Multi-static Scattering of Targets and Rough Interfaces in Ocean Waveguides

by

Jaiyong Lee

B.S., Naval Architecture, Seoul National University, 1991
M.S., Naval Architecture & Ocean Engineering, Seoul National University, 1993

Submitted to the Department of Ocean Engineering
in partial fulfillment of the requirements for the Degree of

Doctor of Philosophy in Acoustics

at the

MASSACHUSETTS INSTITUTE OF TECHNOLOGY

February 1999

Author .....
Department of Ocean Engineering
December 2, 1998

Certified by .....
Professor Henrik Schmidt
Department of Ocean Engineering
Thesis Supervisor

Accepted by .....
Professor J. Kim Vandiver
Chairman, Department Committee on Graduate Students

Multi-static Scattering of Targets and Rough Interfaces in Ocean Waveguides

by
Jaiyong Lee

Submitted to the Department of Ocean Engineering
on December 2, 1998 in partial fulfillment of the
requirements for the Degree of
Doctor of Philosophy in Acoustics

Abstract

The diffusive nature of shallow water environment limits the fidelity of high performance target sonar systems. The multi-layered ocean waveguide increases the reverberation and the stochastic nature of interface inhomogeneities distorts the target signal. In order to improve the performance in such an environment, an accurate description and a better understanding of background reverberant field are essential. As a theoretical approach, two numerical models have been developed in a consistent framework to simulate multi-static scattered fields produced by rough interfaces and targets in ocean waveguides.

The first model describes a scattered field generated by interface roughness in a multi-layered medium. The strong interaction between seismo-acoustic waves and rough interfaces causes a significant amount of surface reverberation. A perturbational approach has been developed for the rough interface scattering. It was combined with 3-D OASES – a seismo-acoustic wave propagation model for a horizontally stratified medium, in order to express multi-layered media efficiently. The model is capable of producing random realizations and spatial statistics of scattered fields in a 3-D space with arbitrary horizontal stratification. Its deterministic scattering formulation for random roughness enables the use of a wide range of roughness types as well as experimental roughness data directly.

The second model describes deterministic target scattering. It is based on the plane wave scattering functions of various targets in a free space and the single scattering approximation. As the target models, a rigid sphere, a pressure-release sphere, and a finite cylindrical elastic shell have been used. A scattering theory of finite cylindrical elastic shells has been chosen to investigate the 3-D effects caused by an aspect-dependent object. The plane wave scattering functions are incorporated with 3-D OASES to produce a unified target scattering model within multi-layered media. Compared to the discretization models using full wave theories, the target scattering model developed in this thesis provides a fast way to understand the physics of target scattering in multi-layered media without the heavy computational burden of the discretization models.

Finally, the rough interface and target scattering models are combined to build a numerical simulator. The numerical simulator is capable of simulating multi-static scattered fields produced by a target in a reverberant background. In order to investigate the feasibility of using a multi-static system, a numerical experiment is performed by using the numerical simulator and the scenario of the GOATS '98 experiment. The numerical simulator provides a realistic forward modeling to aid in understanding the physics of seismo-acoustic scattering in multi-layered media.

Thesis Supervisor: Henrik Schmidt
Title: Professor, Department of Ocean Engineering

To My Wife, Crystal,
&
My Son, Justin.

This page is blank.

Contents

This page is blank.

List of Figures

This page is blank.

List of Tables

This page is blank.

Chapter 1

Introduction

Sonars are important tools for detecting and classifying targets (objects) in the ocean. The real oceanic environment includes several layers of penetrable bottom structure and the air-ocean interface. The interfaces of the bottom layers have roughness which varies from region to region in a statistical sense. These layers may contain volume inhomogeneities such as temporal density fluctuation (e.g. internal waves), cavities, bubbles, cracks, and bio-creatures. These inhomogeneities cause reverberation which may hamper sonar operation. Therefore, the identification of reverberation mechanisms is a critical factor in regard to sonar performance. However, it may be impossible to develop an acoustical theory or model that can embody all the complexities. Therefore, it is necessary to eliminate insignificant effects and concentrate on the acoustically dominant inhomogeneities for the development of theory and numerical model.

In this thesis, scattering caused by rough interface and its reverberation are considered. While ambient noises are independent of the acoustic source field, the rough interface scattering is driven by the source field. For example, noise generated by surface wave breaking and ships passing near-by remains constant within temporal window of sonar operation while the rough interface reverberation varies with incident acoustic field. In addition to the rough interface scattering, a scattering model for various targets in waveguides is developed in this thesis. Since the target and the reverberation features are located in a waveguide, it is essential to incorporate waveguide effects into the scattering models.

1.1 Description of Problem

In this thesis, theories and numerical models are developed for the realistic simulation of multi-static bottom target sonar systems such as shown in Figure 1-1. A multi-static target sonar system can consist of a single source array and multiple receiver arrays around a target. For example, arrays can be moored at a fixed position, carried by AUV[1]s, or towed by ships. The main advantage of using a multi-static system instead of a monostatic system is that with multiple receiver arrays, the actual aperture of the sonar is increased in the spatial domain potentially achieving improved resolution without increasing the source frequency. The wide coverage of the spatial field provides the detail description of environment as well as of target. With multiple receiver arrays, it may be possible to take a snapshot of the field and find scattering features which may not be resolved by a monostatic system.

[1] Autonomous Underwater Vehicle

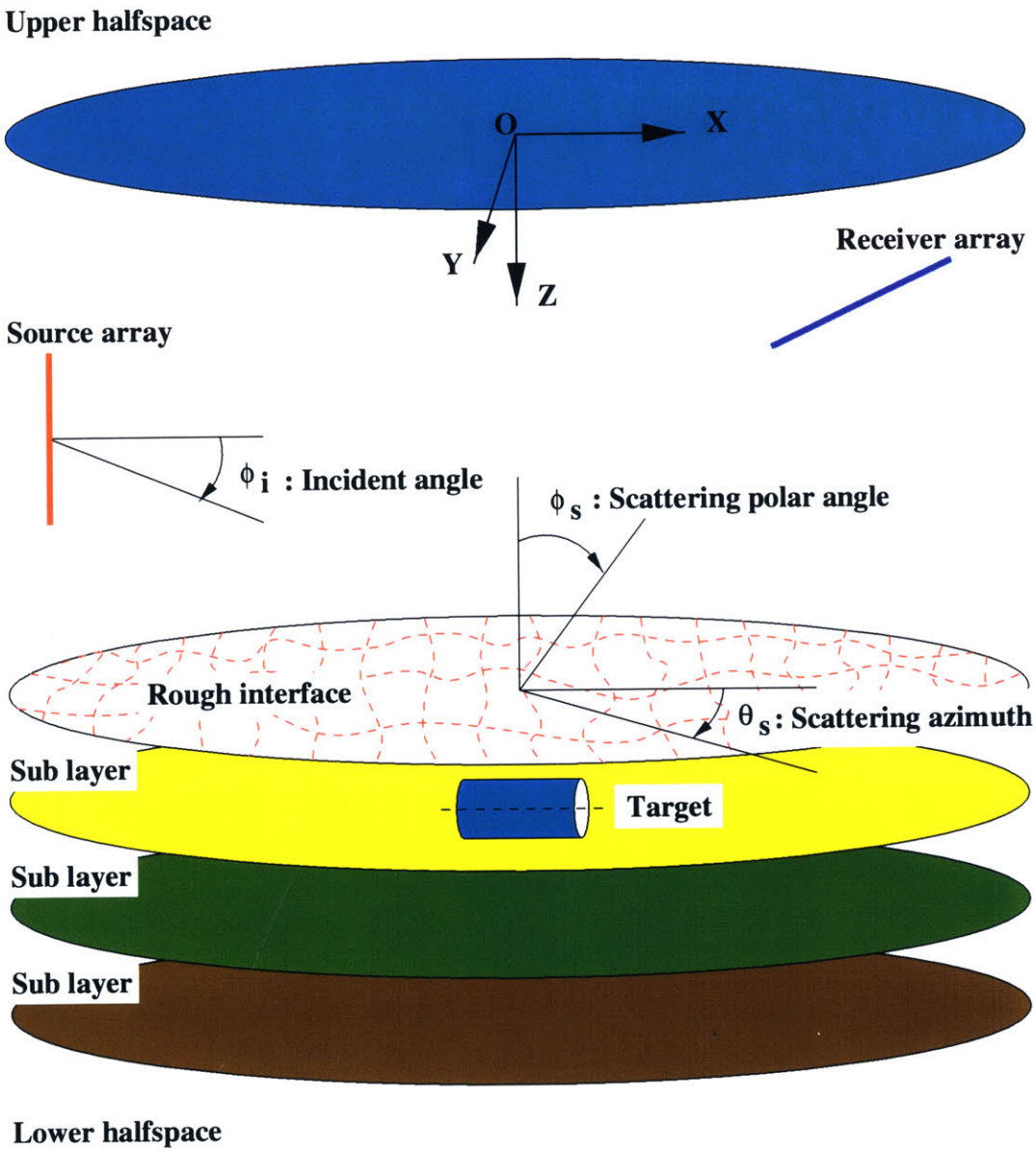

Figure 1-1: Scenario of a multi-static bottom target sonar system.

For a multi-static configuration of a bottom target sonar system, there are two dominant mechanisms of scattering – target scattering and seabed roughness reverberation. The target under consideration such as mines are often buried or partially buried in the bottom structure. Therefore, the penetration of the incident field into the bottom is essential in order to insonify a target. Depending on the incident field (angle and frequency) and the bottom layering, the target is excited in different ways. For example, a lower frequency source may increase the bottom penetration capability at a shallow incident grazing angle. Since the sonar system is looking for a target near or in the bottom, seabed roughness generates an 'undesirable' scattered field – the reverberation. If a bottom target sonar system is operated in a shallow water environment, the existence of the waveguide also affects the target scattering and the seabed roughness reverberation by generating a multi-path signal structure. Therefore, the theories and models must be capable of representing both the target scattering and the rough interface reverberation, and the waveguide physics.

1.2 Objective

The main goal of this thesis is to develop numerical models for the target scattering and the rough interface scattering in a multi-layered waveguide. The numerical models provide tools to understanding the physics of scattering in multi-layered ocean waveguides. Compared to traditional monostatic scattering theories and models, the multi-static scattering is more challenging in modeling and understanding because of its inherent 3-D nature. Therefore, the development of multi-static scattering theories and numerical models becomes an important part of the objective of this thesis. Because model verification is important, several numerical benchmarks are performed as part of the development of numerical models.

With the verified numerical models, a numerical simulator is built for multi-static scattering scenarios in ocean waveguides. The numerical simulator consists of three numerical models – REVERB, TARGET, and OASES. Figure 1-2 shows an overview of the numerical simulator as a block diagram. Each numerical model (module) is based on different acoustical theories. REVERB and TARGET represent the scattering components generated by the interface roughness and the target, respectively. OASES is a numerical model for seismo-acoustic wave propagation in horizontally stratified media [42, 44]. Even though these modules are different in theoretical background, the REVERB and TARGET models can be integrated into OASES by using the spectral representation of the scattering contributions. By utilizing the numerical simulator, an understanding of the scattering physics can be achieved and the controlling physical parameters can be identified. The correlations between the physical parameters and the scattered field can be studied through a controlled numerical experiment using the simulator. Feedback from actual experiments can provide feedback for theoretical and modeling improvement. Figure 1-3 shows how the numerical simulator and experiment can be connected to help physical understanding. The study of physical parameters and their physical interpretation are at the core of this thesis along with the development of numerical models.

1.3 Theoretical Approach

The theoretical approach is based on existing acoustical theories. Because the approach relies on three different theories, it is crucial to combine them seamlessly in a consistent model. A new way of representing scattering components in horizontally stratified waveguides is introduced for the creation of an efficient and consistent numerical model.

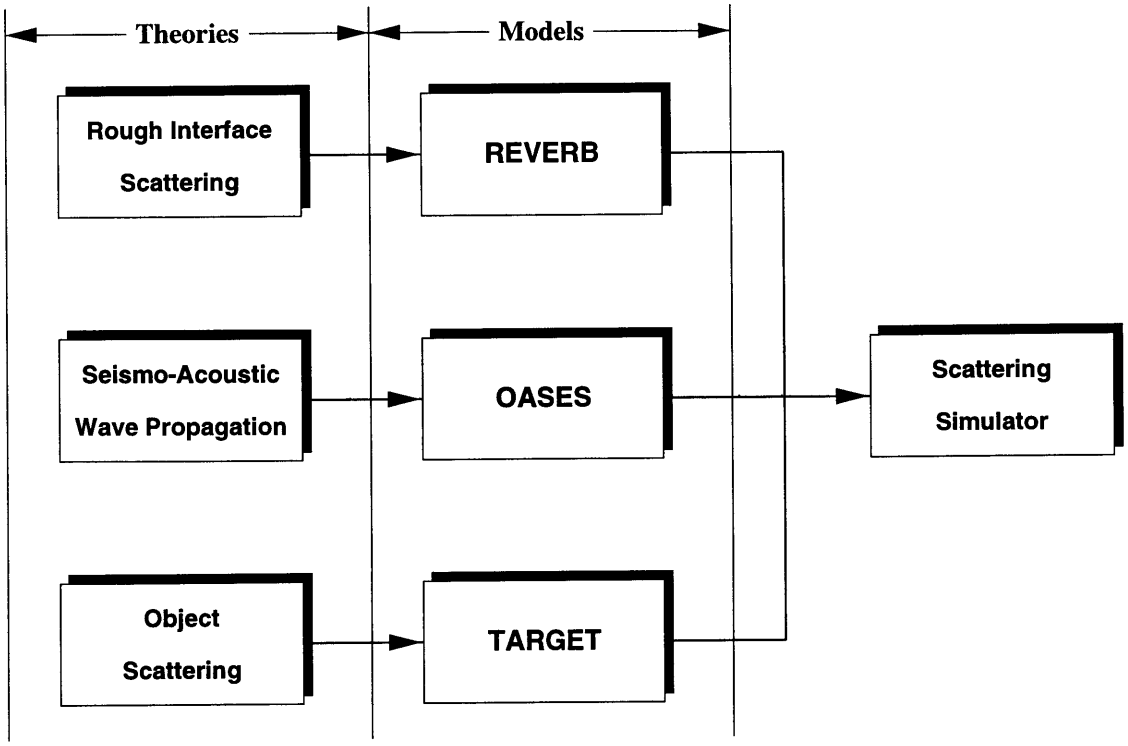

Figure 1-2: Diagram of a numerical multi-static scattering simulator.

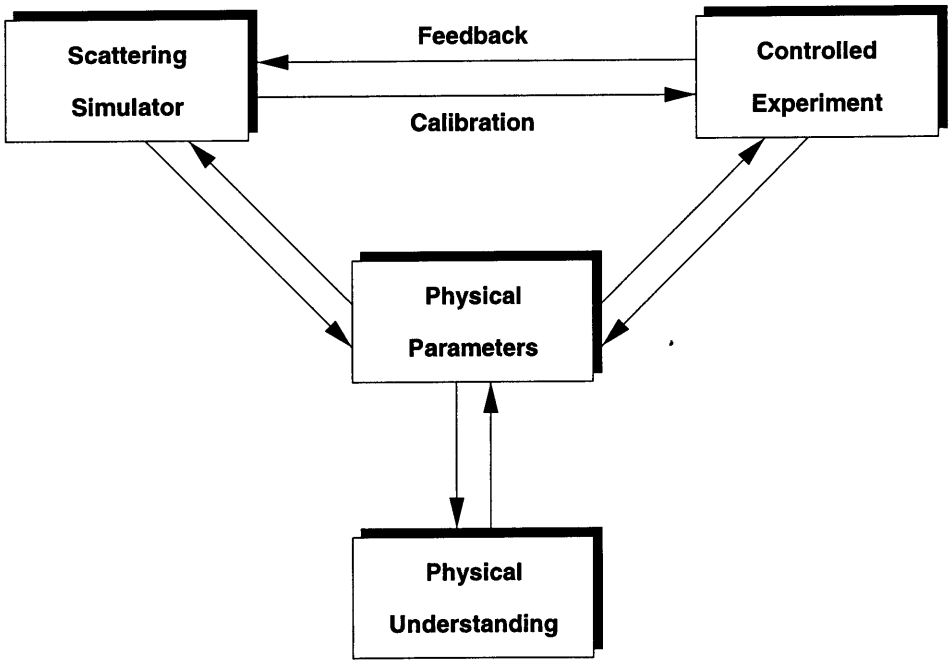

Figure 1-3: Big picture of physical understanding through modeling and experiment.

The selection of each numerical model is based on the requirements of a typical bottom target sonar system. A multi-layered environment is modeled as a horizontally stratified medium. The assumption of horizontal stratification enables an efficient field evaluation using a wavenumber integration method. The numerical technique is based on SAFARI / OASES [42, 44], which solves for the propagation of seismo-acoustic waves in a horizontally stratified medium with 2-D and 3-D receiver configurations. The arbitrary choice of layering structure is a main advantage of using the OASES model.

For the rough interface scattering part, the method of small perturbation (MSP) is chosen. Compared to other interface scattering theories, the MSP can be generalized for vector wave scattering with general boundary conditions (i.e. penetrable boundaries) [36]. The MSP for rough interface scattering has been modified and combined with the 3-D OASES for efficient computation of scattering in horizontally stratified media. Due to the inherently random nature of oceanic interfaces, the scattered fields generated by randomly rough interfaces exhibit stochastic behavior. The MSP formulation used here handles the roughness as a deterministic phenomenon. However, because the numerical model is extremely efficient, the statistical properties of scattered fields are obtainable using 'Monte-Carlo' style simulations.

For the target scattering model of this thesis, the single scattering approximation is utilized with plane-wave scattering functions [21]. The target model is combined with the 3-D OASES code to express a field scattered by a target in a horizontally stratified medium. A rigid sphere, a pressure-release sphere, a finite cylindrical elastic shell are used as targets. For a finite cylindrical elastic shell, Rumerman's scattering model is utilized [41], which is especially useful to investigate the 3-D scattering effects caused by aspect-dependent targets. With the beampatterns of targets in multi-layered media, the equivalent scattering source functions are computed. The corresponding scattered fields are obtained efficiently by the 3-D OASES code. This numerical implementation is similar to that of the rough interface scattering model. Even though the single scattering approximation used in the target scattering model ignores the multiple scattering between the target and the boundaries, the target model does account for the effects of a multi-layered medium (i.e. waveguide effects). The reflection and transmission of scattered energy through interfaces are allowed because the target scattering model uses the Green's function of a multi-layered medium.

1.4 Thesis Organization

This thesis consists of five chapters and six appendices. This chapter includes the description of the problem, the objective of thesis, the theoretical approaches, the thesis organization, and the contributions of thesis.

In Chapter 2, the rough interface scattering theory of this thesis is described along with the background of other rough surface scattering theories. The mathematical formulation is derived along with its theoretical limitations. The numerical model is merged with the wavenumber integration techniques – 2-D / 3-D OASES [44, 46], to allow the computation of the rough interface scattering in multi-layered media. Since the rough interface scattering is closely related to the statistical properties of the rough surfaces, a section is devoted to the statistical properties of various roughness types and the syntheses of roughness. A benchmark case is presented to verify the rough interface scattering model. Various numerical simulations and their physical interpretations are presented to investigate the effects of medium properties, roughness properties, and waveguide on the rough interface scattering.

In Chapter 3, the target scattering model is presented. Using exact and approximate representations for target scattering in free space, the scattering contribution is expressed as a point

source with an effective beampattern in a waveguide. Beampatterns of two axisymmetric targets and one 'aspect-dependent' target are derived and utilized for the numerical implementation of the target scattering model. The model is incorporated into a 3-D wavenumber integration method (3-D OASES), which extends the target scattering model to multi-layered media. The model verification is done by reproducing scattered fields in a free space generated by a rigid sphere, a pressure-release sphere, and a finite cylindrical elastic shell. Effects of medium properties, layering configuration, and target properties are studied through a series of numerical examples. Time domain solutions for target scattering are also performed to illustrate the physics of target scattering in the time domain.

In Chapter 4, the concept and components of the 'numerical simulator' is addressed. To demonstrate the usability of the numerical simulator, numerical experiments are designed and conducted according to an actual multi-static scattering experiment. The results of time domain solutions are analyzed with an array signal processing technique.

In Chapter 5, the summary and conclusion of the thesis are presented. Future work is suggested such as extending current models to include other types of scattering mechanisms and improving those models by analyzing 3-D scattered field data collected from the GOATS '98 experiment[2].

Appendix A reviews the 3-D DGM (Direct Global Matrix) formulation – the wavenumber integration technique of 3-D OASES [46].

In Appendix B, the rough interface scattering formulation is derived in the spatial domain utilizing the method of small perturbation. The contribution of rough interface scattering is expressed as a distributed source function, which is called 'roughness virtual source'.

Appendix C describes the transformation technique used to compute the spectral domain response of the rough interface scattering virtual source. The transformation technique was introduced in Reference [10]. Errors in the original formulation were identified and corrected in this thesis.

In Appendix D, the plane wave scattering function of a finite cylindrical elastic shell by Rumerman is described in detail [41] and its analytic continuation is implemented for evanescent incident and scattered waves.

Appendix E presents the scattering functions of fluid-loaded and void spherical elastic shells. These scattering functions are expected to be included as target models in the future.

In Appendix F, the user's manual for the computational package 'SCATT', which has been developed for this thesis, is included. The manual explains the installation of the package and the usage of the programs included in the package.

1.5 Contributions

Kuperman and Schmidt combined a perturbation approach for rough interface scattering with a wavenumber integration method to model rough interface scattering in multi-layered media [27]. A numerical implementation was performed for a 1-D rough interface. LePage introduced the spatial domain perturbation formulation of rough interface scattering [29]. He introduced a virtual source distribution to express a scattering contribution in terms of source distribution. LePage and Schmidt extended the 2-D roughness formulation to compute the mean reflection coefficients of a rough ice sheet incorporating the effects of scattering into ice plate modes [30]. The reflection coefficient was expressed as a convolution integral of the roughness spectrum, the incident wave vector, and the receiver wave vector. Fan [10] utilized the spatial domain formulation by

[2] Generic Oceanographic Array Technology Sonar

LePage. He introduced a transformation of the virtual source distribution from Cartesian coordinates to cylindrical coordinates in the wavenumber domain. In his numerical implementation, a 2-D roughness patch was used to represent a 2-D rough interface between the water and an elastic seabed. 3-D OASES, the numerical model developed by Schmidt and Glattetre [46], was integrated in order to add the effects of waveguide propagation.

Here, the spatial domain formulation is extended to handle the scattering caused by a rough interface between two elastic media allowing modeling of sub-bottom interface scattering. The numerical model is validated using a benchmark case for which analytical solutions are available. The efficiency and accuracy of the numerical model are improved by introducing the 2-D fast Fourier integral (2-D FFI), which is used to transform the scattering expression from the spatial domain to the wavenumber domain (Section C.2). Also, time domain simulation of 2-D roughness patch scattering is enabled by the improved efficiency. In order to investigate the 3-D nature of rough interface scattering, various numerical simulations are performed in this thesis. Surface models with Gaussian power spectra, Goff-Jordan power spectra (power-law), and ripple spectra are studied. Effects of geometric parameters of rough interfaces on the scattered field such as correlation length, fractal dimension, and anisotropic angle are thoroughly investigated. In addition to the roughness itself, the effects of medium properties, layering configuration, and waveguide effects are extensively studied. Time domain analyses are also done to investigate the physics of scattering in the time domain. The results of analyses of rough interface scattering are summarized in the conclusion (Section 5.2).

In addition to the contributions to the numerical model for 2-D rough interface scattering, a model of target scattering in a multi-layered environment is extended in this thesis. The target scattering model developed here combines the single scattering approximation with a 3-D wavenumber integration method. Analytic continuation [2] is utilized to allow the evanescent incidence and scattering, which are important to model scattering from a buried target with an evanescent insonification. The target models include scattering by a rigid sphere, a pressure-release sphere, and a finite cylindrical elastic shell. The solution for the finite cylindrical elastic shell is adopted from the previous theoretical work done by Rumerman [41]. The target scattering theory by Rumerman was later reviewed and numerically implemented by Ricks [40]. In this thesis, Rumerman's target model is adopted to multi-layered media and expanded to include evanescent wave fields. The implementation of the finite cylindrical elastic shell has significance in the target scattering model because Rumerman's model allows the interaction between the shear and compressional scattered waves in the target as well as the aspect dependence of target. Here, the target scattering model is developed in the spectral domain and the numerical implementation is done in a consistent framework to be incorporated into the wavenumber integration method – 3-D OASES [46]. The numerical model is developed to perform wideband simulation efficiently. The target models are validated in several benchmark cases in this thesis. In order to investigate the effects of various parameters involved in target scattering, various numerical simulations are conducted. The effects of target properties on the scattering are studied. Also, the effects of medium configuration on target scattering such as the existence of a waveguide, thickness of sublayers, and burial depths of the target are investigated. In addition to the investigation of time harmonic cases, time domain simulations of target scattering are conducted to investigate 3-D effects of scattered fields generated by finite cylindrical elastic shells. The summary of the target scattering results is presented in the conclusion part (Section 5.2).

In addition to developing the numerical models for rough interface and target scattering, a new numerical simulator is developed to simulate realistic multi-static sonar systems. The numerical simulator is intended to investigate the feasibility of using multi-static systems to identify targets in reverberant backgrounds. The simulator includes the rough interface and target scattering mod-

els. Since both numerical models are developed together in a consistent framework, the numerical simulator handles general 3-D target and seabed scattering scenarios in multi-layered configurations. It also includes post-processing modules to analyze synthesized scattering data. A series of numerical experiments are carried out to simulate the GOATS '98 experiment [45, 50]. The numerical simulator can be used to analyze a wide range of experimental data and to design a future multi-static experiment. This simulator has been used to investigate the 3-D physics associated with scattering from target buried below a rippled seabed (e.g. demonstrating the strong aspect dependence of the ripple-induced reverberation) [49].

Chapter 2

Rough Interface Scattering Model

The roughness characteristics of the seabed greatly affect how the scattered energy is distributed in space and time. Besides the properties of the roughness, the most significant scattering effects are determined by the medium properties of the stratification, in particular the layers separated by the rough interface.

For many seismo-acoustic problems, the environment is conveniently represented by a range-dependent, or horizontally stratified sequence of layers, separated by plane interfaces. A homogeneous fluid layer allows only compressional wave (P) while a homogeneous elastic layer allows two polarized shear waves (SH and SV) along with the compressional wave. A homogeneous poro-elastic layer, in addition to the three wave types allowed in a homogeneous elastic layer, supports another type of wave – a slow compressional wave (slow P) [4]. When two or more types of waves exist, they are often called a 'vector waves' because they are conveniently expressed mathematically as a vector quantity [36]. The different types of waves are coupled through interaction with interfaces. Depending on its complexity, the numerical model handles some or all of those coupling mechanisms (e.g. OASES [44]). Another coupling mechanism is provided by rough interfaces. As for seismo-acoustic wave propagation, various types are involved in rough interface scattering theories. For example, the scattered field produced by a compressional incident wave on a rough interface between two homogeneous elastic layers may produce P, SH, and SV scattered waves.

In this chapter, a scattering theory will be numerically implemented by considering two important aspects of a waveguide – medium properties and layering configuration. The theory will be capable of describing the field scattered by a rough interface anywhere in the stratification. The numerical model will utilize 3-D OASES – a seismo-acoustic wave propagation model for a 3-D horizontally stratified waveguide [46] – and compute the scattered fields involving P, SH, and SV waves. Scattering of slow P waves is excluded because the poro-elastic layer model has not been implemented for 3-D OASES. Implementation of the slow P wave scattering will be regarded as a possible future work when the poro-elastic layer model is implemented for 3-D OASES.

2.1 Theory

Theories for interface or surface scattering of acoustic waves, electro-magnetic waves and elastic waves, and their numerical implementation have long and abundant background. The following subsections address several well-known scattering models.

2.1.1 Interface Scattering Models

Several commonly used interface scattering models will be mentioned in this section. Each model will be briefly described in terms of its theory, advantages, shortcomings, and applicability.

Kirchoff Approximation

The Kirchoff approximation is the most widely used theory for wave scattering. Its formulation is based on the Helmholtz integral equation and it approximates the scattering surface as if it were part of an infinite plane parallel to the local slope. For this reason, it is often called the 'tangent plane method'. This simplification leads to a simple expression of the integral equation to approximate the scattered field. The wide usage of the Kirchoff approximation is due to its understandable physics. Since the Kirchoff approximation originated from the study of light diffraction through an aperture, an intuitive relationship exists between physics and formulation. Like the solutions by many other physically intuitive approximations, the accuracy of the solution obtained by the Kirchoff approximation is not easily quantifiable.

As previously mentioned, the approximation on the scattering surface imposes the limits of Kirchoff approximation. Since the surface is treated as a part of an infinite plane, the Kirchoff approximation gives the exact solution for an infinite plane surface, but the approximation starts to break down for finite, non-planar, and rough surfaces. Therefore, the Kirchoff approximation is expected to give a good approximation for a surface with slowly changing gradients. Even though there is no specific restriction on the height or slope of surface, a general rule for the validity of the Kirchoff approximation in the scalar wave scattering case [3] is :

$$k_1 a \sin^3 \theta_1 \gg 1, \tag{2.1}$$

where k_1 is the medium wavenumber, a is the local curvature of the surface and θ_1 is the grazing angle of the incident wave. Thus, the restriction (2.1) is imposed on the relative local curvatures $k_1 a$ and on the grazing angle θ of the incident wave. The requirement on the grazing angle implies that the approximation is best for incident waves close to the normal direction of surface. For the case of a penetrable interface, the restriction becomes more severe. Since the condition (2.1) also applies to the transmitted field, the angle of validity becomes narrower. When the incident grazing angle corresponds to the critical angle of two media, the grazing angle of the transmitted wave becomes zero, which clearly violates the condition (2.1). By considering the transmitted wave in the lower medium, the above limit can be modified as :

$$k_1 a \sin^2 \theta_1 \sin\left(\frac{k_1}{k_2}\theta_1\right) \gg 1, \tag{2.2}$$

where k_2 is the medium wavenumber of the transmitted field. When the phase speed of the transmitted field becomes large compared to that of the incident medium, the above restriction becomes more stringent on the angle of the incident wave.

Even though the implementation of Kirchoff approximation for vector wave scattering (e.g. elastic wave scattering) is possible with mathematical formulations of significant complexity, the actual implementation is not widely realized. Consequently, the Kirchoff approximation is not appropriate for scattering in a general waveguide.

Perturbation Method

The perturbation method, which allows for solutions of a weak disturbance to be approximated based on solutions without any disturbance, has been widely used. The solution form and the corresponding boundary conditions are expanded in the order of perturbation parameters. Then, by collecting the same orders from the governing equation, a set of equations is obtained in either explicit or implicit form.

For a rough interface scattering problem, the formulation is rather straightforward. The assumption of small disturbances is associated with the restrictions on the surface height function $h(x, y)$.

$$k|h(x,y)| \ll 1, \qquad |\nabla h(x,y)| \ll 1, \tag{2.3}$$

where k is an incident wavenumber. Under these restrictions, the scattered field is expected to be small compared to the unperturbed field, which is the field produced without roughness (or by the mean surface). Consequently, the order of magnitude for perturbed field at most follows the order of the parameter kh, which is often called the 'smallness parameter' or 'relative roughness height'. Thus, the total field can be expressed by the sum of the unperturbed solution and its correcting perturbed terms caused by small roughness.

$$\phi(\vec{x}) = \phi^{inc}(\vec{x}) + \sum_{n=0}^{\infty} \phi_n^{sc}(\vec{x}), \tag{2.4}$$

where the solution ϕ represents any kind of physical quantity to be sought. It can be a scalar potential or vector potential of displacement or velocity. The total solution consists of the incident field ϕ^{inc} and the subsequent n th order scattered field. The zeroth order simply implies the reflected field produced by mean surface. The n th order term represents the scattered field caused by roughness height deviated from the mean surface with the n th order accuracy of kh. In order to complete the system of equations with the perturbation method, the boundary conditions should be expanded in orders of the perturbation parameter. For the unperturbed case, the boundary conditions are imposed on the mean surface. The perturbation method approximates the boundary conditions on the mean surface with considering effects of roughness. In most of the cases, the boundary condition is expanded by the Taylor series with respect to the mean surface. The form of boundary conditions depends on the types of scattering problems. For a scalar wave scattering case, the boundary condition can be expressed by the scalar function $f(x, y, z)$. Then, the function $f(x, y, z)$ on the rough surface is evaluated by the Taylor series with respect to the mean surface h_0.

$$f(x,y,z)\Big|_{z=h(x,y)} = f(x,y,z)\Big|_{z=h_0} + (h-h_0) f_{,z}(x,y,z)\Big|_{z=h_0} + \frac{1}{2}(h-h_0)^2 f_{,zz}(x,y,z)\Big|_{z=h_0} + \ldots . \tag{2.5}$$

By combining the total solution and boundary condition and collecting terms with the same order, a set of equations is obtained. The resulting equation varies by orders and it can have an implicit form. By solving the equations from lower to higher orders, the total solution is approximated.

The most distinctive advantage of perturbation method is that the formulation is very flexible and therefore can be adopted to various scattering problems. It can be easily modified to the vector scattering formulation and its formulation can be obtained in either spectral or spatial domain. For small roughness cases, the perturbation method provides good approximation to the solution in efficient way.

Boss Models

Multiple scattering effects become significant when the gradient of rough surface increases, and when the incident and scattering angles deviate from the normal direction of the surface. There are several scattering models allowing multiple scattering mechanism in partial or complete sense. As a practical approximation to the multiple scattering theory, boss models have been developed.

Fundamentally, boss models represent surface scattered field with distributed 'bosses' or protuberances. The individual scattering behavior of each boss is assumed to be well known. The bosses are randomly distributed on otherwise even surface with specified statistics to model a random surface. Most real rough surfaces do not share similarity with the surface of the distributed bosses (embossed surface). Despite this fact, the scattered field by the embossed surface often reproduces the key features of rough surface scattering.

There are two different boss models. One of them is based on the 'effective boundary condition' which determines effective boundary condition for the smooth reference plane, on which the bosses are distributed. It computes the monopole and dipole strengths of bosses to express the boundary condition. Multiple scattering mechanism is only allowed among bosses while interaction between boss and the reference plane is ignored. The other approach is called 'Green's function method'. It simply represents the scattered field as sum of individual boss scattering effects. Its treatment of scattering among bosses is based on far field assumption since the individual scattered field of each boss is obtained in far field. One of the distinctive features of the boss models is that it can produce the experimentally observed surface wave on the reference plane by multiple interaction among bosses [36].

The boss models have several shortcomings. Firstly, the extension to vector wave scattering (e.g. elastic wave scattering in seismo-acoustic field) requires great complexity of mathematical formulation for both methods of boss models. For Dirichlet and Neumann boundary conditions, the formulations for boss models are well known. However, as the boundary condition and Green's function of system become complicated, the generalization of boss model become prohibitive. Secondly, the representation of real rough surface by bosses of specific shape gives unclear relationship between the scattered fields produced by real rough surface and embossed surface. Thirdly, boss models' applicabilities are limited to surfaces with reasonable packing distance and small roughness or to surfaces with arbitrary level of roughness and low packing density. The first limitation implies that each boss is a weak scatterer while later one implies that the interaction among adjacent bosses should be small.

Even with these shortcomings, boss models are known to be effective and useful for scatter for near grazing angles of incidence and for the propagation of surface waves associated with multiple scattering.

Small Slope Approximation

Compared to the classical scattering theories such as the Kirchoff approximation and perturbation method, there is a new class of scattering theories which overcomes the various limits imposed by the classical scattering theories. The small slope approximation (SSA) was suggested by Voronovich [58]. It is intended to fill the gap between the Kirchoff approximation and the perturbation method in terms of validity.

The small slope approximation includes the mathematical aspects coming from both the Kirchoff approximation and the small perturbation method. By shifting the origin of coordinates along the rough surface, the restriction on the roughness heights imposed by small perturbation method is removed. The shift of origin is equivalent to using the Kirchoff approximation because

the amount of shifting in the scattering kernel is equal to the scattering kernel of Kirchoff approximation. Then, the scattering expression is expanded in an integral-power series which is similar to the Taylor series. Since the n th order term in the resulting integral-power series is proportional to the n th power of the surface gradient, the integral-power series will converge when the magnitude of the surface gradient is less than one. This integral-power series is called the 'small slope expansion'. The only restriction on the roughness for the small slope approximation is the small surface gradient. Similar to the perturbation approach, the higher order formulation can be derived in the small slope approximation by using the surface gradient as the smallness parameter. In Reference [58], it is demonstrated that the limit of the reflection coefficient by the small slope approximation is equal to the reflection coefficient by the perturbation method when the vertical wavenumber of scattered wave approaches to zero. For large *RMS* height, the deviation between the small slope approximation and the perturbation method increases.

The formulation of the small slope approximation can be expressed by Green's function in spectral domain. However, generalizing 'vector wave scattering' or 'general waveguide case' is difficult due to the complexities involved in implementation of a numerical Green's function to the integral-power series of small slope approximation. The same problem arises when the small slope approximation is applied to mode conversion among different wave types. Even though there are simple benchmark cases proving that the small slope approximation is valid beyond the Kirchoff approximation and the perturbation method, the actual numerical implementation for general problems has not been extensively developed.

2.1.2 Born Approximation

In this thesis, the method of small perturbation (MSP) combined with the Born approximation is used as basis for the rough interface scattering model. The main reasons to choose the method of small perturbation are the followings.

- Flexible formulation to handling full seismo-acoustic wave field.
- Both spatial and spectral domain formulations are readily available for efficient computation and direct interface to seismo-acoustic wave propagation model.
- The mean field is approximated by the unperturbed field using the Born approximation.

Compared to other higher order perturbation methods, the method of small perturbation relies on the first order approximation. Therefore, its perturbation limits are more strict than those of higher order methods. Inherently, the Born approximation violates the conservation of energy due to the assumption that the mean field can be replaced with unperturbed field. Therefore, by using the Born approximation, the total energy of the system is increased. These effects can be shown by comparing with higher order results. The comparison of scattering results between the Born approximation and higher order perturbation method (i.e. self-consistent perturbation approach [28]) was performed recently for rough interface scattering problem in waveguide [48]. In this particular comparison, the mathematical relationship between scattered field and mean field is the same for both methods. But, the mean field computation by self-consistent perturbation approach was done implicitly considering interface roughness statistics. As a result, the mean field produced by 'self-consistent perturbation approach' is lower than the unperturbed field. Consequently, the corresponding scattered field is lower. Therefore, the Born approximation gives the upper limit for the scattered fields produced by self-consistent perturbation approach. Physically, the higher order methods consider the reduction of mean field by scattering while the Born approximation ignores it. Nevertheless, the Born approximation provides the same scattering trends

as that of self-consistent approach. The method of small perturbation combined with the Born approximation, instead of self-consistent perturbation approach, is chosen in this thesis because of extreme mathematical and computational difficulties involved in mean field computation by the self-consistent method.

Previous Developments of Perturbation Methods in Ocean Waveguides

Kuperman and Schmidt developed a perturbation model incorporating rough interface scattering into horizontally stratified elastic waveguide [27]. A wavenumber integration method was utilized to express the horizontal stratification of waveguide. Later, they modified the perturbation model to include the effects of the interface curvature and extended it to a 'self-consistent approach' [28]. Self-consistent approach is an implicit second order perturbation model which can account for the coherent loss of the mean field caused by interface roughness.

Liu, Schmidt and Kuperman utilized the self-consistent perturbation approach to propose the scattering at rough elastic interface as a main cause of deep ocean ambient noise in the infrasonic ($f = 1Hz - 10Hz$) regime [32].

Subsequently, LePage and Schmidt used the self-consistent perturbation approach to model the coherent transmission loss of acoustic wave propagation in the central Arctic [30]. A three dimensional perturbation formulation was used to compute the average reflection coefficients on the rough elastic ice cover. The prediction of transmission loss agreed with historical data and suggested that scattering into the flexural modes of the ice cover is the major loss mechanism for long range propagation in the Arctic environment.

The same approach was also used to demonstrate how reverberation affects the spatial correlation of the acoustic field and the associated degradation in performance of matched field processing approaches [48].

Tracey combined the self-consistent perturbation approach with KRAKEN [38] – A normal mode acoustic propagation model – to develop the normal mode scattering model [54]. A noticeable difference in his approach other than the usage of normal mode method, is that he applied perturbation theory to incorporate the scattering produced by the fluctuation of sound speed and density in acoustic media.

Tracey and Schmidt used the same normal mode scattering model to study the spatial statistics of scattered fields caused by rough interfaces and volume inhomogeneities in ocean waveguides [55].

Boundary Operator Formulation

Since the goal of this thesis is to model the seismo-acoustic scattered field in a horizontally stratified medium, the formulation of wave field should handle the medium stratification in an efficient way. Fundamentally , the scattering formulations in this thesis share a common ground with seismic-acoustic wave propagation models : 2-D / 3-D versions of OASES [42, 44, 47, 46]. Therefore, mathematical formulation for wave propagation model should be addressed prior to the scattering formulations. Since the scope of thesis will cover up to elastic medium, any further complicated media will not be considered. For a homogeneous and isotropic elastic medium, the seismo-acoustic wave field can be expressed in terms of three displacement potentials $\phi(\vec{x})$, $\Lambda(\vec{x})$ and $\psi(\vec{x})$, which represent compressional wave (P), vertically polarized shear wave (SV), and horizontally polarized shear wave (SH) respectively. Here, the wave field is assumed to be time harmonic and has time dependency of $\exp(\iota\omega t)$. For horizontally stratified media, wave field in

each layer can be represented by three displacement potentials :

$$\chi_i(\vec{x}) = \begin{cases} \phi_i(\vec{x}) & \text{P waves} \\ \Lambda_i(\vec{x}) & \text{SV waves} \\ \psi_i(\vec{x}) & \text{SH waves} \end{cases}. \tag{2.6}$$

At each interface, there exists boundary condition stating continuity of displacement and stress field in compact operator form :

$$B_i(\vec{x})\chi_{i;i+1}(\vec{x}) = 0, \qquad i = 1, 2, \ldots, N-1, \tag{2.7}$$

where N is total number of layers and the boundary operator B_i is a matrix form of linear differential operators, which represents the discontinuity of displacement and stresses. The boundary operator B changes according to medium properties of two adjacent layers. For example, between two fluid (acoustical) layers, continuity condition of tangential displacements and stresses vanishes. In order to have non-trivial solution, there must be an external forcing term in the above boundary conditions. Assuming the physical sources are confined to a single depth z_s, the boundary condition can be rewritten as follows :

$$B_i(\vec{x})\chi_{i;i+1}(\vec{x}) = -f_s(\vec{x})\delta(z_i - z_s), \tag{2.8}$$

where $f_s(\vec{x})$ is the distribution function of physical sources. The solution techniques to solve the above equation are well described in References [47, 46]. Its numerical implementation was also done in extremely efficient way. By applying Hankel transform and Fourier series expansion on both sides of above equation, m th order Fourier component becomes :

$$\tilde{B}(k_r)\tilde{\chi}^m(k_r) = -\tilde{f}_s^m(k_r), \tag{2.9}$$

where $\tilde{B}(k_r)$ is a n by n matrix function of horizontal wavenumber k_r. $\tilde{\chi}^m(k_r)$ and $\tilde{f}_s^m(k_r)$ are vectors of n elements. The efficiency of solution technique comes from the fact that $\tilde{B}$ is independent of azimuthal Fourier order m. For each horizontal wavenumber k_r, only one inversion of matrix $\tilde{B}$ is enough to solve $\tilde{\chi}^m$. After obtaining $\tilde{\chi}^m$, transform to spatial domain is done by inverse Fourier expansion and inverse Hankel transform, which are done by the wavenumber integration technique. Number of azimuthal Fourier orders depends on properties of forcing term $f_s(\vec{x})$. As its azimuthal (angular) variation becomes rapid, more azimuthal orders are required.

The whole concept of computing scattered fields based on the above technique is simple and straightforward. Since the seismo-acoustic wave fields can be solved efficiently by the wavenumber integration technique, the scattered field can be obtained in the same fashion by computing the equivalent distribution function for each scattering components. Therefore, solving seismo-acoustic scattered fields in horizontally stratified medium becomes simply evaluation of equivalent distribution function, which is called 'virtual sources' with contrast to 'physical' or 'real sources'.

$$B_i(\vec{x})\chi_{i;i+1}(\vec{x}) = -f_v(\vec{x})\delta(z_i - z_v), \tag{2.10}$$

where $f_v(\vec{x})$ is the virtual source distribution function and z_v is the projected depth of scatterer.

Scattering Virtual Source

Based on the boundary operator formulation, the scattering forcing term (virtual source) is derived from the boundary operator form for stratified elastic waveguides. Previously, the formulation was developed in References [28, 29] and subsequently, it was further extended to the spatial domain formulation to represent the scattering contributions from the roughness patches in the stratified elastic waveguides [10].

The starting point of the perturbation formulation is the definition of coordinate transform. In order to match boundary conditions on the rough interface, the physical quantities involved in boundary conditions are expressed in the new coordinate system as shown in Figure 2-1. This coordinate transform is caused by the rotation of the surface with respect to the reference surface. Since the displacement and traction vectors are physical variables to be matched on the interface, coordinate transform of these variables are necessary. In Reference [17], the coordinate transform of displacement d and traction τ is defined by the following tensor notation.

$$d_i' = \Psi_{ij} d_j, \qquad \tau_i' = \sigma_{i3}' = \Psi_{ij} \sigma_{jk} \Psi_{3k}, \tag{2.11}$$

where Ψ is a coordinate transformation tensor and the subscript i is the coordinate index ($x = 1$, $y = 1$, $z = 3$). For a 3-D rectangular coordinate system, the rotational tensor Ψ is expressed in the following matrix form :

$$\Psi = \begin{bmatrix} \cos\theta_x & 0 & \sin\theta_x \\ 0 & \cos\theta_x & \sin\theta_y \\ -\sin\theta_x & -\sin\theta_y & \cos\theta_x \cos\theta_y \end{bmatrix}, \tag{2.12}$$

where the angles of rotation are related to the roughness height function $\gamma(\vec{x})$:

$$\theta_x = \arctan\left(\frac{\partial\gamma}{\partial x}\right), \quad \theta_y = \arctan\left(\frac{\partial\gamma}{\partial y}\right). \tag{2.13}$$

In Appendix B, the detail of the coordinate rotation is fully described. Due to the small slope assumption of the first order perturbation theory as (2.3), the rotation of coordinate system becomes a linear transform with a roughness slope vector $\nabla\gamma$. The displacement vector, stress tensors, and related variables in the original and rotated coordinate systems are defined as follows :

w	: normal displacement in $x-y$ plane,
$\vec{u}$	: tangential displacement vector in $x-y$ plane,
n	: normal stress in $x-y$ plane ($=\sigma_{zz}$),
$\vec{t}$	: tangential stress vector in $x-y$ plane,
W	: normal displacement in rotated plane,
$\vec{U}$	: tangential displacement vector in rotated plane,
N	: normal stress in rotated plane,
$\vec{T}$	: tangential stress vector in rotated plane,
σ_{xx}	: normal stress in $y-z$ plane,
σ_{yy}	: normal stress in $z-x$ plane,
σ_{xy}	: tangential stress of x direction in $z-x$ plane.

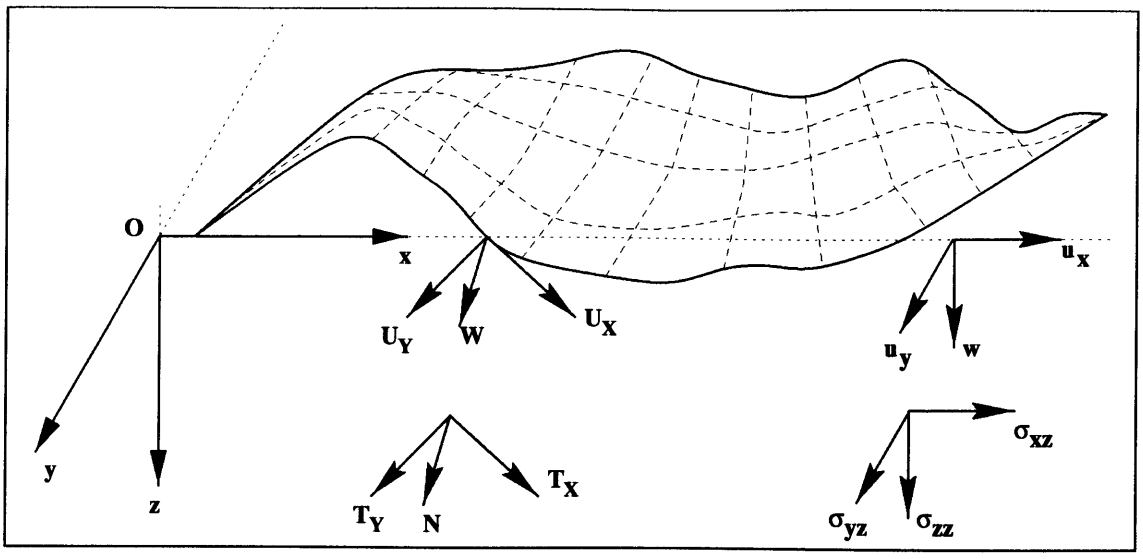

Figure 2-1: Rotation of the coordinate system caused by roughness : $[u_x, u_y, w, \sigma_{xz}, \sigma_{yz}, \sigma_{zz}]^T$ is matched on the interface in the original coordinate system while $[U_x, U_y, W, T_x, T_y, N]^T$ is matched locally on the rough interface in the rotated coordinate system.

Then, the relations among the above variables become :

$$\begin{aligned} W &= w - \vec{u}\cdot\nabla\gamma, \\ \vec{U} &= \vec{u} + w\nabla\gamma, \\ N &= n - 2\vec{t}\cdot\nabla\gamma, \\ \vec{T} &= \vec{t} + \begin{pmatrix} \sigma_{zz}-\sigma_{xx} & -\sigma_{xy} \\ -\sigma_{xy} & \sigma_{zz}-\sigma_{yy} \end{pmatrix}\nabla\gamma, \end{aligned} \tag{2.14}$$

which are satisfied up to the first order of local roughness slopes.

Consequently, B^*, the boundary operator in the rotated coordinate system, has a similar form as that of the displacement and traction vectors :

$$B^* = B + \nabla\gamma \circ b, \tag{2.15}$$

where $\circ$ is a linear operator defined in Reference [28]. Again, this new boundary operator can be expanded by the Taylor series so that it can be applied on the mean surface level $z = z_v$. The Taylor expansion is also based on the assumption of small perturbation (2.3) :

$$B^*\big|_{z=z_v+\gamma} = \left(1+\gamma\frac{\partial}{\partial z}\right)B^*\Big|_{z=z_v} + O(\gamma^2). \tag{2.16}$$

From the above two equations, the first order boundary operator on the mean surface $z = z_v$ is obtained as follows :

$$B^*\big|_{z=z_v+\gamma} = \left[\left(1+\gamma\frac{\partial}{\partial z}\right)(B+\nabla\gamma\circ b)\right]\Big|_{z=z_v} + O(\gamma^2) = \left(B+\gamma\frac{\partial B}{\partial z}+\nabla\gamma\circ b\right)\Big|_{z=z_v} + O(\gamma^2), \tag{2.17}$$

where the higher order terms of the roughness slope and height (i.e. the cross and high power

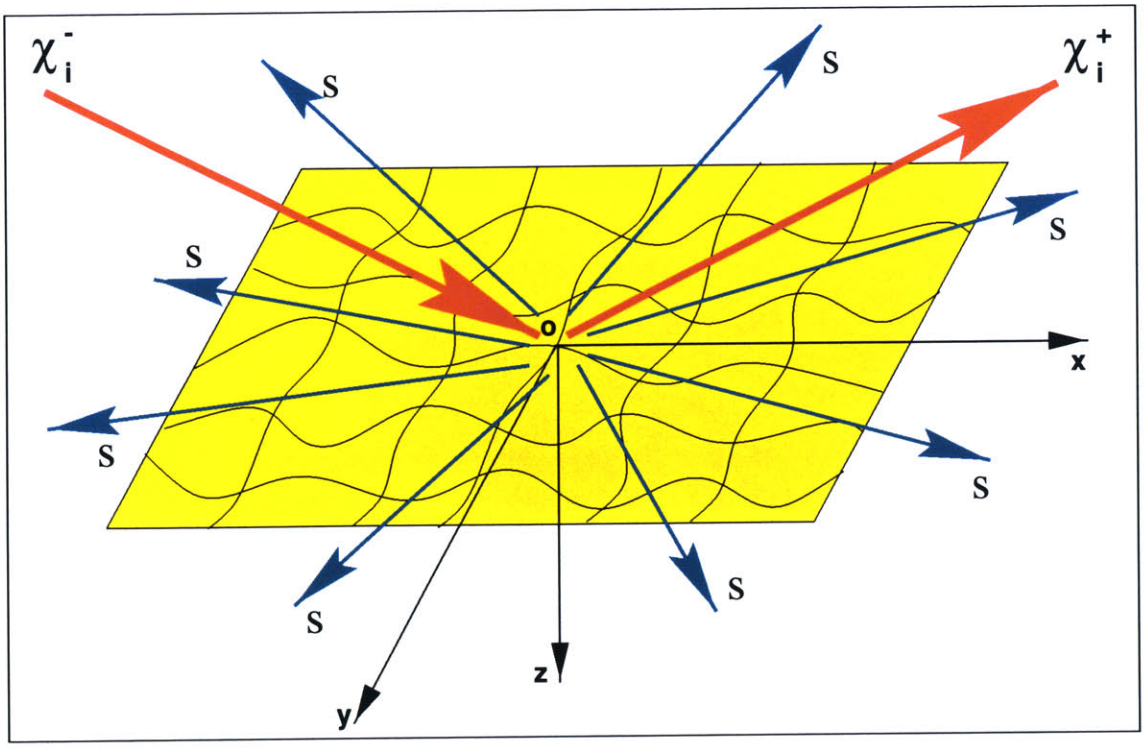

Figure 2-2: Illustration of mean and scattered fields.

terms) are eliminated. The above boundary operator means that the vertical projections of the rotated physical variables to the reference surface are matched to the approximate boundary conditions on the rotated plane. As long as the limits of small perturbation (2.3) are valid, the above linearized boundary operator is adequate. The total solution χ is defined as the sum of the mean field $\langle\chi\rangle$ and the scattered field s represented as follows :

$$\chi_i = \langle\chi_i\rangle + s_i. \tag{2.18}$$

By the assumption that the mean field can be replaced by its unperturbed field for small disturbance and by the fact that the unperturbed solution satisfies the equation of the unperturbed system (2.8), the corresponding scattered field takes the following form :

$$B_i(\vec{x})\, s_{i;i+1}(\vec{x}) = -f_v(\vec{x})\,\delta(z_i - z_v), \tag{2.19}$$

where $f_v(\vec{x})$ is a linear function of the boundary operators, the roughness height function, and the unperturbed field.

$$f_v(\vec{x}) = \left[\gamma\frac{\partial B_i(\vec{x})}{\partial z} + \nabla\gamma \circ b_i(\vec{x})\right]\langle\chi_{i;i+1}(\vec{x})\rangle\Big|_{z=z_v}. \tag{2.20}$$

The subscript v denotes the 'virtual source' because it represents the scattering contribution in the form of a physical source. The virtual source in the spatial domain is derived as a linear matrix form described in Appendix B. The form of the matrix is the combination of linear matrix operators, roughness height and slope matrices, and unperturbed displacement potential vectors. Since the solution of scattering formulation is obtained by the wavenumber integration technique of 3-D

OASES, the forcing term $f_v(\vec{x})$ should be transformed into the wavenumber domain by the numerical Hankel transformation. The form of the virtual forcing term (2.20) implies that the scattering contribution is the multiplication between the roughness profile function and the unperturbed field. Physically, it means that the scattering contribution from the rough interface is concentrated on the surface where the incident energy is focused. In other words, the major scattering events occur on the surface which the incident wave insonifies. Therefore, the computation of the virtual forcing term should be performed on the surface where the insonification is concentrated. There are several situations where the insonification of acoustic wave is confined to a small area which is called 'sonar footprint'. For a high performance sonar system, its source array is capable of focusing acoustic energy on a small area. Also, for a multi-static bottom sonar system, the source and receiver arrays have their own beampatterns which overlap on a small area of the bottom interface. Figure 2-3 shows an illustration of a sonar footprint produced by beampatterns of a multi-static system.

By only considering the insonified portion of the rough interface (i.e. sonar footprint), the rough interface can be modeled as a rough patches of the finite dimension. The outlines of the sonar footprints can be represented by either a square or rectangular shape. The main advantages of using rough patches over a roughness spectra are as follows :

- The convolution integral between the roughness spectra and the unperturbed field spectrum in the spectral formulation is unnecessary.
- The roughness data can be directly used without a spectral domain processing such as the spectral estimate of the roughness profile.

In addition to the spatial domain formulation, the scattered field equation (2.19) is a deterministic expression which is general to any roughness profiles. Since most of the rough interfaces are stochastic processes, the statistical properties of the scattered field are obtained by the field ensembles produced by the random roughness profiles with the same statistical properties. This type of numerical approach is often called 'Monte-Carlo' method. The main reason to use 'Monte-Carlo' style computation is to avoid prohibitively heavy computation involving multiple integrals. When those statistical properties of the scattered field are expressed in mathematical terms, they take the form of multiple integrals. Also, the dimension of the integral increases as the dimension of the roughness profile increases. For 1-D roughness cases, these multiple integrals can be evaluated directly [28]. In Reference [54], the normal mode scattering theory, based on KRAKEN [38], was developed to study the roughness reverberation statistics produced by 1-D roughness in ocean waveguides. The multiple integral expression for the spatial correlation function of the scattered field was reduced to the sum of modal contributions to the scattered field. Each modal contribution was obtained by evaluating the inner portions of the multiple integrals analytically. For 2-D roughness cases, the evaluation of statistical properties become extremely difficult. Firstly, the transformation between spatial and spectral domain becomes a double convolution-type integral. Secondly, the averaging operator in the mathematical formulation becomes a double integral and the number of this double integral increases proportional to the number of random variables.

For example, the spatial correlation function of the scattered field has the following mathematical expression :

$$C_s(\vec{r}_1, z_1, \vec{r}_2, z_2) = \langle s_m(\vec{r}_1, z_1)\, s_n^*(\vec{r}_2, z_2) \rangle, \tag{2.21}$$

where m and n are the layer numbers which includes two receiver depths z_1 and z_2, respectively.

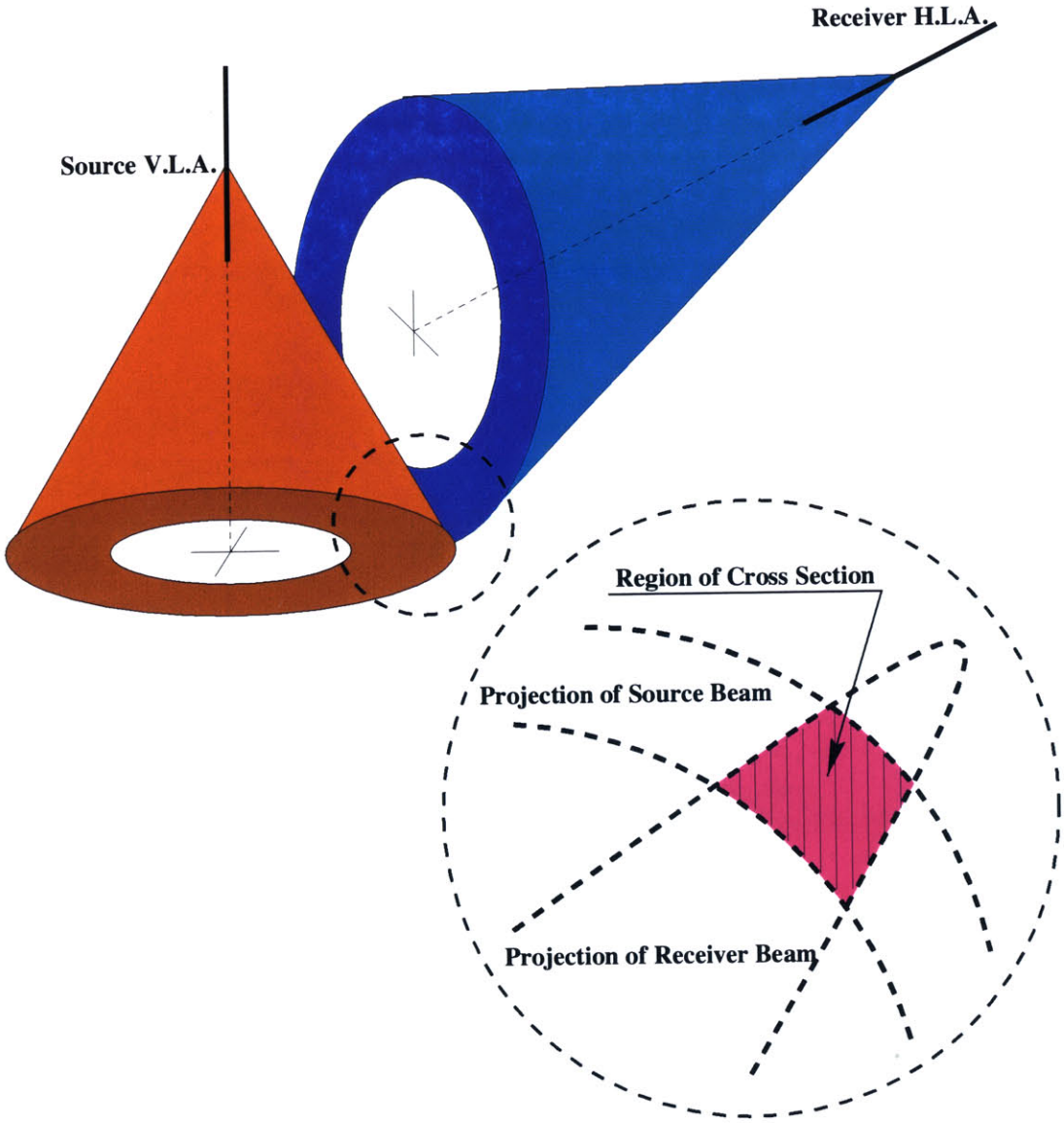

Figure 2-3: Illustration of the sonar footprint : the overlap between beampatterns of the source and receiver arrays.

The formal expression in Reference [48] was derived as follows :

$$C_s(\vec{r}_1, z_1, \vec{r}_2, z_2) = \frac{\sigma_\gamma^2}{(2\pi)^3} \int \left\{ d^2\vec{p}\, P_\gamma(-\vec{p}) \left[\int A_m(z_1, \vec{q}, \vec{q}+\vec{p})\, e^{-\imath\vec{q}\cdot\vec{r}_1}\, d^2\vec{q} \right] \right. \\ \left. \times \left[\int A_n(z_2, \vec{q}, \vec{q}+\vec{p})\, e^{-\imath\vec{q}\cdot\vec{r}_2}\, d^2\vec{q} \right]^* \right\}. \tag{2.22}$$

In the above equation, the scattering kernel A_m is defined as :

$$A_m(z, \vec{q}, \vec{k}) = e_m(z, \vec{q})\, \tilde{T}_{i;m}(\vec{k}, \vec{q})\, \langle \tilde{\chi}^{\mp}_{i;i+1}(\vec{k}) \rangle, \tag{2.23}$$

where $e^m(z, \vec{q})$ is a diagonal matrix representing the exponential behavior of the upward and downward plane wave components in layer m, and $\langle \tilde{\chi} \rangle$ is the spectral decomposition of the mean field derived by Fourier transform. $T_{i;m}(\vec{k}, \vec{q})$ is the reverberation T-matrix representing the transition from the mean field components with wave vector $\vec{k}$ in the layers separated by interface i, to the reverberation components of wave vector $\vec{q}$ in layer m. The scattering kernel, A_m, comes from the spectral expression of the scattered field, $\tilde{s}$, which is the convolution integral between the roughness spectrum and the scattering kernel. The above integral expresses the spatial correlation function by six multiple integrals with kernels in the spectral domain. Also, two of double integrals are in the form of a convolution integral, and they are functions of the spatial coordinates. The direct numerical evaluation of the above multiple integral is extremely inefficient for computing the correlation function values over a set of spatial points (i.e. the correlation matrix).

Another way to compute the spatial correlation function is to use the ensembles of the spatial fields using the roughness realizations. Since computing each spatial field snapshot involves a 2-D Fourier transform and a wavenumber integration and, it is extremely efficient. The correlation function can be obtained by a 'Monte-Carlo' style simulation. The numerical efficiency of the scattering computation is accomplished by the following techniques :

- The Hankel transform of spatial virtual source is performed using a 2-D fast Fourier integral based on FFT (Appendix B) .
- The boundary operator of 3-D OASES is independent of the azimuthal Fourier orders [46].

Compared to the direct integral method, the number of kernel sampling is several orders less in magnitude to achieve the same order of accuracy.

Validity of Small Perturbation

In the tensor notation, the displacement d_i' and traction τ_i' can be expanded by the Taylor series of the unrotated displacement vector d_i and stress tensor σ_{ij} about the reference level ($z = x_3 = 0$).

$$d_i' = \Psi_{ij}\left(d_j^0 + \gamma\, d_{j,3}^0\right) + O(\gamma^2), \tag{2.24}$$

where d_j^0 is the displacement vector at the reference level. Then the displacement perturbation Δd becomes :

$$\Delta d_i = d_i' - d_i^0 = (\Psi_{ij} - \delta_{ij})\, d_j^0 + \gamma\, \Psi_{ij}\, d_{j,3}^0 + O(\gamma^2), \tag{2.25}$$

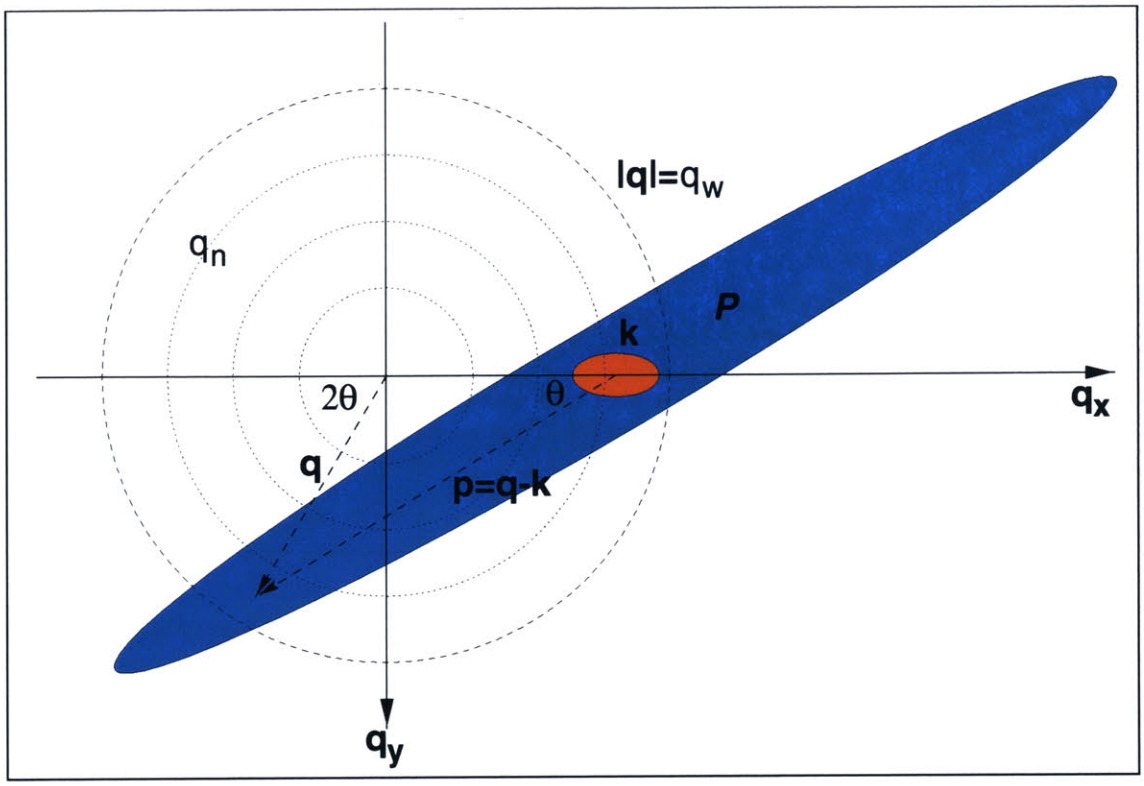

Figure 2-4: Illustration of the roughness spectrum and the incidence kernel in the wavenumber domain.

where δ_{ij} is the Kronecker delta and defined as follows :

$$\delta_{ij} = \begin{cases} 1 & \text{if } i = j \\ 0 & \text{if } i \neq j \end{cases}. \tag{2.26}$$

For the traction vector, the same expansion is used to derive the traction perturbation $\Delta\tau$. The traction vector in the rotated coordinate system is defined as follows :

$$\tau_i' = \Psi_{ij}\left(\sigma_{jk}^0 + \gamma\sigma_{jk,3}^0\right)\Psi_{3k} + O(\gamma^2), \tag{2.27}$$

where σ_{jk}^0 is the stress tensor at the reference level. Then the traction perturbation becomes :

$$\Delta\tau_i = \tau_i' - \tau_i^0 = (\Psi_{ij}\Psi_{3k} - \delta_{ij}\delta_{3k})\sigma_{jk}^0 + \gamma\Psi_{ij}\sigma_{jk,3}^0\Psi_{3k} + O(\gamma^2), \tag{2.28}$$

where τ_i^0 is the traction vector at the reference level. In order to evaluate the above perturbation at higher orders, the rotational tensor Ψ should be used as shown in (2.12). This rotational tensor is often linearized in terms of a local roughness slope. In most cases, this approximation is utilized to express the scattered fields in terms of roughness spectra. If there exists a higher order in the roughness height function, it is prohibitive to use the roughness spectra directly in most of the perturbation formulations. By assuming that the unperturbed field can replace the mean field, the scattering theory in this thesis also uses the linearized rotational operator. Therefore, the theoretical error caused by the linearized rotational operator can explain a validity of the theory.

The error between the exact and approximated rotational tensors occurs when the cosine and the sine of the local angles are approximated by 1 and the tangent of the surface, respectively. The relative errors ϵ between the exact and the first order become :

$$\epsilon_c = \frac{1-\cos\theta}{\cos\theta} = \sqrt{1+\tan^2\theta}-1, \qquad \epsilon_s = \frac{\tan\theta-\sin\theta}{\sin\theta} = \sqrt{1+\tan^2\theta}-1, \tag{2.29}$$

where the subscripts c and s represents the errors for the cosine and sine, respectively. The above relative errors simply mean that the square of the roughness slope should be much smaller than 1 in order to reduce the error, which is already stated by the second condition of the small perturbation limit in the equation (2.3). Since the relative errors for the cosine and sine are the same, it is possible to estimate the mean errors for each roughness type based on the roughness realizations.

Figure 2-5 shows three examples of errors produced by different roughness power spectra. Each error plot is generated by averaging 1024 ensembles. Since the 2-D Hanning window is applied on each roughness realization, the peaks of errors are located near the origin. As fast varying components of roughness increase, the relative errors become greater. Figure 2-5(a) is the error caused by an isotropic Gaussian power spectrum. The peak values are less than 3%, while isotropic Goff-Jordan power spectra produce greater error in Figure 2-5(b) and Figure 2-5(c). When the fractal dimension of Goff-Jordan power spectrum increases from 2.0 to 2.5 in Figure 2-5(b) and Figure 2-5(c), the relative peak error becomes 63% because of the stiffer local slopes.

In addition to the exact rotational tensor, the higher order derivatives of unperturbed displacements and stresses should be available. Since the unperturbed solution is based on the spectral representation in the form of a wavenumber integral, the partial derivatives of any related physical quantities can be derived exactly by multiplying the integral kernel by the corresponding wavenumber. In other words, the partial derivative operators in the spatial domain become the multiplication operator in its spectral domain. In Appendix B, the evaluation of partial derivatives in Cartesian and cylindrical coordinates is described.

Therefore, it is feasible to evaluate the higher order perturbations. The forms of the displacement and traction perturbations are no longer a linear functional of the roughness height function. The exact rotational tensor, Ψ, includes the square terms of the roughness slopes. The cross term between the roughness height and its rotational tensor makes the perturbations behave in a nonlinear fashion. Previously, the first order perturbation states that the magnitudes of perturbation and its resulting field are linearly proportional to the roughness height function. Once any terms higher than the first order are involved in the formulation, the previous statement becomes invalid especially when the roughness increases. Increasing roughness linearly means that the first order term of perturbation increases in the same linear scale but the higher order terms behave differently.

When compared to the first order perturbation using the approximated rotational tensor, the first order perturbation using the exact rotational tensor varies in the following ways. The perturbational formulation can be applied to the roughness with high slopes because the perturbational limit on the roughness slope is eliminated. Because the perturbational expressions (2.25) and (2.26) include the cross terms between the roughness height and slope, their averages become non-zero. In other words, the coherent scattered field will be non-zero [36]. The coherent scattered field corrects the assumption that the mean field can be replaced by the unperturbed field. Physically, this correction term represents the reduction of the total coherent field (mean field) caused by scattering.

Compared to the perturbation in the spectral domain, it is straightforward to implement the perturbation using the exact rotational tensor in the spatial domain. The effort required to compute

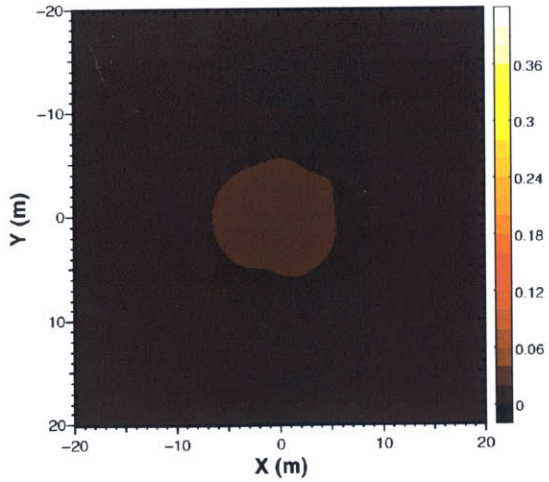

(a) Gaussian power spectrum.

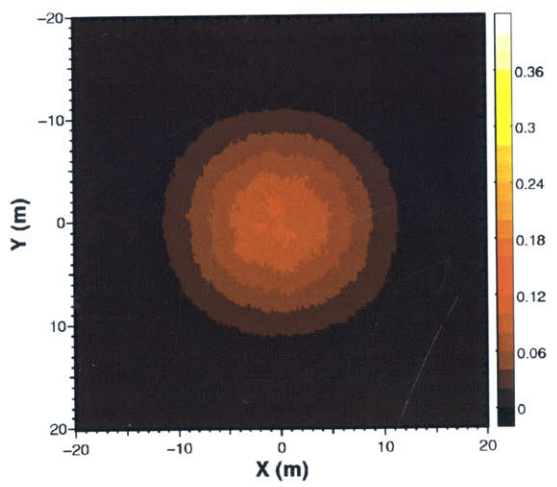

(b) Goff-Jordan power spectrum with fractal dimension $D = 2.0$.

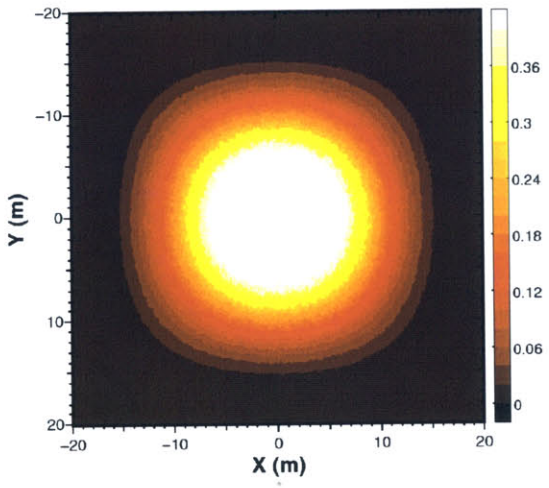

(c) Goff-Jordan power spectrum with fractal dimension $D = 2.5$.

Figure 2-5: The averaged relative errors of local cosine values based on the realization of 2-D isotropic roughness patches : *RMS* roughness height is $1m$ and the correlation length is $4m$. After bias and trend are removed from each realization, the 2-D Hanning window is applied.

the rotational tensor is equivalent to that of the approximated rotational tensor (i.e. roughness slope matrix). Therefore, it might be worth while to investigate the effects of coherent scattered field using the exact rotation tensor. However, the exact rotational tensor is not implemented in this thesis because it is beyond the scope of this thesis.

2.2 Description of Roughness

Description of roughness is an important aspect in rough interface scattering theories. Since most rough surfaces have stochastic behavior, this behavior can be described statistical terms. Those rough surfaces are defined in Reference [36] as follows :

> "No two rough surfaces are identical and even those formed by a well controlled process, such as turning, will each possess a unique surface form. For surface created under less stringent conditions, such as windswept seas, landscapes or fracture surfaces, it is not possible to predict the profile of any part of the surface from knowledge of the profiles of adjacent parts of the surface and the random nature is even more apparent. Such a surface may therefore be regarded as a random process: i.e. 'a process that has no memory'. Statistical techniques are required for describing such surfaces."

Besides the description of a rough surface, the type of rough surface can affect the validity of rough surface scattering models [36].

2.2.1 Statistical Description

There are many ways to describe random rough surfaces in statistical terms. One of the most basic way is by the first order statistic, which describes the characteristic for each of the individual data points. The typical values of first order statistics are mean and variance. The first order statistic is often called a 'one point statistic' because its statistic values are independent of the relative relationship among data points. By this reason, it is quite possible that two visually different random surfaces share the same first order statistics. Mathematically, the first order statistic is solely expressed by probability density functions (i.e., height distribution function $p(\gamma)$) or its equivalents, where $p(\gamma)\,d\gamma$ is the probability of any surface point being at a height between γ and $\gamma + d\gamma$ away from the mean surface. However, this description is often not sufficient to differentiate between two random processes.

In order to describe details of random surface, higher order statistics are required. The second order statistic (i.e., 'two point statistic') is most often used to describe the characteristic of the random variable. The second order statistics describe the correlation between two separate data points, and are often represented by the power spectrum (i.e. power spectral density function) or height correlation function. The definition of power spectrum can be obtained by its relationship with the corresponding correlation function :

$$P_\gamma(\vec{k}) = \frac{\sigma_\gamma^2}{(2\pi)^2} \int_{-\infty}^{\infty} C_\gamma(\vec{R})\, e^{i\vec{k}\cdot\vec{R}}\, d^2\vec{R}, \tag{2.30}$$

where $\sqrt{\sigma_\gamma^2}$ is the *RMS* roughness height and $C(\vec{R})$ is the normalized correlation function of roughness. In other words, the power spectrum is the Fourier transform of the unnormalized correlation function. The power spectrum is also directly related to the surface profile function by replacing the surface correlation function $C(\vec{R})$ with the following definition. For an infinite roughness surface, the normalized correlation function is defined as the following limit.

$$C_\gamma(\vec{R}) = \lim_{A_M \to \infty} \frac{1}{A_M \sigma_\gamma^2} \int_{A_M} \gamma(\vec{r})\gamma(\vec{r}+\vec{R})\, d^2\vec{r}, \tag{2.31}$$

where A_M is the area of mean (or reference) surface. By substituting the above definition to the power spectrum,

$$P_\gamma(\vec{k}) = \lim_{A_M \to \infty} \frac{1}{4\pi^2 A_M} \left| \int_{A_M} \gamma(\vec{r}) e^{i\vec{k}\cdot\vec{r}}\, d^2\vec{r} \right|^2. \tag{2.32}$$

The power spectrum can describe the spread of height distributions as well as the height variation along the surface. The *RMS* roughness height and *RMS* average for higher order derivatives can be conveniently expressed by the power spectrum.

$$\sigma_\gamma^2 = \int_{-\infty}^{\infty} P_\gamma(\vec{k})\, d^2\vec{k}, \qquad \left\langle \left(\frac{\partial^n \gamma}{\partial x^n} \right)^2 \right\rangle_s = \int_{-\infty}^{\infty} P_\gamma(\vec{k}) \vec{k}^{2n}\, d^2\vec{k}. \tag{2.33}$$

The most common form of power spectrum is one with a Gaussian surface correlation function.

$$P_\gamma(\vec{k}) = \frac{\sigma_\gamma^2}{2\pi\sqrt{|Q|}} \exp\left[-\frac{u^2(\vec{k})}{2} \right], \qquad C_\gamma(\vec{x}) = \exp\left[-\frac{r^2(\vec{x})}{2} \right], \tag{2.34}$$

where a positive-definite, the symmetric matrix Q and a function $u(\vec{k})$ and $r(\vec{x})$ are defined as :

$$Q = \frac{1}{C_{L1}^2} \hat{\mathbf{e}}_1 \hat{\mathbf{e}}_1^T + \frac{1}{C_{L2}^2} \hat{\mathbf{e}}_2 \hat{\mathbf{e}}_2^T, \tag{2.35}$$

$$u(\vec{k}) = \left[\vec{k}^T Q^{-1} \vec{k} \right]^{1/2}, \tag{2.36}$$

$$r(\vec{x}) = \left[\vec{x}^T Q^{-1} \vec{x} \right]^{1/2}. \tag{2.37}$$

The determinant of Q is a constant independent of the coordinate system.

$$|Q| = \left(\frac{1}{C_{L1} C_{L2}} \right)^2. \tag{2.38}$$

The unit vectors $\hat{\mathbf{e}}_1$ and $\hat{\mathbf{e}}_2$ are orthogonal to each other and they are aligned to the direction of anisotropy. When the angle of anisotropy is θ_s with respect to horizontal axis (x axis) in the counter-clockwise direction, $\hat{\mathbf{e}}_1$ and $\hat{\mathbf{e}}_2$ simply reflect the rotation of coordinate system.

$$\hat{\mathbf{e}}_1 = \begin{pmatrix} \cos\theta_s \\ \sin\theta_s \end{pmatrix}, \qquad \hat{\mathbf{e}}_2 = \begin{pmatrix} -\sin\theta_s \\ \cos\theta_s \end{pmatrix}. \tag{2.39}$$

The corresponding Q matrix, $u(\vec{k})$ and $r(\vec{r})$ are :

$$Q = \begin{bmatrix} C_{L1}^{-2}\cos^2\theta_s + C_{L2}^{-2}\sin^2\theta_s & (C_{L1}^{-2} - C_{L2}^{-2})\cos\theta\sin\theta \\ (C_{L1}^{-2} - C_{L2}^{-2})\cos\theta\sin\theta & C_{L1}^{-2}\sin^2\theta_s + C_{L2}^{-2}\cos^2\theta_s \end{bmatrix}, \tag{2.40}$$

$$u(\vec{k}) = \sqrt{k_x^2 + k_y^2}\sqrt{C_{L1}^2\cos^2(\theta-\theta_s) + C_{L2}^2\sin^2(\theta-\theta_s)}, \tag{2.41}$$

$$r(\vec{x}) = \sqrt{x^2+y^2}\sqrt{C_{L1}^{-2}\cos^2(\theta-\theta_s)+C_{L2}^{-2}\sin^2(\theta-\theta_s)}, \tag{2.42}$$

where C_{L1} and C_{L2} are major and minor correlation lengths of roughness. If the wavenumber vector in the rotated coordinate system is used, Q becomes a diagonal matrix as follows :

$$Q = \begin{bmatrix} C_{L1}^{-2} & 0 \\ 0 & C_{L2}^{-2} \end{bmatrix}, \tag{2.43}$$

and $u(\vec{K})$ and $r(\vec{x})$ become :

$$u(\vec{K}) = \sqrt{C_{L1}^2K_1^2+C_{L2}^2K_2^2}, \qquad r(\vec{X}) = \sqrt{C_{L1}^{-2}X_1^2+C_{L2}^{-2}X_2^2}, \tag{2.44}$$

where (K_1, K_2) and (X_1, X_2) are a local wavenumber vector and a spatial vector in the rotated coordinate system which are related to the original vectors as follows :

$$K_1 = \sqrt{k_x^2+k_y^2}\cos(\theta-\theta_s), \qquad K_2 = \sqrt{k_x^2+k_y^2}\sin(\theta-\theta_s), \tag{2.45}$$

and

$$X_1 = \sqrt{x^2+y^2}\cos(\theta-\theta_s), \qquad X_2 = \sqrt{x^2+y^2}\sin(\theta-\theta_s). \tag{2.46}$$

The form of the power spectrum is the same as the correlation functions. The main advantage of using this type of power spectrum (Gaussian) is that it is very easy to manipulate analytically.

Another type of power spectrum, which is often used to model oceanic bottom surfaces, was suggested by Goff and Jordan [19].

$$P_\gamma(\vec{k}) = \frac{\sigma_\gamma^2\nu}{\pi\sqrt{|Q|}\left[u^2(\vec{k})+1\right]^{(\nu+1)}}, \qquad C_\gamma(\vec{x}) = G_\nu(r(\vec{x}))/G_\nu(0). \tag{2.47}$$

The function G_ν is defined as :

$$G_\nu(r) = r^\nu K_\nu(r) \quad \text{for } \nu \in [0,1], \tag{2.48}$$

where K_ν is the modified Bessel function of the second kind and order ν, and $G_\nu(r)$ has the following limiting value at $r = 0$ [1] :

$$\lim_{r\to 0} G_\nu(r) = \Gamma(\nu)2^{\nu-1}. \tag{2.49}$$

The above power spectrum has an asymptotic roll-off rate equal to $-2(\nu+1)$ when the wavenumber approaches infinity. The parameter ν is related to the fractal (Hausdorff) dimension D as follows :

$$D = 3-\nu, \tag{2.50}$$

which represents the richness of small scale roughness in a stochastic process. Therefore, the parameter ν is inversely related to the roughness. For the limiting case of $\nu = 1$, the rough surface is called an 'Euclidean surface' which has continuous derivatives. For the case of $\nu = 0$, the surface becomes a 'Peano surface' or 'space-filling', which has strong high wavenumber (fast oscillating) components. In contrast to Gaussian power spectrum, 'Goff-Jordan' power spectrum has a longer tail in the high wavenumber regime. The tail in the high wavenumber regime is often useful to

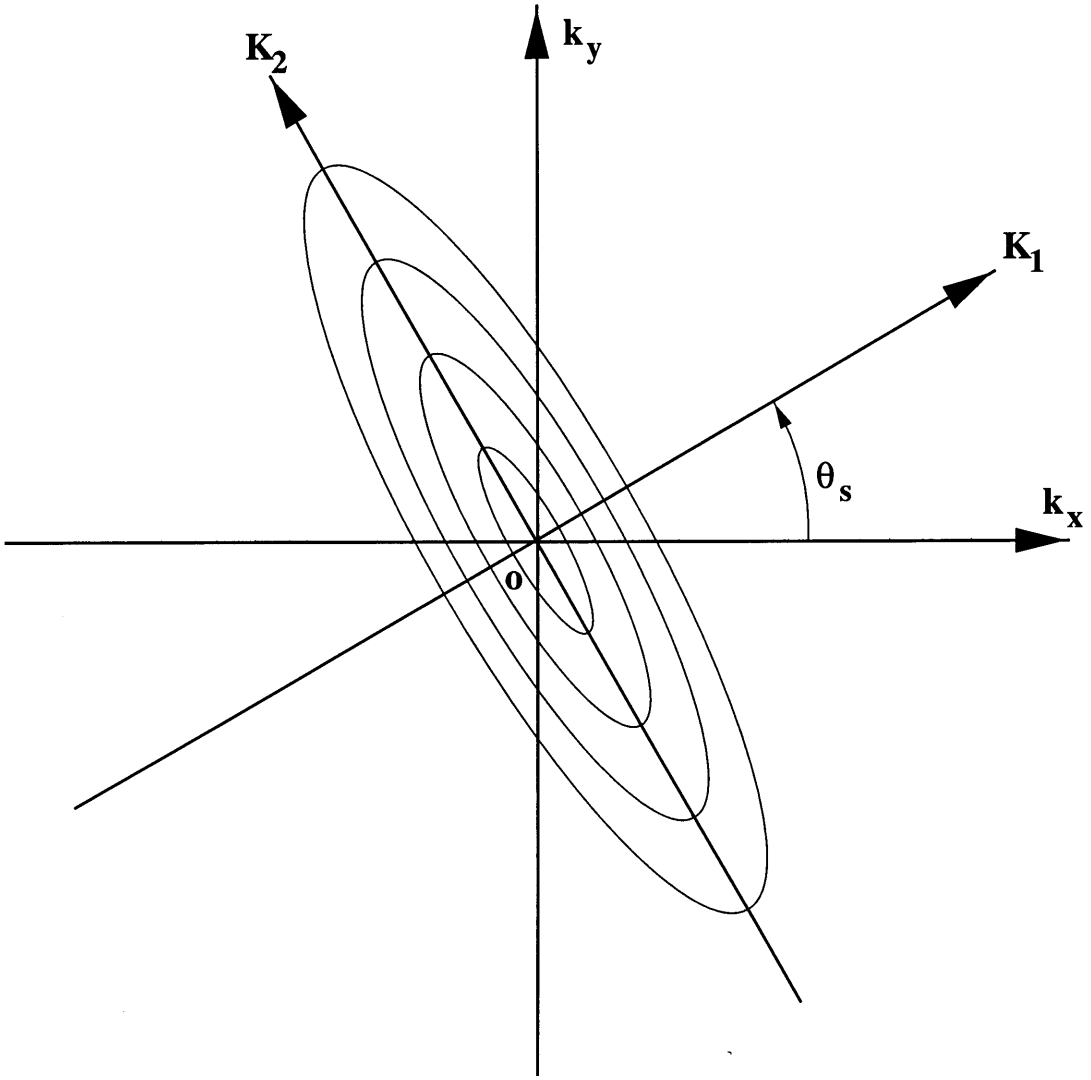

Figure 2-6: Local wavenumber axes : illustrative plots of $u(\vec{k})$. The ellipses are the isolines of $u(\vec{k})$ when $C_{L1} > C_{L2}$.

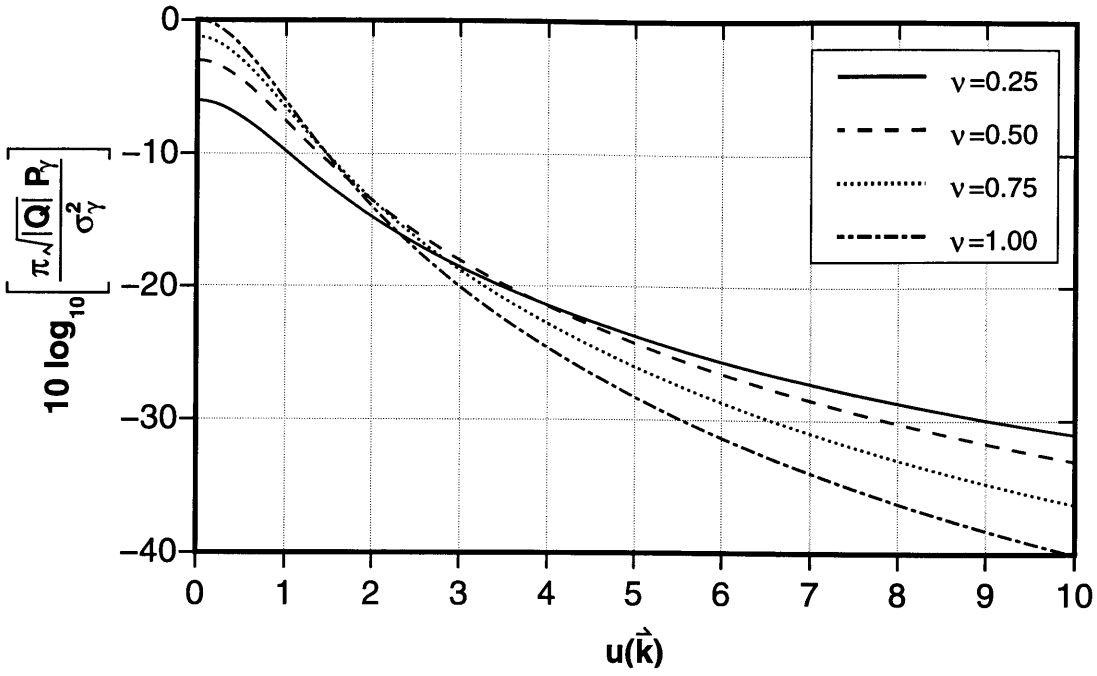

Figure 2-7: Goff-Jordan power spectrum as a function of $u(\vec{k})$: $\nu = 0.25, 0.50, 0.75$, and 1.00 cases.

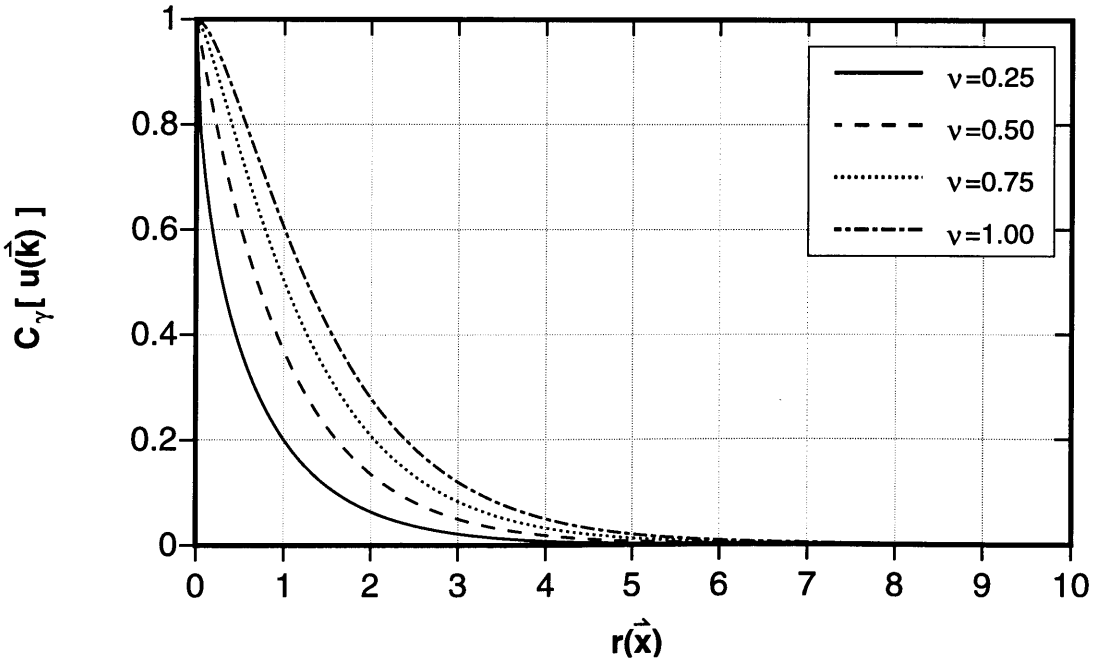

Figure 2-8: Goff-Jordan correlation function as a function of $r(\vec{x})$: $\nu = 0.25, 0.50, 0.75$, and 1.00 cases.

match the experimental roughness data for two reasons.

Firstly, the roughness data collection inherently introduces high wavenumber noise components (fast varying roughness). Secondly, any measurement methods have the limitation on the spatial resolutions, which correspond to the highest measurable wavenumbers. Beyond these wavenumbers, the collection of roughness data is meaningless, except that most of the real oceanic bottom surfaces have small scale features beyond these wavenumbers which are represented insignificantly by Gaussian power spectrum.

Another type of roughness, commonly observed in oceanic bottoms, is often called the 'ripple' or 'ripple structure'. Its most distinctive feature is that the roughness spectrum is centered at a specific wavenumber away from zero wavenumber. In order to describe the ripple roughness in statistical terms, the power spectrum is modified to have a peak at a non-zero wavenumber with a given width of spreading.

$$P_\gamma(\vec{k}) = \frac{\sigma_\gamma^2 C_{L1}^2}{4\pi}\left[\left(1+C_{L1}^2\left|\vec{k}-\vec{k}_0\right|^2\right)^{-3/2}+\left(1+C_{L1}^2\left|\vec{k}+\vec{k}_0\right|^2\right)^{-3/2}\right], \tag{2.51}$$

where $\pm\vec{k}_0$ are the wavenumber vectors for peak positions defined as follows :

$$\vec{k}_0 = \frac{1}{C_{L2}}\begin{pmatrix}-\sin\theta_s\\ \cos\theta_s\end{pmatrix}. \tag{2.52}$$

The above power spectrum is a sum of two isotropic Goff-Jordan power spectra with the fractal dimension 2.5 and the correlation length C_{L1}. It is scaled by the fact that the total power is equal to the variance of roughness. The distance between two peaks is simply the inverse of the second correlation length C_{L2}. In the spatial domain, the first correlation length C_{L1} controls the characteristic length of ripples while the second correlation length C_{L2} controls the width of ripple structure. Since the peak of the power spectrum is not located at the zero wavenumber, it is often called 'off-centered' power spectrum. An example of this power spectrum is shown in Figure 2-17. The same kind of power spectrum can be constructed with two isotropic Gaussian power spectra as follows :

$$P_\gamma(\vec{k}) = \frac{\sigma_\gamma^2 C_{L1}^2}{4\pi}\left[\exp\left(-\frac{C_{L1}^2\left|\vec{k}-\vec{k}_0\right|^2}{2}\right)+\exp\left(-\frac{C_{L1}^2\left|\vec{k}+\vec{k}_0\right|^2}{2}\right)\right]. \tag{2.53}$$

An example of off-centered Gaussian power spectrum is shown in Figure 2-19. The major difference between the above spectra is analogous to that of the Goff-Jordan and Gaussian power spectra. The off-centered Goff-Jordan power spectrum has more energy spreading in the high wavenumber regime as well as near zero wavenumber.

2.2.2 Syntheses of Roughness

In contrast to the other scattering theories, the rough interface scattering formulation in this thesis uses the roughness height functions directly. For measured roughness data sets, the formulation is able to compute the corresponding scattered fields directly. But, when the statistical properties of scattered fields produced by a particular roughness model (i.e. power spectrum) is sought, the most possible way to connect the scattering formulation with the roughness power spectrum is to compute the fields based on the roughness profiles which are synthesized by the roughness power spectrum. With a series of synthesized roughness profiles, the statistical properties of the scattered fields can be obtained in an ensemble sense.

Once a power spectrum or correlation function is determined for a particular roughness statistic, a realization of corresponding roughness is straightforward. The magnitude of roughness spectral component, $\tilde{\gamma}(\vec{k})$, is proportional to the square root of the power spectrum, $P_\gamma(\vec{k})$. Therefore, a realization of the roughness profile, $\gamma(\vec{r})$, is expressed by the following relationship :

$$\gamma(\vec{r}) = \mathbf{F}^{-1}\left[\sqrt{P_\gamma(\vec{k})}\, e^{-i\phi(\vec{k})}\right], \tag{2.54}$$

where $\mathbf{F}^{-1}$ is the inverse Fourier transform. $\phi(\vec{k})$ is a random function with the following probability density function $p(\phi)$:

$$p(\phi) = \begin{cases} (2\pi)^{-1} & \text{for } 0 \le \phi \le 2\pi \\ 0 & \text{otherwise} \end{cases}, \tag{2.55}$$

which is a uniform probability density function.

In order to perform a field computation based on random properties, each random variable should be described by its probability density function. The phase of spectral component is the only random variable which can vary from 0 to 2π. Since there is no prior preference for the phases, the uniform probability density function becomes the natural description of random phases. The square root of the roughness power spectrum provides the amplitudes for the roughness height function in the spectral domain, while the random phase function makes each realization randomly unique.

The basic idea of roughness realization is simple, but its numerical implementation requires several cautions. Regardless of power spectra, the following two facts should be considered for the numerical implementation. Firstly, since the average of the roughness height is zero, therefore, the spectral component at the zero wavenumber should always be zero. Secondly, the roughness height is a real function while the input spectral component is a complex function. Therefore, the spectral components of negative wavenumbers should be equal to the complex conjugation of those in the positive wavenumber regime.

Several examples of the roughness power spectra and their realizations are shown in Figure 2-9 through Figure 2-14. When Figure 2-12 and Figure 2-14 are compared, the most distinctive difference comes from the higher wavenumber components (i.e. small scale roughness). A realization (Figure 2-12) generated by an isotropic Goff-Jordan power spectrum (Figure 2-9) has many rich features of fast varying roughness. However, even with the same correlation length, a realization (Figure 2-14) generated by an isotropic Gaussian power spectrum (Figure 2-13) is very smooth with prevailing features of slowly varying components.

Once an anisotropy is introduced by the second, or minor, correlation length (C_{L2}) and skew angle (θ_s) to a power spectrum such as Figure 2-15, the corresponding roughness realization shows spatial anisotropy such as shown in Figure 2-16. The aspect ratio of anisotropy is determined by the ratio between the major and minor correlation lengths.

Another type of roughness anisotropy, known as a 'ripple structure', is distinguished from the previous roughness anisotropy because its roughness power spectrum has a peak at a non-zero wavenumber. Figure 2-17 is an 'off-centered' Goff-Jordan power spectrum for a ripple structure. Figure 2-18 is a roughness realization based on Figure 2-17. Figure 2-19 and Figure 2-20 are an 'off-centered' Gaussian power spectrum and its roughness realization, respectively. Analogous to the comparison between isotropic Goff-Jordan and Gaussian roughness realizations, Figure 2-18 and Figure 2-20 exhibit the differences in fast and slowly varying roughness components.

Pre-processing of Roughness Data

There are several kinds of methods in collecting roughness data. Raw data of roughness can be underwater photos, bathymetry data, acoustic measurements and even synthesized roughness profiles. Each individual method has own limits in spatial resolution and accuracy. Thus, the resulting statistical values are different in subtle ways. Regardless of data collecting methods, the raw data should be properly processed before any spectral analyses are performed [20]. The general procedures for pre-processing of raw data consist of :

1. Digitization of data.
   The raw data are digitized on the grid points. Interpolation may be used to fill the gaps.

2. Removal of bias and trend.
   The raw data are measured relative to the reference level. For spectral analysis, the mean height and slope should be set to zero by subtracting its least-square plane from the raw data. By doing this, any features with wavelengths longer than the sampling (track) length are eliminated.

3. Windowing and filtering.
   To minimize the spectral distortion, any sharp discontinuity or truncation on data should be removed by a smooth and broad window. While effective surface area is reduced by windowing, side lobes in the spectral domain will be reduced.

As an example, synthesized roughness data are generated to demonstrate the pre-processing procedures. Digitization of data is skipped because the data are synthesized in a digital format. Given a roughness power spectrum or correlation function, roughness is generated on 2-D rectangular grids. Figure 2-9 shows the input power spectrum modeled by an Isotropic Goff-Jordan power spectrum. Figure 2-10 is a single realization of roughness based on the input power spectrum. Unlike the zero mean surface level, the slope of the reference plane is not strictly enforced for the roughness syntheses. Therefore, most of the raw roughness profiles contain non-zero slopes in their mean plane. By subtracting the least-square plane from the raw data, the roughness profile has a zero slope of its mean plane as well as zero mean values. Figure 2-11 shows the roughness data after this procedure. The windowing process removes discontinuity along the boundary of roughness profile in order to eliminate spurious behavior in the spectral domain. Figure 2-12 is the final roughness profile after the pre-processing.

Selection of Patch Length Scale

Determining the length scale of roughness patch requires several physical consideration. The lengths of patch are generally selected by the following factors :

- Size of sonar footprint. The size of sonar footprint is estimated by the angular resolutions of source and receiver arrays, and the distances among interface and arrays.

- Correlation lengths of roughness. In order to express the correlation length on random patches, the length of the patch parallel to each correlation length should be ten times longer than the correlation [36].

Another important length scale is the grid size of the patch. In order to represent various scattered waves, the grid size of the patch should be selected carefully according to the following standards. Depending on the layering structure of the medium, there exist different types of

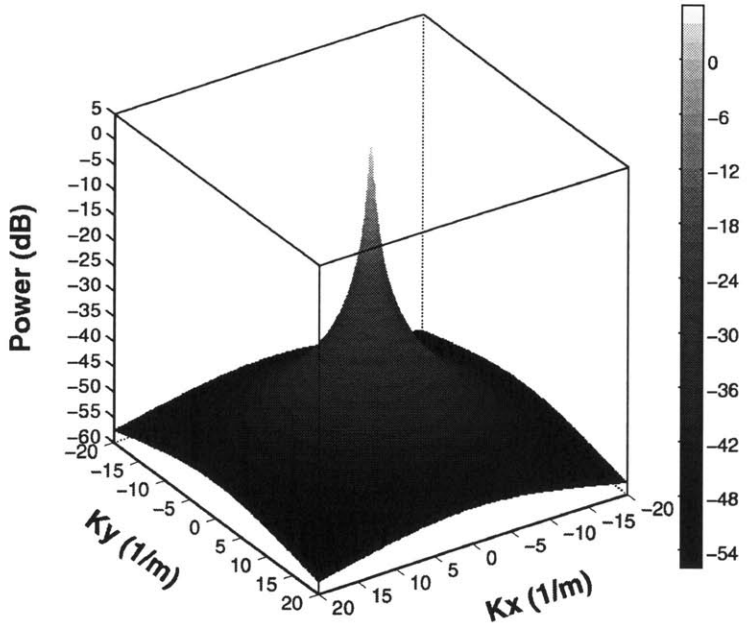

Figure 2-9: Input power spectrum for realization of roughness patch : an isotropic Goff-Jordan power spectrum ($C_L = 4m$, $D = 2.5$, and $\sqrt{\langle \gamma^2 \rangle} = 1m$).

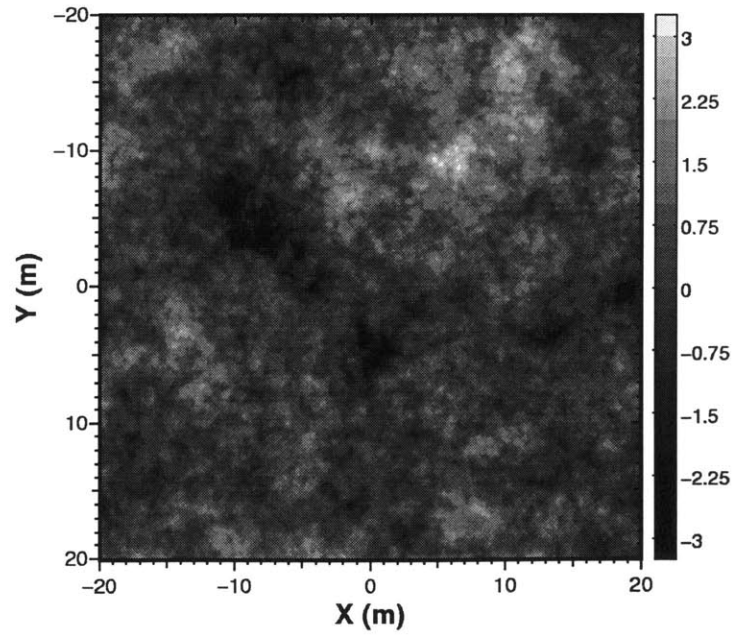

Figure 2-10: Synthesized raw data : an isotropic Goff-Jordan power spectrum ($C_L = 4m$, $D = 2.5$, $l_x = l_y = 40m$, $N_x = N_y = 256$, an $\sqrt{\langle \gamma^2 \rangle} = 1m$).

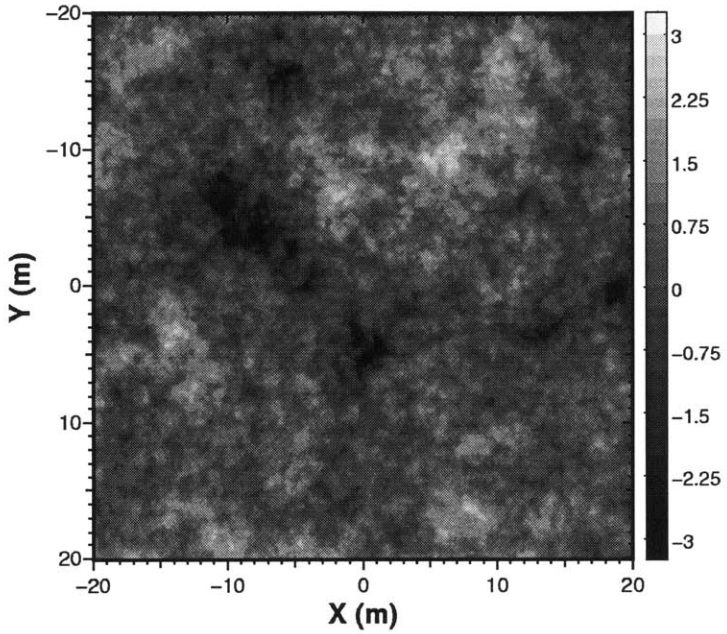

Figure 2-11: Data after removal of bias and trend.

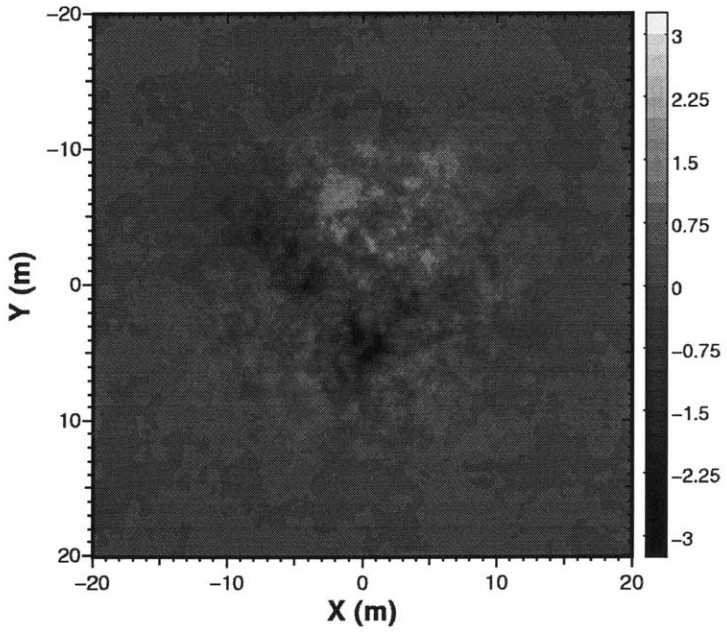

Figure 2-12: Data after 2-D rectangular Hanning windowing.

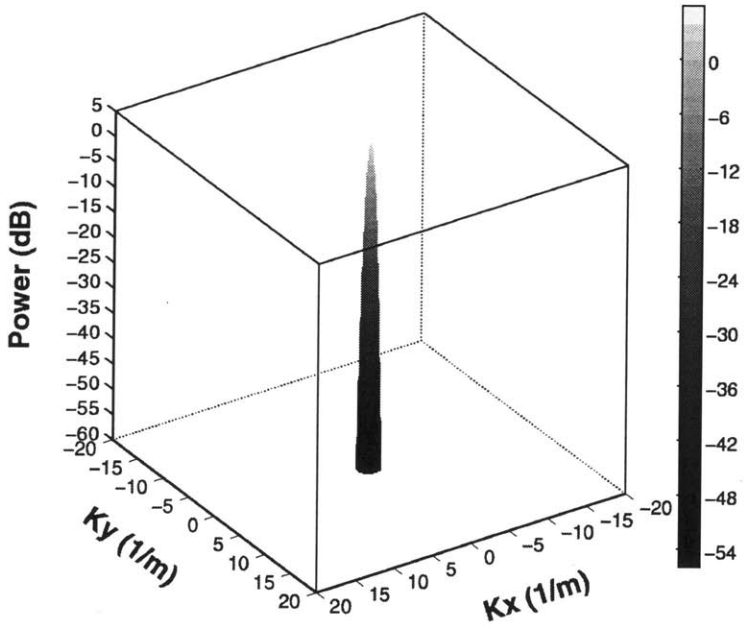

Figure 2-13: Input power spectrum for realization of roughness patch : an isotropic Gaussian power spectrum ($C_L = 4m$ and $\sqrt{\langle \gamma^2 \rangle} = 1m$).

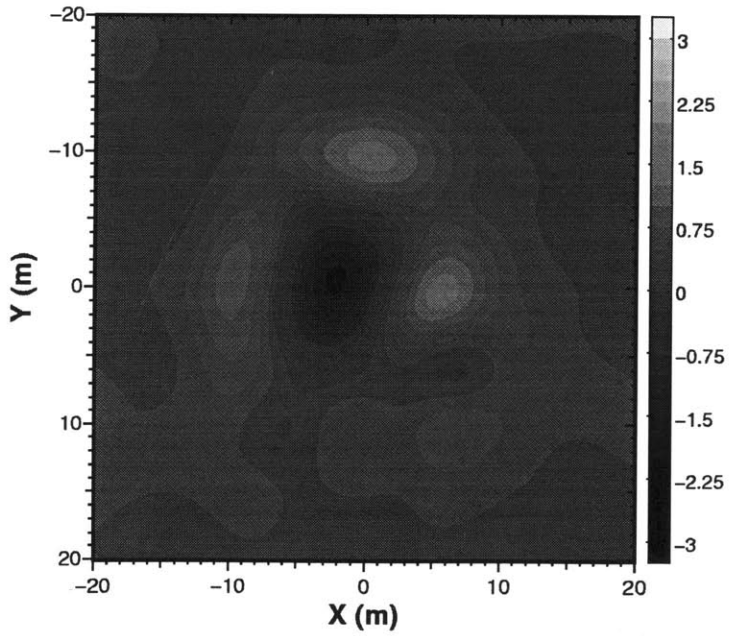

Figure 2-14: Roughness realization by an isotropic Gaussian power spectrum after pre-processing.

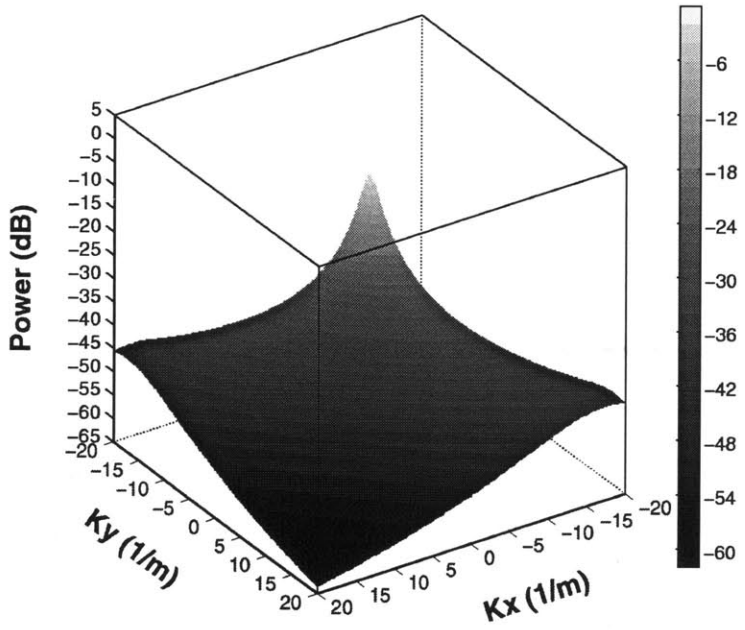

Figure 2-15: Input power spectrum for realization of roughness patch : an anisotropic Goff-Jordan power spectrum ($C_{L1} = 4m$, $C_{L2} = 1m$, $D = 2.5$, $\sqrt{\langle \gamma^2 \rangle} = 1m$, and $\theta_s = 45°$).

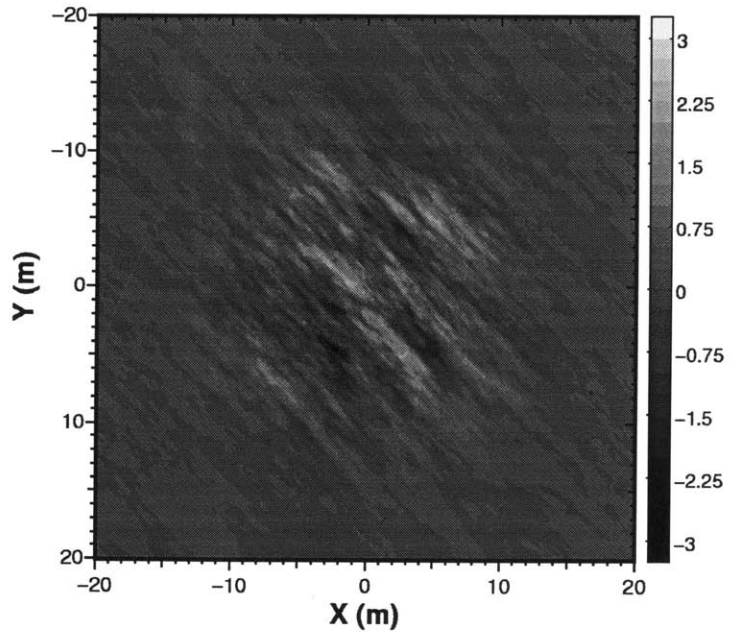

Figure 2-16: Roughness realization by an anisotropic Goff-Jordan power spectrum ($\theta_s = 45°$) after pre-processing.

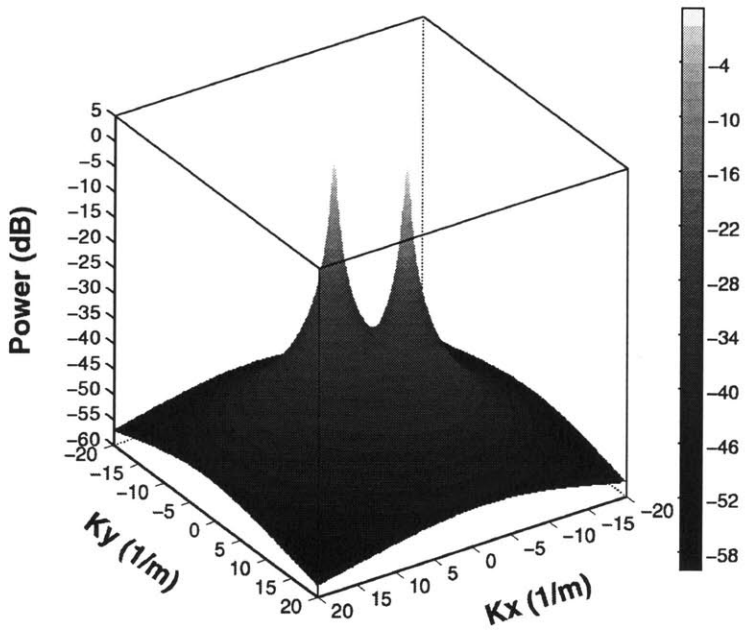

Figure 2-17: Input power spectrum for realization of roughness patch : an off-centered Goff-Jordan power spectrum ($C_{L1} = 4m$, $C_{L2} = 0.25m$, $D = 2.5$, $\sqrt{\langle \gamma^2 \rangle} = 1m$, and $\theta_s = 45°$).

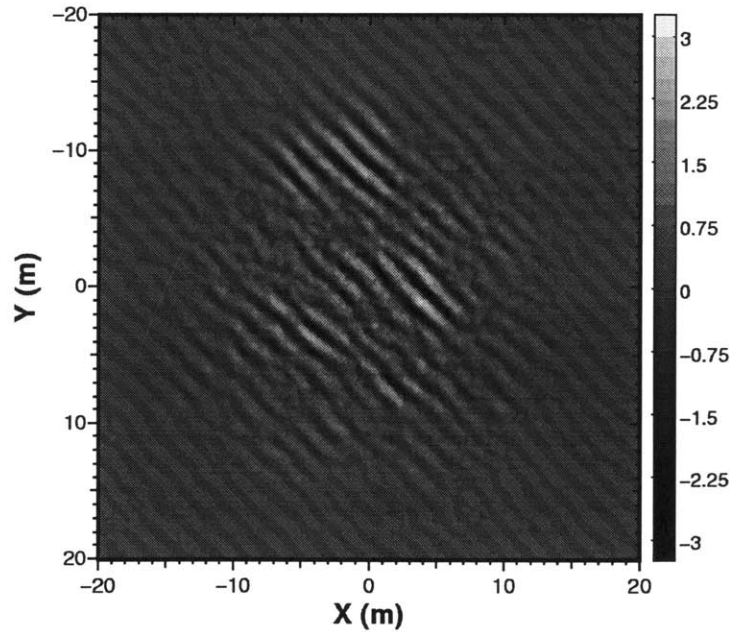

Figure 2-18: Roughness realization by an off-centered Goff-Jordan power spectrum ($\theta_s = 45°$) after pre-processing.

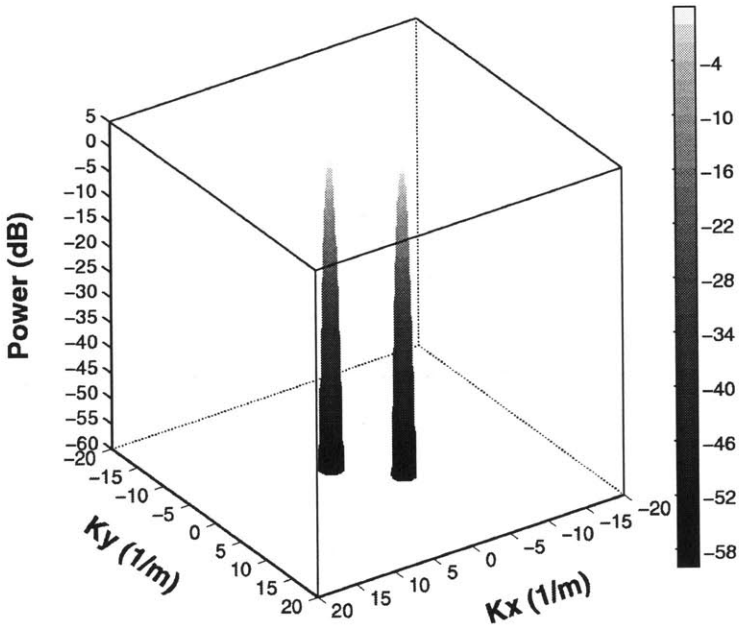

Figure 2-19: Input power spectrum for realization of roughness patch : an off-centered Gaussian power spectrum ($C_{L1} = 4m$, $C_{L2} = 0.25m$, $\sqrt{\langle \gamma^2 \rangle} = 1m$, and $\theta_s = 45°$).

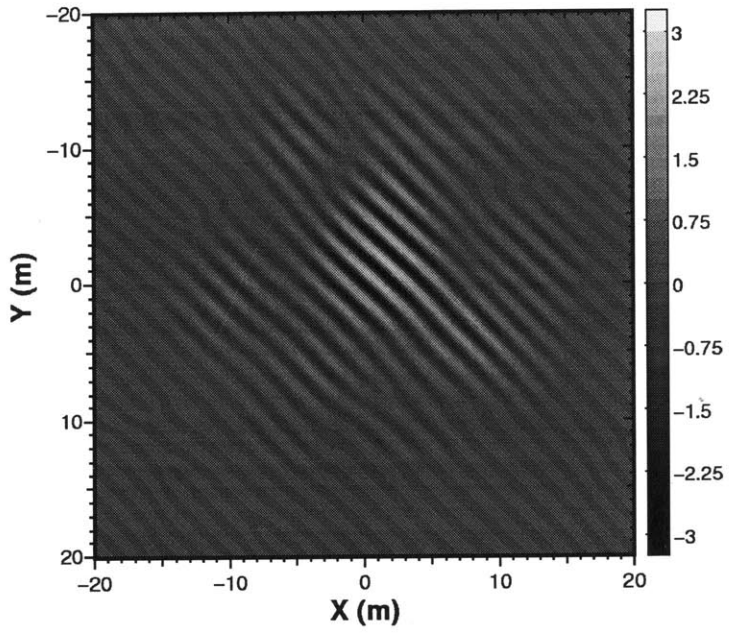

Figure 2-20: Roughness realization by an off-centered Gaussian power spectrum ($\theta_s = 45°$) after pre-processing.

seismo-acoustic waves. These waves are often characterized by their phase speeds. In the spectral domain, these phase speeds are related to the horizontal wavenumber by frequency. The relationship between these characteristic wavenumbers and patch grid size is straightforward. In order to include the effect from each wave type, the maximum patch grid size is determined by the following equality :

$$\Delta_s < \frac{2\pi}{k_c}, \tag{2.56}$$

where Δ_s and k_c are the patch grid size and characteristic wavenumber, respectively. Therefore, the maximum grid size can be found by computing the minimum characteristic wavenumber. There exist surface waves on the interface with an elastic layer. Surface waves are referred to differently depending on the type of medium on the other side. For example, a surface wave is called a 'Rayleigh wave' if it exists on a vacuum-elastic interface and a 'Scholte wave' if it has a fluid-elastic interface. A 'Stonely wave' is a surface wave associated with an elastic-elastic interface. As the pertinent wave type in ocean waveguides, Scholte wave occurs on the interface between a fluid layer and an elastic layer such as bottom interfaces. It has the following characteristics [22] :

- The wave propagates along the interface with exponentially decaying amplitude away from the interface in both medium.
- Particle motion is elliptical in the vertical-horizontal plane.
- There is no low-frequency cut-off.
- The phase speed of the Scholte wave is lower than the shear wave speed of an elastic medium [7].

According to the last item, the grid sizes of patches should be chosen by considering the Scholte wavenumber for a fluid-elastic rough interface. The phase speed of Scholte wave is determined by solving the following characteristic equation [7] :

$$4\sqrt{1-s}\sqrt{1-qs}-(s-2)^2 = \frac{s^2\sqrt{1-qs}}{m\sqrt{1-rs}}, \tag{2.57}$$

where

$$r = \frac{C_{s1}^2}{C_p^2}, \quad q = \frac{C_{s1}^2}{C_{p1}^2}, \quad m = \frac{\rho_1}{\rho}, \quad s = \frac{C_{\text{Scholte}}^2}{C_{s1}^2}, \tag{2.58}$$

where C_p and ρ are the compressional wave speed and the density of the fluid layer while C_{p1}, C_{s1} and ρ_1 are the compressional wave speed, the shear wave speed, and the density of the elastic layer. In Reference [7], the asymptotic behavior of the potential is derived when $m \gg 1$ and $r \gg 1$. The potential amplitude in the fluid medium decreases as the vertical distance from the interface increases. The amplitude is proportional to the following exponential term :

$$\exp\left[-\frac{kz}{2mr(1-q)}\right] \quad \text{for } z > 0, \tag{2.59}$$

where z is the vertical distance from the interface. In order to have significant effects of the Scholte wave in a fluid medium, the above exponential term should be large within the depth of

several wavelengths from the interface. Assuming that the distance z is equal to the compressional wavelength of the fluid, and m and q are kept constant, the condition for the dominant effects of the Scholte wave is obtained as follows :

$$\frac{C_{s1}}{C_p} = \sqrt{r} \gg \sqrt{\pi} \approx 1.77. \tag{2.60}$$

Therefore, when the shear wave speed of the elastic layer exceeds the compression wave speed of the fluid layer by the above ratio, the contribution of Scholte waves to the scattered field is significant.

There is another type of surface wave called the 'leaky wave'. The phase speed of the leaky wave can be calculated by the same characteristic equation as the Scholte wave. The difference is that its phase speed is in a complex plane. The real part of the phase speed exceeds the compressional wave speed of the fluid medium. Even though the real part of phase speed is in the supersonic regime in the fluid medium, the non-zero imaginary part of phase speed produces the decaying behavior of leaky wave which is similar to the other interface wave. Again, the contribution of leaky wave to the scattered field is observable in the vicinity of interface if the rough interface is located between the fluid and the elastic media, or between two elastic media.

Correction of Window Effects

Even synthesized roughness data are required to be pre-processed for any further spectral analysis. For example, biased roughness data are likely to give erroneous results in scattering computation because of non-zero mean height and slopes. Also, computation of the local roughness slopes, which is necessary for a perturbation method, can properly be done only if the edge discontinuity is removed by windowing. The spatial windowing process changes the effective area for scattering computation. There are several ways to compensate for the losses caused by windowing. The most typical approach is to scale up the final results by a predetermined factor. As a rule of thumb, this factor is approximately equal to the ratio between the volume under the specific window and the volume under the rectangular window. For example, the volume ratio by Hanning window is 0.25, which corresponds to half the size of the *RMS* roughness height.

$$\frac{1}{l_x l_y}\int_{-l_y/2}^{l_y/2}\int_{-l_x/2}^{l_x/2}\frac{1}{4}\left[1+\cos\left(\frac{2\pi x}{l_x}\right)\right]\left[1+\cos\left(\frac{2\pi y}{l_y}\right)\right]dx\,dy = \frac{1}{4}. \tag{2.61}$$

Mathematically, this approximation is too crude. In order to compute the correct scaling factor, it is necessary to examine the mathematical expression of the *RMS* roughness height. By definition, the *RMS* roughness height is :

$$\sqrt{\langle \gamma^2 \rangle} = N(0), \tag{2.62}$$

where N is the roughness correlation function defined as follows :

$$N(\vec{x}) = \left\langle \gamma(\vec{x}')\,\gamma(\vec{x}+\vec{x}') \right\rangle, \tag{2.63}$$

where $\gamma(\vec{x})$ is the roughness height function.

Once a window function $h(\vec{x})$ is applied, the new correlation function $N'(\vec{x})$ becomes :

$$\begin{aligned} N'(\vec{x}) &= \left\langle h(\vec{x}')\gamma(\vec{x}')h(\vec{x}+\vec{x}')\gamma(\vec{x}+\vec{x}')\right\rangle \\ &= \left\langle h(\vec{x}')h(\vec{x}+\vec{x}')\right\rangle \times \left\langle \gamma(\vec{x}')\gamma(\vec{x}+\vec{x}')\right\rangle \\ &= N_h(\vec{x}) \times N(\vec{x}). \end{aligned} \tag{2.64}$$

The window correlation function $N_h(\vec{x})$ is :

$$N_h(\vec{x}) = \frac{\int_A h(\vec{x}')h(\vec{x}+\vec{x}')\,d^2\vec{x}'}{\int_A d^2\vec{x}'}, \tag{2.65}$$

and the roughness correlation function can be expressed by the corresponding power spectrum $P(\vec{q})$:

$$N(\vec{x}) = \int P(\vec{q})\,e^{-i\vec{q}\cdot\vec{x}}\,d^2\vec{q}. \tag{2.66}$$

In reality, the above equality can not be exact due to the following two facts :

- The length of the sampling track L_s is finite.
- The spatial resolution of the sampling, Δ_s, is not infinitesimal.

These two facts are valid for both experimental and synthesized roughness data. Therefore, it is necessary to have another expression of the correlation function with the power spectrum. This expression can be derived from the relationship between the sampling limits and integral limits of (2.66) :

$$q_{\min} = \frac{2\pi}{L_s}, \qquad q_{\max} = \frac{2\pi}{\Delta_s}. \tag{2.67}$$

By truncating (2.66) with finite integral range,

$$\begin{aligned} N_t(x,y) &= 2\int_{q_{y\min}}^{q_{y\max}} e^{-iq_y y}\,dq_y \left\{ \int_{q_{x\min}}^{q_{x\max}} \left[P(q_x,q_y)e^{-iq_x x} + P(-q_x,q_y)e^{iq_x x}\right] dq_x \right\} \\ &= 2\int_{q_{x\min}}^{q_{x\max}} e^{-iq_x x}\,dq_x \left\{ \int_{q_{y\min}}^{q_{y\max}} \left[P(q_x,q_y)e^{-iq_y y} + P(q_x,-q_y)e^{iq_y y}\right] dq_y \right\}. \end{aligned} \tag{2.68}$$

Thus, the actual correlation function $N''(\vec{x})$ is :

$$N''(\vec{x}) = N_h(\vec{x}) \times N_t(\vec{x}). \tag{2.69}$$

Therefore, the upper bound of the *RMS* scaling factor is :

$$\frac{\sqrt{\langle\gamma^2\rangle}(\text{window})}{\sqrt{\langle\gamma^2\rangle}(\text{true})} = \sqrt{\frac{N''(0)}{N(0)}} = \sqrt{\frac{N_h(0)N_t(0)}{N(0)}} \le \sqrt{N_h(0)}. \tag{2.70}$$

As an example, the following isotropic Goff-Jordan power spectrum ($D = 2.5$) is used to compute

the correction term $N_t(0, 0)$ to compensate the finite sampling effect.

$$P(q_x, q_y) = \frac{C_l^2}{2\pi\left[1 + (q_x C_l)^2 + (q_y C_l)^2\right]^{3/2}}, \tag{2.71}$$

where the fractal dimension is 2.5, and its correction term is :

$$\begin{aligned} N_t(0,0) = \frac{2}{\pi} \times \Bigg\{ & \arctan\left[\frac{C_l^2 q_{x_2} q_{y_2}}{\sqrt{1 + (C_l q_{x_2})^2 + (C_l q_{y_2})^2}}\right] - \arctan\left[\frac{C_l^2 q_{x_2} q_{y_1}}{\sqrt{1 + (C_l q_{x_2})^2 + (C_l q_{y_1})^2}}\right] \\ & - \arctan\left[\frac{C_l^2 q_{x_1} q_{y_2}}{\sqrt{1 + (C_l q_{x_1})^2 + (C_l q_{y_2})^2}}\right] + \arctan\left[\frac{C_l^2 q_{x_1} q_{y_1}}{\sqrt{1 + (C_l q_{x_1})^2 + (C_l q_{y_1})^2}}\right] \Bigg\}, \end{aligned} \tag{2.72}$$

where C_l is the correlation length, q_{x_1}, q_{y_1} are the lower limits of integral (2.68), and q_{x_2}, q_{y_2} are the upper limits. Figure 2-21 shows $N_t(0, 0)$ when $q_{x1} = q_{y1}$ and $q_{y_1} = q_{y_2}$.

As an example, the correlation function of a 2-D rectangular Hanning window is considered. When the rectangular Hanning window is defined as :

$$h(x, y) = \begin{cases} \frac{1}{4}\left[1 + \cos(2\pi x/l_x)\right]\left[1 + \cos(2\pi y/l_y)\right] & \text{for } |x| < l_x,\ |y| < l_y \\ 0 & \text{otherwise} \end{cases}, \tag{2.73}$$

its auto-correlation function becomes :

$$\begin{aligned} N_h(x, y) = & \frac{1}{(16\pi)^2}\left\{\frac{2\pi}{l_x}(l_x - |x|)\left[2 + \cos(2\pi x/l_x)\right] + 3\sin(2\pi|x|/l_x)\right\} \\ & \times\left\{\frac{2\pi}{l_y}(l_y - |y|)\left[2 + \cos(2\pi y/l_y)\right] + 3\sin(2\pi|y|/l_y)\right\}, \quad \text{for } |x| < l_x,\ |y| < l_y, \end{aligned} \tag{2.74}$$

and the square root value of $N_h(x, y)$ at the origin is :

$$\sqrt{N_h(0, 0)} = \frac{3}{8}. \tag{2.75}$$

The 2-D rectangular Hanning window and its correlation function are shown in Figure 2-22 and Figure 2-23. The maximum for the scaling factor becomes 0.375 for the 2-D Hanning window, which is less than 0.5 by the volume ratio method. This number corresponds to an effective area ratio of 0.140625. It should be also emphasized that the simple scaling of roughness is not enough to compensate for the window effects. There are additional windowing effects to be considered.

In order to investigate the windowing effects on the input power spectrum, a pair of 1-D power spectrum and its correlation function are used to compute the effective power spectrum caused by a 1-D Hanning window function. The power spectrum and correlation function are defined as follows :

$$C_\gamma(x) = e^{-|x|/L}, \qquad P_\gamma(k) = \frac{\sigma_\gamma^2 L}{\pi\left(k^2 L^2 + 1\right)}, \tag{2.76}$$

where L is the correlation length. For the 1-D Hanning window, the window correlation function

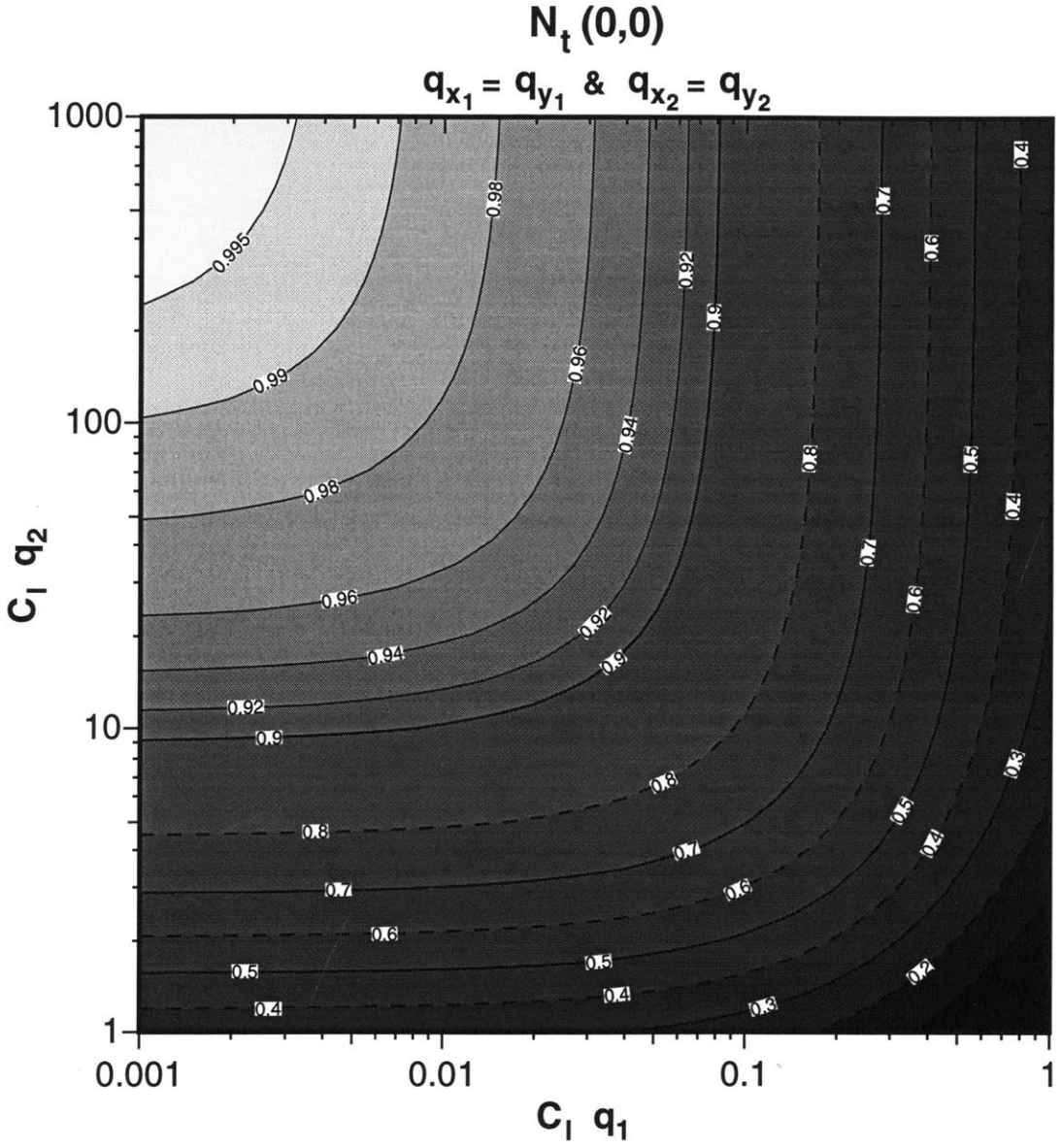

Figure 2-21: Correction term $N_t(0, 0)$ to compensate for the finite sampling effect for $q_{x_1} = q_{y_1}$ and $q_{y_1} = q_{y_2}$.

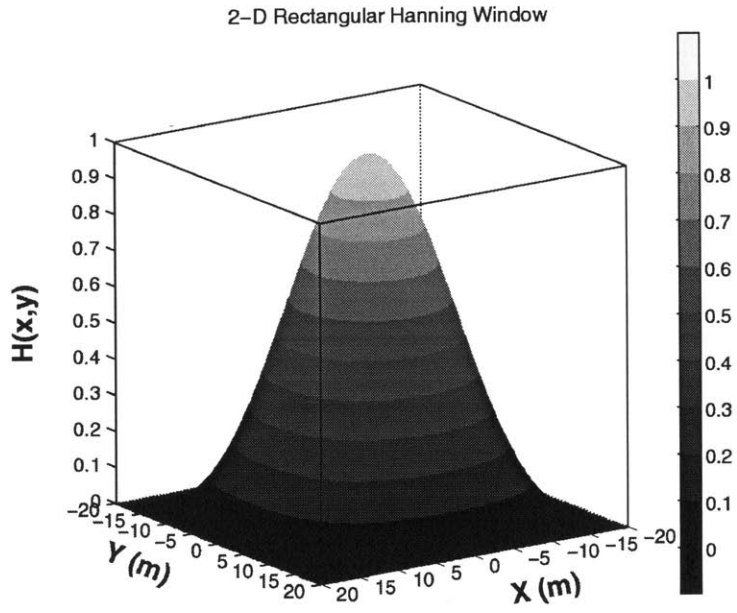

Figure 2-22: 2-D rectangular Hanning window : $l_x = l_y = 40m$ and $N_x = N_y = 128$.

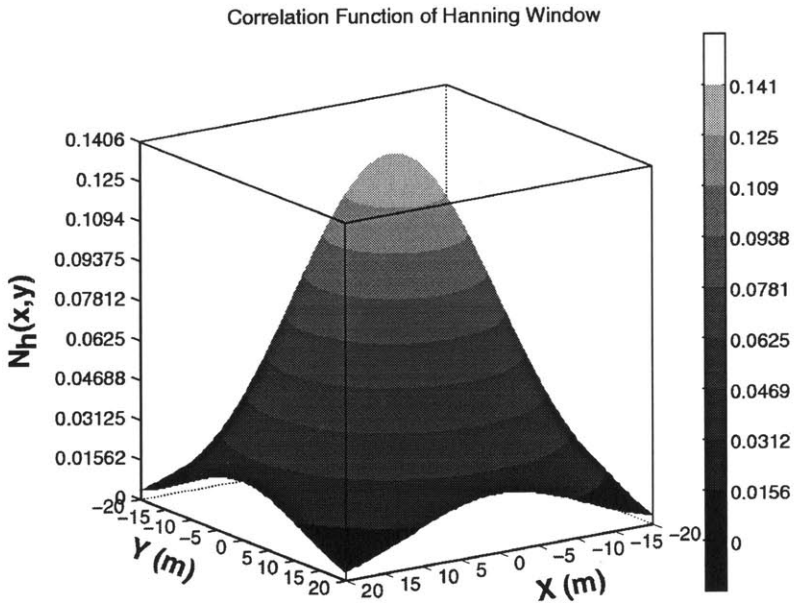

Figure 2-23: Auto-correlation function of a 2-D rectangular Hanning window.

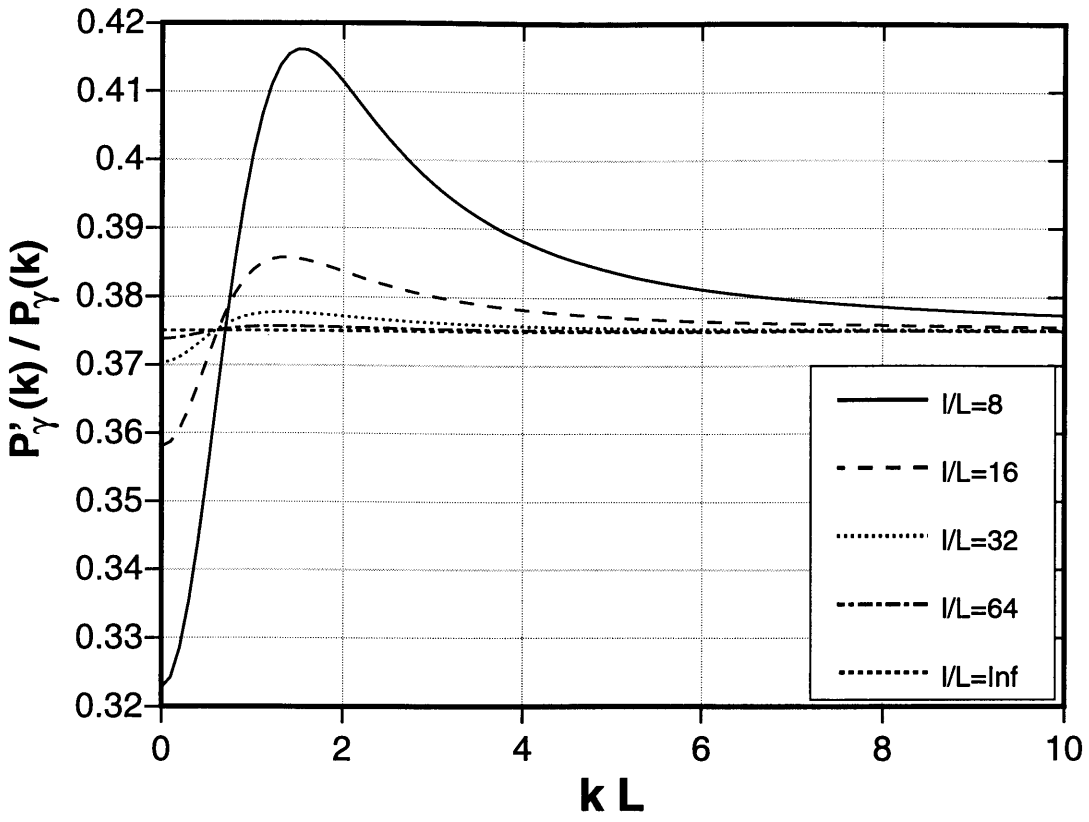

Figure 2-24: Ratio of a windowed power spectrum $P'_\gamma(k)$ to the original power spectrum $P_\gamma(k)$ as a function of dimensionless wavenumber kL and the length ratio l/L.

is :

$$N_h(x) = \begin{cases} \frac{1}{8l}(l-|x|)\,[2+\cos(2\pi x/l)] + \frac{3}{16\pi}\sin(2\pi|x|/l)| & \text{for } |x| < l \\ 0 & \text{otherwise} \end{cases}, \tag{2.77}$$

where l is the window length. By the definition, the correlation function after applying Hanning window becomes :

$$\begin{aligned} C'_\gamma(x) &= N_h(x)e^{-|x|/L} \\ &= \begin{cases} \left\{\frac{1}{8l}(l-|x|)\,[2+\cos(2\pi x/l)] + \frac{3}{16\pi}\sin(2\pi|x|/l)\right\}e^{-|x|/L} & \text{for } |x| < l/2 \\ 0 & \text{otherwise} \end{cases} \end{aligned} \tag{2.78}$$

From the above correlation function, the modified power spectra can be expressed as a function of a dimensionless patch length kL and correlation length l/L. The ratios among the modified power spectra and input power spectrum are plotted in Figure 2-24.

After the pre-processing, actual statistical analysis can be performed. The general interests of roughness data are focused on the first and the second order statistics. The height probability density function (PDF) is the most common form of first order statistics, while the auto-correlation function is the most common form for the second order. Often, the power spectrum of roughness

heights is used instead because it is a Fourier transform pair of the corresponding auto-correlation. It should also be emphasized that the first and second order statistics are completely independent. For example, two different rough surfaces can share the same first order statistics while their second order statics are completely different [36].

2.3 Numerical Implementation of Rough Interface Scattering Model

In order to solve the scattered field $s(\vec{x})$ by the same solution technique used for the unperturbed field, $f_v(\vec{x})$ is expanded in an azimuthal Fourier series and transformed using the Hankel transform. The unknown coefficients of the displacement potentials in the spectral domain are obtained by matching boundary conditions [46]. The azimuthal Fourier expansion and the Hankel transform of the spatial virtual source is described in Appendix C. Solving for the scattered field is an evaluation of the virtual source distribution function $\tilde{f}_v^m(k_r)$.

$$\tilde{B}(k_r)\,\tilde{s}^m(k_r) = -\tilde{f}_v^m(k_r). \tag{2.79}$$

Figure 2-25 is a flow chart for implementing the patch scattering model. The left hand of the diagram shows the roughness patch realization and process while the right hand side shows the computation of the unperturbed field potentials including the incident field. By combining the roughness and the unperturbed potentials, the cylindrical virtual force is evaluated by numerical Hankel transform and the azimuthal Fourier series. Finally, the virtual forcing term is inverted by 3-D OASES to yield the scattered field.

2.4 Benchmark

In order to verify the validity of the 'patch' scattering model, a benchmark is performed against an analytic perturbation solution. For comparison purpose, in-plane scattering strengths are computed. The scattering strength is defined in Reference [57] :

$$S_{s,v}\left(\vec{k}_s, \vec{k}_i\right) = 10\log_{10}\left[\lim_{r\to\infty} \frac{I_s\left(\vec{k}_s, \vec{k}_i, r\right) r^2}{I_i\left(\vec{k}_i\right) r_{ref}^2}\right] \text{(dB re } r_{ref}\text{)}, \tag{2.80}$$

where the subscripts s and v represent surface and volume scattering, respectively. $\vec{k}_s$ is the wavenumber vector in the scattering direction and $\vec{k}_i$ corresponds to the incident wavenumber vector. I_s is the scattering intensity generated by a scatterer of unit area or volume (i.e. $1m^2$ for surface scatterer or $1m^3$ for a volume scatterer), which is measured at range r. I_i is the intensity of the incident plane wave. In Reference [3], a wave scattering formulation is derived based on the first order perturbation theory. The medium consists of two fluid half spaces divided by a rough interface. Assuming the power spectrum of rough interface is known, the intensity is expressed as :

$$I_s\left(\vec{k}_s, \vec{k}_i\right) = A_M \frac{k_1^4}{R_i^2 R_s^2} \left|F\left(\vec{k}_i, \vec{k}_s\right)\right|^2 P_\gamma\left(\vec{\kappa}_s - \vec{\kappa}_i\right), \tag{2.81}$$

where R is the distance from the center of the scattering surface to the source or observation point and A_M is the area of the reference scattering surface. $\vec{\kappa}$ is the projection of the wave vector $\vec{k}$ on the horizontal plane. The subscripts i and s indicate 'incident' and 'scattered' wave components, respectively. Figure 2-26 shows the coordinate system with the incident and scattered wave

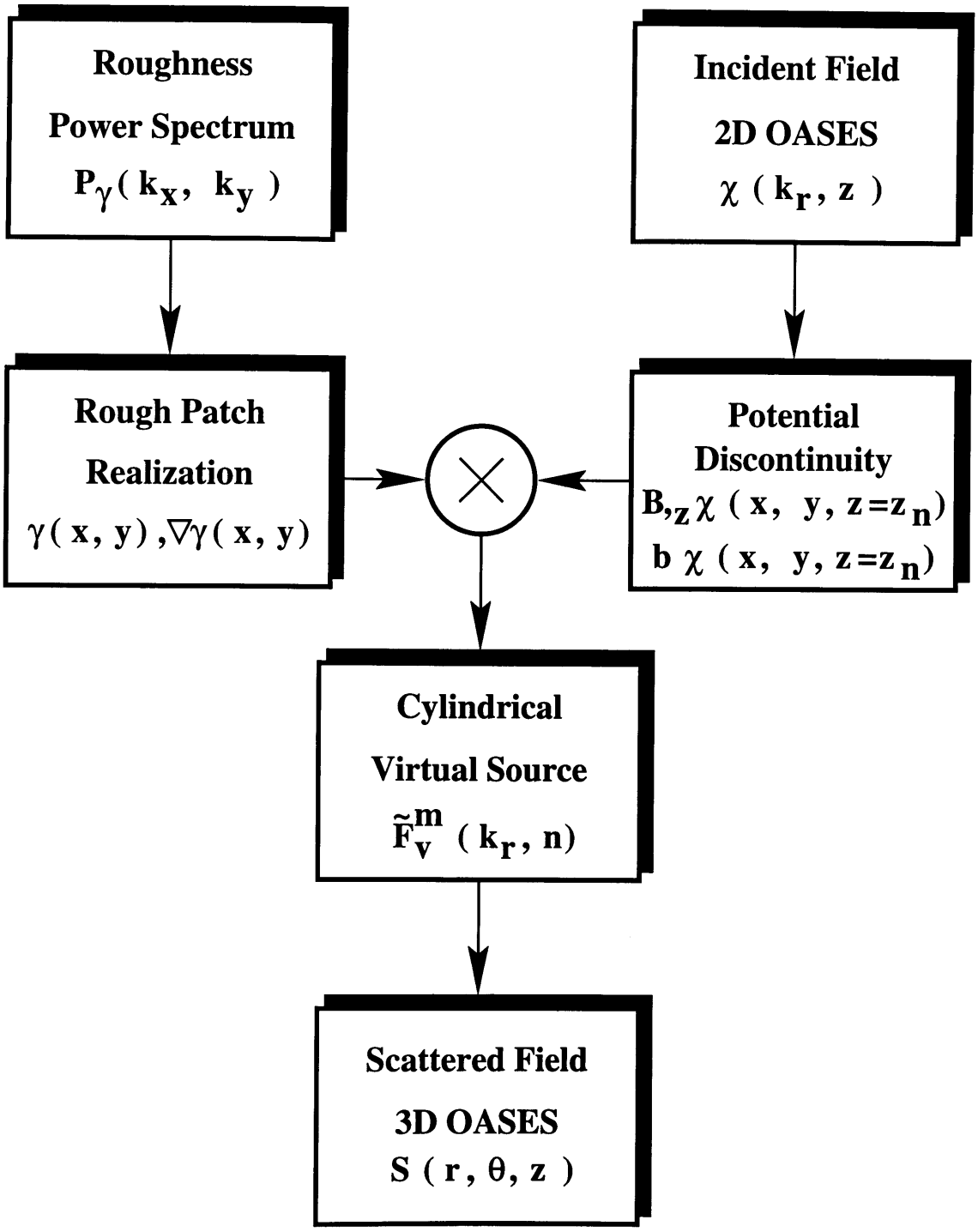

Figure 2-25: Diagram of the patch scattering model.

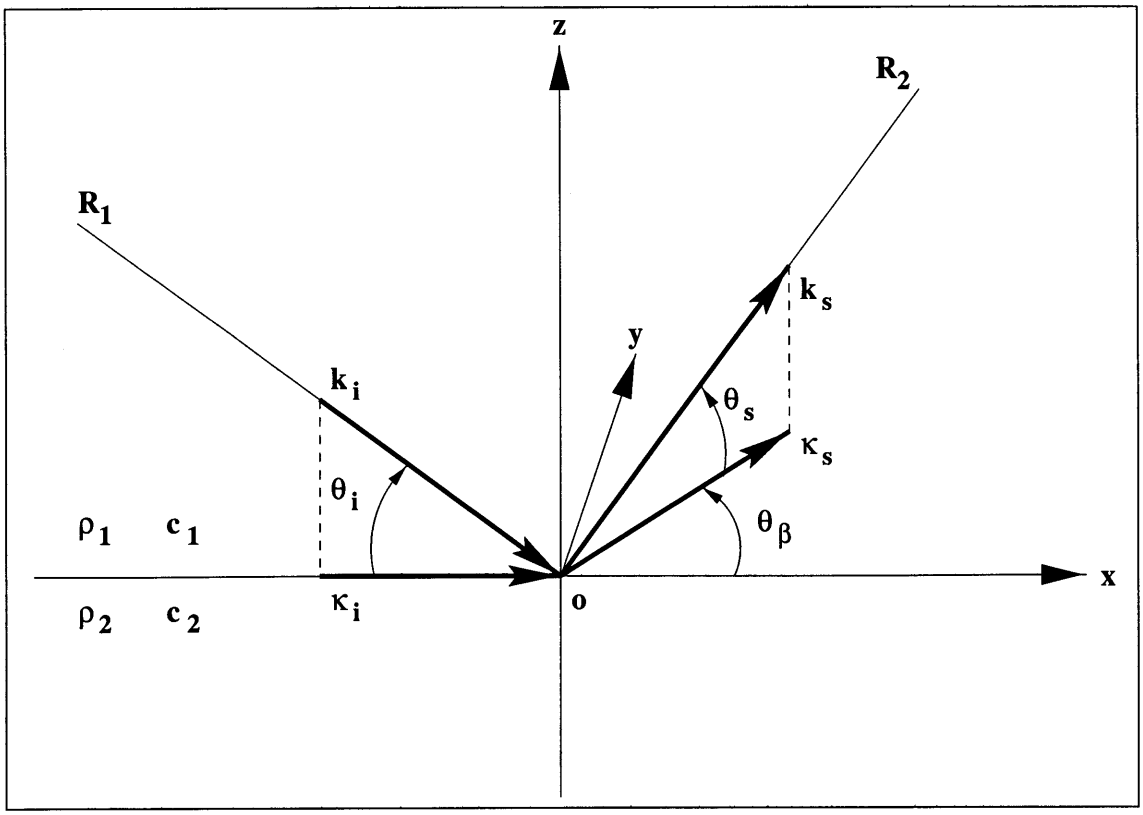

Figure 2-26: Configuration of incident and scattered wave vectors in two fluid half spaces with a rough interface.

vectors. The corresponding scattering strength is :

$$S_s\left(\vec{k}_s, \vec{k}_i\right) = 10\log_{10}\left[k_1^4\left|F\left(\vec{k}_i, \vec{k}_s\right)\right|^2 P_\gamma\left(\vec{\kappa}_s - \vec{\kappa}_i\right)\right]. \tag{2.82}$$

The function F is defined as :

$$\begin{aligned} 2k_1^2 F\left(\vec{k}_s, \vec{k}_i\right) = & \frac{(\rho_2 - \rho_1)\sqrt{k_1^2 - \left|\vec{\kappa}_s\right|^2}}{\rho_1\sqrt{k_2^2 - \left|\vec{\kappa}_s\right|^2} + \rho_2\sqrt{k_1^2 - \left|\vec{\kappa}_s\right|^2}} \\ & \times\left\{\left[-\vec{k}_i \cdot \vec{\kappa}_s + \frac{k_1^2\rho_2 - k_2^2\rho_1}{\rho_2 - \rho_1}\right]\left[1 + V\left(\vec{k}_i\right)\right] - \sqrt{k_2^2 - \left|\vec{\kappa}_s\right|^2}k_{iz}\left[1 - V\left(\vec{k}_i\right)\right]\right\}, \end{aligned} \tag{2.83}$$

where wave vectors $\vec{k}_i$, $\vec{k}_s$, $\vec{\kappa}_i$ and $\vec{\kappa}_s$ are defined as follows :

$$\begin{aligned} \vec{k}_i &= k_1(\cos\theta_i, 0, -\sin\theta_i), \\ \vec{k}_s &= k_1(\cos\theta_s\cos\theta_\beta, \cos\theta_s\sin\theta_\beta, \sin\theta_s), \\ \vec{\kappa}_i &= k_1(\cos\theta_i, 0, 0), \\ \vec{\kappa}_s &= k_1(\cos\theta_s\cos\theta_\beta, \cos\theta_s\sin\theta_\beta, 0). \end{aligned} \tag{2.84}$$

The plane wave reflection coefficient V is a function of the incident grazing angle θ_i.

$$V = \frac{(\rho_2/\rho_1)\sin\theta_i - \sqrt{(c_1/c_2)^2 - \cos^2\theta_i}}{(\rho_2/\rho_1)\sin\theta_i + \sqrt{(c_1/c_2)^2 - \cos^2\theta_i}} = \frac{\zeta\sin\theta_i - \sqrt{\eta - \cos^2\theta_i}}{\zeta\sin\theta_i + \sqrt{\eta - \cos^2\theta_i}}, \tag{2.85}$$

where ζ and η are defined as :

$$\zeta = \rho_2/\rho_1, \qquad \eta = (c_1/c_2)^2. \tag{2.86}$$

F is a function of incident and scattered wave vectors. Close examination of this function reveals that it is independent of frequency and that it can be expressed as a function of incident angle, scattered angle, bistatic angle, density ratio, and the ratio of compressional phase speeds as follows :

$$\begin{aligned} F(\theta_i, \theta_s, \theta_\beta) = & \frac{1}{2}\frac{(\zeta - 1)\sin\theta_s}{\sqrt{\eta - \cos^2\theta_s} + \zeta\sin\theta_s} \\ & \times \left\{ \left[\frac{\zeta - \eta}{\zeta - 1} - \cos\theta_i \cos\theta_s \cos\theta_\beta \right](1 + V) + \sin\theta_i \sqrt{\eta - \cos^2\theta_s}(1 - V) \right\}. \end{aligned} \tag{2.87}$$

The benchmark scenario chosen here is shown in Figure 2-27. The upper half space is a fluid medium (water) with C_p = 1500m/s and ρ = 1g/cm^3. The lower half space is basalt which is modeled as either fluid or elastic medium with C_p = 5000m/s, C_s = 2000m/s and ρ = 2.2g/cm^3. The interface between the two half spaces is rough. Its roughness is modeled by an isotropic Goff-Jordan power spectrum with fractal dimension 2.5 and 6m correlation length. The dimension of roughness patches is 256m by 256m and the number of grids is 512 in each direction. The incident wave is a compressional plane wave with f = 250Hz and a 5° grazing angle. Figure 2-28 shows the in-plane scattering strengths of 3 cases. The solid line is computed using the formal averaging formulation in Bass and Fuks [3]. The dashed line is obtained using the patch scattering model in this thesis with 256 ensembles of scattering realization. The dotted line is also from the patch scattering model, but the lower basalt half space allows an additional elastic property, shear wave speed. The thin solid lines correspond to the compressional critical angles while the thin dashed lines indicate the shear critical angles in the forward and backward directions. With only 256 ensembles, the patch scattering model can reproduce the analytical solution derived by the formal averaging of scattered field. Computation of each ensemble was completed within the order of minutes on a desktop workstation. While the numerical model is accurate over most of the angular regime, a small discrepancy in the forward direction arises as the scattering grazing angle approaches to zero. The numerical model produces a lower scattered field than the analytic solution. This effect is caused by the reduced projected area of the finite-sized roughness patch for the numerical model when the scattering grazing angle become small. In other hand, the projected area of the insonified region is infinite for the analytic solution. This discrepancy is not practically important in a real situation because the area of insonification is finite for sonar systems with finite beam widths. Therefore, using a roughness patch of finite size for scattering computation is closer to a real situation.

The benchmark case shows that the patch scattering model is correctly implemented. When the layering of a medium becomes complex or contains elastic properties, there is no analytic solution available in a compact form such as the above solution by Bass and Fuks. Also, the model can compute the scattered field caused by beam incidence, too. The examples suggest that the efficiency of the model can be exploited further for the simulation of narrow band pulses in the

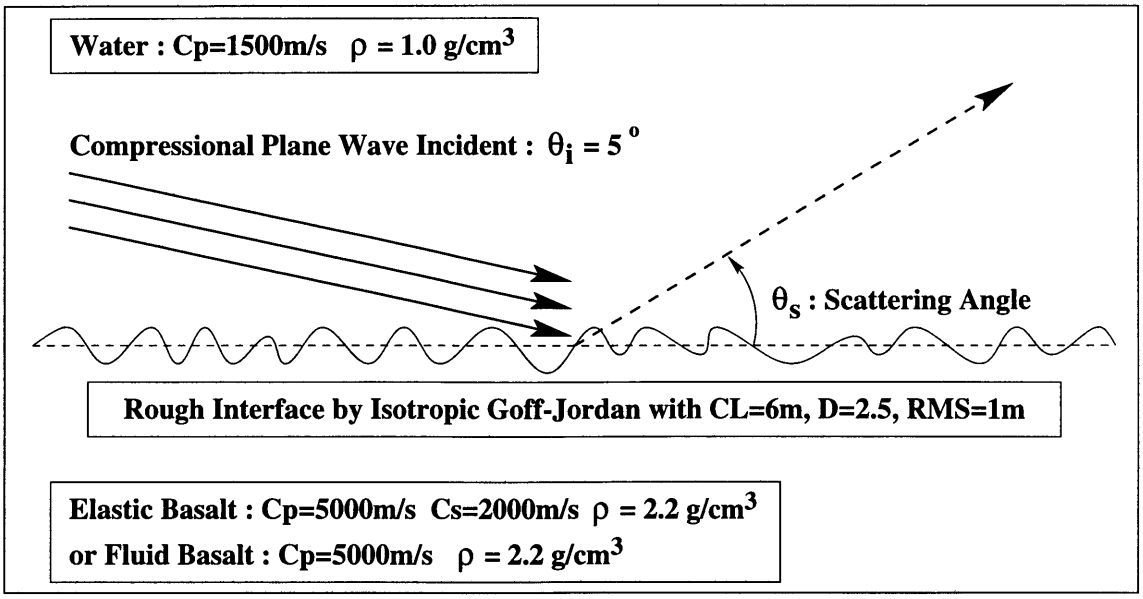

Figure 2-27: Benchmark scenario for the rough interface scattering model : case of two fluid half spaces divided by a rough interface.

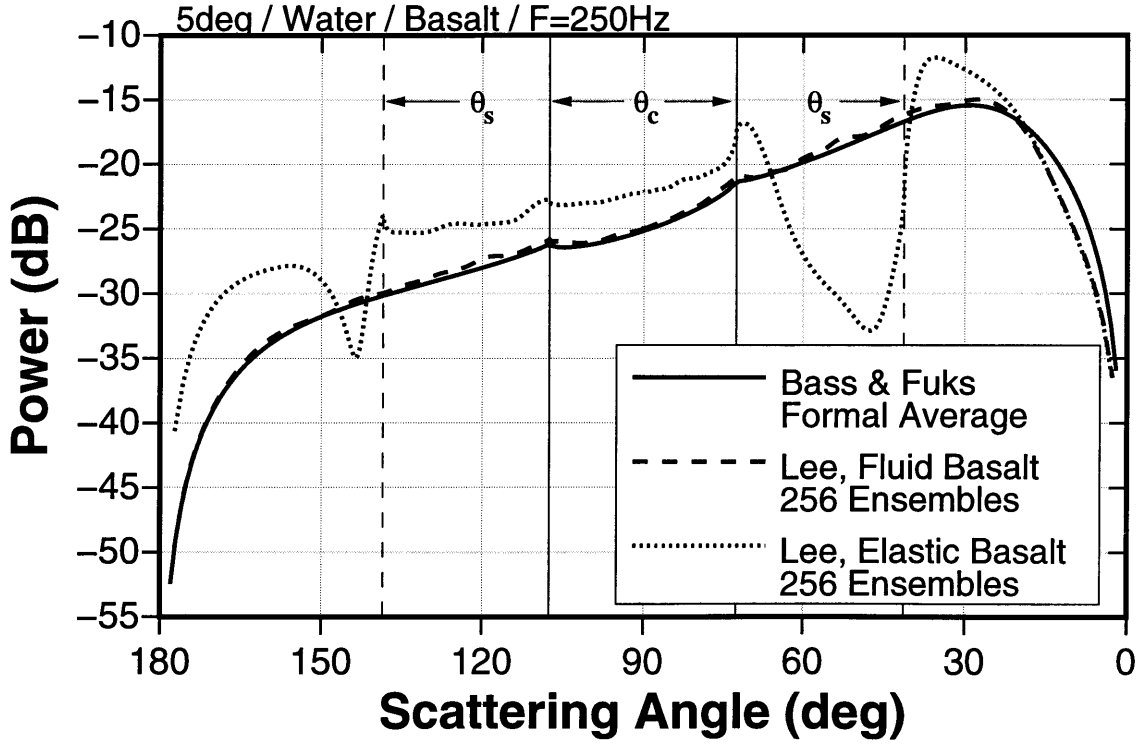

Figure 2-28: Comparison with an analytic perturbation solution : a formal average solution for fluid basalt, a numerical solution for fluid basalt, and a numerical solution for elastic basalt.

time domain as well as the computation of statistical properties in the spatial domain.

2.5 Effect of Medium Properties

From this section to the end of the chapter, many numerical simulation results are presented. In order to clarify the numerical results, the coordinate system is explained and each type of plots is described before the discussion on numerical results.

The coordinate systems used in the numerical results are Cartesian and polar coordinates shown in Figure 2-29. The Cartesian coordinates (x, y, z) follow the right-hand-side rule with the depth coordinate z pointing down. The polar coordinate system uses the polar angle ϕ measured from the negative z axis. There are four types of major numerical results presented in this thesis.

The first type of plot is called 'angular spectrum contour of scattered field'. The angular spectrum shows the distribution of the scattered energy as a function of polar and azimuthal angles. In Figure 2-29, the polar angle ϕ is represented using the radial coordinate while the azimuthal angle θ is represented using the azimuthal coordinate.

The second type of plot is called 'in-plane scattering plot' as shown in Figure 2-30. The in-plane scattering plot shows the angular spectrum of the scattered field when the bistatic angle is set to 0 or π. The in-plane scattering angle Θ is related to the scattering polar angle ϕ.

The third and fourth types of plot types are the 'scattered field cuts' in the horizontal and vertical planes as shown in Figure 2-31. The term 'scattered field' refers to the transmission loss of the scattered wave. The horizontal scattered field corresponds to the field parallel to the $x-y$ plane while the vertical scattered field is normal to the $x-y$ plane.

Two roughness patches are generated for the first roughness patch scattering scenario shown in Figure 2-34. The first roughness patch (Figure 2-32) is generated using an isotropic Goff-Jordan power spectrum. The second roughness patch (Figure 2-33) is generated using an anisotropic Goff-Jordan power spectrum. Severe anisotropy ($C_{L1}/C_{L2} = 8$ and $\theta_s = 45°$) is expected to produce a strong scattered field in the out-of-plane directions.

2.5.1 Comparison between Elastic and Fluid Cases

The first scattering scenario in Figure 2-34 is used to demonstrate medium effects such as shear properties. The scenario is the case of two half spaces separated by a rough interface. The incident field is a compressional plane wave at $f = 3kHz$ and the incident grazing angle is either 15° or 45°. With the water upper half space, several types of media are chosen for the lower half space to investigate the effects of elastic properties on rough interface scattering.

The first set of numerical results are in-plane scattered fields with elastic sand, fluid sand, and elastic limestone half spaces. The incident angle is 15°, which is a subsonic incidence to compressional waves in the lower half spaces. An isotropic roughness patch (Figure 2-32) is used. When the elastic sand (Figure 2-35(a)) and the fluid sand (Figure 2-35(b)) cases are compared, one major difference is observed. The scattered energy in the elastic sand half space is about $12dB$ higher than fluid sand case. This difference is caused by the shear property of elastic sand half space. By allowing shear waves, the elastic sand half space can support scattered energy in the form of SH and SV waves. This conclusion can be drawn by examining the major scattering angles in the lower half space. By applying Snell's law between compressional waves in the water half space and shear waves in the elastic sand half space, this angle is confirmed to correspond to shear waves. When the limestone lower half space is used instead, strong shear conversion of the incident wave is observed in Figure 2-35(c). The scattered shear wave also follows Snell's law. The major difference between elastic sand and limestone can be found in the shallow polar angle regime ($\phi < 20°$). A strong scattered field is observed in this regime for the elastic limestone case. This can be explained by the higher compressional phase speed of elastic limestone. By increasing

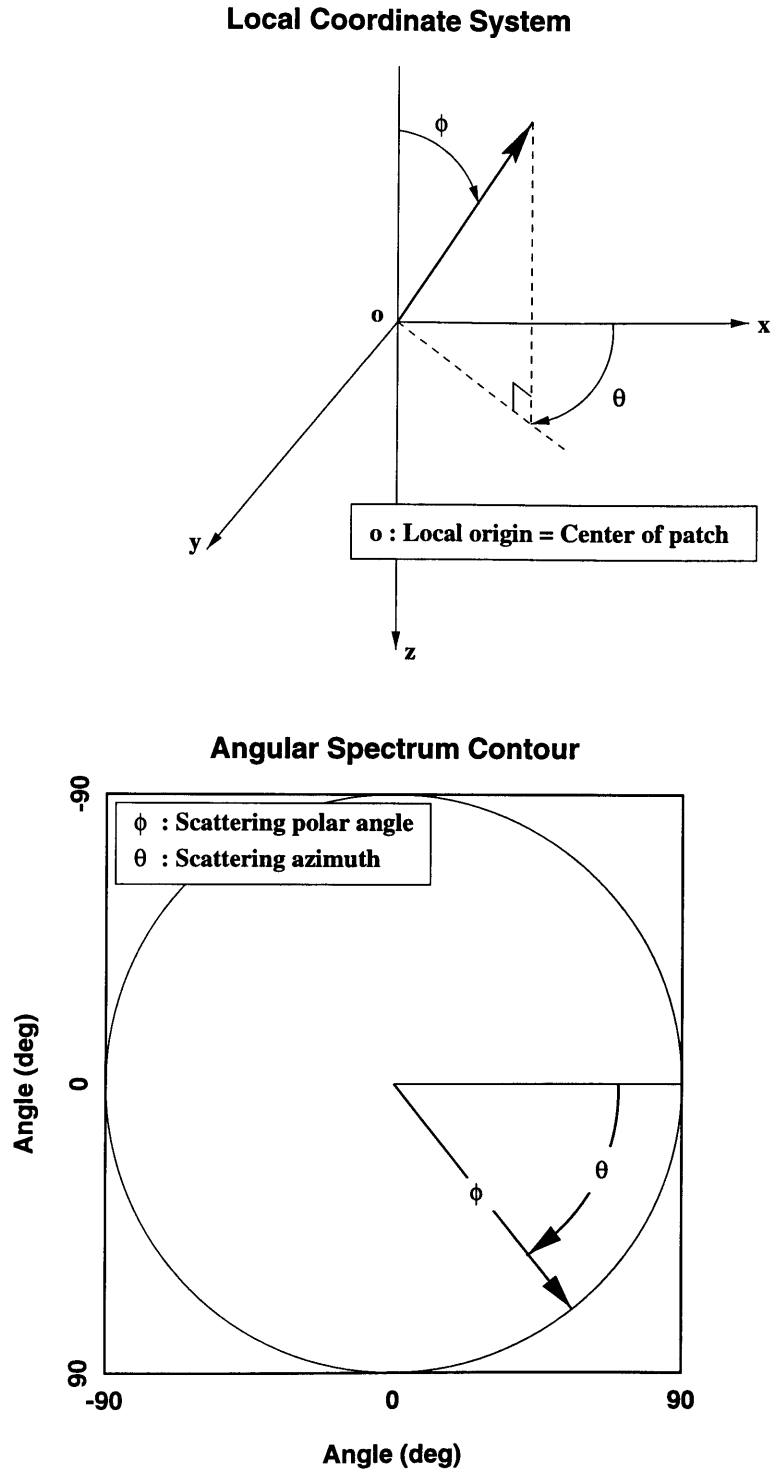

Figure 2-29: Coordinate notations in angular spectrum plots. The radial coordinate corresponds to the scattering polar angle ϕ and the angular coordinate corresponds to the scattering azimuthal (bistatic) angle θ.

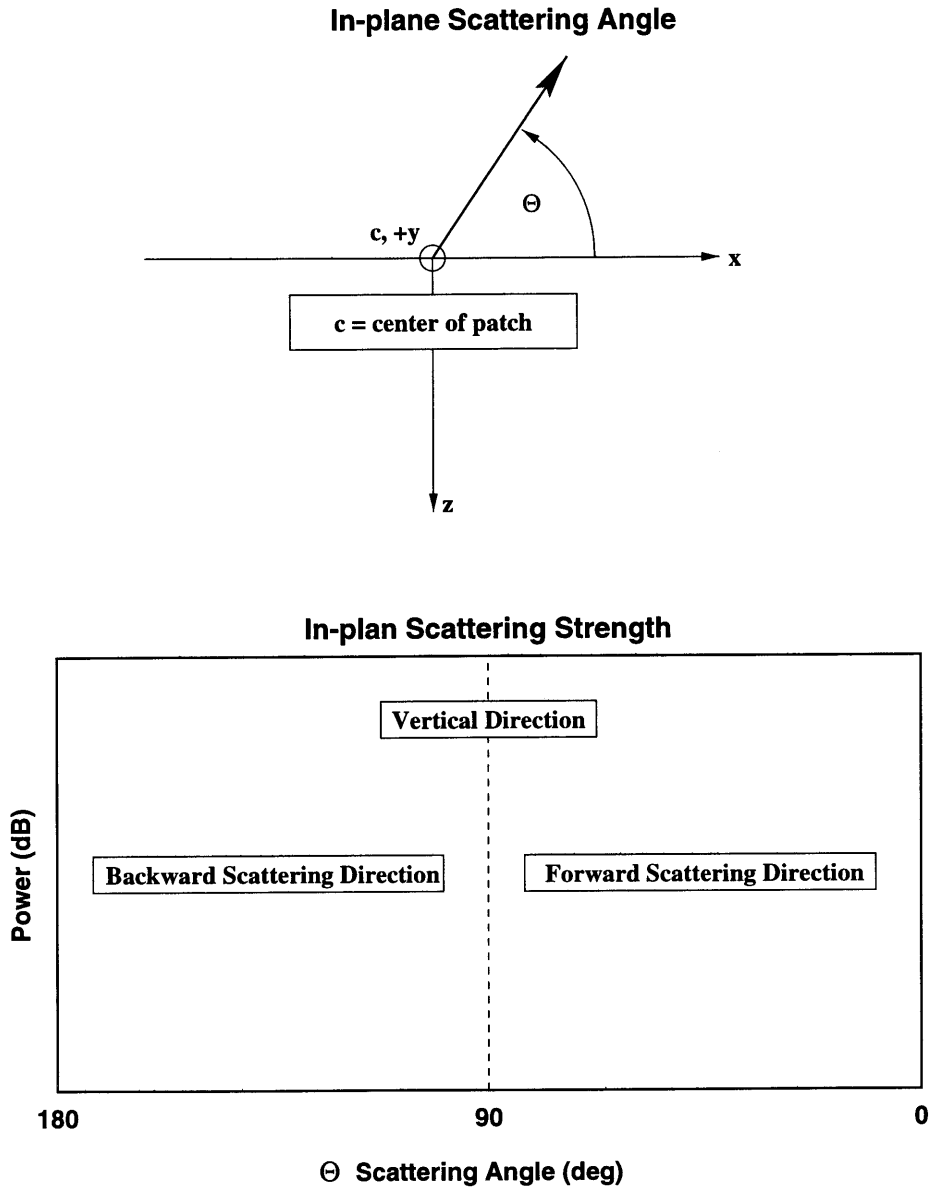

Figure 2-30: Coordinate notation for in-plane scattering strength plots. When the in-plane scattering angle Θ is between 0 and $\pi/2$, it is equal to $\pi/2 - \phi$ with the bistatic angle $\theta = 0$ (i.e. forward scattering direction). For $\pi/2 < \Theta < \pi$, the bistatic angle θ is fixed at π (i.e. backward scattering direction) and Θ corresponds to $\pi/2 + \phi$.

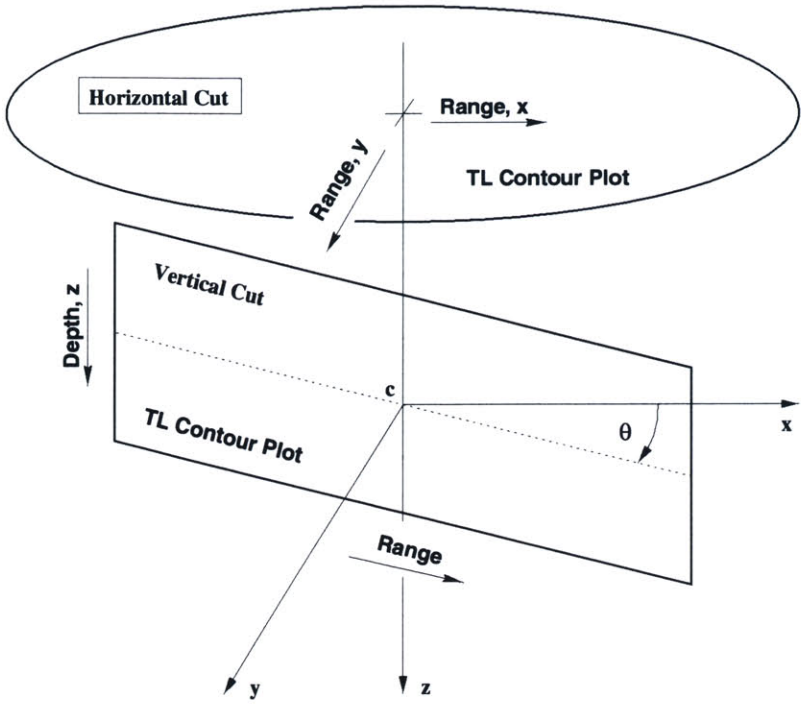

Figure 2-31: Coordinate notation for transmission loss contour plots. Horizontal field cuts are obtained at fixed depths (z = const), while vertical fields are computed at fixed azimuthal angles (θ = const). In-plane vertical cut corresponds to the case of $\theta = 0, \pi$.

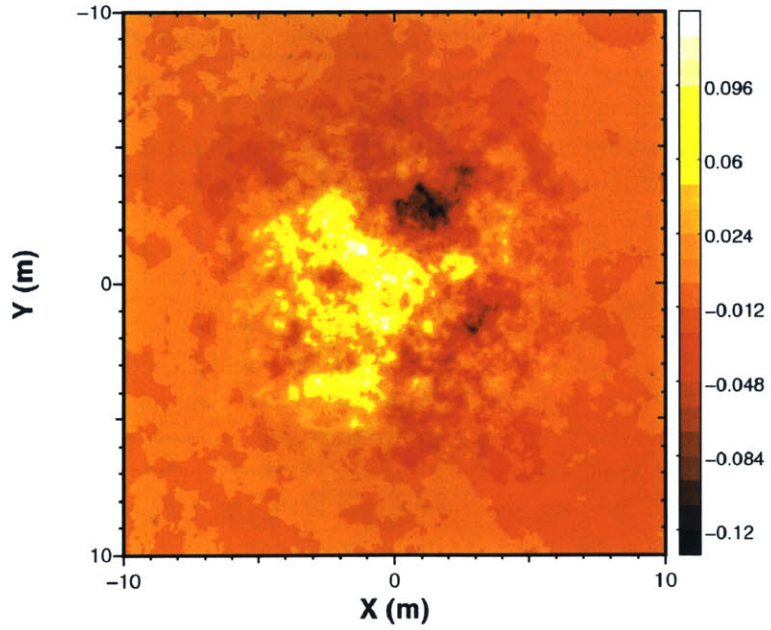

Figure 2-32: Roughness patch generated by an isotropic Goff-Jordan power spectrum ($N_x = N_y = 512$, $l_x = l_y = 20m$, $C_L = 2m$, $D = 2.5$, and $\sqrt{\langle \gamma^2 \rangle} = 6.25cm$).

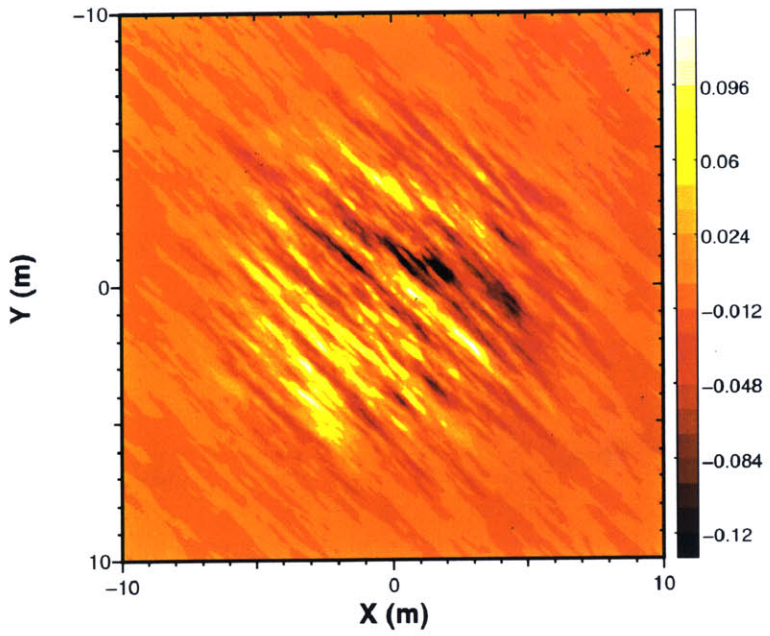

Figure 2-33: Roughness patch generated by an anisotropic Goff-Jordan power spectrum ($N_x = N_y = 512$, $l_x = l_y = 20m$, $C_{L1} = 2m$, $C_{L2} = 0.25m$, $\theta_s = 45°$, $D = 2.5$, and $\sqrt{\langle \gamma^2 \rangle} = 6.25cm$).

the compressional critical angle, the scattered wave in the upper half space can propagate within a wider angular space.

The next numerical examples (Figure 2-36) show the effect of elasticity on horizontal scattered field when the roughness is strongly anisotropic. The anisotropic roughness patch (Figure 2-33) is located between the water upper half space and the elastic (or fluid) sand lower half space. For both cases, the strong anisotropy of the roughness causes dominant scattered field at $\theta = \pi/2$ as well as in the forward direction ($\theta = 0$). The noticeable differences between the two cases are as follows. Elastic sand scatters energy in a relatively wider azimuthal range ($\pi/2 < \theta < 3/2\pi$). Fluid sand produces forward scattering which is $6dB$ higher than in the case of elastic sand, but the azimuthal energy distribution is relatively narrow.

The next numerical examples show in-plane scattered fields (vertical cuts) when the incident angle becomes 45°. The roughness patch is the isotropic patch used in the previous cases. Because the incident angle is in the supersonic regime in the sand lower half space, the scattered compressional waves in the sand half space can be observed in both cases. Unlike fluid sand, elastic sand exhibits steep shear scattered waves in the lower half space as well as interface wave. The interface wave decays exponentially away from the center of the roughness patch.

The significance of the shear wave can be explained by examining the reflection coefficients from the half space with varying the shear wave speed. Figure 2-38 shows the reflection coefficients between water and sand half space. As the shear wave speed of the sand half space increases, the reflection coefficient decreases before and after the compressional critical angle ($\theta_c = 33.6°$). The decrease in the reflection coefficient means that some portion of the energy is transmitted to the lower space as shear waves. In the plots, the reflection coefficients do not change dramatically until the shear wave speed of the sand exceeds $300m/s$, which is 20% of the compressional wave speed in the water half space. Therefore, the effects of shear waves on the scattered field in the upper space are not considered to be significant when the shear wave speed is much lower than

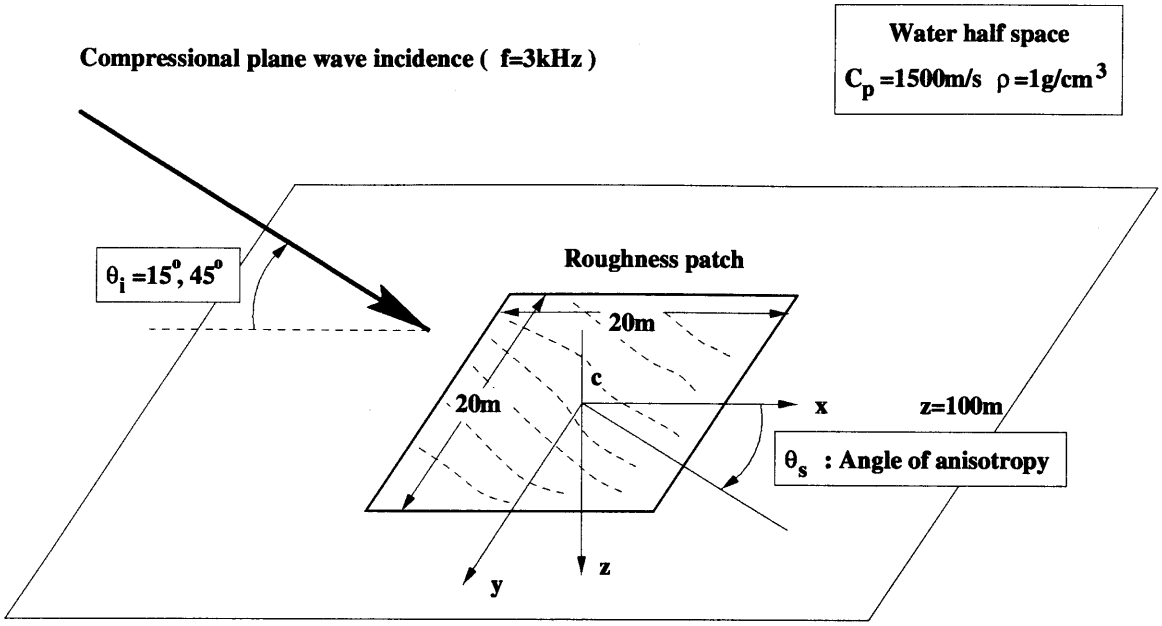

Lower half space	C_p (m/s)	C_s (m/s)	ρ (g/cm^3)
Elastic limestone	2500	1000	2.2
Fluid limestone	2500	0	2.2
Elastic sand	1800	600	1.6
Fluid sand	1800	0	1.6
Elastic basalt	5000	2000	2.4

patch scenario #1

Figure 2-34: Patch scattering scenario : The medium consists of a water upper half space and various types of lower half spaces.

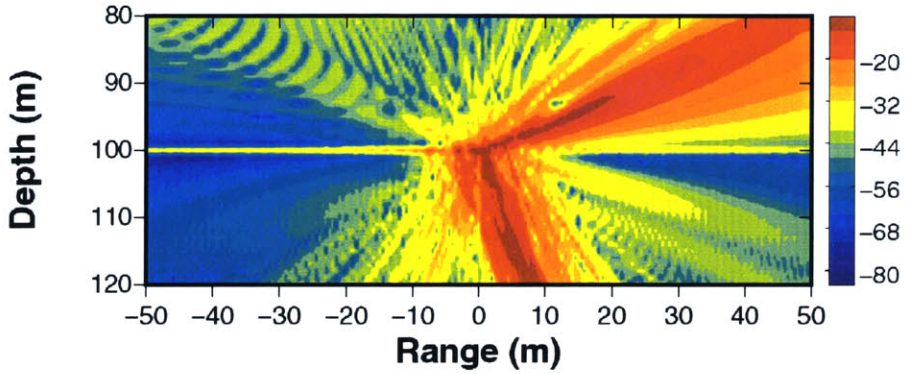

(a) Case of elastic sand lower half space.

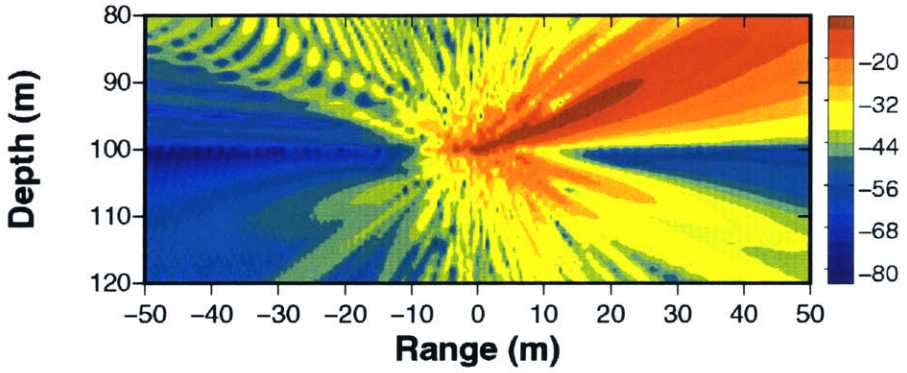

(b) Case of fluid sand lower half space ($C_s = 0m$).

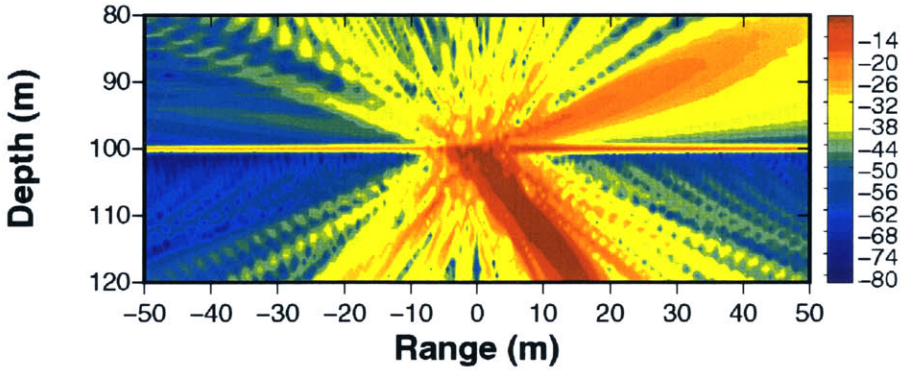

(c) Case of elastic limestone lower half space.

Figure 2-35: In-plane cut of scattered field produced by an isotropic roughness patch (Figure 2-32). The medium is divided at $100m$ depth. Roughness patch is centered at $100m$ depth and $0m$ range. The incident field is a compressional plane wave with 15° grazing angle (θ_i) in the water half space. The incident wave is coming from the left hand side of plot.

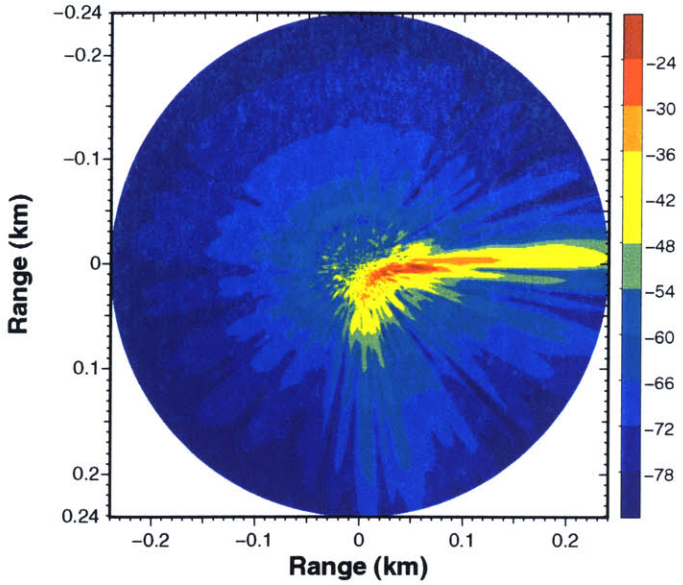

(a) Case of elastic sand lower half space.

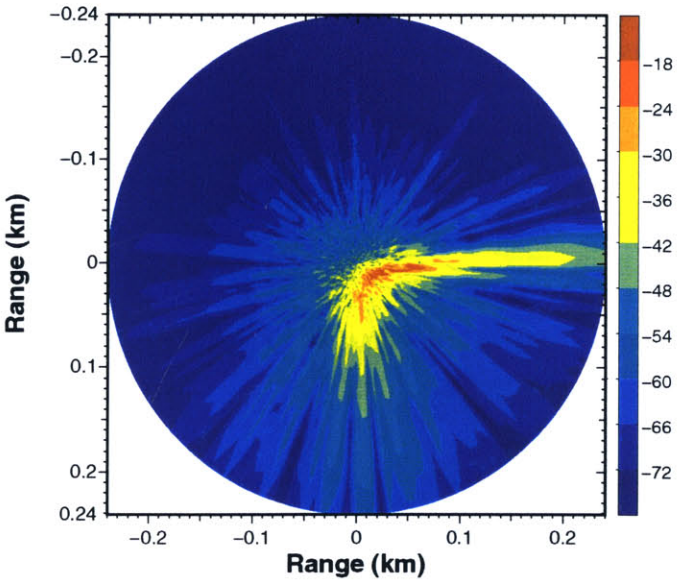

(b) Case of fluid sand lower half space ($C_s = 0m$).

Figure 2-36: Horizontal cut of scattered field at $20m$ above an anisotropic roughness patch (Figure 2-33). The medium is divided at $100m$ depth. Roughness patch is centered at $100m$ depth and $0m$ range. The incident field is a compressional plane wave ($\theta_i = 15°$) in the water half space. The incident wave is coming from the left hand side of plot.

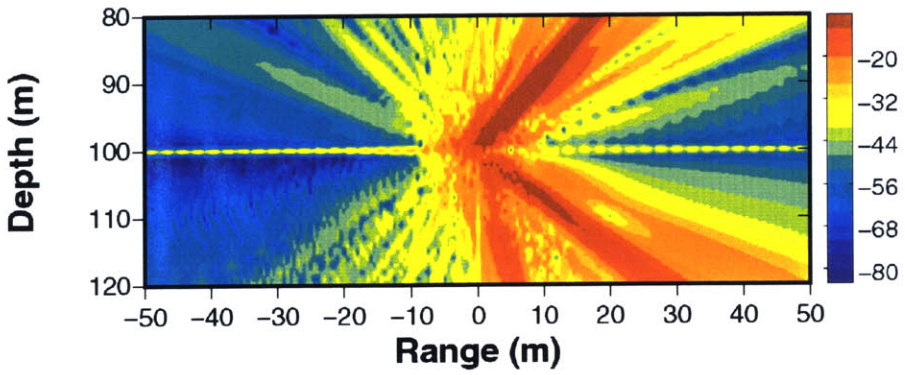

(a) Case of elastic sand lower half space.

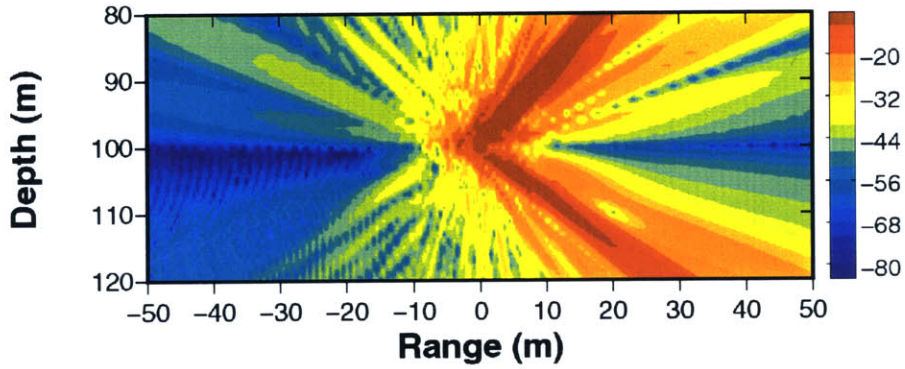

(b) Case of fluid sand lower half space ($C_s = 0m$).

Figure 2-37: In-plane cut of scattered field produced by an isotropic roughness patch (Figure 2-32). The medium is divided at $100m$ depth. Roughness patch is centered at $100m$ depth and $0m$ range. The incident field is a compressional plane wave ($\theta_i = 45°$) in the water half space. The incident wave is coming from the left hand side of plot.

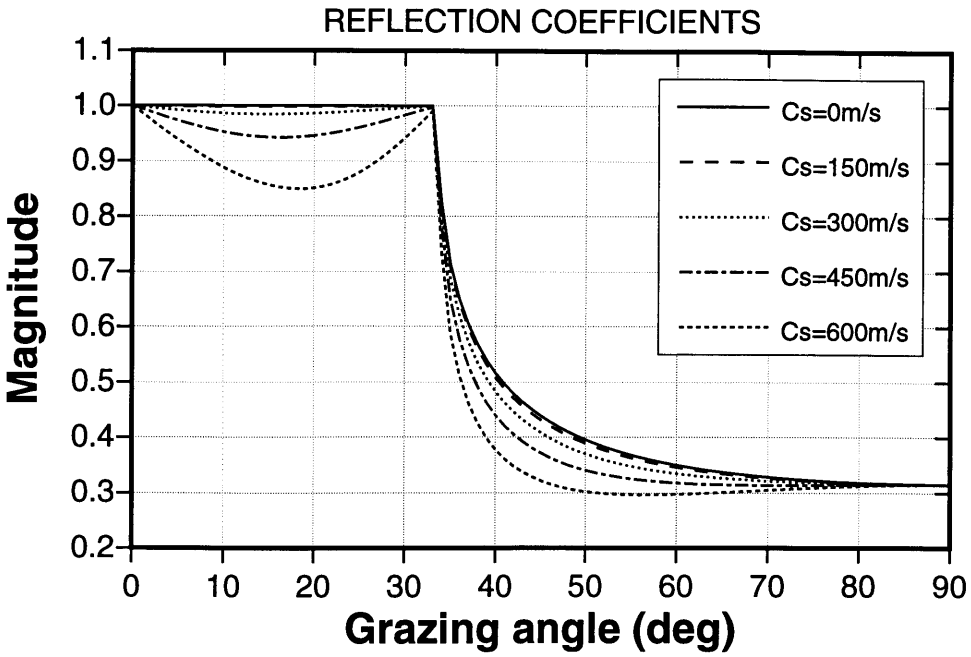

Figure 2-38: Reflection coefficients between water half space (C_p = 1500m/s and ρ = 1.0g/cm^3) and sand half space (C_p = 1800m/s and ρ = 1.6g/cm^3). The shear wave speed of the sand half space (C_s) varies from 0m/s to 600m/s.

the compressional wave speed of the upper space because the shear conversion of incident energy into the lower space is small.

2.5.2 Waveguide Effects

The presence of a waveguide can change the way scattered energy propagates. To demonstrate waveguide effects on rough interface scattering phenomena, a simple numerical scenario is used (Figure 2-39) using the previous isotropic patch. The medium consists of a water column and an elastic sand half space. The incident field is a compressional plane wave at $f = 3kHz$ and the incident angle is either 15° or 45°. As the rough interface scattering formulation (2.20) implies, the scattered field is a function of the unperturbed field. Since the unperturbed field depends on the configuration of the medium, the existence of the waveguide can change the scattered field.

Figure 2-40(a) shows the in-plane scattered field when the incident angle is 15° and the water column is 100m thick. The main scattering features are similar to the case without a waveguide. In the water column, the scattered field is severely distorted in the depth direction. This change is caused by the propagating modal structure of the waveguide. Generally, the modal structure is confined below the critical angle. For this case, most of scattered energy is concentrated below the critical angle because of the shallow incident angle. When the incident angle becomes steep (θ_i = 45°) for the same scenario, the scattered field (Figure 2-40(b)) changes in the water column. Because a major portion of the scattered energy is in the shallow polar angle regime (i.e. close to $\phi = 0$), the scattered wave is relatively unaffected by the modal structure. In order to interfere (or couple) for the scattered wave and the modal structure of the waveguide, their dominant angular regimes must overlap.

The next three sets of numerical results demonstrate the effects of waveguide thickness by taking ensemble averages of scattered fields. As stated in Reference [16], the number of propa-

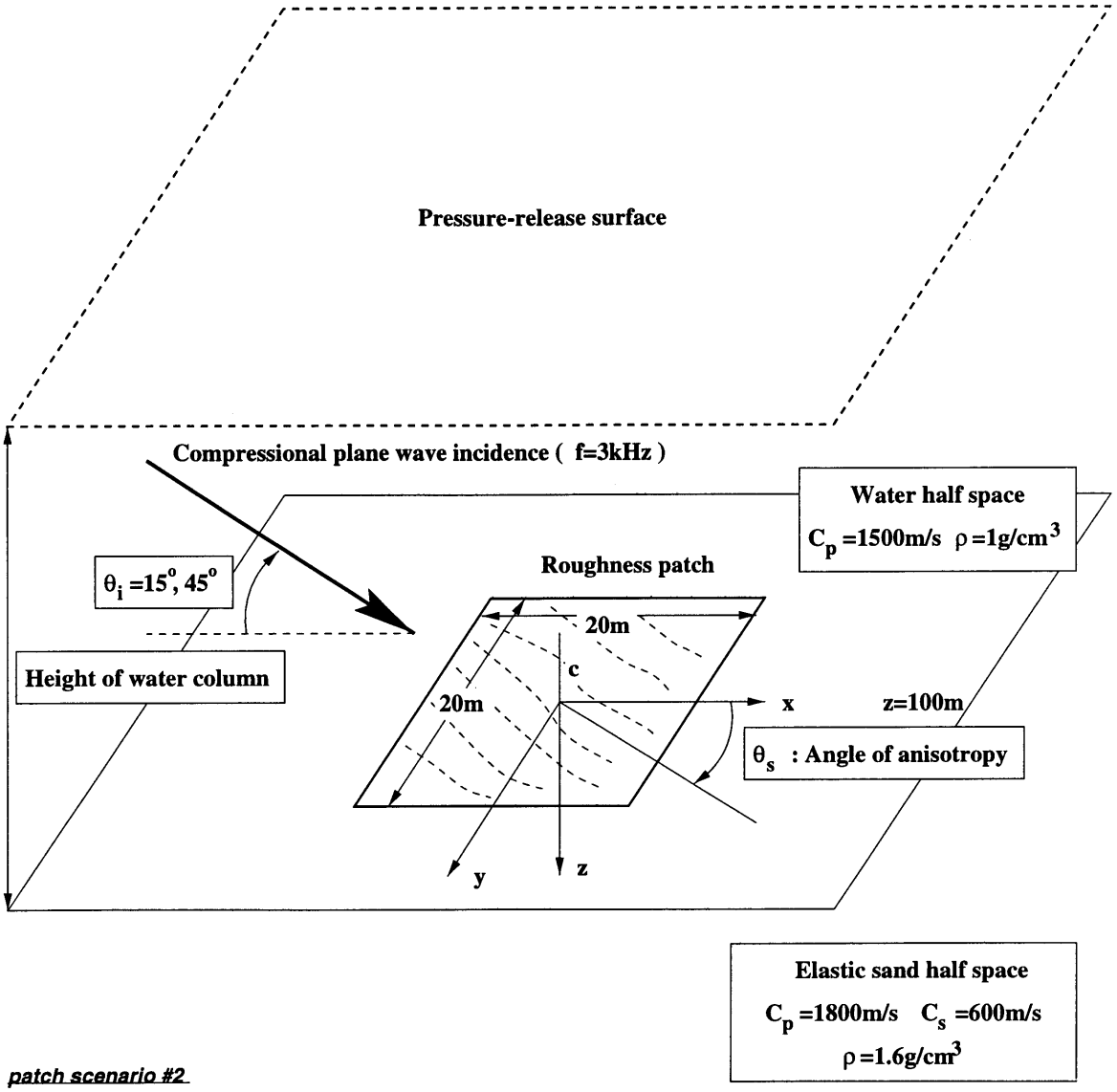

Figure 2-39: Patch scattering scenario – patch scattering in a waveguide. Case of a water column with varying depths over an elastic sand half space.

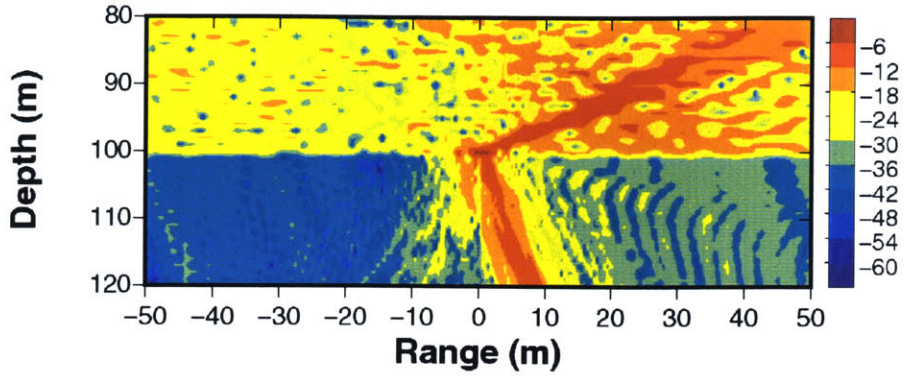

(a) Compressional plane wave incidence at $\theta_i = 15°$.

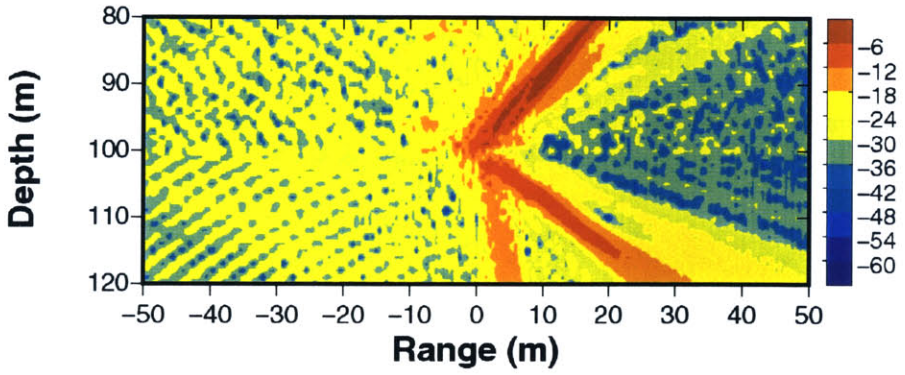

(b) Compressional plane wave incidence at $\theta_i = 45°$.

Figure 2-40: In-plane cut of scattered field produced by an anisotropic roughness patch (Figure 2-33) at $100m$ depth. The medium consists of a $100m$ water column and an elastic sand lower half space. The incident wave is coming from the left hand side of plot.

gating modes in a waveguide is proportional to the thickness of the waveguide. The condition of propagating mode number is :

$$\frac{(n-1/2)\lambda}{2h} < 1, \tag{2.88}$$

where λ is the incoming wavelength and h is the waveguide thickness. It also implies that the thicker waveguide allows steeper modes.

The examples in Figures 2-41, 2-42, and 2-43 have the identical parameters except the waveguide thickness. The incident field is a plane wave at $f = 3kHz$ and $\theta_i = 15°$. The lower half space is elastic sand. The waveguide thickness varies from $20m$ to $40m$ in $10m$ increments. The roughness has an isotropic Goff-Jordan power spectrum. The number of ensembles (N_e) is 64 in each case. Each set of plots consists of three sub-plots – averaged horizontal scattered fields, averaged angular spectrum contours, and in-plane scattering coefficients. In the angular spectrum contours, the circular interference patterns is a results of the modal structure of the scattered field. As the waveguide thickness increases, the number of these circular patterns increases as well. The circular pattern in the angular spectrum correspond to the peaks in the in-plane scattering coefficient plot. Besides increasing the number of circular patterns, the thicker waveguide decreases the width of the trough near $\Theta = \pi/2$ by allowing the steeper modes. As an additional remark, it is noticeable that the results are converged well even with a small number of ensembles.

2.5.3 Layering Effects

The following patch scattering scenario is designed to demonstrate the effect of layering on the scattered fields. Here, the layer effects refer to the effects caused by the thickness of the layer below the rough interface. Figure 2-44 shows the scattering scenario. The medium consists of a water half space, an elastic sand sublayer, and an elastic limestone half space. The incident field is a compressional plane wave in the water half space with $f = 3kHz$ and $\theta_i = 15°$. Roughness patches are generated using an isotropic Goff-Jordan power spectrum with $C_L = 2m$, $D = 2.5$, and $\sqrt{\langle\gamma^2\rangle} = 6.25cm$.

Figure 2-45 shows in-plane scattered fields caused by two sublayers with different thicknesses ($2m$ and $4m$). The major scattering features such as the scattered shear wave and the forward scattered wave, are almost identical. The main difference can be found in the sublayers. The scattered fields exhibit the modal structure within sublayers. In order to investigate this scattering feature, the corresponding 'ensemble averaged' scattered fields are computed. 128 ensembles of scattered fields are computed for four media – an elastic limestone half space, a $2m$ elastic sand sublayer over elastic limestone, a $4m$ elastic sand sublayer over elastic limestone, and an elastic sand half space. Figure 2-46 shows the comparison of in-plane scattering coefficients in the water half space among these cases. When a half space is used, there is no modal interference pattern (solid and dashed lines in the plot). Once a sublayer of finite thickness is introduced, the modal structure of the scattered field can be observed in the upper half space. When the thickness increases, the number of interference patterns increases. This trend can be explained in a similar way as for the waveguide.

Once the incident wave interacts with the rough interface and transfers energy into the sublayer in the form of a scattered wave, a complicated energy partitioning process occurs. When the scattered grazing angle ($\pi/2 - \phi$) is less than the critical angle between water and elastic sand, the scattered energy propagates to the upper half space. When this angle is higher than the critical angle, scattered energy moves to the sublayer and the lower half space. Some portion of the scattered energy is trapped and it propagates in the sublayer, exhibiting modal peaks. These modal peaks in

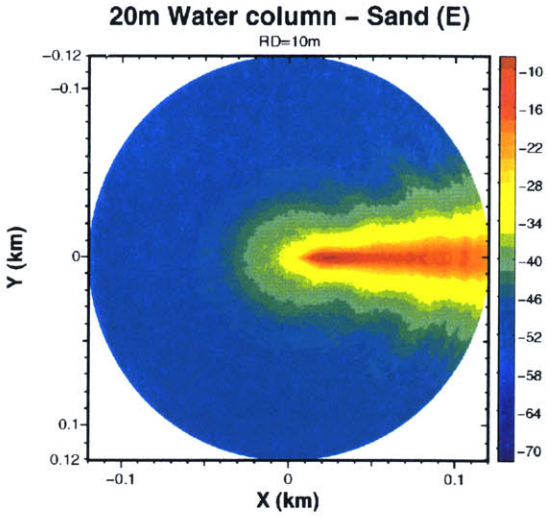

(a) Averaged horizontal scattered field in water column at $10m$ above the rough interface.

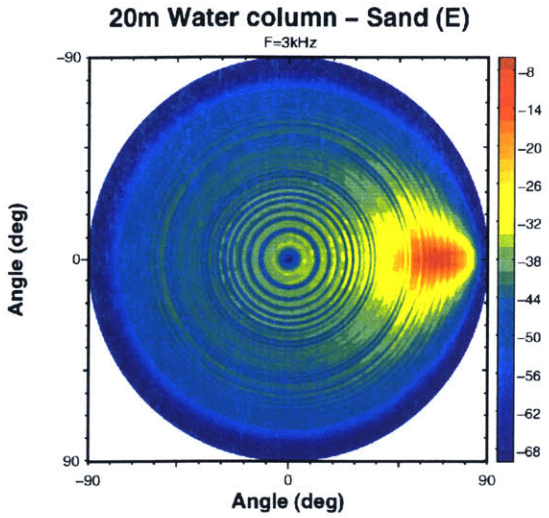

(b) Averaged angular spectrum of scattered field in water column.

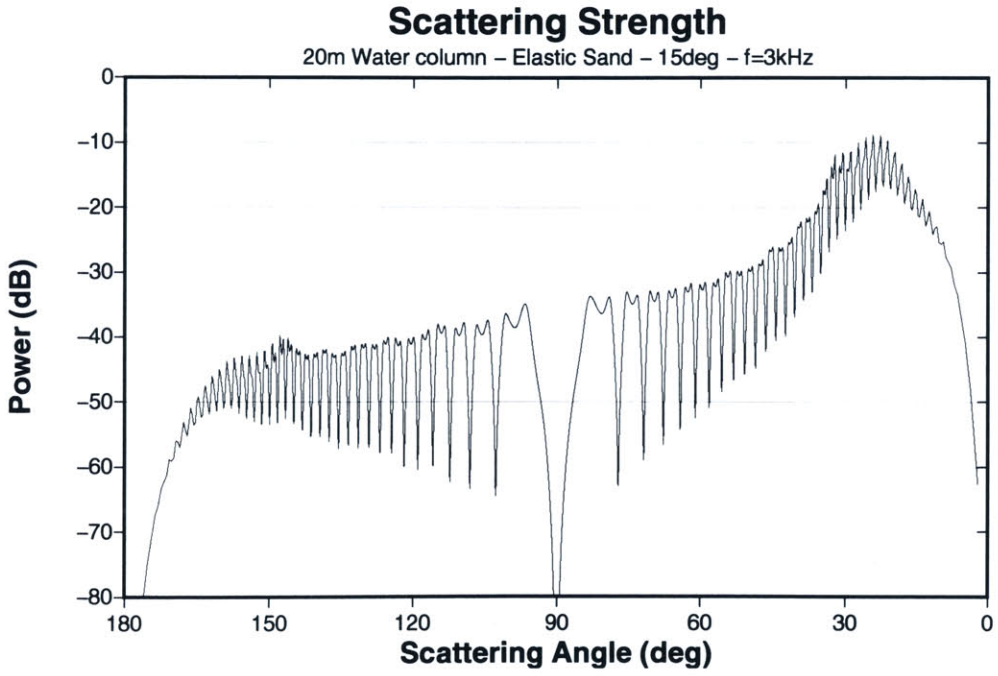

(c) Averaged in-plane scattering strength in water column.

Figure 2-41: Ensemble average of scattered field in waveguide. The medium consists of a $20m$ water column and an elastic sand half space. Roughness is modeled by an isotropic Goff-Jordan power spectrum ($C_L = 2m$, $D = 2.5$, and $\sqrt{\langle \gamma^2 \rangle} = 6.25cm$). The incident field is a compressional plane wave ($f = 3kHz$ and $\theta_i = 15°$). The incident wave is coming from the left hand side of plot. Number of ensembles (N_e) is 64.

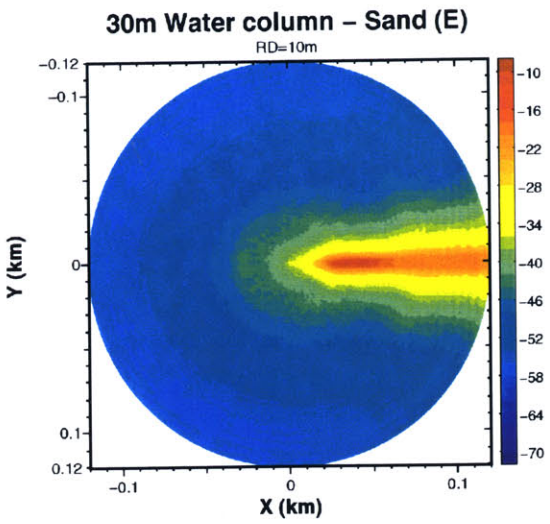

(a) Averaged horizontal scattered field in water column at $20m$ above the rough interface.

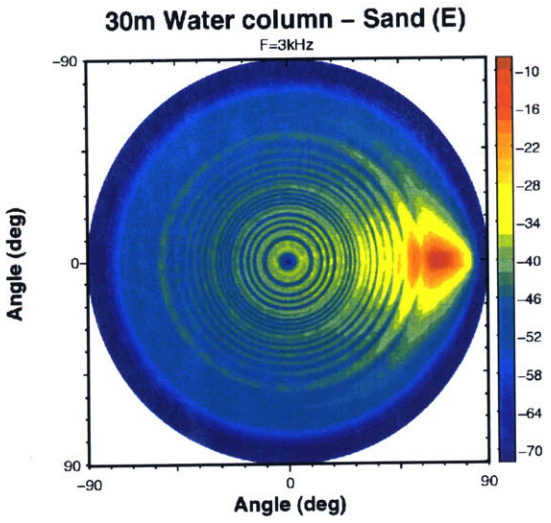

(b) Averaged angular spectrum of scattered field in water column.

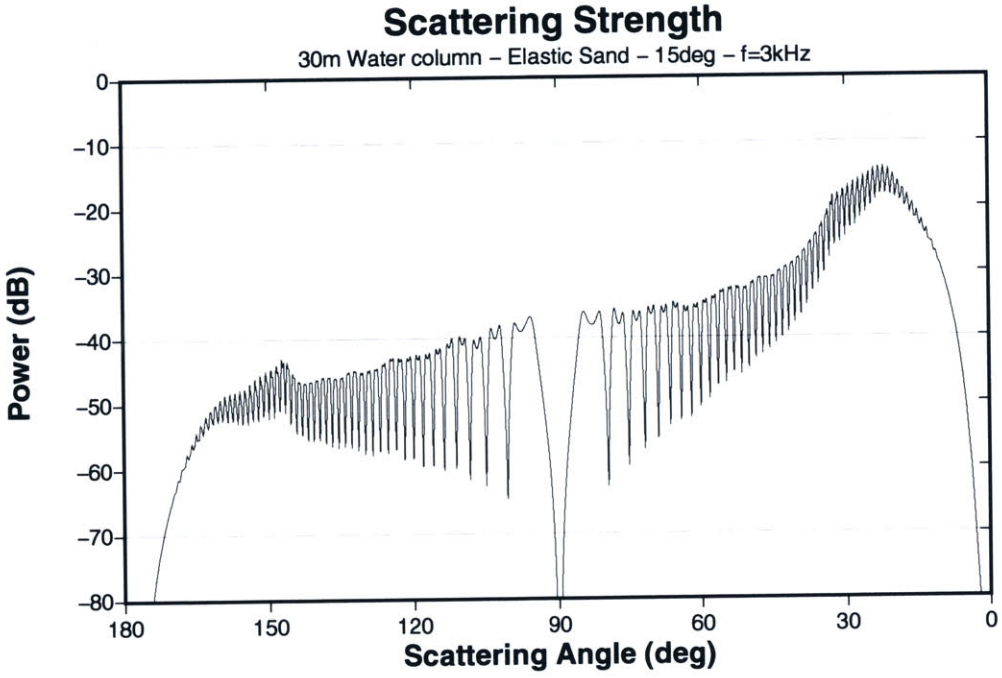

(c) Averaged in-plane scattering strength in water column.

Figure 2-42: Ensemble average of scattered field in waveguide ($N_e = 64$). The medium consists of a $30m$ water column and an elastic sand half space . Roughness is modeled by an isotropic Goff-Jordan power spectrum ($C_L = 2m$, $D = 2.5$, and $\sqrt{\langle \gamma^2 \rangle} = 6.25cm$). The incident field is a compressional plane wave coming from the left side of plot with ($f = 3kHz$ and $\theta_i = 15°$).

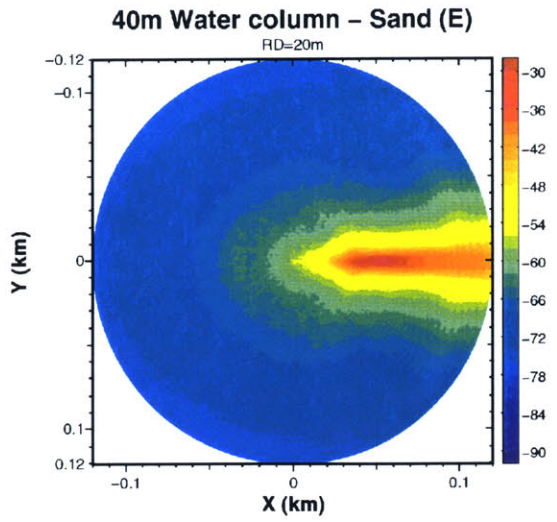

(a) Averaged horizontal scattered field in water column at $20m$ above the rough interface.

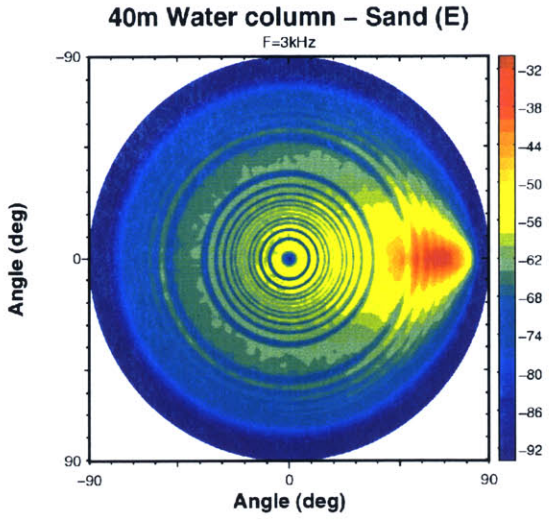

(b) Averaged angular spectrum of scattered field in water column.

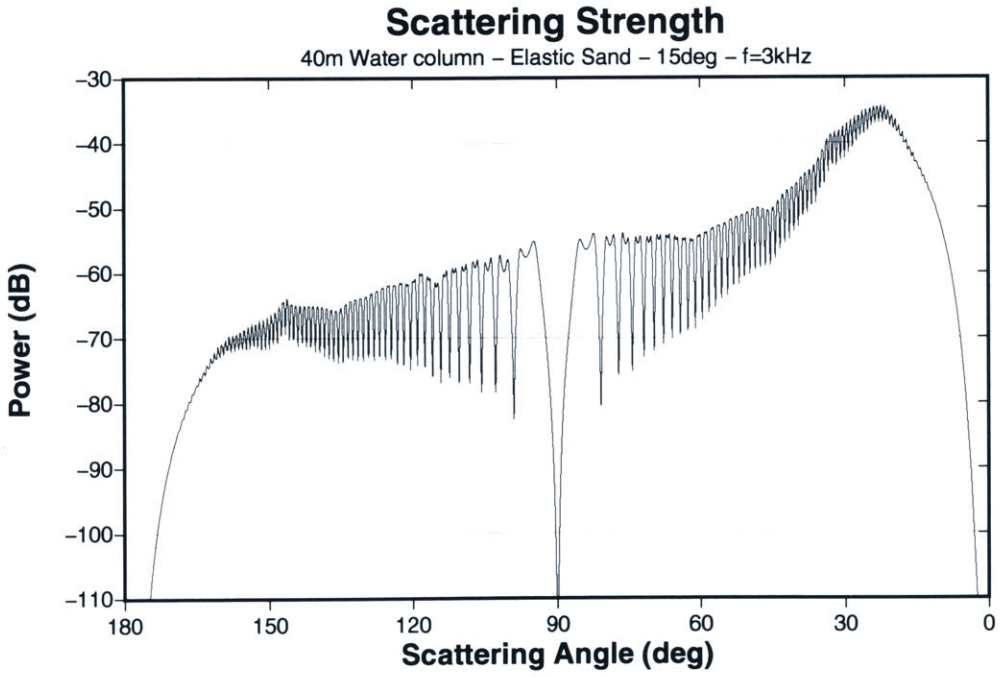

(c) Averaged in-plane scattering strength in water column.

Figure 2-43: Ensemble average of scattered field in waveguide ($N_e = 64$). The medium consists of a $40m$ water column and an elastic sand half space. Roughness is modeled by an isotropic Goff-Jordan power spectrum ($C_L = 2m$, $D = 2.5$, and $\sqrt{\langle \gamma^2 \rangle} = 6.25cm$). The incident field is a compressional plane wave coming from the left side of plot with $\theta_i = 15°$.

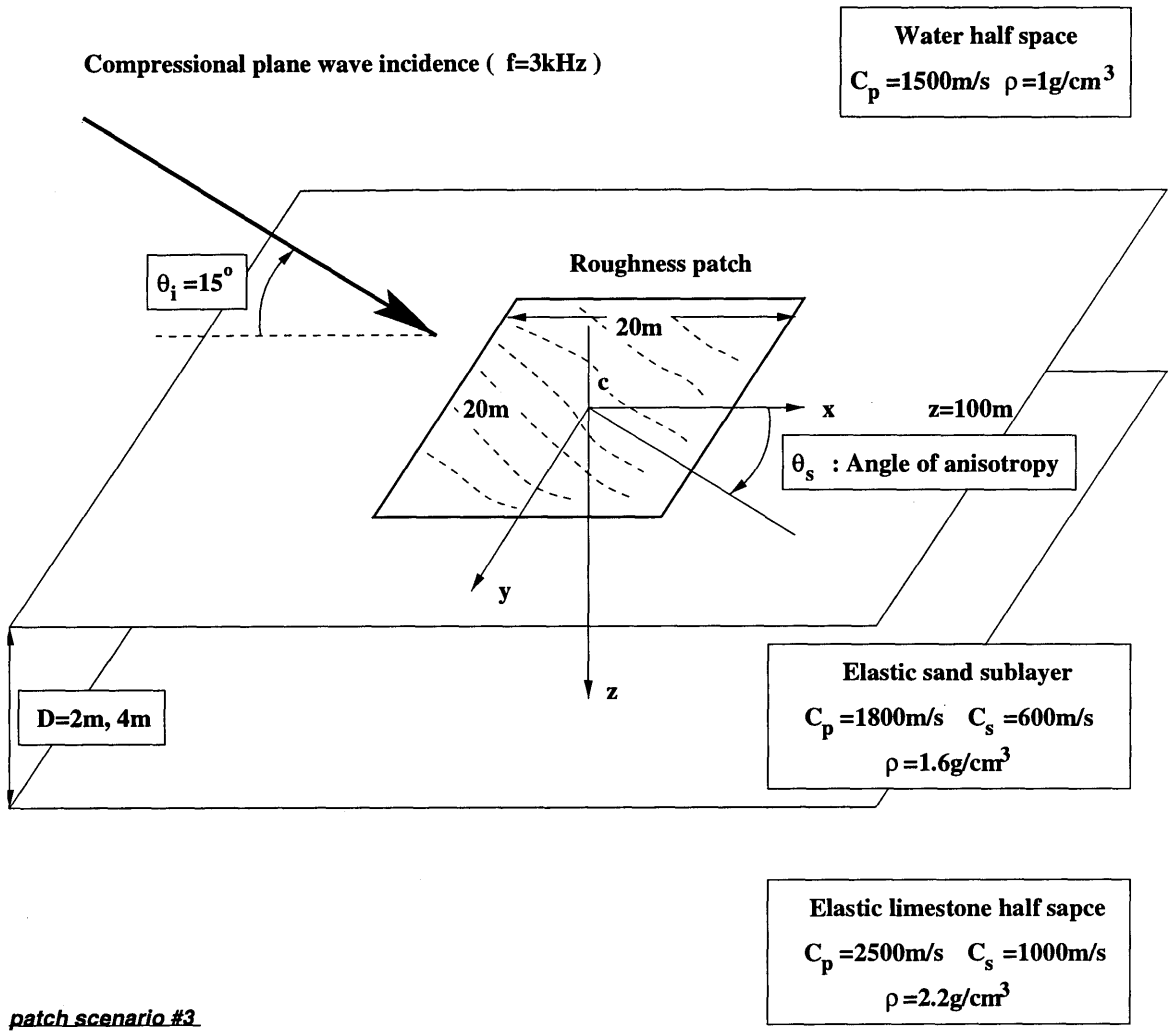

Figure 2-44: Patch scattering scenario – case of an elastic sublayer between two half spaces. The depth of sublayer varies to demonstrate the layering effect on the rough interface scattering.

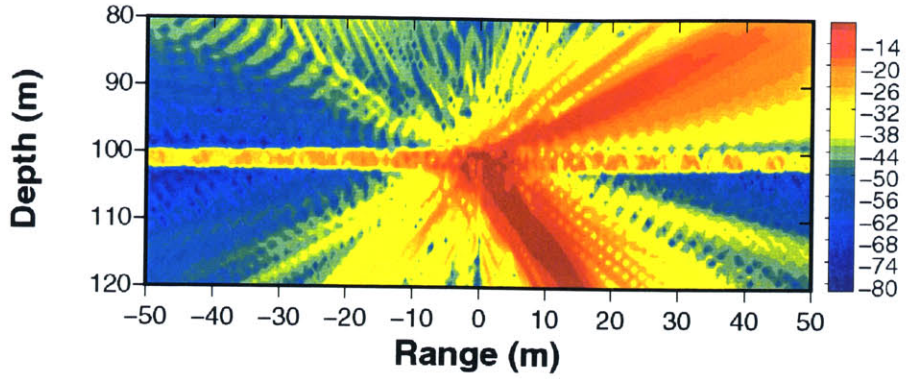

(a) Case of $2m$ elastic sand sublayer.

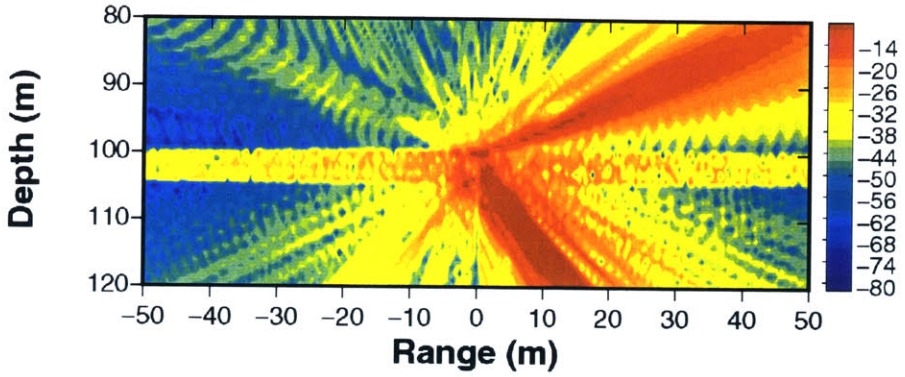

(b) Case of $4m$ elastic sand sublayer.

Figure 2-45: In-plane cuts of scattered field generated by an isotropic roughness patch (Figure 2-32) at $100m$ depth. The incident field is produced by a plane compressional wave ($f = 3kHz$ and $\theta_i = 15°$). The medium consists of a water half space, an elastic sand sublayer, and an elastic limestone half space.

the sublayer can be seen as series of steep (or sharp) minima in the in-plane scattering coefficients plot. Between two adjacent modes in the sublayer, part of scattered energy can propagate to the upper and lower half spaces. They can be observed as smoother peaks in the in-plane scattering coefficients plot.

When the scattered wave has a scattered grazing angle higher than the critical angle, the scattered energy escapes to the upper and lower half spaces. When the incident angle becomes close to $\phi = 0$, the effects of sublayer thickness decreases. In this angular regime, the in-plane scattering coefficients for an elastic sand half space and elastic sand sublayers agree. Also, the same trend can be observed in the shallow angular regime ($\pi/2 - \phi < \pi/6$).

Figure 2-47 shows 'ensemble averaged' angular spectrum contour plots for four different medium configurations. Half space cases do not have modal structures shown in sublayer cases. Figure 2-47(b) and Figure 2-47(c) exhibit similar trends except for their different modal structures. The $4m$ elastic sand sublayer produces more modal patterns than the $2m$ sublayer. Other than their modal structures, the elastic sand sublayer cases are close to the sand half space case

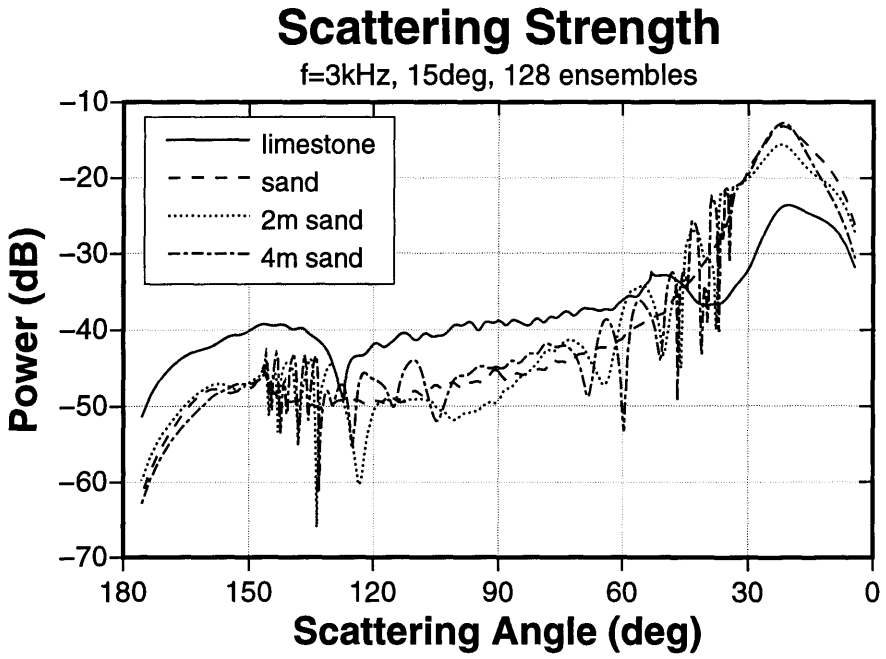

Figure 2-46: Comparison of in-plane scattering strengths among different layer configurations. The medium consists of a water upper half space, an elastic sand sublayer, and an elastic limestone lower half space.

(Figure 2-47(a)). The lower elastic limestone half space below the sublayer does not affect the scattered fields in the upper water half space.

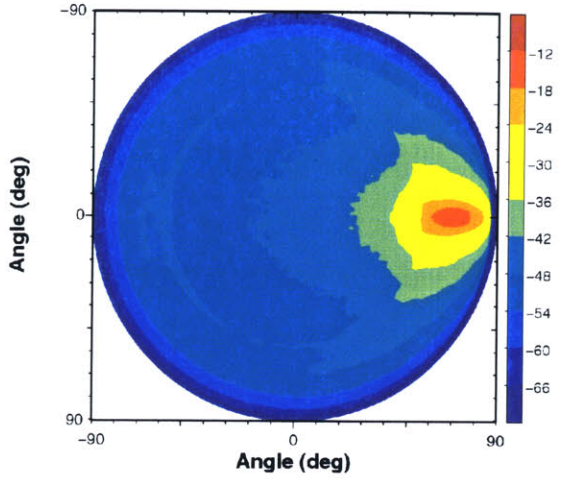

(a) Case of elastic sand half space.

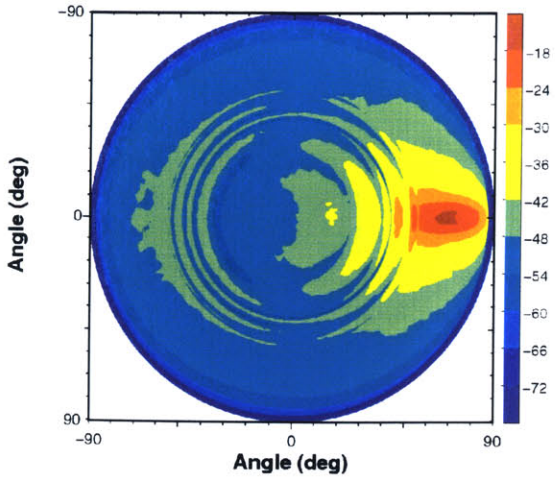

(b) Case of $2m$ elastic sand sublayer over elastic limestone half space.

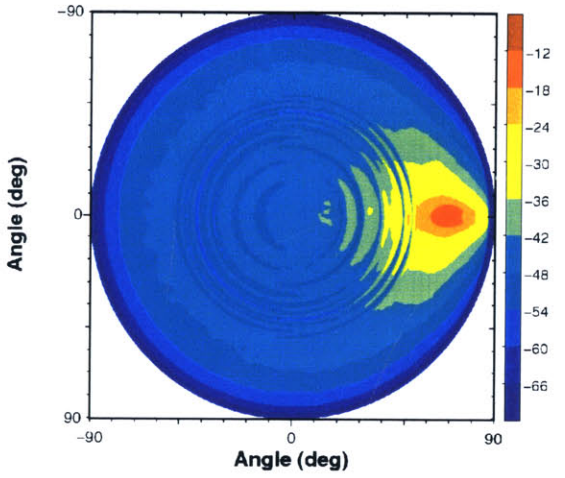

(c) Case of $4m$ elastic sand sublayer over elastic limestone half space.

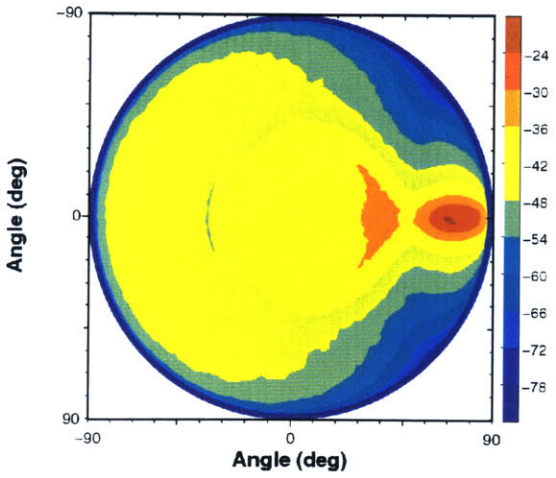

(d) Case of elastic limestone half space.

Figure 2-47: Ensemble averaged angular spectra of roughness scattered fields ($N_e = 128$). Rough interface is modeled by an isotropic Goff-Jordan power spectrum ($C_L = 2m$, $D = 2.5$, and $\sqrt{\langle \gamma^2 \rangle} = 6.25cm$). The incident field is a compressional plane wave ($f = 3kHz$ and $\theta_i = 15°$).

2.6 Effect of Roughness Properties

In this section, the effects of various roughness parameters on the scattered fields are discussed along with numerical examples. The parameters studied include correlation length (C_L), fractal dimension (D), angle of anisotropy (θ_s) ,and other types of anisotropic roughness.

2.6.1 Correlation Length

The numerical results in Figures 2-48, 2-49, 2-50, and 2-51 demonstrate the effects of roughness correlation length on the scattered field. The scattering scenario is similar to the previous half space cases. The medium consists of a water upper half space and an elastic sand lower half space. The incident field is generated by a plane wave at $f = 3kHz$ and $\theta_i = 15°$. The roughness is modeled using an isotropic Goff-Jordan power spectra with $D = 2.5$ and $\sqrt{\langle\gamma^2\rangle} = 6.25cm$. The roughness correlation lengths are $1m$, $2m$, and $4m$.

Figure 2-48 shows the in-plane scattering strengths. In the backward scattering direction, the scattering strength increases as the correlation length decreases. This trend continues in the forward direction until the compressional critical angle is reached (i.e. $\Theta = \theta_c = 33.6°$). The forward peak value increases and the width of the peak becomes narrower as the correlation length increases. These two features can be explained as follows. When the correlation length increases, the peak value of the roughness power spectrum at the origin ($k = 0$) increases and its tail becomes shorter. A higher roughness spectrum peak value produces a stronger forward scattered field and the shorter tail leads to a weaker convolution of the roughness and incident spectra in the backward direction.

When these cases are compared in spatial and angular domains, the following trends can be found in the horizontal scattered fields and angular spectrum contours. As the correlation length increases :

- Horizontal scattered field – the spatial width of the forward scattering beam becomes narrower.
- Angular spectrum – the angular width of the forward peak becomes smaller.

2.6.2 Fractal Dimension

Another important roughness parameter is the fractal (Hausdorff) dimension (D) of the roughness power spectrum. For the Goff-Jordan power spectrum, the fractal dimension can vary from 2 to 3 (excluding $D = 3$). The fractal dimension indicates the slope of the power spectrum on a log-scaled plot. Figure 2-7 shows Goff-Jordan power spectra with different fractal dimensions, where the parameter ν is related to the fractal dimension by $D = 3 - \nu$. As shown in Figure 2-7, the power spectrum becomes flatter when the fractal dimension increases. In other words, the high wavenumber component of the power spectrum increases as the fractal dimension increases. Since the scattered field is obtained as the convolution of the roughness spectrum and the incident spectrum, the angular spreading of the scattered field increases as the fractal dimension becomes larger.

The scattering scenario for the study of the fractal dimension is the case of a water half space overlying an elastic sand half space. The incident field is a plane wave at $f = 3kHz$ and $\theta_i = 15°$. The roughness is modeled using an isotropic Goff-Jordan power spectra with $C_L = 2m$ and $\sqrt{\langle\gamma^2\rangle} = 6.25cm$. The fractal dimension varies from 2.00 to 2.75. Figure 2-52 shows 'ensemble averaged'

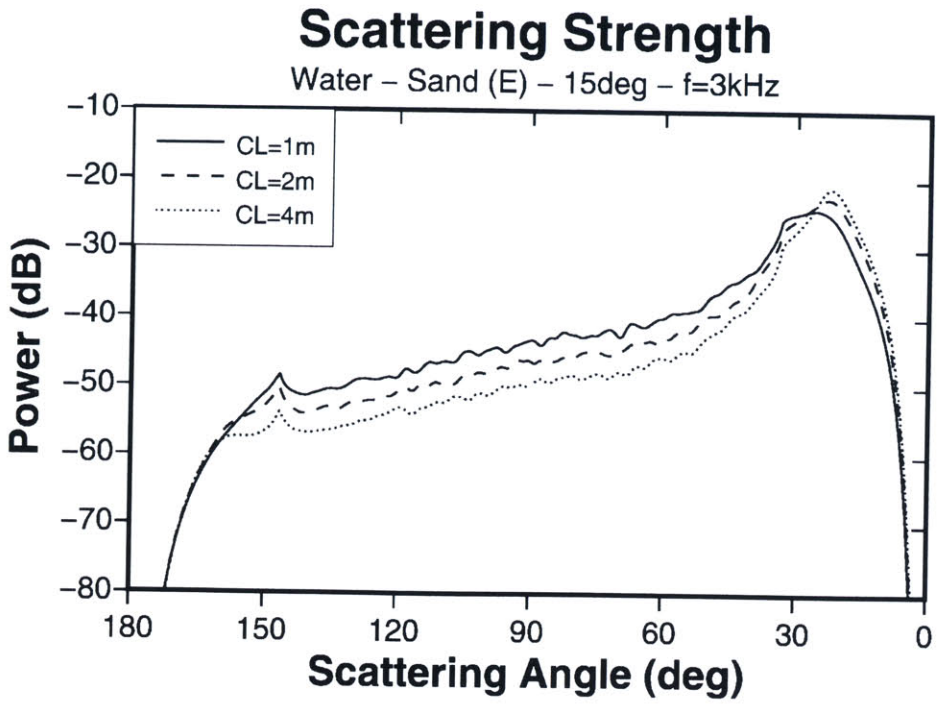

Figure 2-48: Comparison of average in-plane scattering strengths among different roughness correlation lengths. Roughness is modeled by an isotropic Goff-Jordan power spectra ($D = 2.5$ and $\sqrt{\langle \gamma^2 \rangle} = 6.25cm$). The medium consists of a water half space and an elastic sand lower half space. The incident field is a plane wave ($f = 3kHz$ and $\theta_i = 15°$).

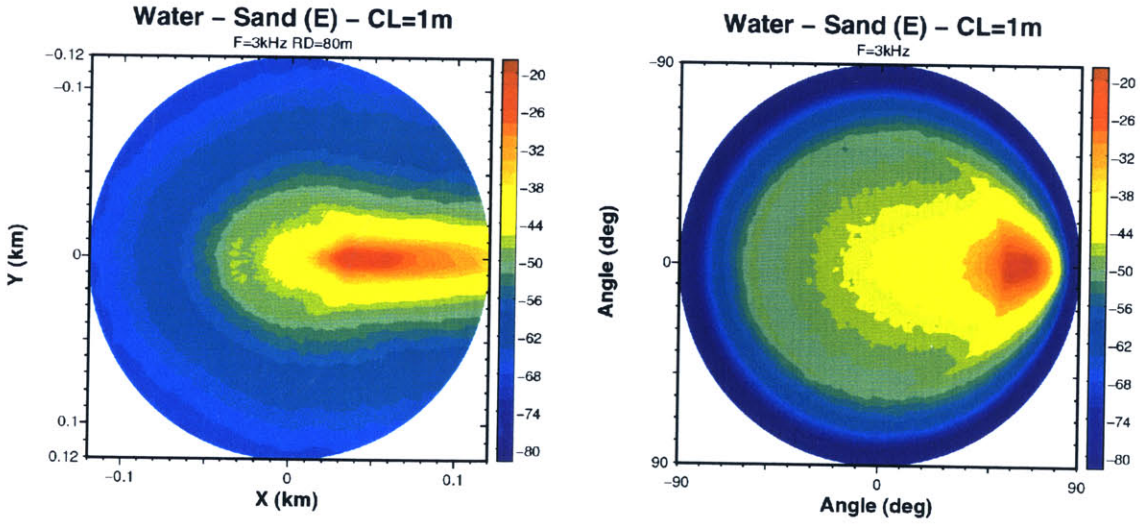

(a) Averaged horizontal scattered field at $20m$ above the rough interface.

(b) Averaged angular spectrum of scattered field in water half space.

Figure 2-49: Ensemble average of scattered field ($N_e = 64$). Roughness is modeled by an isotropic Goff-Jordan power spectrum ($C_L = 1m$, $D = 2.5$, and $\sqrt{\langle \gamma^2 \rangle} = 6.25cm$).

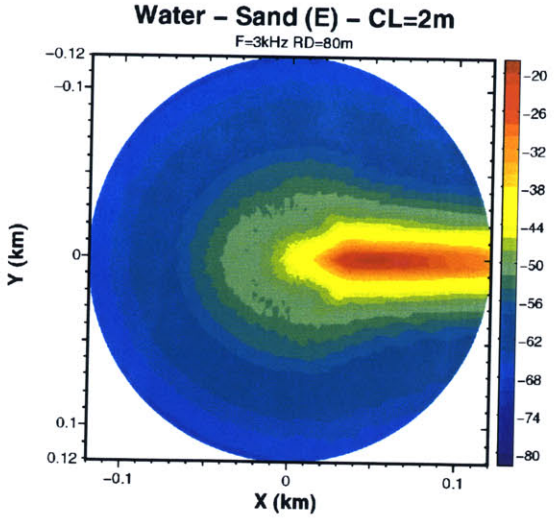

(a) Averaged horizontal scattered field at $20m$ above the rough interface.

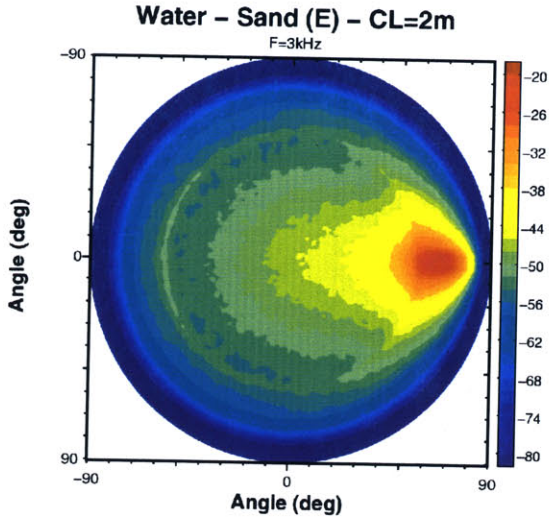

(b) Averaged angular spectrum of scattered field in water half space.

Figure 2-50: Ensemble average of scattered field ($N_e = 64$). Roughness is modeled by an isotropic Goff-Jordan power spectrum ($C_L = 2m$, $D = 2.5$, and $\sqrt{\langle \gamma^2 \rangle} = 6.25cm$).

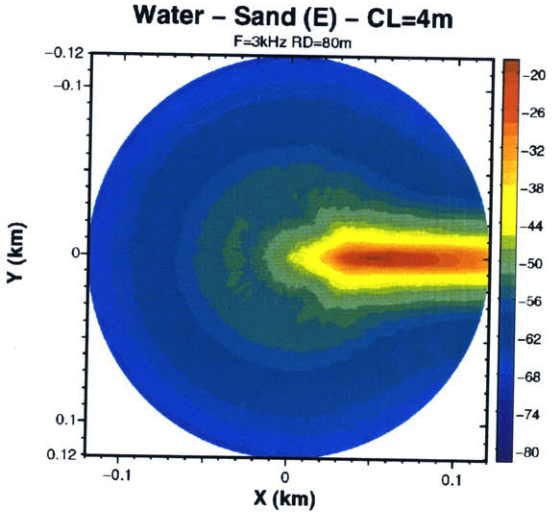

(a) Averaged horizontal scattered field at $20m$ above the rough interface.

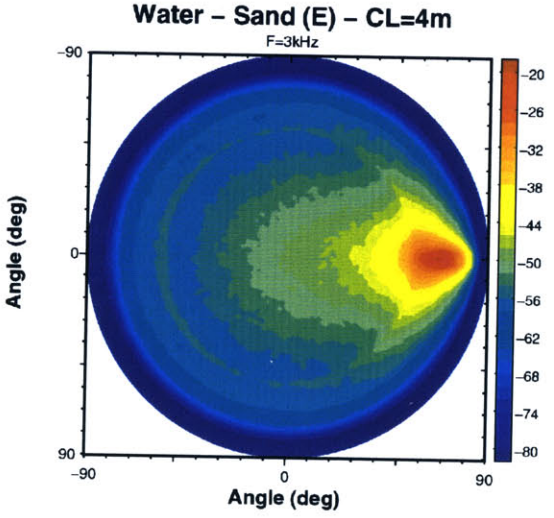

(b) Averaged angular spectrum of scattered field in water half space.

Figure 2-51: Ensemble average of scattered field ($N_e = 64$). Roughness is modeled by an isotropic Goff-Jordan power spectrum ($C_L = 4m$, $D = 2.5$, and $\sqrt{\langle \gamma^2 \rangle} = 6.25cm$).

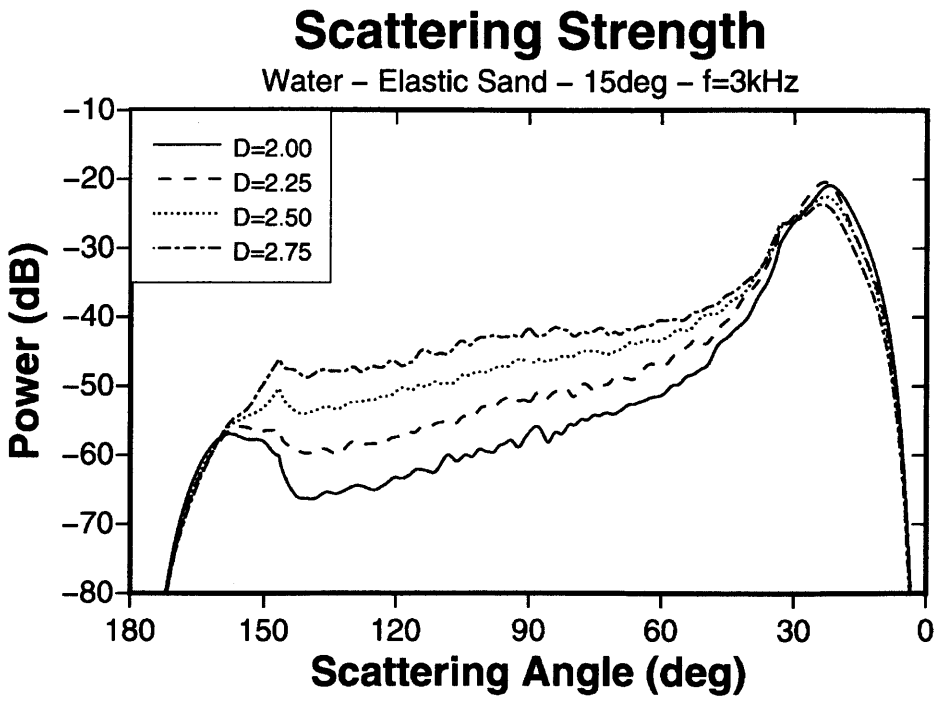

Figure 2-52: Comparison of average in-plane scattering strengths among different roughness fractal dimensions. Roughness is modeled by isotropic Goff-Jordan power spectra ($C_L = 2m$ and $\sqrt{\langle\gamma^2\rangle} = 6.25cm$). The medium consists of a water half space and an elastic sand lower half space. The incident field is a compressional plane wave ($f = 3kHz$ and $\theta_i = 15°$).

in-plane scattering strengths for different fractal dimensions. For shallow angular regimes in the forward scattering direction, there is no significant dependency on fractal dimension because it does not change the behavior of the roughness spectrum near the origin ($k = 0$). Once the scattering angle is away from the forward scattering direction, the roughness with higher fractal dimension produces a stronger scattered field for $\Theta > \theta_c = 33.6°$.

2.6.3 Roughness Anisotropy

Roughness anisotropy can be easily found in nature because the processes of generating rough interfaces generally have directional preferences such as the direction of sediment transportation by an ocean current. In the following, effects of roughness anisotropy are addressed with several numerical examples of scattered fields. The first set of numerical examples has the scattering configuration shown in Figure 2-57. The medium consists of a water half space, a $5m$ elastic sand sublayer, and an elastic limestone half space. The incident field is produced by a compressional plane wave with $f = 3kHz$ and $\theta_i = 30°$. Roughness patches of $20m$ by $20m$ size are synthesized for the scattering computation.

Figures 2-58 and 2-59 show realizations of the roughness patches and their corresponding horizontal scattered fields with the scattering configuration shown in Figure 2-57. The incident plane wave is coming from the left side of the roughness patches. Anisotropic patches are generated using Goff-Jordan power spectra with $C_{L1} = 2m$, $C_{L2} = 0.25m$, $D = 2.5$, and $\sqrt{\langle\gamma^2\rangle} = 6.25cm$. The anlge of anisotropy θ_s is set at 0°, 45°, and 90°. For comparative purposes, an isotopic patch is also generated with $C_L = 2m$ (Figure 2-59(c)). When the angle of anisotropy changes from 0° to

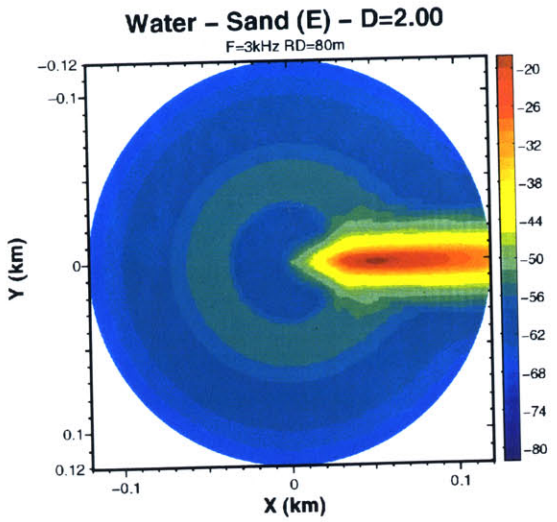

(a) Averaged horizontal scattered field at $20m$ above the rough interface.

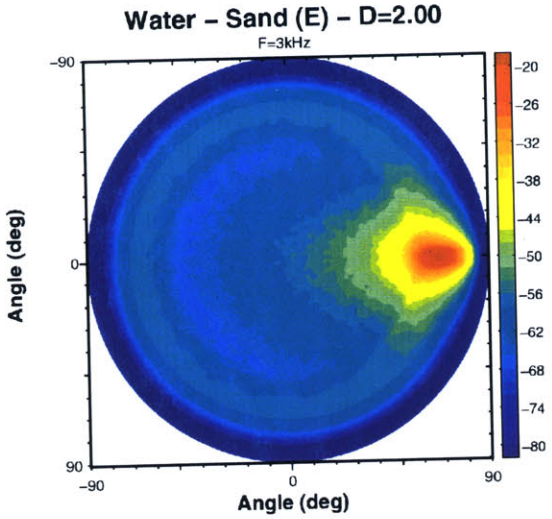

(b) Averaged angular spectrum of scattered field in water half space.

Figure 2-53: Ensemble average of scattered field ($N_e = 64$). Roughness is modeled by an isotropic Goff-Jordan power spectrum ($D = 2.00$, $C_L = 2m$, and $\sqrt{\langle \gamma^2 \rangle} = 6.25cm$).

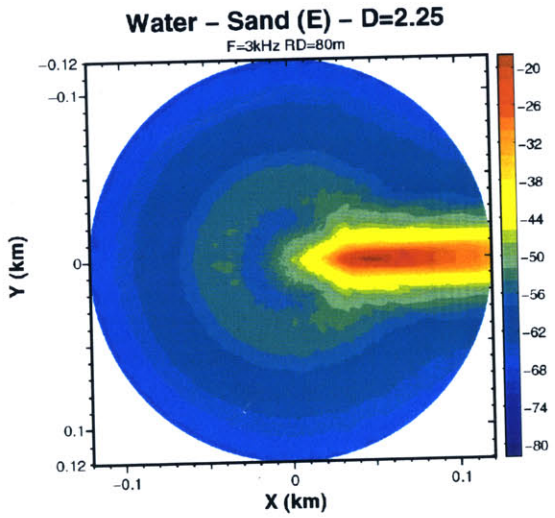

(a) Averaged horizontal scattered field at $20m$ above the rough interface.

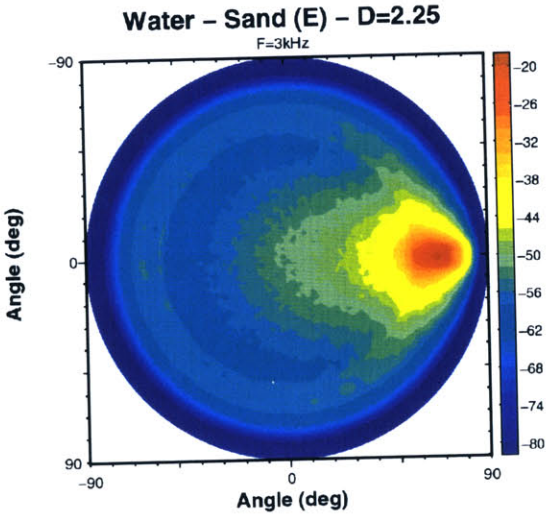

(b) Averaged angular spectrum of scattered field in water half space.

Figure 2-54: Ensemble average of scattered field ($N_e = 64$). Roughness is modeled by an isotropic Goff-Jordan power spectrum ($D = 2.25$, $C_L = 2m$, and $\sqrt{\langle \gamma^2 \rangle} = 6.25cm$).

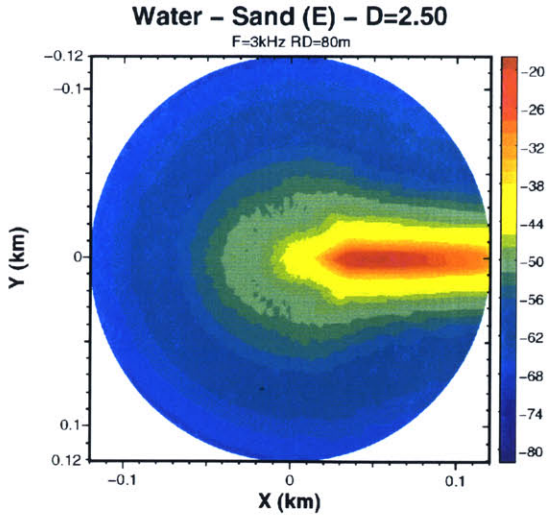

(a) Averaged horizontal scattered field at $20m$ above the rough interface.

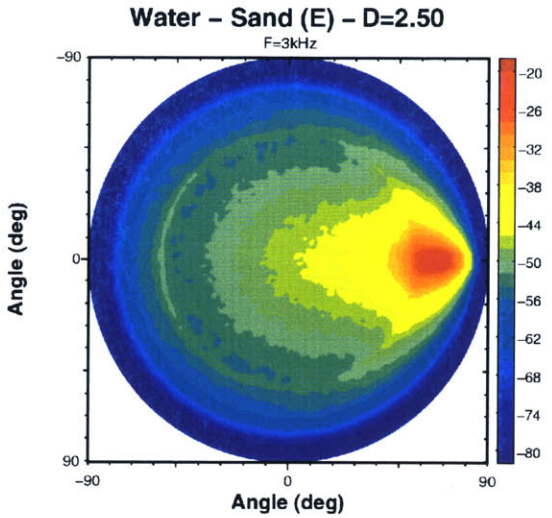

(b) Averaged angular spectrum of scattered field in water half space.

Figure 2-55: Ensemble average of scattered field ($N_e = 64$). Roughness is modeled by an isotropic Goff-Jordan power spectrum ($D = 2.50$, $C_L = 2m$, and $\sqrt{\langle \gamma^2 \rangle} = 6.25cm$).

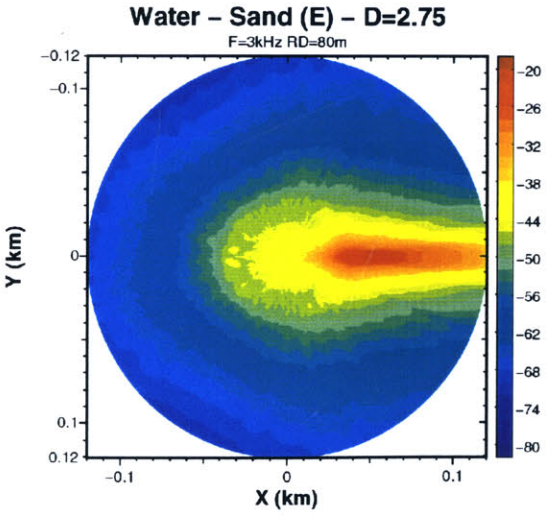

(a) Averaged horizontal scattered field at $20m$ above the rough interface.

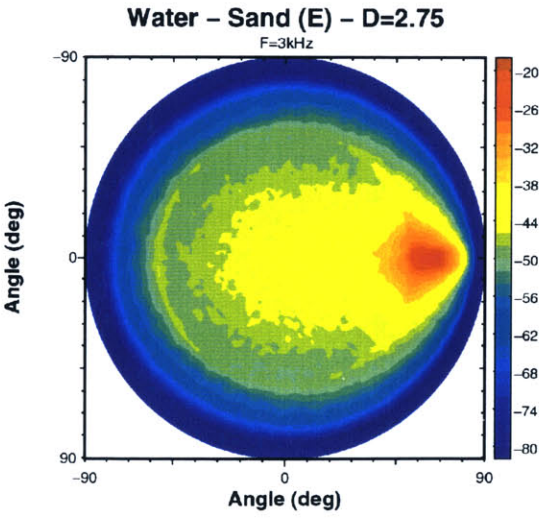

(b) Averaged angular spectrum of scattered field in water half space.

Figure 2-56: Ensemble average of scattered field ($N_e = 64$). Roughness is modeled by an isotropic Goff-Jordan power spectrum ($D = 2.75$, $C_L = 2m$, and $\sqrt{\langle \gamma^2 \rangle} = 6.25cm$).

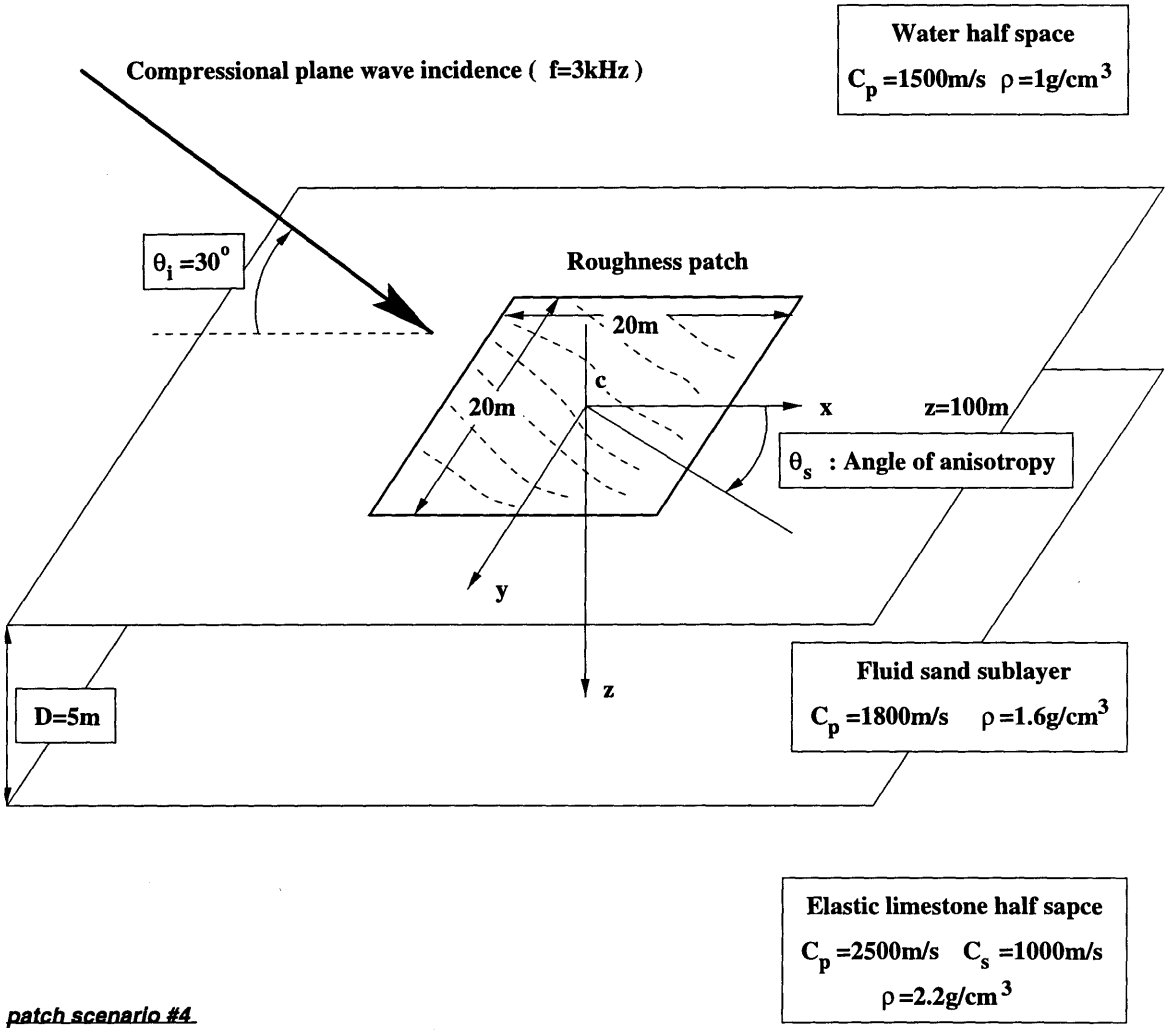

Figure 2-57: Patch scattering scenario : The medium consists of a water half space, an elastic sand sublayer, and an elastic limestone half space. Roughness patches with different anisotropy are realized for the scattered field computation.

90°, the most noticeable difference is 'minor' (or 'sideway') scattering pattern. The term 'minor' is used to differentiate it from the 'forward' scattering peak at $\theta = 0$. The minor scattering pattern is observed in the direction specular to the anisotropy. For example, the 45° anisotropic patch produces a minor scattering pattern at $\theta = 90°$ while the 90° anisotropic patch has a minor scattering pattern in the backward scattering direction ($\theta = 180°$). This trend can be easily explained using a schematic diagram of roughness spectrum and incident kernel (Figure 2-4). According to the diagram, the angular spectrum of the scattered field for anisotropic roughness spans from $\theta = 0°$ to $\theta = 2\theta_s$. The angle $2\theta_s$ corresponds to the specular direction of anisotropy. While anisotropic roughness generates strong spatial anisotropy in the scattered field, isotropic roughness distributes scattered energy evenly in space with a forward scattering peak (Figure 2-59(d)).

Previous numerical results show anisotropic effects with single realizations of scattered fields. In order to study these effects in more precise terms, average scattered fields should be examined instead. From Figure 2-60 to Figure 2-64, five anisotropic and isotropic roughness cases are presented. The averaging process is done in an ensemble sense and the number of ensembles for each case is 64.

The scattering scenario is a case of two half spaces similar to Figure 2-34. The upper half space is water and the lower half space is elastic sand. The incident field is a plane wave with $f = 3kHz$ and $\theta_i = 15°$. The dimensions of the roughness patch are $20m$ by $20m$. Each set of plots includes the horizontal scattered field, the angular spectrum contour, and the in-plane scattering strength. Figure 2-60 shows the average scattered field due to an anisotropic rough interface. The rough interface is generated using a Goff-Jordan power spectrum with $C_{L1} = 2m$, $C_{L2} = 0.25m$, $D = 2.5$, $\sqrt{\langle\gamma^2\rangle} = 6.25cm$, and $\theta_s = 0°$. When the direction of the incident field is aligned with the roughness anisotropy as this case, strong forward scattering is expected. The average angular spectrum contour (Figure 2-60(b)) confirms that the scattered energy is concentrated in the forward direction. When the anisotropy angle changes to 45°, another scattering peak is observed in Figure 2-61. As predicted by a scattering diagram (Figure 2-4), the scattered energy is concentrated between the forward direction ($\theta = 0°$) and the side direction ($\theta = 2\theta_s = 90°$). There is also a slight enhancement ($4dB$) of backward scattering power compared to the $\theta_s = 0$ case. When the roughness anisotropy is perpendicular to the direction of the incident wave, backward scattering ($\theta = 180°$) becomes stronger. Compared to the $\theta_s = 0°$ case, backward scattering is enhanced by $24dB$. The main feature of the scattered field is that the angular distribution of scattered energy is limited to the in-plane direction (i.e. cut along $\theta = 0$ and $\theta = 180°$ lines). In other words, the out-of-plane scattered field is relatively weak.

In order to investigate anisotropy further, two isotropic cases are presented for comparative purposes. Figure 2-63 shows the average scattered field caused by an isotropic Goff-Jordan power spectrum with $C_L = 2m$, $D = 2.5$, and $\sqrt{\langle\gamma^2\rangle} = 6.25cm$. The scattered energy is evenly distributed in the spatial domain with a forward scattering peak. The scattered field is similar to the case of $\theta_s = 0°$ anisotropy, but the forward scattering peak is very narrow. This difference can be explained by comparing shapes of roughness power spectra. An isotropic power spectrum has circularly-shaped contours while an anisotropic power spectrum has elliptically-shaped contours. Elliptically shaped distribution of roughness enables the wider spreading of scattered energy in forward peak.

Another isotropic roughness case is presented in Figure 2-64. The correlation length of the roughness is $C_L = 0.25m$, which is equal to the minor correlation length of previous anisotropic cases. When the correlation length becomes smaller, the roughness spectrum becomes wider and contains a significant amount of energy in the high wavenumber regime. Therefore, the resulting scattered field is evenly distributed. The difference between the forward and backward scattering

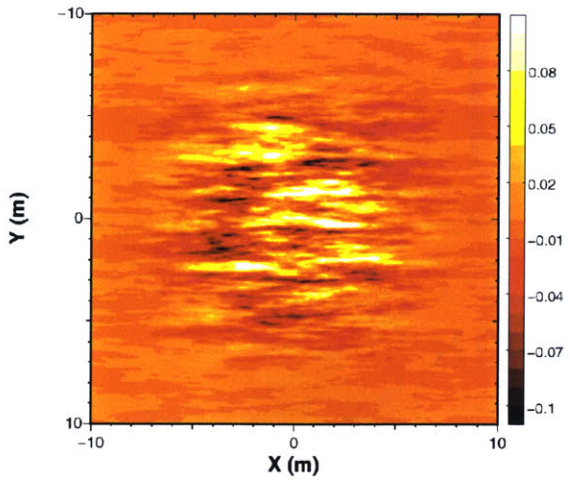

(a) Anisotropic patch with $\theta_s = 0°$.

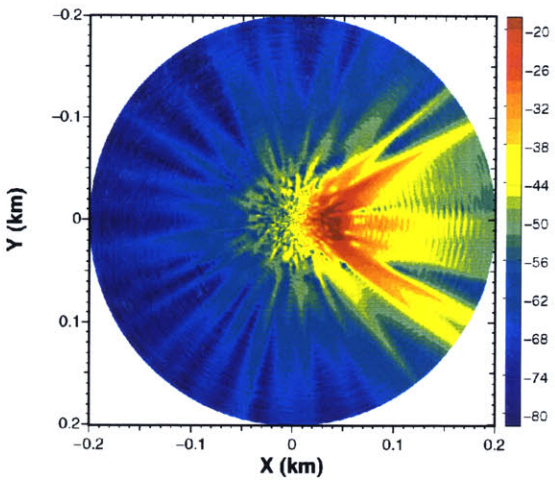

(b) horizontal scattered field by (a).

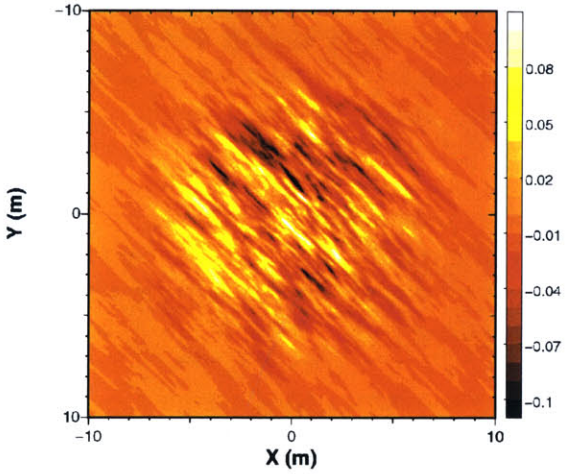

(c) Anisotropic patch with $\theta_s = 45°$.

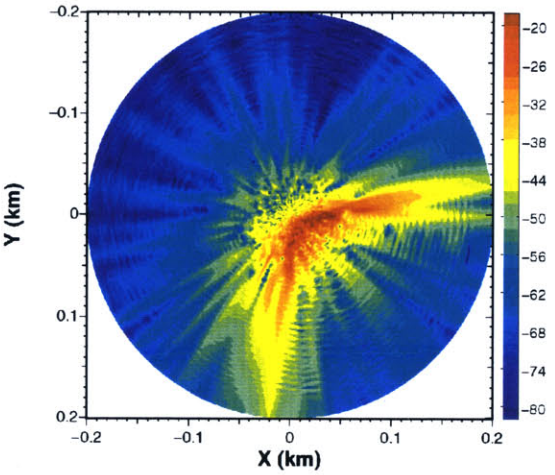

(d) horizontal scattered field by (c).

Figure 2-58: Anisotropic roughness patches and the corresponding horizontal scattered fields in a water half space at $20m$ above the patches. Patches are generated by a Goff-Jordan power spectrum ($C_{L1} = 2m$, $C_{L2} = 0.25m$, $D = 2.5$, and $\sqrt{\langle \gamma^2 \rangle} = 6.25cm$).

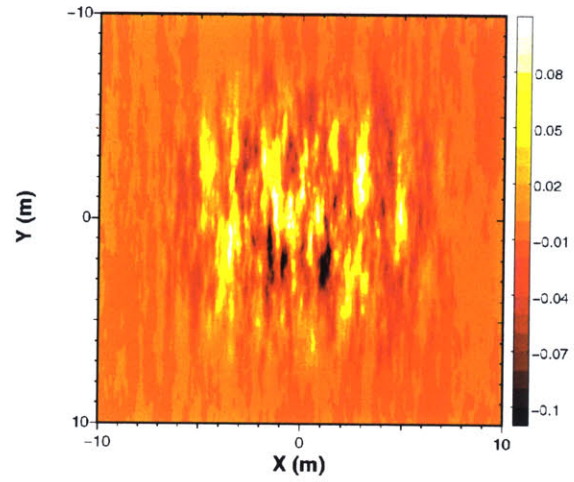

(a) Anisotropic patch with $C_{L1} = 2m$, $C_{L2} = 0.25m$, and $\theta_s = 90°$.

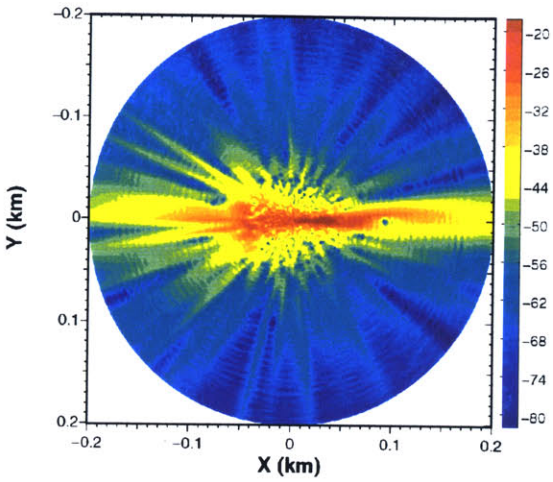

(b) horizontal scattered field by (a).

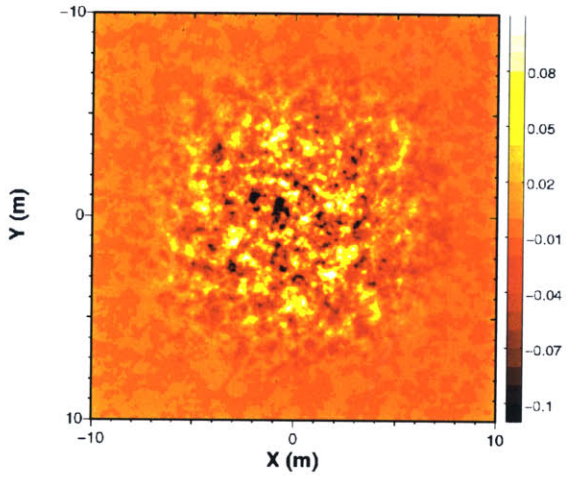

(c) Isotropic patch with $C_L = 2m$.

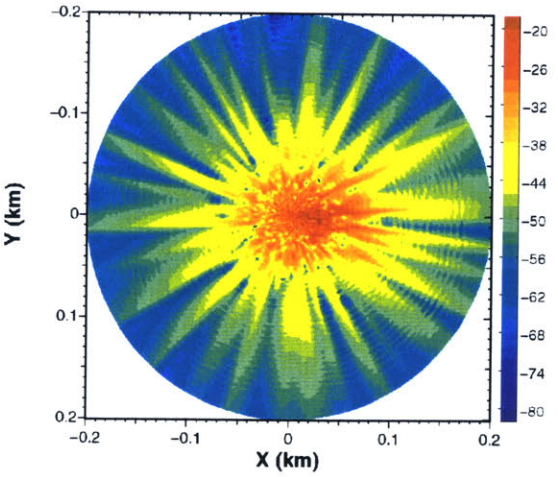

(d) horizontal scattered field by (c).

Figure 2-59: Roughness patches and the corresponding horizontal scattered fields in a water half space at $20m$ above the patches. Patches are generated by a Goff-Jordan power spectrum ($D = 2.5$ and $\sqrt{\langle \gamma^2 \rangle} = 6.25cm$).

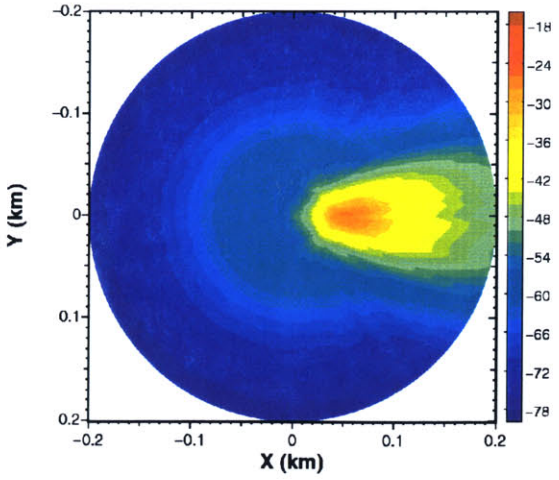

(a) Averaged scattered field in water half space at $20m$ above the rough interface.

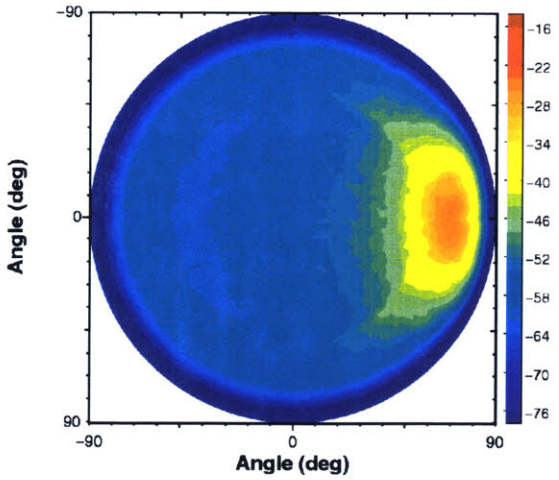

(b) Averaged scattering angular spectrum in water half space.

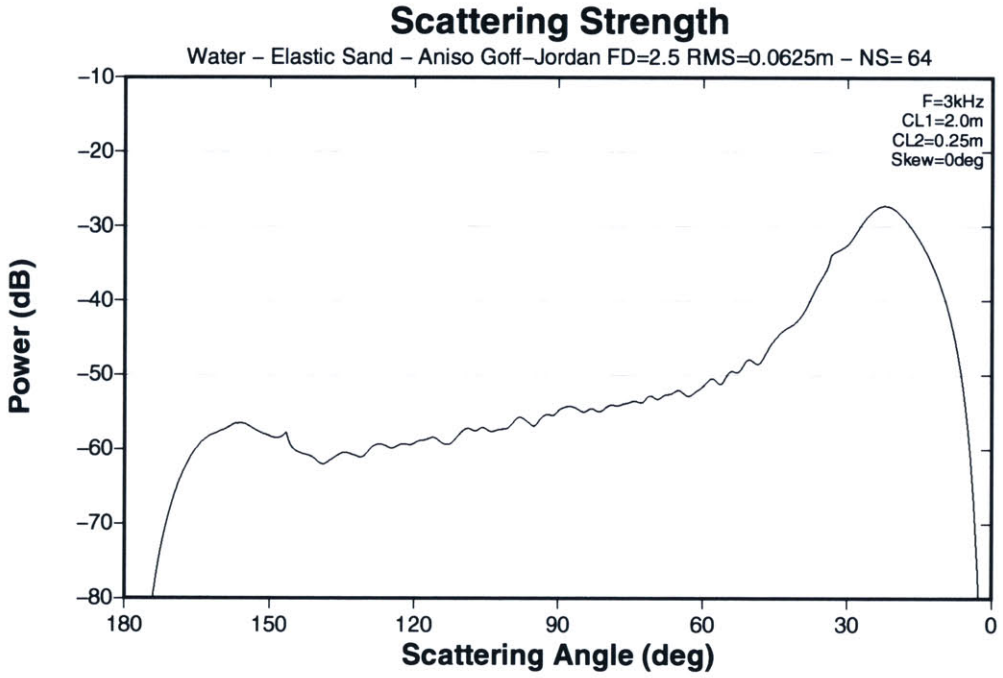

(c) Averaged in-plane scattering strength in water half space.

Figure 2-60: Ensemble average of scattered field ($N_e = 64$). The medium consists of a water upper half space and an elastic sand lower half space. The incident field is a plane wave ($f = 3kHz$ and $\theta_i = 15°$). Roughness is modeled by an anisotropic Goff-Jordan power spectrum ($C_{L1} = 2m$, $C_{L2} = 0.25m$, $\theta_s = 0°$, $D = 2.5$, and $\sqrt{\langle \gamma^2 \rangle} = 6.25cm$).

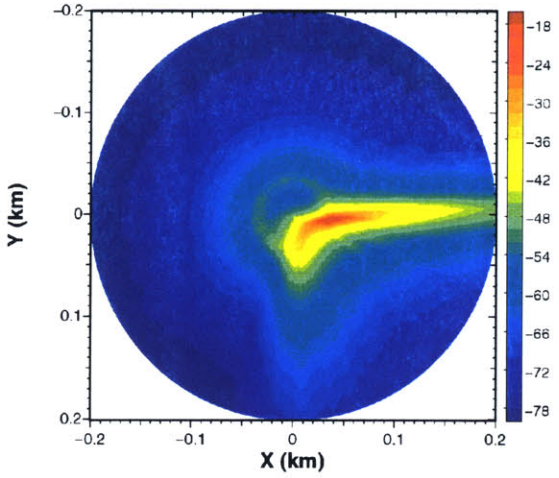

(a) Averaged scattered field in water half space at $20m$ above the rough interface.

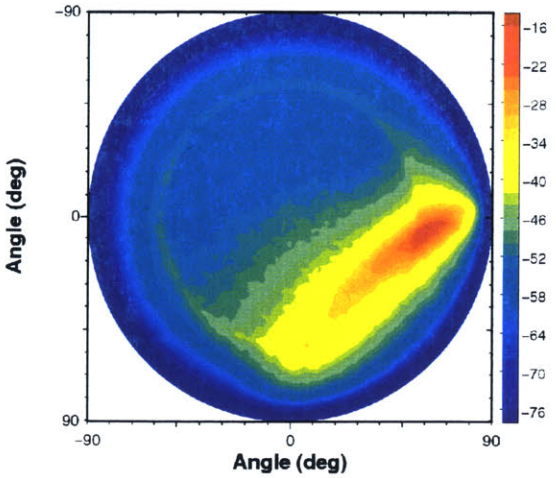

(b) Averaged scattering angular spectrum in water half space.

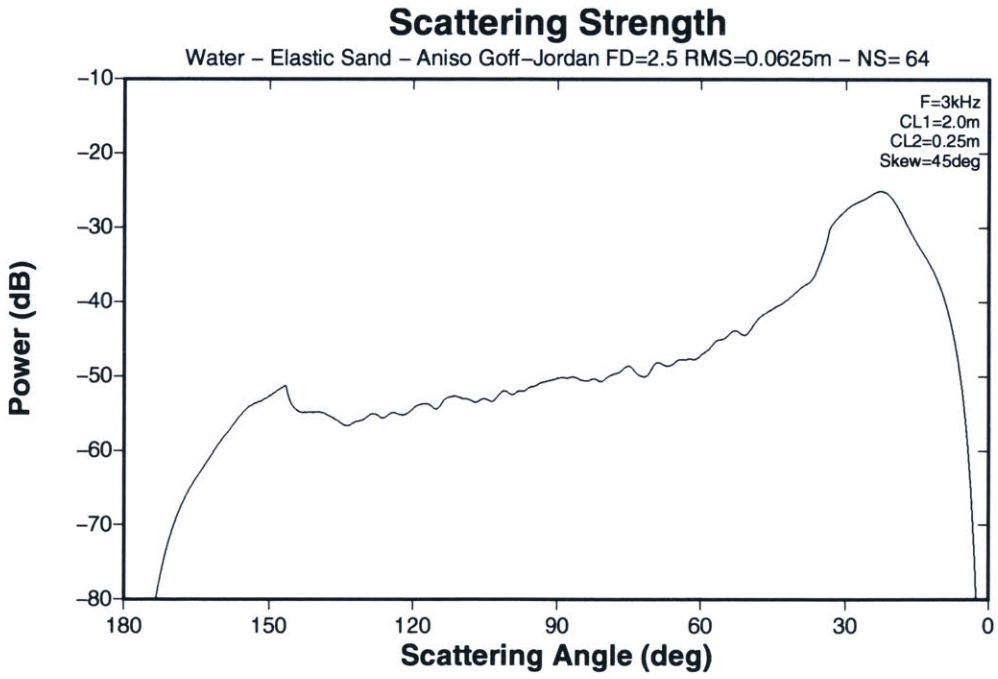

(c) Averaged in-plane scattering strength in water half space.

Figure 2-61: Ensemble average of scattered fields. Roughness is modeled by an anisotropic Goff-Jordan power spectrum ($C_{L1} = 2m$, $C_{L2} = 0.25m$, $\theta_s = 45°$, $D = 2.5$, and $\sqrt{\langle \gamma^2 \rangle} = 6.25cm$).

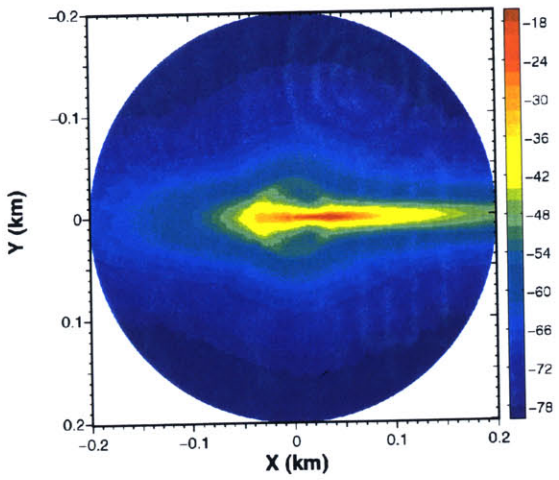

(a) Averaged scattered field in water half space at $20m$ above the rough interface.

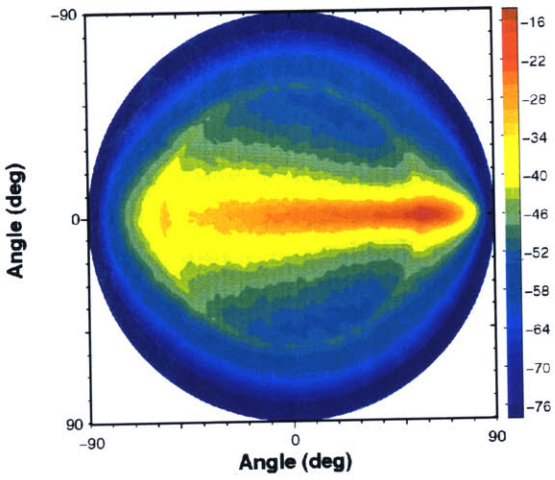

(b) Averaged scattering angular spectrum in water half space.

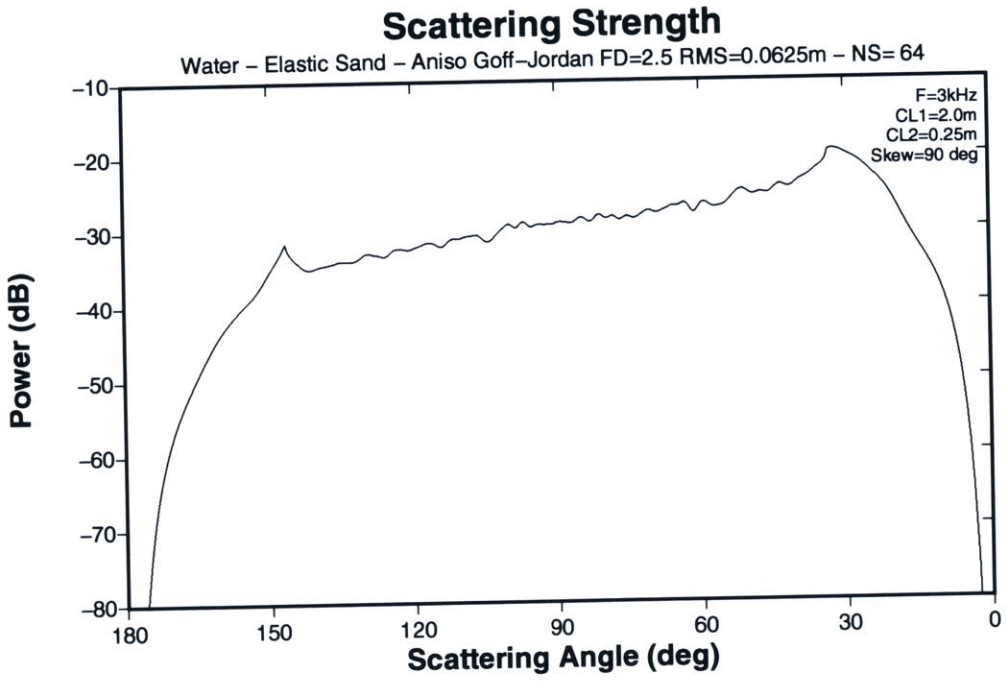

(c) Averaged in-plane scattering strength in water half space.

Figure 2-62: Ensemble average of scattered fields. Roughness is modeled by an anisotropic Goff-Jordan power spectrum ($C_{L1} = 2m$, $C_{L2} = 0.25m$, $\theta_s = 90°$, $D = 2.5$, and $\sqrt{\langle \gamma^2 \rangle} = 6.25cm$).

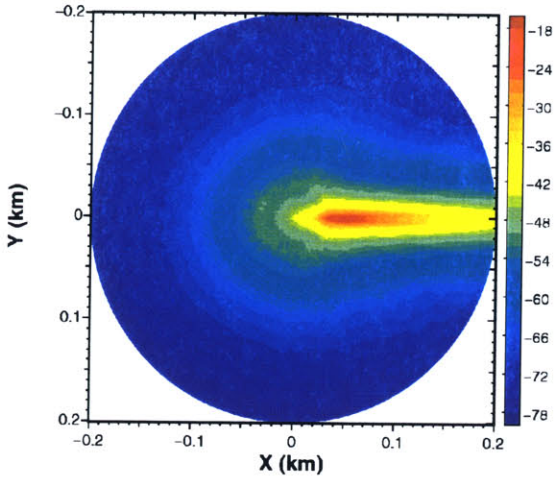

(a) Averaged scattered field in water half space at $20m$ above the rough interface.

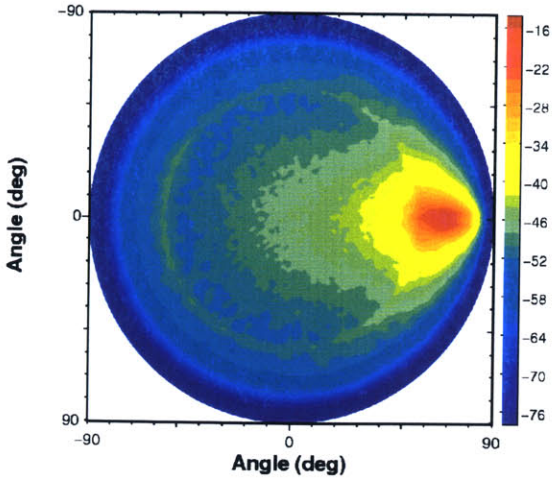

(b) Averaged scattering angular spectrum in water half space.

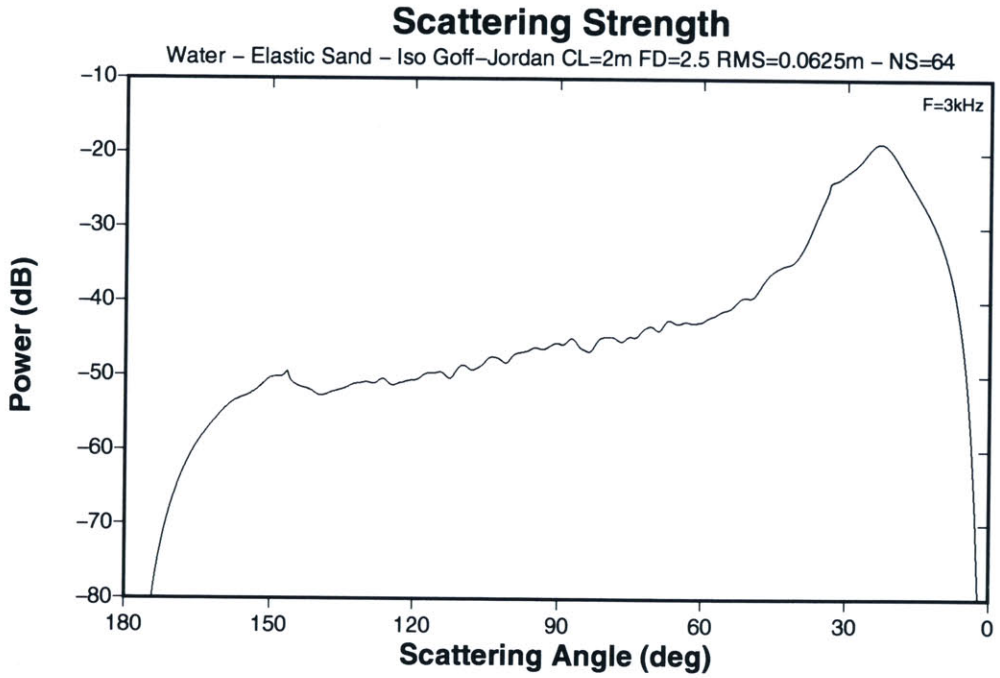

(c) Averaged in-plane scattering strength in water half space.

Figure 2-63: Ensemble average of scattered fields. Roughness is modeled by an isotropic Goff-Jordan power spectrum ($C_L = 2m$, $D = 2.5$, and $\sqrt{\langle \gamma^2 \rangle} = 6.25cm$).

peaks is approximately $12dB$ while the previous isotropic case has a $22dB$ difference. Overall, the in-plane scattered field becomes weaker but the out-of-plane scattered field becomes stronger compared to the previous isotropic case.

In the previous examples of roughness anisotropy, only Goff-Jordan power spectra with peaks at zero wavenumber were considered. There exists another class of roughness anisotropy – 'ripple structure'. The main feature of 'ripple structure' is that it has a pair of off-centered symmetric peaks in the power spectrum. The distance between the origin and one of the peaks represents the wavenumber of dominant roughness features and the orientation of the two peaks corresponds to the angle of anisotropy. For the following scattering computation, off-centered Goff-Jordan power spectra (2.51) are used to generate ripple structures. Figure 2-4 shows a schematic diagram of roughness spectra and incident kernel. Compared to the ordinary Goff-Jordan power spectra, ripple spectra are convolved with the incident kernel in a different way. Since the peaks of ripple spectra are off-centered, it is possible to have one of peaks outside the medium wavenumber such as $\theta_s = 45°$ and $\theta_s = 90°$ cases. When a peak of the roughness power spectrum is outside the medium wavenumber, its contribution to the scattered field is insignificant because it is located in the evanescent wavenumber regime. For $\theta_s = 0°$ case, the two peaks of the roughness spectrum are located within the medium wavenumber circle. This roughness spectrum produces two peaks off the forward scattering direction ($\theta = 0°$). This kind of scattering situation is true when a certain correlation length C_{L2} is used. When C_{L2} becomes smaller, it is possible to have none of the roughness spectrum peaks within the medium wavenumber circle. Consequently, it can produce an insignificant scattered field in throughout the angular regime. The following three scattering examples involving ripple structures have the scattering mechanism shown in Figure 2-65.

Figure 2-66(b) shows the ensemble averaged scattered field produced by an off-centered Goff-Jordan power spectrum with $\theta_s = 0°$, $C_{L1} = 2m$, $C_{L2} = 0.125m$, and $\sqrt{\langle\gamma^2\rangle} = 6.25cm$. As seen in the average angular spectrum, it produces two peaks at the out-of-plane direction. The angular distance between these peaks is determined by C_{L2} while the spreading of each peak is controlled by C_{L1}. When the anisotropic angle θ_s becomes 45° in Figure 2-67(b), the peak of the scattered field becomes one and moves sideways. The exact azimuthal location of the peak in the averaged angular spectrum seems to be 45°. However, the exact location is determined by the distance between the roughness spectrum peaks ($2/C_{L2}$) and the angle of anisotropy (θ_s). When the anisotropic angle becomes 90°, the averaged scattered field (Figure 2-68(b)) shows strong forward scattering. Compared to the previous cases of Goff-Jordan power spectra, this case produces a scattering peak at a steep angle ($\phi = 19.1°$). Figure 2-69 shows estimates of peak azimuthal angle as a function of anisotropic angle θ_s. This estimation is obtained with the assumption that the scattering peak coincides with the roughness spectral peak located inside the medium wavenumber circle shown in Figure 2-65. The assumption might be crude, but the estimation is quite accurate for the current cases. It should be noticed that the structure of scattering peaks for ripple structures depends on the frequency (or medium wavenumber). In the formulation shown in Figure 2-69, the position of the scattering peak is also function of medium wavenumber k_w, correlation length C_{L2}, and incident grazing angle θ_i. When the frequency (or medium wavenumber) becomes smaller, there can be cases which do not have scattering peaks in the angular spectrum. It is also possible to have two peaks in the angular spectrum for any anisotropic angles when the frequency and the incident grazing angle are high.

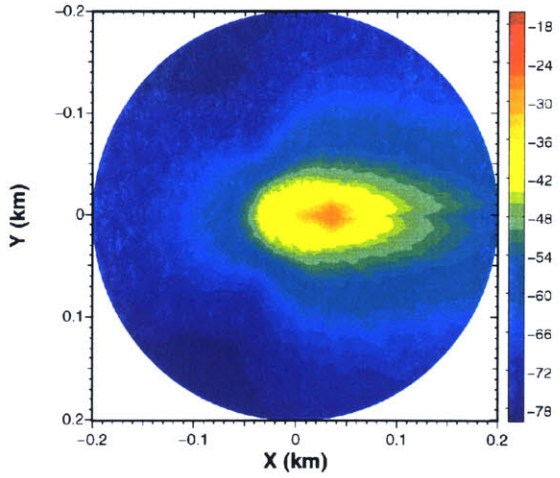

(a) Averaged scattered field in water half space at $20m$ above the rough interface.

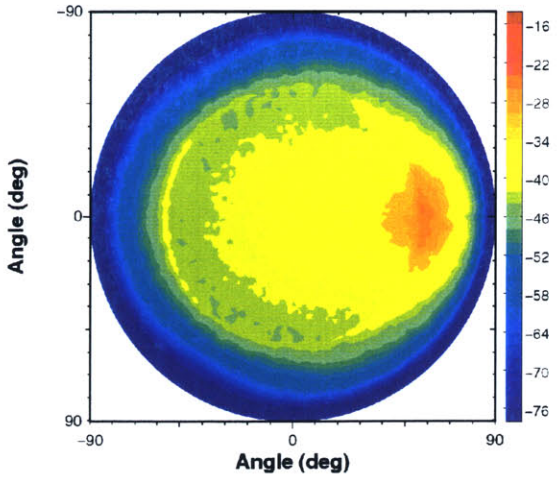

(b) Averaged scattering angular spectrum in water half space.

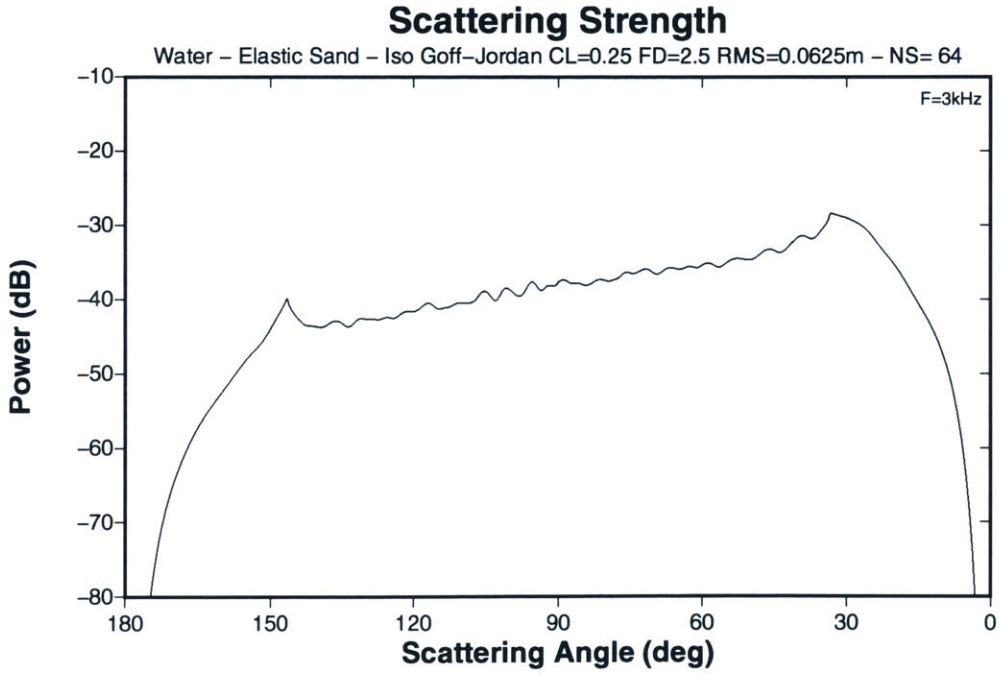

(c) Averaged in-plane scattering strength in water half space.

Figure 2-64: Ensemble average of scattered fields. Roughness is modeled by an isotropic Goff-Jordan power spectrum ($C_L = 0.25m$, $D = 2.5$, and $\sqrt{\langle \gamma^2 \rangle} = 6.25cm$).

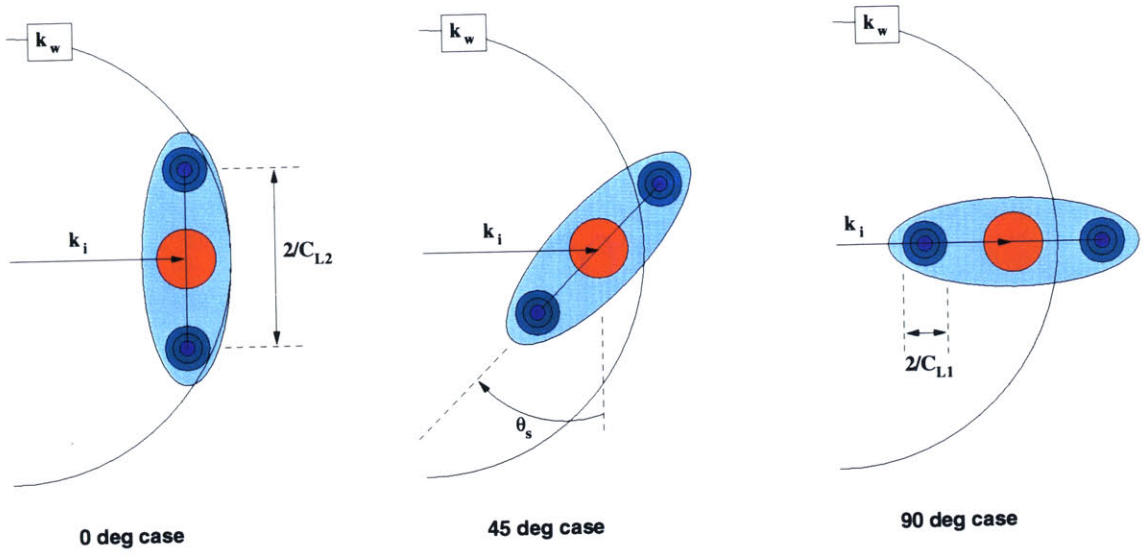

Figure 2-65: Schematic diagrams of ripple spectra and incident kernel for different anisotropic angles. Red (dark) circle corresponds to the incident wavenumber kernel and blue (light) ellipse with two peaks represents the roughness spectrum for ripple structure. k_w is the medium wavenumber and k_i is the incident wavenumber.

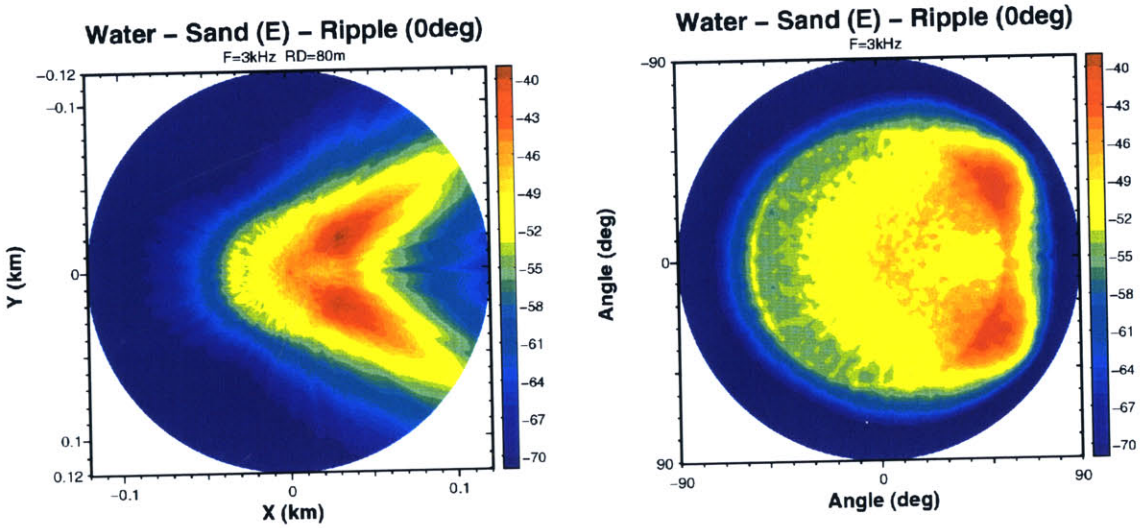

(a) Averaged horizontal scattered field at $20m$ above the rough interface.

(b) Averaged angular spectrum of scattered field in water half space.

Figure 2-66: Ensemble average of scattered fields ($N_e = 64$). Roughness is modeled by an off-centered Goff-Jordan power spectrum ($C_{L1} = 2m$, $C_{L2} = 0.125m$, $\theta_s = 0°$, and $\sqrt{\langle \gamma^2 \rangle} = 6.25cm$). The incident field is a compressional plane wave ($f = 3kHz$ and $\theta_i = 15°$).

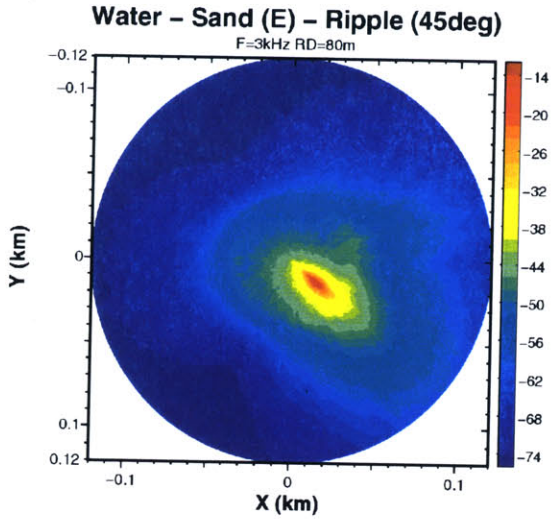

(a) Averaged horizontal scattered field at $20m$ above the rough interface.

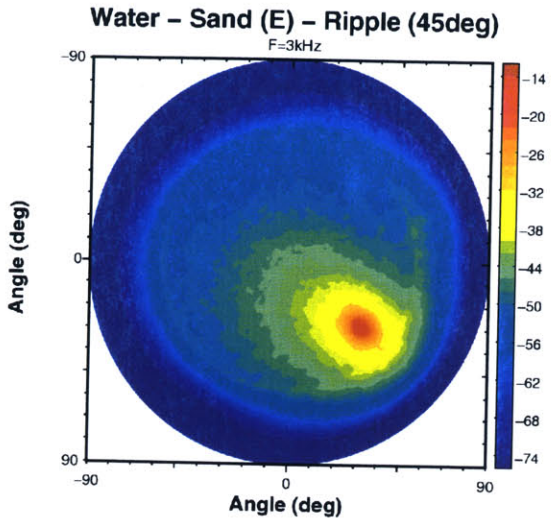

(b) Averaged angular spectrum of scattered field in water half space.

Figure 2-67: Ensemble average of scattered fields ($N_e = 64$). Roughness is modeled by an off-centered Goff-Jordan power spectrum ($C_{L1} = 2m$, $C_{L2} = 0.125m$, $\theta_s = 45°$, and $\sqrt{\langle \gamma^2 \rangle} = 6.25cm$). The incident field is a compressional plane wave ($f = 3kHz$ and $\theta_i = 15°$).

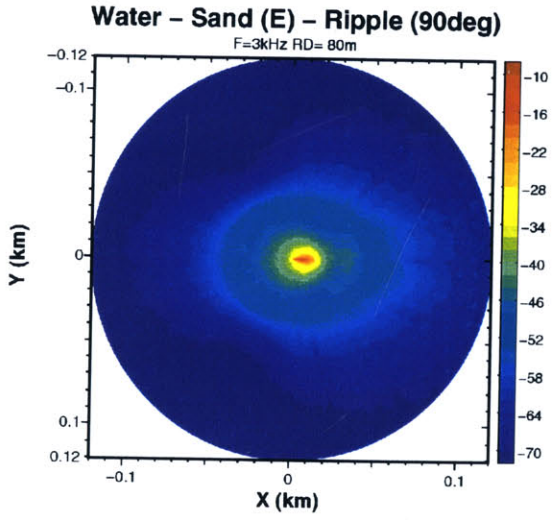

(a) Averaged horizontal scattered field at $20m$ above the rough interface.

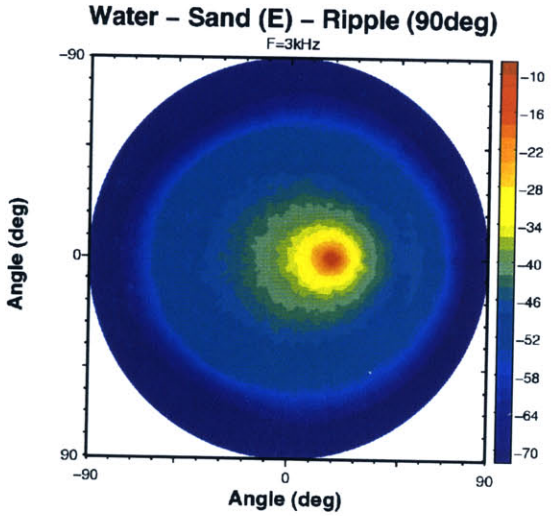

(b) Averaged angular spectrum of scattered field in water half space.

Figure 2-68: Ensemble average of scattered fields ($N_e = 64$). Roughness is modeled by an off-centered Goff-Jordan power spectrum ($C_{L1} = 2m$, $C_{L2} = 0.125m$, $\theta_s = 90°$, and $\sqrt{\langle \gamma^2 \rangle} = 6.25cm$). The incident field is a compressional plane wave ($f = 3kHz$ and $\theta_i = 15°$).

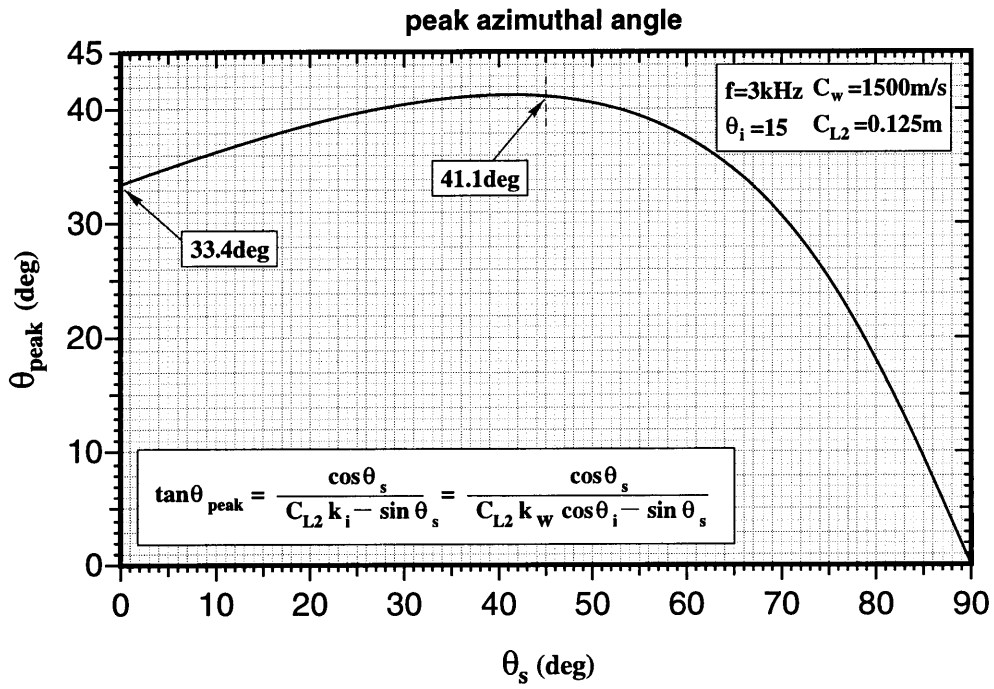

Figure 2-69: Peak azimuthal angle θ_{peak} as a function of the anisotropic angle θ_s for an off-centered Goff-Jordan power spectrum.

2.7 Time Domain Solutions

Practically, time domain (i.e. wideband) scattering solutions are necessary to predict or compare with experimental data because CW (continuous wave or single frequency) sources are not commonly used for acoustical experiments. Since the rough interface scattering formulation gives a single frequency (CW) solution for a single realization of roughness patch, Fourier synthesis is utilized to produce a time domain solution. Fourier synthesis simply means that the time domain solution is represented by a weighted sum of a finite number of single frequency solutions.

This section will present a series of time domain rough interface scattering solutions for various configurations. The scattering scenario for time domain solutions is shown in Figure 2-70. The incident field is generated by an $8m$ long vertical line array (VLA) with 128 elements. The center of the VLA is $20m$ above the rough interface. The amplitudes of VLA elements are weighted by a Hanning window and their phases are weighted so as to be tilted down by 15° and focused on the center of roughness patch. The center frequency of the source is $F_c = 3kHz$ and the bandwidth of pulse is $\Delta F = 1kHz$. The time window is set at $0.1s$. The shape of incident pulse is a sine wave weighted by a Hanning window. The rough interface is represented as a $20m$ by $20m$ roughness patch.

The first time domain scattering case involves two half spaces with an isotropic patch (Figure 2-71). The medium consists of a water upper half space and an elastic sand ($C_p = 1800m/s$, $C_s = 600m/s$, and $\rho = 1.6g/cm^3$) lower half space. Figure 2-72 shows the in-plane incident field in the time domain. These time snap shots are obtained by 2-D OASP (pulse module of OASES) and PP (pulse processor) [44]. The location of the roughness patch center in the incident field plot is $40m$ in range and $100m$ in depth.

As the incident beam pulse sweeps the rough interface, the scattered field begins to be produced in the time domain. Figure 2-73 shows a series of in-plane (vertical) time snapshots. White lines in the plots indicate the mean interface level ($z = 100m$) and the red line corresponds to the direction of specular reflection (15°). The blue lines represent the forward compressional critical angle (33.6°) and the green line are the angle of the transmitted shear wave in the lower half space (67.3°). In the early part of the time snapshots ($T < 0.06s$), there are some numerical artifacts (light blue contour area above and below interface) due to aliasing (wrap-around). The under-sampling in the frequency domain due to the use of a small time window ($0.1s$ for this case) causes aliasing in the time domain. This is due to the periodicity assumed by the discrete Fourier transform. This can be eliminated by using longer time windows (i.e. finer frequency sampling) or introducing complex frequency. The former method simply moves the wrap-arounds to earlier and later time points mathematically by increasing the aliasing time period. The later method reduces the wrap-around effects in the later part of signal by moving the frequency integration contour away from the real axis [44, 22].

For the field computation at fixed points within a limited spatial separation instead of time snapshots, having excessively long time windows is computationally impractical. For example, in order to eliminate the aliasing by using longer time windows for these snapshots, the time window should be longer than $0.167s$. This number comes from the time required for a shear scattered wave ($C_s = 600m/s$) to travel $100m$. There are four major groups of scattered waves in the results. In the lower elastic sand half space, scattered shear and compressional waves are observed. Shear waves travel along the green line (i.e. angle of transmitted shear wave) while compressional waves moves at shallow angles. There are two clues that the scattered wave at shallow angles is a compressional wave. Firstly, its traveling speed is faster than that of steep shear scattered waves. Secondly, its amplitude is about $12dB$ lower than the shear wave because the incident wave is subsonic for compressional waves in the lower half space. In the upper half space, two

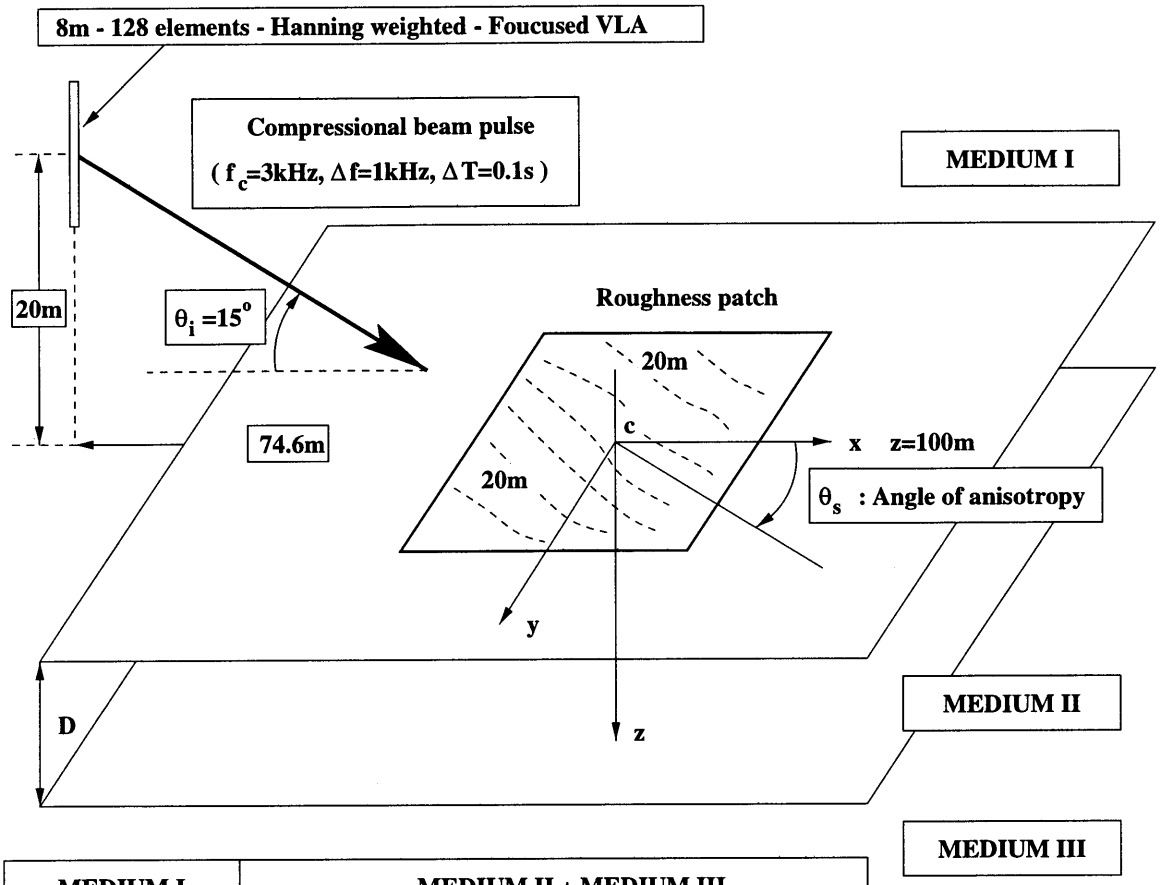

MEDIUM I	MEDIUM II + MEDIUM III
Water half space	Elastic sand half space
Water half space	Elastic limestone half space
Water half space	Elastic basalt half space
Water half space	4m elastic sand layer + elastic limestone half space
Water half space	2m elastic sand layer + elastic limestone half space
20m water column	2m elastic sand layer + elastic limestone half space

patch scenario #5

Figure 2-70: Patch scattering scenario for time domain solutions. The incident field is generated by a focused vertical linear array.

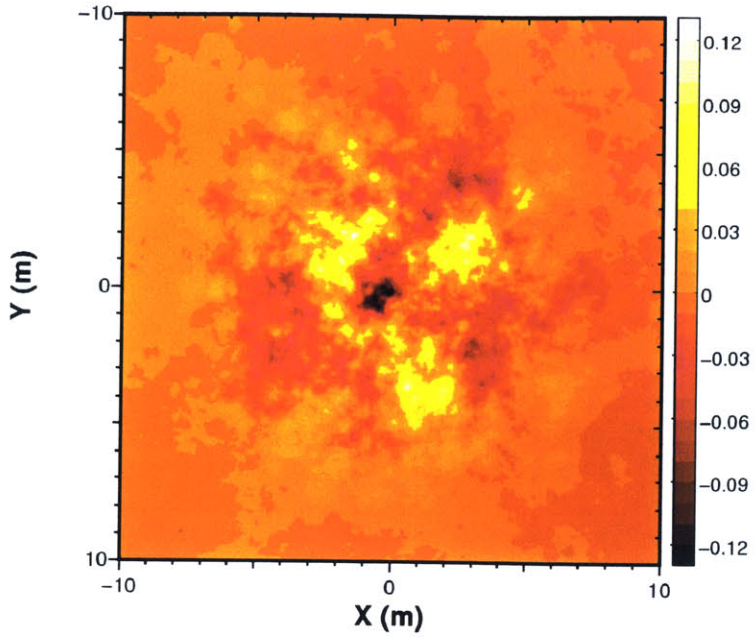

Figure 2-71: Isotropic Goff-Jordan roughness patch ($C_L = 2m$, $D = 2.5$, $\sqrt{\langle \gamma^2 \rangle} = 6.25cm$, $l_x = l_y = 20m$, and $Nx = N_y = 512$).

groups of compressional scattered waves are observed. Between the blue line (i.e. forward critical angle) and the red line (direction of specular reflection), compressional scattered waves move in the forward direction. Also, another compressional wave is scattered in the backward direction.

The next example has a similar scattering scenario as the previous case except that an elastic limestone ($C_p = 2500m/s$, $C_s = 1000m/s$, and $\rho = 2.2g/cm^3$) lower half space is used instead of elastic sand. Figure 2-74 shows time snapshots of the incident beam pulse. Compared to the elastic sand case (Figure 2-72), the elastic limestone half space has the transmitted shear wave at a shallower angle.

Figure 2-75 shows the resulting snapshots of the in-plane scattered field. When they are compared against the case of an elastic sand half space, there are three major differences :

- strong backward scattering in both half spaces.
- shallower shear scattered wave in the lower space.
- backward shear scattering is stronger than forward compressional scattering in the lower space.

As the compressional and shear wave speeds increase in the lower half space, scattering in the backward direction is enhanced significantly in both spaces. Also, the transmitted energy in the form of compressional waves is lower than that of elastic sand because of the limestone's higher compressional wave speed. This explains the reason the backward shear scattering is stronger than forward compressional scattering.

The following scattering example is the case of an elastic basalt ($C_p = 5000m/s$, $C_s = 2000m/s$, and $\rho = 2.4g/cm^3$) half space. Unlike the previous two cases (sand and limestone), the shear wave speed of elastic basalt exceeds the compressional wave speed of water. As shown in Figure 2-76,

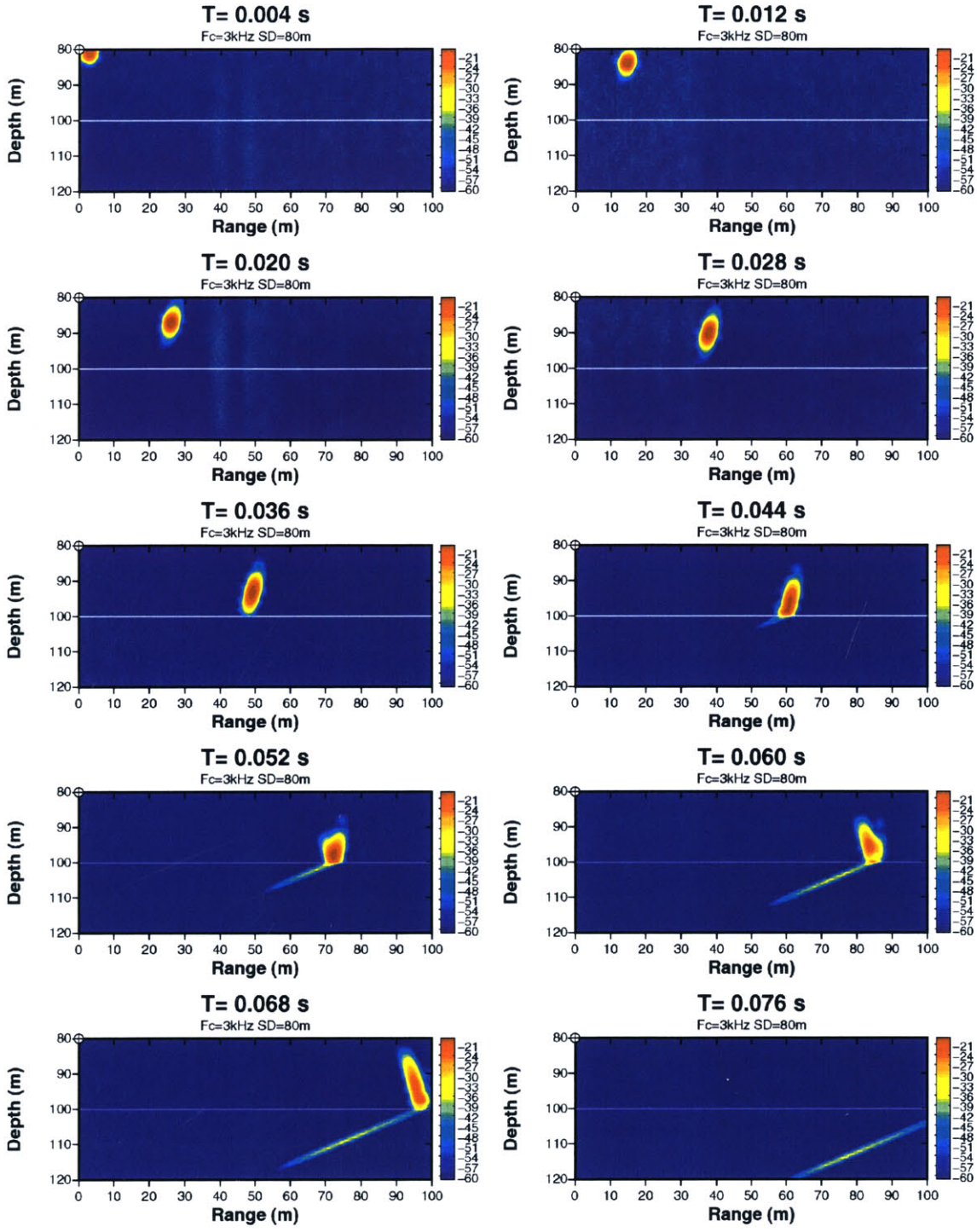

Figure 2-72: Time snapshots of in-plane incident beam pulse : a water half space and an elastic sand half space. The center of vertical array is located at 80m depth. The length of array is 8m and the number of elements is 128. The main lobe is focused at 100m depth with 15° tilt angle. $F_c = 3kHz$ (center frequency) and $\Delta F = 1kHz$ (bandwidth).

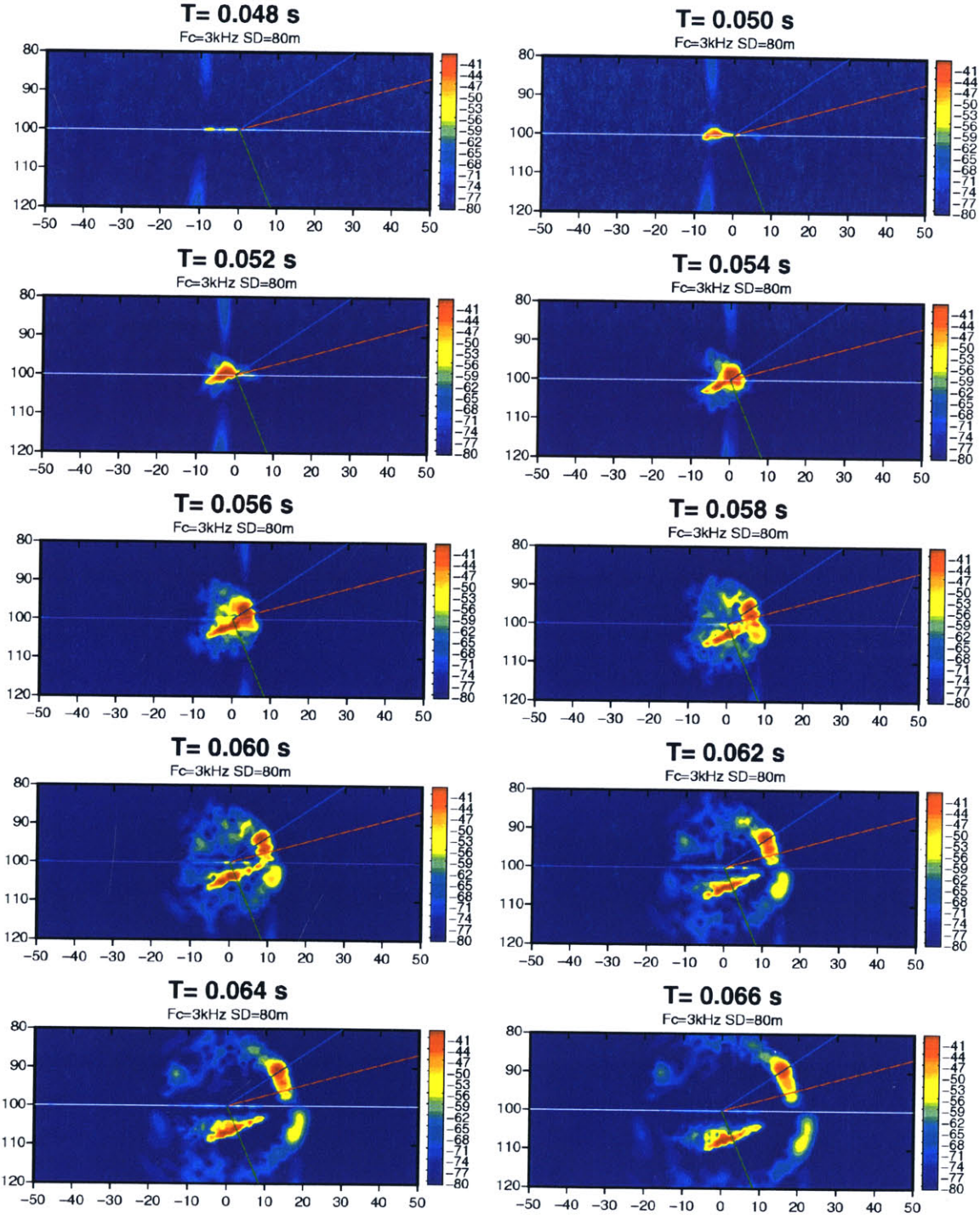

Figure 2-73: Time snapshots of in-plane scattered field : a water half space and an elastic sand half space. The center of roughness patch (Figure 2-71) is located at $100m$ depth and $0m$ range. The incident pulse is shown in Figure 2-72.

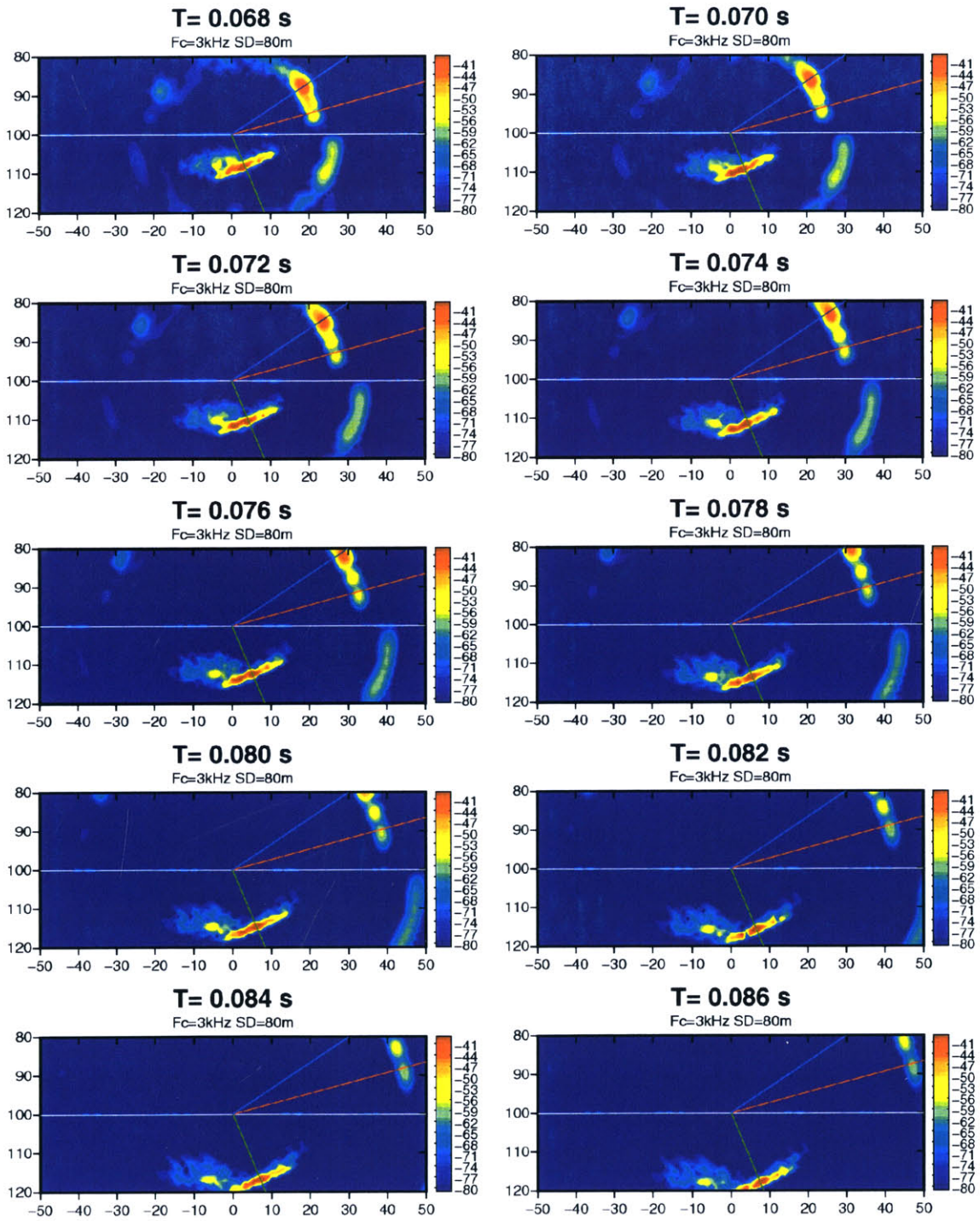

(Figure 2-73 continued)

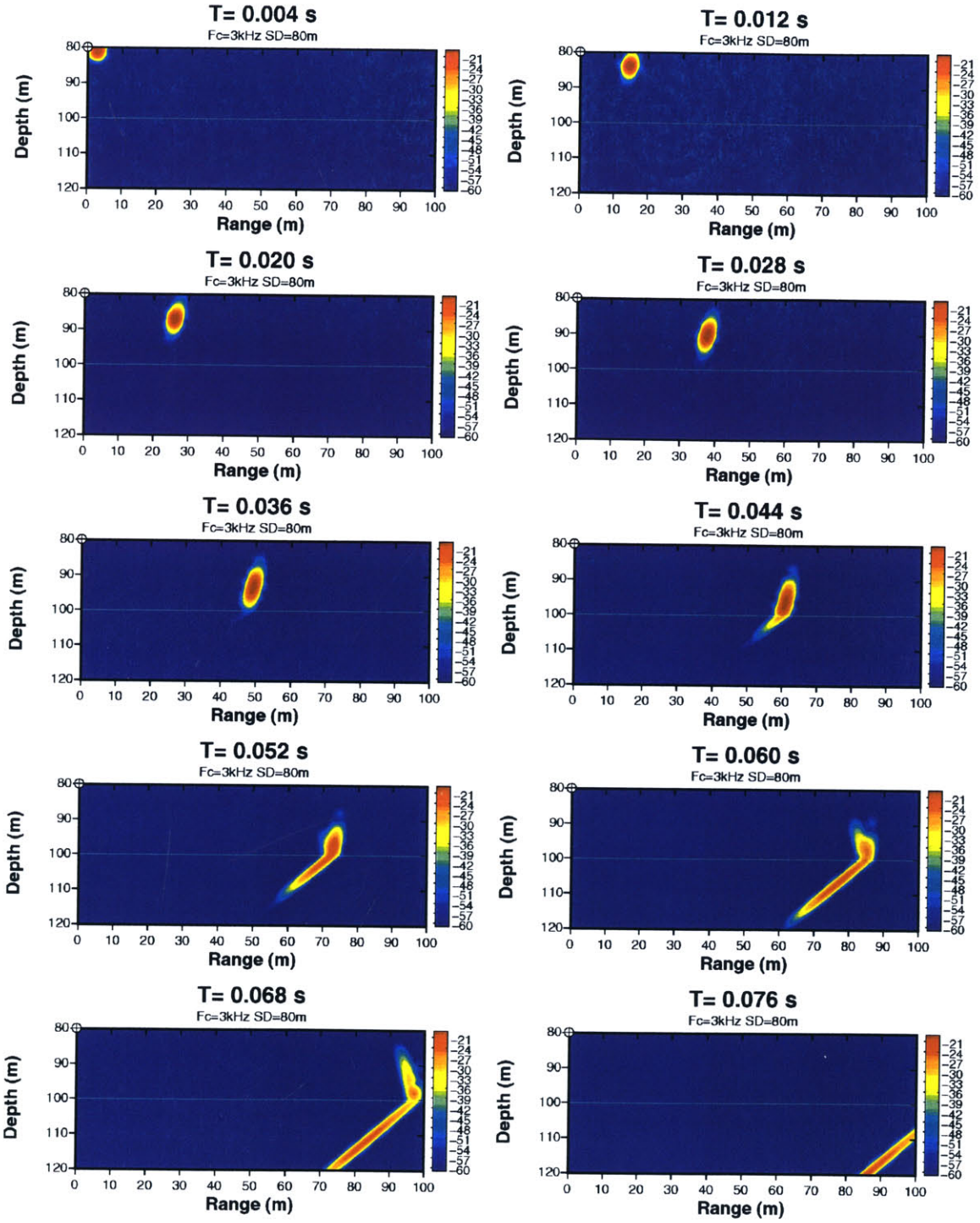

Figure 2-74: Time snapshots of in-plane incident beam pulse : a water half space and an elastic limestone half space. The center of vertical array is located at $80m$ depth. The length of array is $8m$ and the number of elements is 128. The main lobe is focused at $100m$ depth with 15° tilt angle. $F_c = 3kHz$ and $\Delta F = 1kHz$.

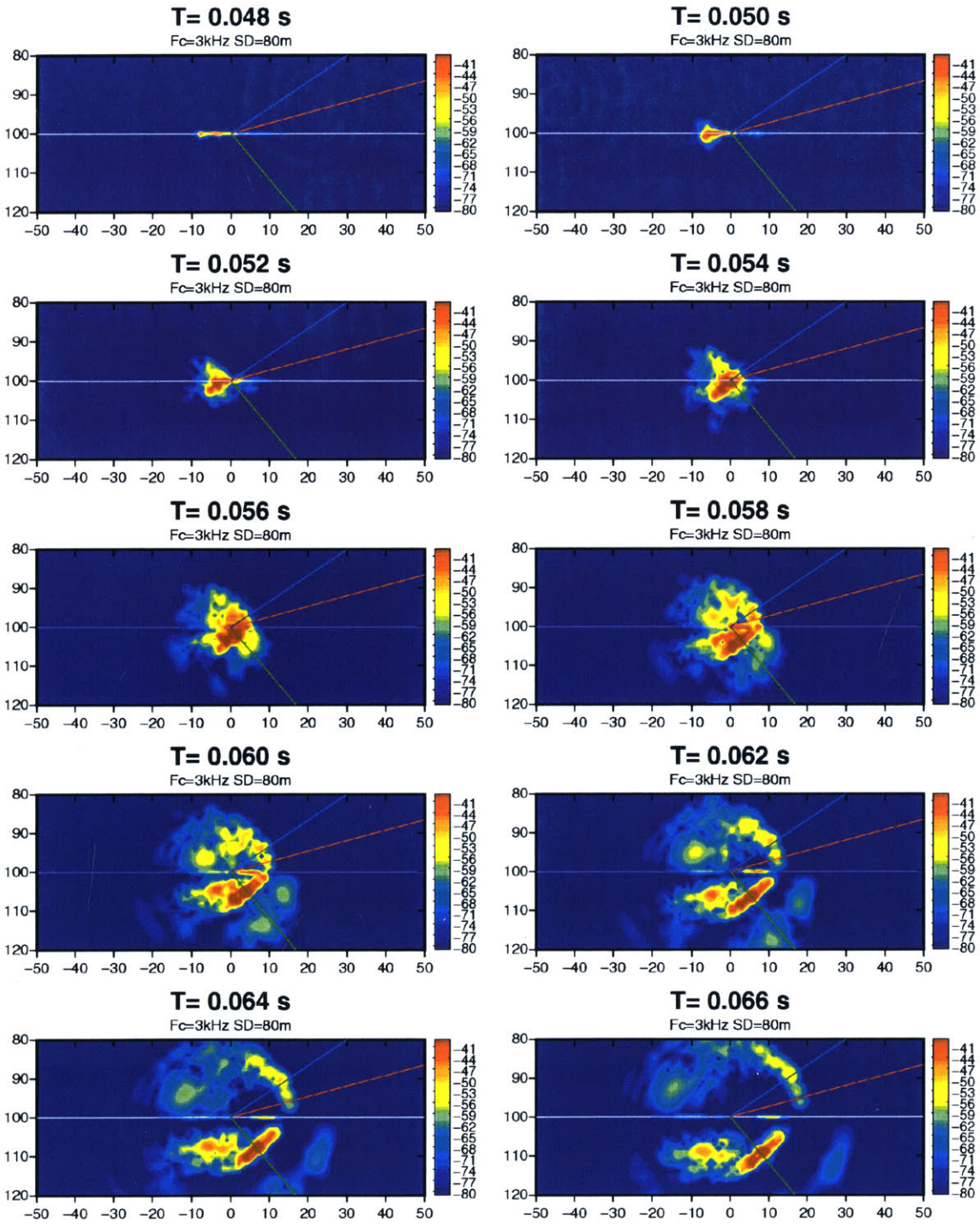

Figure 2-75: Time snapshots of in-plane scattered field : a water half space and an elastic limestone half space. The center of roughness patch (Figure 2-71) is located at 100m depth and 0m range. The incident pulse is shown in Figure 2-74.

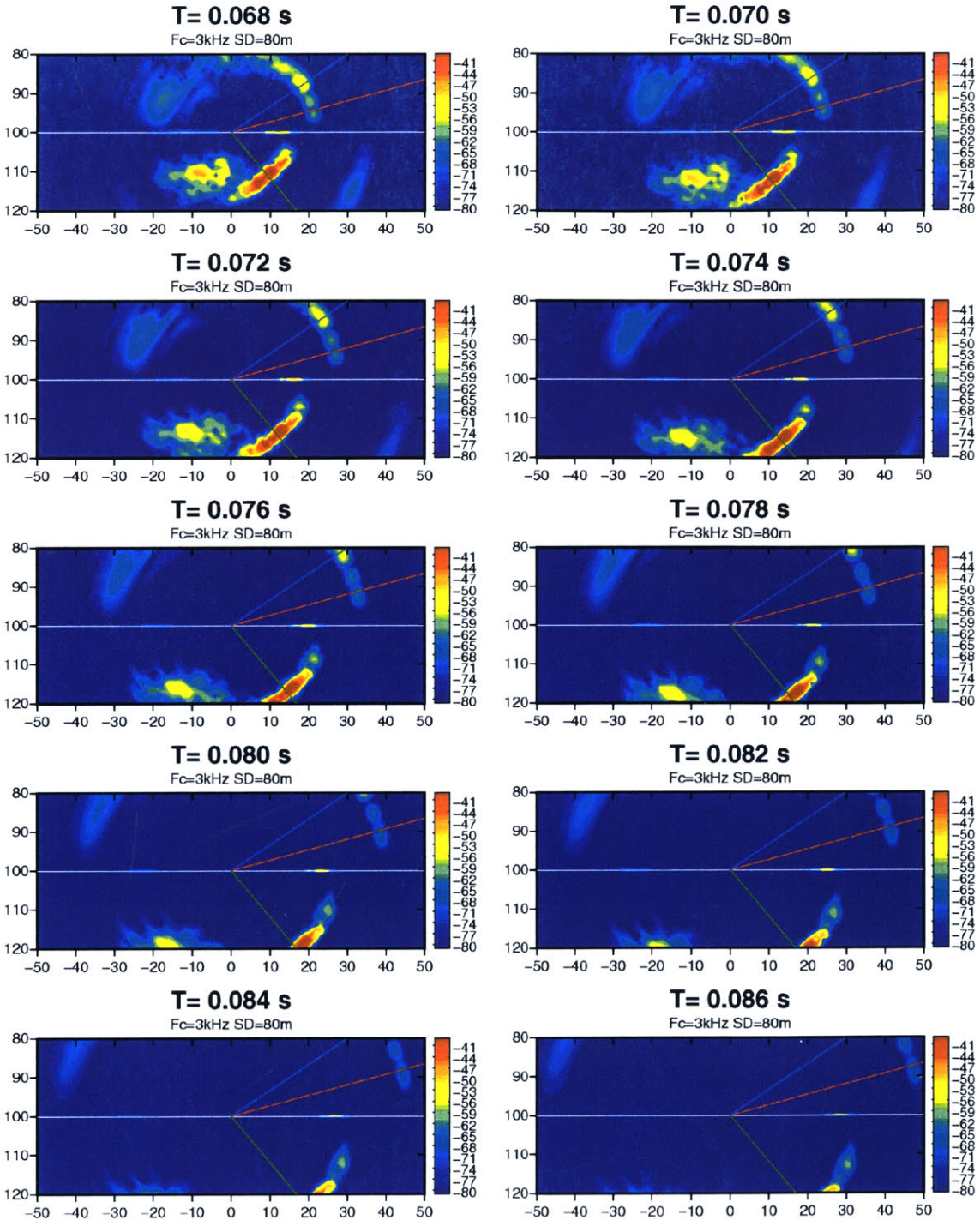

(Figure 2-75 continued)

the transmitted field in the lower half space is at least $40dB$ less than the field in the upper half space.

Figure 2-77 shows the resulting time snapshots of the in-plane scattered field. The most interesting scattering feature is the existence of a scattered interface wave (Scholte wave). This type of wave occurs when both shear and compressional waves are evanescent in the lower space. By searching for a pole in the evanescent wavenumber regime, the phase speed of the Scholte wave is obtained. For this example, it is $C_{\text{Scholte}} = 1455.5m/s$ which is very close to the compressional speed of water. Since the interface wave decays in both upper and lower spaces, its effects are most pronounced near the interface. In Figure 2-77, the scattered interface waves in the forward and backward directions can be observed clearly. The time evolution also confirms that the phase speed of the interface wave is very close to the compressional wave speed of water. In the upper half space, both backward and forward scattering are strong because of the large medium contrast between the two half spaces. The shear and compressional scattered waves in the lower half space are relatively weak.

The next scenario has an elastic sublayer between two half spaces. The medium consists of a water half space, a $4m$ elastic sand sublayer, and an elastic limestone lower half space. Figure 2-78 shows the time evolution of the incident beam pulse. Since the incident field is subsonic to compressional wave speeds in both the sublayer and the lower half space, most of transmitted energy is carried by shear waves in the lower media. The incident field in the upper half space is almost identical to that of an elastic sand half space (Figure 2-72).

Figure 2-79 shows the corresponding snapshots of the in-plane scattered field. Since the incident field in the upper half space is similar to that of an elastic sand half space, it is interesting to ask how the additional elastic sublayer changes the scattered field in the upper half space. There are three observable differences between the two cases. The sublayer case produces :

- enhanced backward scattering.
- two additional packets of scattered waves later in time ($T > 0.068s$).

Enhanced backscattering in the upper half space is due to the existence of a limestone half space which is faster than elastic sand. The limestone half space reflects shear and compressional waves back to the upward direction, which is not possible in the case of water - sand half spaces. This enhancement is very similar to the case of an elastic limestone half space. Two additional scattered waves in the upper half space are generated by shear and compressional scattered waves in the sublayer. The scattered waves in the sublayer propagate through the layer and re-radiate the scattered energy into the upper half space. The scattered packet with the later arrival has significant meaning because of its long time lag ($\Delta t > 12ms$) from the forward scattered field in the upper half space.

The next three examples demonstrate the effects of roughness anisotropy in time domain scattering solutions. For this purpose, three roughness patches (Figures 2-81, 2-83, and 2-85) are generated by anisotropic Goff-Jordan power spectra with varying anisotropic angles (θ_s). The scattering environment consists of a water upper half space, a $2m$ elastic sand sublayer, and an elastic limestone half space. The incident field is generated using the same VLA used in the previous cases. Figure 2-80 shows the snapshots of the in-plane incident beam pulse. It is very similar to the previous case of a $4m$ elastic sand sublayer.

Figure 2-81 is the roughness patch used for the first scattering case. Roughness has anisotropic angle $\theta_s = 0°$, which is aligned with the incident direction. As demonstrated in the frequency domain solutions (Figure 2-58(b) and Figure 2-60), this kind of anisotropy enhances the forward scattering and keeps the backward scattering at lower levels.

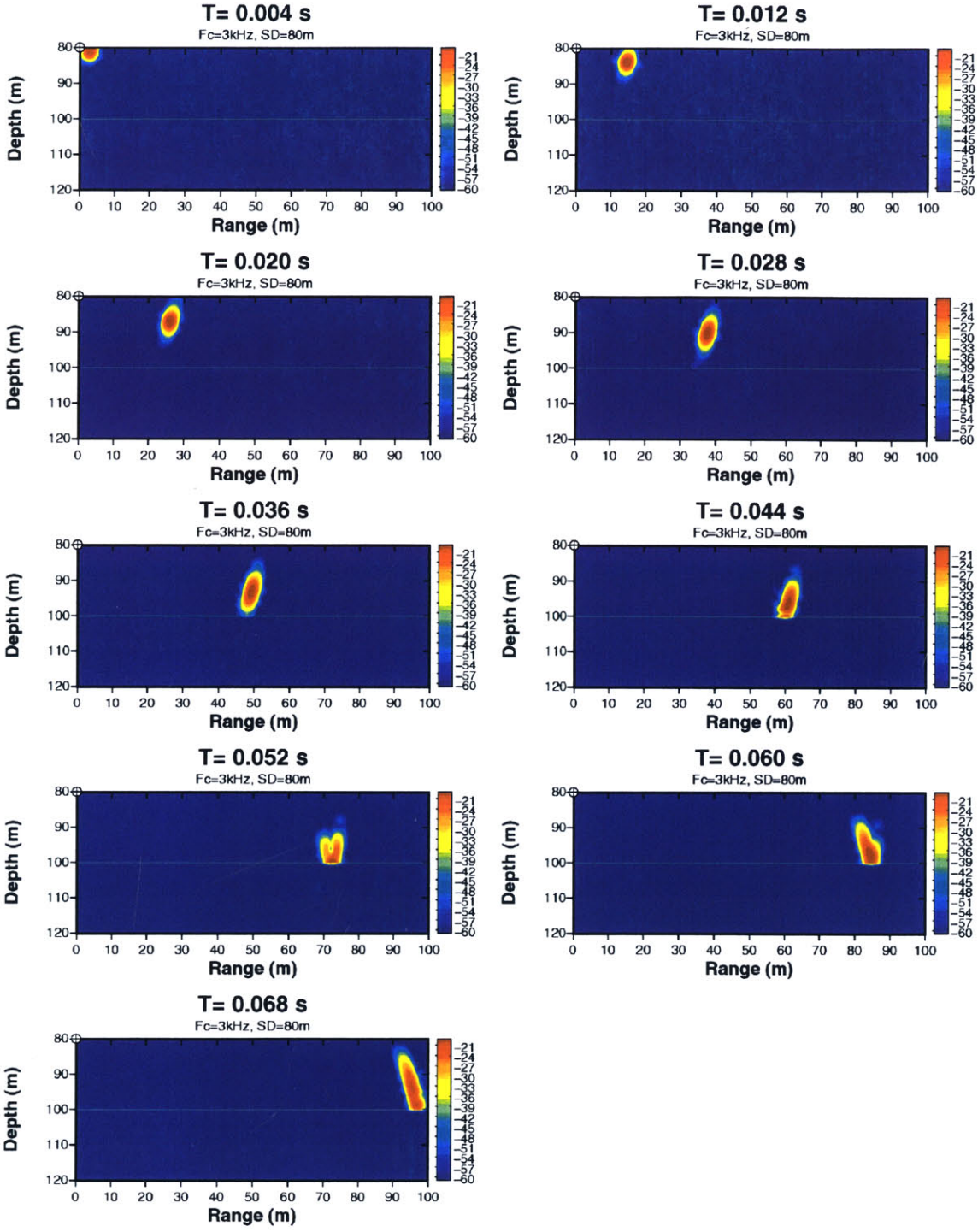

Figure 2-76: Time snapshots of in-plane incident beam pulse : a water half space and an elastic basalt half space. The center of vertical array is located at 80m depth. The length of array is 8m and the number of elements is 128. The main lobe is focused at 100m depth with 15° tilt angle. $F_c = 3kHz$ and $\Delta F = 1kHz$.

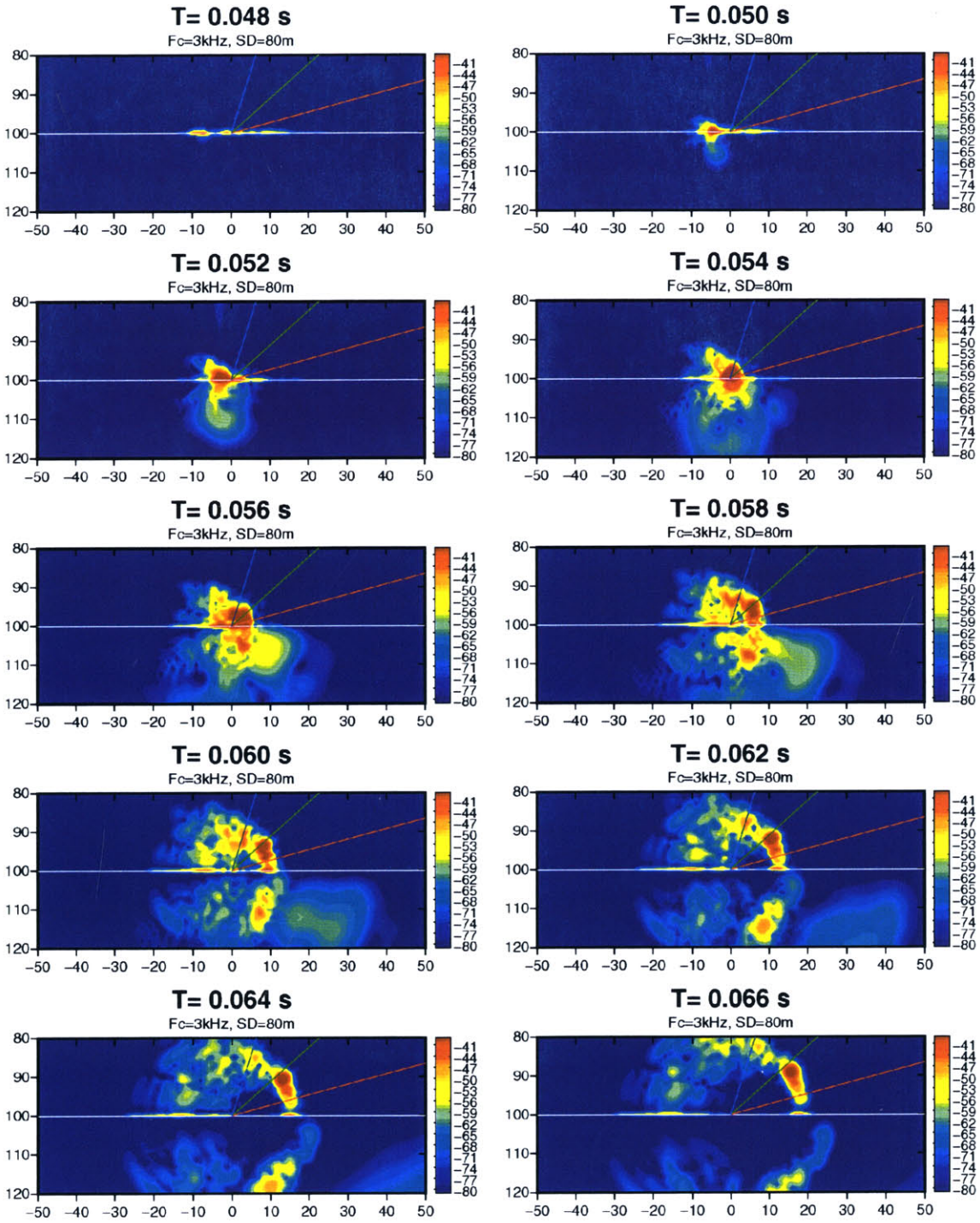

Figure 2-77: Time snapshots of in-plane scattered field : a water half space and an elastic basalt half space. The center of roughness patch (Figure 2-71) is located at $100m$ depth and $0m$ range. $F_c = 3kHz$ and $\Delta F = 1kHz$.

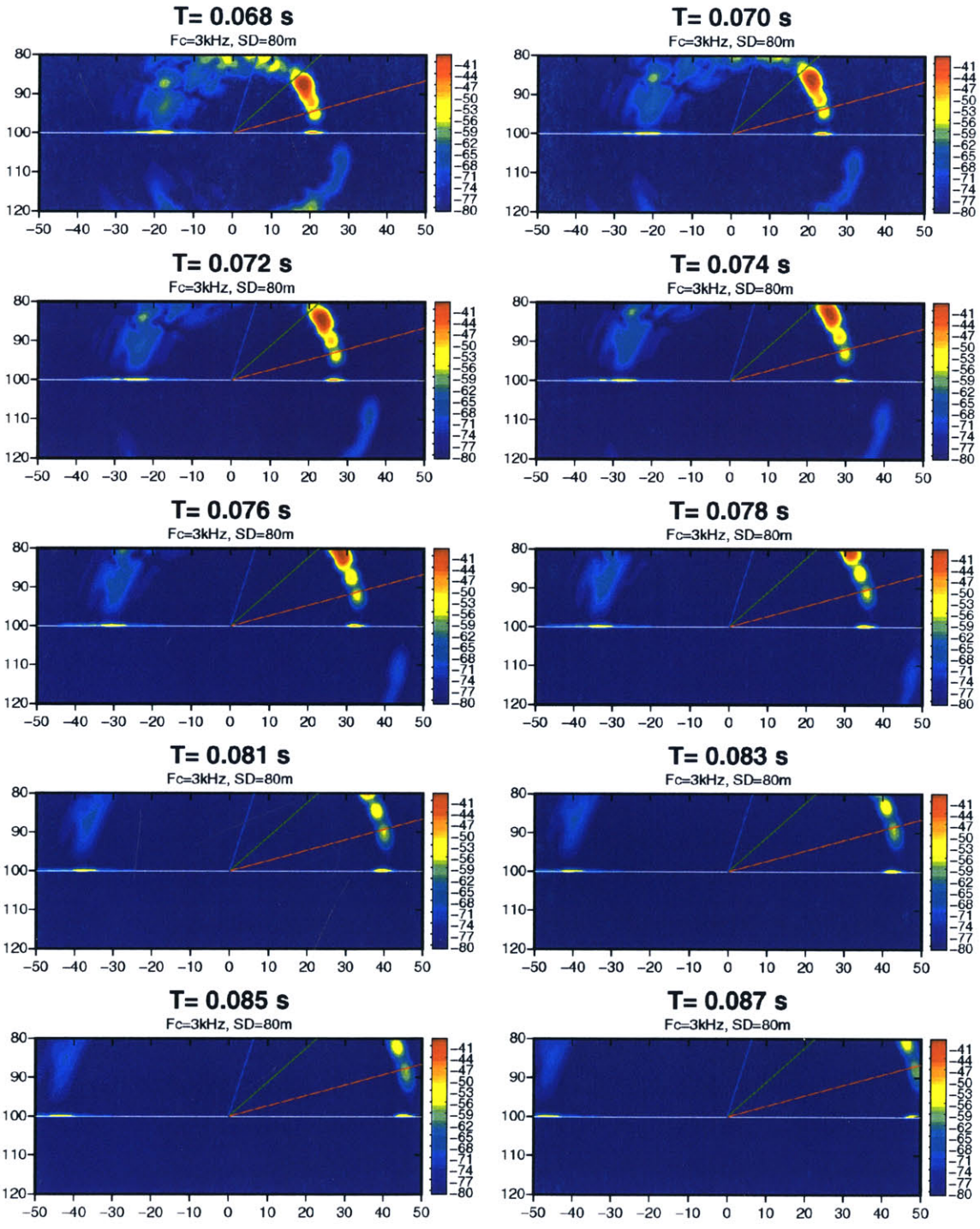

(Figure 2-77 continued)

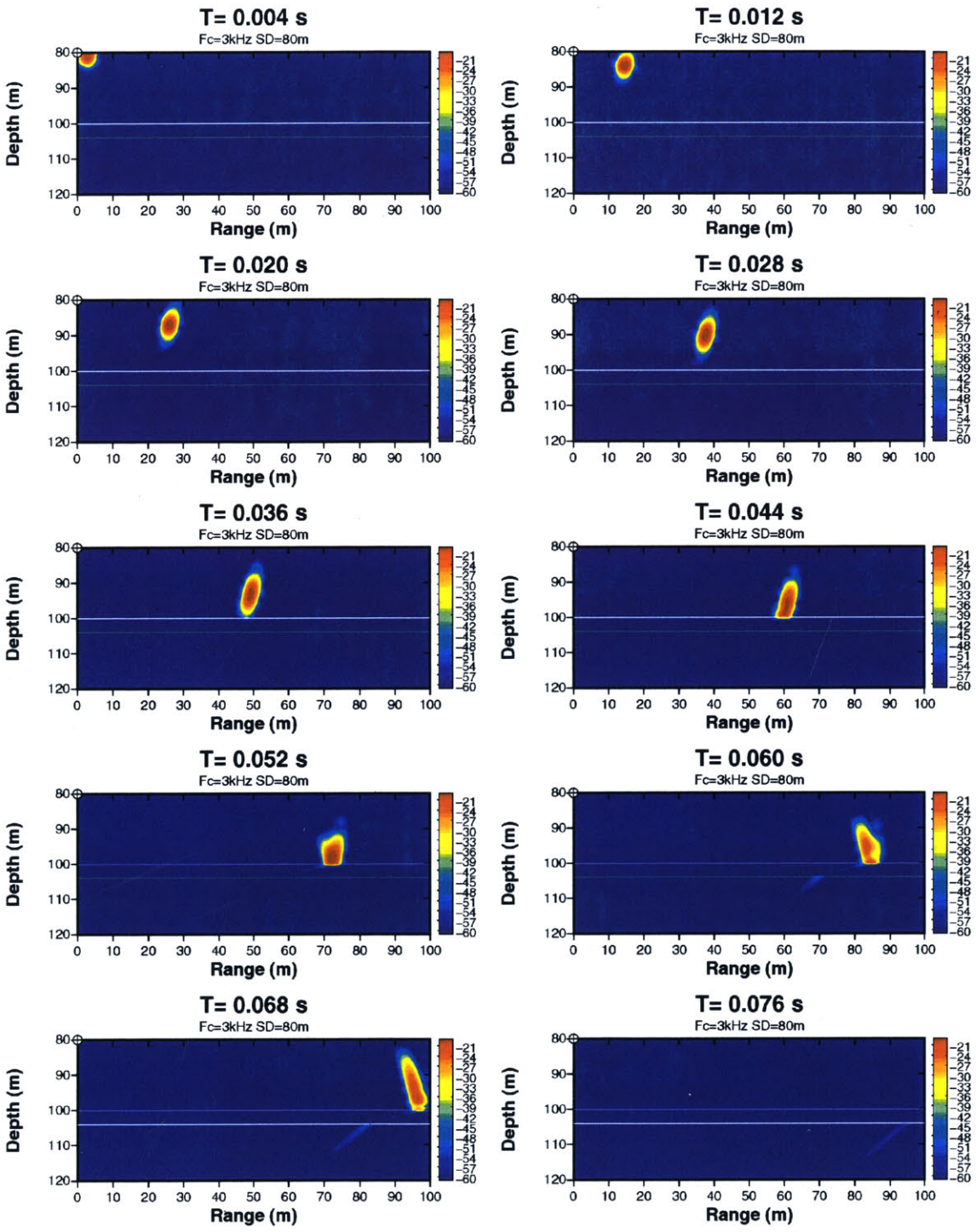

Figure 2-78: Time snapshots of in-plane incident beam pulse : a water half space, a $4m$ elastic sand layer, and an elastic limestone half space. The center of vertical array is located at $80m$ depth. The length of array is $8m$ and the number of elements is 128. The main lobe is focused at $100m$ depth with 15° tilt angle. $F_c = 3kHz$ and $\Delta F = 1kHz$.

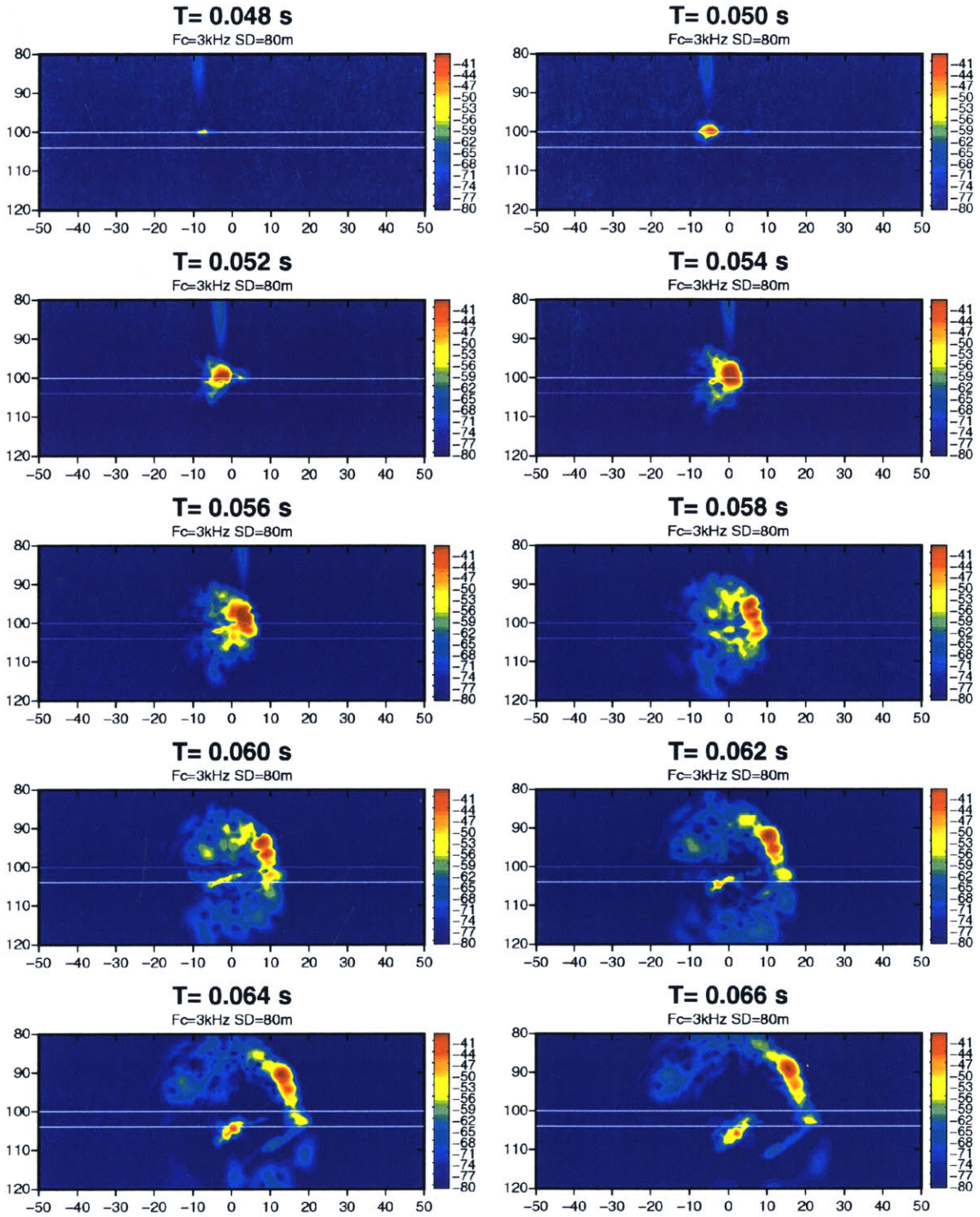

Figure 2-79: Time snapshots of in-plane scattered field : a water half space, a $4m$ elastic sand layer, and an elastic limestone half space. The center of roughness patch (Figure 2-71) is located at $100m$ depth and $0m$ range. $F_c = 3kHz$ and $\Delta F = 1kHz$.

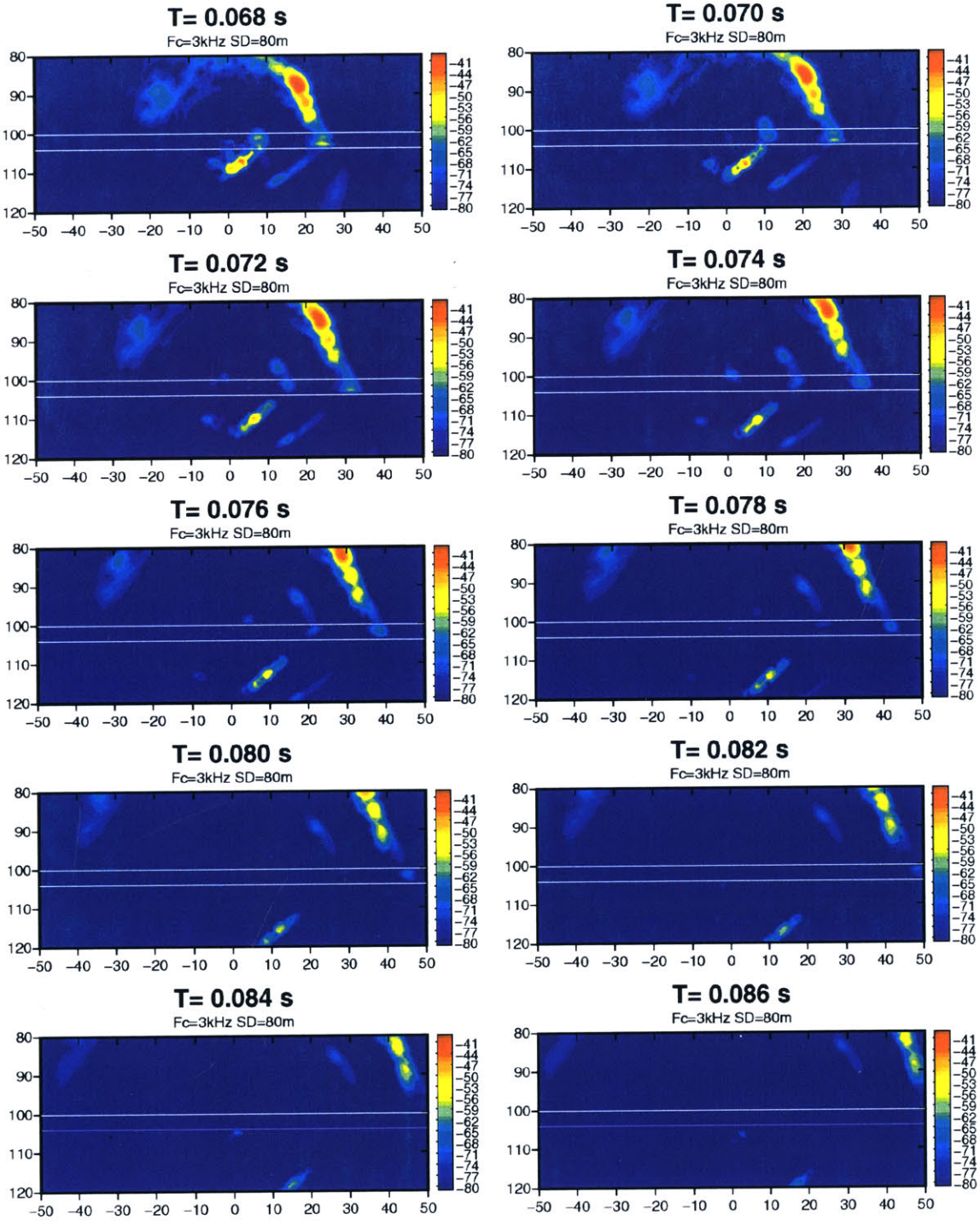

(Figure 2-79 continued)

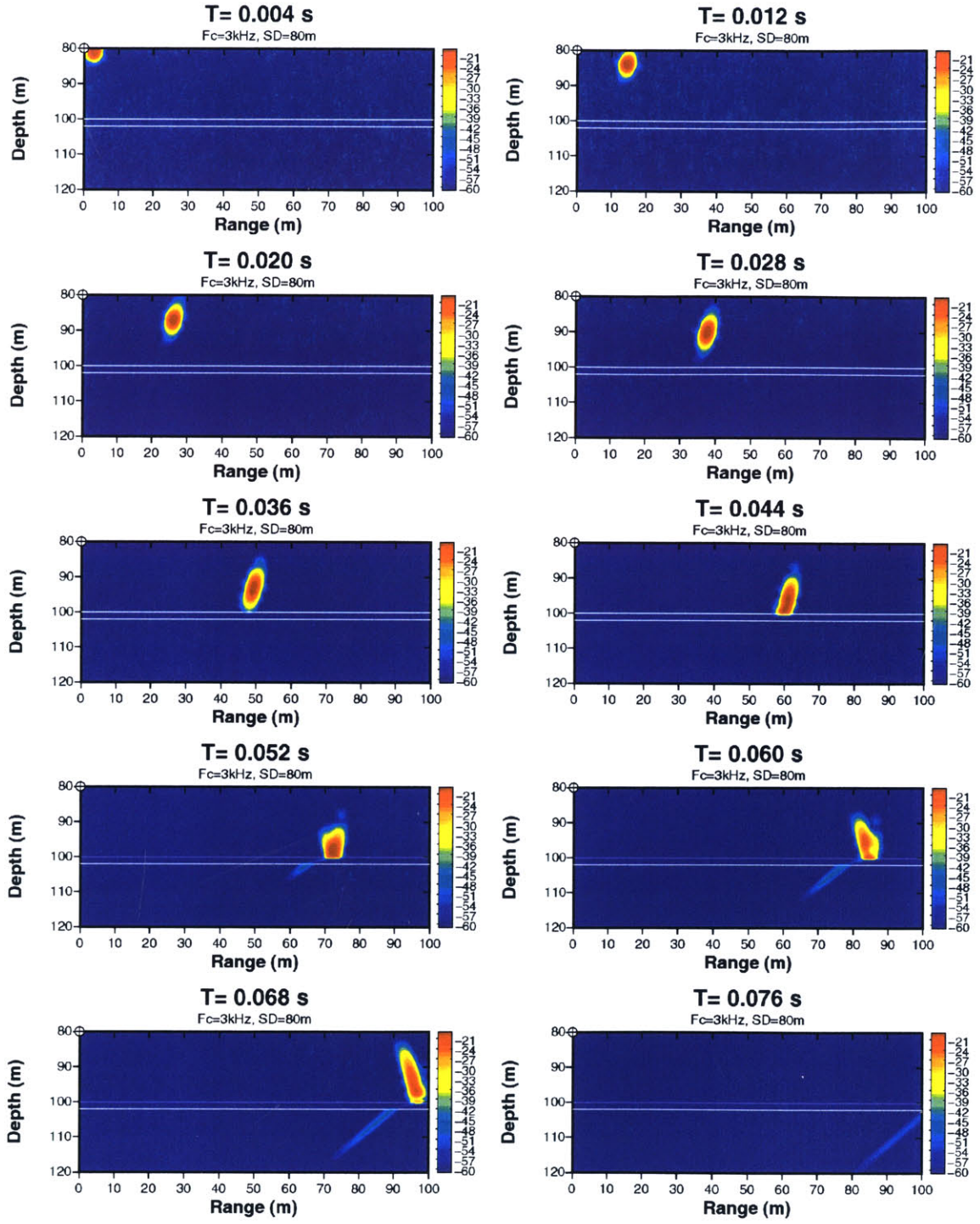

Figure 2-80: Time snapshots of in-plane incident beam pulse : a water half space, a $2m$ elastic sand layer, and an elastic limestone half space. The center of vertical array is located at $80m$ depth. The length of array is $8m$ and the number of elements is 128. The main lobe is focused at $100m$ depth with 15° tilt angle. $F_c = 3kHz$ and $\Delta F = 1kHz$.

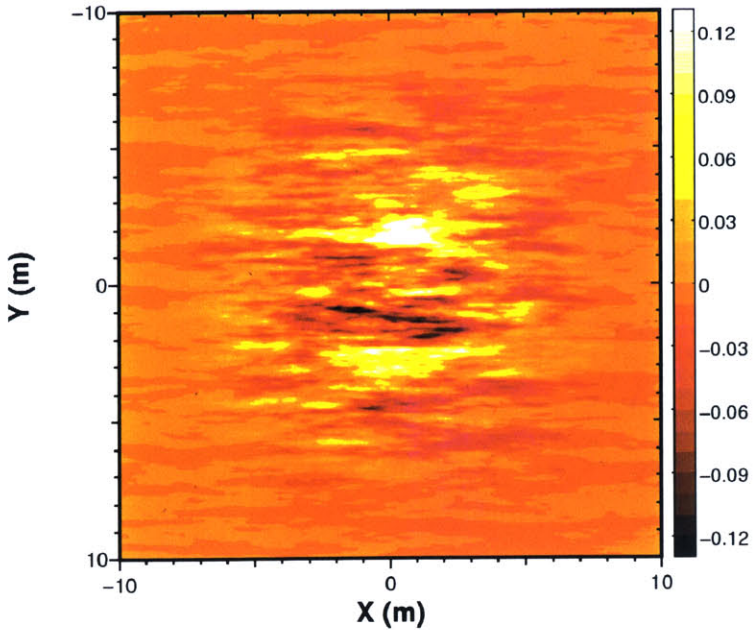

Figure 2-81: Anisotropic Goff-Jordan roughness patch ($C_{L1} = 2m$, $C_{L2} = 0.25m$, $\theta_s = 0°$, $D = 2.5$, $\sqrt{\langle \gamma^2 \rangle} = 6.25cm$, $l_x = l_y = 20m$, and $N_x = N_y = 512$).

Figure 2-82 is the in-plane scattered field in the time domain. Compared to the case of an isotropic patch with a $4m$ elastic sand sublayer, the backward scattering level is low while the forward scattering remains at a similar level. Other scattering features such as re-radiation of shear and compressional waves from the sublayer into the upper half space can be observed as well.

Another time domain scattering computation is performed on the anisotropic roughness patch (Figure 2-83) with the same scattering configuration (i.e. medium and incident field). The only difference is the anisotropic angle of the roughness patch. The angle of anisotropy becomes $\theta_s = 90°$, which is perpendicular to the the direction of incidence. As explained in the frequency domain cases, this type of anisotropy increases the backward scattering levels significantly.

Figure 2-84 shows the snapshots of the in-plane scattered field. As predicted, the backward scattered fields are relatively strong in both upper and lower half spaces. The scattered energy in the elastic sand sublayer propagates to both forward and backward directions and then re-radiates into the upper and lower media. Unlike the case of the $4m$ elastic sand sublayer, re-radiation of scattered energy to the forward direction in the lower medium is clearly observed. The difference can be explained as follows. The thickness of the elastic sand sublayer controls the amount of energy passing through the sublayer by changing the modal structure in the layer. Generally, the thicker sublayers allow more propagating modes so that the total amount of trapped energy is increased. In other words, this thin sublayer allows more scattered energy to interact with the lower medium and produces stronger re-radiation of scattered waves.

The third case of roughness anisotropy uses the roughness patch with $\theta_s = 45°$ shown in Figure 2-85. The preferred scattering directions for this anisotropic angle are the forward direction and positive y direction (i.e. bistatic angle $\theta = 90°$). Unlike the previous roughness patches ($\theta_s = 0°, 90°$) , this type of roughness patch can produce a non-symmetric scattered field in an average sense (Figure 2-61).

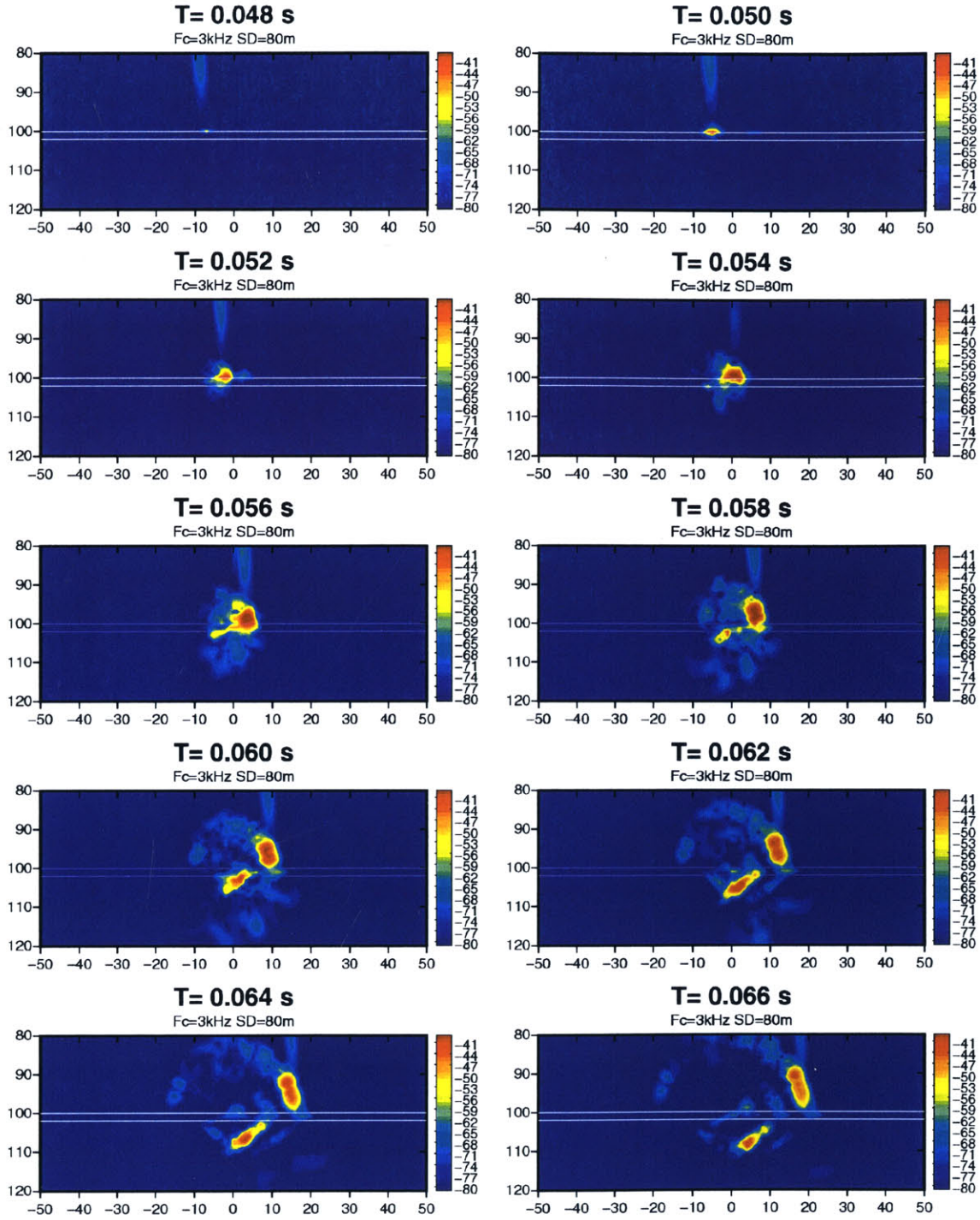

Figure 2-82: Time snapshots of in-plane scattered field : a water half space, a $2m$ elastic sand layer, and an elastic limestone half space. An anisotropic roughness patch with $\theta_s = 0°$ (Figure 2-81) is located at $100m$ depth and $0m$ range. $F_c = 3kHz$ and $\Delta F = 1kHz$.

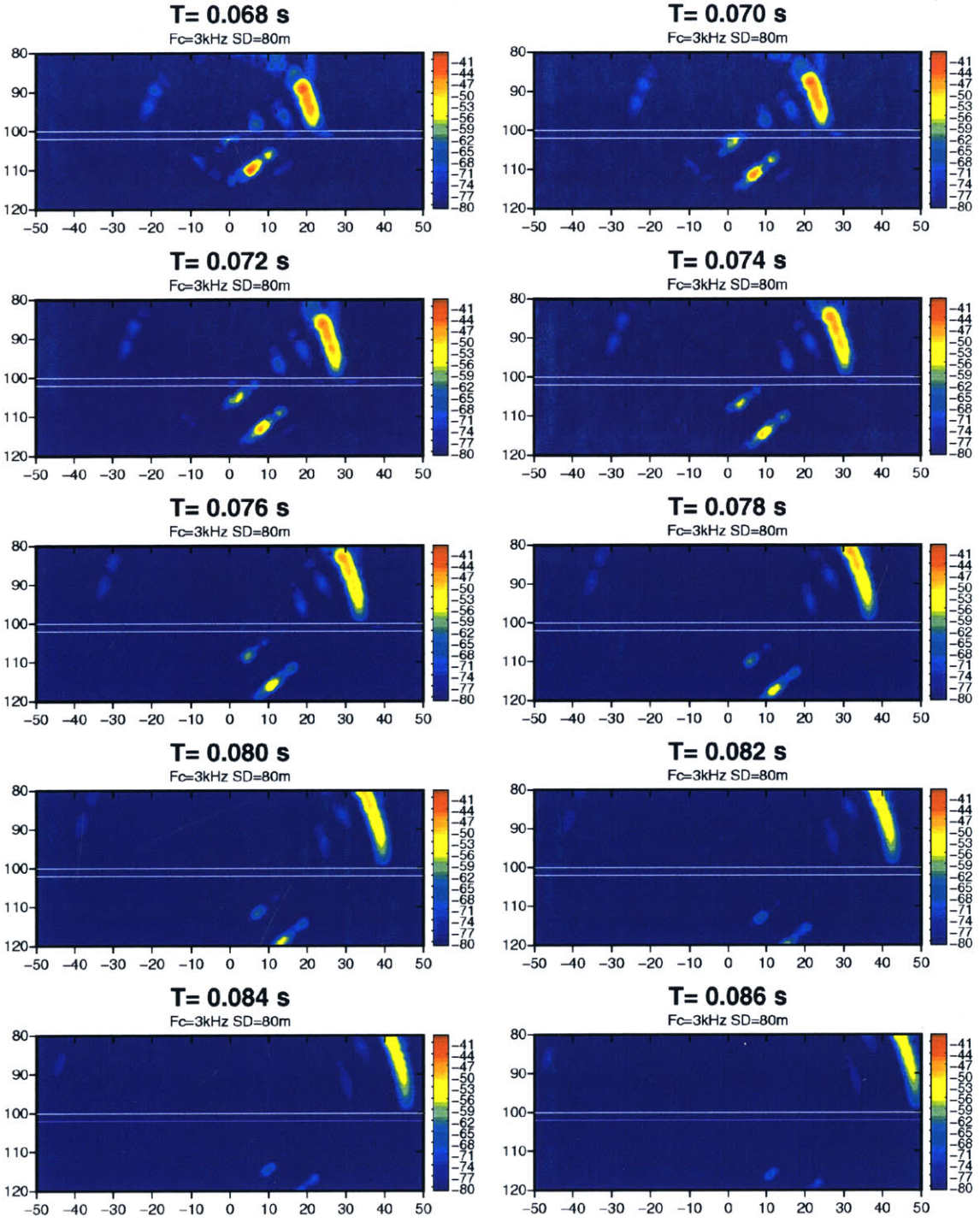

(Figure 2-82 continued)

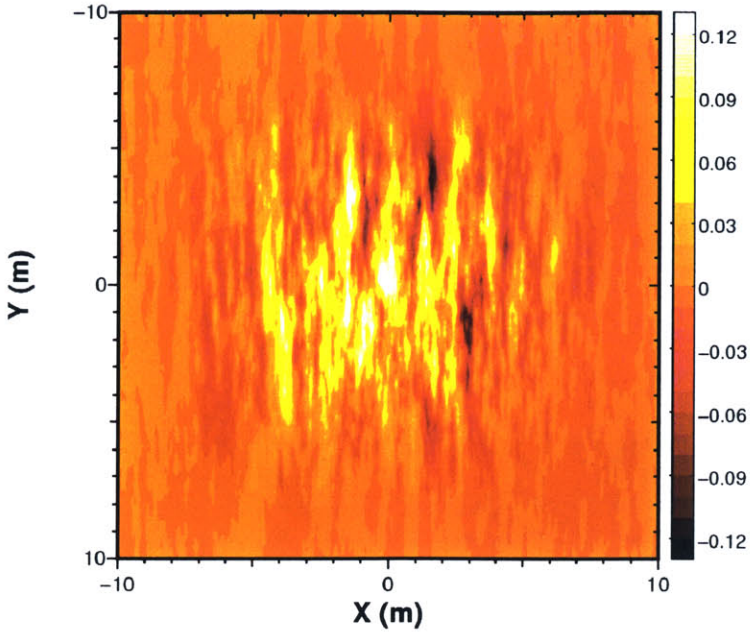

Figure 2-83: Anisotropic Goff-Jordan roughness patch ($C_{L1} = 2m$, $C_{L2} = 0.25m$, $\theta_s = 90°$, $D = 2.5$, $\sqrt{\langle \gamma^2 \rangle} = 6.25cm$, $l_x = l_y = 20m$, and $N_x = N_y = 512$).

Figure 2-86 shows the snapshots of the in-plane scattered field caused by the anisotropic patch ($\theta_s = 45°$). The in-plane scattered field is similar to that of the $\theta_s = 0°$ case except that the amplitude of the backward scattered wave is stronger. However, the in-plane scattered snapshots are not sufficient to describe the case of $\theta_s = 45°$ since the out-of-plane scattering is dominant at this anisotropic angle.

In order to observe the out-of-plane scattering event, vertical cuts at $\theta = 90°$ and $\theta = 270°$ are used for the time snapshots of the scattered field (Figure 2-87). In the plots, the right side corresponds to the positive y axis ($\theta = 90°$) and the downward direction is aligned with the positive z direction. The dominant feature in this case is the strong right side ($\theta = 90°$) scattered wave in the upper half space. Unlike the upper half space, an almost equal amount of scattered waves propagates to the left and right sides. There is a subtle difference in the right side of the lower space. A packet of scattered waves follows the first scattered wave. This may be caused by the shear conversion of the shear scattered wave in the sublayer. It is unlikely that the compressional wave in the sublayer causes an observable scattering event because of subsonic incidence from the upper space. Close observation of snapshots at $T = 72ms$ and $T = 74ms$ reveal that this packet has a steeper propagation angle. This implies that the scattered shear wave in the sublayer is transmitted to the lower half space in the form of compressional and shear waves with a time lag (about $6ms$).

The last example of wideband rough interface scattering involves an upper medium with a pressure-release surface (i.e. water column). For this example, an isotropic patch with shorter correlation length is used (Figure 2-88). Because of the smaller correlation length, the roughness patch is expected to allow coupling with high wavenumber components (i.e. backward scattering). The medium consists of a $20m$ water column, a $2m$ elastic sand sublayer, and an elastic limestone half space. The rough interface is located at $20m$ depth. The source configuration is identical to the previous examples.

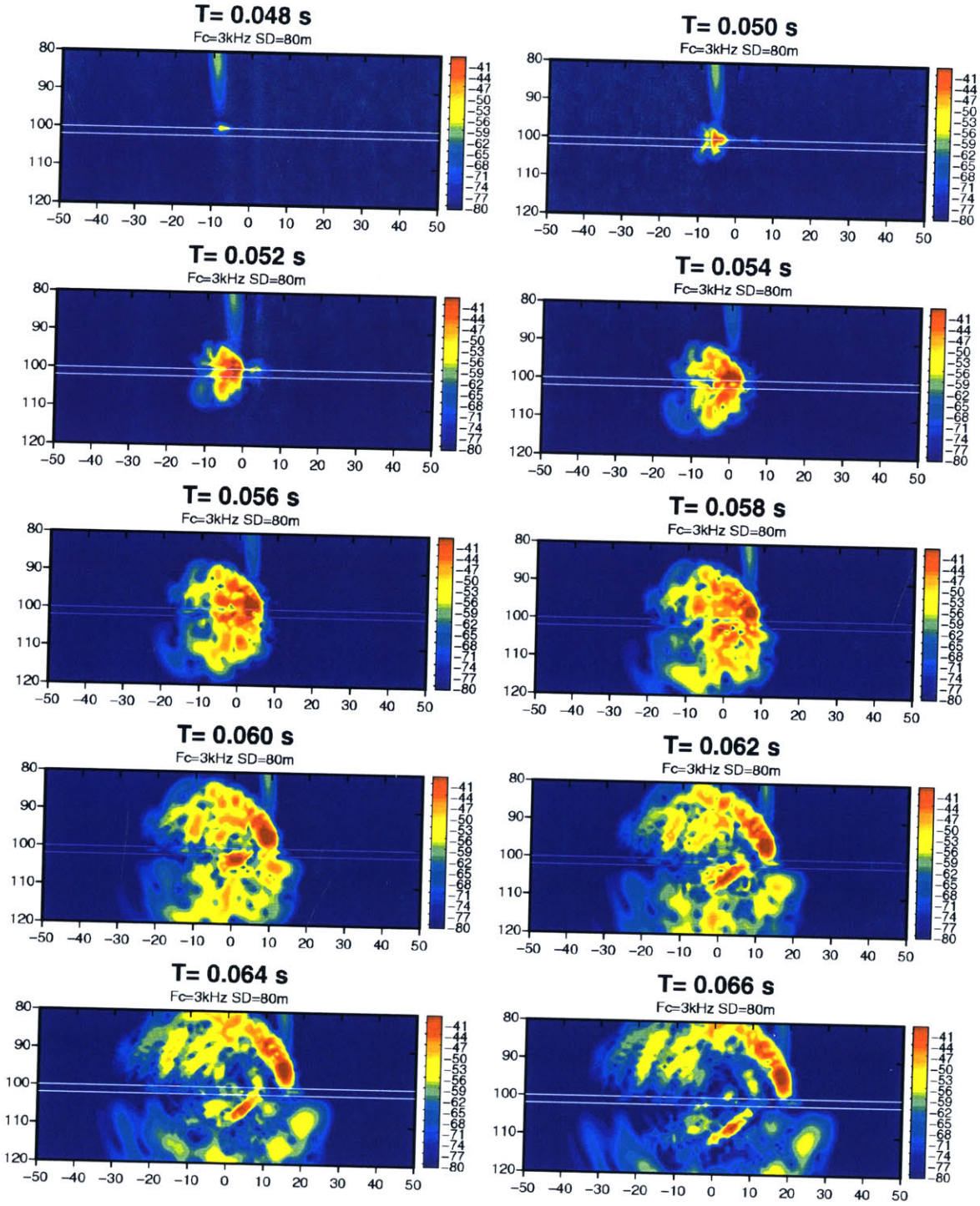

Figure 2-84: Time snapshots of in-plane scattered field : a water half space, a $2m$ elastic sand layer, and an elastic limestone half space. An anisotropic roughness patch with $\theta_s = 90°$ (Figure 2-83) is located at $100m$ depth and $0m$ range. $F_c = 3kHz$ and $\Delta F = 1kHz$.

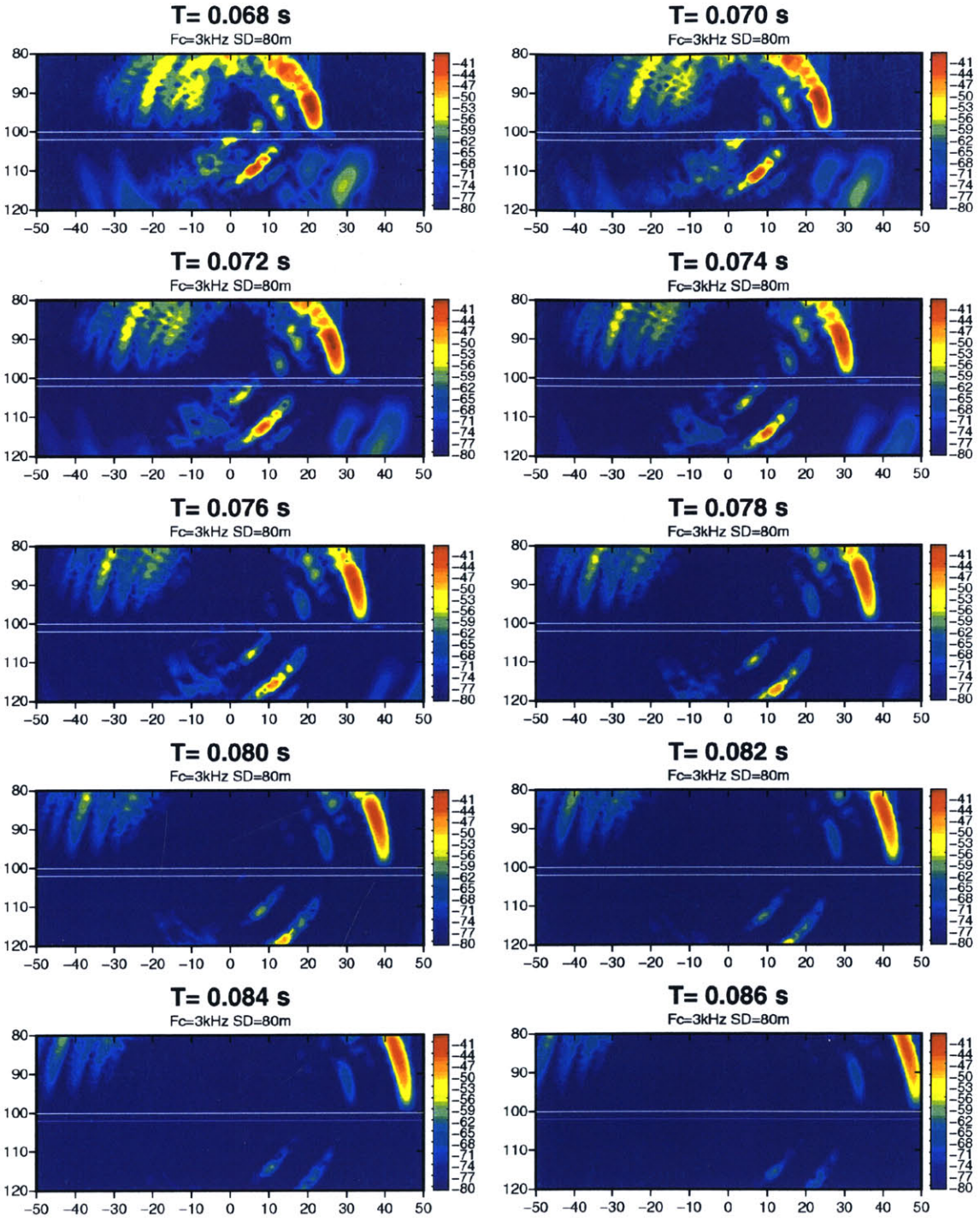

(Figure 2-84 continued)

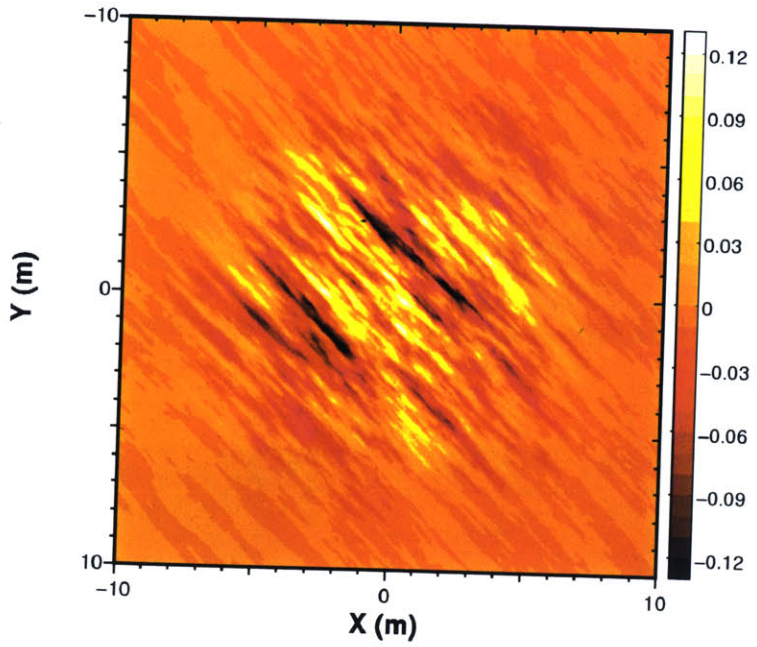

Figure 2-85: Anisotropic Goff-Jordan roughness patch : ($C_{L1} = 2m$, $C_{L2} = 0.25m$, $\theta_s = 45°$, $D = 2.5$, $\sqrt{\langle \gamma^2 \rangle} = 6.25cm$, $l_x = l_y = 20m$, and $N_x = N_y = 512$).

Figure 2-89 shows the snapshots of the in-plane incident field. The incident packet does not interact with the pressure-release surface until it passes the roughness patch.

Figure 2-90 is the resulting in-plane scattered field caused by a roughness patch in the waveguide. As a reference point, a cross mark indicates the center of the VLA in the scattered field plots. As predicted, the scattered energy in the backward direction is relatively strong. Until the wave front of scattered energy reaches the pressure-release surface, the scattered field is similar to the case without a pressure-release surface. Once the scattered wave hits the pressure-release surface, it is reflected in the downward direction with a grazing angle steeper than the direct scattered wave. If a monostatic[1] VLA receiver is used, there can be two major arrivals in the time series. The first arrival ($T = 52ms - 54ms$) is the direct scattered wave with upward direction close to the broadside[2] of the array. The second arrival ($T = 58ms - 62ms$) is the surface-reflected scattered wave with downward direction close to the end-fire[3] of the array. This demonstrates the possibility that a direct scattered wave in a waveguide can be separated from the surface-reflected scattered wave by analyzing time lag and angle of arrival. This kind of analysis can be performed through array beamforming [24].

[1] Arrays are called 'monostatic' when the source position coincides with the receiver position.
[2] For a line array, 'broadside' is referred to the direction perpendicular to the array.
[3] For a line array, 'end-fire' is the direction parallel to the array.

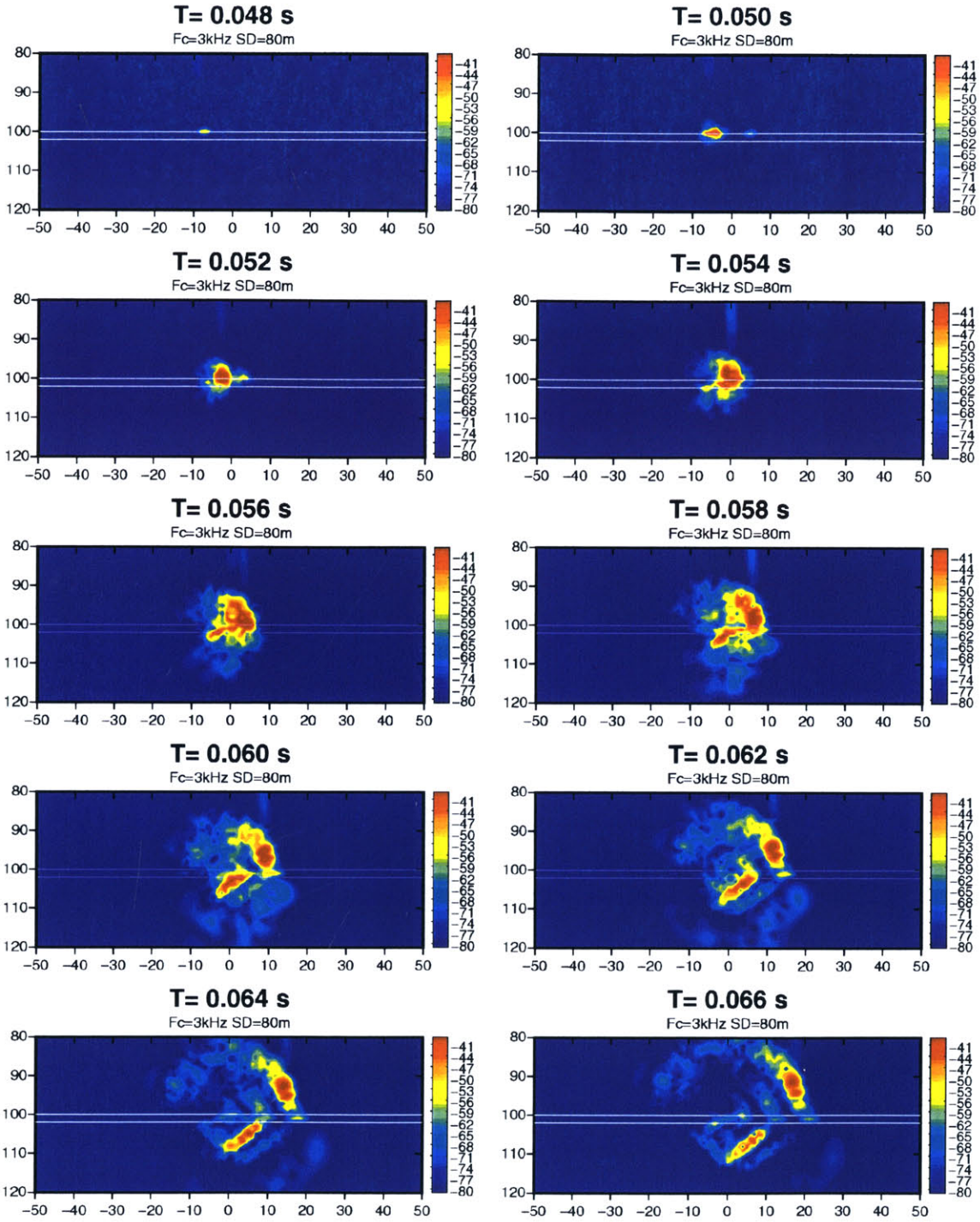

Figure 2-86: Time snapshots of in-plane scattered field : a water half space, a $2m$ elastic sand layer, and an elastic limestone half space. An anisotropic roughness patch with $\theta_s = 45°$ (Figure 2-85) is located at $100m$ depth and $0m$ range. $F_c = 3kHz$ and $\Delta F = 1kHz$.

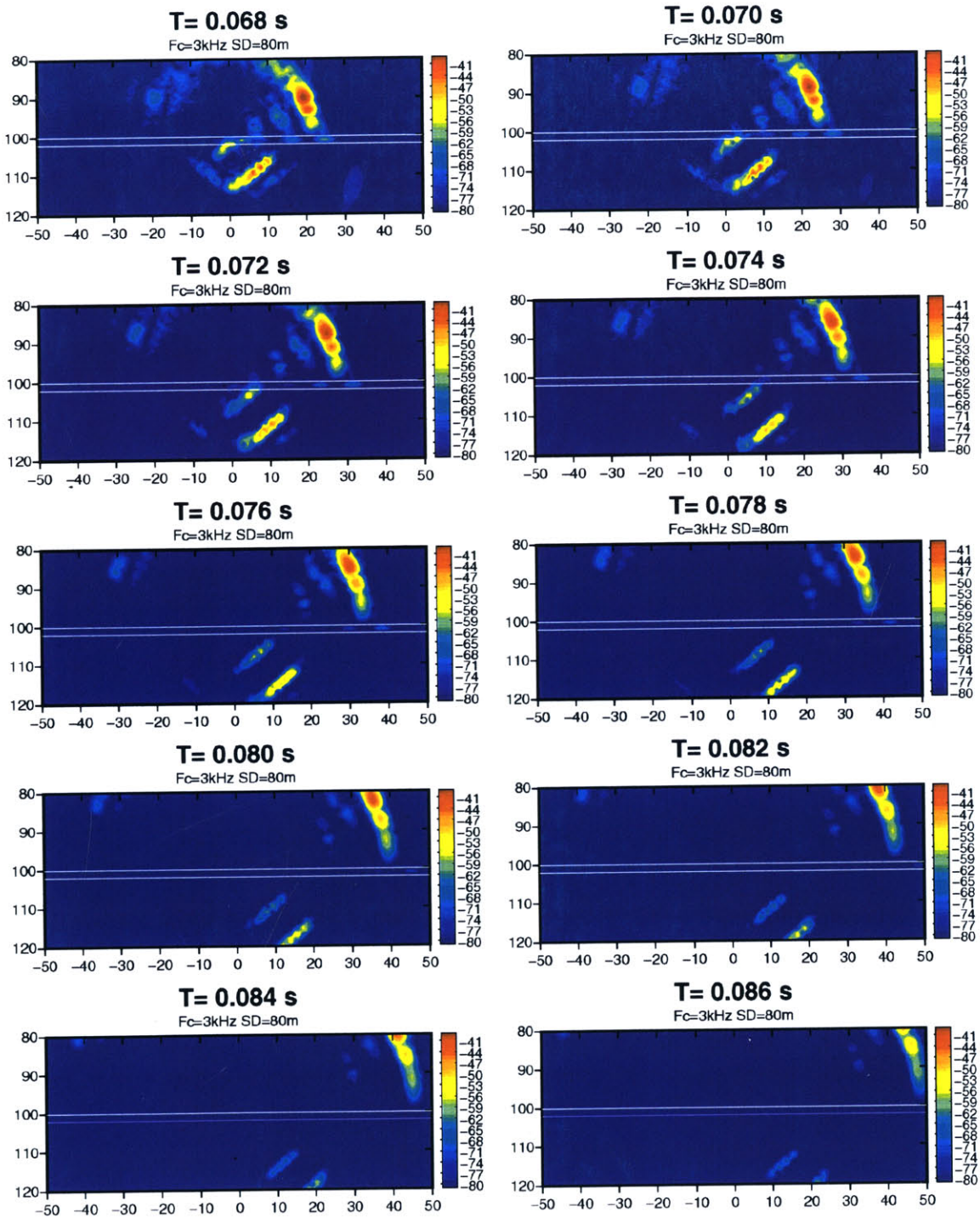

(Figure 2-86 continued)

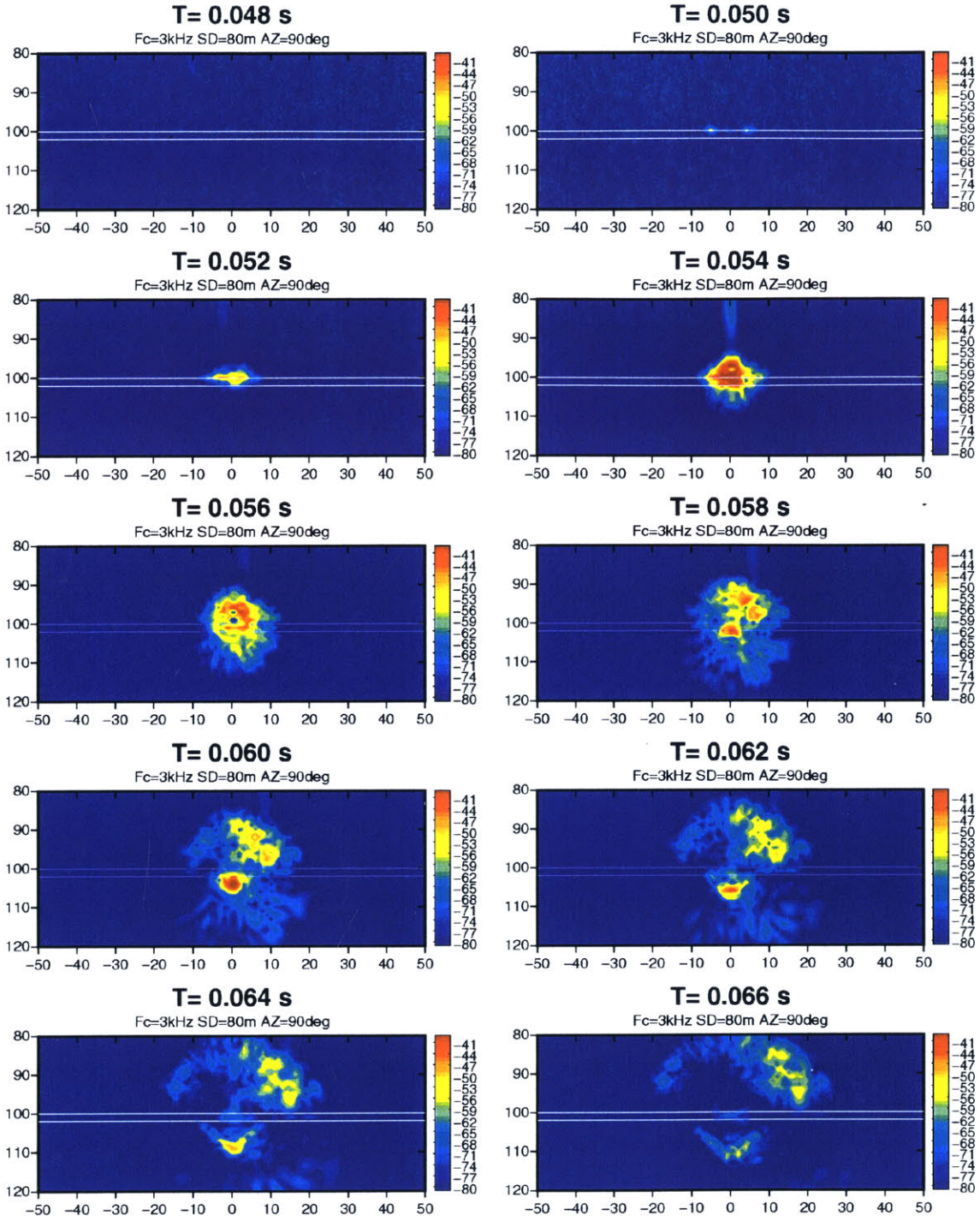

Figure 2-87: Time snapshots of scattered field in 90° azimuthal plane : Configuration is identical to the previous case (Figure 2-86). Horizontal axis corresponds to the y axis and the positive x direction points into the paper.

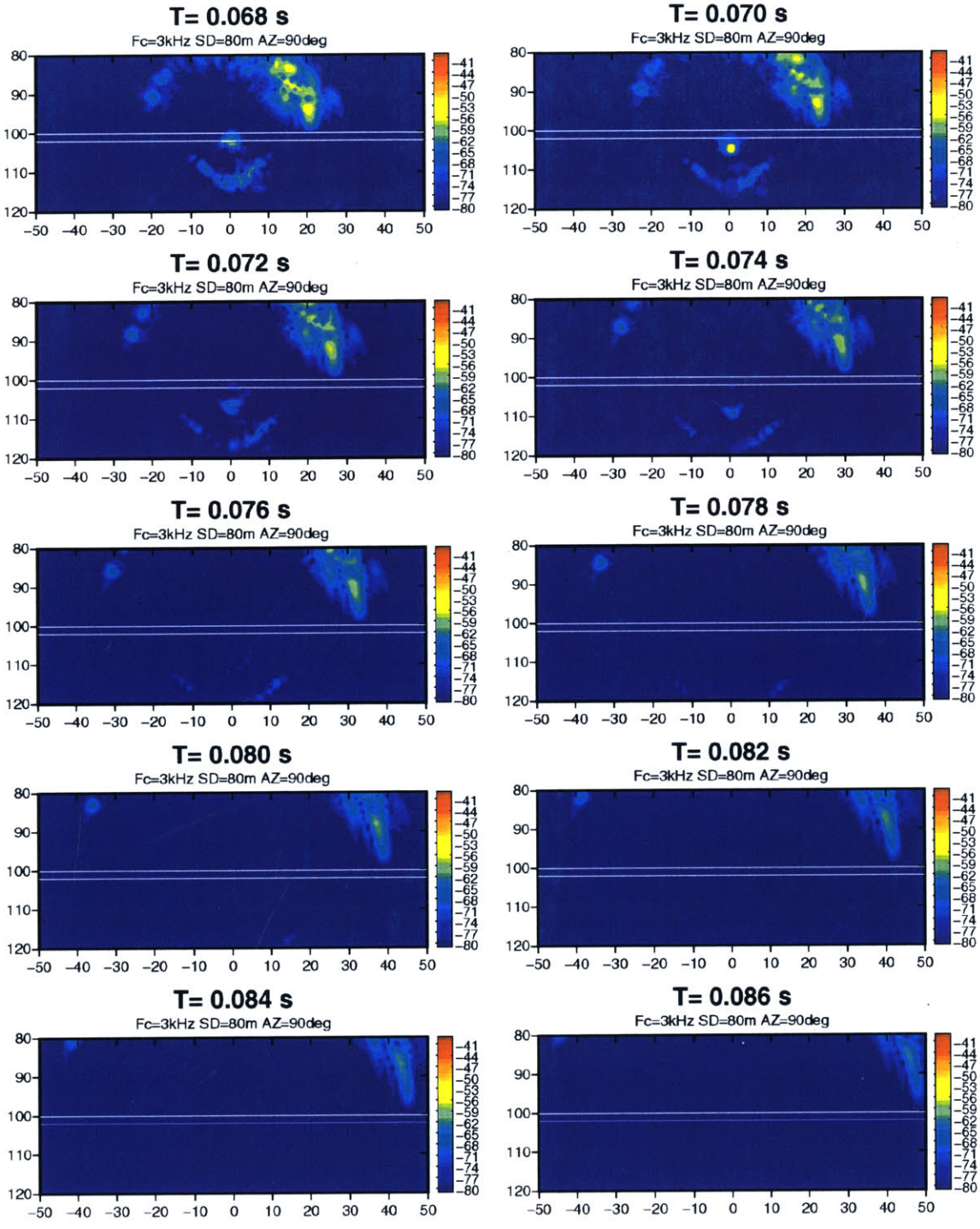

(Figure 2-87 continued)

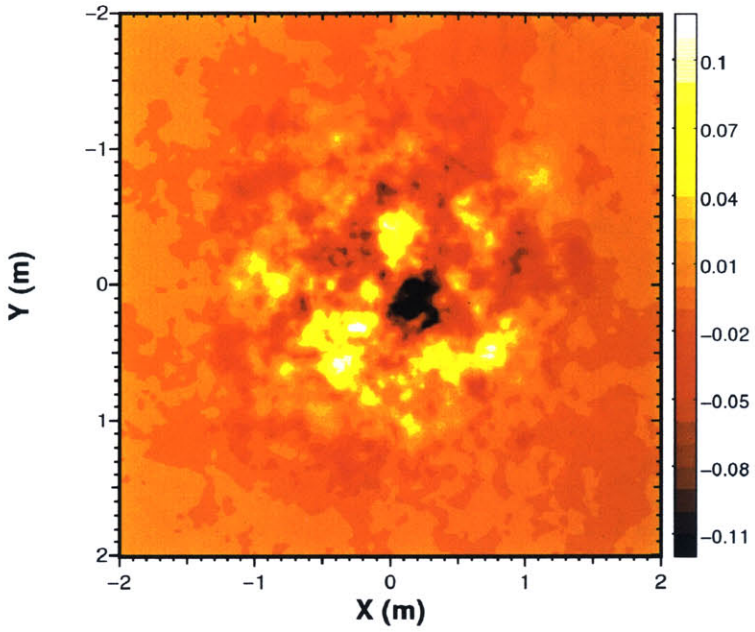

Figure 2-88: Isotropic Goff-Jordan roughness patch ($C_L = 0.3m$, $D = 2.5$, $\sqrt{\langle \gamma^2 \rangle} = 6.25cm$, $l_x = l_y = 4m$, and $N_x = N_y = 128$).

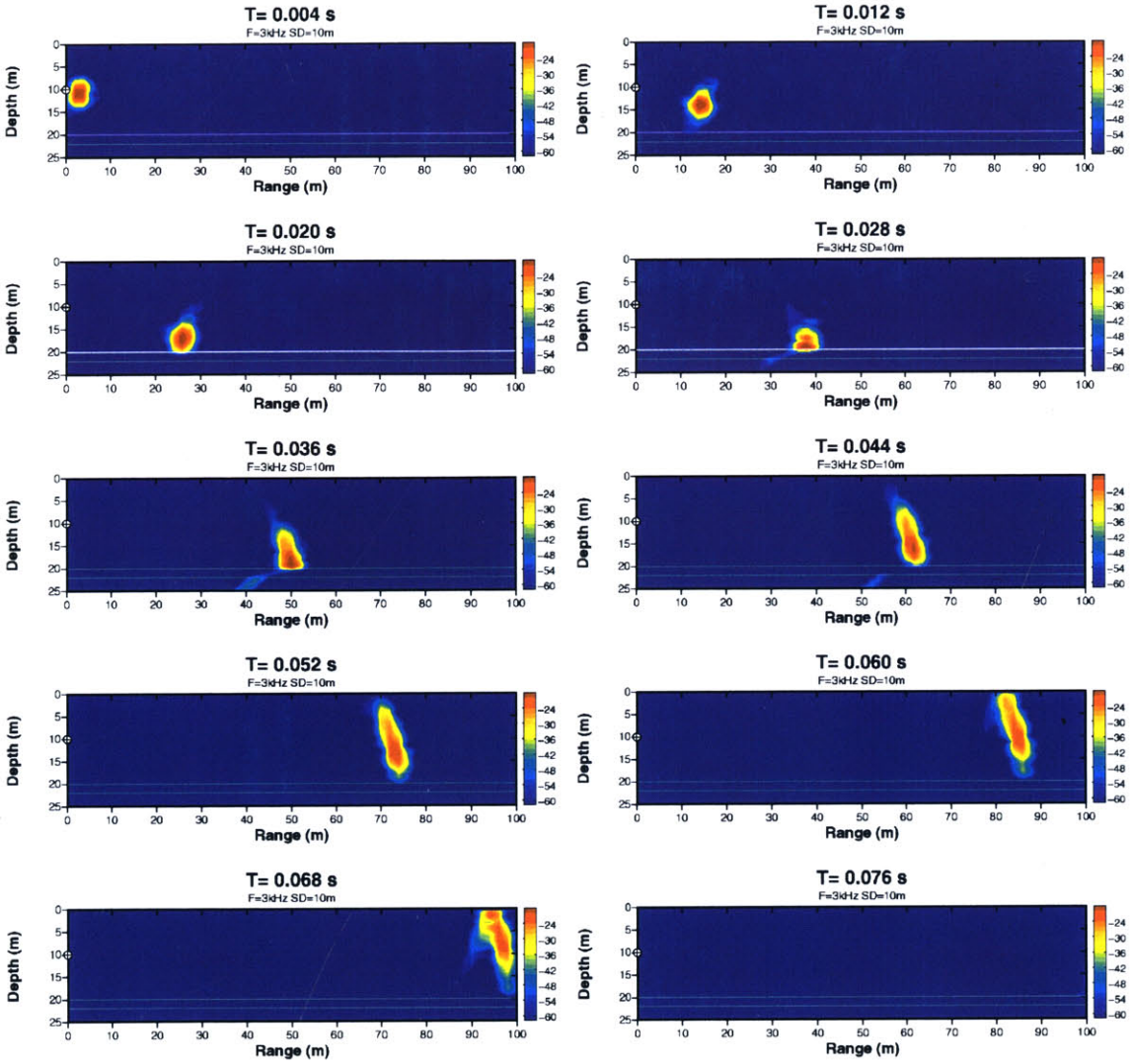

Figure 2-89: Time snapshots of in-plane incident beam pulse : a $20m$ water column, a $2m$ elastic sand layer, and an elastic limestone half space. The center of vertical array is located at $10m$ depth. The length of array is $8m$ and the number of elements is 128. The main lobe is focused at $100m$ depth with 15° tilt angle. The center coordinate of roughness patch is $(x, z) = (37.3m, 20m)$. $F_c = 3kHz$ and $\Delta F = 1kHz$.

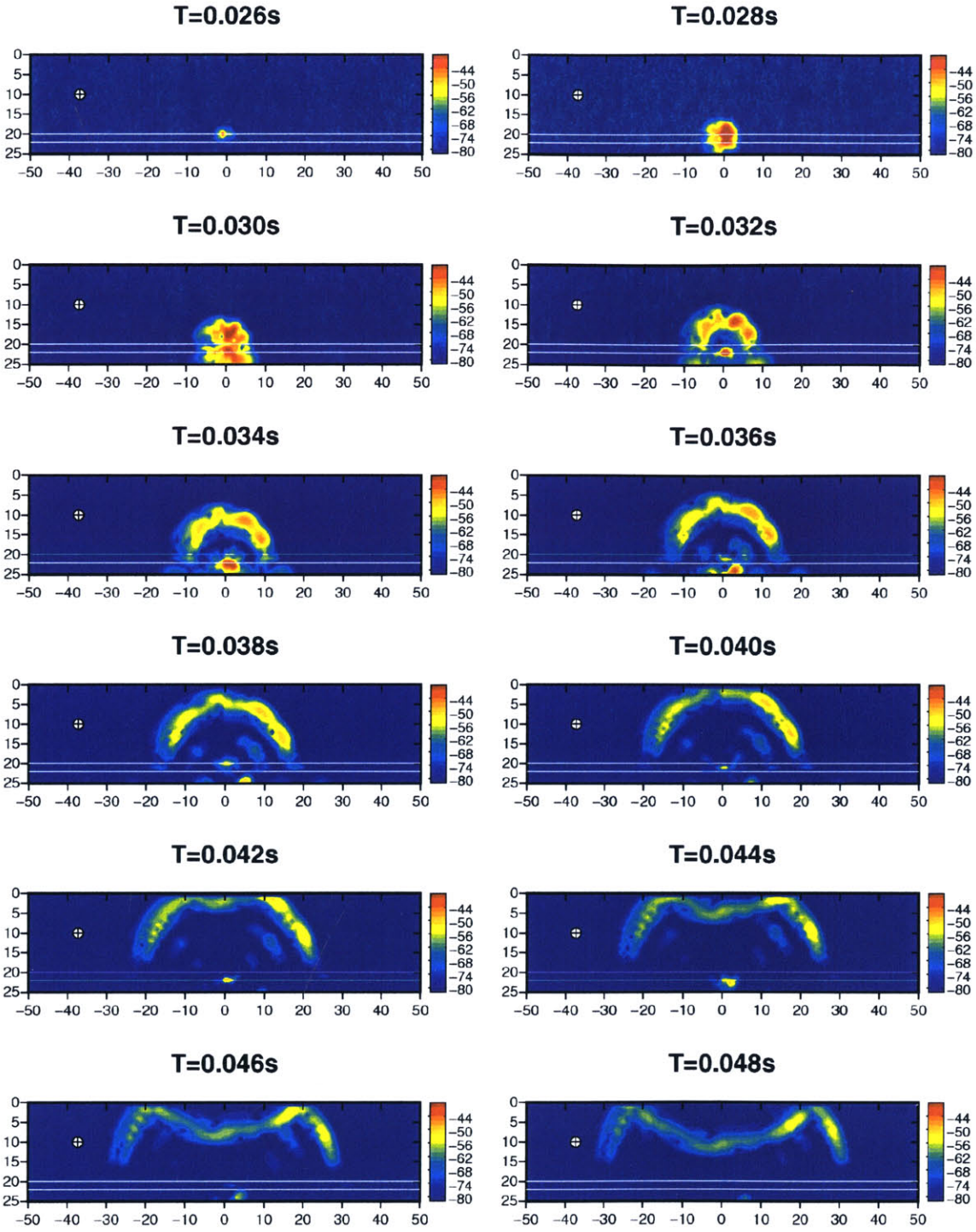

Figure 2-90: Time snapshots of in-plane scattered field : a $20m$ water column, a $2m$ elastic sand layer, and an elastic limestone half space. An isotropic roughness patch (Figure 2-88) is located at $20m$ depth and $0m$ range. $F_c = 3kHz$ and $\Delta F = 1kHz$.

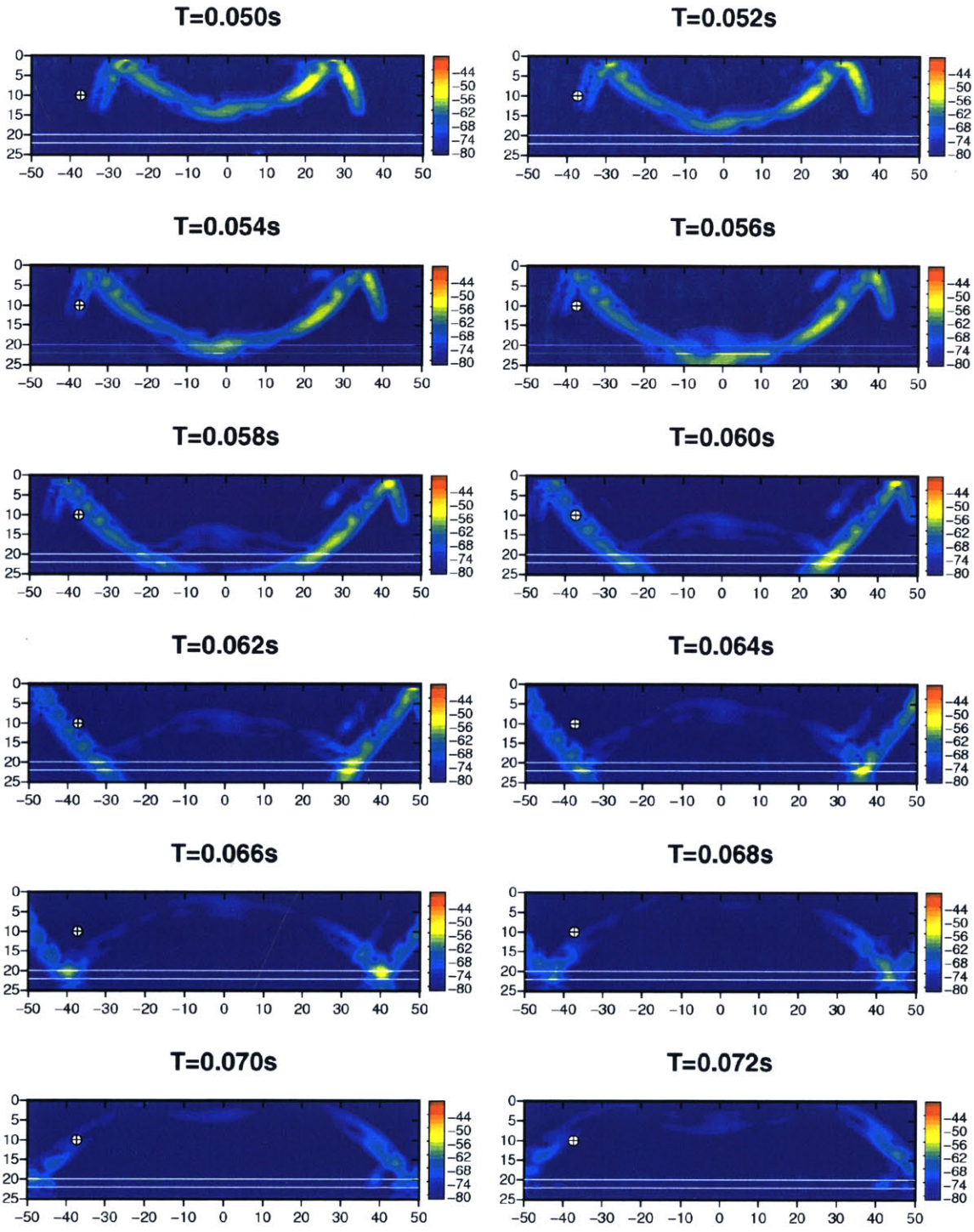

(Figure 2-90 continued)

Chapter 3

Target Scattering Model

The scattered field produced by a target in a waveguide is greatly affected by several factors – geometric and material properties of a target, medium properties of a surrounding layer, and layering configuration of a waveguide. In this chapter, several numerical models for target scattering theories will be reviewed. A target scattering model, which can account for these factors, will be chosen for numerical implementation. Using the target scattering model developed in this thesis, several effects of target scattering in a waveguide will be investigated.

3.1 Theory

There is a wide range of target scattering models. Computationally, the object scattering models are divided into two categories – discretization methods and analytic methods. Even though analytic methods provide a compact form of solution which readily explains physical meaning, analytic solutions are available for only a handful of simple problems. Discretization methods can be useful to solve problems involving a scatterer in complex media. However, the physical interpretation of solutions by discretization methods is difficult compared to analytic methods. The implementation of discretization models require large amounts of book keeping and computational resources. Therefore, using a discretization method often loses the practicality when a fast field evaluation is necessary.

Discretization Models

Discretization models are considered to be the most general methods for solving the field caused by a target with complex geometry and properties. Here, only local discretization methods are reviewed. As major methods, there exist finite elements (FE), finite deference (FD), and boundary elements (BE). These approaches use different solution techniques to approximate true solutions of physical systems which are generally expressed by partial differential equations or integral equations. Depending on the type of governing equation, one method can perform better than the others. There are several hybrid numerical techniques to combine these methods to solve a system of equations. Usually, hybrid methods utilize the specific advantages of individual discretization methods. For example, a hybrid method combining FE and BE, treats a complex scatterer as an inner problem by FE and expresses the surrounding medium as an outer problem by BE. This type of hybrid method utilizes the radiation condition automatically satisfied by BE and the capability of FE to represent a complex geometry with inhomogeneous material properties.

Even with these differences and variations, there are common mathematical and computational

limits for any types of discretization methods. These limits come from the behavior of the solution for system variables. Since local discretization methods approximate the solution by nodal values and interpolation between two adjacent nodal values, the rate of change in the true solution should not exceed the length of the discretization (i.e. grid size). This limit is analogous to the Nyquist condition of the discrete Fourier transform. The quantitative criteria vary according to types of governing equations and their parameters. For linear seismo-acoustic wave problems including propagation and scattering, the general form of governing equation is the Helmholtz equation. Consequently, the behavior of the solution is oscillatory and the rate of oscillation increases as the local medium wavenumber increases. In Reference [14], the convergence test results for FE, FD, and BE are shown. A general rules to achieve reasonable convergence with FE, FD, and BE is to use a discretization length smaller than 1/10 of the local wavelength for scalar wave cases (i.e. compressional wavelength of a fluid medium) and 1/20 of the local wavelength for vector wave cases (i.e. compressional and shear wavelengths of an elastic medium). These limits are much more severe than the Nyquist limit for an equivalent wavelength. The number of nodes N for the Helmholtz equation follows the rules below.

$$N \propto \begin{cases} \dfrac{(kL)^d}{\delta t} & \text{for FE and FD} \\ \dfrac{(kL)^{d-1}}{\delta t} & \text{for BE} \end{cases}, \tag{3.1}$$

where k, L, d, and δt correspond to the local wavenumber, the length scale of the problem, the dimension of the spatial coordinates, and the time resolution of the solution, respectively. The recent invention of high performance computing technologies has made these methods feasible. For two dimensional and low frequency problems, the implementation of discretization methods has been achieved recently. An implementation of FE to seismo-acoustic wave propagation was addressed by Chin-Bing and Murphy [8]. FD was applied to solve the scattered field produced due to an ice keel by Fricke [15]. Series of BE models have been developed to solve the scattering produced by volume inhomogeneities such as a cavity and a non-planar surface [6, 5, 9]. A hybrid method combining BE and a spectral method (i.e. wavenumber integration technique) was implemented by Gerstoft and Schmidt [18] to solve the scattered field produced by a 2-D object in a horizontally stratified waveguide. By including a spectral method, the representation of a horizontally stratified waveguide is efficiently done by using the Green's function of a horizontally stratified medium instead of the free space Green's function to express each waveguide interface. Later, the same approach was modified by Fan for a '$2\frac{1}{2}$-D object' scatterer which is a 2-D scatterer not perpendicular to the incident wave vector [10]. This model is capable of considering the angular anisotropy of a 2-D volume scatterer. A hybrid method combining BE with a spectral method was applied by Tadeu [51] to solve the scattered field produced by a 2-D volume inclusion in a half space. Even though these implementations of BE / spectral hybrid method are efficient compared to the ordinary BE method, they still require a great amount of computing resources so that the practical use of these methods is often prohibitive for high frequency cases or higher dimensional cases (i.e. 3-D and time domain). Recently, another kind of discretization target scattering model was introduced by Fawcett [12]. This model uses a coupled-mode solution technique to solve the scattered field produced by an axisymmetric object in a horizontally stratified waveguide. An axisymmetric object is represented by layers of isotropic circular discs. Originally, the coupled-mode solution technique had been used in range dependent acoustic wave propagation models.

Because the partial goal of this thesis is to make an extremely efficient and realistic numerical model to simulate multi-static bottom target sonar operation, discretization methods for the target

scattering problem are excluded.

3.2 Single Scattering Approximation

The basic assumption of the single scattering approximation [21] is that once the scattered wave leaves a scatterer, it does not return to the scatterer. In the case of a volume scatterer in a waveguide, this assumption implies that once the incident wave has interfered with a scatterer and the scattered wave propagates away from the scatterer, the scattered wave reflected from the interface does not interact with the scatterer any more. It is important to clarify the definition of the incident field for waveguide cases before further theoretical explanation. The definition of the incident field throughout this chapter is the same as the definition of the unperturbed field in Chapter 2. To restate the definition of the incident field in the waveguide, it is a field generated by physical source in a waveguide without scatterers. Thus, it includes the transmitted and reflected waves from the interfaces of the waveguide layers. When the incident wave arrives at a scatterer in the waveguide, the first scattered wave travels to and interacts with the adjacent interfaces. Then, the reflected portion of the scattered wave from these interfaces can possibly propagate back to the scatterer and it can be re-scattered by the same scatterer. This process continues iteratively in the time domain until the scattered wave dissipates. The single scattering approximation simply ignores the contribution of the re-scattered wave from the scatterer. The model approximates the scattered field by considering only the first scattering interaction between a scatterer and the incident field. In the case of multiple scatterers, the single scattering approximation ignores re-scattered fields among scatterers. In other words, the model treats each scatterer as if it exists alone.

The single scattering approximation in the case of a scatterer in a waveguide has advantages and disadvantages. The advantage of the single scattering approximation is that the model can be applied to any scatterers which have known solutions in free space. These solutions can be analytic solutions or semi-analytic solutions. Thus, the computation of the scattered field is very efficient. While the assumptions behind the single scattering approximation simplify its numerical implementation, the disadvantages comes from the same assumptions. Since the model ignores the re-scattered field, a complete description of the scattered field cannot be achieved.

There is an issue of validity in using the single scattering approximation when a target is located close to the interface. As explained by Fawcett [13], the model using the single scattering approximation gives excellent agreement with the multiple scattering solution over a wide range of frequencies for the case when the depth separation of the target is twice the target radius. In Reference [11], the multiple scattering formulation was expressed in an infinite series. The first term of the series is equivalent to the expression of the single scattering approximation. The difference between the multiple scattering formulation and the single scattering formulation is that the former has extra higher order terms which has the incremental factor $-S \times B$. S is the free-space scattering function of the target and R is a reflection coefficient times twice the vertical phase difference between the interface and the target. In the case of a target submerged in a fast fluid bottom, the reflection coefficient from the lower space to the upper space is relatively small and the series of scattering expression converges fast. Therefore, the error caused by the single scattering approximation is reduced. In Reference [33], several cases of a pressure-release sphere within a waveguide were used to demonstrate errors caused by the single scattering approximation. By neglecting the multiple scattering, the total field at the surface of the pressure-release sphere does not vanish and it increases as the waveguide thickness decreases with respect to the radius of the sphere. In a practical sense, the quality of solutions using the single scattering approximation must be checked against the experimental scattering data for a known target.

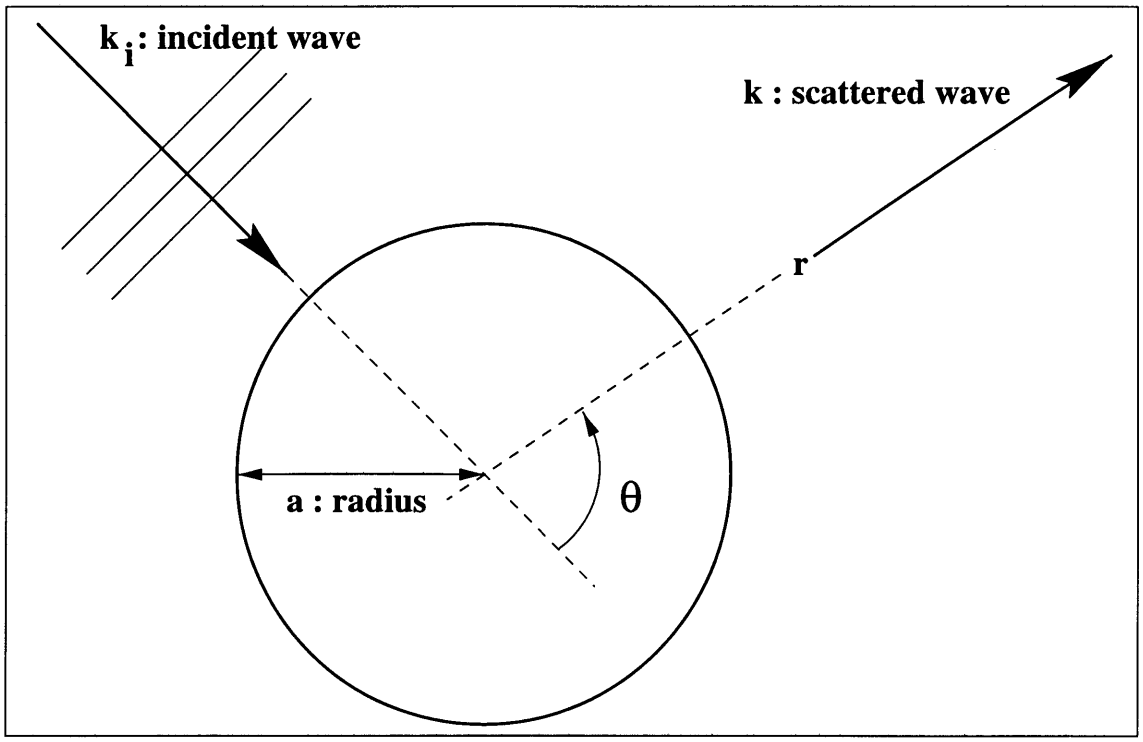

Figure 3-1: Geometry of rigid and pressure-release spheres.

In this thesis, the single scattering approximation is applied to three known solutions – a rigid sphere, a pressure-release sphere, and a finite cylindrical shell. The rigid sphere and pressure-released spheres have analytic solutions while the finite cylindrical shell has a semi-analytic solution. Their plane wave scattering functions in free space are utilized to compute the effective beampatterns in the waveguide given an incident field. The target model is modified to be compatible with the 3-D OASES propagation model. This modification is similar to the modification of the perturbation method used for rough interface scattering in Chapter 2.

3.2.1 Sphere Solutions

The sphere solution is the simplest target model available and there exist many references and numerical simulations for scattering from a sphere.

In this thesis, rigid and pressure-release spheres are used as volume scatterers. The solutions for rigid and pressure-release spheres are derived from the same mathematical form. The geometry of the spherical scatterer is shown in Figure 3-1 where θ is the angle between the incident wave vector and the scattered wave vector. First, the time harmonic plane incident wave in free space is decomposed into spherical harmonics [1].

$$P_{inc}(kr,\theta) = \exp(\imath kr\cos\theta) = \sum_{n=0}^{\infty}(2n+1)\imath^n P_n(\cos\theta)\, j_n(kr), \tag{3.2}$$

where j_n is the n th order spherical Bessel function of the first kind and P_n is the n th order Legendre polynomial. Here, the time dependence is assumed to be $\exp(-\imath\omega t)$. Then, an appropriate boundary condition is imposed on the total pressure field (sum of incident pressure and scattered

pressure).

Rigid Sphere

For a rigid sphere in fluid free space, the scattered field produced by a unit plane incident wave can be obtained analytically [35, 25]. The boundary condition on the surface of the sphere is that the radial particle velocity is zero. With the above time dependence, the radial velocity v_r is :

$$v_r = \frac{1}{\imath\rho\omega}\frac{\partial P}{\partial r}. \tag{3.3}$$

The boundary condition becomes :

$$\left.\frac{\partial P_{sc}}{\partial r}\right|_{r=a} = -\left.\frac{\partial P_{inc}}{\partial r}\right|_{r=a}. \tag{3.4}$$

Considering the time dependence, a proper solution form of P_{sc} can be an infinite series of spherical Hankel functions of the first kind with unknown amplitudes. The spherical Hankel functions of the first kind correspond to propagating waves away from the sphere.

$$P_{sc}(kr,\theta) = \sum_{n=0}^{\infty} A_n h_n^{(1)}(kr). \tag{3.5}$$

From the incident pressure and boundary condition, the unknown coefficients A_n are obtained. The scattered pressure field generated by a rigid sphere of radius a becomes :

$$P_{sc}(kr,\theta,ka) = -\sum_{n=0}^{\infty}(2n+1)\imath^n P_n(\cos\theta)\frac{j'_n(ka)}{h'^{(1)}_n(ka)}h_n^{(1)}(kr), \tag{3.6}$$

where θ is the angle between the incident wave and the receiver direction. k, r, and a are the medium wavenumber of the fluid, the distance from the center of the sphere to the receiver position, and the radius of sphere, respectively. $h_n^{(1)}$ is the n th order spherical Hankel function of the first kind. The boundary condition applied to obtain the above expression is that the normal derivative of the total pressure on the surface of sphere is zero. The convergence of the above series depends on the non-dimensional radius of the sphere ka. The required number of terms increases as ka becomes large because of the oscillatory behavior of the spherical Bessel function. There are approximate solutions for rigid sphere scattering in the limits of low and high frequencies. The above expression converges to the same approximations in both the low and high frequency cases [37, 25].

Pressure-release Sphere

When a sphere has pressure-release surface, the corresponding boundary condition on the sphere surface is :

$$P_{sc}\big|_{r=a} = -P_{inc}\big|_{r=a}. \tag{3.7}$$

With the same solution form as the rigid sphere case, the unknown coefficients A_n are obtained from the above boundary condition and incident field. The scattered field generated by a plane

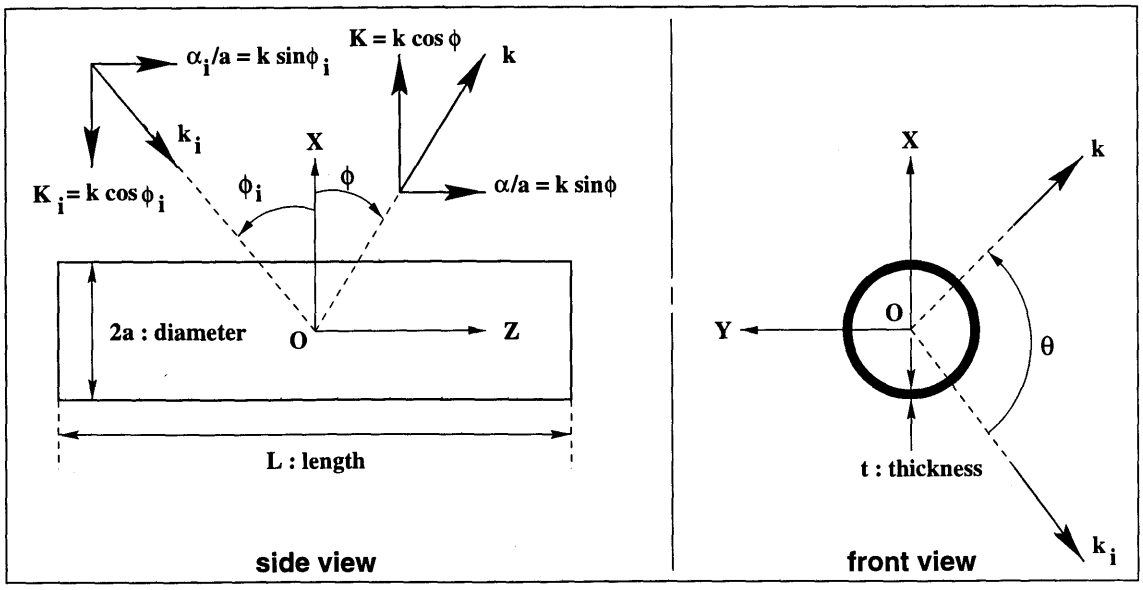

Figure 3-2: Geometry of a finite elastic cylindrical shell.

wave incidence becomes :

$$P_{sc}(kr, \theta, ka) = -\sum_{n=0}^{\infty}(2n+1)i^n P_n(\cos\theta)\frac{j_n(ka)}{h_n^{(1)}(ka)}h_n^{(1)}(kr). \tag{3.8}$$

3.2.2 Finite Cylindrical Shell Scattering Solution

A finite cylindrical shell scattering model was introduced in Reference [41]. This model approximates the bistatic scattering of supersonic traveling (re-radiating) membrane waves from a finite cylindrical shell excited by a plane incident wave. The major assumptions of this model are :

- The contribution of the bending wave in the higher wavenumber regime is ignored. In other words, in-plane displacements and stress vectors are approximated by membrane wave components only.
- The modal impedances of the finite shell can be approximated by those of an infinite length shell in the same surrounding fluid medium. This implies the neglect of modal coupling through the fluid medium.
- The inside of the shell is void and both ends of the shell are attached to two semi-infinite coaxial rigid cylindrical baffles of the same radius as shell.

In Reference [40], the scattering contribution from the void portion of the shell was added to the original formulation by Rumerman. The scattered field from a void cylinder is described by Junger and Feit [25].

In Reference [25], the difference between rigid and elastic body scattering is described as follows :

> "While a rigid scatterer distorts the sound field by interfering the propagation of the incident field, the dynamic response of an elastic scatterer excited by the incident wave further modifies the resultant sound field."

An elastic scatterer permits the transmission and reflection of incident wave through and on its boundary as well as the vibration of surface. By allowing these mechanisms, the field is a result of complex interactions among various dynamic responses of the scatterer and the incident wave field. On the other hand, a rigid scatterer changes the sound field by simply blocking the propagation of the incident wave. The above statement can be written in mathematical form. Let the scattered pressure by an elastic scatterer be represented by P_{se} and let the scattered pressure by the infinite-impedance boundary coinciding with the elastic scatterer be represented by $P_{s\infty}$. The total field becomes :

$$P = P_i + P_{se}, \tag{3.9}$$

where P_i is the incident pressure. If P_{se} is expressed as :

$$P_{se} = P_{s\infty} + P_r, \tag{3.10}$$

the remaining term P_r is the pressure radiated by elastic effects representing the difference between the elastic scatterer and the corresponding rigid scatterer. In other words, P_r consists of terms necessary for satisfying elastic boundary conditions. Since $P_{s\infty}$ is easily available, solving the scattered field by an elastic body becomes an exercise in finding P_r in terms of P_r and P_i with the proper boundary conditions.

$$\frac{\partial P}{\partial \xi_0} = -\rho \ddot{w}, \quad \text{on } S(R_0), \tag{3.11}$$

where $\ddot{w}$ is the surface normal acceleration and ξ_0 is the surface normal coordinate. The above boundary condition is satisfied if the following conditions are satisfied.

$$\left.\begin{aligned} \frac{\partial P_r}{\partial \xi_0} &= -\rho \ddot{w} \\ \frac{\partial P_{s\infty}}{\partial \xi_0} &= -\frac{\partial P_i}{\partial \xi_0} \end{aligned}\right\}, \quad \text{on } S(R_0). \tag{3.12}$$

Based on References [25, 41, 40], the scattered pressure field is derived in Appendix D. The geometry of the finite cylindrical shell is shown in Figure 3-2 along with the definitions of incident and scattered wave vectors. Assuming the time dependence $\exp(-\imath\omega t)$, the scattered pressure P_{se} generated by unit plane wave incidence is :

$$P_{se}(R,\theta,\phi) = \frac{\imath k a e^{\imath kR}}{2\pi KR} \sum_{n=0}^{N_{\max}} \left\{ \frac{\epsilon_n \cos(n\theta)}{H'^{(1)}_n(Ka)} \left[\frac{J'_n(K_i a) K_i Q_{n5}}{k} - \frac{2\rho c Q_n}{Z_n(\Omega, \alpha_i)\pi K_i a H'^{(1)}_n(K_i a)} \right] \right\}, \tag{3.13}$$

where J'_n is the first derivative of the Bessel function of the first kind and order n and $H'^{(1)}_n$ is the first derivative of the Hankel function of the first kind and order n. The subscript i refers to incident wave components. The other parameters are defined as :

$$\epsilon_n = \begin{cases} 1 & \text{for } n = 0 \\ 2 & \text{for } n > 1 \end{cases},$$

$\Omega = \omega a / c_p$ (dimensionless frequency),

c_p = (compressional wave speed of shell),

θ_{sk} = (skew angle with respect to the range coordinate x),

θ = (circumferential angle),

ϕ_i = (incident polar angle),

ϕ = (scattered polar angle),

k = (medium wavenumber of surrounding fluid),

$K = k\cos\phi$ (receiver radial wavenumber),

$K_i = k\cos\phi_i$ (incident radial wavenumber),

$\alpha_r = ka\sin\phi$ (dimensionless receiver axial wavenumber),

$\alpha_i = ka\sin\phi_i$ (dimensionless incident axial wavenumber),

α_n = (dimensionless shear modal axial wavenumber),

β_n = (dimensionless compressional modal axial wavenumber),

Z_n = (modal system impedance).

The modal axial wavenumbers are zeros of the system impedance function Z_n.

The finite length of the shell causes the radiation from the shell to have sinc[1]-like beampatterns in the axial wavenumber domain. Each beampattern is centered at one of the modal axial wavenumbers or the incident axial wavenumber. There are five types of beam patterns defined as :

$$
\begin{aligned}
Q_{n1} &= \frac{\bar{A}_n}{\sin(\alpha_n \bar{L})} \frac{1-\exp\left[-\imath\bar{L}(\alpha_r-\alpha_n)\right]}{\alpha_n-\alpha_r}, \\
Q_{n2} &= \frac{\bar{B}_n}{\sin(\beta_n \bar{L})} \frac{1-\exp\left[-\imath\bar{L}(\alpha_r-\beta_n)\right]}{\beta_n-\alpha_r}, \\
Q_{n3} &= -\frac{\bar{C}_n}{\sin(\alpha_n \bar{L})} \frac{1-\exp\left[-\imath\bar{L}(\alpha_r+\alpha_n)\right]}{\alpha_n+\alpha_r}, \\
Q_{n4} &= -\frac{\bar{D}_n}{\sin(\beta_n \bar{L})} \frac{1-\exp\left[-\imath\bar{L}(\alpha_r+\beta_n)\right]}{\beta_n+\alpha_r}, \\
Q_{n5} &= 2\imath \frac{1-\exp\left[-\imath\bar{L}(\alpha_r-\alpha_i)\right]}{\alpha_i-\alpha_r}, \\
Q_n &= Q_{n1}+Q_{n2}+Q_{n3}+Q_{n4}+Q_{n5},
\end{aligned}
\tag{3.14}
$$

where $\bar{L} = L/a$ and $\bar{A}_n$, $\bar{B}_n$, $\bar{C}_n$, $\bar{D}_n$ are modal coefficients defined in Reference [41]. The full mathematical formulation of the scattered field is derived in Appendix D. Figure 3-3 shows an example of solutions of modal axial wavenumbers for a cylindrical shell. Each mode has a set of shear and compressional modal wavenumbers, which corresponds to the axial beampattern at a specific angle with respect to the shell axis. These modal axial wavenumbers represent either a propagating scattered field or an evanescent scattered field. If α_n (dimensionless shear modal axial wavenumber) is quasi-real[2] and the circumferential mode number n is less than $ka\sin\phi_s$[3]

[1] $\mathrm{sinc}(x) = \begin{cases} 1 & \text{for } x = 0 \\ \dfrac{\sin(x)}{x} & \text{otherwise} \end{cases}$.

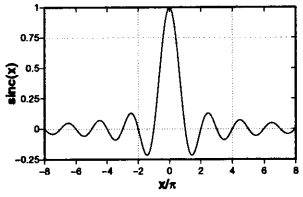

[2] Complex number with dominant real part.

[3] ϕ_s is the shear critical angle measured from the radial axis of shell.

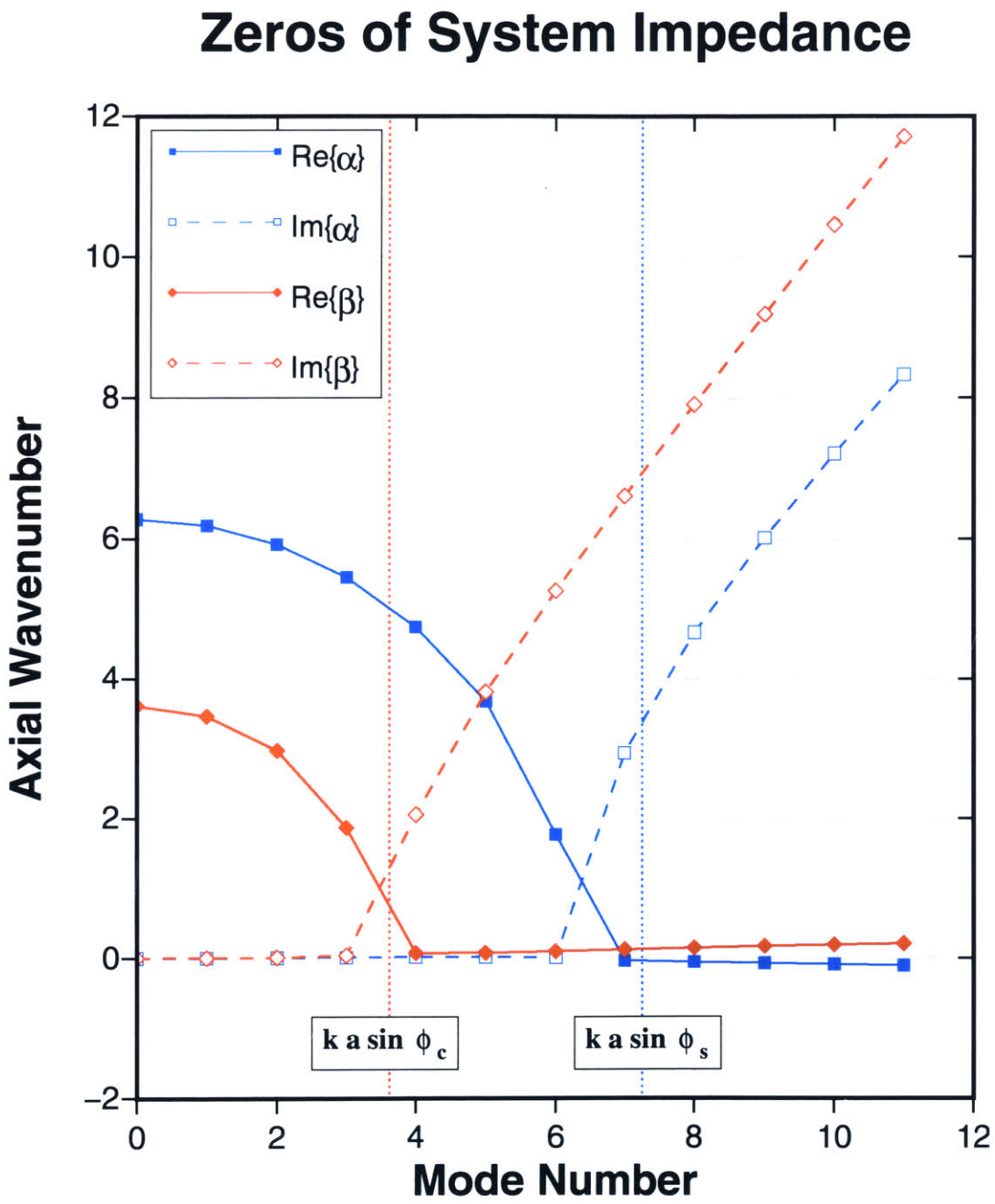

Figure 3-3: Real and imaginary parts of modal axial wavenumbers – a steel cylindrical shell ($a = 1m$, $t = 5cm$, $\rho = 7.8g/cm^3$, $C_p = 5200m/s$, and $C_s = 2600m/s$) in a water space ($\rho = 1.0g/cm^3$ and $C_p = 1500m/s$) at $f = 3kHz$. α is the dimensionless shear axial wavenumber and β is the dimensionless compressional axial wavenumber.

(dimensionless shear critical wavenumber), the scattered wave becomes a propagating field. If α_n is quasi-imaginary[4] and the mode number n is greater than $ka\sin\phi_s$, the scattered wave becomes an evanescent field. The same analogy also applies to the dimensionless complex modal wavenumber β_n.

The main lobes of the beampatterns Q are controlled by the shell's aspect ratio $\bar{L}$. As the aspect ratio of the cylinder increases, the width of the main lobe decreases but the number of side lobes increases. This behavior is quite similar to the beampattern of a line array.

3.3 Numerical Implementation of Target Scattering Model

The idea of including target models into a waveguide was inspired from the far-field approximation of the target scattered field. In the far field, the target models previously mentioned can be approximated by a point source with a specific beampattern in angular space. A unit point source in free space (i.e., $|P_o| = 1Pa$ at $r = 1m$) is described as :

$$P_o(kr) = \frac{e^{\imath kr}}{r}, \tag{3.15}$$

where the source is located at the origin of the coordinate system. When a scattered field produced by a target is observed in the far field, the mathematical expression of the field can be represented as :

$$P_{se} = \frac{e^{\imath kr}}{r}\beta(\theta_r, \phi_r; \theta_i, \phi_i), \tag{3.16}$$

where β is the beampattern of the target in the far-field. The beampattern β is independent of receiver range and is determined by source and receiver angles. Therefore, the effects of target scattering can be approximated by using a point source with a far-field beampattern instead of using a full-wave numerical model. Figure 3-4 illustrates a schematic comparison between a point source and a point source with the effective beampattern of a target. The difference is that the source representing the target produces the energy in a non-uniform way. This non-uniform distribution of energy is described by a beampattern.

Even though the beampattern is expressed as a function of angular variables ϕ and θ only, it is possible to obtain the scattered fields in the evanescent wavenumber regime. Since the evanescent wavenumber regime can not be expressed using the real angles, analytic continuation [2] is used to define the beampattern outside the real angular regime. Scattering caused by evanescent incident waves is especially important when the penetration of the incident wave shallower than the critical incident angle is considered. Also, the scattered waves in the evanescent regime are important because they can be propagating waves in other layers. Therefore, including the target beampattern in the evanescent wavenumber regime is essential to express the scattering from a target buried in a layer. By replacing the angular variable with the horizontal wavenumber, both propagating and evanescent waves can be handled smoothly.

For rigid and pressure-release sphere target models, far-field beampatterns are easily obtained by taking the limit of the following function [1].

$$\lim_{kr\to\infty} -(\imath)^n h_n^{(1)}(kr) = \imath\frac{e^{\imath kr}}{kr}. \tag{3.17}$$

[4] Complex number with dominant imaginary part

$$P_o = \frac{e^{i k R}}{R}$$

Unit Point Source

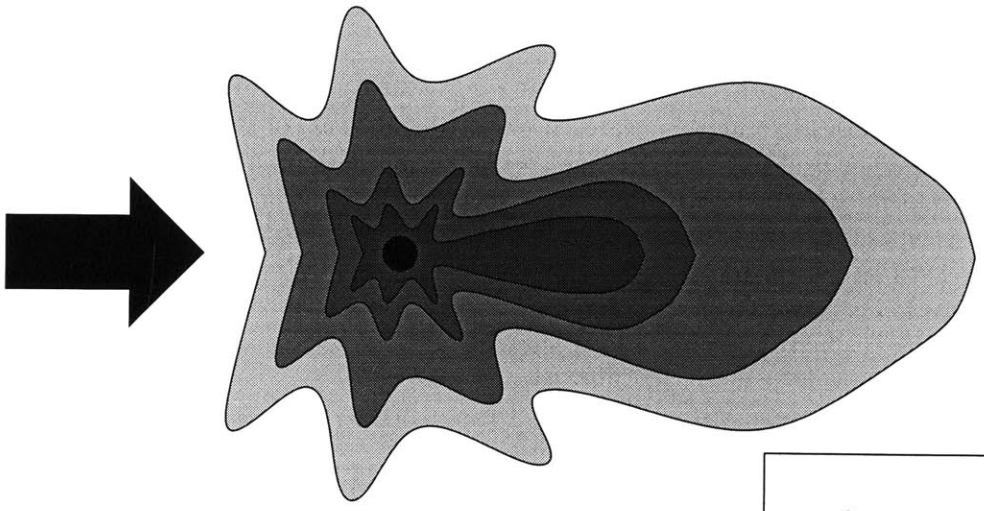

$$P = \beta(\theta, \phi)\ \frac{e^{i k R}}{R}$$

Target Beam Pattern

Figure 3-4: Target model by an effective beampattern. The arrow indicates the direction of incident wave.

Therefore, beampatterns for rigid and pressure-release spheres become :

$$\beta_{rigid} = \frac{\iota}{k}\sum_{n=0}^{\infty}(2n+1)\frac{j'_n(ka)}{h'^{(1)}_n(ka)}P_n(\cos\theta), \tag{3.18}$$

$$\beta_{pressure-release} = \frac{\iota}{k}\sum_{n=0}^{\infty}(2n+1)\frac{j_n(ka)}{h^{(1)}_n(ka)}P_n(\cos\theta), \tag{3.19}$$

where $\cos\theta$ is the directional cosine between the incident wavenumber vector $\vec{k}_i$ and the receiver wavenumber vector $\vec{k}_r$. The above expressions are generally converged when the number of summation is in the same order of ka.

$$\cos\theta = \frac{\vec{k}_i \cdot \vec{k}_r}{k_0^2}, \tag{3.20}$$

where k_0 is the wavenumber of the surrounding medium. Figure 3-5 and Figure 3-6 show examples of normalized angular beampatterns for rigid and pressure-release spheres in free space. As the dimensionless frequency ka increases, the forward scattered field becomes stronger and the scattered fields in other direction become uniform. When the rigid and pressure-release spheres are compared at the same dimensionless frequency, the pressure-release sphere produces a stronger forward field than a same-sized rigid sphere. Also, the pressure-release sphere exhibits less fluctuation of beampattern than the rigid sphere.

When a target is buried in a lower half space or a sublayer, the target may be excited by subsonic (evanescent) waves. The scattering beampattern of a target insonified by an evanescent plane wave is obtained by applying analytic continuation to the corresponding plane wave scattering function. Figure 3-7 shows examples of angular scattering beampatterns for a rigid sphere (ka = 5.0) insonified by evanescent plane waves. Compared to the case of supersonic incidence, evanescent incidence breaks the symmetry of the angular beampattern for a rigid sphere. As the dimensionless incident wavenumber ($k_i a$) increases, the degree of asymmetry in the scattering beampatterns increases.

For Rumerman's finite cylindrical shell model, the far-field beampattern is readily available. Since the formulation is derived from the stationary phase integral of the scattering function, it already includes the far-field approximation. Therefore, its far-field beampattern is simply the scattering term normalized by a unit point source.

$$\beta_{cylinder} = \frac{\iota ka}{2\pi K}\sum_{n=0}^{N_{\max}}\frac{\epsilon_n\cos(n\theta)}{H'^{(1)}_n(Ka)}\left[\frac{J'_n(K_i a)K_i Q_{n5}}{k} - \frac{2\rho c Q_n}{Z_n(\Omega,\alpha_i)\pi K_i a H'^{(1)}_n(K_i a)}\right], \tag{3.21}$$

where the angle θ is defined in Appendix D.

As examples of beampatterns for the cylindrical shells, Figure 3-8 compares normalized polar beampatterns for cylindrical shells with different lengths. The axes of cylindrical shells are perpendicular to the direction of the incident wave. The polar beampattern is a beampattern obtained on a plane normal to the axial direction of the shell. Apparently, the normalized polar beampattern is not changed as the aperture of the shell (L/a) increases. Since the beampatterns are normalized by the length of shell, the magnitude of the resulting scattered field is proportional to the length of shell.

Figure 3-9 shows the normalized azimuthal beampatterns of the same cylindrical shells used in Figure 3-8. The azimuthal beampattern is obtained on a plane parallel to the shell axis. The angular beam width of the main lobe in the forward direction becomes smaller as the aperture of

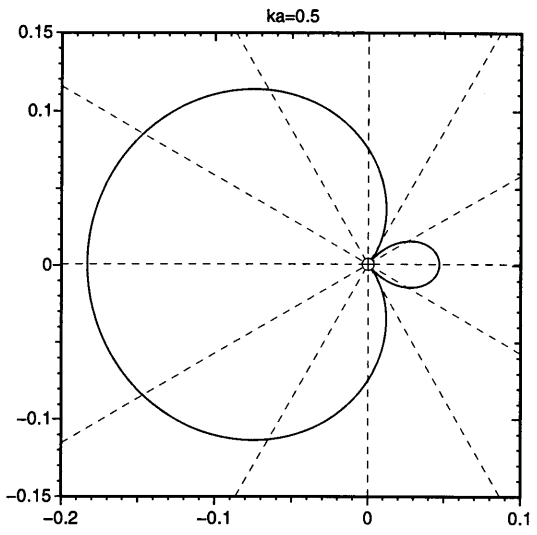

(a) $ka = 0.5$

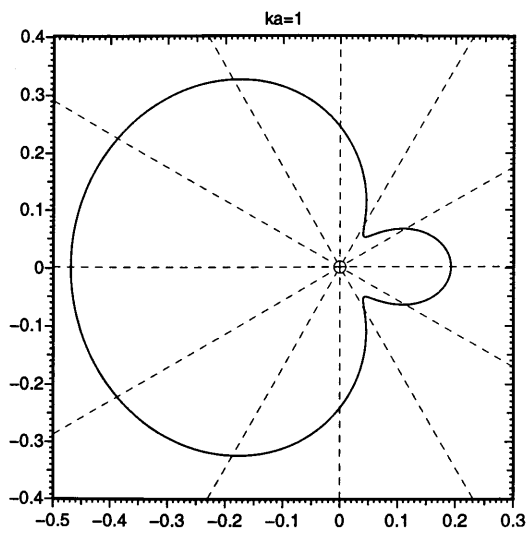

(b) $ka = 1$

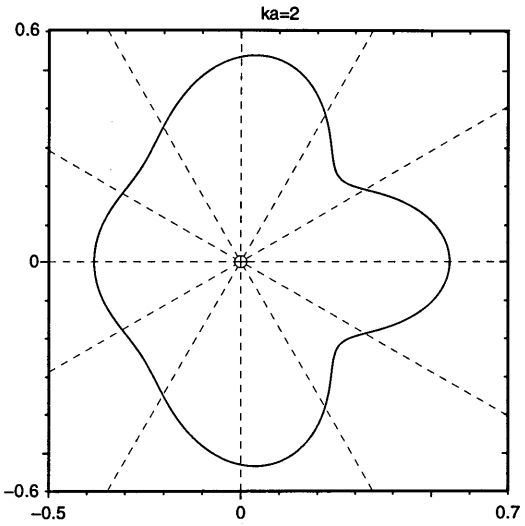

(c) $ka = 2$

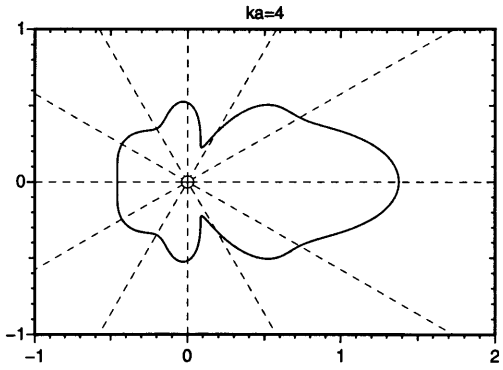

(d) $ka = 4$

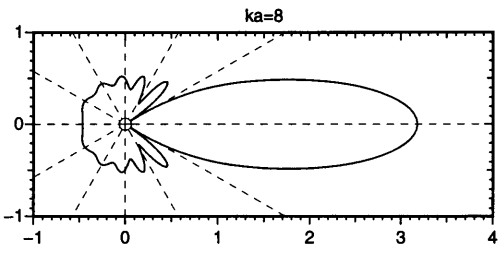

(e) $ka = 8$

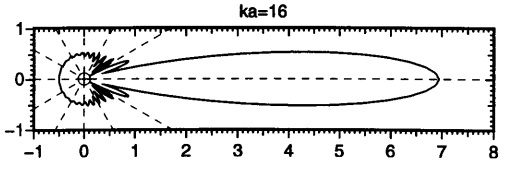

(f) $ka = 16$

Figure 3-5: $|\beta_{rigid}|/a$: angular beampatterns of rigid spheres. The right hand side is the forward scattering direction.

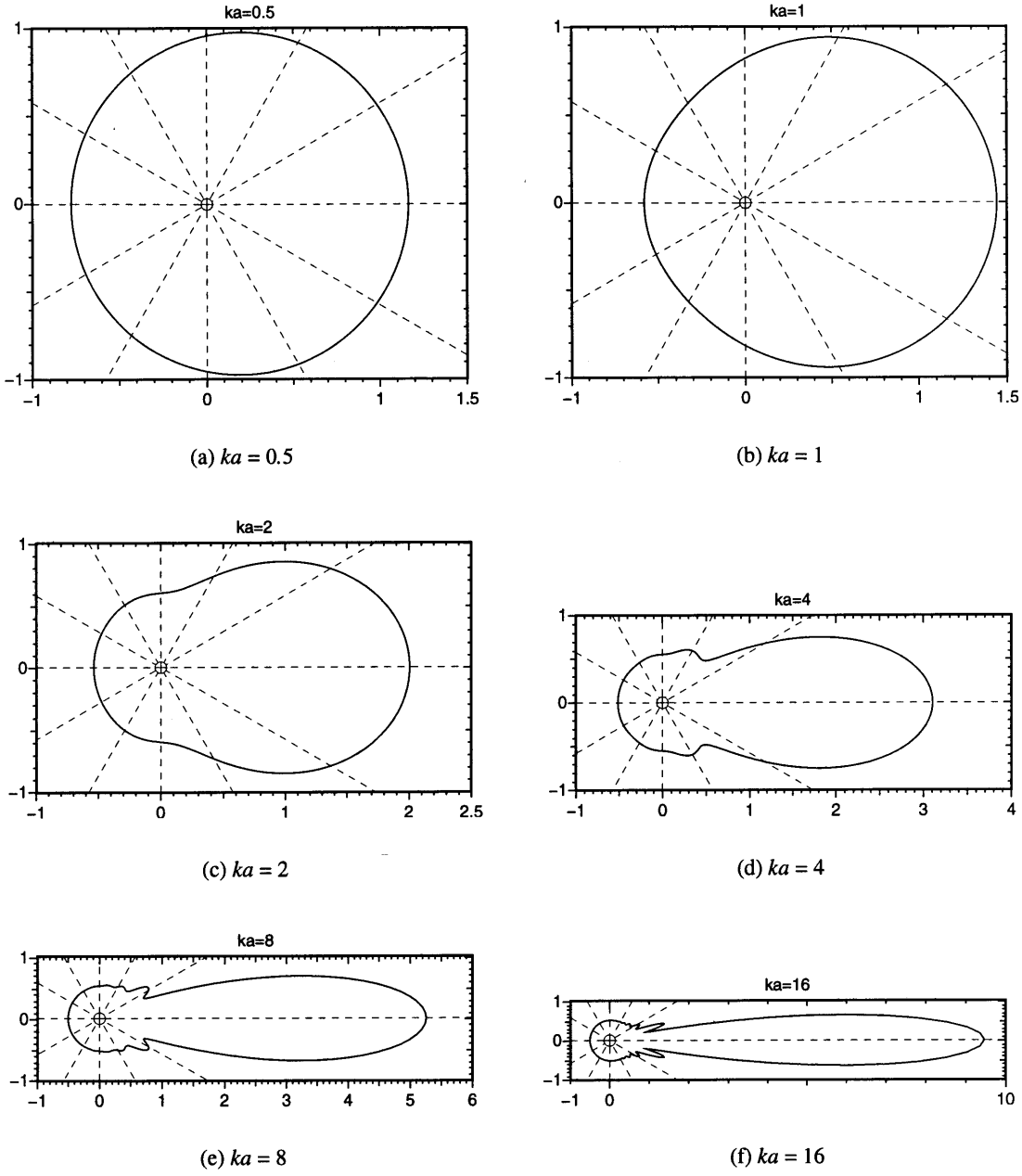

(a) $ka = 0.5$

(b) $ka = 1$

(c) $ka = 2$

(d) $ka = 4$

(e) $ka = 8$

(f) $ka = 16$

Figure 3-6: $|\beta_{pressure-release}|/a$: angular beampatterns of pressure-release spheres. The right hand side is the forward scattering direction.

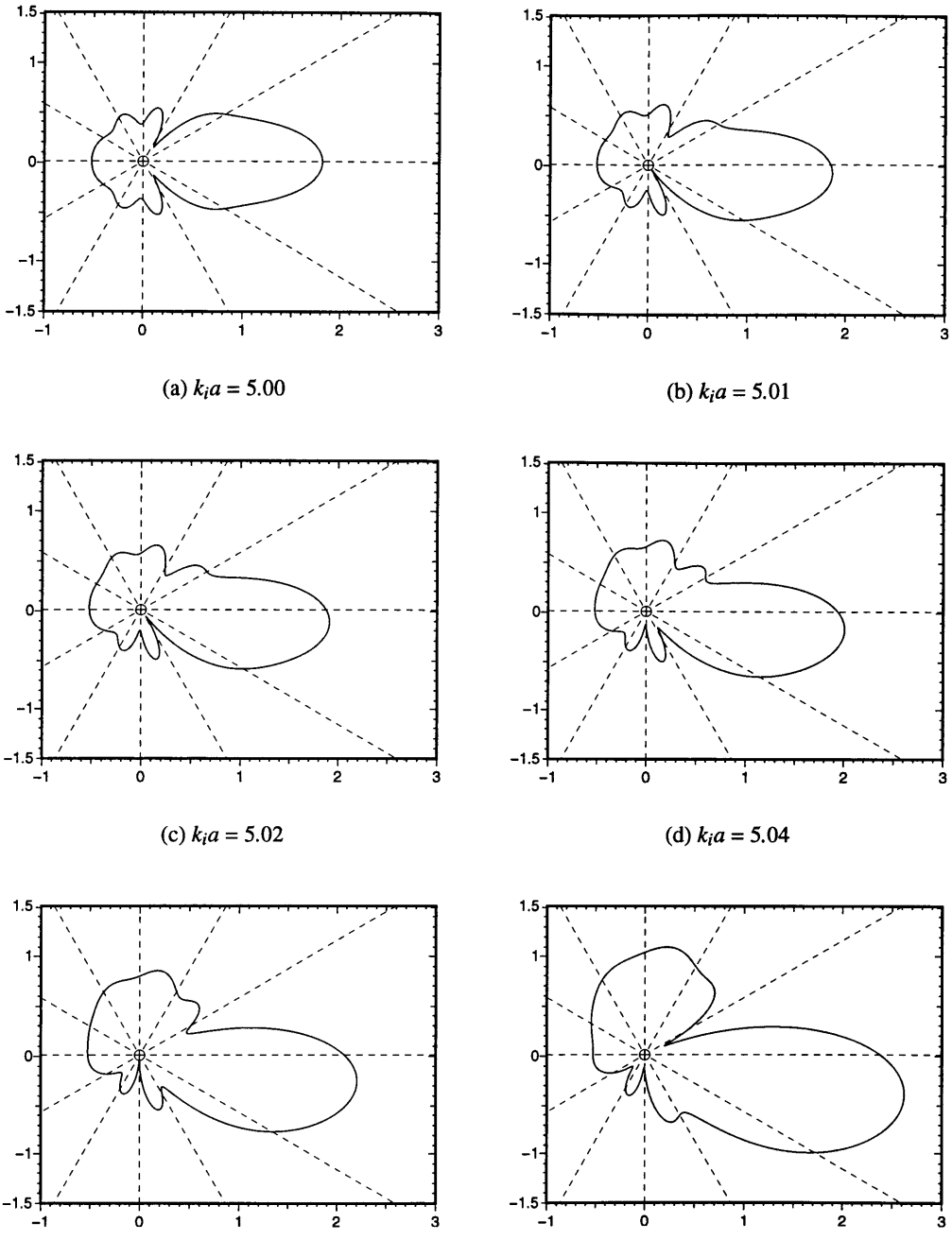

(a) $k_i a = 5.00$

(b) $k_i a = 5.01$

(c) $k_i a = 5.02$

(d) $k_i a = 5.04$

(e) $k_i a = 5.08$

(f) $k_i a = 5.16$

Figure 3-7: $|\beta_{pressure-release}|/a$: angular beampatterns of a rigid sphere insonified by an evanescent plane wave. The dimensionless medium wavenumber (ka) is 5.00 and the dimensionless incident wavenumber ($k_i a$) varies from 5.00 to 5.16. The incident plane wave is coming from the upper left corner of the plot. The right hand side corresponds to the forward scattering direction.

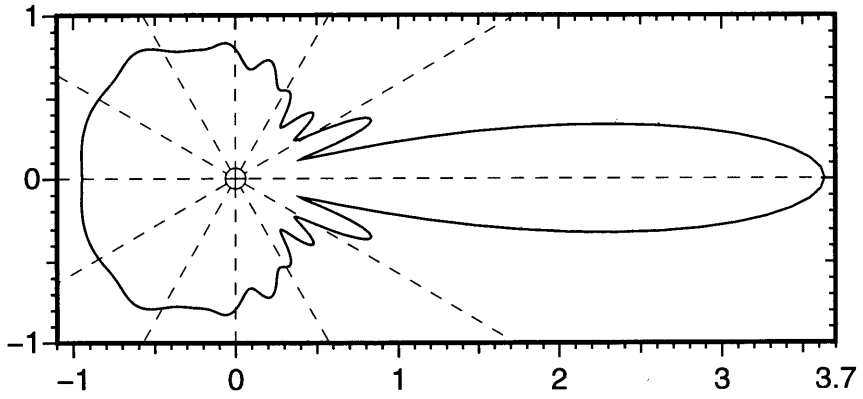

(a) $L = 2m$

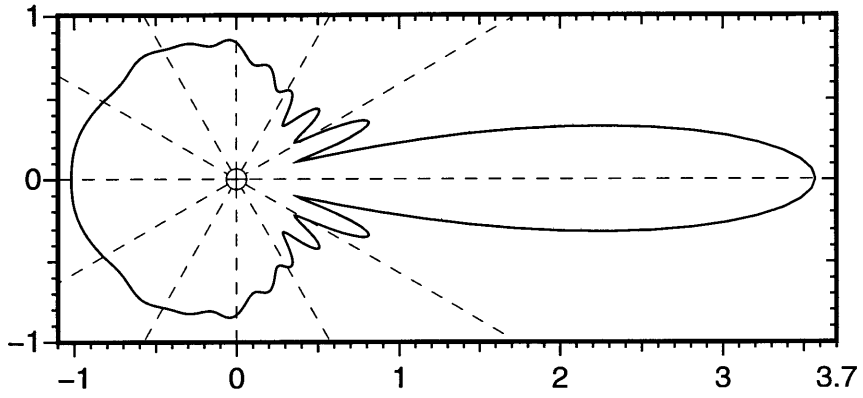

(b) $L = 4m$

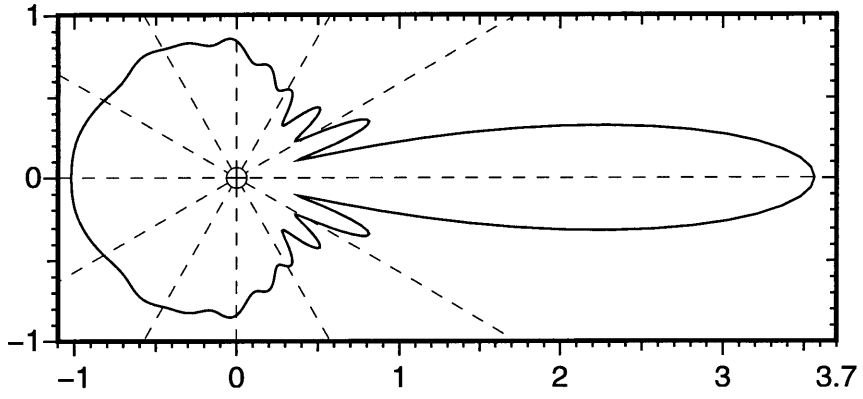

(c) $L = 8m$

Figure 3-8: $|\beta_{cylinder}|/L$: polar beampatterns of cylindrical finite shells – broad-sided (90°) steel shells ($a = 1m$, $t = 5cm$, $\rho = 7.8g/cm^3$, $C_p = 5200m/s$, and $C_s = 2600m/s$) in a water space ($\rho = 1.0g/cm^3$ and $C_p = 1500m/s$) at $f = 3kHz$. The right hand side is the forward scattering direction.

shell increases. This trend is similar to the beampattern of a line array.

Figure 3-10 shows the azimuthal beampatterns produced by cylindrical shells of different azimuthal orientations. Since a cylindrical shell is an aspect-dependent target, the scattered field of a cylindrical shell becomes asymmetric when the shell is neither perpendicular to nor aligned with the direction of the incident wave. The azimuthal beampatterns in the figure show that there are two major features of the scattered field. One is in the forward direction and the other is in the specular direction of the incident wave with respect to the shell axis.

In order to incorporate these beampatterns into a spectral method, the wavenumber integration technique of the 3-D OASES [46] is used. Since the above beampatterns are derived from the case of single plane incident wave, the equivalent point source strength in a layer is the sum of the contributions from upward and downward traveling plane wave components existing in that layer. In other words, the beampattern in a layer is the superposition of beampatterns from up-going and down-going plane wave components. In the case of an incident beam, the same technique is used to compute the equivalent beampattern. Once a beampattern is obtained, its equivalent source spectrum is determined for each horizontal wavenumber. This approach implicitly assumes that multiple scattering of the target is ignored, which does not allow re-scattering of scattered waves. Figure 3-11 shows a diagram describing the overview of the numerical implementation regarding the target scattering model. The left hand side shows the procedure to obtain the plane wave scattering function of a target and the right hand side describes the incident field. When the plane wave scattering function and the incident field are combined, the effective beampattern of the target is obtained. This beampattern is transformed in order to be compatible with the 3-D OASES. The polar angle ϕ of the beampattern is replaced by horizontal wavenumber and the azimuthal dependency (i.e. θ of beampattern) is expressed by the azimuthal Fourier series. Then, the 3-D OASES computes the resulting scattered field by using the spectral representation of the target beampattern.

3.4 Benchmark

In order to validate the target scattering model developed in this thesis, several benchmarks were conducted against the baseline case of target scattering in an unbounded homogeneous medium. Figure 3-12 describes the first and second benchmark cases. The target is either a rigid sphere or a pressure-release sphere. The radius of the sphere is $0.5m$ and the incident field is a compressional plane wave with 45° grazing angle at $f = 3kHz$. The surrounding medium is water. Since the numerical model for target scattering requires interfaces above and below the target, the medium is divided into two water half spaces and one water layer between the two half spaces. The depth of the layer is $10m$ and the target is located at the center depth of the layer. Even though there are no physical interfaces, this medium configuration has two transparent interfaces above and below the sphere. The benchmark compares the scattered pressures along these interfaces for the numerical model and the analytic solution.

Figure 3-13 shows an in-plane vertical cut of the scattered field[5]. With respect to the direction of the incident wave (45°), the scattered exhibits symmetry. The scattered pressures along the upper and lower interfaces are computed for comparison purposes.

Figure 3-14 shows two plots comparing the scattered pressures along the upper and lower interfaces for the numerical model and the analytic solution. There are four curves in each plot. The solid line is the scattered pressure computed using the true solution. The dotted line is computed

[5] defined in Figure 2-31.

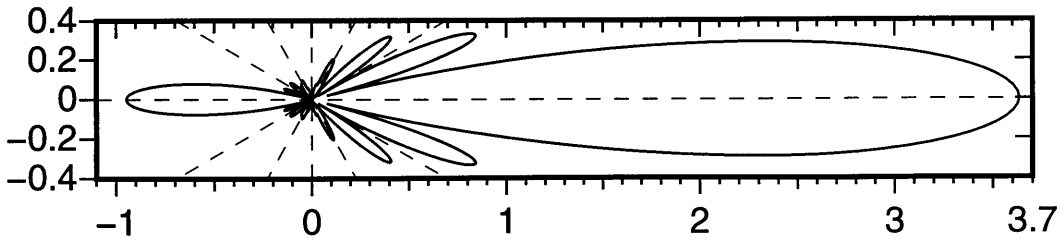

(a) $L = 2m$

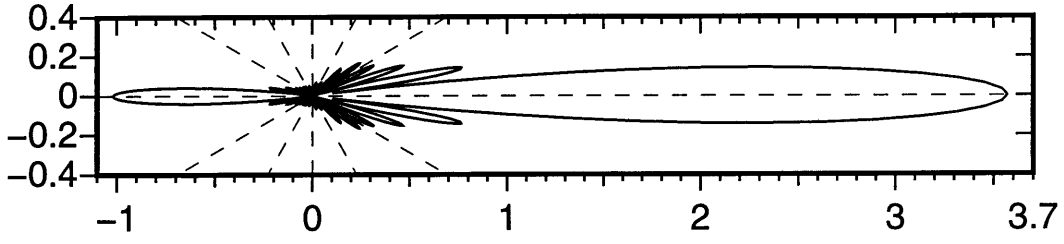

(b) $L = 4m$

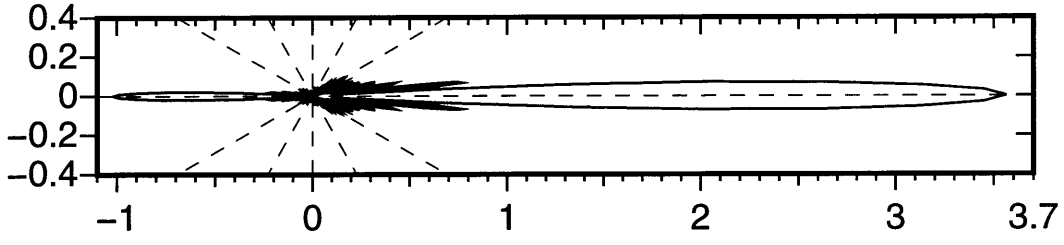

(c) $L = 8m$

Figure 3-9: $|\beta_{cylinder}|/L$: azimuthal beampatterns of cylindrical finite shells – broad-sided (90°) steel shells ($a = 1m$, $t = 5cm$, $\rho = 7.8g/cm^3$, $C_p = 5200m/s$, and $C_s = 2600m/s$) in a water space ($\rho = 1.0g/cm^3$ and $C_p = 1500m/s$) at $f = 3kHz$. The right hand side is the forward scattering direction.

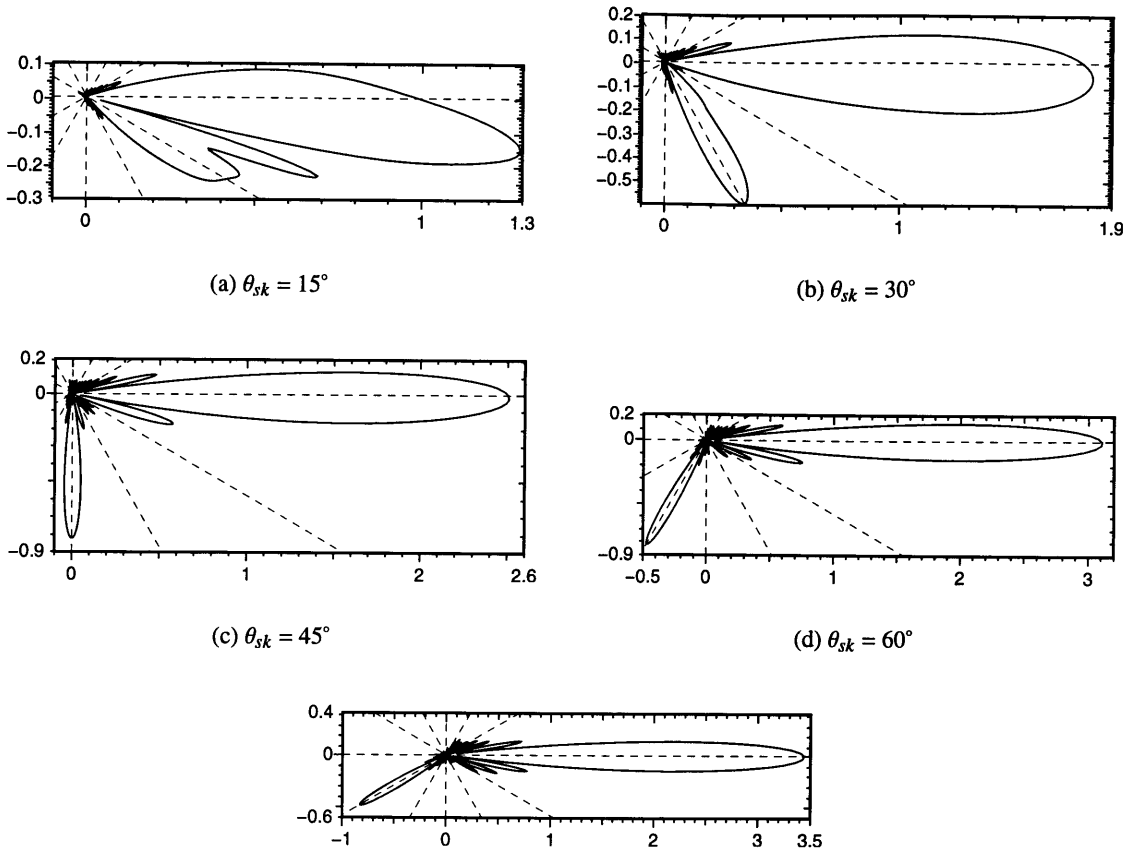

(a) $\theta_{sk} = 15°$

(b) $\theta_{sk} = 30°$

(c) $\theta_{sk} = 45°$

(d) $\theta_{sk} = 60°$

(e) $\theta_{sk} = 75°$

Figure 3-10: $|\beta_{cylinder}|/L$: azimuthal beampatterns of cylindrical finite shells with different azimuthal orientations – steel shells ($a = 1m$, $L = 4m$, $t = 5cm$, $\rho = 7.8g/cm^3$, $C_p = 5200m/s$, and $C_s = 2600m/s$) in a water space ($\rho = 1.0g/cm^3$ and $C_p = 1500m/s$) at $f = 3kHz$. The right hand side is the forward scattering direction.

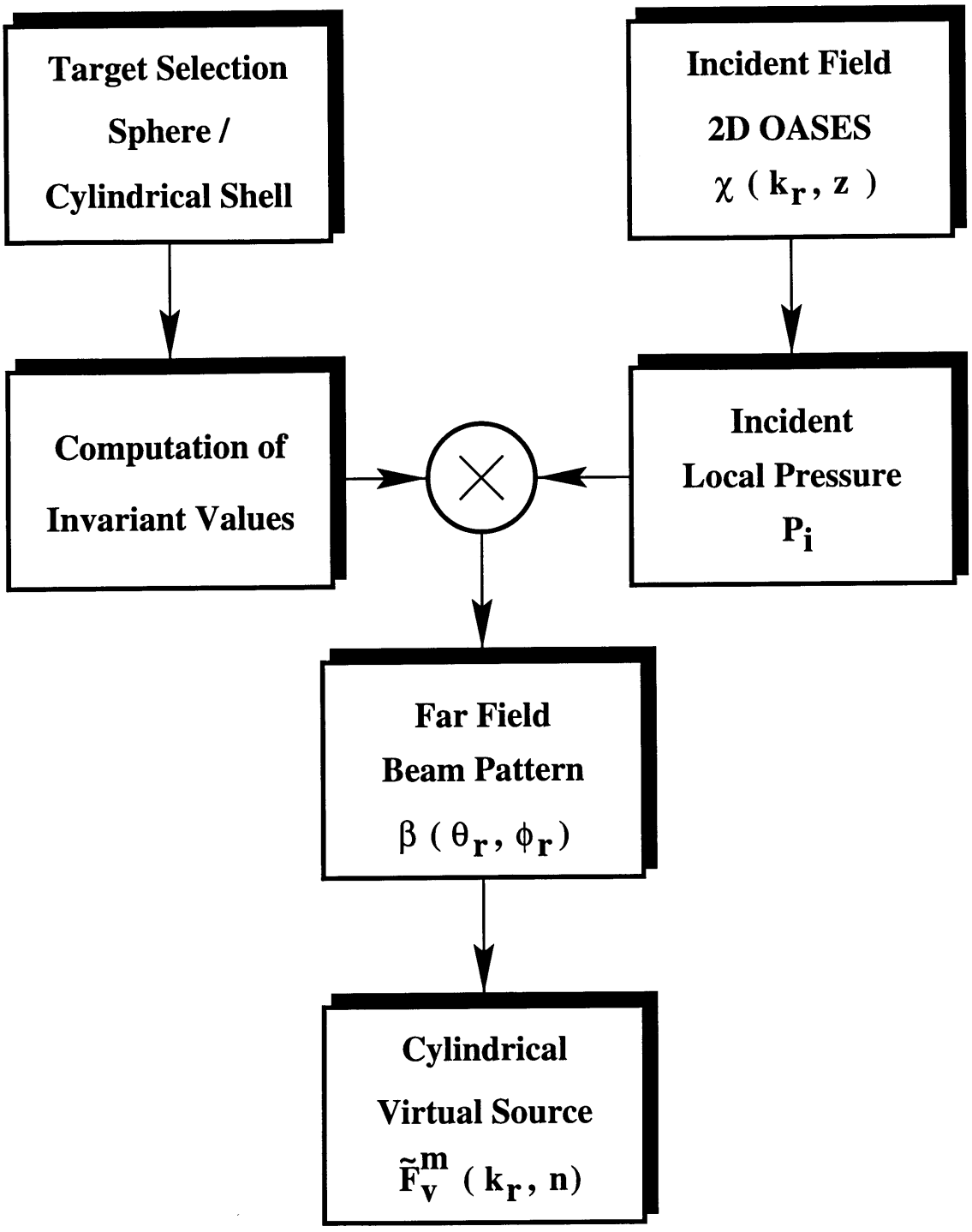

Figure 3-11: Diagram of the target scattering model.

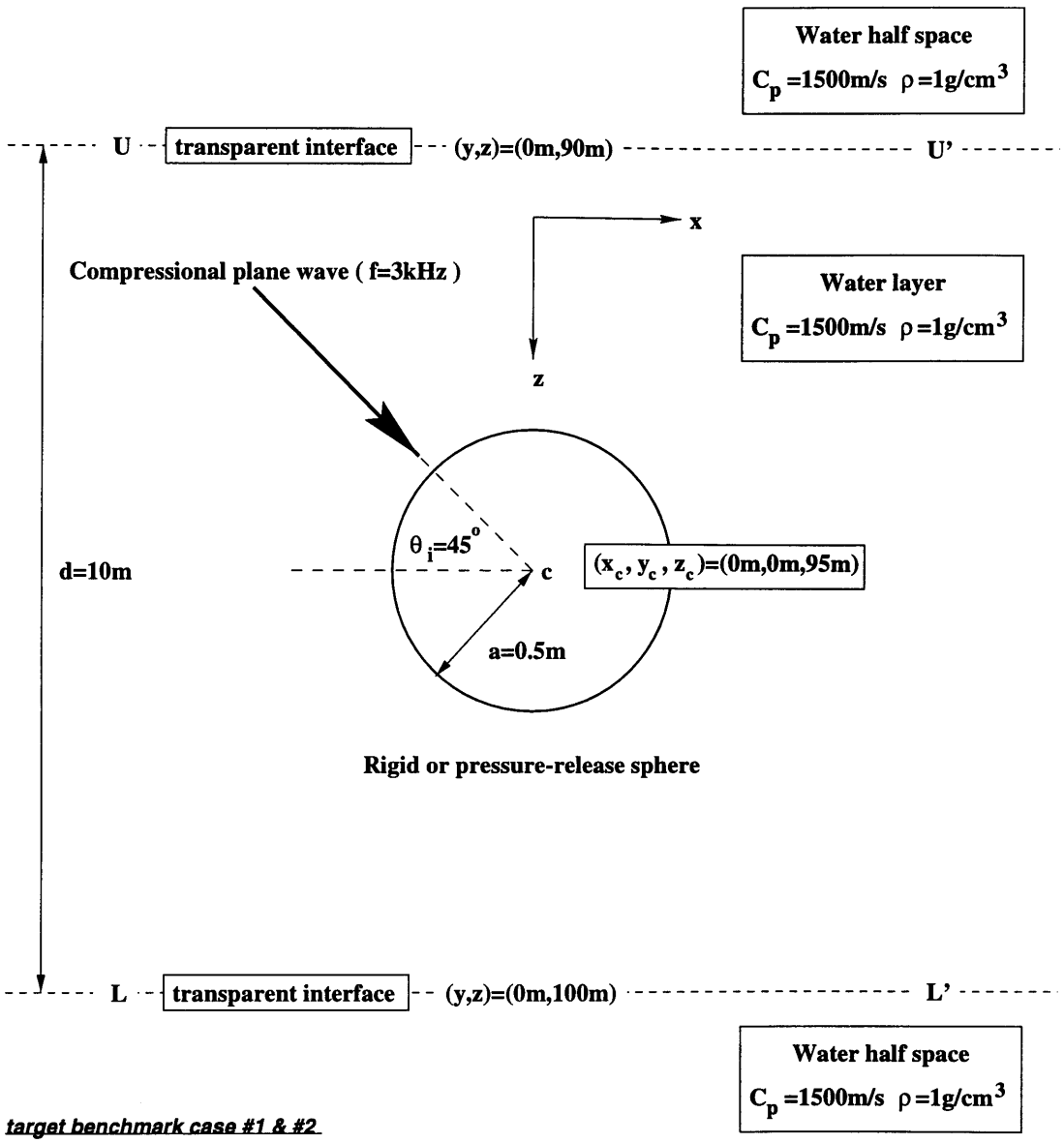

Figure 3-12: Benchmark scenario for the target scattering model : case of a spherical target in a free space.

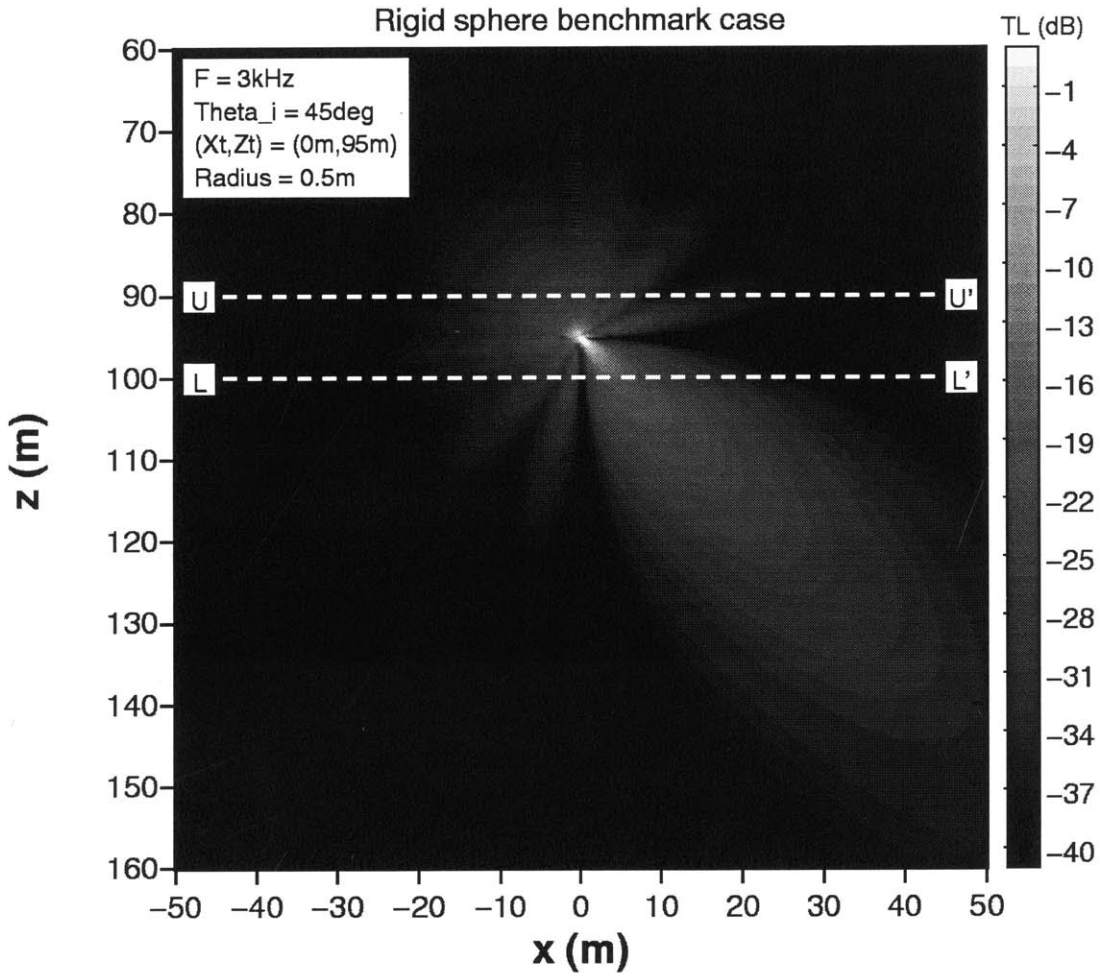

Figure 3-13: In-plane transmission loss of a rigid sphere ($a = 0.5m$) in a free space ($C_p = 1500m/s$ and $\rho = 1.0g/cm^3$). The incident field is a compressional plane wave coming from the left upper direction with $\theta_i = 45°$. Dashed lines $U - U'$ and $L - L'$ correspond to the upper and lower transparent interfaces between the water half spaces and the water layer.

using the far-field approximation of the true solution (i.e. the limiting case of the true solution as the field point goes to infinity). The dashed line is a numerical solution evaluated by the numerical model developed in this chapter. The computation of the scattered pressure in this case is done by the 3-D OASES using the full expression for the Bessel functions in the wavenumber integration. The dash-dotted line is another numerical solution with the same numerical model, however the scattered pressures are obtained by the 3-D OASES using the asymptotic forms of the Bessel functions in the wavenumber integration[6]. The plots show excellent agreements among the different solutions on both interfaces. The only discrepancy found is the oscillatory behavior of the numerical solution in the backward direction. This is caused by a numerical instability when the coefficients of the azimuthal Fourier series are evaluated. Since the backward direction ($\theta = \pi$) corresponds to the cancellation of terms in the Fourier transformation, the amount of error in the backward direction is bigger than that of the forward direction.

The solution obtained by the numerical model and the 3-D OASES using the asymptotic Bessel functions shows the greatest error at zero range. This error is expected because the asymptotic expression of the Bessel functions is not valid for small arguments. The asymptotic expression of the Bessel functions in the wavenumber integration is still useful because it produces accurate solutions in the far-field efficiently. Other solutions have errors less than $1dB$.

Figure 3-15 is the in-plane vertical cut of the scattered field caused by the pressure-release sphere shown in Figure 3-12. Like the case of the rigid sphere, the symmetry of the scattered field with respect to the direction of the incident wave is observed.

Figure 3-16 shows the comparison of the scattered pressure along the upper and lower interface for the numerical model and the true solution. Except the solution obtained using the asymptotic version of the Bessel functions, the numerical solution shows excellent agreement with the true solution.

Two benchmark cases involving a finite cylindrical shell were also performed to validate the numerical target model. Figure 3-17 shows the benchmark scenario for a broad-sided cylindrical shell. The length, radius and thickness of the shell are $2m$, $0.5m$, and $5cm$, respectively. The compressional wave speed of the shell is $C_p = 5200m/s$, the shear wave speed is $C_s = 2600m/s$, and the density is $7.8g/cm^3$. The cylindrical shell is oriented to be perpendicular to the direction of the incident plane wave. The incident grazing angles are 30° and 45°. Other configurations for the benchmark scenario are exactly the same as the previous scenario (Figure 3-12).

Figure 3-18 is the in-plane vertical cut of scattered field produced by the cylindrical shell when the incident gazing angle is 30°. Similarly to the previous benchmark cases, the scattered field is symmetric with respect to the direction of the incident wave.

Figure 3-19 shows the comparison of the scattered pressure for the numerical model and the analytic solution. Since the exact solution for the scattered field produced by a finite cylindrical elastic shell is not available yet, Rumerman's approximate solution is used as a reference solution. Compared to the previous case, the error between the numerical solution and analytic solution is relatively large. This is especially true for the combination of the target model and the 3-D OASES using the full expression of the Bessel functions. It produces large errors along the upper interface (Figure 3-19(a)). When the 3-D OASES uses the asymptotic expressions for the Bessel functions in the wavenumber integration, these errors are decreased. Unlike the previous benchmark cases, the reference solution for the cases of cylindrical target is already a far-field solution. Therefore, the reference solution can be reproduced better by the solution using the 3-D OASES and the asymptotic expressions for the Bessel functions. Using the asymptotic forms of the Bessel functions in the wavenumber integration is equivalent to the far-field approximation.

[6] This type of wavenumber integration is called FFP (fast field program) integration scheme [22].

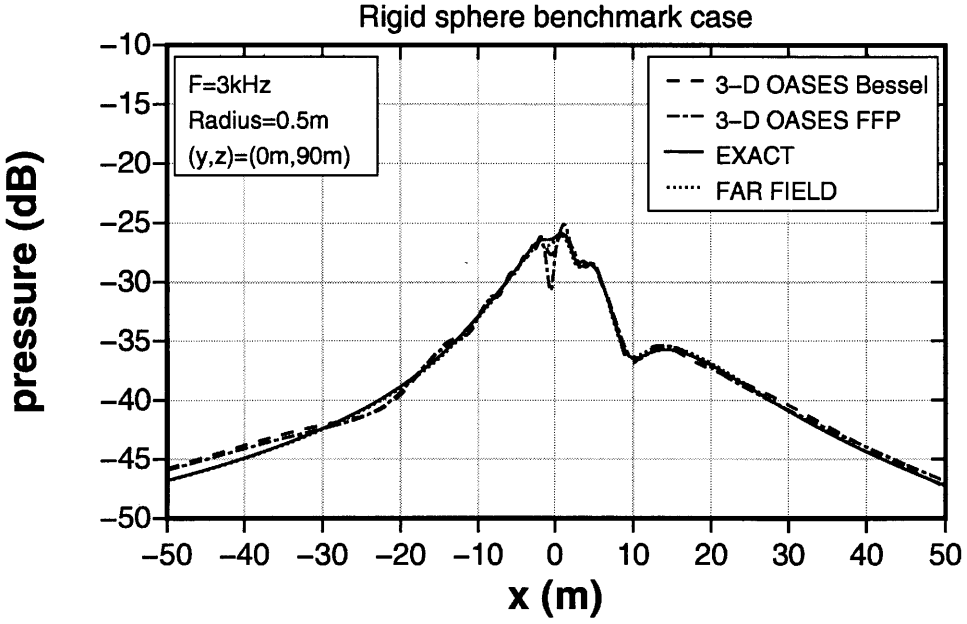

(a) Transmission loss at $5m$ above the center of rigid sphere ($U - U'$).

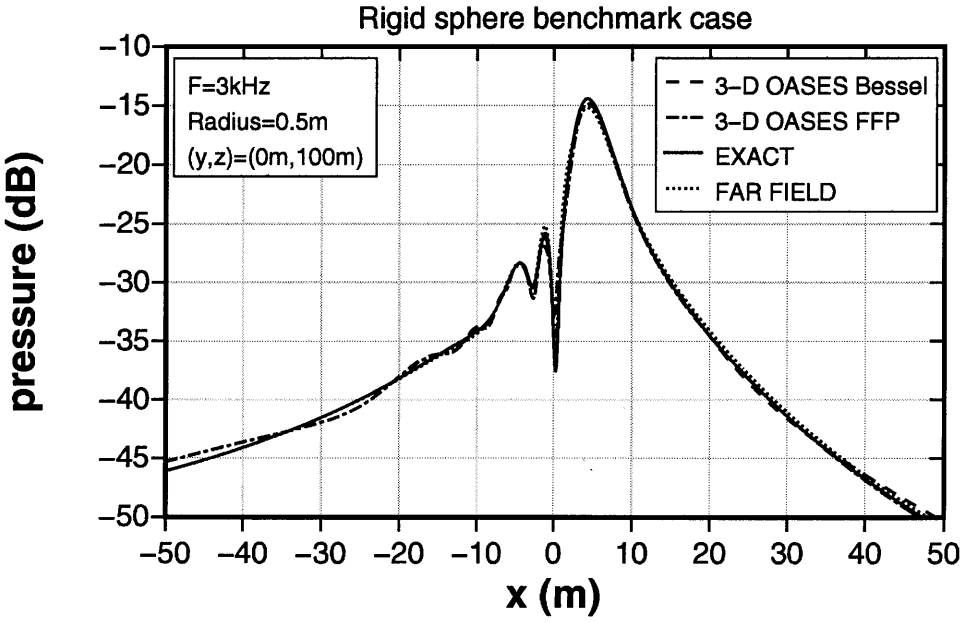

(b) Transmission loss at $5m$ below the center of rigid sphere ($L - L'$).

Figure 3-14: Comparison of in-plane transmission losses by a numerical method (3-D OASES) and two analytic expressions. The target is a rigid sphere with radius $0.5m$ in Figure 3-12. The incident field is a compressional plane wave ($f = 3kHz$ and $\theta_i = 45°$). Comparisons are along the lines $U - U'$ and $L - L'$ of Figure 3-13.

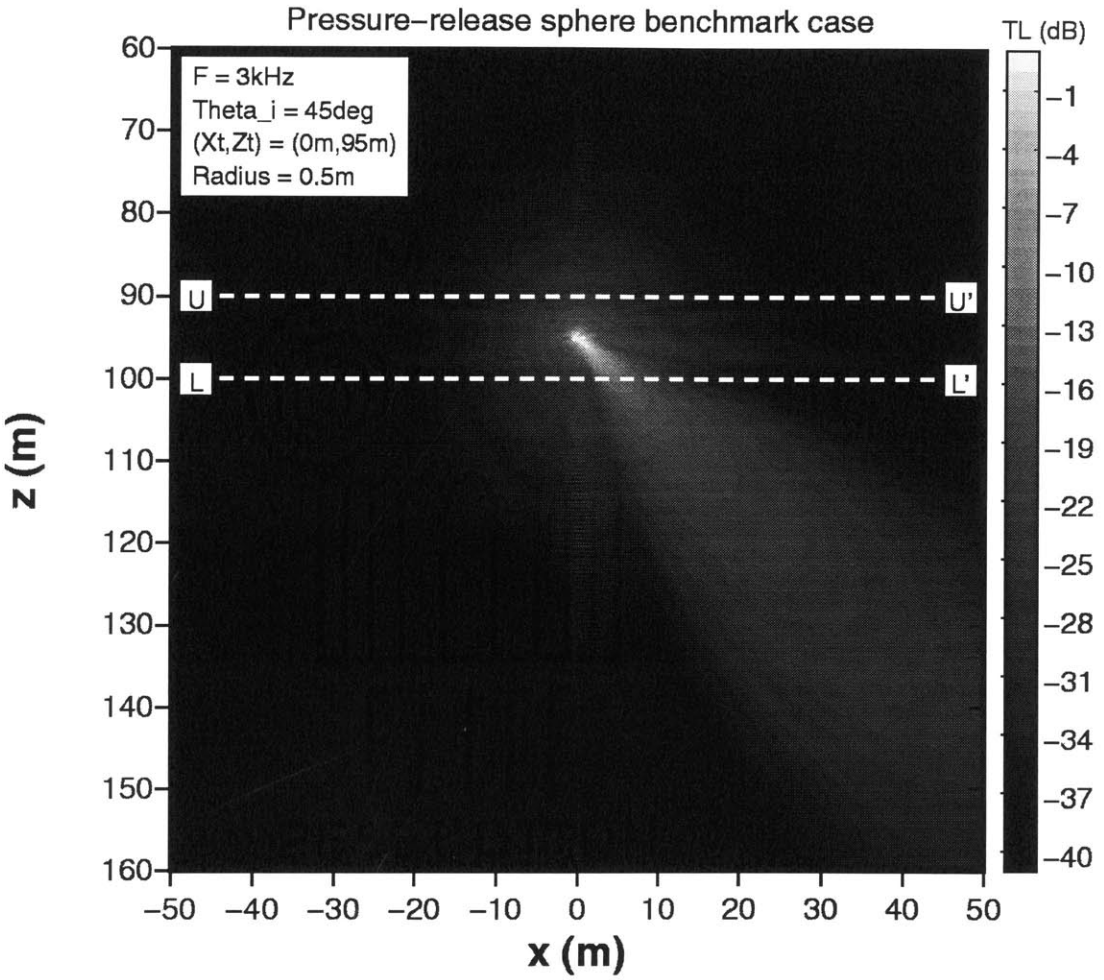

Figure 3-15: In-plane transmission loss of a pressure-release sphere ($a = 0.5m$) in a free space ($C_p = 1500m/s$ and $\rho = 1.0g/cm^3$). The incident field is a compressional plane wave coming from the left upper direction with 45° grazing angle. Dashed lines $U - U'$ and $L - L'$ correspond to the upper and lower transparent interfaces between the water half spaces and the water layer.

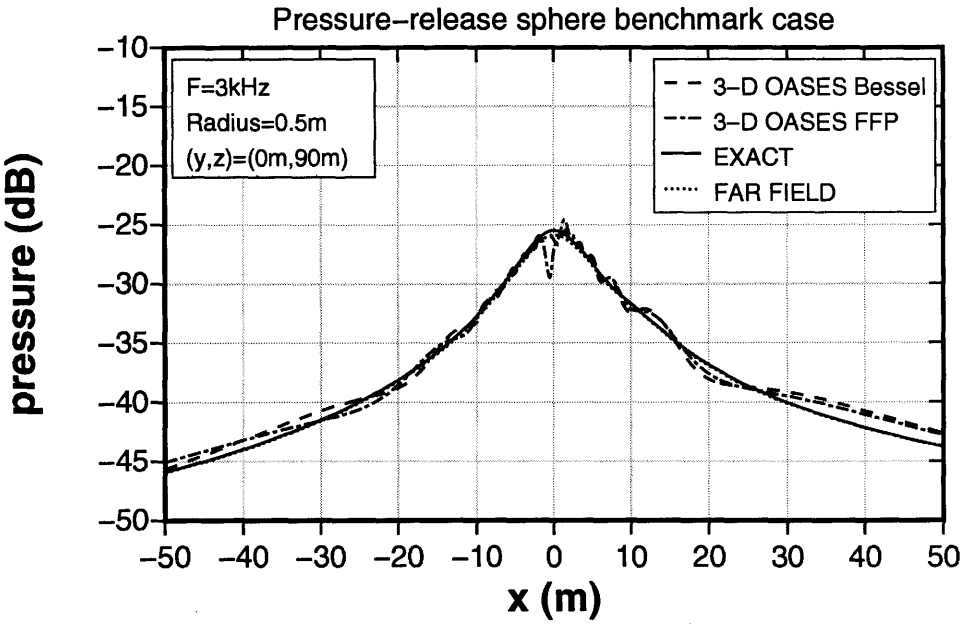

(a) Transmission loss at $5m$ above the center of pressure-release sphere ($U - U'$).

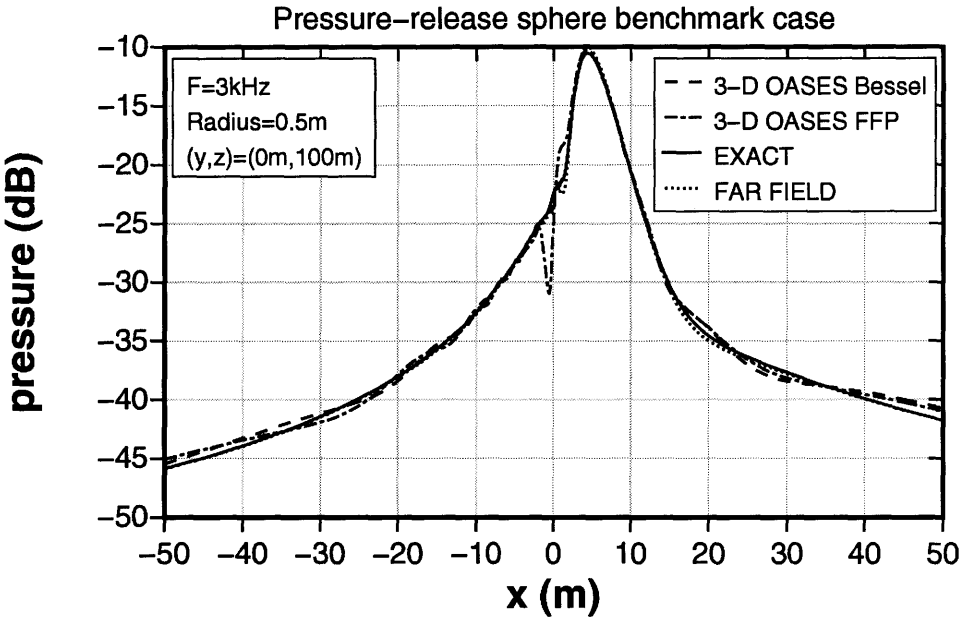

(b) Transmission loss at $5m$ below the center of pressure-release sphere ($L - L'$).

Figure 3-16: Comparison of in-plane transmission losses by a numerical method (3-D OASES) and two analytic expressions. The target is a pressure-release sphere with radius $0.5m$ in Figure 3-12. The incident field is a compressional plane wave ($f = 3kHz$ and $\theta_i = 45°$). Comparisons are along the lines $U - U'$ and $L - L'$ of Figure 3-15.

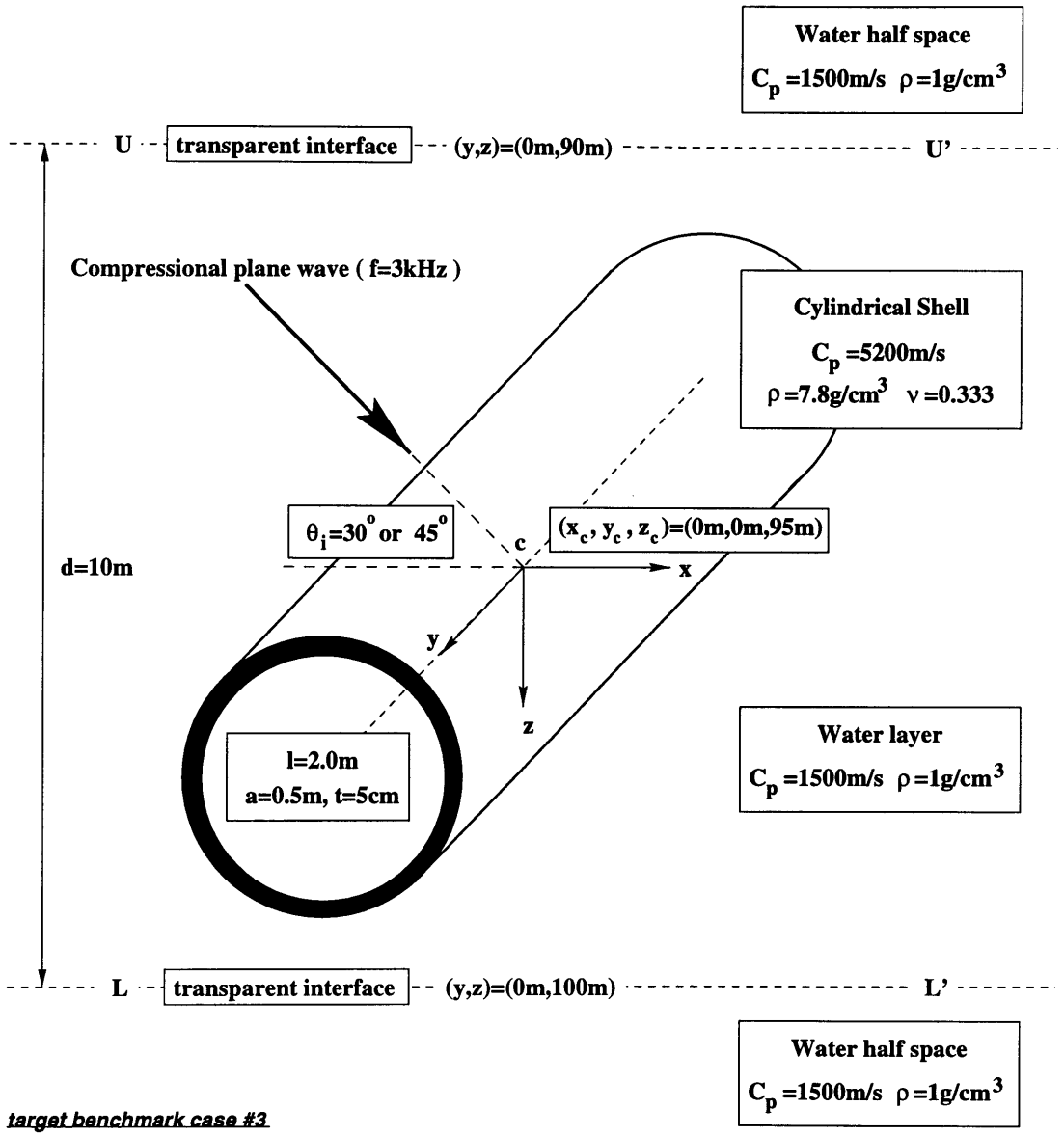

Figure 3-17: Benchmark scenario for the target scattering model : case of a cylindrical target in a free space.

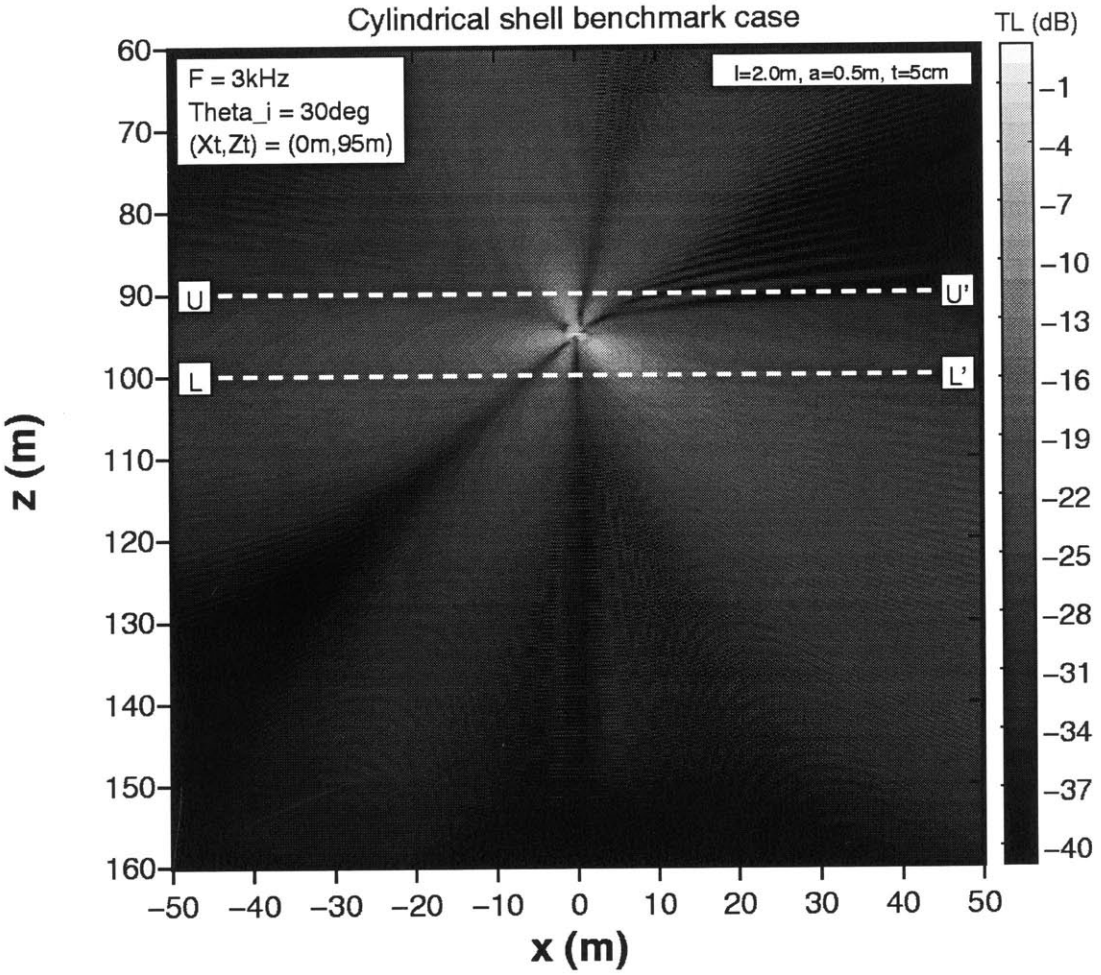

Figure 3-18: In-plane transmission loss of a cylindrical steel shell ($l = 2m$, $a = 0.5m$, $t = 5cm$, $\rho = 7.8g/cm^3$, $C_p = 5200m/s$, and $C_s = 2600m/s$) in a free space ($C_p = 1500m/s$ and $\rho = 1.0g/cm^3$). The incident field is a compressional plane wave coming from the left upper direction with 30° grazing angle. Dashed lines $U - U'$ and $L - L'$ correspond to the upper and lower transparent interfaces between the water half spaces and the water layer.

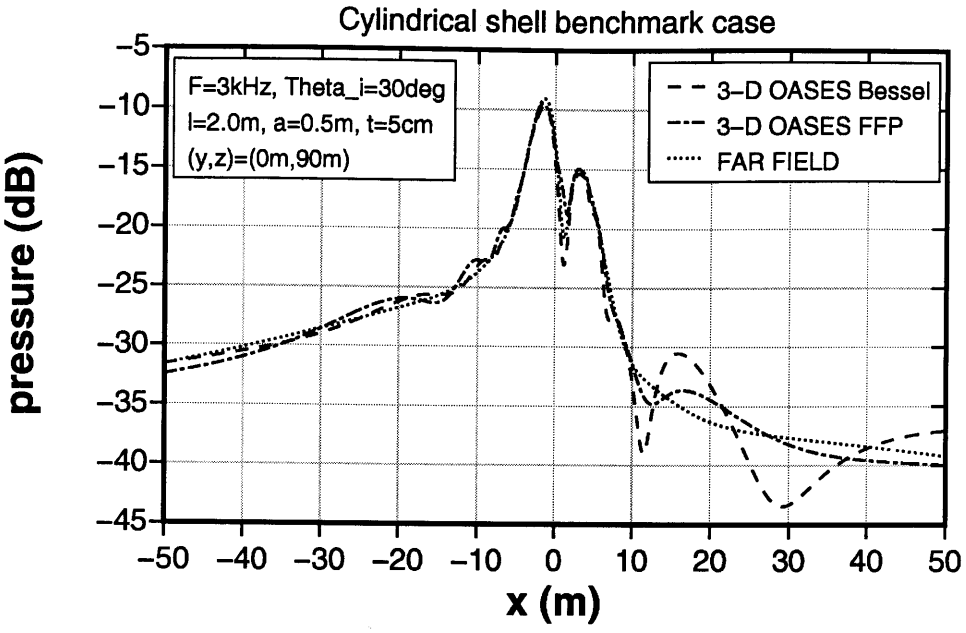

(a) Transmission loss at $5m$ above the center of cylindrical shell ($U - U'$).

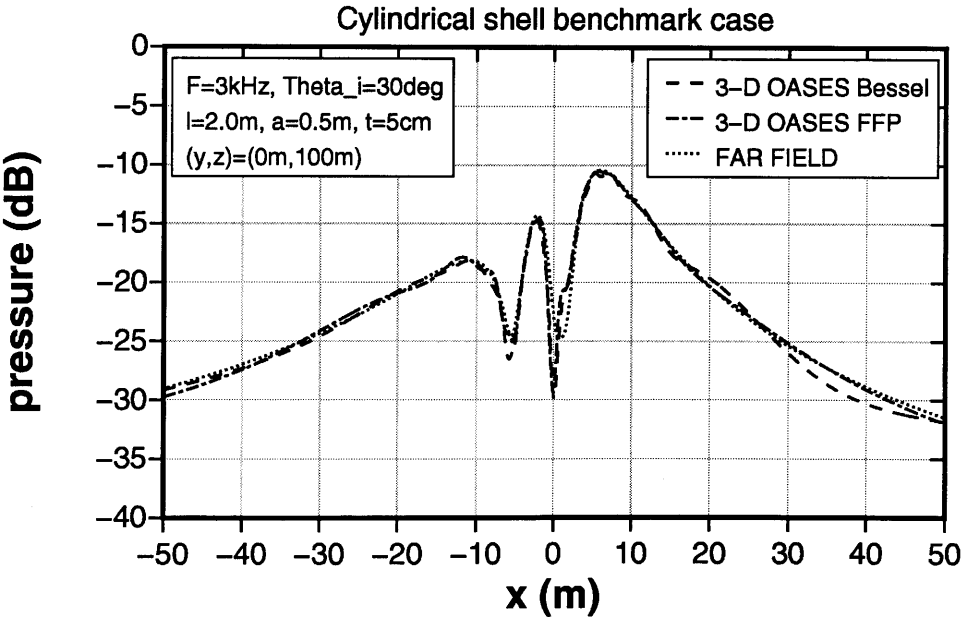

(b) Transmission loss at $5m$ below the center of cylindrical shell ($L - L'$).

Figure 3-19: Comparison of in-plane transmission losses by a numerical method (3-D OASES) and two analytic expressions. The target is a cylindrical steel shell ($l = 2m$, $a = 0.5m$, and $t = 5cm$). The incident field is a compressional plane wave ($f = 3kHz$ and $\theta_i = 30°$). Comparisons are along the lines $U - U'$ and $L - L'$ of Figure 3-18.

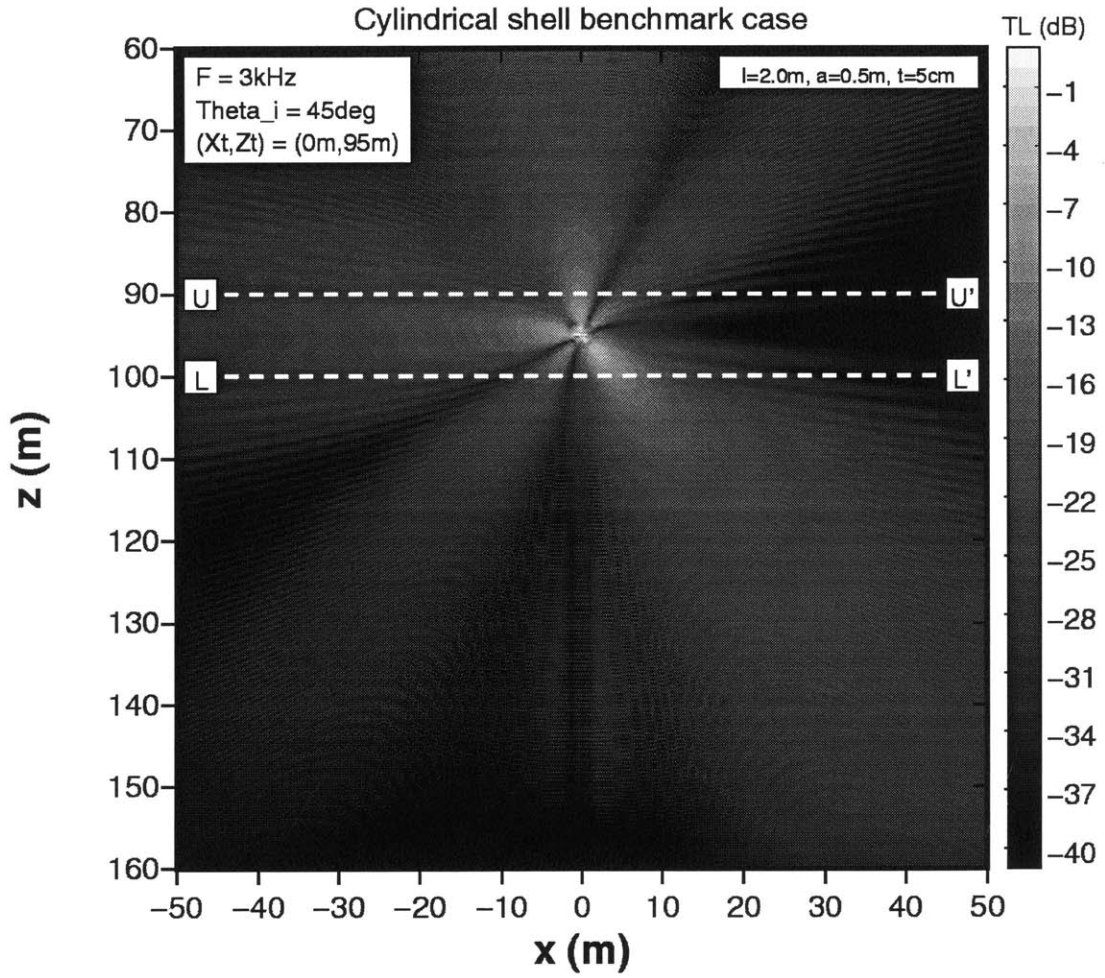

Figure 3-20: In-plane transmission loss of a cylindrical steel shell ($l = 2m$, $a = 0.5m$, $t = 5cm$, $\rho = 7.8g/cm^3$, $C_p = 5200m/s$, and $C_s = 2600m/s$) in a free space ($C_p = 1500m/s$ and $\rho = 1.0g/cm^3$). The incident field is a compressional plane wave coming from the left upper direction with 45° grazing angle. Dashed lines $U - U'$ and $L - L'$ correspond to the upper and lower transparent interfaces between the water half spaces and the water layer.

Figure 3-20 shows the in-plane vertical cut of the scattered field produced by the cylindrical shell for a plane incident wave at the grazing angle 45°. The symmetry of the scattered field is observed as the previous cases.

Figure 3-21 shows the comparison of scattered pressures along the upper and lower interfaces. Similarly to the previous case of a cylindrical shell, the scattered pressures are matched better by the numerical target model with the 3-D OASES using the FFP integration scheme (i.e. using the asymptotic expressions for the Bessel functions).

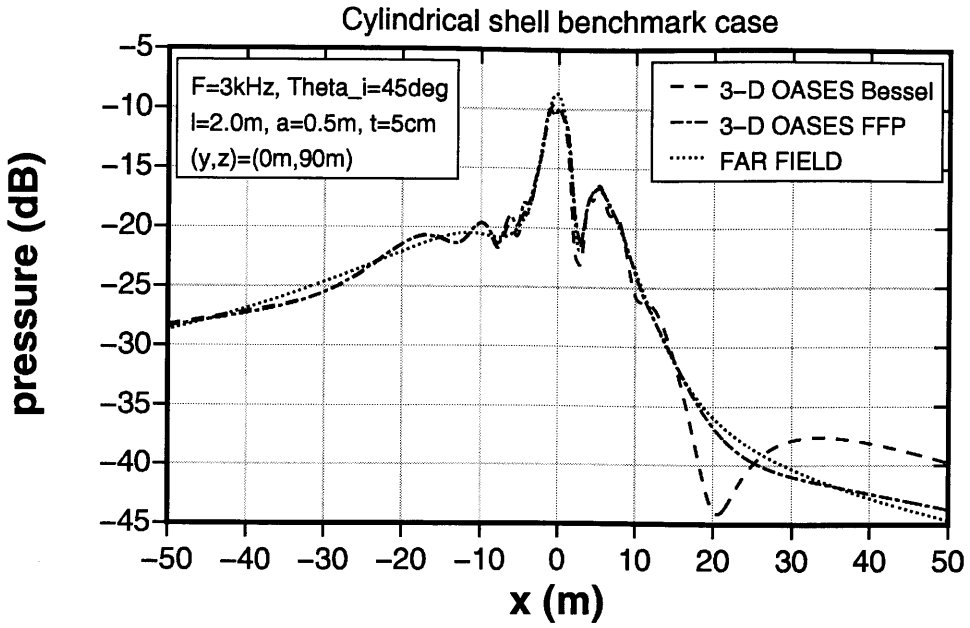

(a) Transmission loss at $5m$ above the center of cylindrical shell ($U - U'$).

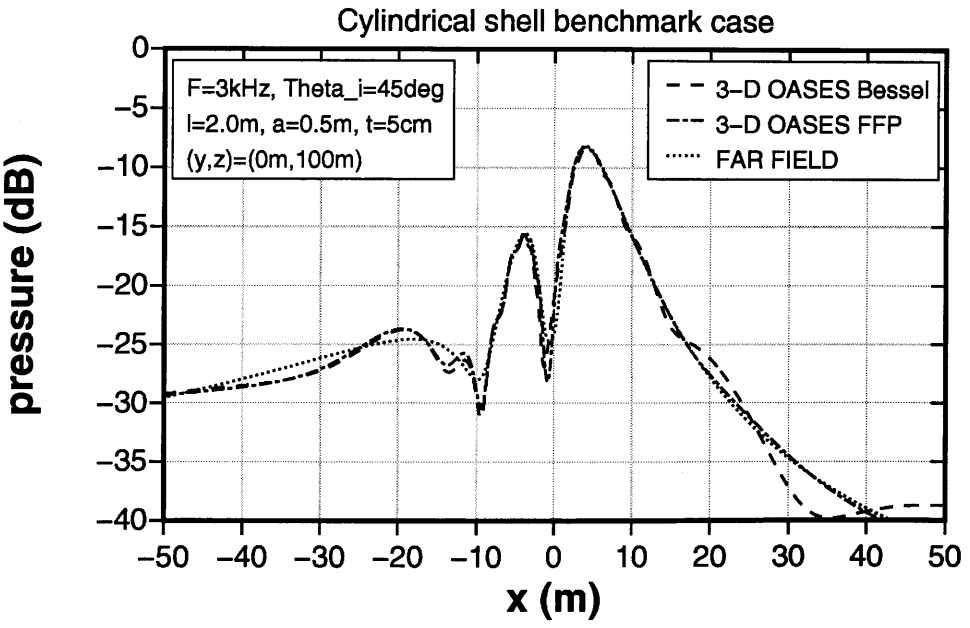

(b) Transmission loss at $5m$ below the center of cylindrical shell ($L - L'$).

Figure 3-21: Comparison of in-plane transmission losses by a numerical method (3-D OASES) and two analytic expressions. The target is a cylindrical steel shell ($l = 2m$, $a = 0.5m$, and $t = 5cm$). The incident field is a compressional plane wave ($f = 3kHz$ and $\theta_i = 45°$) Comparisons are along the lines $U - U'$ and $L - L'$ of Figure 3-20.

3.5 Effects of Medium Configuration

This section presents series of numerical simulations of target scattering caused by spherical and cylindrical targets with different medium configurations. Along with the numerical results, the effects of medium configurations on target scattering will be discussed. The formats of the various resulting plots are identical to those presented in Section 2.5 – Horizontal scattered field, in-plane scattered field, in-plane scattering coefficient plot, and angular spectrum contour. The numerical simulations in this section includes the following three cases.

- Target above different bottom media.
- Target flush buried in sublayers with different thicknesses.
- Target in a waveguide.

For the first two cases, only rigid and pressure-release spheres are used. Two types of cylindrical shells are included for the last case.

3.5.1 Effects of Medium Properties

A target scattering case is designed to demonstrate the effects of the lower half space medium on the scattered field. The target is either a rigid or a pressure-release sphere with radius $a = 0.5m$. Figure 3-22 shows the target scattering scenario – a target sitting on a half space. The upper medium is water and the lower medium is modeled as one of elastic limestone, fluid limestone, elastic sand, and fluid sand. The elastic and fluid cases are used together to show the effects of shear properties. The incident field is a plane wave at $f = 3kHz$. Two cases of grazing angles are considered – 15° and 45°.

Figure 3-23 shows the in-plane scattered field caused by a rigid sphere and a plane wave with grazing angle $\theta_i = 15°$ for different bottom properties. When fluid cases are compared with elastic cases, they produce a stronger forward and backward scattered field in the upper half space. This is caused by the shear waves supported by elastic media. The direct scattered waves from the target interact with the lower half space and are both reflected to the upper half space and transmitted to the lower half space. The elastic lower half space allows supersonic transmission of scattered waves in the form of shear waves. For the current examples, scattered waves are always supersonic to the shear phase speeds ($1000m/s$ for limestone and $600m/s$ for sand) in the lower half space. When the elastic and fluid limestone cases are compared, the elastic limestone (Figure 3-23(a)) has strong transmitted scattered wave in a narrow angular space. This angle of transmitted wave agrees to the shear transmission angle of forward scattering beam, which is $\theta = 49.9°$. The same type of transmitted shear wave exists for the elastic sand case (Figure 3-23(c)). The supersonic transmission to the compressional waves in the lower space is also allowed but within the compressional critical angular regimes ($\theta_c = 53.1°$ for limestone and $\theta_c = 33.6°$ for sand). This can be shown by observing the scattered field in the lower half space. When the fluid limestone case (Figure 3-23(b)) and the fluid sand case (Figure 3-23(d)) are compared, the sand half space allows more scattered energy at shallow angles in the forward direction while the limestone case does not have significant scattered field in that region.

Figure 3-24 shows the corresponding horizontal scattered field caused by four different types of lower half spaces. As shown in the in-plane scattered field plots (Figure 3-23), fluid limestone and sand half spaces produce similar scattered fields. A strong forward reflection of direct scattered wave and relatively high backward scattering are observed. For the elastic half space cases, the forward reflection and backward scattering are noticeably decreased. When elastic

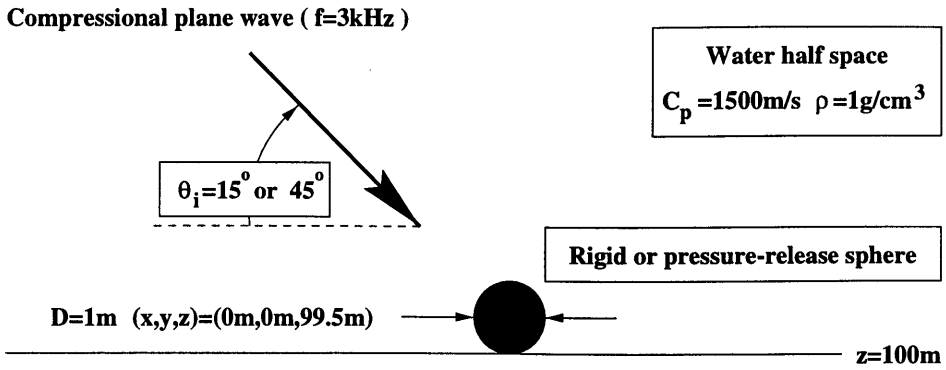

Lower half space	C_p (m/s)	C_s (m/s)	ρ (g/cm^3)
Elastic limestone	2500	1000	2.2
Fluid limestone	2500	0	2.2
Elastic sand	1800	600	1.6
Fluid sand	1800	0	1.6

target scenario #1 & #2

Figure 3-22: Target scattering scenario – case of a spherical target sitting on the interface between two half spaces. The target is a rigid or pressure-release sphere with radius $a = 0.5m$. The medium consists of a water upper half space and various lower half spaces. The incident field is a compressional plane wave ($f = 3kHz$ and $\theta_i = 15°, 45°$).

limestone and sand cases are compared, the limestone half space produces the scattered field confined to shallow scattering polar angle (ϕ), which corresponds to the compressional critical angle ($\theta_c = 53.1°$). These differences in the scattered fields are mainly caused by the elasticity of lower half space. When the shear wave is supported by a medium below a target, it provides a wide angular regime where the direct scattered waves from target escape to the lower space. The contrast in compressional wave speed and density controls the amount of reflected scattered energy.

Figure 3-25 compares in-plane scattering coefficients among different lower half spaces. As previously discussed, the fluid limestone and sand (dashed lines) have similar trends while the elastic lower spaces produce different scattering patterns. The elastic limestone has very low backward and forward scattering coefficients, because of its high compressional critical angle.

The next scattering example is exactly same as the previous one except the target is a pressure-release sphere instead of a rigid sphere. The pressure-release sphere produces stronger forward scattered field with uniform backward scattering at frequency $f = 3kHz$ and radius $a = 0.5m$. As shown in Figure 3-26, the in-plane scattered fields of pressure-release sphere have similar trends as the rigid sphere case. The major differences can be found in the reflected forward scattered wave in the upper space and transmitted scattered wave in the lower space.

The corresponding horizontal scattered fields are shown in Figure 3-27. The overall trend is similar to the case of rigid sphere. One observable difference between the elastic and fluid cases can be found in out-of-plane scattered waves. When the elastic and fluid sand cases (Figure 3-27(c) and Figure 3-27(d)) are compared, the out-of-plane scattering feature in the forward direction is

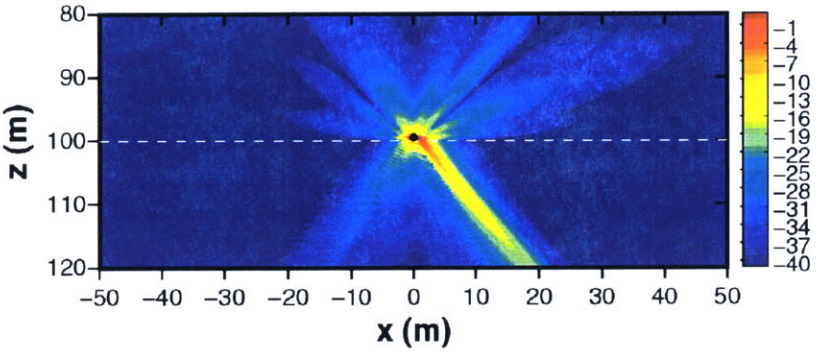

(a) Elastic limestone lower half space.

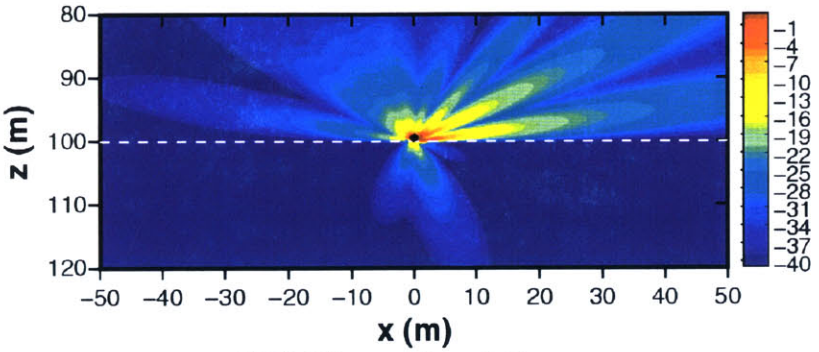

(b) Fluid limestone lower half space.

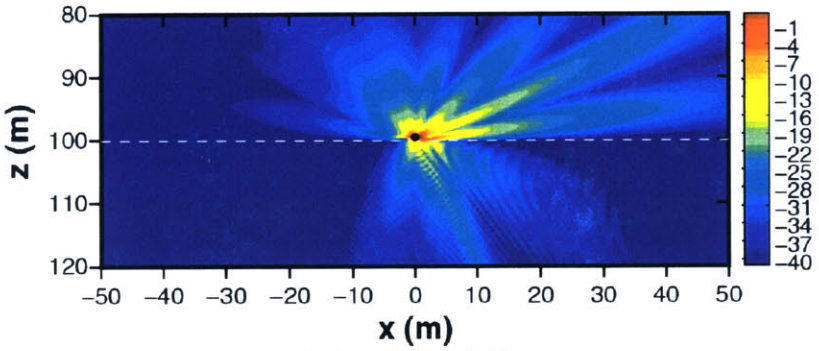

(c) Elastic sand lower half space.

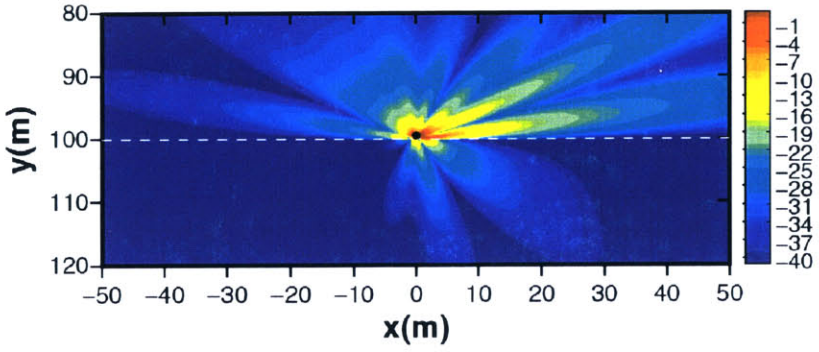

(d) Fluid sand lower half space.

Figure 3-23: In-plane scattered fields caused by a rigid sphere and a compressional plane wave ($f = 3kHz$ and $\theta_i = 15°$).

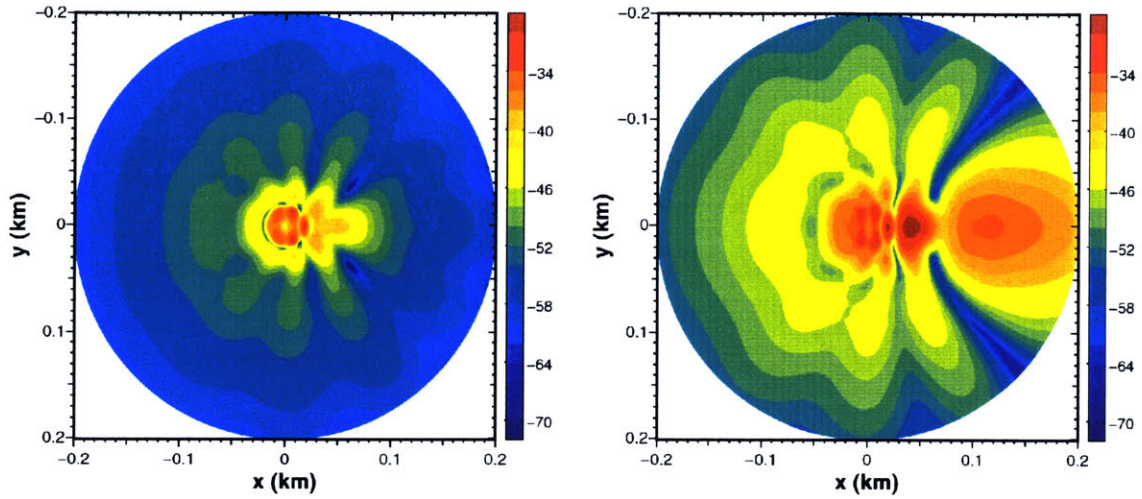

(a) Elastic limestone lower half space.

(b) Fluid limestone lower half space.

(c) Elastic sand lower half space.

(d) Fluid sand lower half space.

Figure 3-24: Horizontal scattered fields at $20m$ above the interface. The target is a rigid sphere with $0.5m$ radius and the incident field is generated by a compressional plane wave ($f = 3kHz$ and $\theta_i = 15°$).

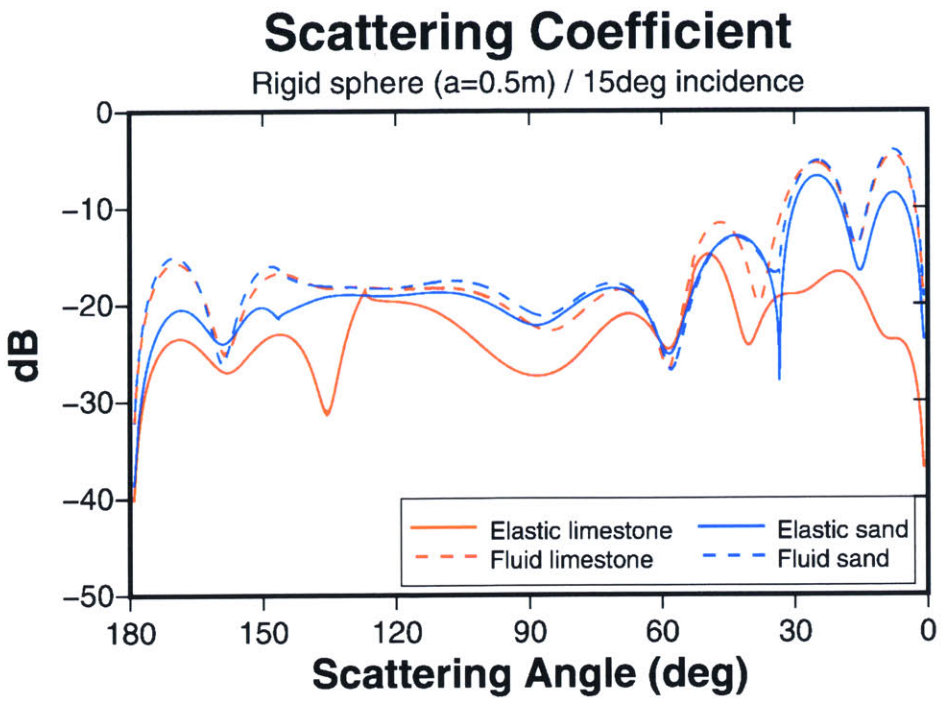

Figure 3-25: In-plane scattering coefficients. Cases of a rigid sphere sitting on different lower half spaces. The incident field is a compressional plane wave ($f = 3kHz$ and $\theta_i = 15°$).

reduced in the elastic sand case. In the free space case, out-of-plane scattering manifests itself as side lobes in the same direction as the main lobe. Since the lower (downward) portion of side lobe pattern has a higher grazing angle than main lobe, this portion of the scattered energy can be transmitted to the lower space as shear waves in the elastic case.

Figure 3-28 compares scattering coefficients produced by the pressure-release sphere across various lower half spaces. The elastic and fluid sand cases have similar values between the backward shear critical angle ($\theta_c = 66.4°$) and the forward specular reflection angle (15°). Outside of this regime, where transmission of direct scattered energy is very low, the scattering coefficients for fluid sand are almost identical to those of fluid limestone. In the case of elastic limestone, the transmission of scattered energy is dominant due to the wide angular regime of supersonic incidence in the lower space.

In the next two scattering examples (Figures 3-29, 3-30, and 3-31), the grazing angle of incident plane wave is 45° instead of 15°. Having a high grazing angle changes the partition of scatterer energy between the upper and lower spaces. Generally, high incident grazing angles reduce reflection and increase transmission. Figure 3-29 shows the in-plane scattered fields caused by a rigid sphere with radius $a = 0.5m$. Unlike the case of shallow grazing incidence, elastic and fluid sand lower half spaces allow the main lobe to be transmitted to the lower space with less distortion. The reflection of the scattered field is not significant in the forward direction. This results in an insignificant reflection of the main lobe. This dominant transmission can be explained by the fact that the incident grazing angle is higher than the compressional critical angle ($\theta_c = 33.6°$). For the cases of elastic and fluid limestone, the compressional critical angle ($\theta_c = 53.1°$) exceeds the grazing incident angle. Therefore, the transmission of scattered waves into the lower space is relatively weak compared to the cases of sand half spaces. This high grazing angle still permits more scattered energy to be transmitted than a shallow grazing angle. The backward scattered

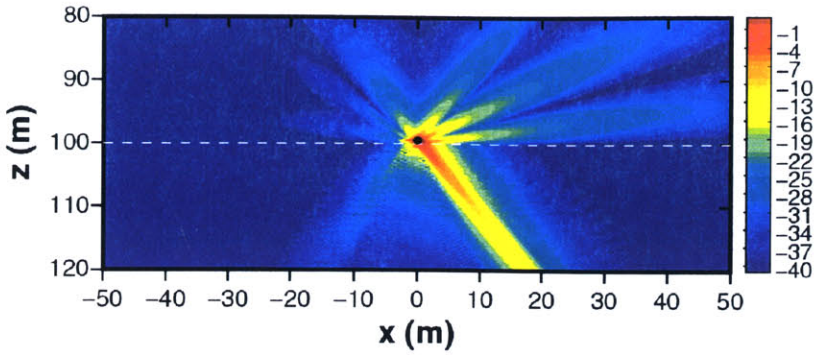

(a) Elastic limestone lower half space.

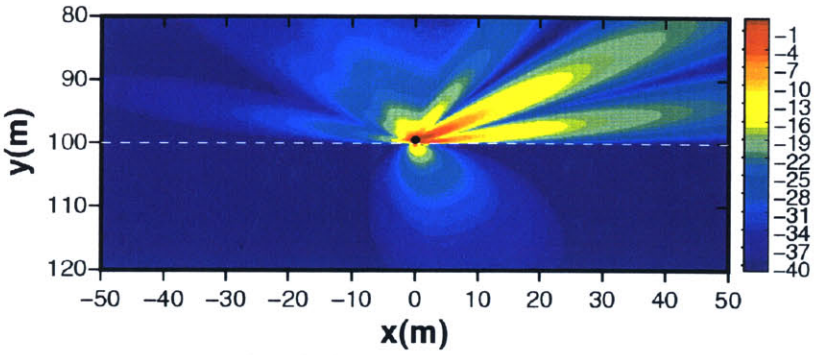

(b) Fluid limestone lower half space.

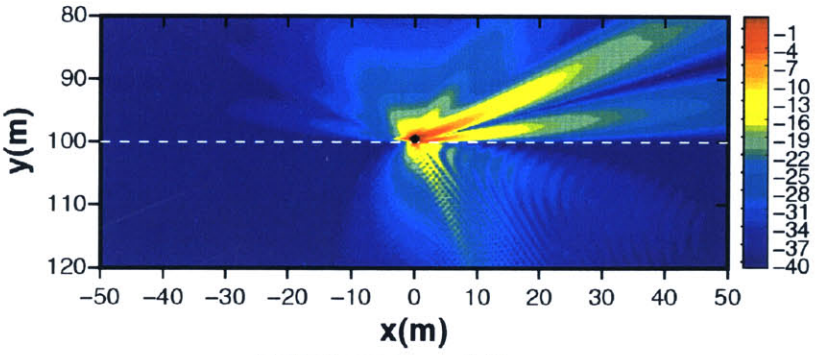

(c) Elastic sand lower half space.

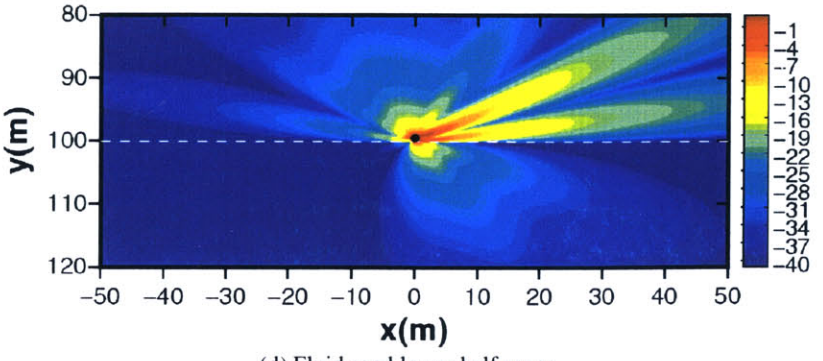

(d) Fluid sand lower half space.

Figure 3-26: In-plane scattered field caused by a pressure-release sphere and a compressional plane wave ($f = 3kHz$ and $\theta_i = 15°$) for different bottom properties.

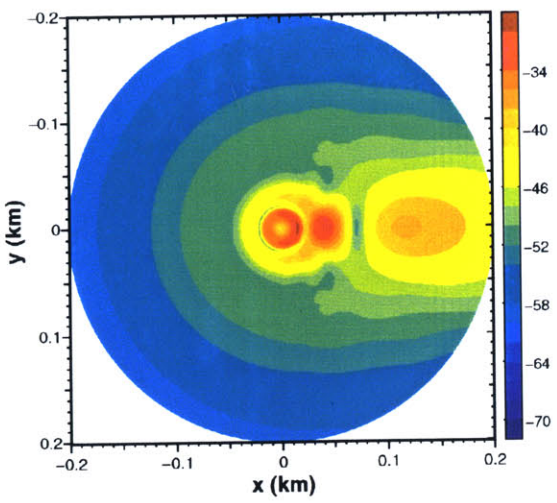

(a) Elastic limestone lower half space.

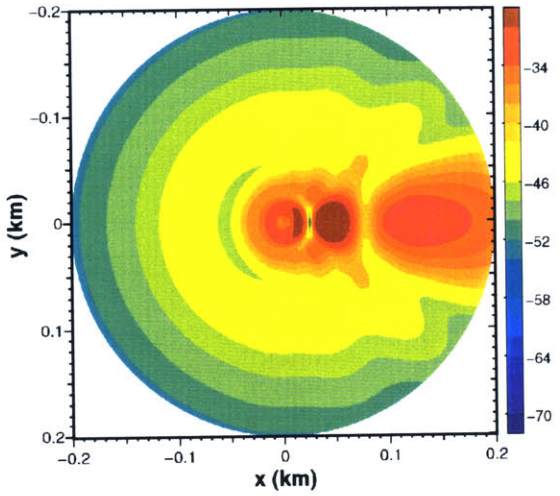

(b) Fluid limestone lower half space.

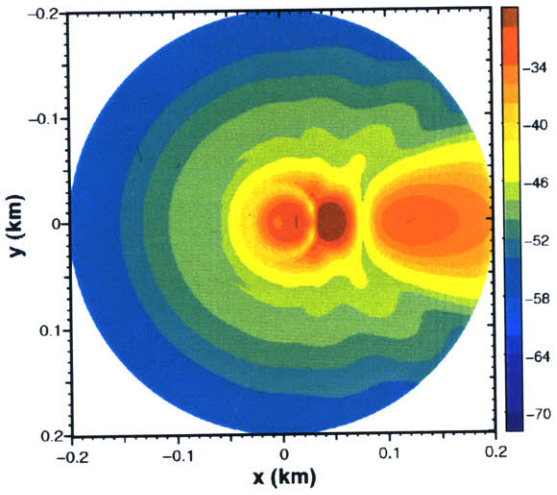

(c) Elastic sand lower half space.

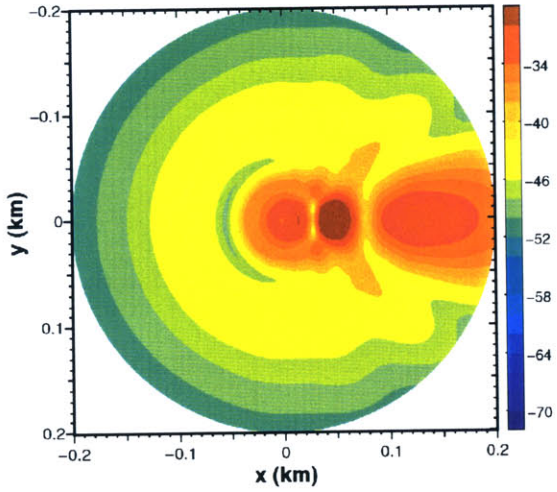

(d) Fluid sand lower half space.

Figure 3-27: Horizontal scattered fields at $20m$ above the interface. The target is a pressure-release sphere with $0.5m$ radius and the incident field is generated by a compressional plane wave ($f = 3kHz$ and $\theta_i = 15°$).

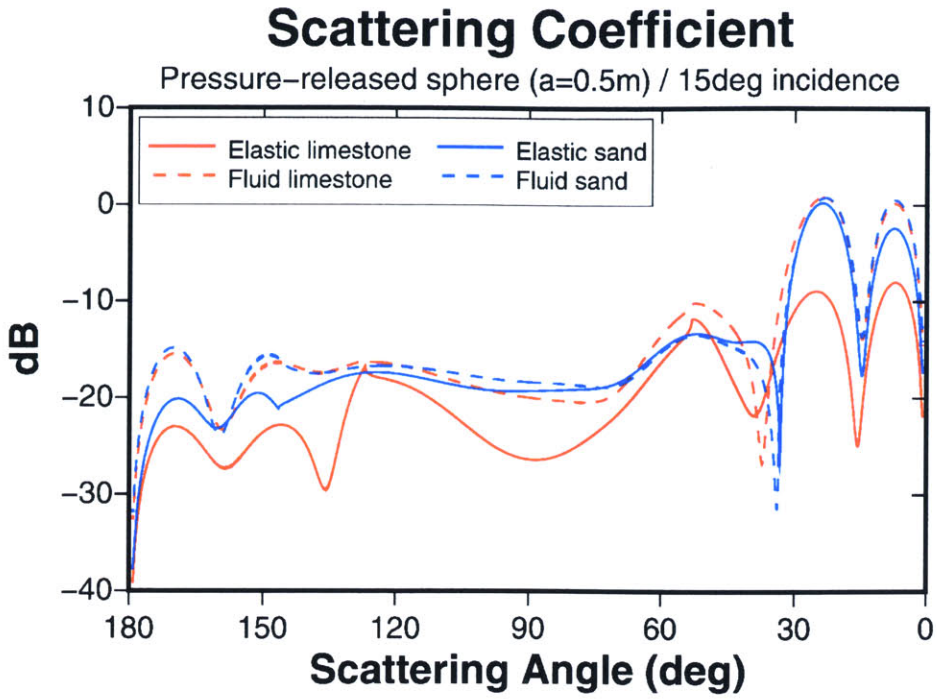

Figure 3-28: In-plane scattering coefficients. Cases of a pressure-release sphere sitting on different lower half spaces. The incident field is a compressional plane wave ($f = 3kHz$ and $\theta_i = 15°$).

field is less affected by the existence of an interface than the shallow grazing case.

Figure 3-30 shows the corresponding horizontal scattered fields. As discussed with the in-plane scattered fields, the elastic and fluid sand half spaces generate similar scattered fields in out-of-plane direction as well. The limestone cases have different trends compared to the cases of a sand half space because of their high compressional grazing angles. Elastic limestone permits scattered energy to be transmitted as shear waves in the lower space while the reflection of scattered energy is dominant in the fluid sand case.

Figure 3-31 shows the comparison among different in-plane scattering coefficients. Elastic sand and fluid sand yield very similar values of scattering coefficients. While elastic limestone and sand limestone have similar scattering coefficients near the vertical direction (i.e. shallow scattering polar angle regime : $0 < \phi < 30°$), the forward and backward scattered fields for elastic limestone are relatively weaker than case of fluid limestone.

The following scattering case of high grazing angle is identical to the previous one except the pressure-release sphere ($a = 0.5m$) is used instead of the rigid sphere. Figure 3-32 shows the corresponding in-plane scattered field. As in the case of a rigid sphere at 45° grazing incident angle, the majority of forward scattered energy is transmitted to the lower space. The case of elastic limestone (Figure 3-32(a)) is different from the other cases because the incident wave and a major portion of the main scattering lobe are both supersonic to the shear wave of lower medium. In the in-plane scattered field plot (Figure 3-32), the transmitted shear wave with a steep angle (about 60°) dominates the lower half space. When elastic and fluid sand cases are compared, they are almost identical except the scattered field in the steep angular regime of the lower half space is affected by the transmitted shear waves of elastic sand.

Figure 3-33 shows the horizontal cuts of scattered fields caused by a pressure-release sphere with a plane wave of 45° grazing angle. As mentioned in the rigid sphere case, the forward

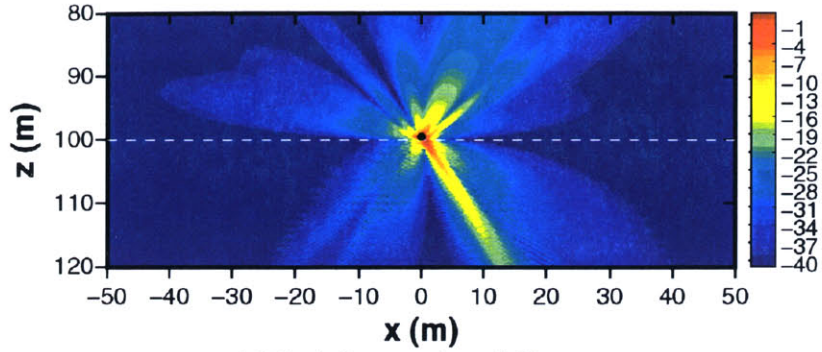

(a) Elastic limestone lower half space.

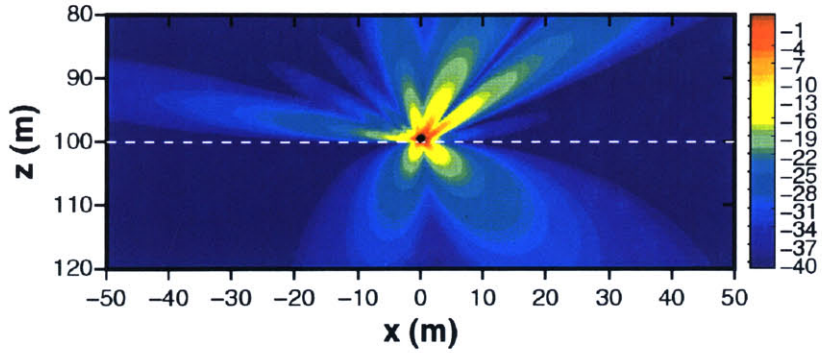

(b) Fluid limestone lower half space.

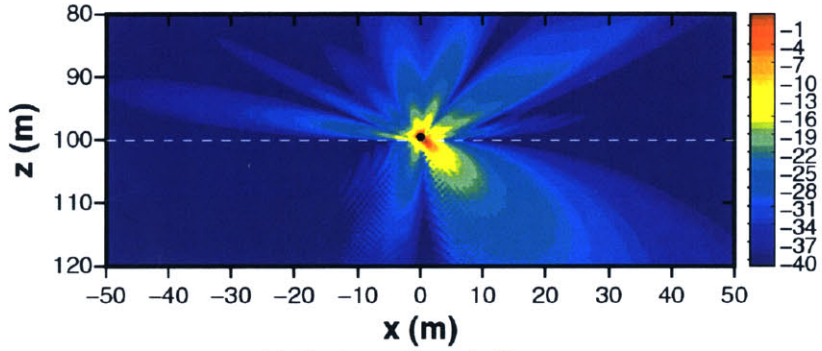

(c) Elastic sand lower half space.

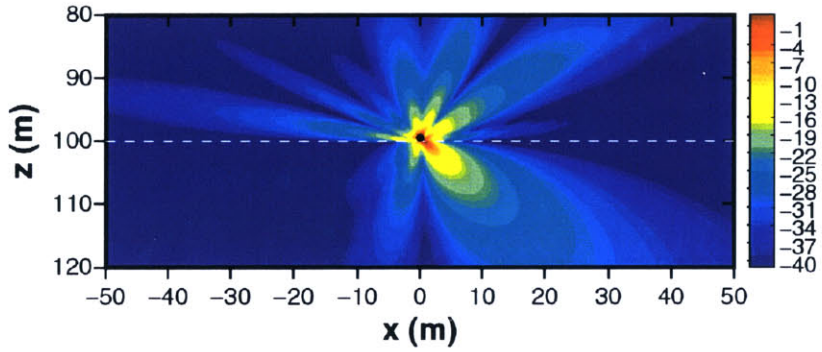

(d) Fluid sand lower half space.

Figure 3-29: In-plane scattered fields caused by a rigid sphere and a compressional plane wave ($f = 3kHz$ and $\theta_i = 45°$).

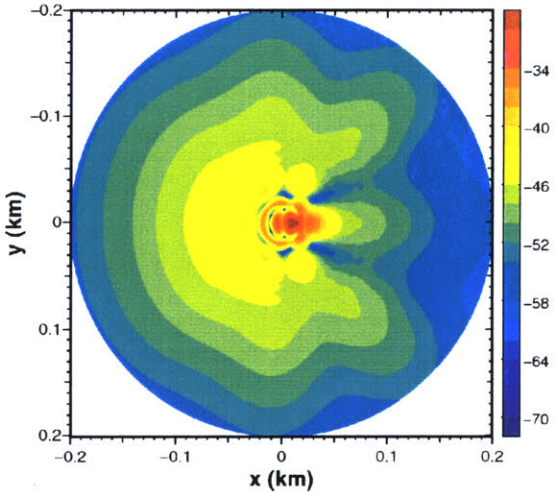

(a) Elastic limestone lower half space.

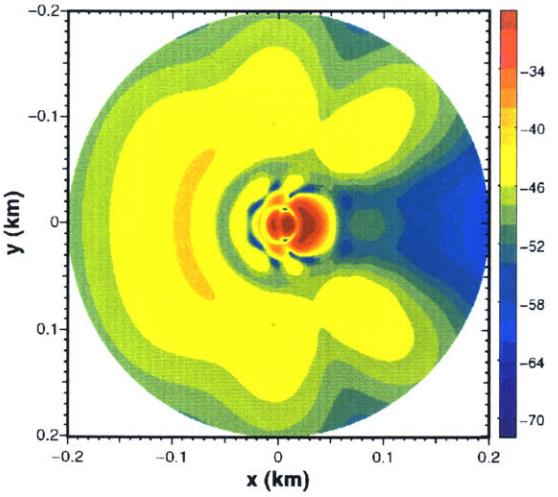

(b) Fluid limestone lower half space.

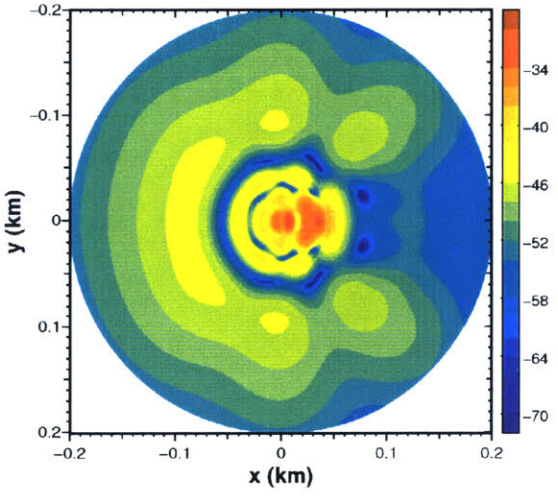

(c) Elastic sand lower half space.

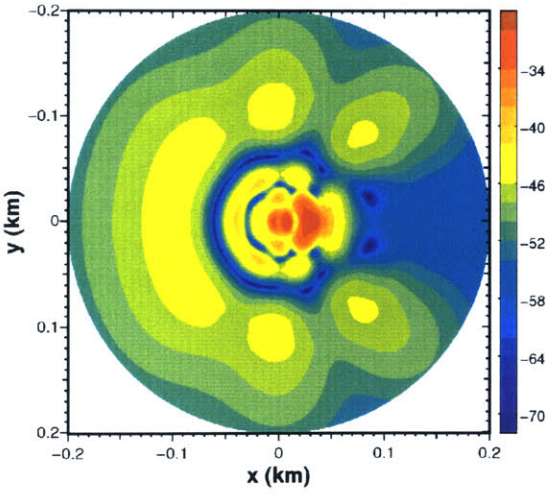

(d) Fluid sand lower half space.

Figure 3-30: Horizontal scattered fields at $20m$ above the interface. The target arget is a rigid sphere with $0.5m$ radius and the incident field is generated by a compressional plane wave ($f = 3kHz$ and $\theta_i = 45°$).

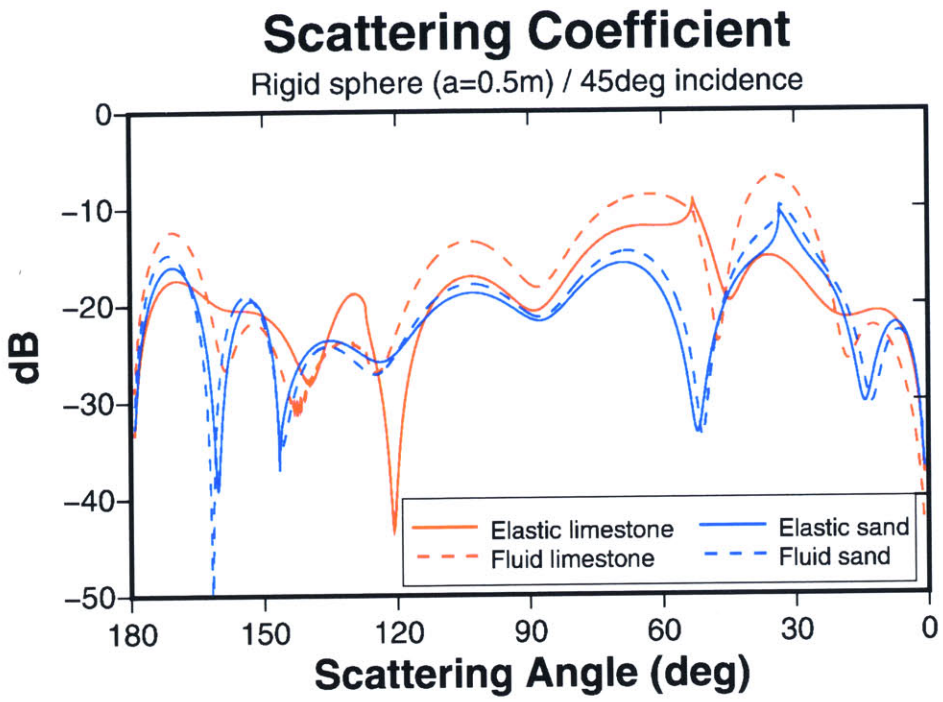

Figure 3-31: In-plane scattering coefficients. Cases of a rigid sphere sitting on different lower half spaces. The incident field is a compressional plane wave ($f = 3kHz$ and $\theta_i = 45°$).

scattering peaks caused by the reflection of main lobes are insignificant. For the case of an elastic limestone half space, the backward and out-of-plane scattering are fairly uniform compared to the fluid limestone case. The comparison between elastic and fluid sand reveals a similar difference found in the case of a shallow grazing incident angle (Figure 3-27(c) and Figure 3-27(d)). Out-of-plane scattering features in the forward direction disappear with the elastic sand case. This is caused by the transmission of forward side lobes into the lower space.

Figure 3-34 compares in-plane scattering coefficients. Elastic and fluid sand cases agree within $3dB$ throughout the entire angular regime. Elastic and fluid limestone also agree well in the vicinity of the forward specular direction. In the angular regime away from the forward specular direction, the elastic limestone case produces a low scattered field due to transmitted shear waves in the lower space.

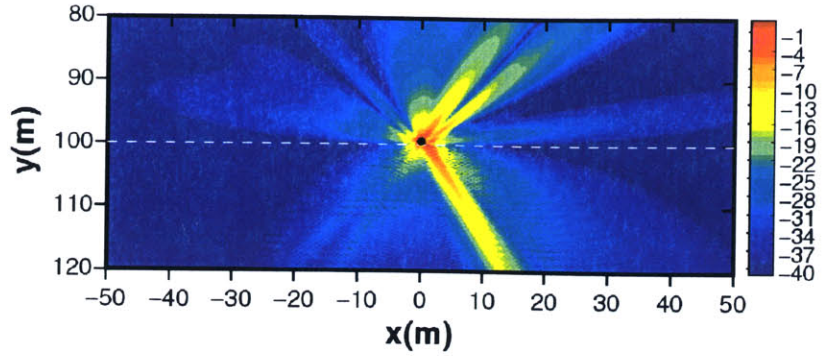

(a) Elastic limestone lower half space.

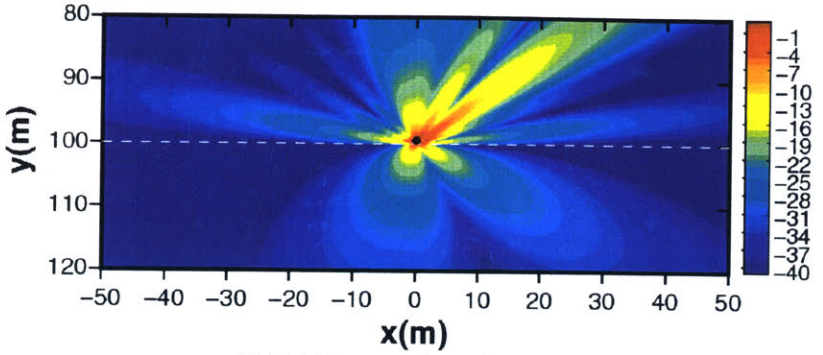

(b) Fluid limestone lower half space.

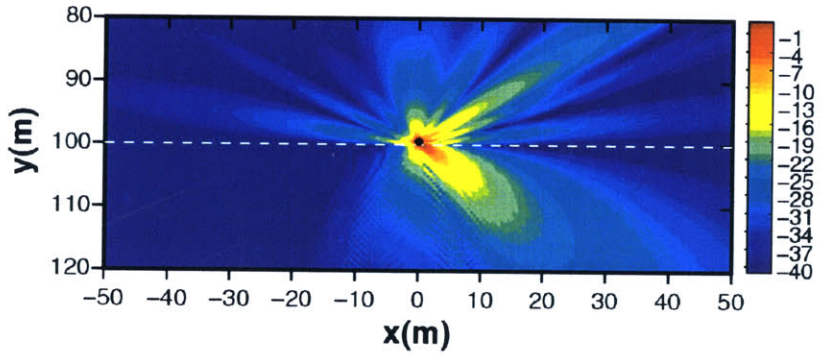

(c) Elastic sand lower half space.

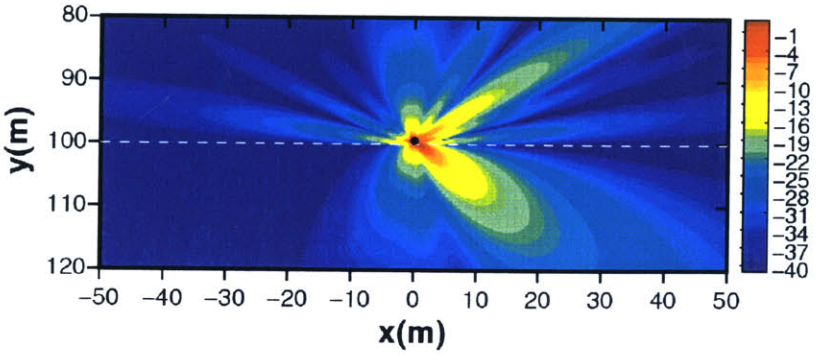

(d) Fluid sand lower half space.

Figure 3-32: In-plane scattered fields caused by a pressure-release sphere and a compressional plane wave ($f = 3kHz$ and $\theta_i = 45°$).

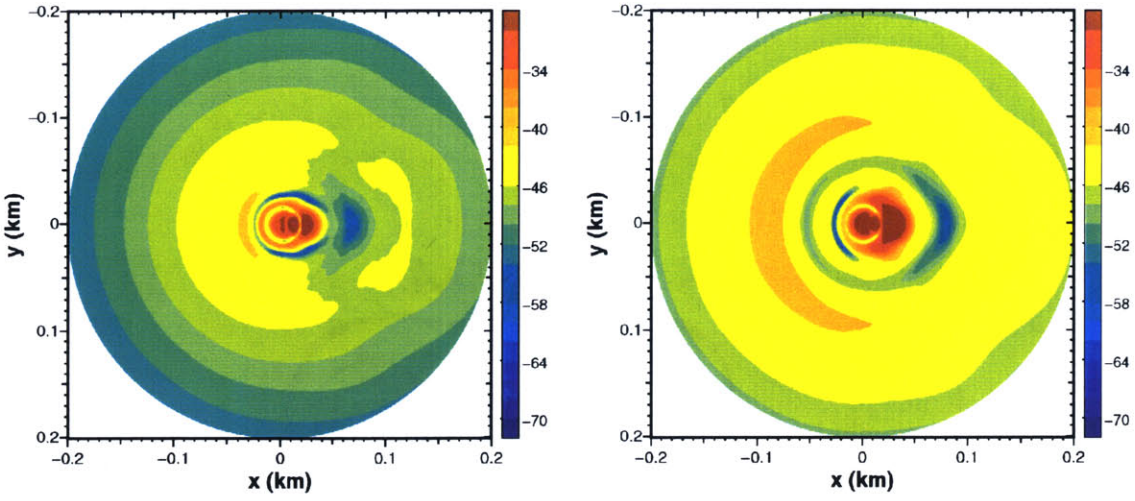

(a) Elastic limestone lower half space.

(b) Fluid limestone lower half space.

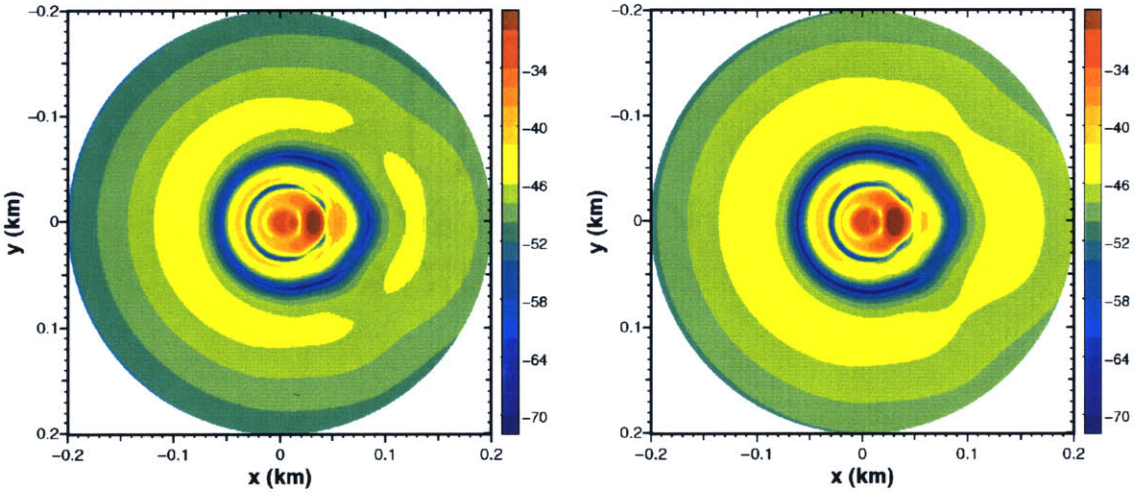

(c) Elastic sand lower half space.

(d) Fluid sand lower half space.

Figure 3-33: Horizontal scattered fields at $20m$ above the interface. The target is a pressure-release sphere with $0.5m$ radius and the incident field is generated by a compressional plane wave ($f = 3kHz$ and $\theta_i = 45°$).

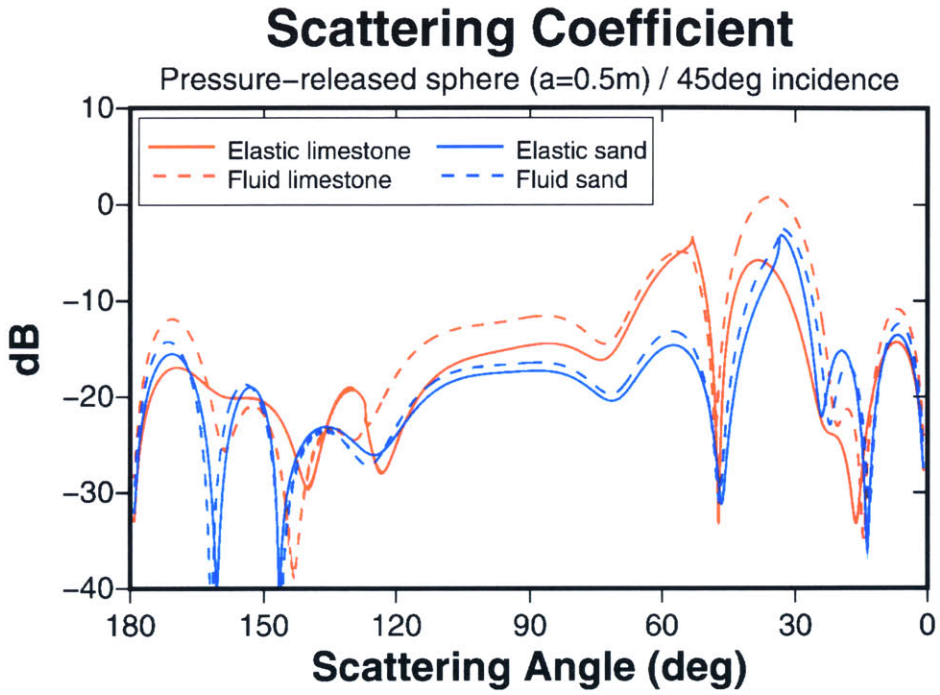

Figure 3-34: In-plane scattering coefficients. Cases of a pressure-release sphere sitting on different lower half spaces. The incident field is a compressional plane wave ($f = 3kHz$ and $\theta_i = 45°$).

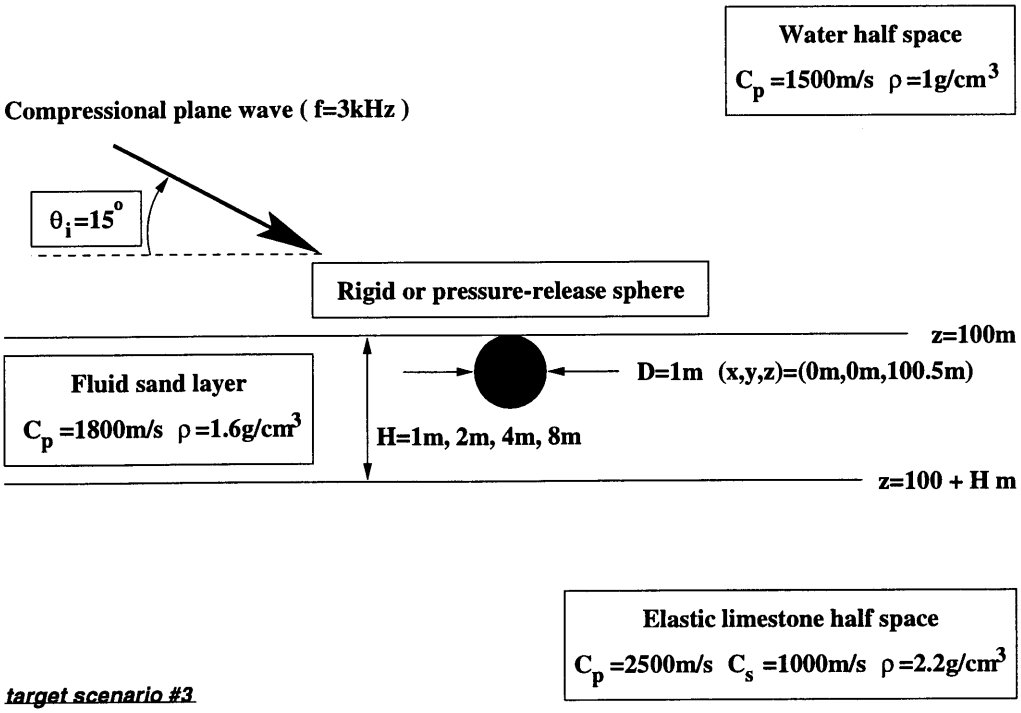

Figure 3-35: Target scattering scenario – a target in a fluid sand sublayer between a water half space and an elastic limestone lower half space. The target is a rigid sphere or a pressure-release sphere ($a = 0.5m$) flush buried below the water - sand interface. The thickness of fluid sand sublayer varies from $H = 1m$ to $H = 8m$. The incident field is a compressional plane wave ($f = 3kHz$ and $\theta_i = 15°$).

3.5.2 Layering Effects

Another possible target scattering scenario is the case of a target flush buried in the sublayer of a bottom structure. Figure 3-35 shows such a target scattering scenario with variable thickness (H) of a sublayer – $1m$, $2m$, $4m$, and $8m$. This configuration is designed to observe the effects of sublayer thickness on the resulting target scattered field. The medium is assumed to consist of water upper half space, fluid sand sublayer with variable thickness, and elastic limestone half space. Since the target scattering model used in this thesis is not applicable to a target surrounded by an elastic medium, only a fluid sublayer is considered. Other than the medium surrounding the target, any combination of elastic and fluid media are allowed. The incident field is a plane wave with $f = 3kHz$ and $\theta_i = 15°$. The target is either a rigid or pressure-release sphere with radius $a = 0.5m$.

Figure 3-36 shows the in-plane scattered fields produced by a rigid sphere flush buried in the sublayer with variable thickness. The incident field from the water half space becomes subsonic in the fluid sand sublayer. Subsonic incidence produces less of a scattered field because of its exponential decaying behavior. Compared to the previous case of a rigid sphere sitting on the half spaces, the scattering level is about $20dB$ lower. Even with the subsonic incidence, the burial depth of the target in the scenario is shallow enough to generate significant scattered fields. The direct scattered field from the target re-radiates to the upper and lower half spaces. Generally, re-radiation to the upper space is dominated by supersonic transmission of scattered energy. By observing four

cases of sublayer thickness, one common feature at the scattered fields is the dominance of the forward scattered field in angles higher than the compressional critical angle ($\theta_c = 33.6°$). The direct scattered wave has three possible re-radiation routes to the lower half space. Since the shear wave speed of elastic limestone is always lower than the phase speed of scattered wave, a portion of the scattered energy is transmitted to the lower half space. The remainder of the scattered energy is either reflected at the interface or transmitted to the lower space according to the scattering angle and compressional critical angle ($\theta_c = 43.9°$ for sand and limestone). The first case of fluid sand sublayer has thickness $H = 1m$. The angle of scattering peak in the elastic limestone half space indicates that the transmitted scattered wave becomes a shear wave. The angle agrees with the transmission angle (49.9°) from water to limestone at incident angle 15°. As the thickness of sublayer increases, this transmitted shear wave disappears. This can be explained by examining the scattered field in the sublayer. As the sublayer thickness increases, the amount of energy blocked by the lower interface increases due to the modal structure of the sand sublayer. It does not block the scattered energy at the upper interface because of the slower compressional phase speed of the water half space. At the lower interface, some portion of scattered energy is reflected due to the faster compressional phase speed of limestone. Consequently, it will be transmitted to the upper half space. The remaining scattered energy leaks to the lower space through lower shear phase speed ($C_s = 1000m/s$) when the scattering angle is steeper than the compressional critical angle ($\theta_c = 43.9°$).

Figure 3-37 shows the corresponding horizontal scattered fields at $20m$ above the water - sand interface. The most noticeable difference are the circular interference patterns. As the thickness increases the number of interference patterns increases. These interference patterns are generated by the modal structure in the sand sublayer. Generally, the number of modes is proportional to the thickness of the waveguide. This rule applies to the scattered field generated by a target flush buried in a sublayer. Another effect of the sublayer is enhancement of the scattered field in both forward and out-of-plane directions. When Figure 3-37(a) ($H = 1m$ case) and Figure 3-37(b) ($H = 2m$ case) are compared, the scattered field in both water columns is noticeably increased by the thicker sublayer. This can also be explained by the existence of a modal structure in the sublayer. When the sublayer thickness is small, only a few modes with shallow grazing angles are allowed ; most of the direct scattered energy escapes to the lower half space, as shown in Figure 3-36(a). The thicker sublayer allows re-radiation of scattered energy in higher modes which enhances the scattered field in the upper space.

Figure 3-38 is the corresponding in-plane scattering coefficient plot. As a reference, the case of a target flush buried in fluid sand half space ($H = \infty$) is presented. When the $H = 1m$ case is compared to other cases of finite sublayers, it does not show oscillation of scattering coefficients. Oscillation would be the evidence of modal structure. This explains the clear dominance of the transmitted shear wave in the lower half space (Figure 3-36(a)). For other sublayers with finite thickness ($H = 2m$, $4m$, and $8m$), the in-plane scattering coefficients fluctuate in region of angles higher than the compressional critical angle between water and sand ($\theta_c = 33.6°$). In the shallow angular regime, for both forward and backward directions, they agree with the in-plane scattering coefficients of fluid sand half space.

The next example (Figure 3-39) uses a pressure-release sphere with $a = 0.5m$ instead of rigid sphere. Other than the target, the scattering configuration is identical to the previous case. Figure 3-39 shows the in-plane scattered fields produced by a pressure-release sphere. As discussed with the previous rigid sphere case, the re-radiation of the direct scattered field is controlled by the thickness of fluid sublayer and consequently its modal structure. Overall, the dominant angular regime in the upper half space is set by the compressional critical angle between water and sand ($\theta_c = 33.6°$). As with the rigid sphere, the $H = 1m$ case produces strong transmitted shear waves

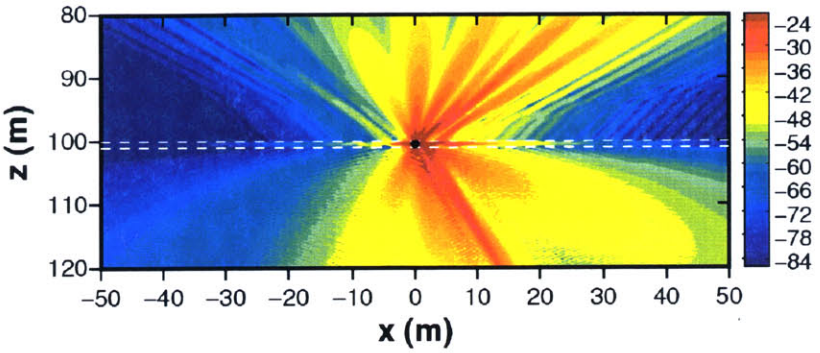

(a) $H = 1m$ case.

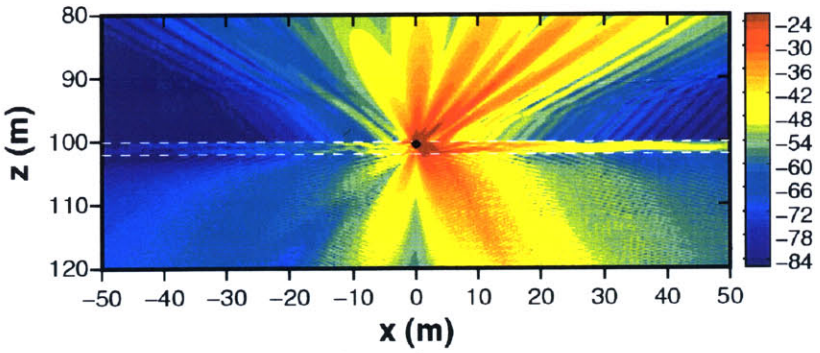

(b) $H = 2m$ case.

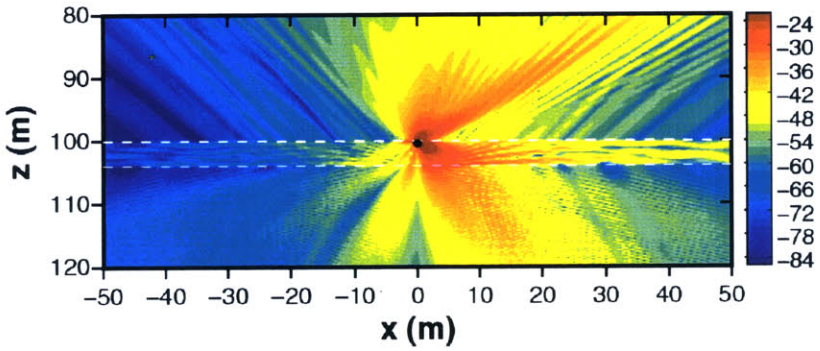

(c) $H = 4m$ case.

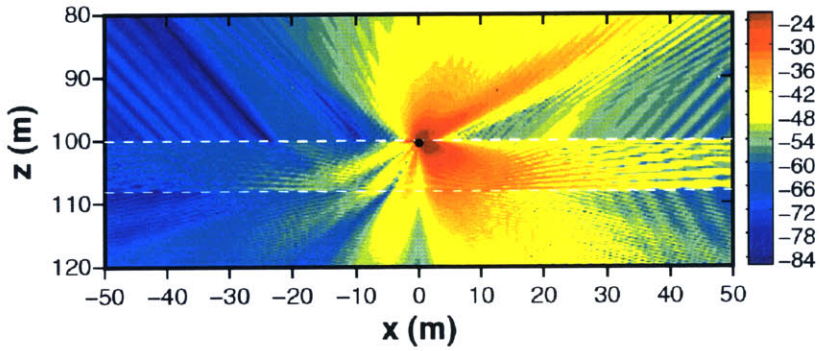

(d) $H = 8m$ case.

Figure 3-36: In-plane scattered fields caused by a rigid sphere. The target is flush buried in the fluid sand sublayers with different layer depths.

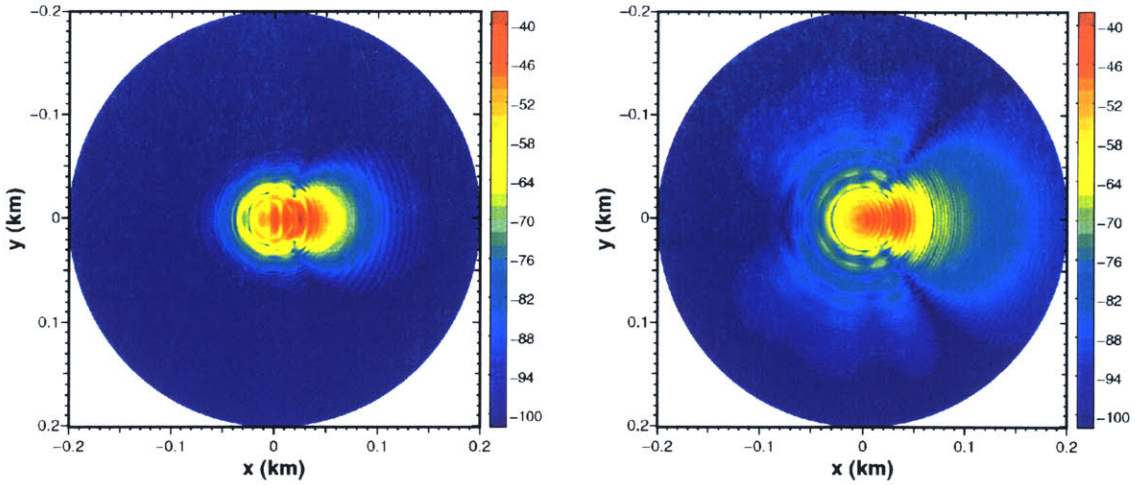

(a) $H = 1m$ case.

(b) $H = 2m$ case.

(c) $H = 4m$ case.

(d) $H = 8m$ case.

Figure 3-37: Horizontal scattered fields at 20m above the upper interface of fluid sand sublayer. The target is a rigid sphere flush buried in the sublayers with different layer depths.

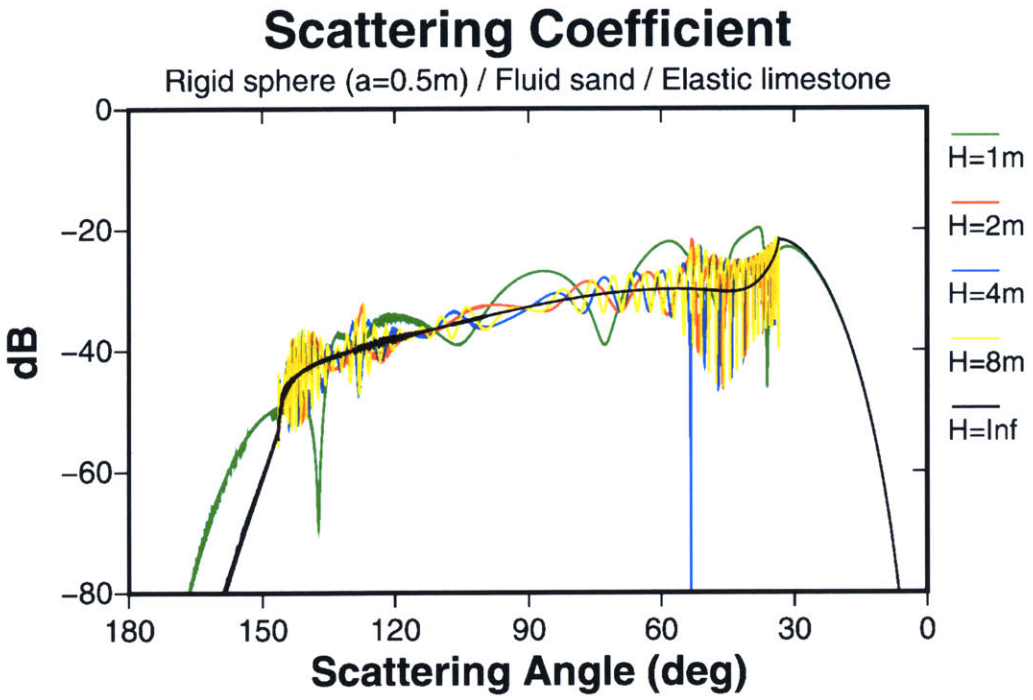

Figure 3-38: In-plane scattering coefficients. Cases of a rigid sphere flush buried in the fluid sand sublayers with different thickness.

in the lower half space. Other cases exhibit similar behavior.

Figure 3-40 shows the corresponding horizontal scattered fields at $20m$ above the interface. Again, the results confirms the scattering trends and their physical interpretation discussed for the case of a rigid sphere. As the layer thickness increases, modal structure and enhancement of both the forward and out-of-plane scattered fields are clearly observed. When the grazing angle is steeper than the compressional critical angle (i.e. center portion of contours), the scattered fields across different configurations are similar.

Figure 3-41 shows the comparison of in-plane scattering coefficients by different sublayers. As a reference, the in-plane scattering coefficient for the case of a fluid sand half space is included. The plot shows trends similar to the case of a rigid sphere. One major difference can be found with the case of $H = 1m$. Deviation of the in-plane scattering coefficient for $H = 1m$ case from that of fluid sand half space is not significant, while the deviation is noticeable for the case of rigid sphere. A possible physical reason should be found in the scattering beampatterns. In this frequency regime, the pressure-release sphere produces a more uniform beampattern in angular space, while the rigid sphere of same size has a series of local minima in its angular beampattern. Because of the difference in the beampatterns, the pressure-release sphere cases generate less fluctuation in the in-plane scattering coefficients.

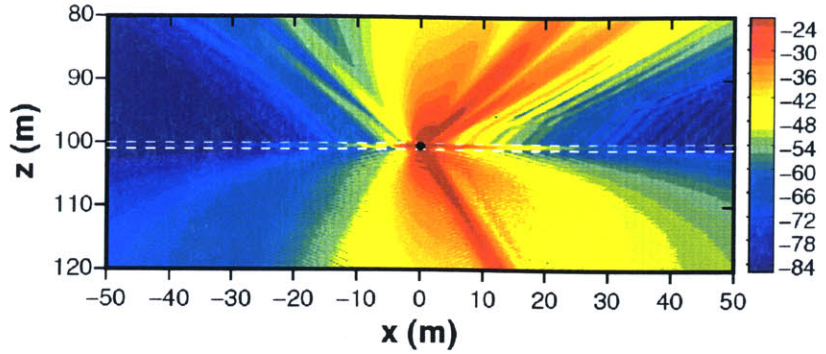

(a) $H = 1m$ case.

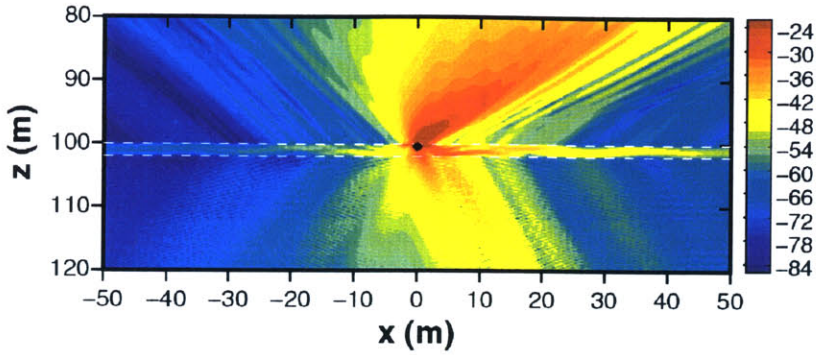

(b) $H = 2m$ case.

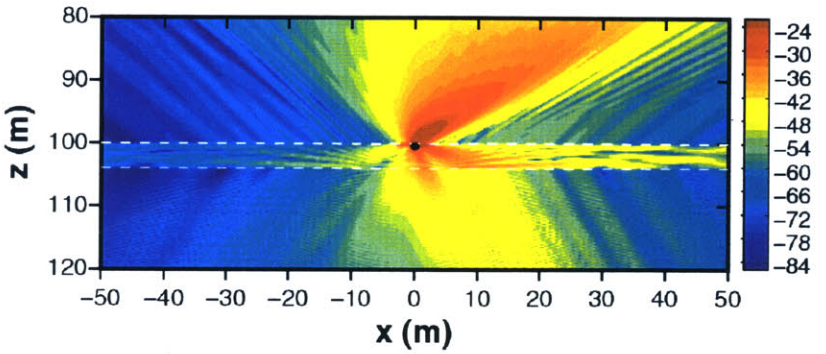

(c) $H = 4m$ case.

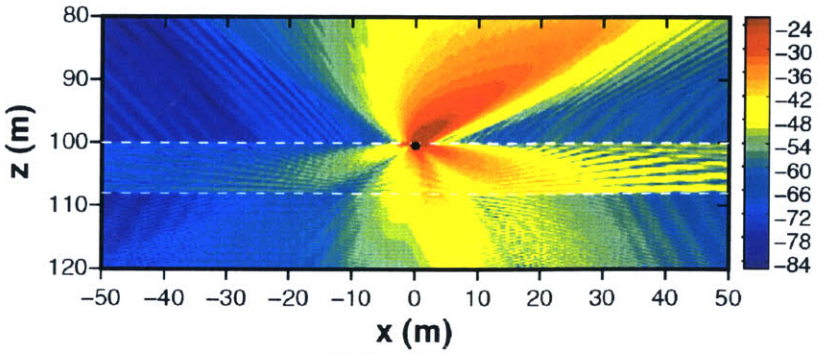

(d) $H = 8m$ case.

Figure 3-39: In-plane scattered fields caused by a pressure-release sphere. The target is flush buried in the fluid sand sublayers with different layer depths.

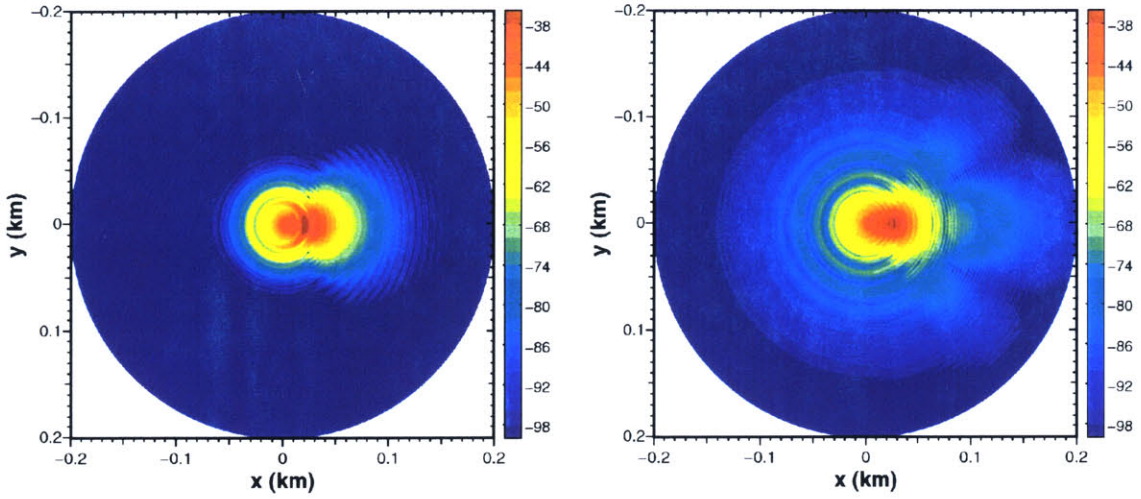

(a) $H = 1m$ case.

(b) $H = 2m$ case.

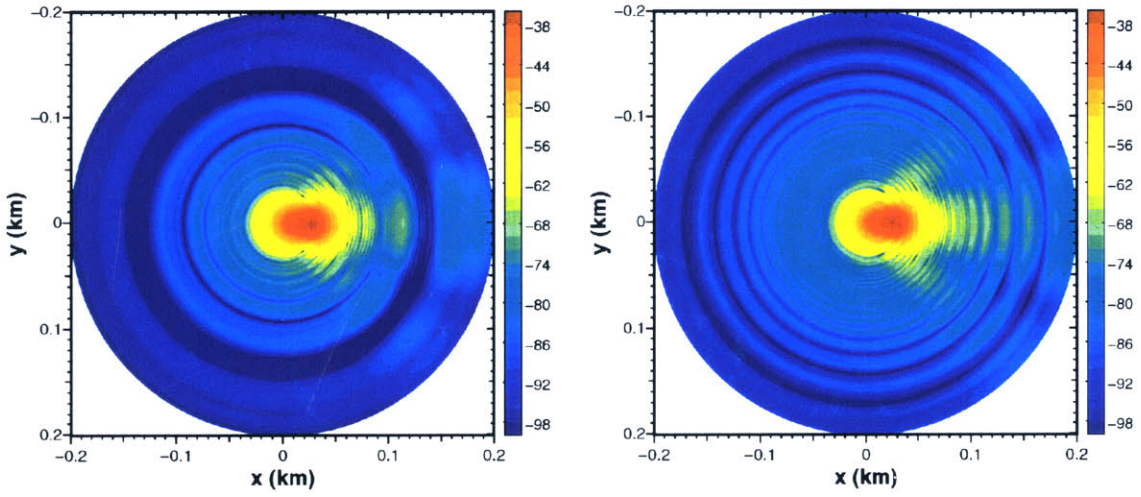

(c) $H = 4m$ case.

(d) $H = 8m$ case.

Figure 3-40: Horizontal scattered fields at 20m above the upper interface of fluid sand sublayer. The target is a pressure-release sphere flush buried in the sublayers with different layer depths.

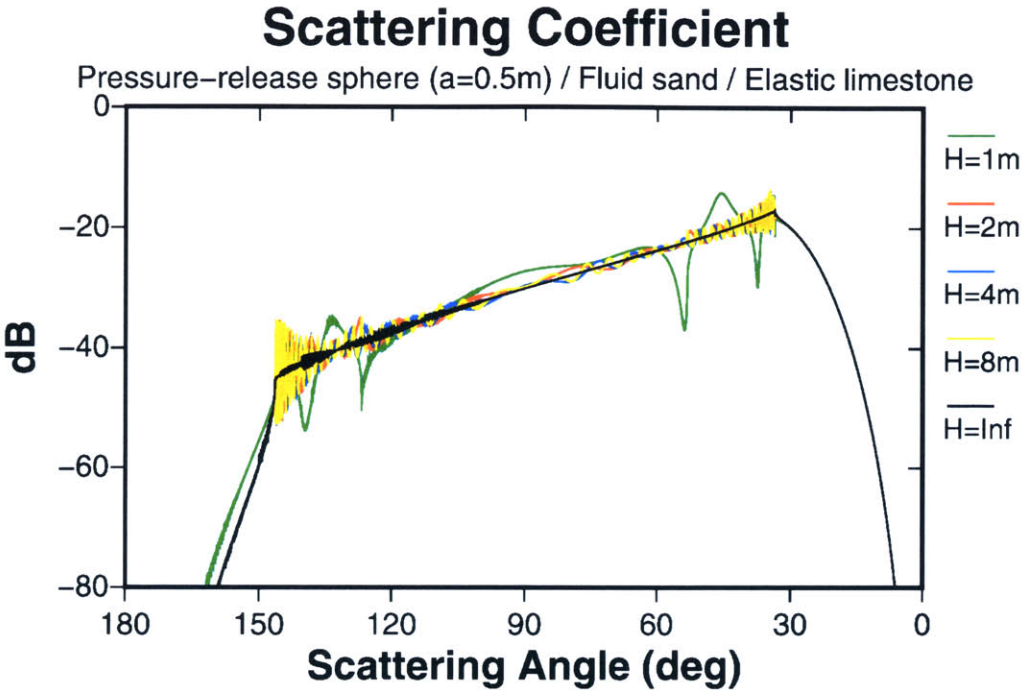

Figure 3-41: In-plane scattering coefficients. Cases of a pressure-release sphere flush buried in the fluid sand sublayers with different thickness.

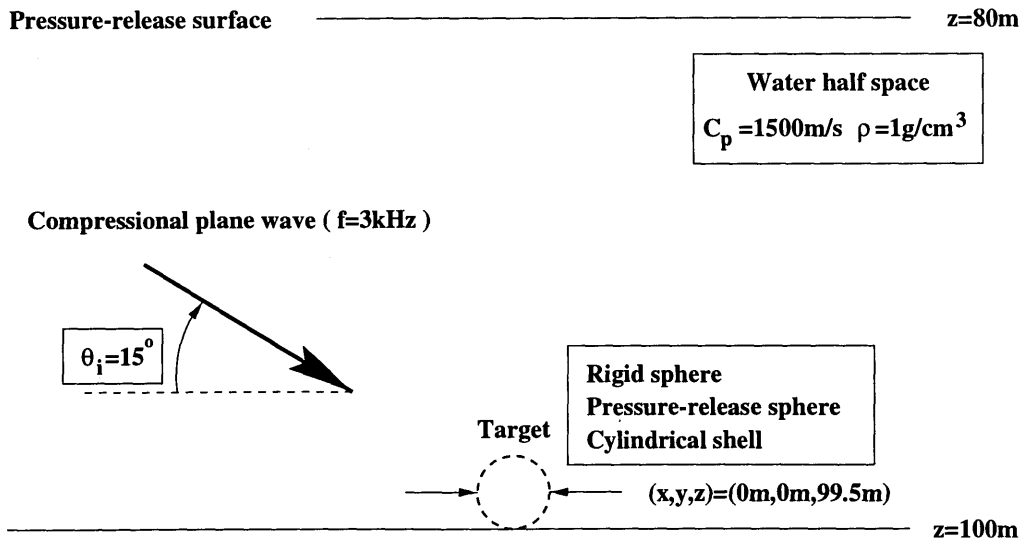

Lower half space	C_p (m/s)	C_s (m/s)	ρ (g/cm^3)
Elastic limestone	2500	1000	2.2
Elastic sand	1800	600	1.6

target scenario #4

Figure 3-42: Target scattering scenario – A target is sitting on the interface between water column and lower half space. Water column has a pressure-release surface at $20m$ above the interface. A rigid sphere, a pressure-release sphere, a broad-sided cylindrical shell ($\theta_{sk} = 90°$), and a slanted cylindrical shell are used as a target. The incident field is a compressional plane wave in the water column ($f = 3kHz$ and $\theta_i = 15°$). The lower half space is an elastic limestone or sand.

3.5.3 Waveguide Effects

Another important case of target scattering is the case of a target within the waveguide. When a target is located inside the waveguide, the resulting scattered field follows the physics of the waveguide. Figure 3-42 shows such a target scattering scenario, composed of $20m$ water column with an elastic lower half space (limestone or sand). The incident field is a plane wave with $f = 3kHz$ and $\theta_i = 15°$. There are four kinds of targets used for this scenario – a rigid sphere ($a = 0.5m$), a pressure-release sphere ($a = 0.5m$), a broad-sided cylindrical steel shell ($L = 2m$, $a = 0.5m$, $t = 5cm$, and $\theta_{sk} = 90°$), and a slanted cylindrical steel shell ($L = 2m$, $a = 0.5m$, $t = 5cm$, and $\theta_{sk} = 45°$). The targets are sitting on the interface between the water column and the lower half space. The existence of a waveguide provides the series of preferred angles (i.e. modes) in the water column. The incident field and the resulting scattered field are affected by this modal structure.

Figure 3-43 shows the in-plane scattered fields produced by various targets with an elastic limestone lower half space. Both rigid and pressure-release spheres (Figure 3-43(a) and Figure 3-43(b)) in the water column produce in-plane scattered fields similar to those produced by rigid and pressure-release spheres in the water half space (Figure 3-23(a) and Figure 3-26(a)). Transmission of direct scattered field into the lower space is dominated by the shear wave in limestone. In the

water column, the scattered fields exhibit complicated interference patterns made by reflections from the pressure-release surface. Despite the complexity of interference patterns in the time harmonic solution (i.e. single frequency solution), there is a possibility these interference patterns may be resolved by a space-time domain solution. Similar scattering behavior to the scattering sphere is exhibited (with the exception of the actual scattered beampattern) in cases where one is scattered from a cylindrical shell. The broad-sided cylindrical shell (Figure 3-43(c)) produces extremely complex interference patterns due to its strong in-plane scattered field throughout the entire angular regime. The backward scattered wave in the lower space is caused by a side lobe of target beampattern. The slanted cylindrical shell (Figure 3-43(d)) has a low level backward scattered field because the slanted shell produces a strong scattered field in the forward direction at a bistatic angle of $\theta = 90°$.

Figure 3-44 shows the corresponding horizontal scattered fields at 10m below the pressure-release surface. All four cases clearly show the circular interference patterns which correspond to the modal structure of water column. One noticeable scattering feature is found in the case of the slanted cylindrical shell. Out-of-plane scattering at $\theta = 90°$ is dominant. This feature exists in the free space target beampattern. It interacts with the modal structure and produces an oscillating scattered field of relatively high level near $\theta = 90°$. Other target cases also shows severe interaction of scattered fields within the waveguide.

Figure 3-45 shows another example of target scattering in a waveguide. This case is identical to the previous one except the lower half space is elastic sand. Compared to the case of an elastic limestone half space, the elastic sand transmits less scattered energy into the lower space via shear waves. Instead, the reflected scattered wave in the waveguide is relatively stronger than the elastic limestone case. The modal interference patterns also exist, and they distort the scattered fields in the water column.

Figure 3-46 shows the corresponding horizontal scattered fields. Overall trends are similar to the case of an elastic limestone half space. A noticeable difference between the limestone and sand cases is the amount of out-of-plane scattered energy in the upper space. When the cases of broad-sided cylindrical shells (Figure 3-46(c) and Figure 3-44(c)) are compared with each other, the elastic sand produces more scattered energy in the out-of-plane direction. The elastic limestone half space converts more scattered energy to shear waves in the lower space and this process reduces the reflection of scattered waves originating from the side lobes of the target beampattern.

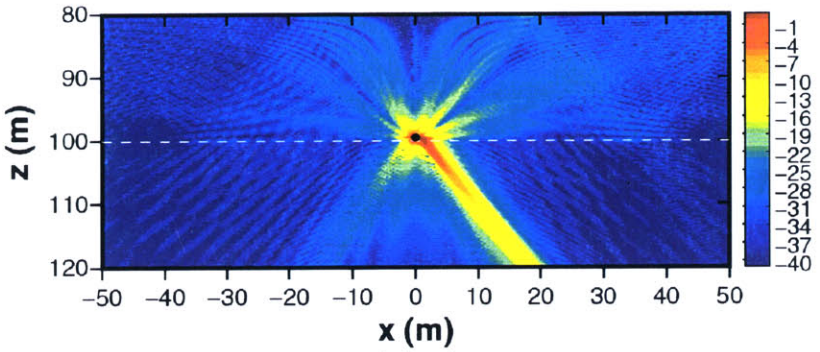

(a) Rigid sphere.

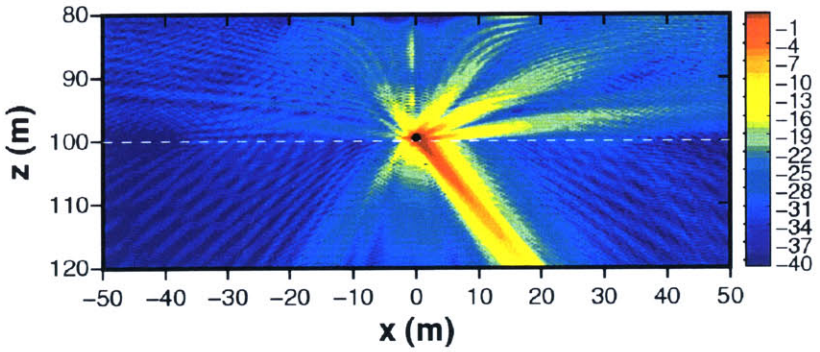

(b) Pressure-release sphere.

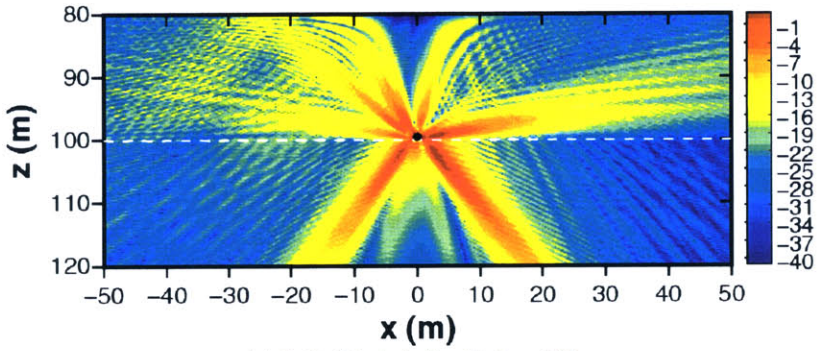

(c) Cylindrical shell with $\theta_{sk} = 90°$.

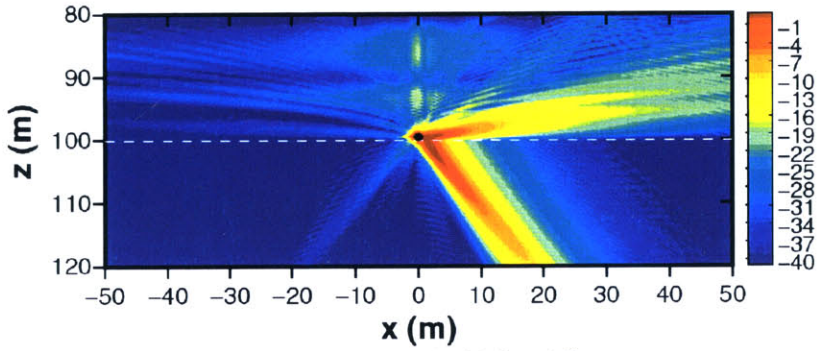

(d) Cylindrical shell with $\theta_{sk} = 45°$.

Figure 3-43: In-plane scattered fields – targets in a $20m$ waveguide over an elastic limestone half space.

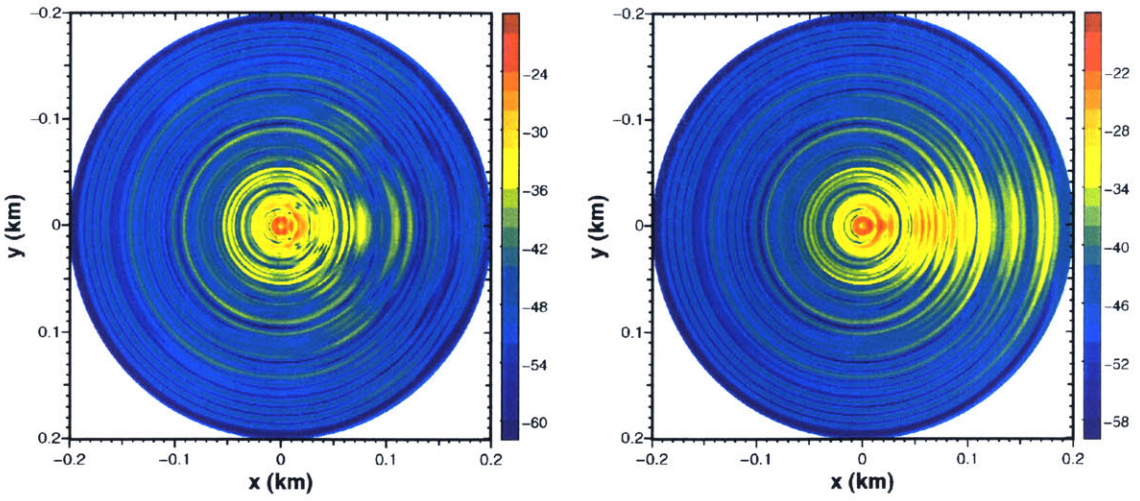

(a) Rigid sphere.

(b) Pressure-release sphere.

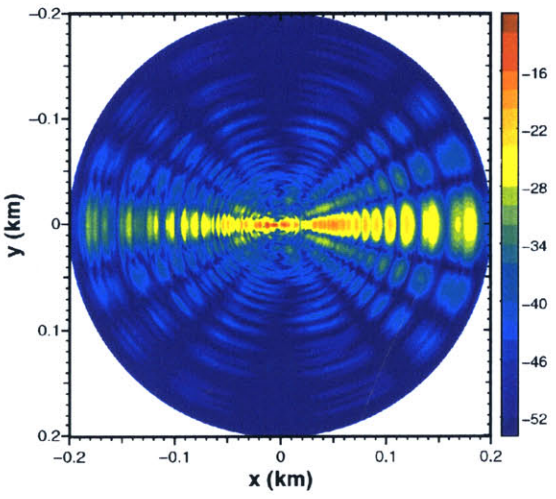

(c) Cylindrical shell with $\theta_{sk} = 90°$.

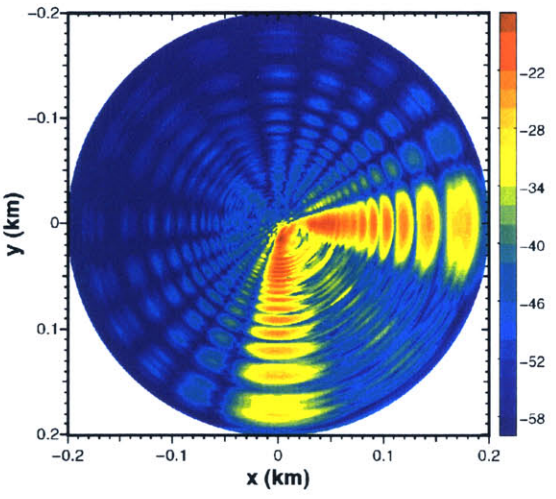

(d) Cylindrical shell with $\theta_{sk} = 45°$.

Figure 3-44: Horizontal scattered fields at $10m$ above the interface – targets in a $20m$ waveguide over an elastic limestone half space.

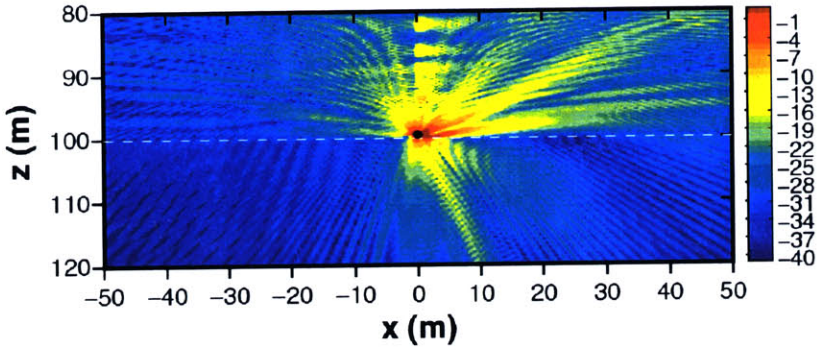

(a) Rigid sphere.

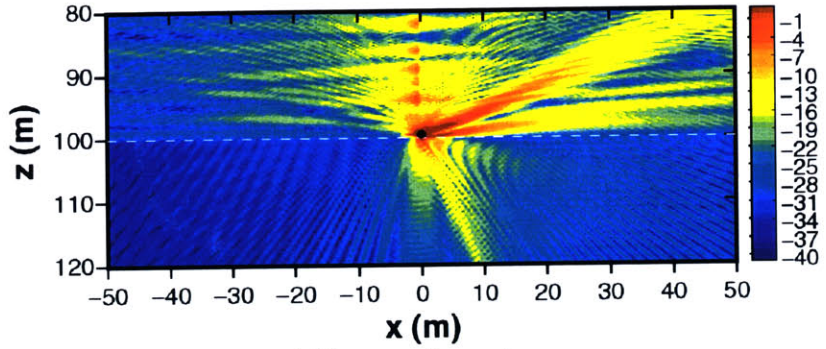

(b) Pressure-release sphere.

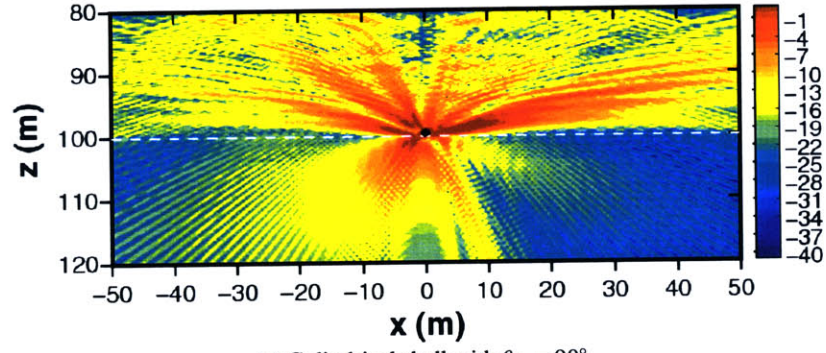

(c) Cylindrical shell with $\theta_{sk} = 90°$.

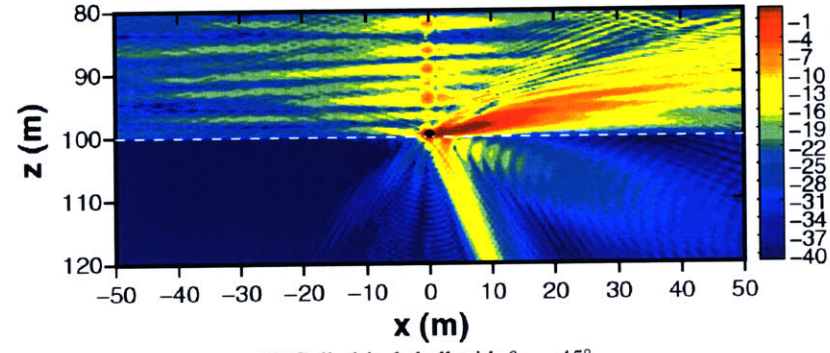

(d) Cylindrical shell with $\theta_{sk} = 45°$.

Figure 3-45: In-plane scattered fields – targets in a $20m$ waveguide over an elastic sand half space.

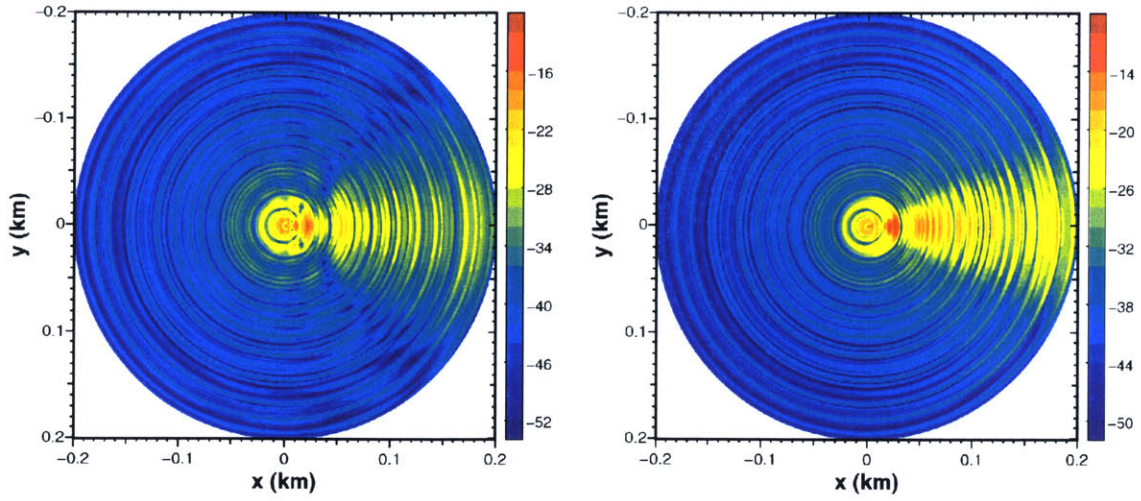

(a) Rigid sphere.

(b) Pressure-release sphere.

(c) Cylindrical shell with $\theta_{sk} = 90°$.

(d) Cylindrical shell with $\theta_{sk} = 45°$.

Figure 3-46: Horizontal scattered fields at $10m$ above the interface – targets in a $20m$ waveguide over an elastic sand half space.

3.6 Effects of Target Configuration

Besides medium configuration, the target field is greatly affected by target configurations such as orientation, burial depth, and etc. This section will present several target scattering cases involving different target configurations – anisotropy of target orientation and burial depth of target.

3.6.1 Anisotropy Effects

The term 'anisotropy' is used to indicate that the target has directionality in solid angle space. Any non-spherical targets have asymmetric geometries with respect to a solid angle. In this thesis, an anisotropy target is modeled by an elastic cylindrical shell with finite aperture. Since a cylindrical shell can be rotated about its radial axis, or tilted with respect to its axial direction, there are two orientation degrees of freedom. In this thesis, only the rotation of a cylindrical shell is considered. Figure 3-47 shows the scattering scenario. Three anisotropic angles – $\theta_{sk} = 0°$, $45°$, and $90°$ – are used for the numerical simulation. The target has $2m$ length, $0.5m$ radius, and $5cm$ thickness and its material properties are $C_p = 5200m/s$, $\rho = 7.8g/cm^3$, and $\nu = 0.333$. The target is sitting on an interface between the water half space and lower space. The lower space is an elastic limestone or sand half space. The incident field is a plane wave with $f = 3kHz$ and $\theta_i = 15°$. Generally, maximum scattering is expected in the forward and backward directions when the shell's axis is perpendicular to the incident direction.

Figure 3-48 shows the in-plane scattered fields caused by cylindrical shells with different anisotropic angles over the elastic limestone half space. As expected, the forward and backward scattered fields are maximized at anisotropic angle $\theta_{sk} = 90°$ (Figure 3-48). The case of $\theta_{sk} = 0°$ shows the relatively weak backward scattered field. The shear conversion of scattered energy in the lower half space is clearly observed in all three cases at the same angle as the shear transmission angle of the incident wave.

Figure 3-49 shows the corresponding horizontal scattered fields. The horizontal scattered field plot clearly shows the preferred directions of scattered energy in the upper space. The distribution of scattered energy is quite sensitive to the anisotropic angle of the cylindrical shell. Generally, two scattering peaks are observed in the incident direction and the specular direction of incident wave with respect to shell's longitudinal axis. The details of the target beampattern, such as number of axial modes and angular beam widths of the main lobe and side lobes, are determined by the free space scattering function and incident field.

Figure 3-50 shows the comparison of scattering coefficients by cylindrical shells with three anisotropic angles. As mentioned earlier, the forward and backward scattering maxima are expected with the broad-sided cylindrical shell ($\theta_{sk} = 90°$). When the longitudinal axis of the cylindrical shell is aligned with the incident direction, the scattered field becomes low because the excitations of axial modes are reduced by the shallow local incident angle with respect to the longitudinal axis of the shell. The slanted cylindrical shell ($\theta_{sk} = 45°$) produces a forward scattered field with an almost equal strength as in the case of the broad-sided cylindrical shell.

The next case is identical to the previous, except the lower half space is elastic sand instead of elastic limestone. Figure 3-51 shows the in-plane scattered fields produced by three configurations of cylindrical shell. In all cases, strong shear conversion of the scattered field in the lower space is observed. Compressional conversion of the scattered energy is weakly observed at the forward shallow angle. The case of a broad-sided shell produces a strong backward scattered field in the upper and lower half spaces. When compared to the previous limestone case, the forward scattered fields are stronger due to less scattered energy transmitted to the lower half space.

Figure 3-52 shows the corresponding horizontal scattered fields. Overall, the horizontal fields

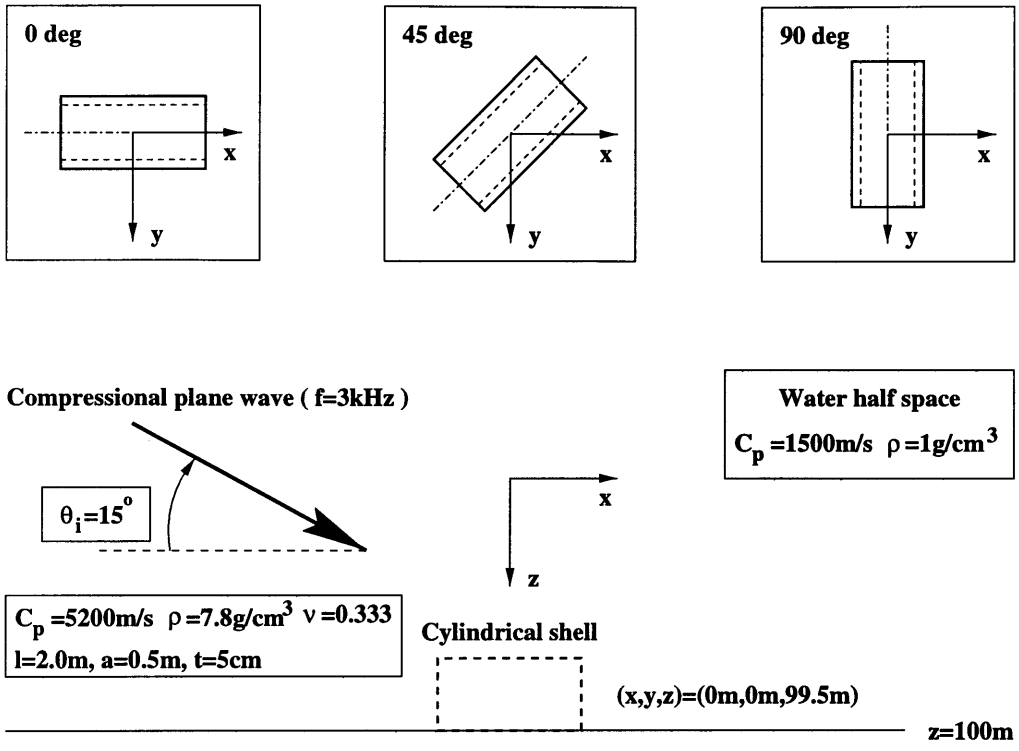

Lower half space	C_p (m/s)	C_s (m/s)	ρ (g/cm^3)
Elastic limestone	2500	1000	2.2
Elastic sand	1800	600	1.6

target scenario #5

Figure 3-47: Target scattering scenario – a cylindrical shell target is sitting on the interface between two half spaces. Orientation of target is varying with respect to the direction of incidence. The medium consists of a water upper half space and an elastic lower half space. The incident field is a compressional plane wave ($f = 3kHz$ and $\theta_i = 15°$).

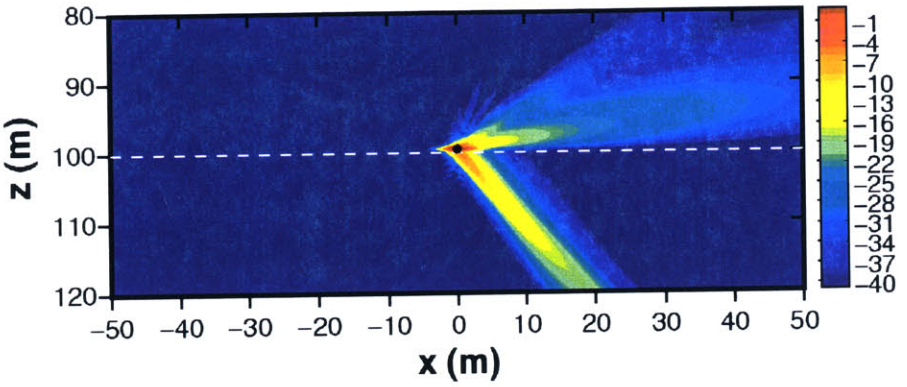

(a) $\theta_{sk} = 0°$ case.

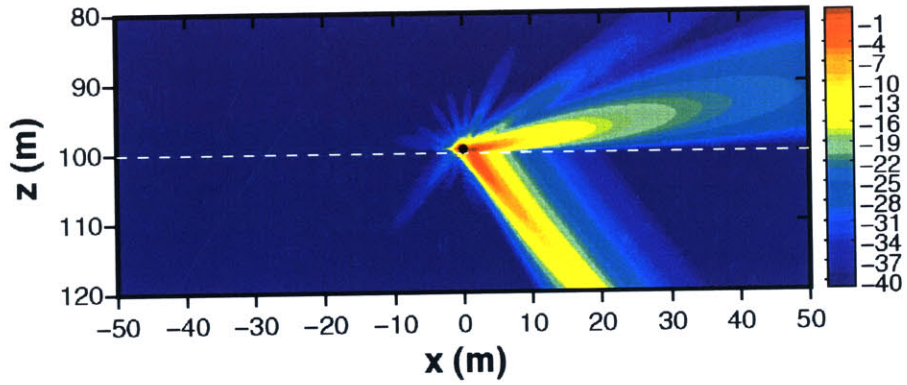

(b) $\theta_{sk} = 45°$ case.

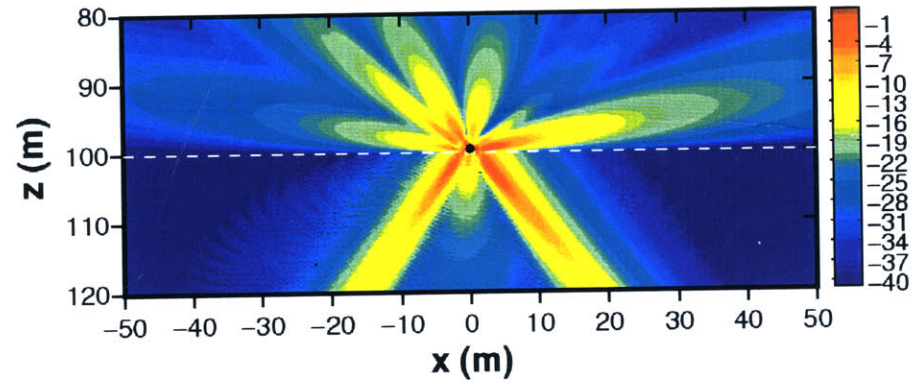

(c) $\theta_{sk} = 90°$ case.

Figure 3-48: In-plane scattered fields caused by a cylindrical shell over an elastic limestone half space. The incident field is a compressional plane wave ($f = 3kHz$ and $\theta_i = 15°$).

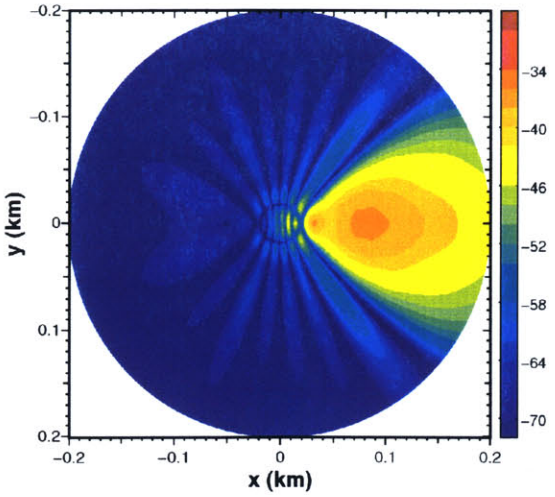

(a) $\theta_{sk} = 0°$ case.

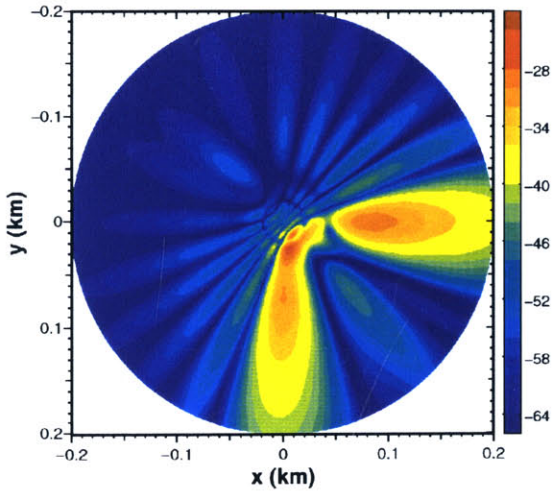

(b) $\theta_{sk} = 45°$ case.

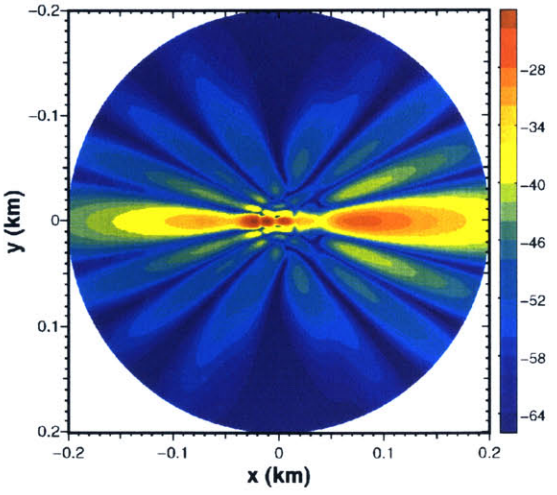

(c) $\theta_{sk} = 90°$ case.

Figure 3-49: Horizontal scattered fields at $20m$ above the interface. The lower half space is elastic limestone. The incident field is a compressional plane wave ($f = 3kHz$ and $\theta_i = 15°$). The cylindrical shell with $\theta_{sk} = 0°$ is aligned with the direction of incidence while the shell with $\theta_{sk} = 90°$ is perpendicular to the incidence.

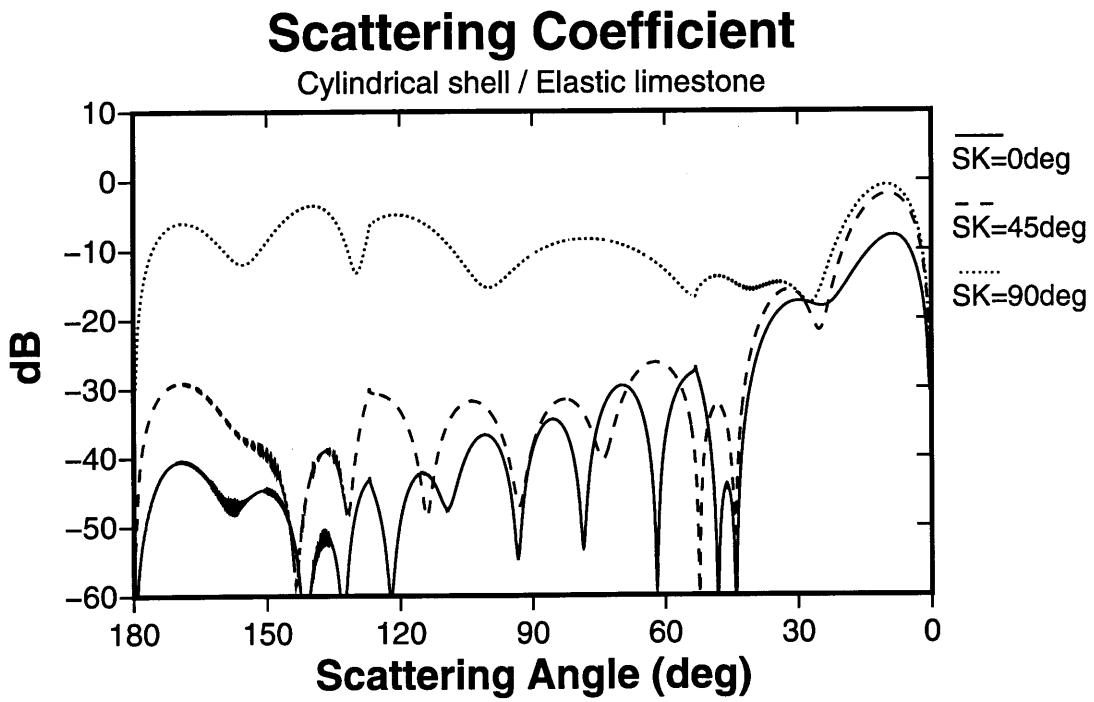

Figure 3-50: In-plane scattering coefficients. Case of a cylindrical shell over an elastic limestone half space.

of a cylindrical shell over elastic sand are similar to those of the elastic limestone cases. The axial modes of cylindrical shells are clearly observable as is the scattering in the specular direction (with respect to the longitudinal axis of the shell). One noticeable difference in the elastic sand lower space is the high scattering level in both the forward and specular directions. This is due to its low transmission of scattered energy into the lower space.

Figure 3-53 shows a comparison of scattering coefficients across different orientations of a cylindrical shell. Compared to the elastic limestone case, the forward scattering level is approximately $4dB$ higher. The slanted cylindrical shell exhibits similar forward scattering levels when the scattering angle is shallower than the compressional critical angle ($\theta_s = 33.6°$). When the scattering angle is greater than the compressional critical angle, the broad-sided cylindrical shell has relatively high backward scattering levels.

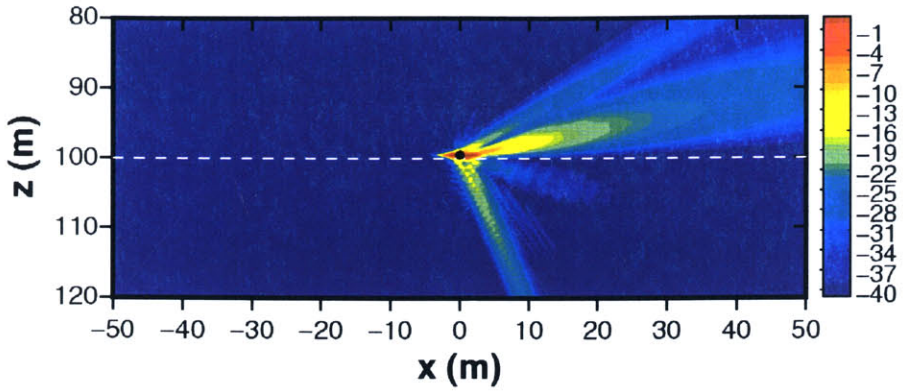

(a) $\theta_{sk} = 0°$ case.

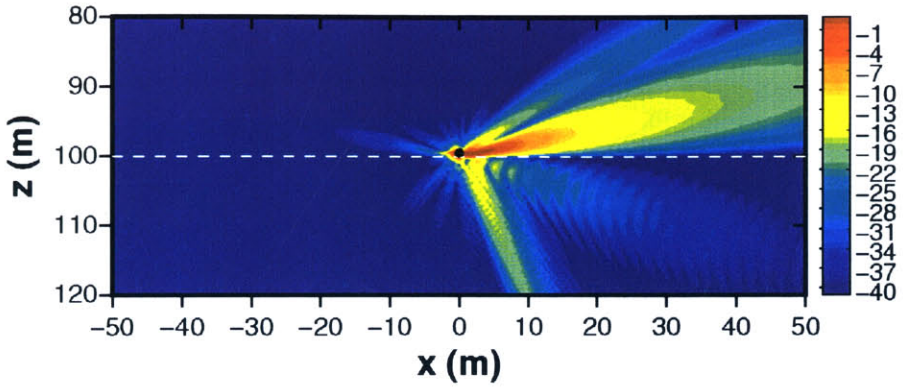

(b) $\theta_{sk} = 45°$ case.

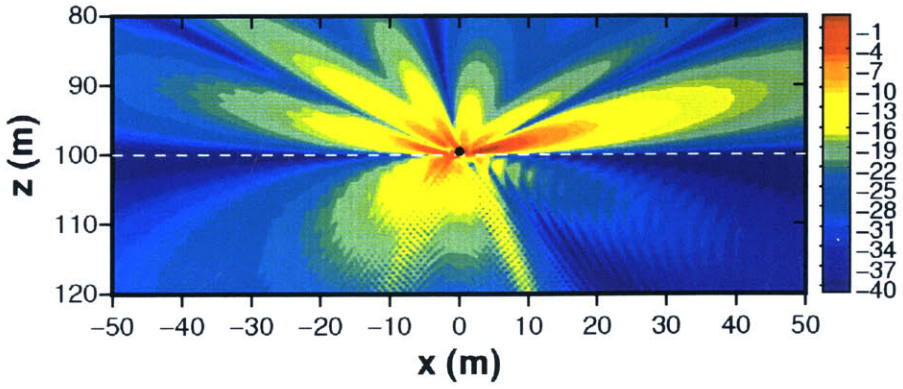

(c) $\theta_{sk} = 90°$ case.

Figure 3-51: In-plane scattered fields caused by a cylindrical shell over an elastic sand half space. The incident field is a compressional plane wave ($f = 3kHz$ and $\theta_i = 15°$).

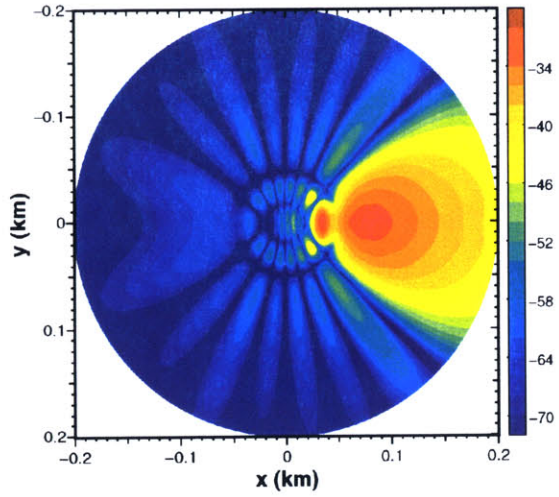

(a) $\theta_{sk} = 0°$ case.

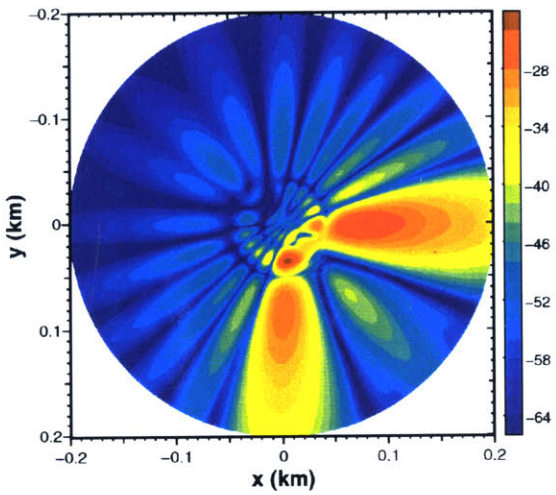

(b) $\theta_{sk} = 45°$ case.

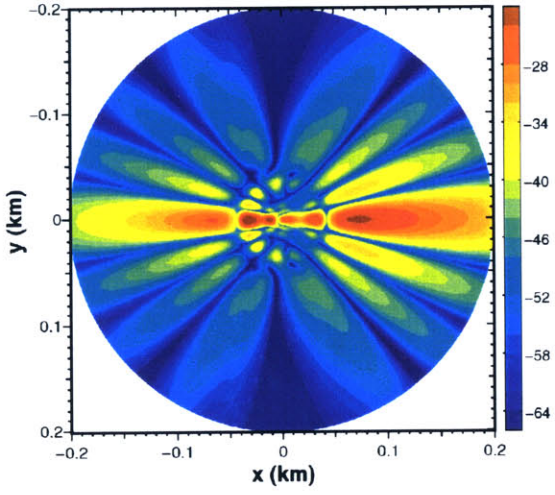

(c) $\theta_{sk} = 90°$ case.

Figure 3-52: Horizontal scattered fields at $20m$ above the interface. Case of a cylindrical shell over an elastic sand half space. The incident field is a compressional plane wave ($f = 3kHz$ and $\theta_i = 15°$).

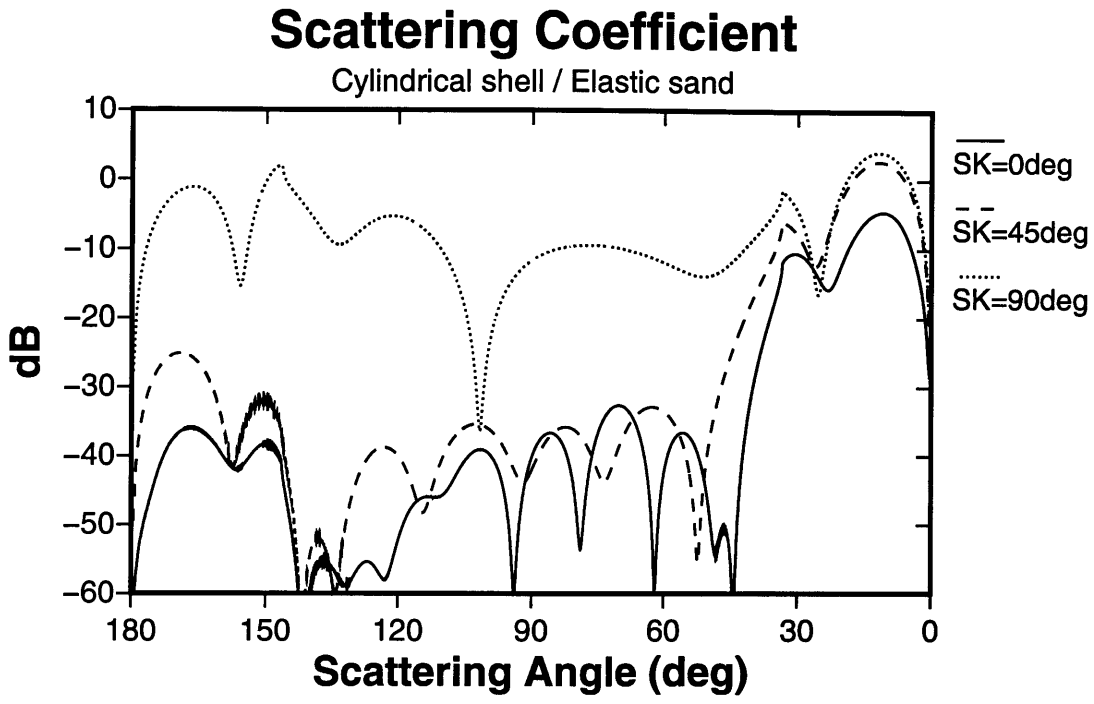

Figure 3-53: In-plane scattering coefficients. Case of a cylindrical shell over an elastic sand half space.

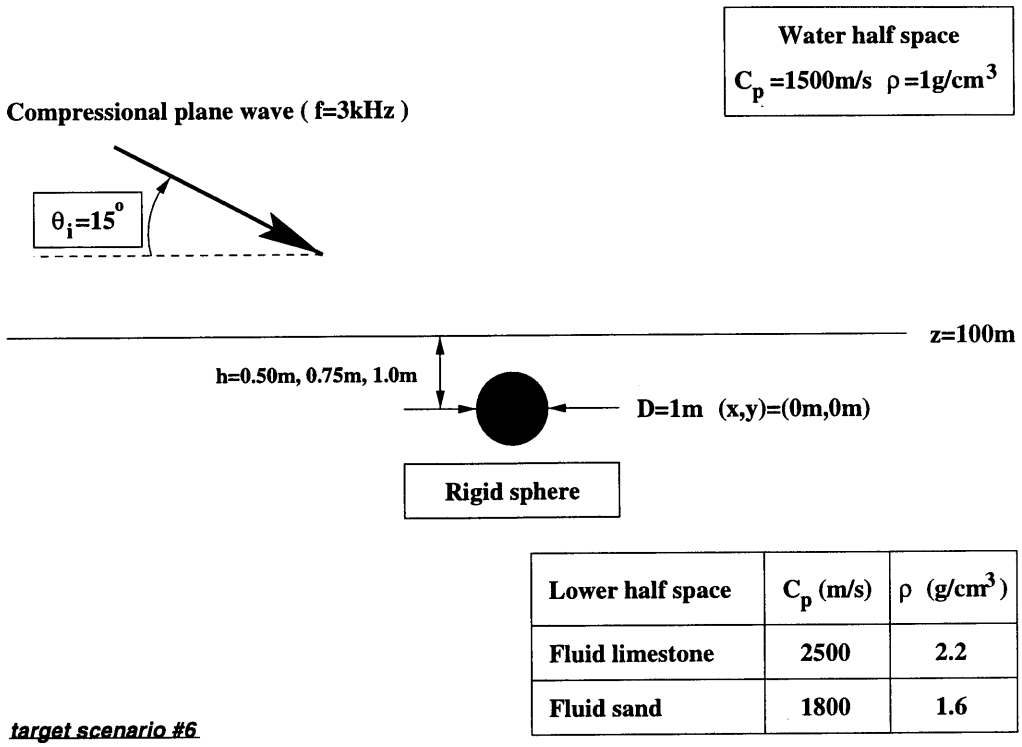

Lower half space	C_p (m/s)	ρ (g/cm^3)
Fluid limestone	2500	2.2
Fluid sand	1800	1.6

Figure 3-54: Target scattering scenario – a rigid sphere buried in a fluid lower half space. The target depth varies from $h = 0.5m$ to $h = 1.0m$ below the interface. The lower half space is a fluid sand or limestone. The incident field is generated by a compressional plane wave ($f = 3kHz$ and $\theta_i = 15°$) in the water half space.

3.6.2 Burial Depth Effects

The following four examples demonstrate the effects of target burial depth on the resulting scattered field. When a target is buried in a lower space, the incident field to the target is reduced by the transmission coefficient, and the incident angle changes by Snell's law. When the incident phase speed is subsonic, the incident field decays exponentially as the target burial depth increases. Figure 3-54 is the target scattering scenario where a rigid sphere ($a = 0.5m$) is buried at the different depths ($h = 0.5m$, $0.75m$, and $1.0m$). The incident field is a plane wave with $f = 3kHz$ and $\theta_i = 15°$. The lower half space is modeled by either fluid limestone or fluid sand.

The first example uses fluid limestone as the lower half space. Figure 3-55 shows the in-plane scattered fields caused by the target at various burial depths (h). As the burial depth increases, the scattered field decreases by approximately $18dB$ per $0.25m$. Even with the fast decay of scattered field, the scattering patterns are very similar for all cases. Since the incident field is subsonic in the lower space, the incident energy exciting the target decays exponentially. The resulting scattered field is supersonic to the upper medium and consequently the transmission of scattered energy is not reduced by the burial depth. The transmission and reflection of scattered fields are controlled by the same mechanism regardless of depth. Therefore, target burial depth affects the scattered field mostly by scaling its amplitude.

Figure 3-56 shows the corresponding horizontal scattered fields. These fields decay as the burial depth increases. One noticeable difference (other than exponential decaying behavior) is

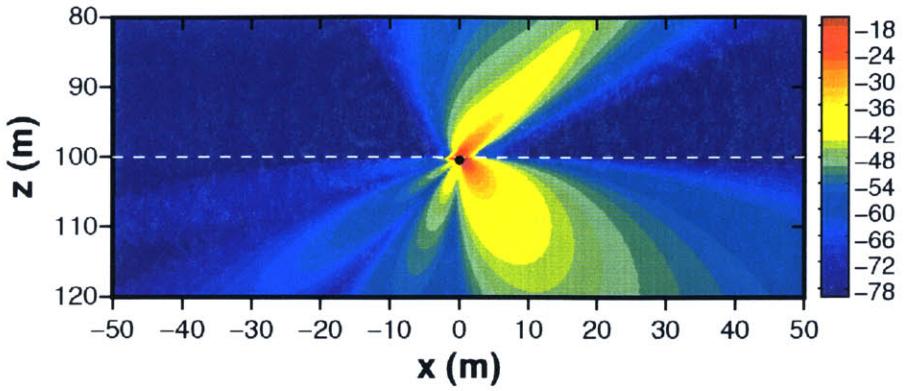

(a) $h = 0.5m$ case.

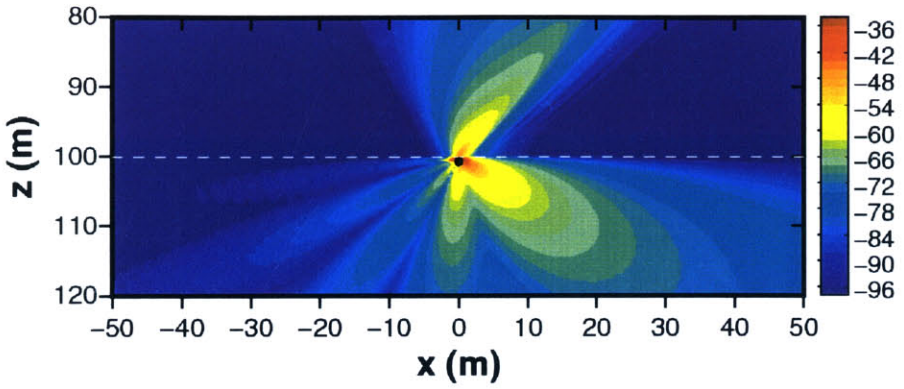

(b) $h = 0.75m$ case.

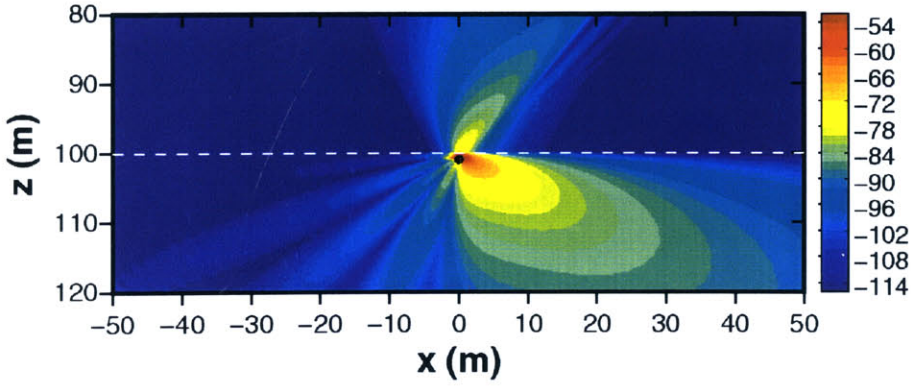

(c) $h = 1.0m$ case.

Figure 3-55: In-plane scattered fields caused by a rigid sphere buried at different depths in the fluid limestone lower half space. The incident field is a compressional plane wave ($f = 3kHz$ and $\theta_i = 15°$).

the low grazing angle scattered wave in the forward direction. As the burial depth increases, the relative strength of the forward scattered wave at the shallow grazing angle increases. The backward scattered fields are quite similar to each other except for their relative amplitudes. This subtle difference was not found in the previous in-plane scattered field plots (Figure 3-55). This is caused by the change in the interference pattern as the center of target moves away from the interface. When the distance between the interface and target is very close, the resulting field is similar to one caused by a source near a pressure-release surface; this is known as the Lloyd mirror effect [16]. Figure 3-57 demonstrates Lloyd mirror effects produced by sources with different depths in a fluid limestone lower half space. The Lloyd mirror effect originally assumes the interface is a pressure-release surface. A similar effect can be observed in cases of penetrable boundaries, such as the interface between water and fluid limestone. In the plots, the similarity between pressure-release surface and penetrable interface is shown. As the source depth increases, the resulting field has additional interference patterns and the angular spread of the field becomes wider. The farthest null range (r_1) of these interference patterns produced by pressure-release interface is determined as follows [16] :

$$r_1 = \frac{kzz_0}{\pi}, \tag{3.22}$$

where k is medium wavenumber, z is receiver depth from the interface, and z_0 is source depth from the interface. As the source depth increases, the null space moves farther away. Consequently, the angle of first interference pattern (i.e. shallowest one) comes closer to the horizontal direction. In the case of water and fluid limestone half spaces, the field in the water space is also affected by the interference patterns in the lower space. As the source depth increases, the angular spectrum in water half space becomes wider, resulting in a significant field at shallow grazing angles. Since the target scattering contribution is represented as a point source with a specific beampattern, this hypothesis can be applied to explain how the forward scattered field in the upper space increases as the target burial depth increases.

Figure 3-58 shows the comparison of scattering strengths by rigid spheres at different burial depths. Their scattering coefficients trends are similar. Again, this confirms the primary effect of target burial depth is field amplitude scaling.

The next scattering example is identical to the previous example except the lower half space is fluid sand instead of fluid limestone. Figure 3-59 shows the in-plane scattered fields by a rigid sphere buried at different depths. Unlike the fluid limestone case, a noticeable difference other than scaling can be seen. The scattering angle in forward direction of the lower half space becomes shallower (or closer to the horizontal direction). The same hypothesis used for the previous case might explain this scattering trend. As the separation of depth increases, the Lloyd mirror effect is reduced and consequently the field in the horizontal direction increases.

Figure 3-60 shows the corresponding horizontal scattered fields. As with the previous case, the relative forward scattered field at a shallow grazing angle is enhanced as the burial depth increases. Compared to the case of fluid limestone (Figure 3-56), the scattering level is high and the angular regime of dominant scattering feature increases.

Figure 3-61 compares in-plane scattering coefficients among rigid spheres with different burial depths in a fluid sand half space. The overall trend is similar and the decaying rate is about $14dB$ per $0.25m$. When compared to the limestone case, the peak scattering level is about $6dB$ higher and the scattering coefficients are uniform between backward and forward compressional critical angles ($\theta_c = 33.6°$). Also, when the scattering grazing angle is shallower than the forward critical angle, the rate decreases as the burial depth increases. This agrees with the horizontal scattered

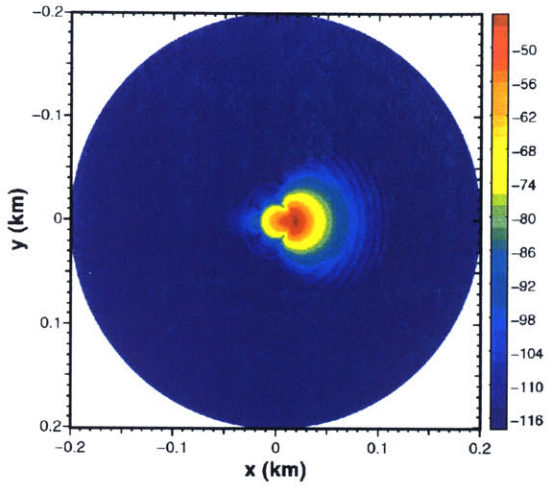

(a) $d = 0.50m$ case.

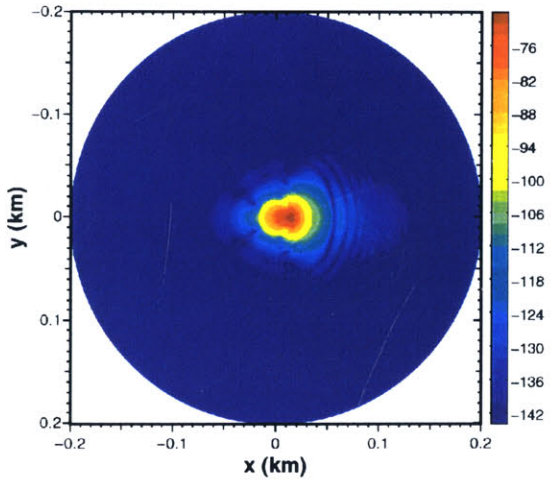

(b) $d = 0.75m$ case.

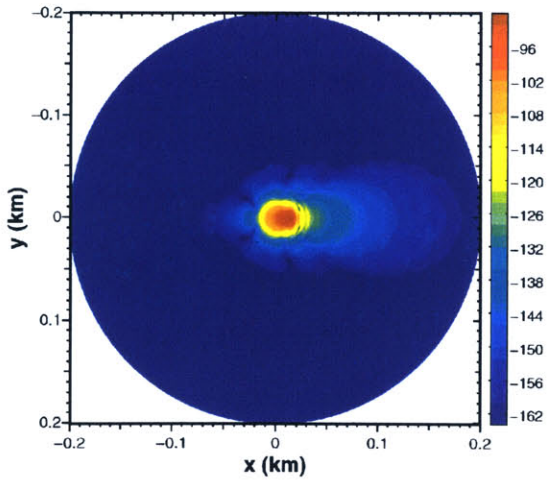

(c) $d = 1.0m$ case.

Figure 3-56: Horizontal scattered fields at $20m$ above the interface. The target is a rigid sphere buried in the fluid limestone half space at different depths.

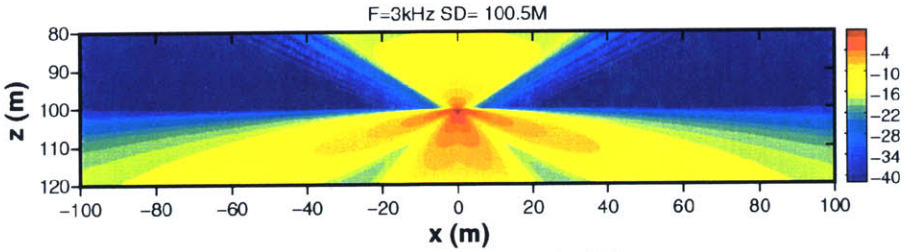

(a) water – fluid limestone : $d = 0.5m$

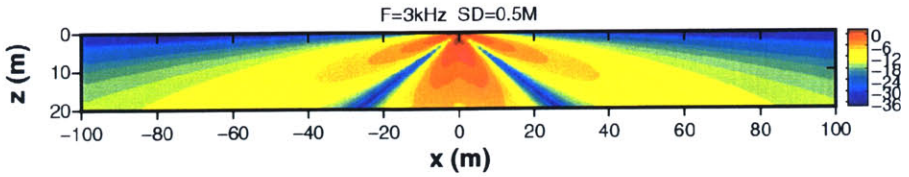

(b) vacuum – fluid limestone : $d = 0.5m$

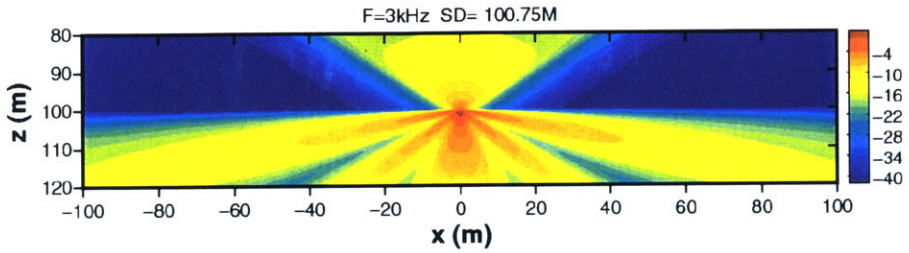

(c) water – fluid limestone : $d = 0.75m$

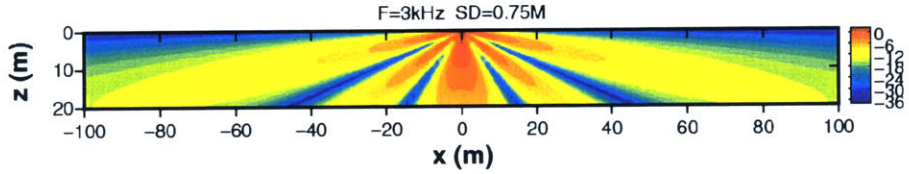

(d) vacuum – fluid limestone : $d = 0.75m$

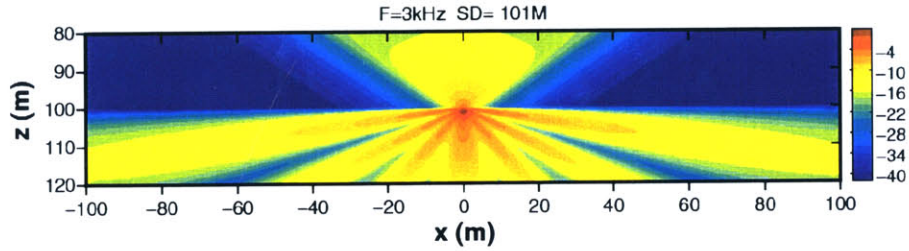

(e) water – fluid limestone : $d = 1.0m$

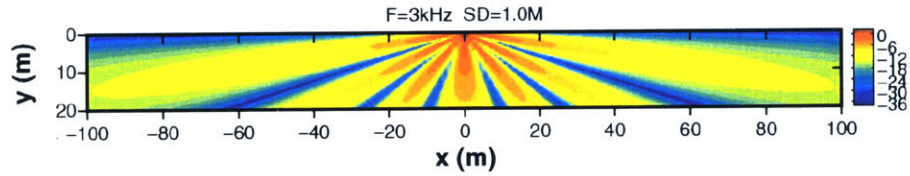

(f) vacuum – fluid limestone : $d = 1.0m$

Figure 3-57: Lloyd mirror effects caused by different source depths between the water and fluid limestone half spaces. As references, cases of vacuum - fluid limestone half spaces are shown. d is the source (or burial) depth from the interface.

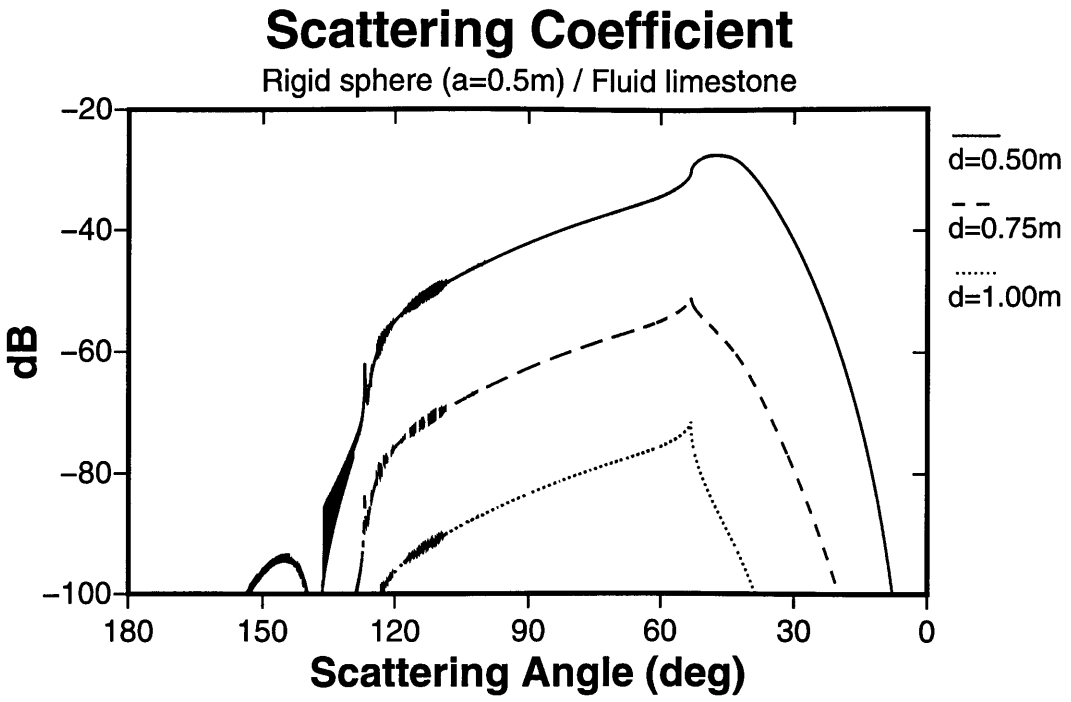

Figure 3-58: In-plane scattering coefficients. Cases of a rigid sphere buried in the fluid limestone half space.

field trends.

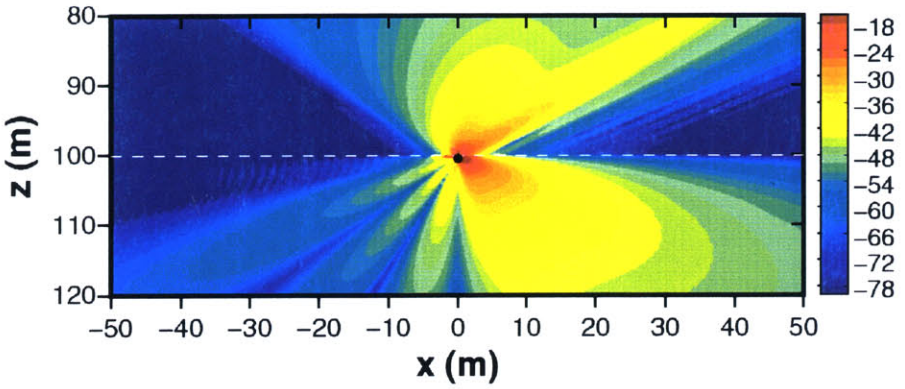

(a) $d = 0.5m$ case.

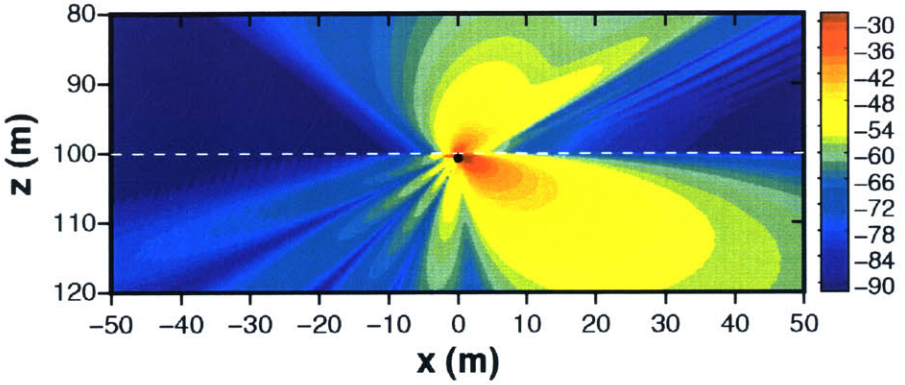

(b) $d = 0.75m$ case.

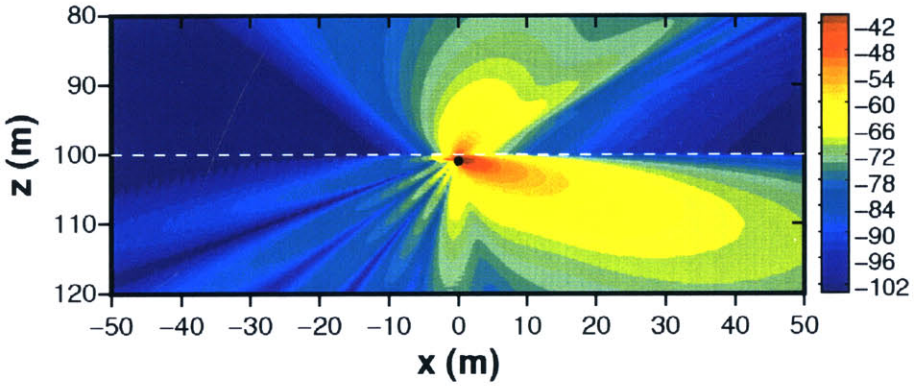

(c) $d = 1.0m$ case.

Figure 3-59: In-plane scattered fields caused by a rigid sphere buried in the fluid sand half space at different depths. The incident field is a compressional plane wave ($f = 3kHz$ and $\theta_i = 15°$).

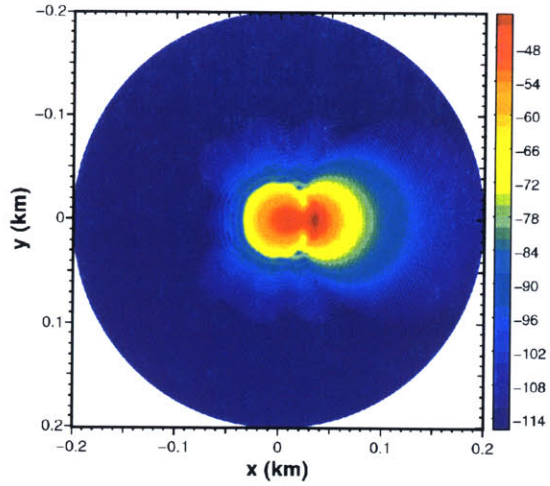

(a) $d = 0.50m$ case.

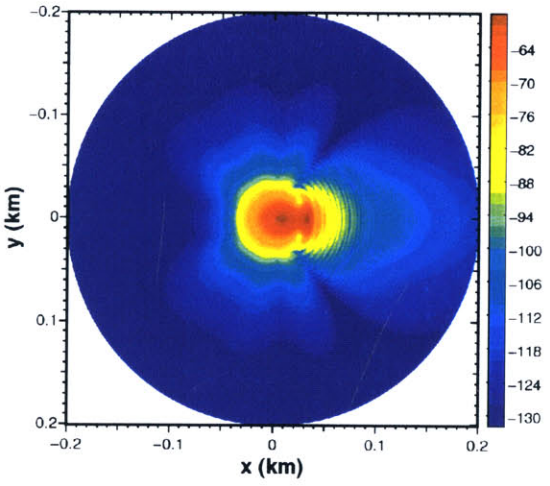

(b) $d = 0.75m$ case.

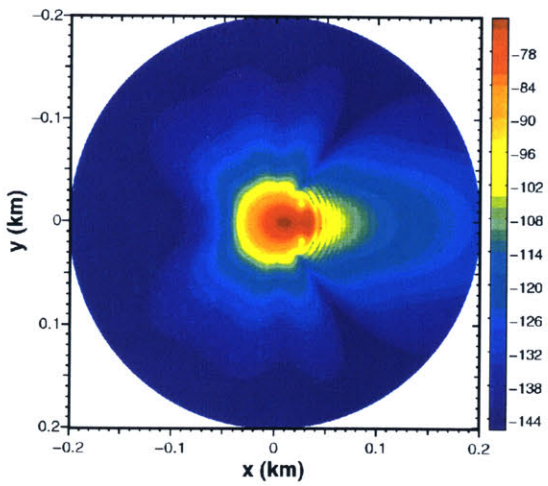

(c) $d = 1.0m$ case.

Figure 3-60: Horizontal scattered fields at $20m$ above the interface. The target is a rigid sphere buried in the fluid sand half space at different depths.

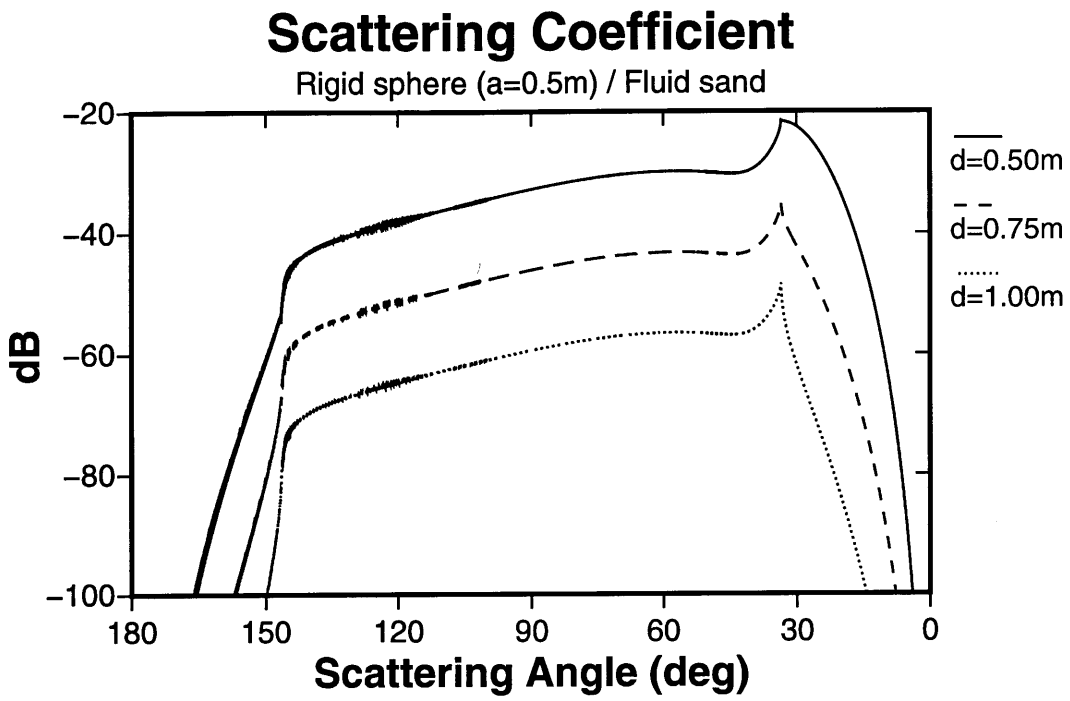

Figure 3-61: In-plane scattering coefficients. Cases of a rigid sphere buried in the fluid sand half space.

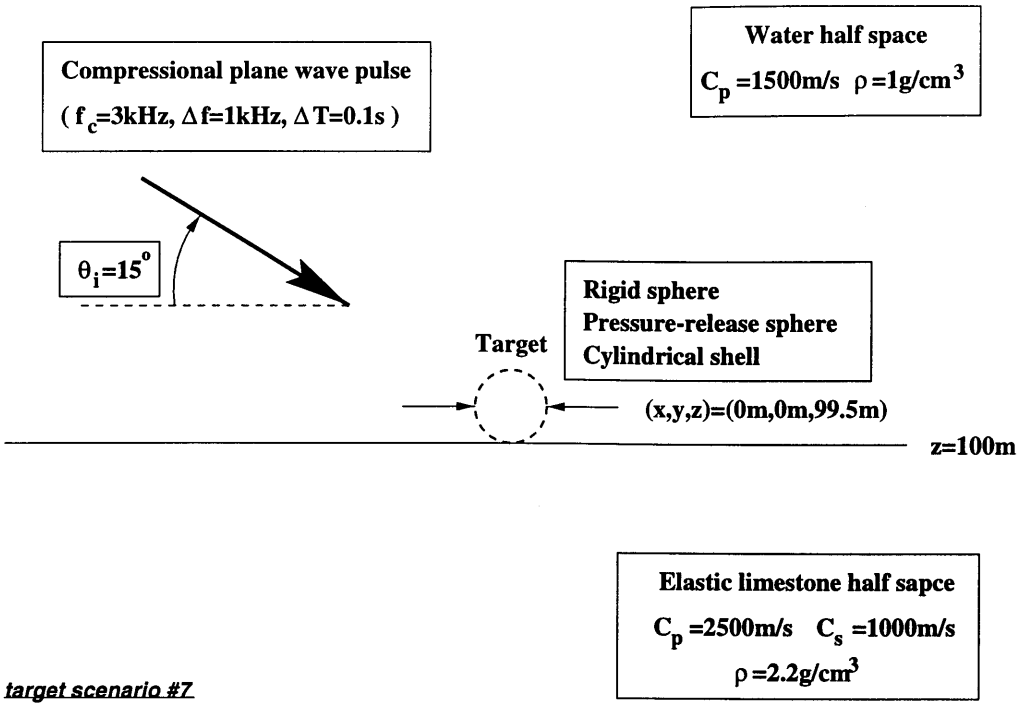

Figure 3-62: Target scattering scenario for time domain solutions. The incident pulse is a Hanning windowed sine wave. The incident field is generated by compressional plane waves ($F_c = 3kHz$ and $\Delta F = 1kHz$). The target is sitting on the interface between the water and elastic limestone half spaces.

3.7 Time Domain Solutions

As mentioned in Section 2.7, time domain scattering solutions are practical when experimental data are needed to be compared or analyzed. The numerical techniques to obtain wideband target scattering solutions are identical to those used in roughness patch time domain solutions : Fourier synthesis of single frequency scattering solutions. Section 2.7 describes the numerical techniques used with the time domain solutions. Figure 3-62 shows the target scattering scenario in time domain. The incident field is a plane wave with grazing angle $\theta_i = 15°$, center frequency $F_c = 3kHz$, bandwidth $\Delta F = 1kHz$, and time window $\Delta T = 0.1sec$. The incoming pulse is a Hanning windowed sine wave. The propagation medium consists of a water half space and an elastic limestone half spaces. The target is sitting on the interface between two half spaces.

The first time domain solution assumes a rigid sphere with radius $a = 0.5m$. Figure 3-63 shows snapshots of in-plane scattered field as a function of time. The most noticeable scattering features are transmitted shear and compressional waves of scattered energy in the lower space. When compared, the transmitted shear wave is slower and steeper than the compressional wave, but the shear waves carry more scattered energy because the transmitted scattered waves are supersonic to the shear wave speed. As shown in the frequency domain solution (Figure 3-23(a)), the peak scattering occurs at the forward direction in the upper space.

The next time domain solution has a pressure-release sphere ($a = 0.5m$) as the target. Figure 3-64 shows the time snapshots of in-plane scattered field. Overall, the time evolution of the scattered field is similar to that of rigid sphere case. The main difference can be found in the

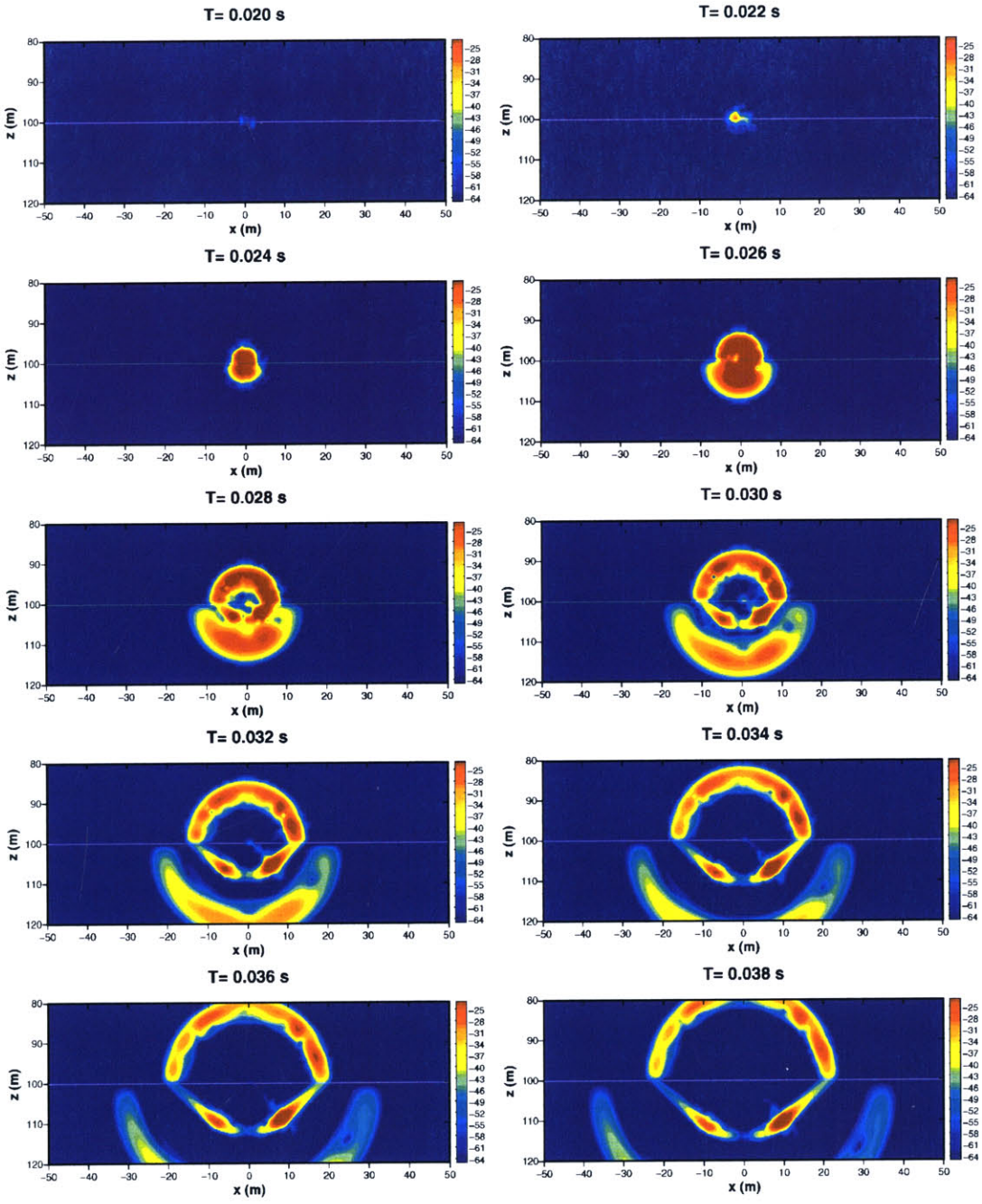

Figure 3-63: Time domain solution : snapshots of in-plane scattered field produced by a rigid sphere ($a = 0.5m$) over an elastic limestone half space.

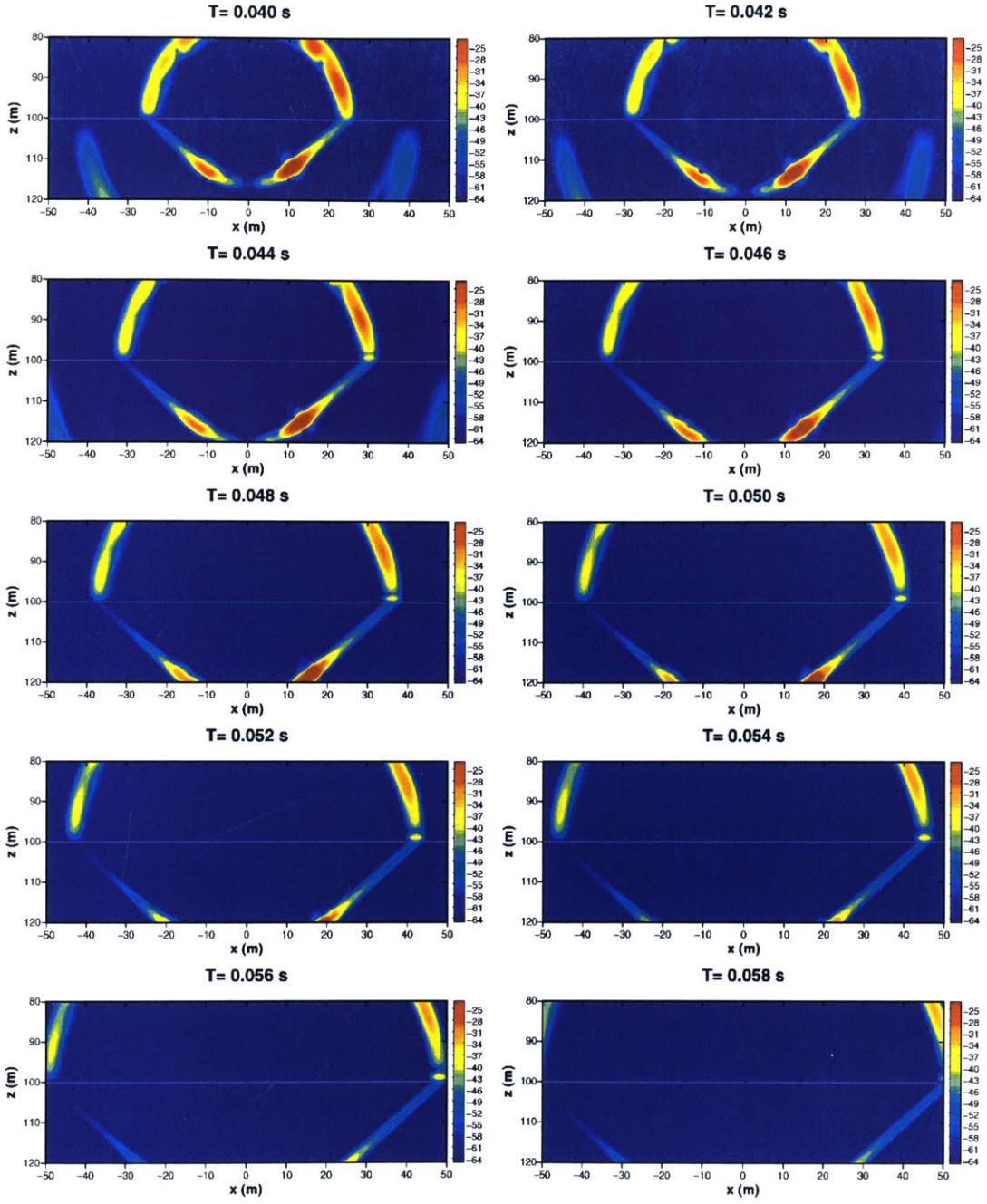

(Figure 3-63 continued)

forward and backward scattered fields. As with the frequency domain solutions (Figure 3-23(a) and Figure 3-26(a)), the pressure-release sphere exhibits a stronger forward scattered field but a weaker backward scattered field in the upper space. The pressure-release sphere has stronger transmitted shear waves in the forward and backward directions of the lower space.

The third case of time domain target scattering example has an identical scattering configuration except the slanted cylindrical steel shell is used instead of a pressure-release sphere. The orientation of the shell is 45° rotated in the counter-clockwise direction. The cylindrical shell has a length of $2m$, radius of $0.5m$, and thickness of $5cm$. The density of the shell is $7.8g/cm^3$, its compressional wave speed is $5200m/s$, and its shear wave speed is $2600m/s$. As shown in the frequency domain, the shell's anisotropic angle causes strong out-of-plane scattering at a bistatic angle of $\theta = 90°$. Figure 3-65 shows the time evolution of the horizontal scattered field at $20m$ above the interface between water and elastic limestone half spaces. There are two noticeable scattering features in the snapshots. Firstly, it is confirmed in time domain that the out-of-plane scattered waves are strong at a bistatic angle of $\theta = 90°$. Secondly, the axial modes can be observed from the beginning of the time evolution. Those axial modes are shown as local peaks in their side lobes, which are 45°. As time passes, the separation of the forward scattered wave and the out-of-plane scattered wave becomes clear. The level of the out-of-plane scattered field is higher than that of the forward scattered field. Therefore, the detection of the target is easier along the out-of-plane direction.

Figure 3-66 shows the time snapshots of the in-plane scattered field. Compared to the cases of rigid and pressure-release spheres, the backward scattered field is low while the forward scattered field is relatively strong in both upper and lower spaces. Transmission of direct scattered energy into the lower space is mostly carried by the shear waves of elastic limestone while the compressional wave is extremely low. Early in the time evolution, scattering of axial modes can be observed at high grazing angles.

Since the slanted cylinder produces significant scattered energy in the out-of-plane direction, it is useful to examine the vertical scattered field parallel to the out-of-plane. Figure 3-67 shows the time snapshots of the vertical cut in 90° azimuthal plane. In both upper and lower spaces, the scattered field at the bistatic angle of $\theta = 90°$ is dominant.

The last case of time domain target scattering solution uses a broad-sided cylindrical steel shell. The scattering configuration and target properties are identical to the previous case. Only the orientation of the cylindrical shell becomes broad-sided to the incoming wave. Since the incident field is perpendicular to the longitudinal axis of the shell, this target is expected to produce strong forward and backward scattered fields and a weak out-of-plane scattered field compared to the slanted shell case. Figure 3-68 shows the time snapshots of the horizontal scattered field at $20m$ above the interface. As expected, the in-plane scattered field is dominant compared to the out-of-plane field. In the early part of the time evolution, the axial modes of the cylindrical shell are observed and they are shown as local peaks in their side lobes. When the forward and backward scattered fields are compared, the backward field is slightly stronger than the forward field. In the frequency domain solution ($f = 3kHz$ case), the amplitude of forward scattered field is slightly higher than that of the backward scattered field (see Figure 3-50). This suggests the distribution of scattered energy is controlled by excitation frequency and that the center frequency may not necessarily determine the overall trend of the scattered field.

Figure 3-69 shows several time snapshots of the corresponding in-plane scattered field. Compared to the slanted shell case (Figure 3-66), the in-plane backward scattered field is strong in both the upper and lower spaces. The transmission of a scattered wave into the lower space is mostly done by the shear waves at a steep angle. Also, the scattered waves at high grazing angle in the backward direction of the upper space are significant. This suggests the detection possibility is

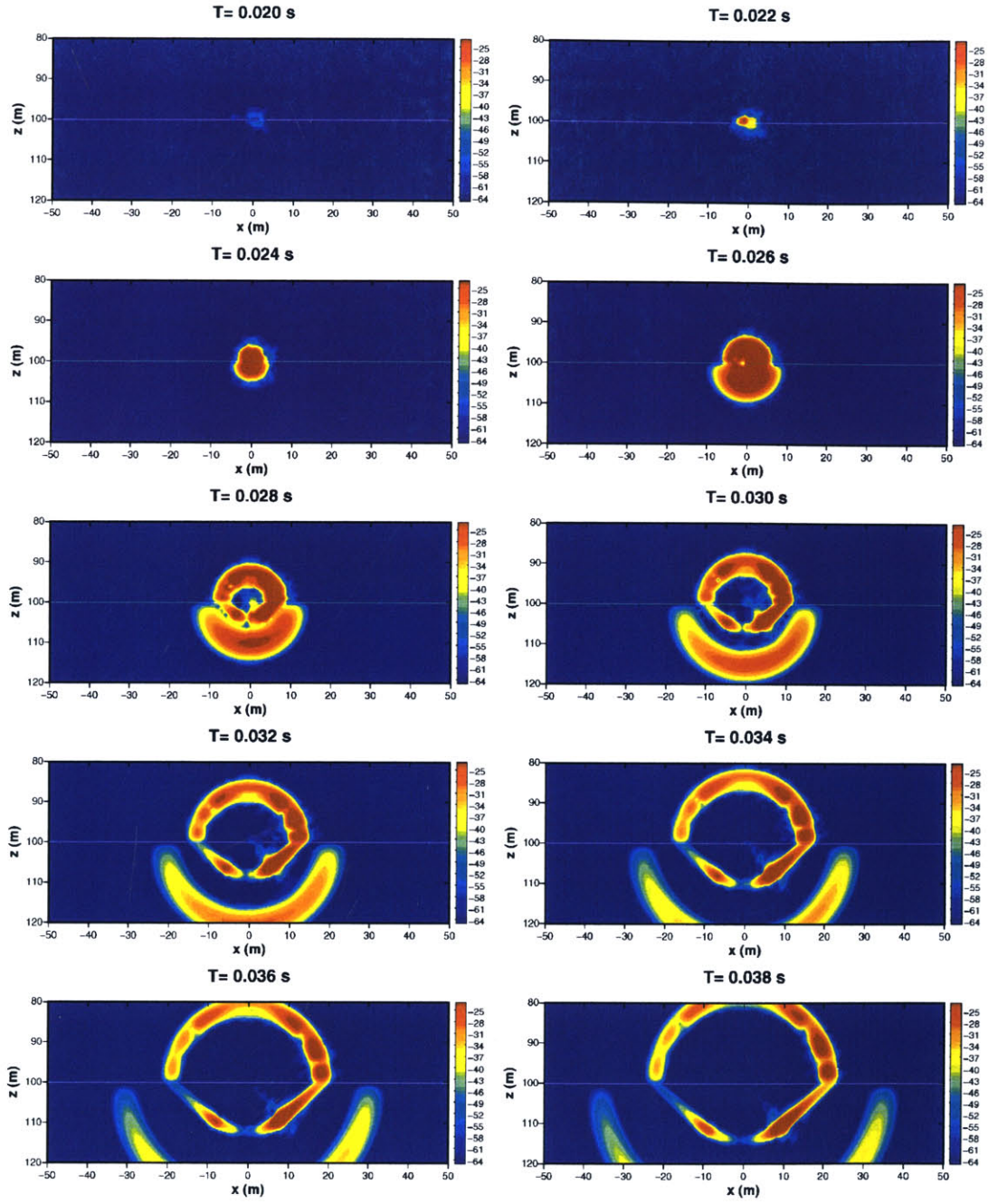

Figure 3-64: Time domain solution : snapshots of in-plane scattered field produced by a pressure-release sphere ($a = 0.5m$) over an elastic limestone half space.

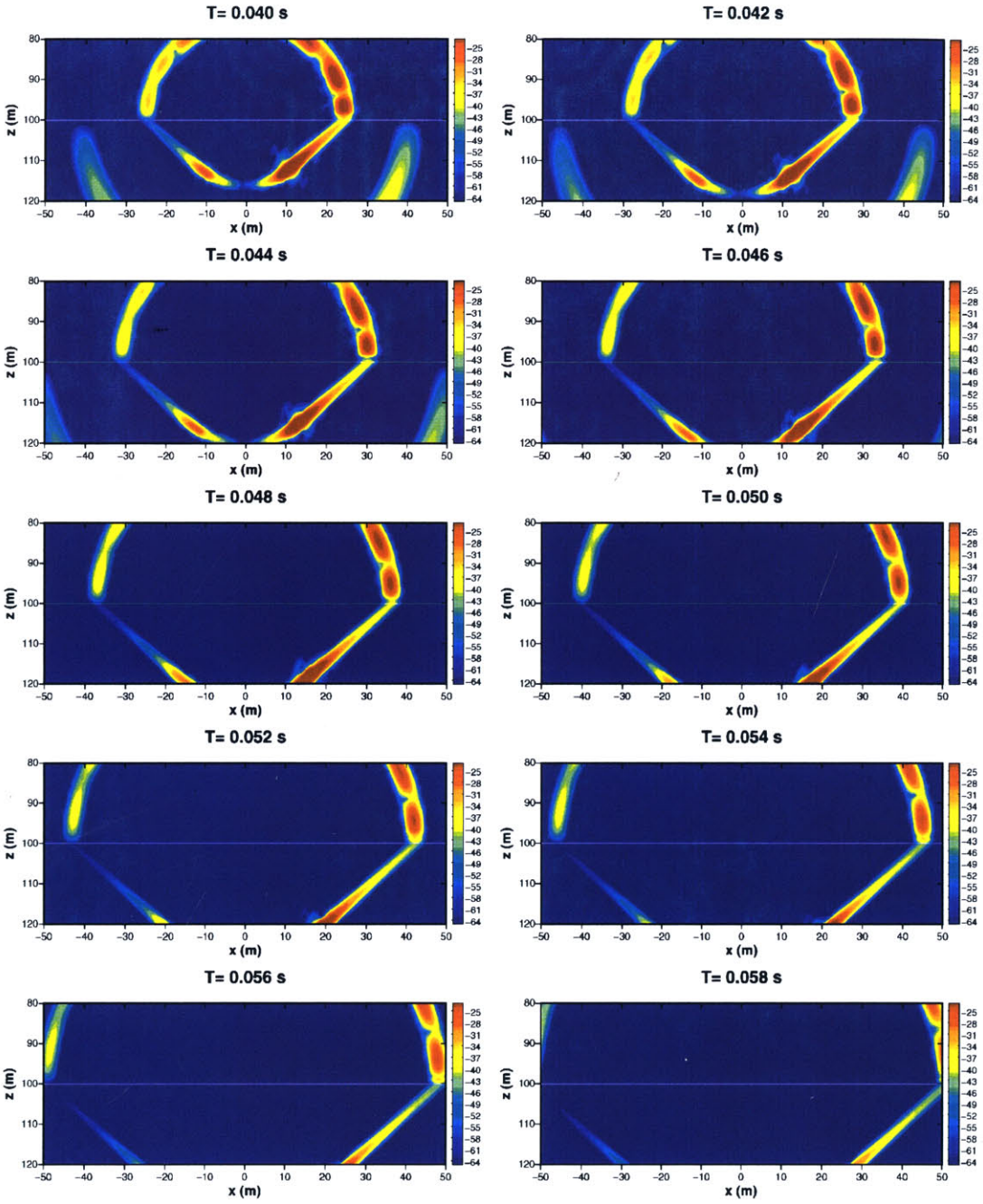

(Figure 3-64 continued)

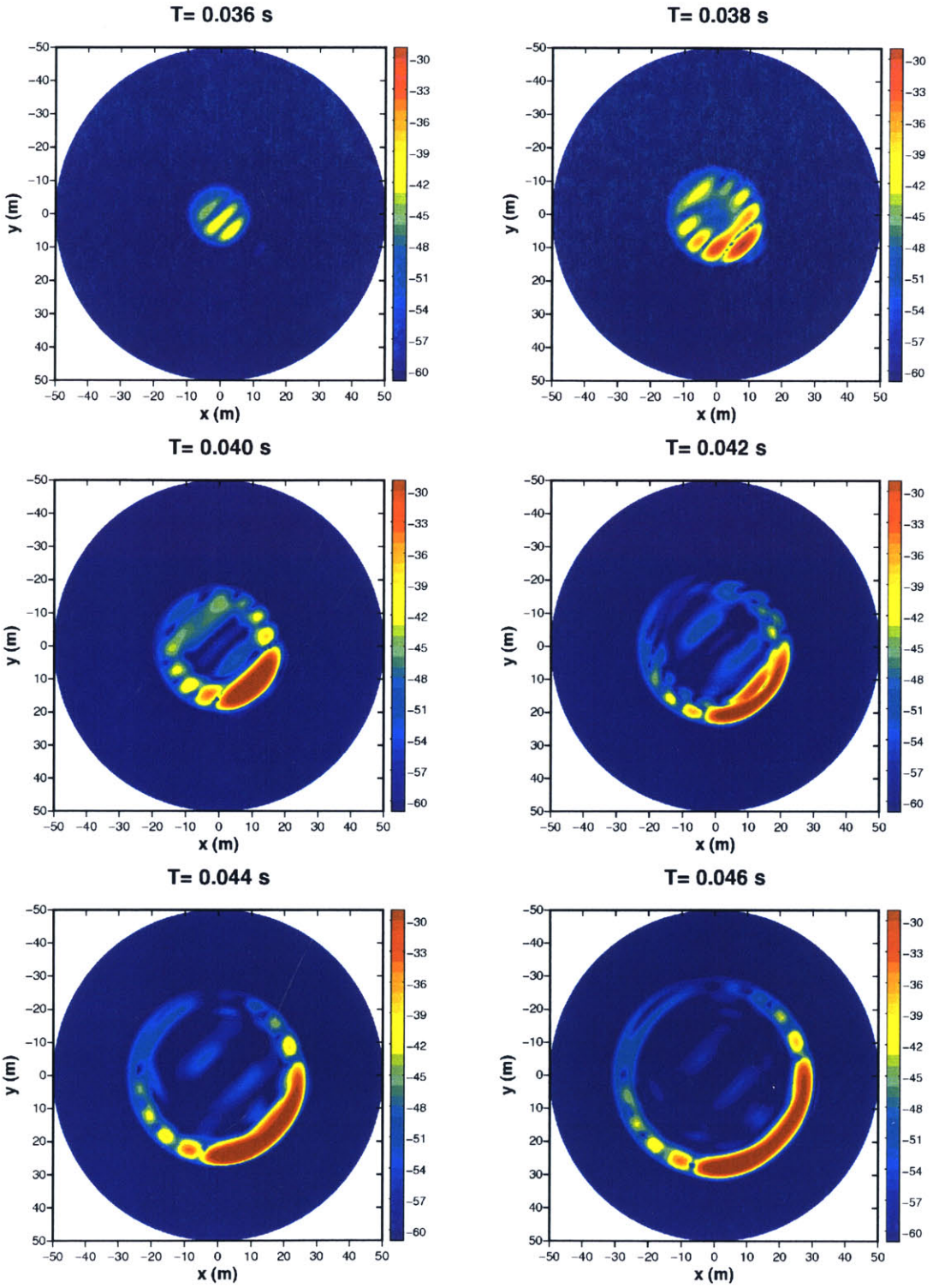

Figure 3-65: Time domain solution : snapshots of horizontal scattered field at $20m$ above the interface produced by a cylindrical shell ($\theta_{sk} = 45°$) over an elastic limestone half space.

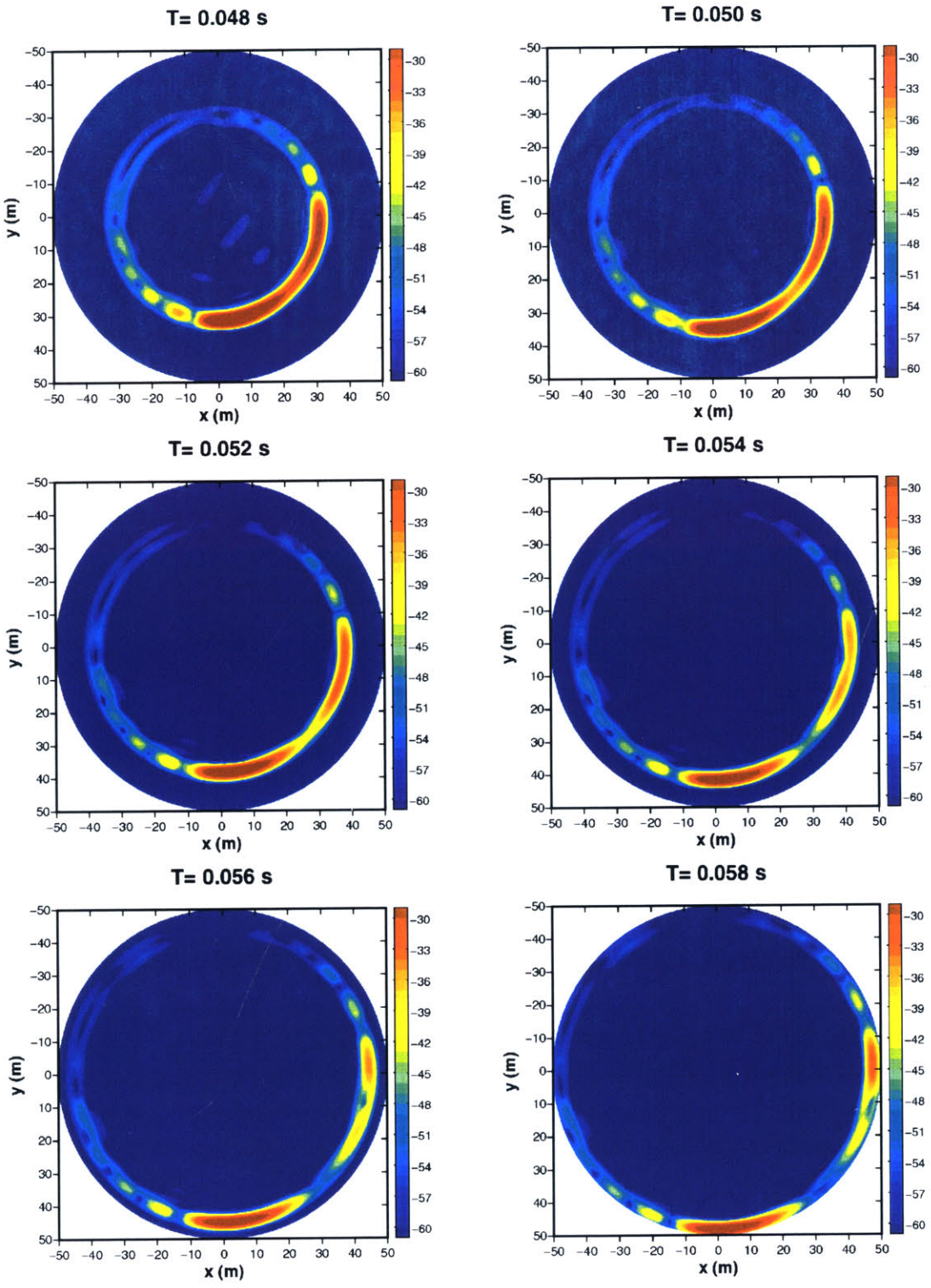

(Figure 3-65 continued)

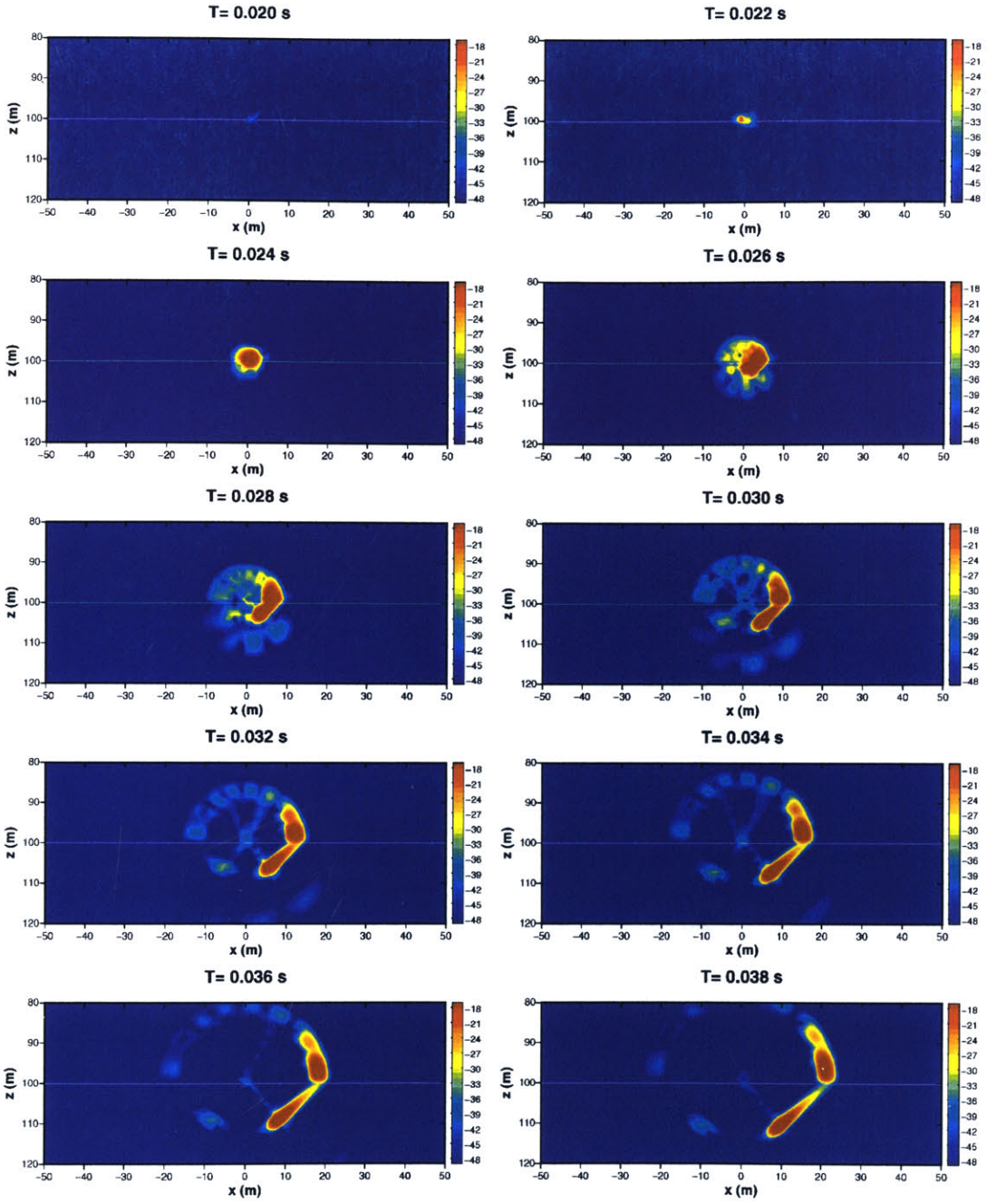

Figure 3-66: Time domain solution : snapshots of in-plane scattered field produced by a cylindrical shell ($\theta_{sk} = 45°$) over an elastic limestone half space.

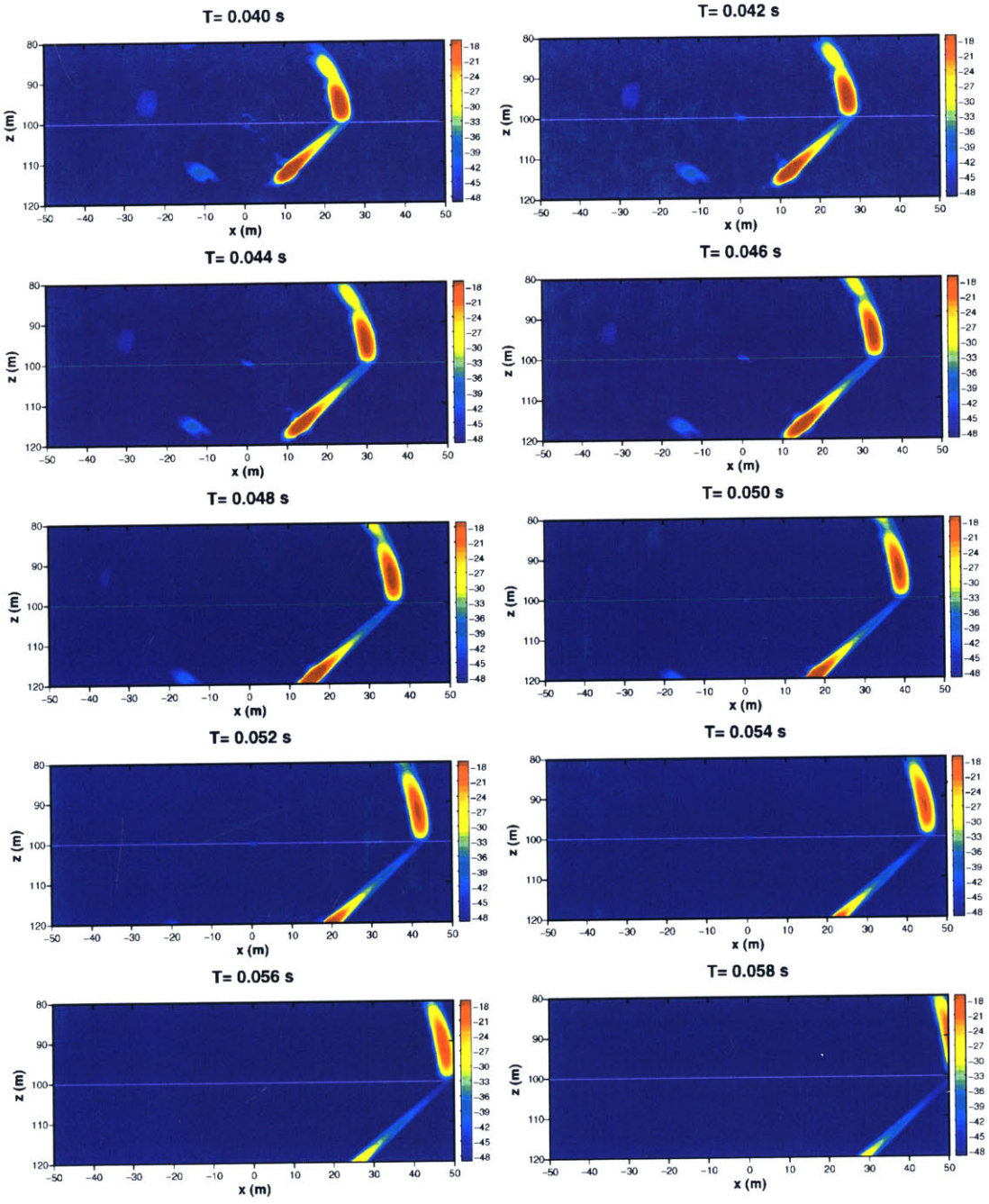

(Figure 3-66 continued)

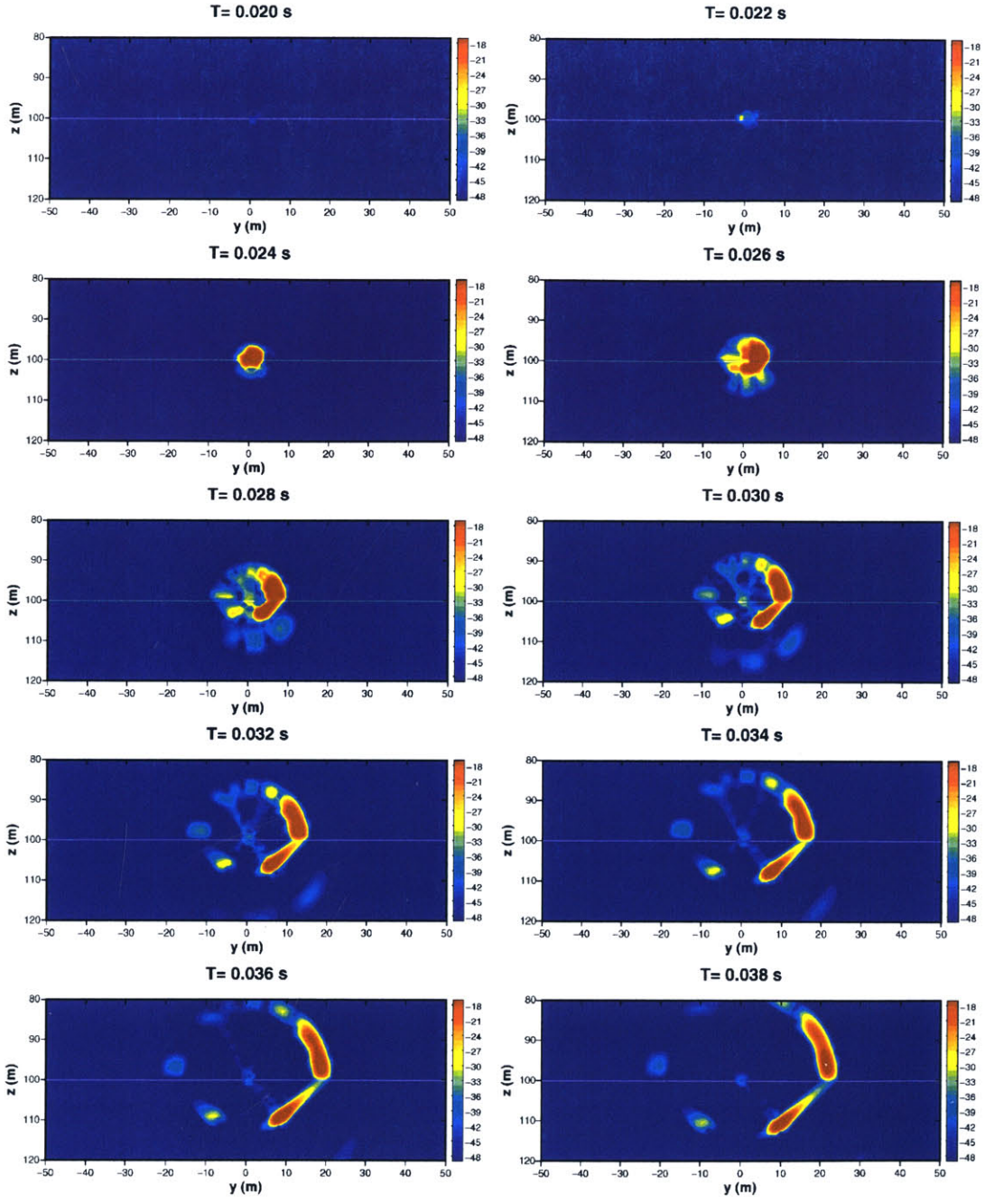

Figure 3-67: Time snapshots in the 90° azimuthal plane. (out-of-plane cuts) : case of a cylindrical shell (θ_{sk} = 45°) over an elastic limestone half space.

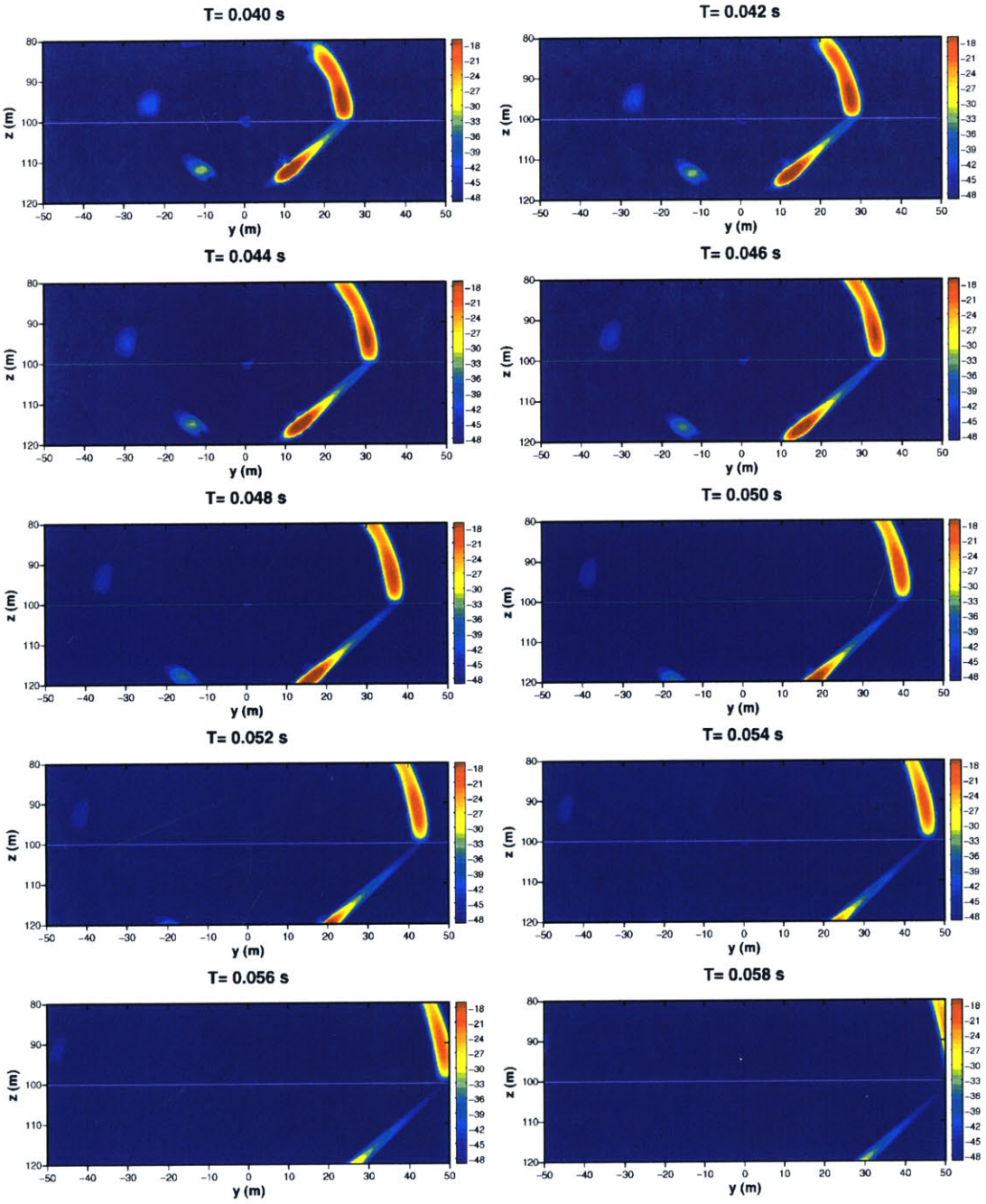

(Figure 3-67 continued)

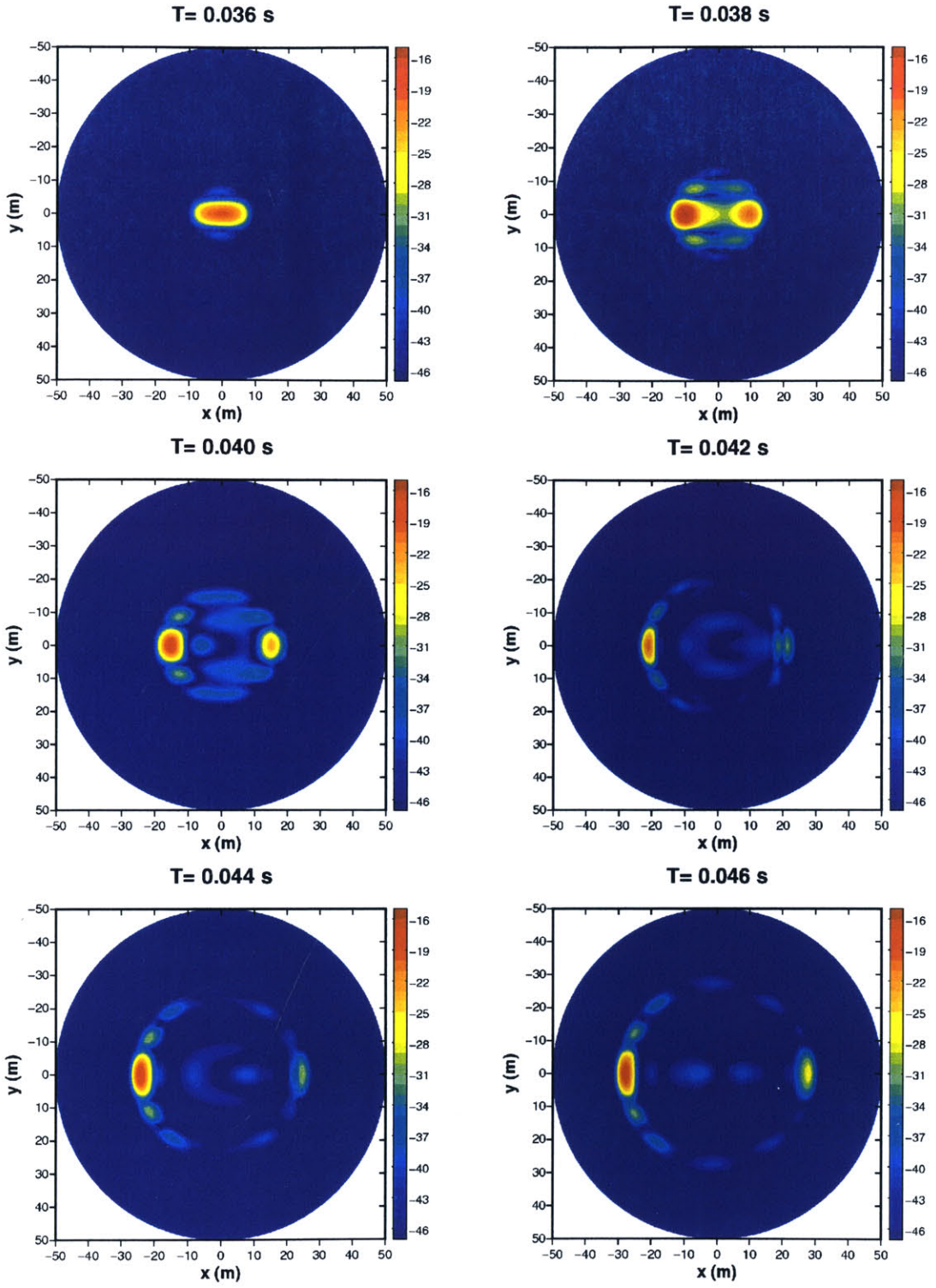

Figure 3-68: Time domain solution : snapshots of horizontal scattered field at $20m$ above the interface produced by a cylindrical shell ($\theta_{sk} = 90°$) over an elastic limestone half space.

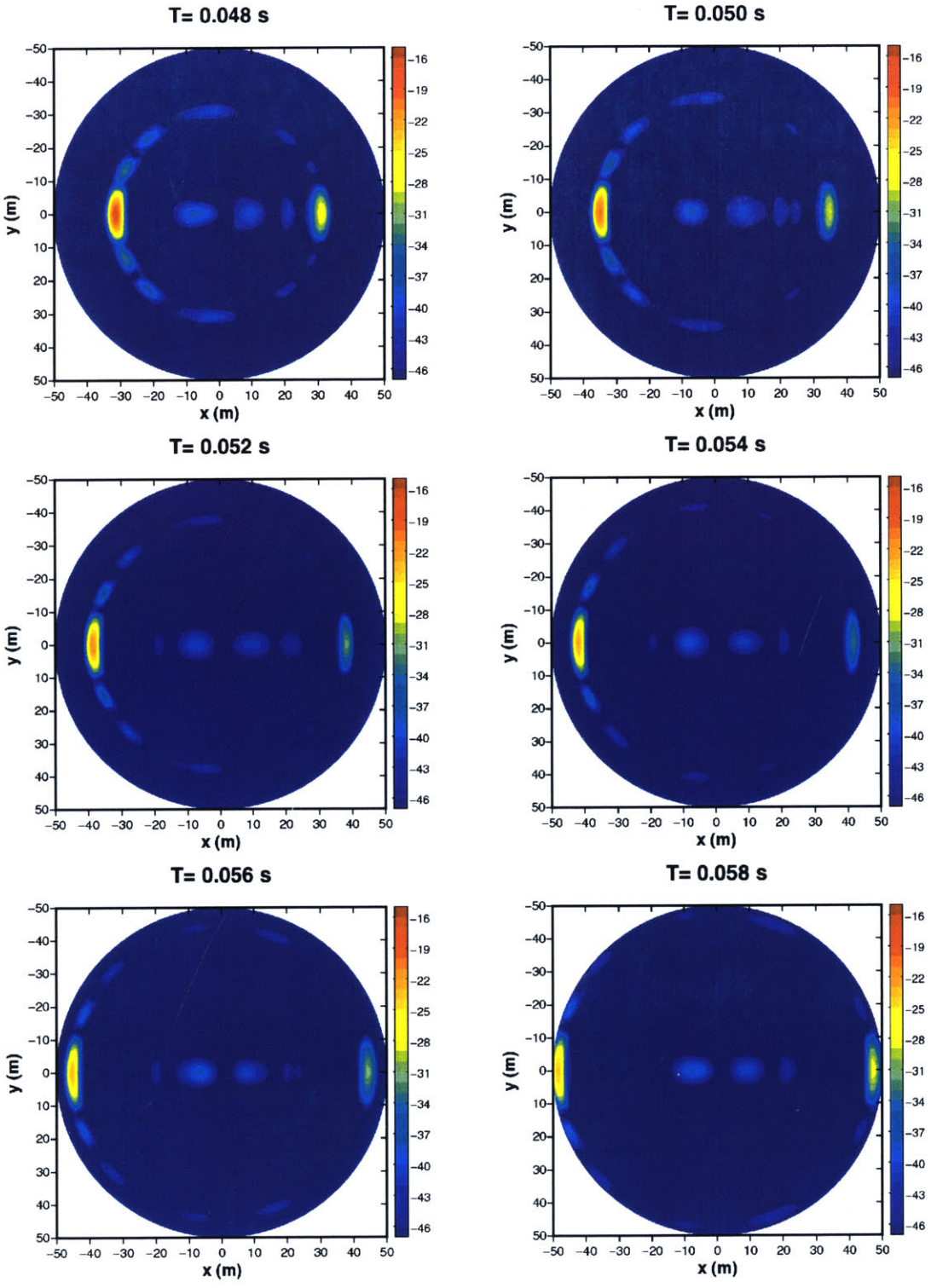

(Figure 3-68 continued)

fairly high at wide angular range in the backward direction.

For comparison purposes, the time snapshots corresponding to a vertical cut in the 90° azimuthal plane are presented in Figure 3-70. Compared to the slanted shell case (Figure 3-67), the side way scattered field is confined to the shallow polar angular regime. Again, this confirms that the broad-sided cylindrical shell produces an insignificant amount of scattered energy in the out-of-plane direction.

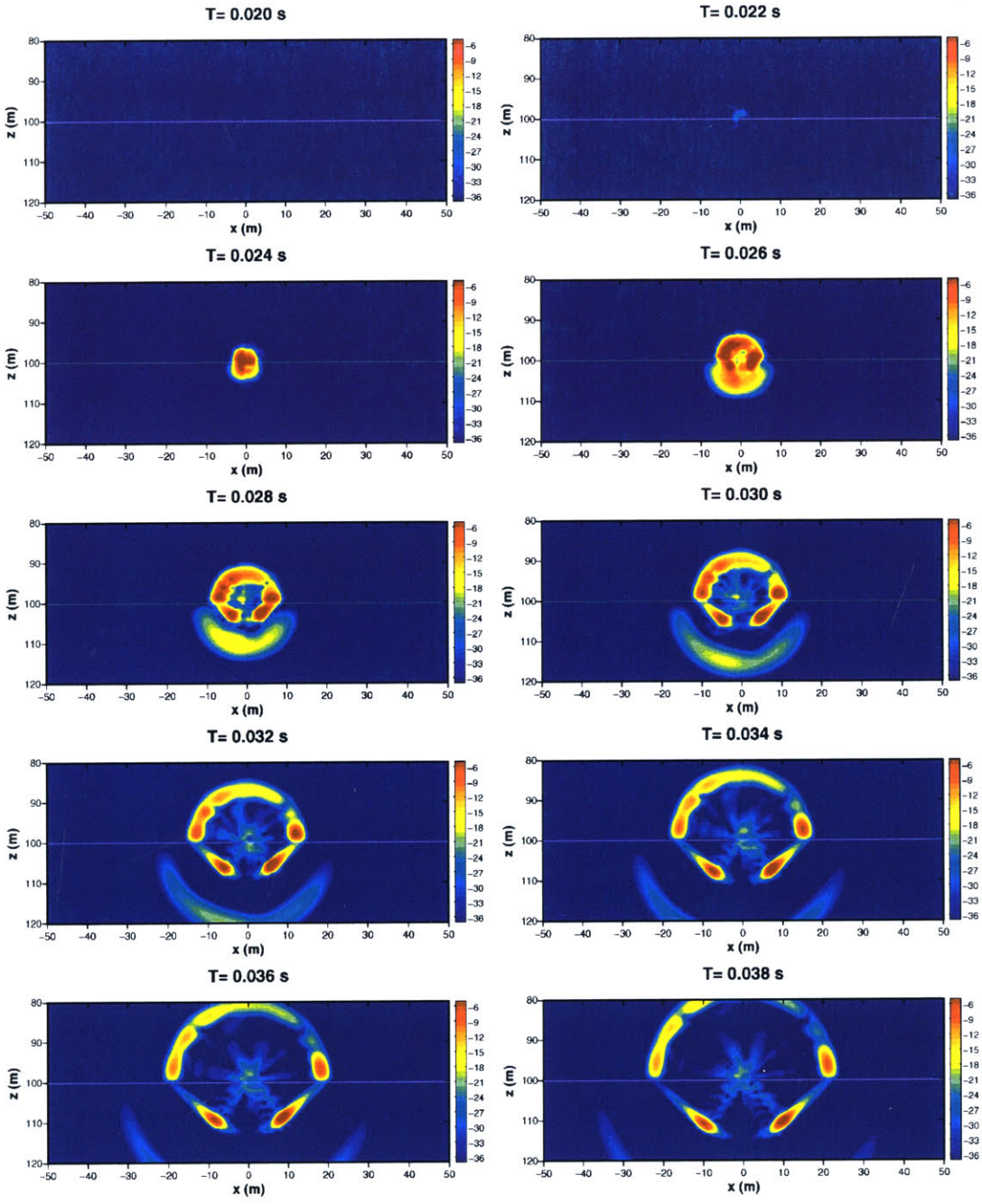

Figure 3-69: Time domain solution : snapshots of in-plane scattered field produced by a cylindrical shell ($\theta_{sk} = 90°$) over an elastic limestone half space.

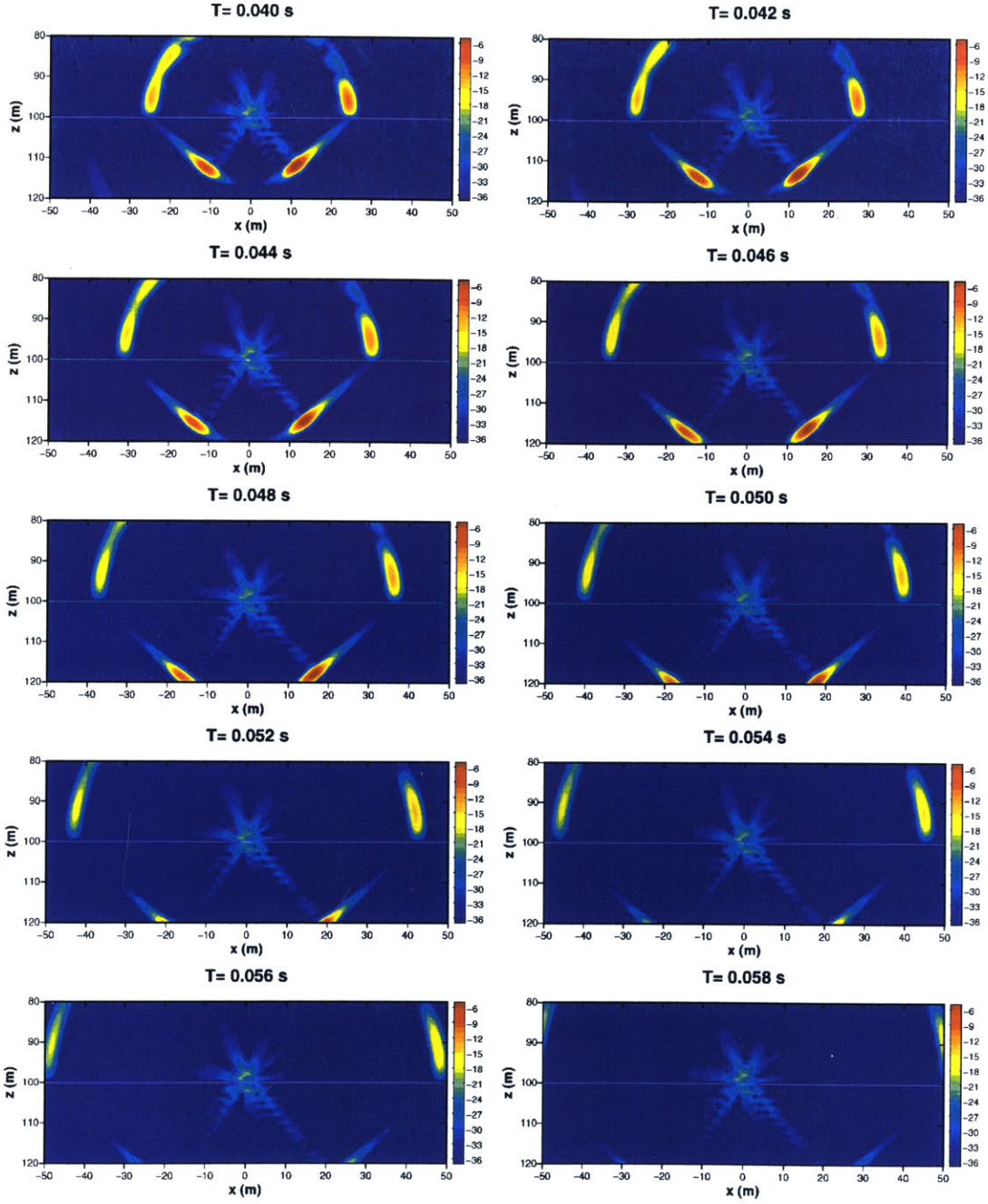

(Figure 3-69 continued)

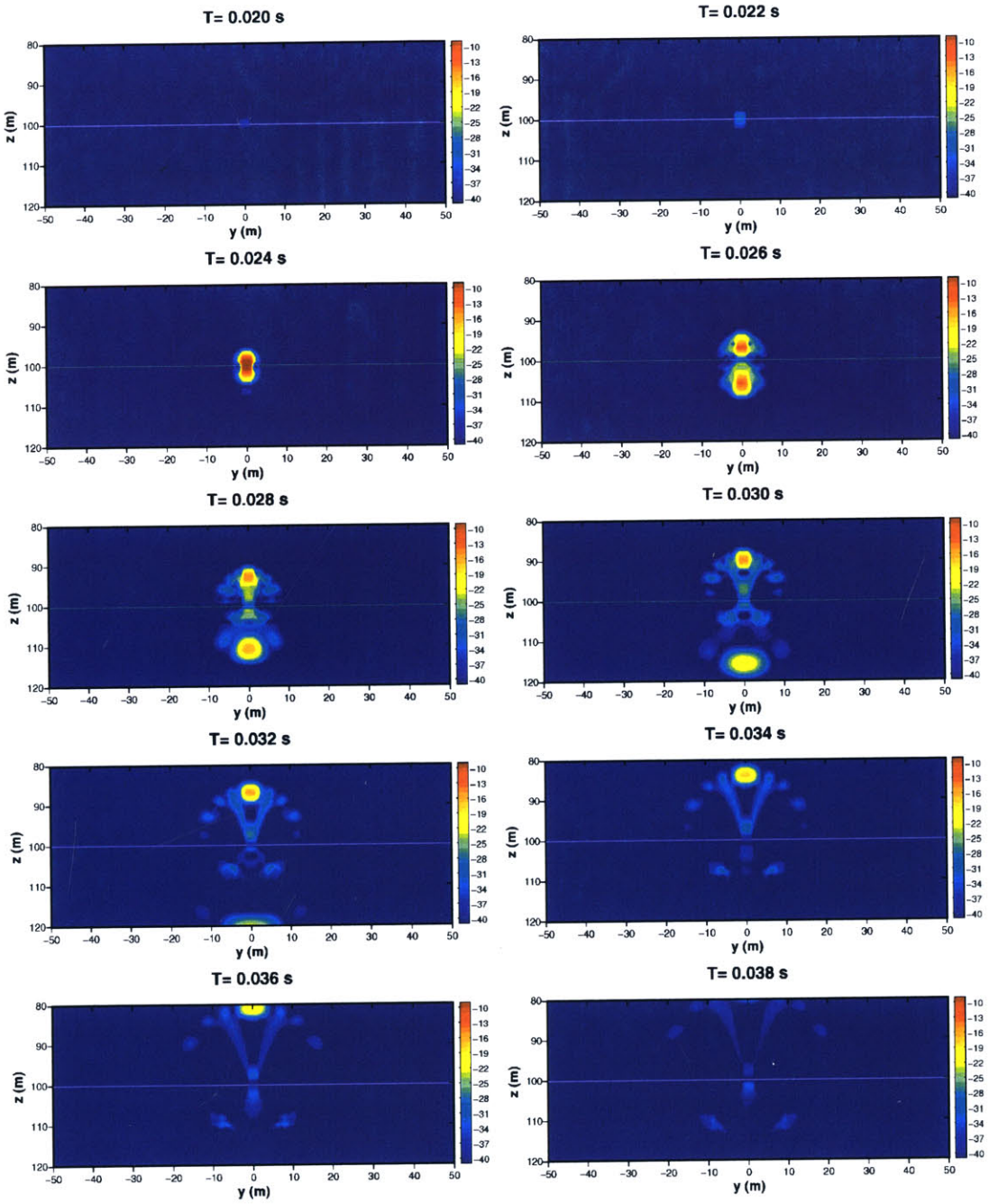

Figure 3-70: Time snapshots of vertical cut in the 90° azimuthal plane (out-of-plane cuts). : case of a cylindrical shell ($\theta_{sk} = 90°$) over an elastic limestone half space.

Chapter 4

Numerical Experiments

In this chapter, the numerical models developed in Chapter 2 and Chapter 3 will be applied to scenarios close to that of an actual experimental environment. This demonstrates the usability of these numerical models and allows to present a physical interpretation of the simulated acoustical data.

Figure 4-1 shows a schematic of the 'numerical simulator' based on two scattering models and one wave propagation model – a rough interface scattering model, a target scattering model, and a wavenumber integration method. The term 'numerical simulator' is used because the ultimate goal of combining different numerical models is to perform numerical experiments – computer simulation of acoustical fields. Since the scattering scenarios in this thesis include heterogeneities such as multiple layers of isotropic elastic and fluid media, rough interfaces, and a target, it is natural to combine the various numerical models to build a 'numerical simulator'. In order to build a numerical simulator with different models, one has to provide consistency or a common ground for every numerical model used by the simulator. In other words, each numerical model in the simulator has to be combined in a consistent way to solve a heterogeneous problem. In this thesis, this 'consistent way' is provided by the 'wavenumber domain formulation'. Each numerical model in the diagram of the numerical simulator expresses the acoustical field as a function of wavenumber. The field decomposition in the wavenumber domain is used to solve the wave equation with its boundary conditions. After obtaining solutions in each wavenumber, the solution in the spatial domain is constructed by wavenumber integration. The first component of the numerical simulator is the 'wavenumber integration model'. The wavenumber integral model provides the incident field necessary for the rough interface and target scattering models. It also computes the scattered fields from the outputs of rough interface and target scattering models. The second component is the 'rough interface scattering model' described in Chapter 2. It uses the method of small perturbation to represent rough interface scattered fields in terms of the source distribution function. This source distribution is transformed into an azimuthal Fourier series in the wavenumber domain. This transformation is necessary to make the rough interface scattering model compatible with the wavenumber integration model. The third component is the 'target scattering model', which is based on the single scattering approximation. In this thesis, there are three types of targets available for computation – rigid sphere, pressure-release sphere, and finite cylindrical elastic shell. The scattered field generated by a target is expressed as a point source with a specific beampattern. This beampattern is obtained from the incident field computed by the wavenumber integration model and the free field scattering function of the target. Then, the point source expression of the target field is transformed to an azimuthal Fourier series in the wavenumber domain. Again, this transformation ensures that the target scattering model is

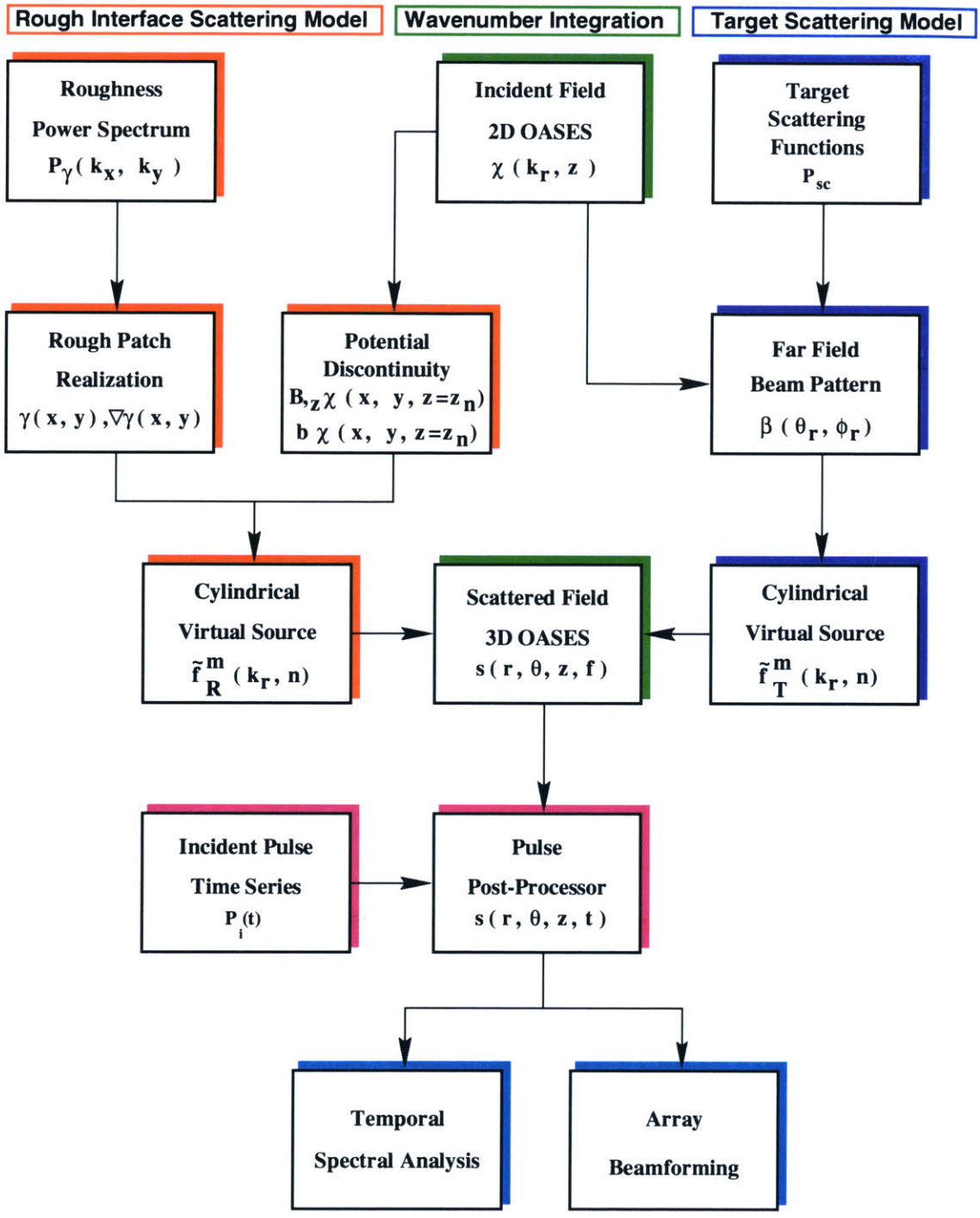

Figure 4-1: Diagram of the numerical simulator.

compatible with the wavenumber integration model for field computations. By using these three models in a consistent way, the scattered field caused by a rough interface and a target in a multi-layered environment can be solved in the spatial domain at a single frequency.

When a wideband (i.e. time domain) simulation is necessary, the 'pulse post-processor module' can be utilized to construct a time domain solution by Fourier synthesis of the frequency domain solutions. Because each frequency domain solution can be used as a transfer function, it is possible to change the input pulse (time series of incident field) without re-computing the single frequency domain solutions. This is possible when the bandwidth of the input pulse is mostly covered by the bandwidth of the frequency domain solutions. After obtaining a time domain solution by the pulse post-processor, further analyses such as temporal spectral analysis and array beamforming can be carried out. This final stage is one of the post-processing works that are done during or after real experiments.

In the following section, numerical experiments will be designed according to the scattering scenario used in the GOATS '98 experiment [45]. These numerical experiments will be conducted by the above numerical simulator and the simulated scattering data will be analyzed and discussed.

4.1 Setup of the Numerical Experiments

Because the numerical experiments are designed based on the GOATS '98 experiment, it is necessary to describe the GOATS '98 experiment. The 'GOATS' stands for 'Generic Oceanographic Array Technology Sonar'. The experiment was performed from May 5 to May 29, 1998 in shallow water outside Marciana Marina, Elba. The schematic figure of the experimental site is shown in Figure 4-2. The test site is very shallow and the depth of the target site is about $14m$ to $15m$. The AUV 'Odyssey' was launched from the research vessel 'Alliance'. It collected acoustical data, and returned to the ship. The shore laboratory and the tug boat 'Manning' deployed and operated 'Topas'[1] source, installed targets, and recorded data from 16 element vertical receiver array attached next to the Topas array and 128 element horizontal receiver array.

Figure 4-3 shows a blowout of the area including the Topas source, the receiver arrays, the target field, and the roughness features. Each target was insonified by the Topas source. In order to maintain a symmetric beampattern of the Topas source at any grazing angle, the latter was steered by a mechanical device instead of using electronic control (i.e. phase shifting and weighting). The sonar footprint of the Topas source was small enough to cover only one or one and half of the targets at a given source position.

Figure 4-4 shows the detailed configuration of the Topas source and the receiver arrays. The horizontal position of the Topas source was controlled by moving the source tower along the rail on the sea floor. By changing the horizontal position, tilt angle, and pan angle of the Topas, the grazing and azimuthal angles of the incident beam with respect to a specific target was determined. A 128 element horizontal array was suspended between two towers and its position and orientation were changed by manually moving array towers. An AUV Odyssey navigated along the desired tracks above the target field and collected acoustical data with an 8 element receiver array. The receiver array was attached to the nose of the AUV and its orientation was parallel to the longitudinal direction of the AUV.

Based on the above detail description of the GOATS '98 experiment, numerical experiments of rough interface and target scattering in a shallow water environment are designed as follows. Since it is difficult to include all the complexities of a real experiment and some parameters are actually

[1] Topographic Parametric Sonar

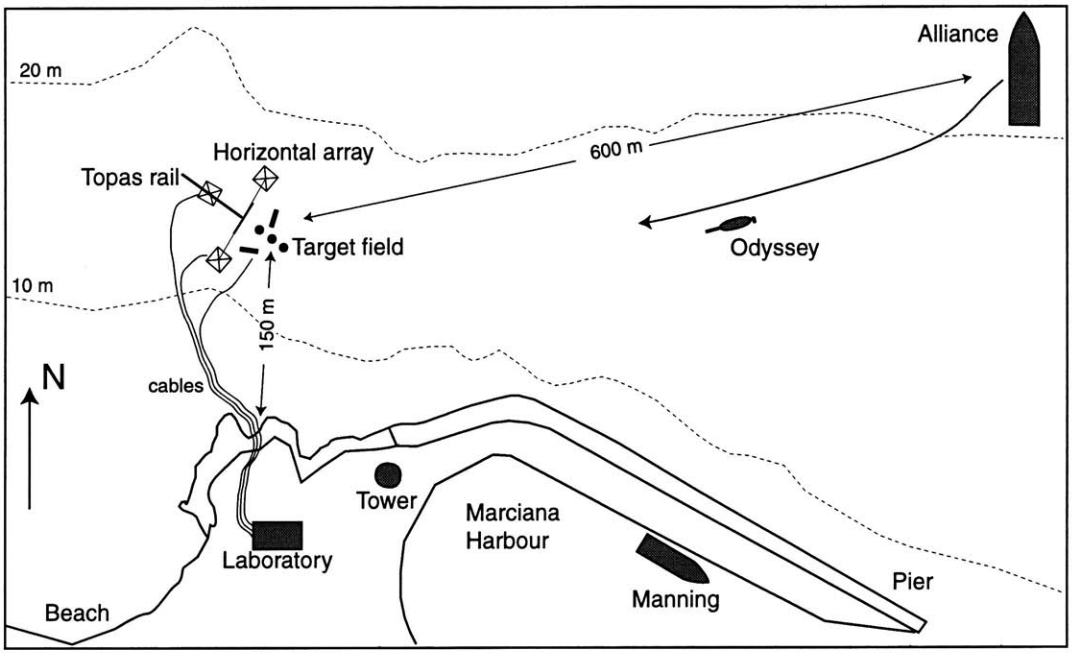

Figure 4-2: The GOATS '98 operational scenario at Marciana Marina, Elba. Shore facility and 'Manning' deployed and operated Topas source, targets etc., and recorded data from 16 element vertical array and 128 element horizontal array. 'Alliance' launched AUV operations from offshore, and served as the data processing centre for the experiment. Courtesy of H. Schmidt et al. [50].

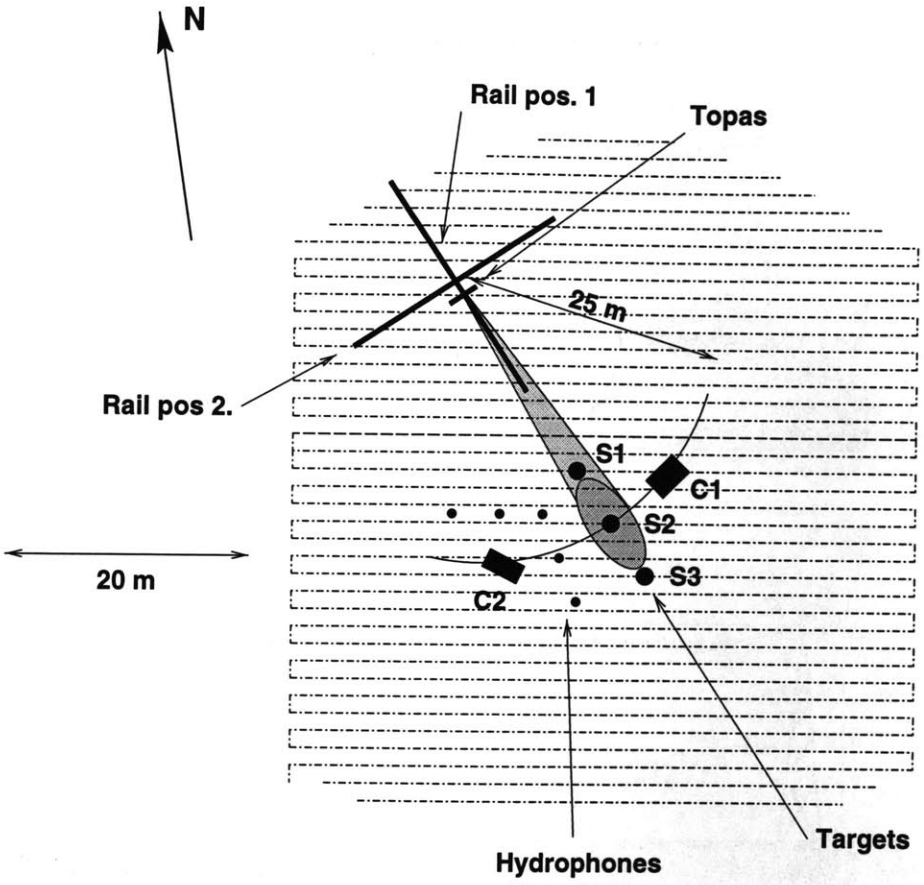

Figure 4-3: The GOATS '98 test area layout. The Topas rail is deployed at an angle of approximately 45° to the ripples, with the targets deployed near the center of the patch. Two perpendicular deployment directions were planned for the rail. The targets included two flush buried cylinders (C1 and C2), two buried spherical shells of $1m$ radii (S1 and S2, and S3), and one half buried spherical shell of $1m$ radius (S3). Courtesy of H. Schmidt [45].

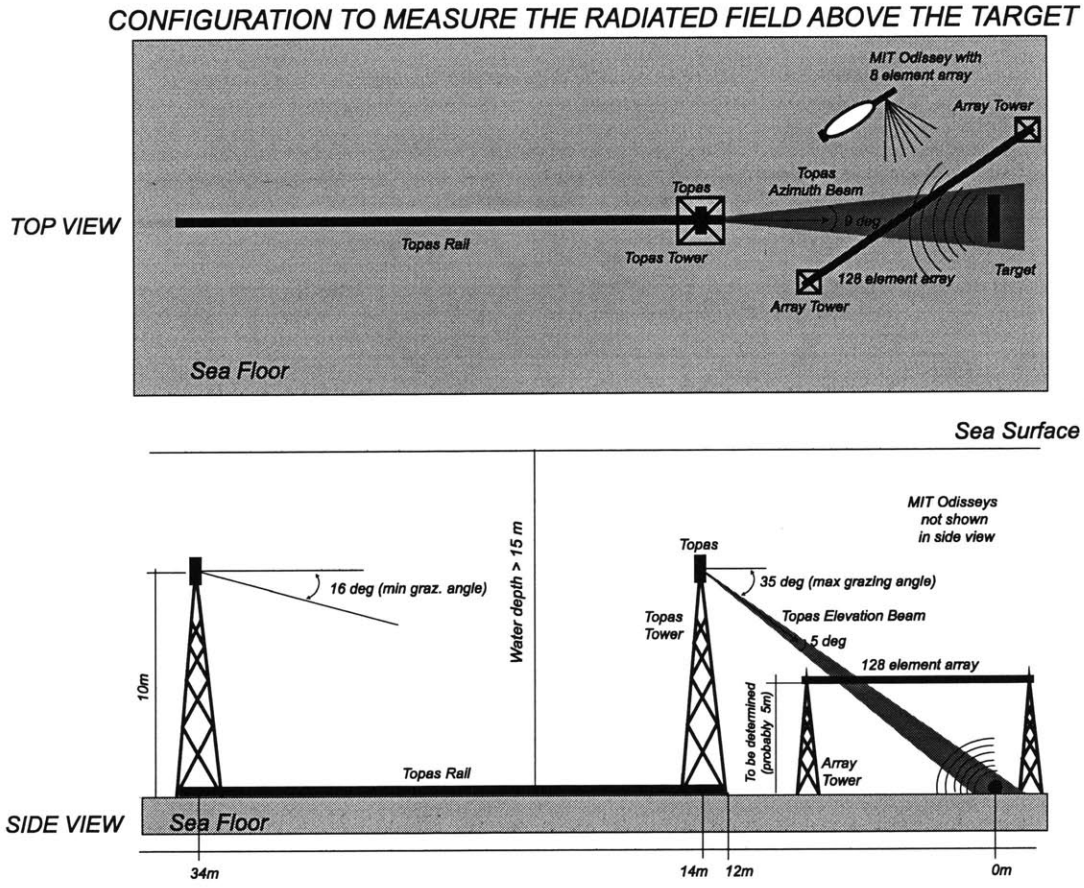

Figure 4-4: The GOATS '98 Topas source tower/rail with a fixed 128 element horizontal array in bistatic configuration, suspended between two $5m$ towers. Courtesy of E. Bovio [45].

unknown, it is necessary to strip down the real experimental scenario to a numerical scenario with manageable complexities. Figure 4-5 is a schematic figure of the numerical experiment designed according to the GOATS '98 configuration. The upper inset of the plot shows the configuration of the medium, source location and properties, and a schematic view of sonar footprint. The medium consists of an isotropic fluid and elastic layers – $15m$ water column, $2m$ fluid sand layer, $2m$ elastic sand layer, and an elastic lower half space. The depth of the rough interface is $15m$, which is between the water column and the fluid sand layer. The lower left inset shows the sound speed and density profiles in the depth direction. The source depth is $5m$ below the pressure-release surface. The source is assumed to have a 5° vertical angular beam width and a 9° horizontal angular beam width. The size of the sonar footprint is determined by the depth separation between the insonified area and the source depth, the vertical angular beam width, and the horizontal beam width. The lower right inset shows two examples of sonar footprint sizes. The nominal incident grazing angle is set at either 15° or 35°. The insonified area remains at the same position while the source moves along the horizontal direction to change the incident angle. The configuration is very similar to that of the GOATS '98, especially when it comes to waveguide depth and source configuration.

In addition to the configuration of the environment and the source, other components of the numerical experiments must be included such as receiver array configuration, rough interface data, and target properties. Figure 4-6 shows the receiver array designed for these numerical experiments. It consists of a horizontal line array (HLA) and a vertical line array (VLA). These line array segments are identical except for their orientation. Each segment is made of 9 elements. The center element is shared by the HLA and the VLA. The array spacing is determined by an anti-aliasing condition at the center frequency of the source spectrum – less than a quarter of a wavelength ($F_c = 3kHz$ and $\Delta_H/\lambda = 0.2$). The aperture ratio of each segment is 1.6 at $3kHz$. The normalized beampattern of line array segment is shown in Figure 4-7. Depending on the window function, the line array segment has a different main beam width and side lobes. In the numerical experiments in this chapter, a Hanning window will be used for each segment of the receiver array. The advantage of using a Hanning window is that it has smaller side lobes compared to the rectangular window case. The reason for using a horizontal and a vertical line array together is to identify the direction of arrival clearly. For example, the HLA segment cannot differentiate the arrivals from the free surface and the ones from bottom if they have the same grazing angle and similar arrival times. In the numerical experiments of this chapter, synthesized data from the HLA and VLA segments will be analyzed separately. More specifications are necessary for the receiver array – global position and orientation of array. The receiver array used in the numerical experiments will move along a circular track with a specific orientation shown in Figure 4-8. The radius of the circular track is $40m$, its center is aligned with the center of the sonar footprint, and the depth of the center element is $4m$ below the pressure-release surface. The main purpose of using a receiver array moving along a circular track is to collect ('synthesize' for numerical experiment) acoustical data at different bistatic angles. Bistatic data can show the spatial structure of the scattered field and may provide a clue to identify properties of a scatterer. The HLA part of the array is aligned with the radial direction and the VLA part is parallel to the depth direction.

In the numerical experimental scenario, two inhomogeneities cause scattering – a rough interface and a target. The rough interface is modeled by a synthesized roughness patch shown in Figure 4-9(a). This roughness patch is generated by an anisotropic Goff-Jordan power spectrum with $\theta_s = 45°$, $C_{L1} = 2m$, $C_{L2} = 0.25m$, $\sqrt{\langle\gamma^2\rangle} = 3.125cm$, and $D = 2.5$. The size of sonar footprint varies depending on the incident grazing angle. Therefore, the synthesized roughness has to be windowed in proportion to the size of the sonar footprint. The nominal dimensions of the sonar

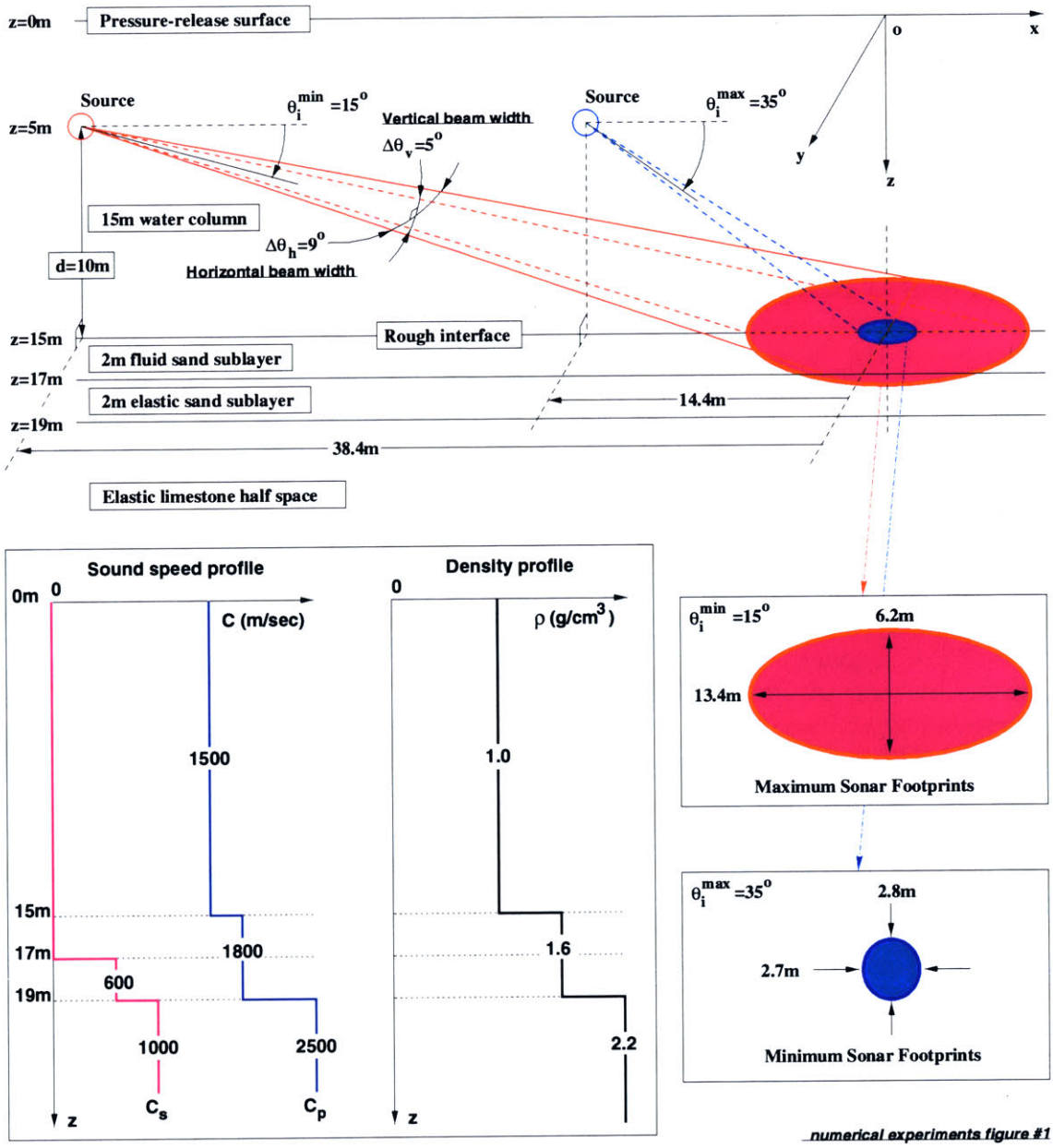

Figure 4-5: Scenario of the numerical experiment based on the GOATS '98 configuration (Figure 4-4). The medium is assumed to be independent of range and the waveguide consists of multiple homogeneous layers. The sound speed and density profiles are presented in the lower left corner.

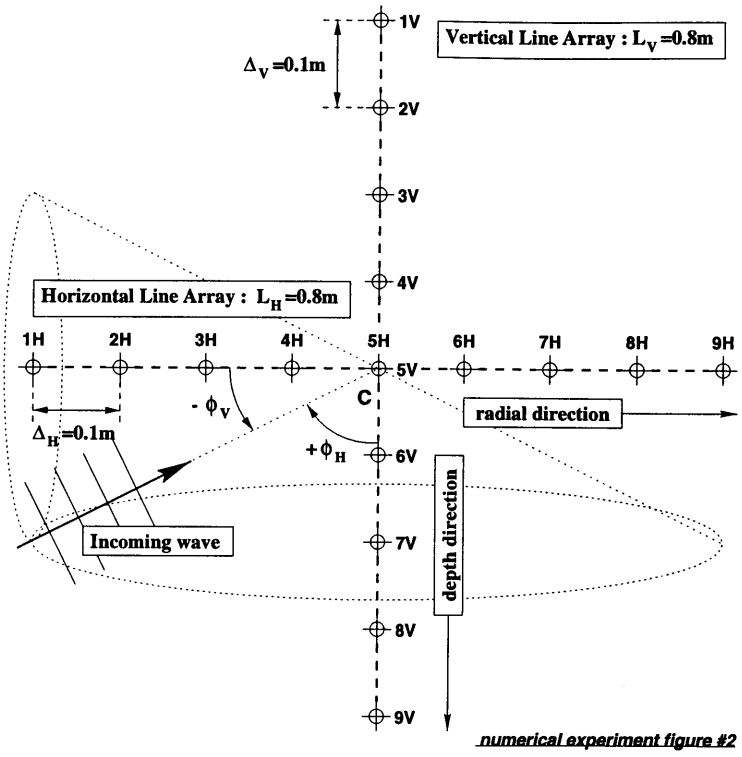

Figure 4-6: Geometry of the receiver array for the numerical experimental scenario – Figure 4-5. The array consists of a horizontal and a vertical line array segments. Each segment consists of 9 elements with $\Delta_H = \Delta_V = 0.1m$ spacing. The center elements $5H$ and $5V$ are shared by the horizontal and vertical arrays. $1H$ corresponds to the innermost element in the radial direction and $1V$ corresponds to the vertical element closest to the pressure-release interface.

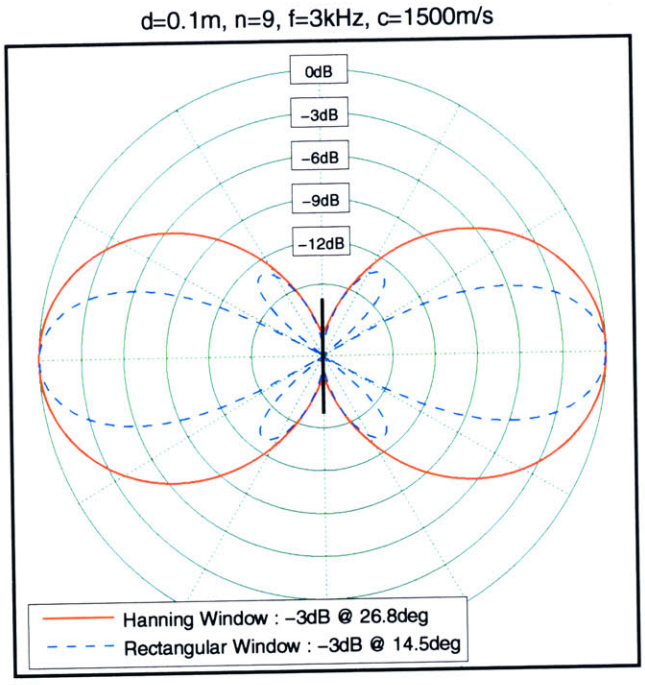

Figure 4-7: Normalized beampatterns for a line array segment of array shown in Figure 4-6. Beampatterns are obtained at $f = 3kHz$ and $c = 1500m/s$. The solid line is a beam pattern produced by a Hanning window while the dashed line is one without windowing. The black thick line represents the orientation of line array.

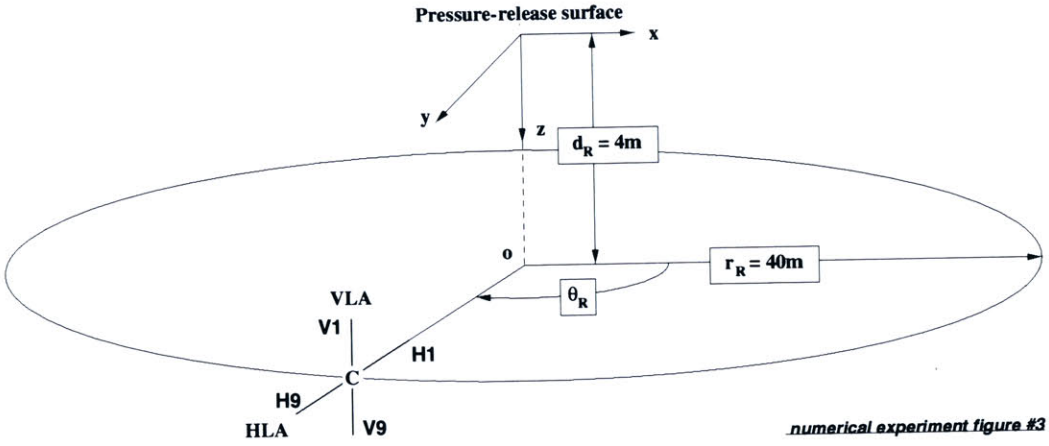

Figure 4-8: Track of the receiver array used in the numerical experiments. The center of array is moving along a circular track of $40m$ radius at $4m$ below the pressure-release interface. The horizontal array is aligned with the radial direction. The horizontal coordinates of the track center coincide with those of the sonar footprints shown in Figure 4-5. θ_R is the azimuthal position of the center element C, measured with respect to the positive x axis.

footprint are determined by the following equations :

$$XL = r_2 - r_1, \qquad YL = 2\tan\left(\frac{\Delta\theta_v}{2}\right)\sqrt{\left(\frac{r_1 + r_2}{2}\right)^2 + d^2}, \tag{4.1}$$

where XL and YL are the lengths of sonar the footprints in the x and y directions, respectively. In the above equation, r_1 and r_2 are defined as :

$$r_1 = \frac{d}{\tan(\theta_i + \Delta\theta_v/2)}, \qquad r_2 = \frac{d}{\tan(\theta_i - \Delta\theta_v/2)}. \tag{4.2}$$

There are two reasons to apply windowing on a raw synthesized roughness patch. Firstly, the non-zero edges of the roughness patch generate unnecessary spectrum in the high wavenumber regime and cause aliasing problems in scattering computations. Secondly, the computational load can be reduced by using a smaller roughness patch. Figure 4-9(b) shows a roughness patch windowed for the case of $\theta_i = 15°$. The dashed rectangle indicates the nominal size of sonar footprint generated by a source with $\theta_i = 15°$, $\Delta\theta_h = 9°$, $\Delta\theta_v = 5°$, and $10m$ depth separation between the source and the interface. The rectangle of solid line corresponds to the size of the 2-D Hanning window applied on the roughness realization (Figure 4-9(a)). The size of the Hanning window has a 25% margin over the nominal size of the sonar footprint. Non-white space in the plot corresponds to the area of computation. Figure 4-9(c) is a roughness patch windowed for the case of $\theta_i = 35°$. Since the size of the sonar footprint is substantially smaller than the synthesized roughness patch (Figure 4-9(a)), the necessary number of grids is reduced to one eighth of the original number of grids. In the numerical experiments, a cylindrical shell is used as a target. Figure 4-10 shows the configuration of the target. The target is a finite cylindrical elastic shell of length $L = 2m$, radius $a = 0.5m$, thickness $t = 5cm$, density $\rho = 7.8g/cm^3$, compressional wave speed $C_p = 5200m/s$, and shear wave speed $C_s = 2600m/s$. Two orientations of cylinder are considered – broad-sided shell ($\theta_{sk} = 90°$ – named as $C90$) and slanted shell ($\theta_{sk} = -45°$ – named as $C45$). The skew angle of the slanted shell is perpendicular to the roughness anisotropic angle ($\theta_s = 45°$). The anisotropic angles of a rough interface and a target are determined to produce possible target detection cases.

In the next section, four sets of numerical experiments that were conducted will be presented along with their post-processed results and physical interpretation.

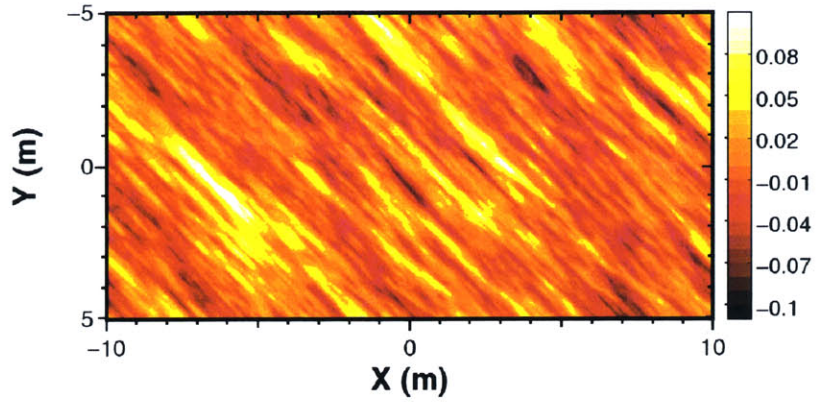

(a) Synthesized roughness patch.

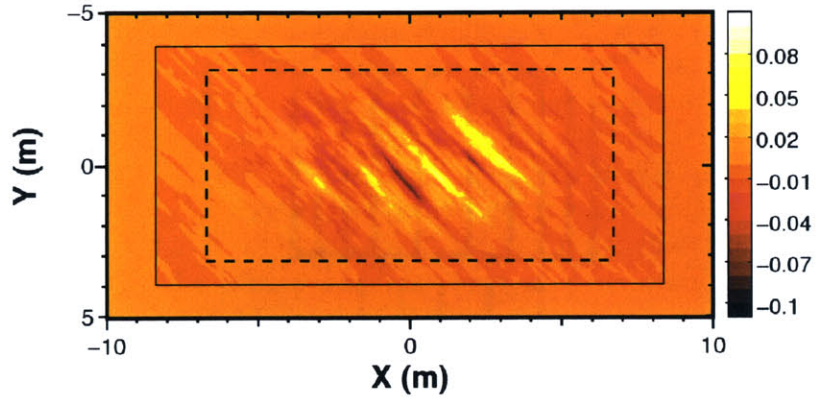

(b) Sonar footprint for $\theta_i = 15°$ case.

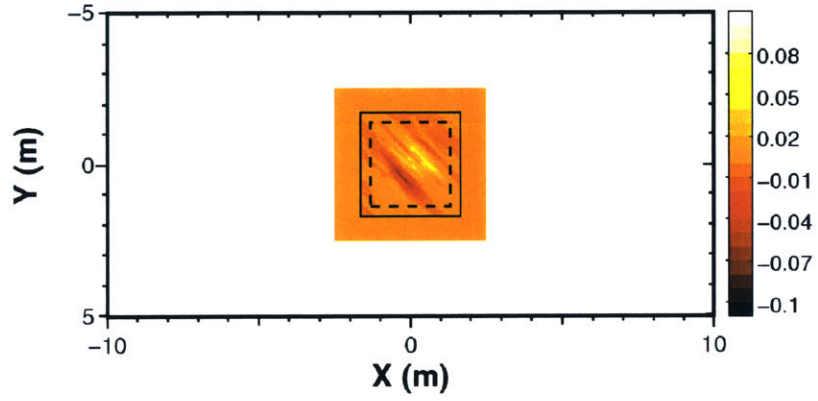

(c) Sonar footprint for $\theta_i = 35°$ case.

Figure 4-9: Sonar footprints for the numerical experiments. Sonar footprints (b) and (c) are obtained from the synthesized roughness patch (a) by applying sonar-footprint-sized 2-D Hanning windows. Roughness is modeled by a Goff-Jordan power spectrum ($C_{L1} = 2m$, $C_{L2} = 0.25m$, $\theta_s = 45°$, $\sqrt{\langle \gamma^2 \rangle} = 3.125cm$, and $D = 2.5$).

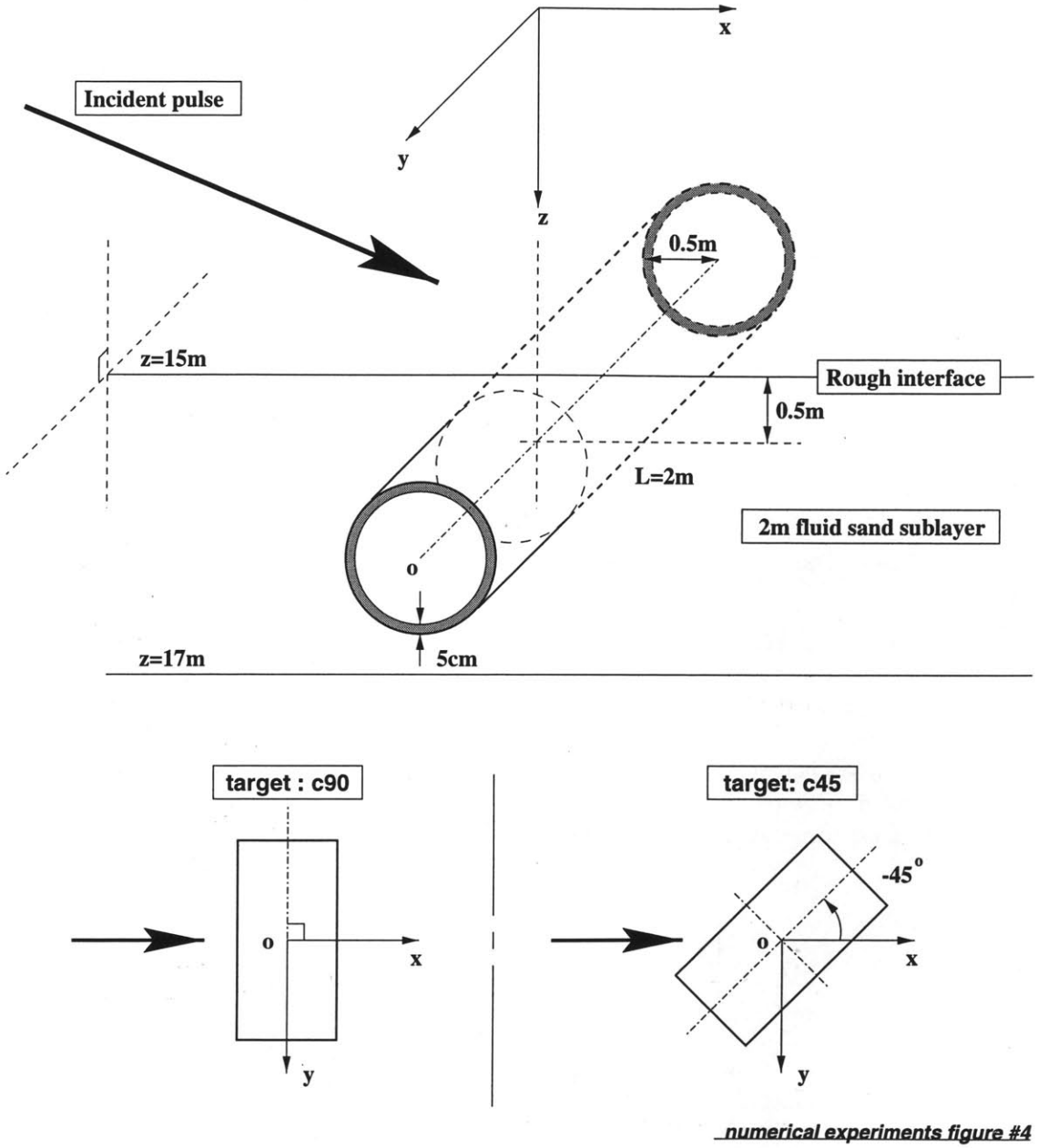

Figure 4-10: Target used in the numerical experimental scenario. The target is a finite cylindrical elastic (steel) shell flush buried in a $2m$ fluid sand layer. The medium properties of the target are $\rho = 7.8g/cm^3$, $C_p = 5200m/s$, and $\nu = 0.333$. Two orientations of the target are considered. $C90$ corresponds to the shell in the broadside ($\theta_{sk} = 90°$) to the incident field while $C45$ is slanted by $\theta_{sk} = -45°$.

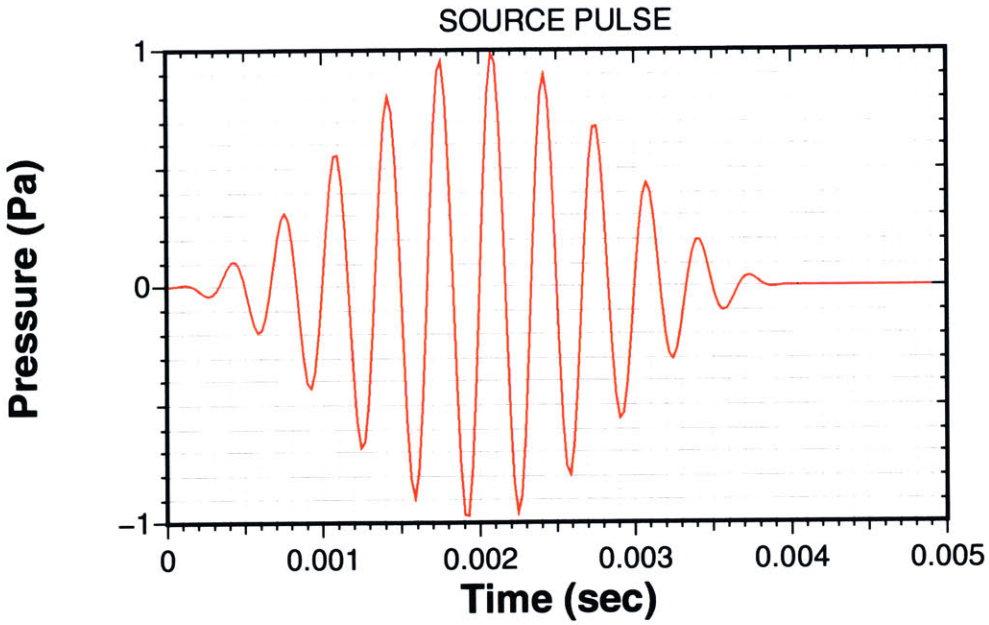

Figure 4-11: The incident pulse. The pulse is a sine wave modulated at $3kHz$ and masked by a Hanning window. The duration of the pulse is $4ms$ and the sampling frequency is $f_s = 40.96kHz$.

4.2 Numerical Results

The numerical experiment designed in the previous chapter does not include the specification of the incident pulse because the time domain solution is obtained by Fourier synthesis of the transfer function (i.e. frequency domain solutions) and the input pulse spectrum. Once the transfer function is computed, any types of input pulses (or spectra) can be used within the Nyquist criterion. In the numerical experiments of this section, the following function will be used to generate incident pulses.

$$P_i(t) = \begin{cases} \frac{1}{2}\sin(2\pi F_c t)\left[1-\cos\left(\frac{\pi}{2}\Delta F\, t\right)\right] & 0 \le t \le \frac{4}{\Delta F} \\ 0 & \text{otherwise} \end{cases}, \tag{4.3}$$

where F_c is the center frequency and ΔF is the bandwidth. This pulse is a sine wave of center frequency F_c and weighted by a Hanning window. The duration of pulse is $4/\Delta F$. Figure 4-11 shows the time series of the input pulse. The center frequency is set at $F_c = 3kHz$ and the bandwidth is $\Delta F = 1kHz$. The number of frequency samples within the band width is 401. The size of corresponding time window is $400ms$, which is long enough to observe scattering events at the receiver position. The distance between the receiver and the center of the target is about $42m$. Considering the pressure-release surface and the multiple interfaces in the bottom structure, the scattering events within the receiver range ($r_R = 40m$) will vanish approximately after $200ms$. Since each frequency domain computation is performed independently, the computation of the transfer function can be done on series of computers in an efficient parallel manner.

Figure 4-12 is the spectrum of the corresponding incident pulse (Figure 4-11). The first nulls coincide with the lower and upper frequency limits ($2.5kHz$ and $3.5kHz$). The pulse spectrum between the lower and upper frequency limits is multiplied by the transfer function of the scattered

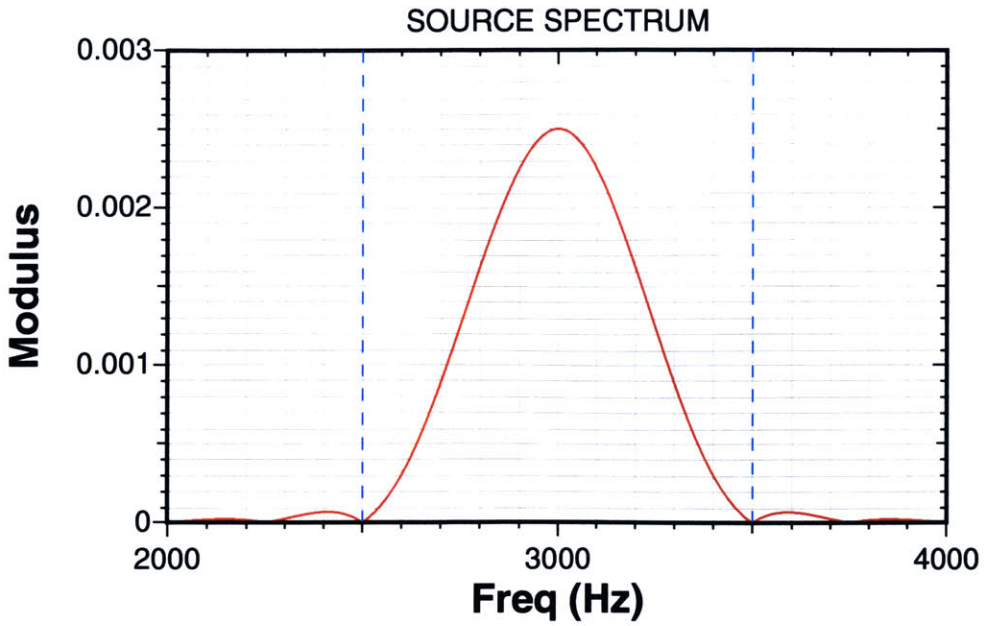

Figure 4-12: Input spectrum of incident wave. The center frequency is $f_c = 3kHz$, the bandwidth is $BW = 1kHz$, and the frequency increment is $\delta f = 2.5Hz$. Dashed lines indicate the lower and upper frequency limits.

field to generate the spectrum of the scattered field. Then, the scattering spectrum is transformed to the time domain solution by inverse FFT.

There are four cases of numerical experiments which are combination of two incident angles ($\theta_i = 15°$ and $35°$) and two target configurations ($C90$ and $C45$). Their numerical results include the time series of acoustical pressure measured at the receiver array shown in Figure 4-6. These time series were examined at four different azimuthal positions of receiver array ($\theta_R = 0°, 90°, 180°$,and $270°$) and one azimuthal position per case is chosen for post-processing. The following subsections will present selected time series and their post-processed results – spectrogram and array beamforming.

A 'spectrogram' is an estimate of the short-term (or temporal) spectral contents of an input time series. Unlike the power spectral density function which covers the entire length of the time series, a spectrogram only shows the temporal spectrum of the signal. It applies a time window on a small region of the time series and performs a Fourier transform to estimate the spectral density. The output is a spectrum as a function of time and frequency. Depending on the size of the time window and the method of Fourier transform, spectrograms show different results.

A 'beamforming' is used in the following subsections to estimate the direction of the scattered wave with respect to the receiver position. The following equations explain the procedure of beamforming in this thesis. First, the time series of elements are transformed to the frequency domain by FFT. To decrease the frequency spacing, zeros can be added at the end of the time series (i.e. zero padding).

$$p_j(t) \xrightarrow{\text{FFT}} \tilde{p}_j(f), \quad j = 1, \ldots, n, \tag{4.4}$$

where n is the total number of channels used in beamforming. Once the Fourier transformed input signals are obtained, their weighted sums are obtained by the following equation. This

formula simply implies the total amount of in-phased components between each channel and the incoming wave from $\phi = \theta_b$ direction. The angle ϕ is defined in Figure 4-6 for a line array. The last exponential term in the equation cancels the channel phases when the beam-angle of the array is equal to the direction of the incoming wave. In that case, the summation yields a maximum value in the frequency domain.

$$\tilde{b}(\theta_b, f) = \sum_{j=1}^{n} w(z_j - z_{ref})\, \tilde{p}_j(f)\, e^{2\pi\imath f (z_j - z_{ref}) \sin(\theta_b)}\, e^{-2\pi\imath f (t_j - t_{ref})}, \tag{4.5}$$

where w is a window function and z_{ref} and t_{ref} are the reference position and time, respectively. With the inverse FFT, the time domain counterpart is obtained as follows :

$$\tilde{b}(\theta_b, f) \xrightarrow{\text{Inverse FFT}} b(\theta, t). \tag{4.6}$$

4.2.1 Case of $C90$, $\theta_i = 15°$, $\theta_R = 180°$

In this case, the target is $C90$, the incident angle is 15°, and the receiver azimuth is 180°. When the target is $C90$, the forward ($\theta_R = 0°$) and backward ($\theta_R = 180°$) scattered fields in the water column are expected to be dominant. For the rough interface scattering part, the forward ($\theta_R = 0°$) and sideway ($\theta_R = 90°$) scattered fields are relatively strong. Therefore, it is most likely to detect the target $C90$ at the backward direction because of a possibly high signal-to-noise ratio (target v.s. rough interface). The numerical results at other angles show that the target signals are overwhelmed by rough interface scattering signals during the entire time window. The receiver at the backward direction receives a target signal which is stronger than the rough interface scattering signal. Figure 4-13 shows the time series corresponding to the scattered signal received on the center channel of array. The overall scattering level from the rough interface is relatively lower than that of the target $C90$ in the backward direction. Therefore, when two scattered fields are combined, the main features of the target can still be found in the time series (i.e. $c90 + p$ of Figure 4-13). A simple geometric calculation shows that the first arrivals of the scattered wave will occur at $t = 54.1ms$, which agrees with Figure 4-13. But, observation of the time series at a specific receiver point does not provide sufficient information about how each scattered wave arrives in the spatial domain.

Figure 4-14 shows three post-processed results from the time series outputs of the receiver array at $\theta_R = 180°$ when only a rough interface is considered. The first plot (Figure 4-14(a)) is the spectrogram of the center channel ($5H$ or $5V$). A peak occurs at $f = 3kHz$ and $t = 58.4m$. Since the duration of the input pulse is $4ms$ and the peak of the input pulse occurs at $t = 2ms$, the peak based on a simple geometric calculation is supposed to occur at $t = 56.1ms$. Thus, this time difference suggests the strongest arrival may not be the direct arrival from the center of the roughness patch. The path of the peak arrival can be found by examining beamforming results from the HLA and VLA segments. Figure 4-14(b) is the beamforming of the HLA segment. The peak angle and time are $\phi_H = 64°$ and $t = 64.0ms$. This peak corresponds to the surface-reflected path from the roughness patch to the receiver. The beamforming corresponding to the VLA segment is shown in Figure 4-14(c). It confirms that the scattered wave is coming from the pressure-release surface. The peak time coincides with the HLA results, but the peak beam-angle (90° – 18°) has approximately an 8° difference compared to the HLA case. Unlike the HLA case, the peak time and angle cannot be matched closely by the geometric calculation. This angular difference can be caused by a relatively small aperture of array ($L/\lambda = 1.6$ at $f = 3kHz$). Since the angular resolution of the line array is proportional to the aperture ratio of the array, there might be

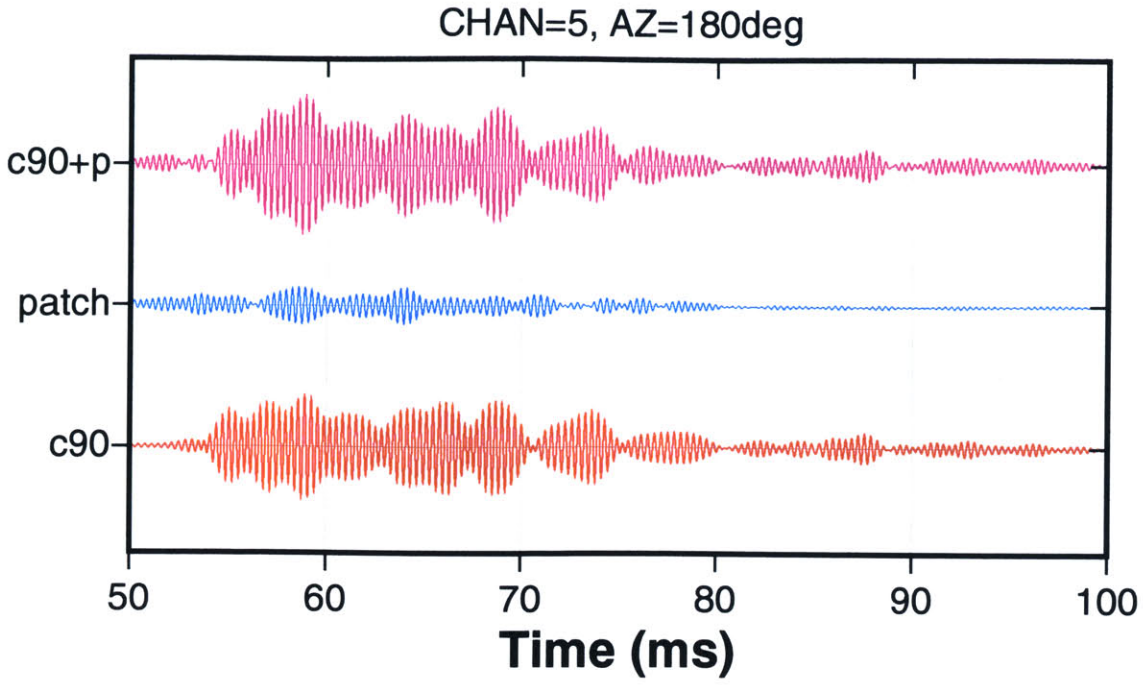

Figure 4-13: Time series received at the center channel ($5H$ or $5V$) from target $C90$ and rough interface (patch) with an incident grazing angle 15°. Azimuth of receiver array is $\theta_R = 180°$. Scales of time series are identical.

wide angular ambiguity for both segments. For this particular case, the HLA segment performs better than the VLA segment based on the geometric calculation of arrival time and angle.

Figure 4-15 shows the post-processed results for target $C90$ only. The spectrogram of the center channel is different from that of the roughness patch case. The peak occurs at a frequency higher than the patch case and the duration of scattered field is relatively longer than of the patch case. The most interesting results can be found in the beamforming plots of the HLA and VLA. Figure 4-15(b) is the beamforming of the HLA segment. The peak arrival occurs at $\phi_H = 50°$. Considering that the scattered waves are originating from the fluid sublayer, the scattered wave may have a path within the sublayer. Indeed, the geometric calculation matches the peak time and angle by taking a pressure-release surface-reflected path including a sub-bottom reflected path from the target to the water-sand interface. VLA beamforming (Figure 4-15(c)) confirms that the scattered wave is coming from the pressure-release surface. Compared to the case of the roughness patch, the angular difference between the HLA and VLA beamforming becomes smaller (6.5°). But, their peak times have an $1.8ms$ difference. In the VLA beamforming plot, a local peak can be located near $t = 59ms$. In addition to the previous hypothesis for this angular difference between the HLA and the VLA, this might be caused by the pressure-release surface. Unlike the HLA segment, the elements of the VLA segment are located at the different depths where the interference pattern in the depth direction rapidly changes because of the pressure-release surface. This effect may cause the degradation of the VLA performance and consequently produce an incorrect peak time and angle.

Figure 4-16 shows the arrival structure of rough interface and target $C90$ scattering. As previously mentioned, the HLA beamforming results agree with the simple geometric estimation of the peak arrivals. This figure shows the incident and scattering paths for a rough interface and a target

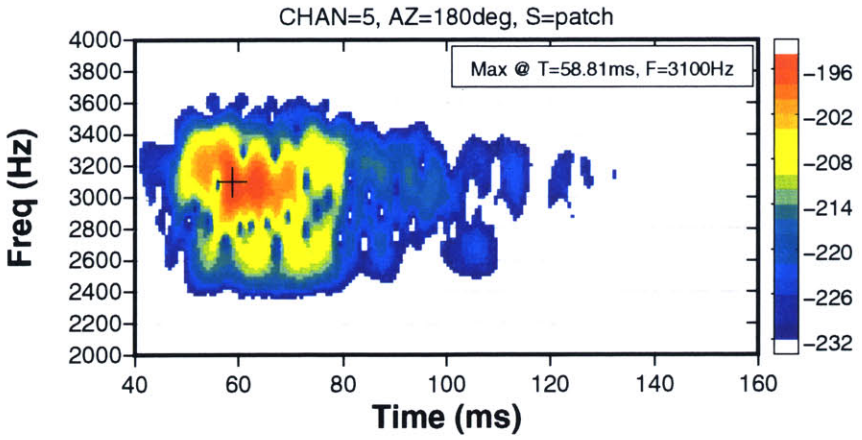

(a) Spectrogram of center channel.

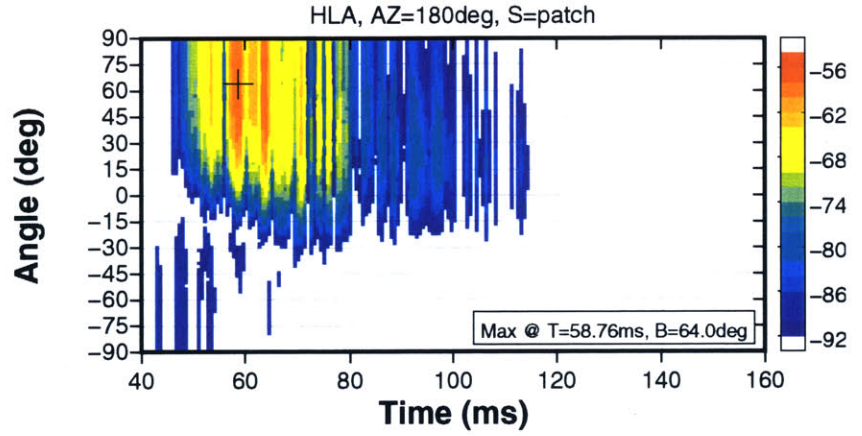

(b) Beamforming of HLA segment.

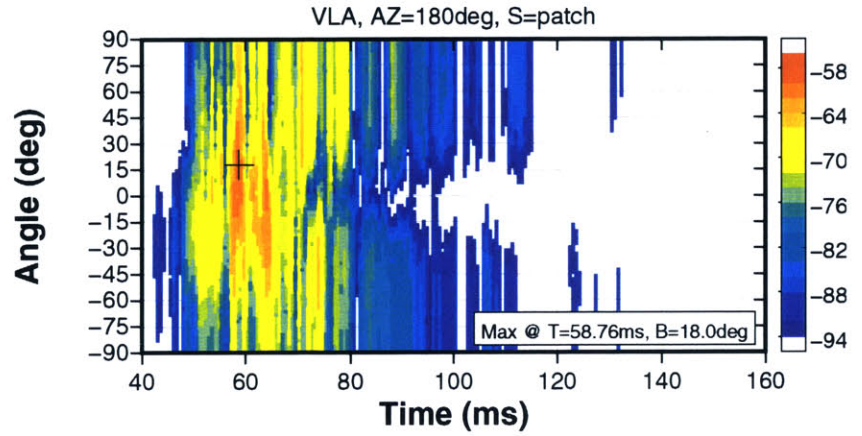

(c) Beamforming of VLA segment.

Figure 4-14: Patch : backward scattering (θ_R = 180°) configuration. Nominal incident angle θ_i is 15°.

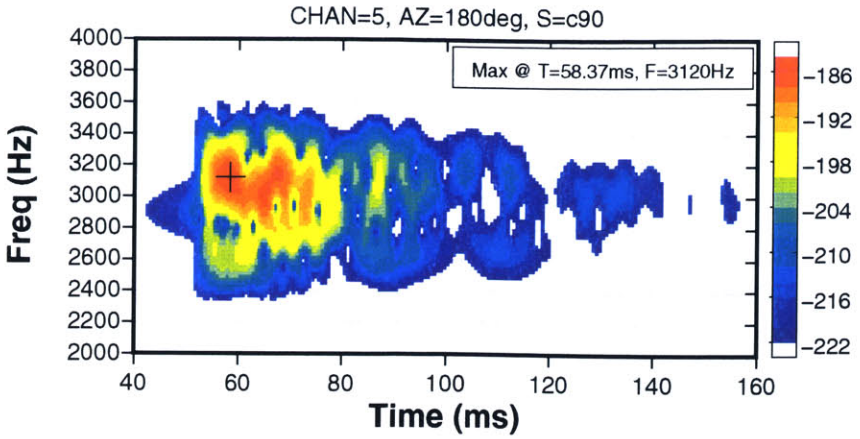

(a) Spectrogram of center channel.

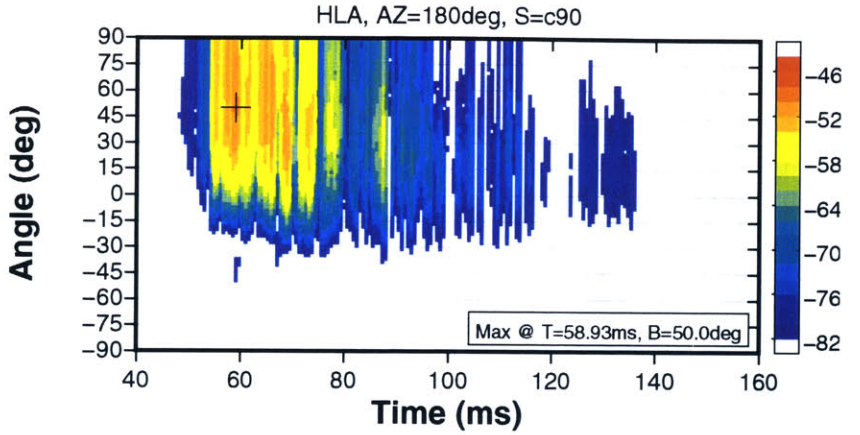

(b) Beamforming of HLA segment.

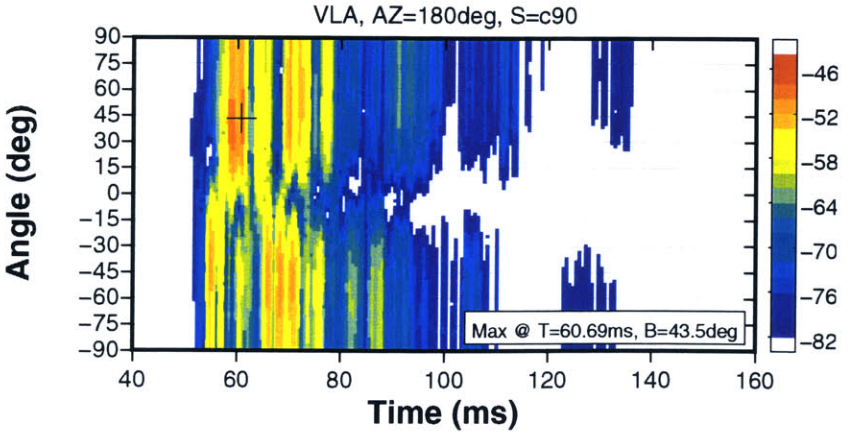

(c) Beamforming of VLA segment.

Figure 4-15: Target $C90$: receiver array at $\theta_R = 180°$. Nominal incident angle θ_i is 15°.

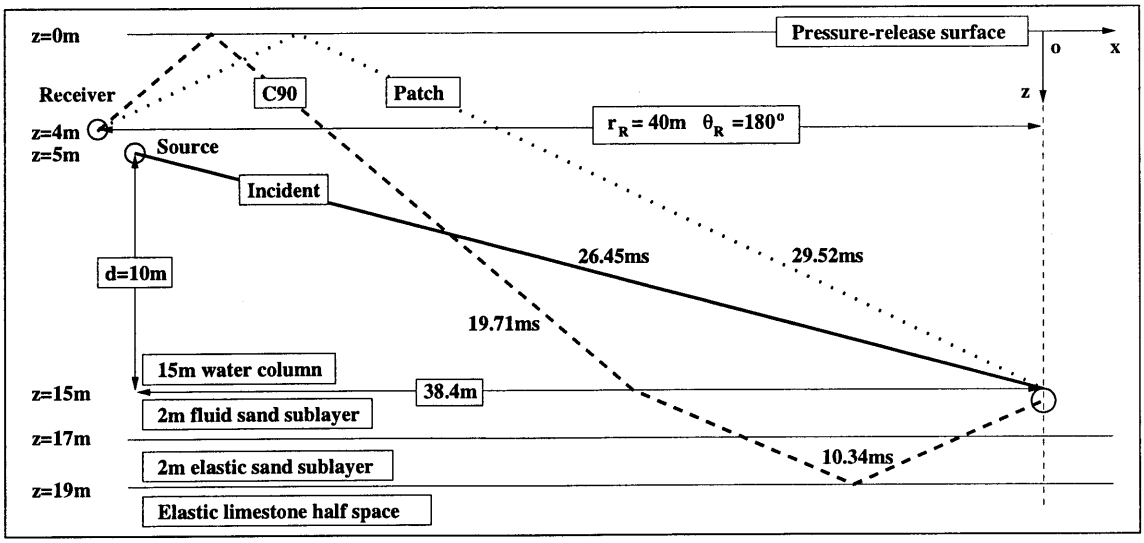

Figure 4-16: Arrival paths of scattered waves – rough interface scattering and target $C90$ scattering in the backward direction. Arrival angles are provided by the HLA beamforming shown in Figure 4-14(b) and Figure 4-15(b).

$C90$ in the backward direction. Travel times in the plots also agree closely with the beamforming results. The most interesting scattering path is the one for the target $C90$. With the grazing angle 50° estimated from the HLA beamforming, the scattered wave can be traced back to the source position with small error. The target scattering takes the following path. First, the direct scattered wave from $C90$ penetrates into the elastic sublayer without any change in angle. Then, it is reflected from the elastic sand and limestone interface. Once it reaches the water and fluid sand interface, it changes the grazing angle according to Snell's law and heads toward the pressure-release surface. Then, the reflected wave from the pressure-release surface arrives at the receiver. The estimated arrival time error between the geometric calculation and the HLA beamforming results is approximately $0.4ms$, which is only 10% of the input pulse duration. Unlike the target $C90$, the HLA beamforming results for rough interface scattering do not agree accurately with the geometric calculation of arrival time and angle. The arrival time error is about $0.8ms$, twice as long as the target case. This larger time error is caused by the following fact. While the target scattering signal is originated from a point, the rough interface scattering signal is generated by a patch of finite area. In other words, the arrival seen on the HLA beamforming results for the roughness patch scattering is made of contributions from distributed sources. Therefore, the peak point may not be predicted accurately by a simple geometric calculation.

Figure 4-17 shows the post-processed results when the contributions from the roughness patch and the target $C90$ are combined. The spectrogram of the center channel (Figure 4-17(a)) is similar to the case of target $C90$. While the peak frequency is same as the target $C90$ case, the peak time moves toward that of the roughness patch case. The HLA beamforming results (Figure 4-17(b)) show a shift in peak angle toward the case of roughness patch. This trend is caused by the interference between the scattered waves from the rough interface and the target $C90$. Since their incoming angles at the HLA location are different ($\phi_H = 64°$ and $\phi_H = 50°$), there are destructive and constructive interferences on each element of the HLA segment resulting in the shift in peak angle. Because the arrival time for the roughness patch case and the target case are so close ($< 0.2ms$), the peak time in the HLA beamforming results does not change. The change of peak

angle causes an error in locating the target. The location of the target computed by the changed peak angle becomes $41.5m$ in range away from the center element and $3.15m$ in depth from the water – sand interface which results in $3m$ of range error. The VLA beamforming results (Figure 4-17(c)) also shows the shift in peak angle toward the roughness patch case. Adding the rough interface reverberation to the target scattering causes incorrect estimation of the target location by changing the interference patterns received by an array. This effect is more noticeable if the arrival times of the reverberation signal and the target scattering signal are within a small time frame such as in the present case.

4.2.2 Case of $C45$, $\theta_i = 15°$, $\theta_R = 270°$

The target $C45$ produces the dominant scattered field in forward ($\theta_R = 0°$) and sideway ($\theta_R = 270°$) directions. With the roughness patch shown in Figure 4-9(b) and the incident angle $\theta_i = 15°$, the target is most likely to be detected at the bistatic angle $\theta_R = 270°$. The time series of the target and the roughness patch show that a relatively high signal-to-noise ratio for the target $C45$ is observed at $\theta_R = 270°$. Therefore, this bistatic angle is chosen to analyze the time series of the scattered field. Figure 4-18 shows the time series at the center channel of the receiver array. The first arrival time of the scattered wave agrees well with the geometric calculation ($t = 53.9ms$).

Figure 4-19 shows the post-processed results of the roughness patch scattering contribution at $\theta_R = 270°$. The spectrogram of the center channel (Figure 4-19(a)) shows a peak at a frequency higher than that of the backward receiver position case (Figure 4-14(a)). The peak time is also different from the backward case. This suggests that the sideway scattered waves might be originated differently from the roughness patch. The peak time and angle of the HLA beamforming results (Figure 4-19(b)) agree well with those of the VLA beamforming results (Figure 4-19(c)). By using the peak angle of the VLA beamforming results, a possible path of the scattered wave is estimated in Figure 4-20. This path shows that the scattered wave leaves the roughness patch to the pressure-release surface at the left edge of the roughness patch (i.e. $y = -5m$ or edge in $\theta_R = 270°$ direction). Then, it is reflected on the pressure-release surface and travels to the receiver position. The estimated travel time is $58.4ms$ which is $1ms$ earlier than the peak time found in the beamforming results of the VLA segment. This time difference might be explained by the following hypothesis. It may take time for the incident wave to interact with the roughness patch before the scattered wave is fully developed.

Figure 4-21 shows three post-processed results for the target $C45$ at the azimuth $\theta_R = 270°$. The beamforming results of the HLA and VLA segments (Figure 4-21(b) and Figure 4-21(c)) show two peaks (i.e. $t = 57ms$ and $59ms$) in the time series (Figure 4-18), respectively. Because the peak arrival time in the beamforming results of the VLA segment is very close to that of the roughness patch scattering arrival and its signal level is not high enough, it will be difficult to differentiate the target signal from the roughness patch signal in this time frame. But, the peak point near $t = 57ms$ can be separated from the roughness patch signal because the time separation is long and its incoming angle is quite different from that of the roughness patch signal. The beamforming results of the VLA segment confirm that the peak at $t = 57ms$ is coming from the bottom. With the angle from the beamforming results of the HLA segment ($\phi_H = 53.5°$), a possible target scattering path is traced back to the target $C45$ in Figure 4-20. The scattered wave moves to the interface between the elastic sand sublayer and the elastic limestone half space. It is reflected and transmitted through the water–sand interface. Then, it propagates to the receiver array. The estimated arrival time is $55.3ms$, which is $1.7ms$ earlier than the peak time in the beamforming results of the HLA segment. This time difference can be caused by a slight error in estimating arrival angles. Even with the error in estimating arrival time, the arriving sequence of roughness

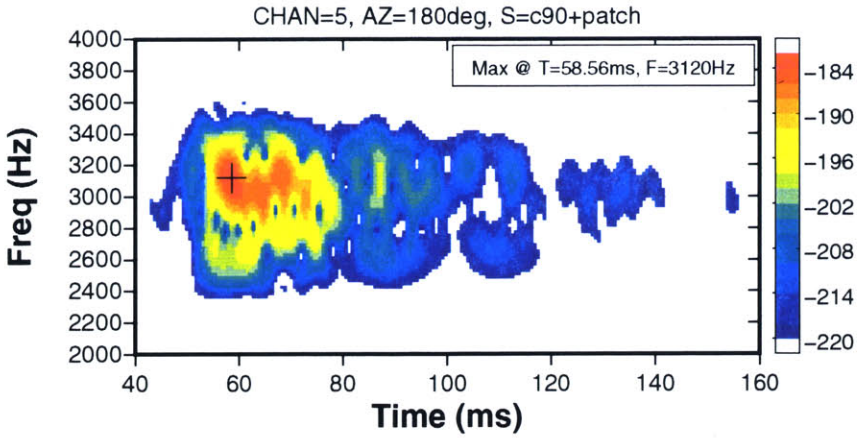

(a) Spectrogram of center channel.

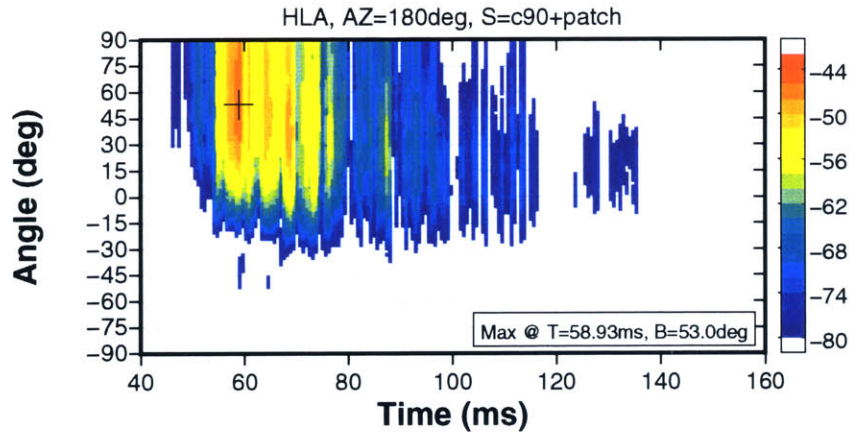

(b) Beamforming of HLA segment.

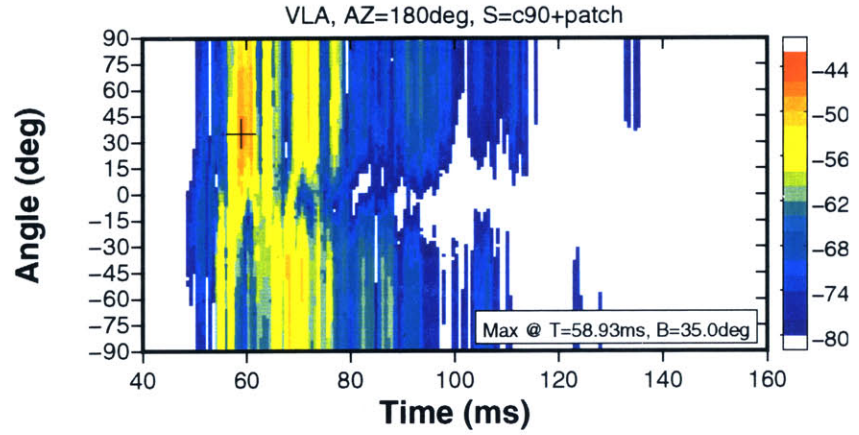

(c) Beamforming of VLA segment.

Figure 4-17: Target $C90$ + Patch : receiver array at $\theta_R = 180°$. Nominal incident angle θ_i is 15°.

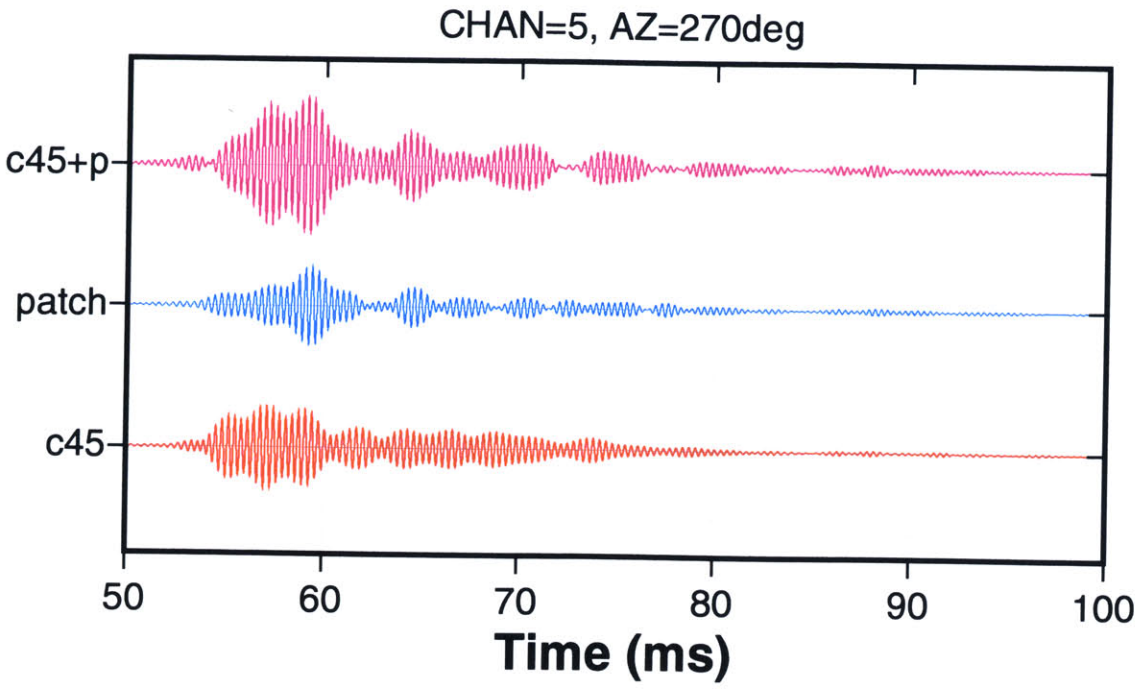

Figure 4-18: Time series received at the center channel from target $C45$ and rough interface (θ_R = 270°). Nominal incident angle θ_i is 15°.

patch scattering and target scattering is preserved.

Figure 4-22 shows the post-processed results when the signals from the target $C45$ and the roughness patch are combined. Because the roughness patch scattering is strong, the post-processed results are similar to the results of roughness patch only. Even though the beamforming results of the HLA (Figure 4-22(b)) clearly include the contribution from the target signals near $t = 55ms$ and $t = 57ms$, it is difficult to locate the target. The reason is that there is no information to determine whether the incoming scattered wave is coming from the pressure-release surface or the bottom interface. But, with the information from the VLA segment, the location of the target might be found. The beamforming results of the VLA (Figure 4-22(c)) give a clue to locate the target by providing a high-valued point near $t = 55ms$ and $\phi_V = -45°$, which is not observed in the beamforming results for the case of roughness patch only. This suggests that all the high-valued points in the beamforming results should be examined in order to find the targets. The maximum point may not correspond to a target when there is a background reverberant field.

4.2.3 Cases of $C90$, $\theta_i = 35°$, $\theta_R = 90°$ and $C45$, $\theta_i = 35°$, $\theta_R = 90°$

In the following two numerical experiments, the incident grazing angle becomes $\theta_i = 35°$. The major difference from the previous cases is that the incident angle is steeper than the critical angle of water and fluid sand. Therefore, bottom penetration by the incident wave is strong and consequently the target excitation is high. Compared to the scattered field caused by the roughness patch (Figure 4-9(c)), the scattered field caused by either $C90$ or $C45$ is dominant in most azimuthal angles. In order to demonstrate the capability of a receiver array in the worst situation where the reverberant field is relatively strong, the azimuthal angle $\theta_R = 90°$ is chosen for post-processing purposes. In the direction of $\theta_R = 90°$, the anisotropic roughness patch (Figure 4-9(c))

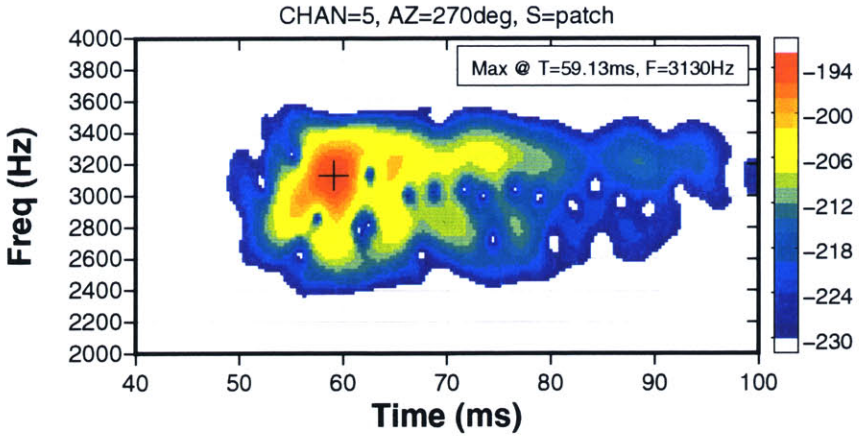

(a) Spectrogram of center channel.

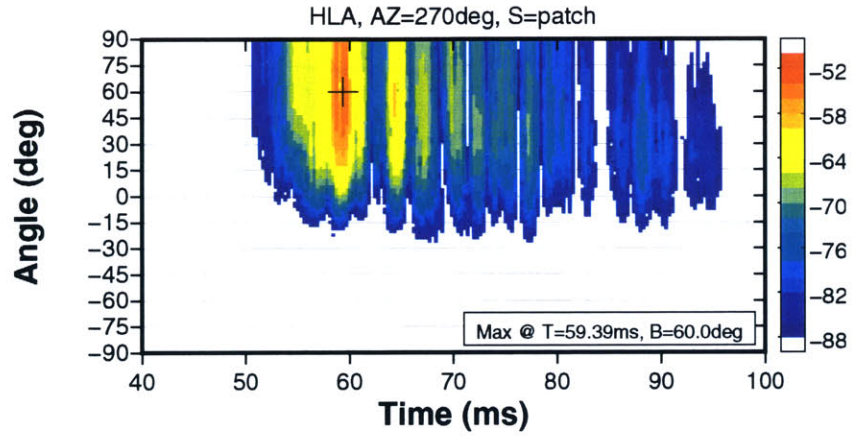

(b) Beamforming of HLA segment.

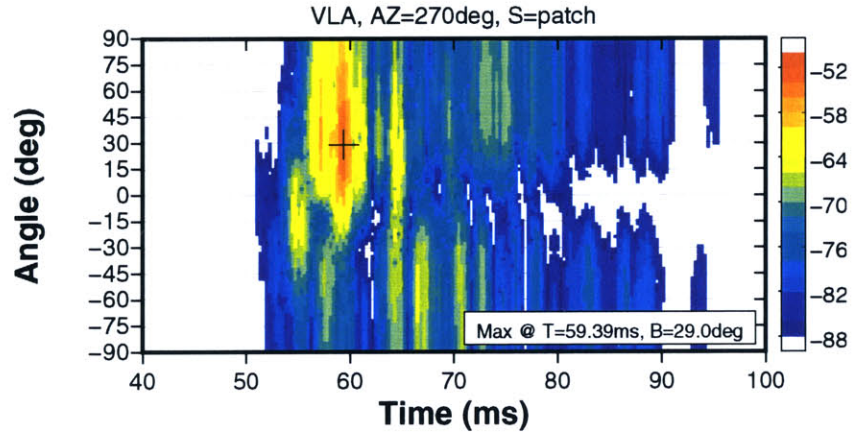

(c) Beamforming of VLA segment.

Figure 4-19: Patch : receiver array at $\theta_R = 270°$. Nominal incident angle θ_i is 15°.

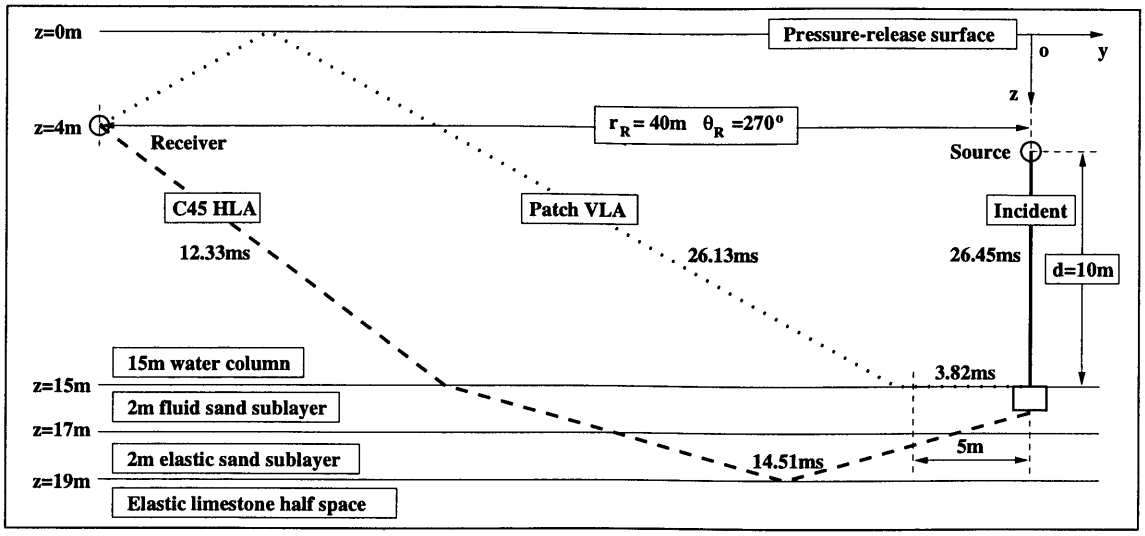

Figure 4-20: Arrival paths of scattered waves – rough interface scattering and target *C*45 scattering in the sideway direction. Arrival angle of roughness patch is provided by the VLA beamforming shown in Figure 4-19(c) while the angle for the target *C*45 comes from Figure 4-21(b).

produces the major out-of-plane scattered field. Figure 4-23 shows the time series corresponding to the scattered fields from the roughness patch, the target *C*90, and *C*45 at the azimuth $\theta_R = 90°$. Because the range from source to the center of the patch is closer than in the previous case, the arrival time of the first signal is sooner ($t = 37ms$).

Figure 4-24 shows the post-processed results of the scattered field caused by the roughness patch. Compared to the case when the incident angle is 15°, the spectrogram (Figure 4-24(a)) shows many local peaks. Also, those peaks come as pairs in time, which suggests the existence of a modal structure in the sub-bottom. The modal structure in the sub-bottom is made possible because of supersonic incidence. This is also confirmed by the slight angle change between two adjacent local peaks of the beamforming results (Figure 4-24(b) and Figure 4-24(c)). By using the peak angle shown in the beamforming results of the VLA segment, a path of the scattered wave is drawn in Figure 4-25.

The arrival path of the scattered wave shows that the scattered wave leaves the interface at the left edge of the roughness patch. Then, the scattered wave is reflected on the pressure-release surface and propagates to the receiver array. According to the beamforming results of the VLA segment, other minor peaks arrive at the receiver array with relatively shallow grazing angles (< 30°) from the pressure-release surface.

Figure 4-26 shows the post-processed results for the target *C*90. At this azimuthal angle, the target *C*90 produces the minimum scattered field. The spectrogram of the center channel (Figure 4-26(a)) has its peak frequency close to the center frequency of the source pulse. Compared to the case of *C*90 with $\theta_i = 15°$, the duration of the target echo becomes longer and the target signal includes multiple local peaks. This suggests that there is an interaction between the scattered wave and the waveguide or sublayers. The beamforming results of the HLA and VLA segments (Figure 4-26(b) and Figure 4-26) also show multiple arrivals from the target *C*90. Because the arrival structure of the target signal is complicated, it is difficult to find the path of a scattered wave by the peak angles and times from the beamforming results. The only obvious path is the direct path from the top of the target to the receiver array. This path is confirmed by the negative

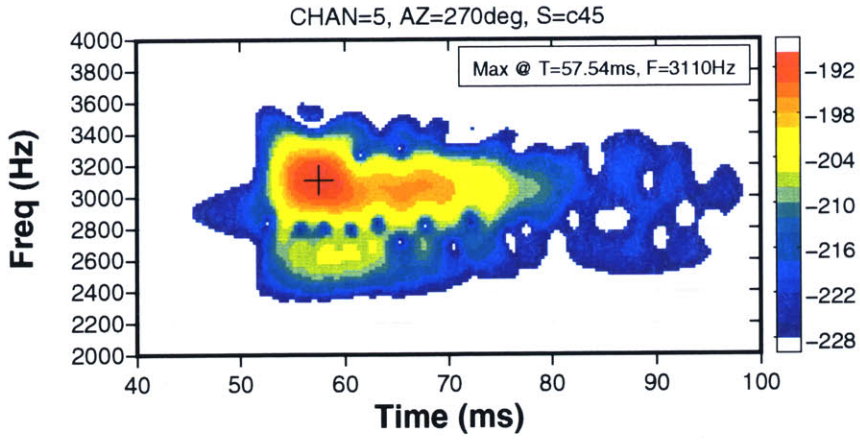

(a) Spectrogram of center channel.

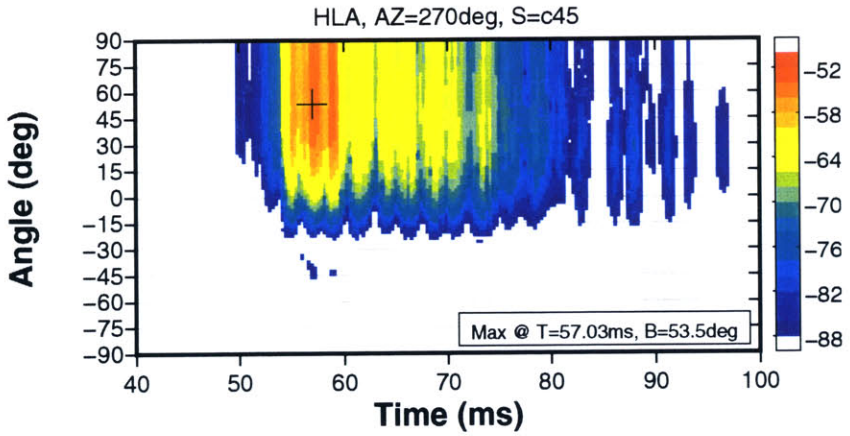

(b) Beamforming of HLA segment.

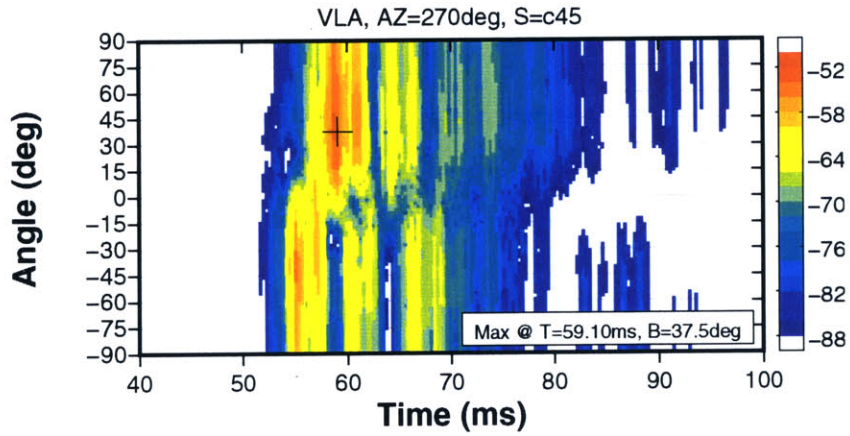

(c) Beamforming of VLA segment.

Figure 4-21: Target $C45$: receiver array at $\theta_R = 270°$. Nominal incident angle θ_i is 15°.

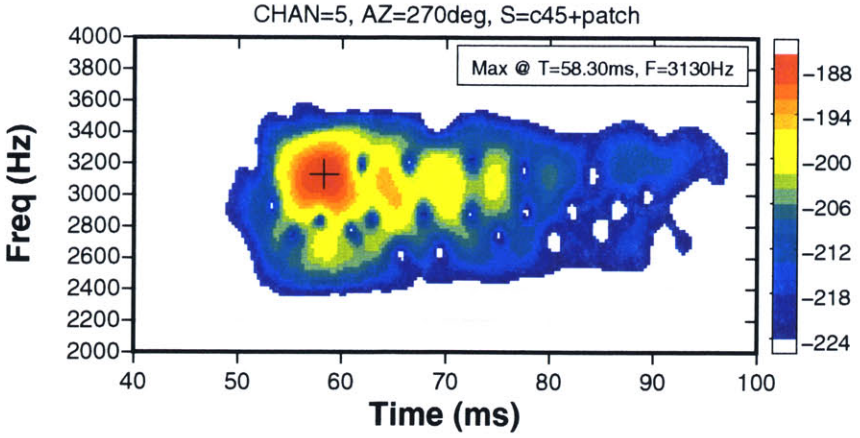

(a) Spectrogram of center channel.

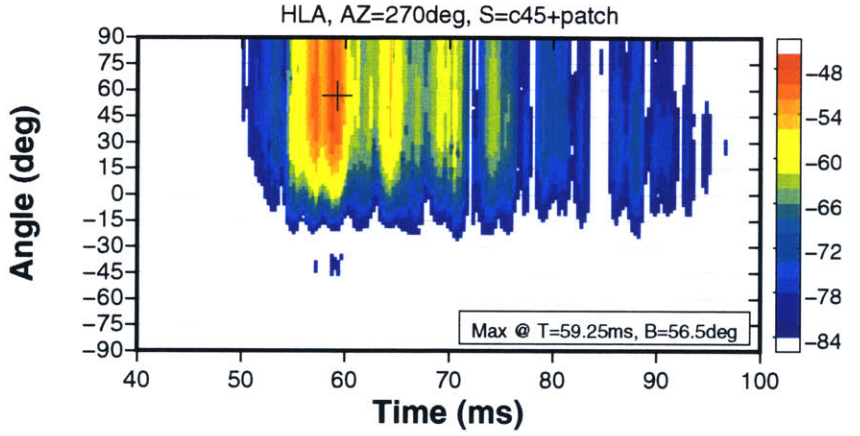

(b) Beamforming of HLA segment.

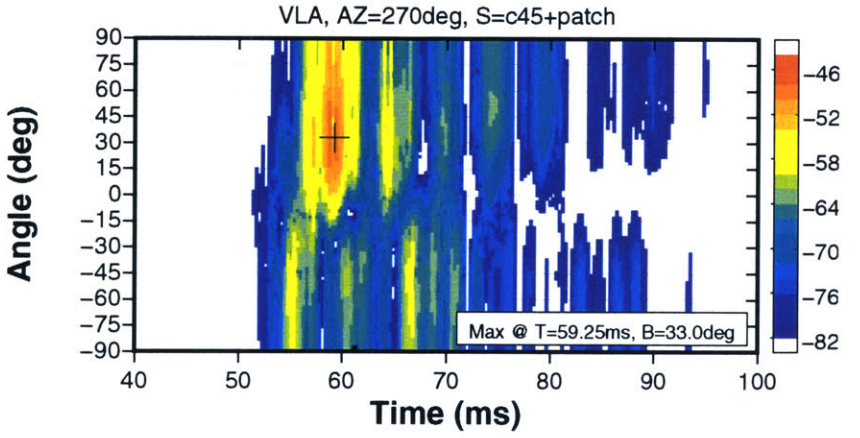

(c) Beamforming of VLA segment.

Figure 4-22: Target $C45$ + Patch: receiver array at $\theta_R = 270°$.

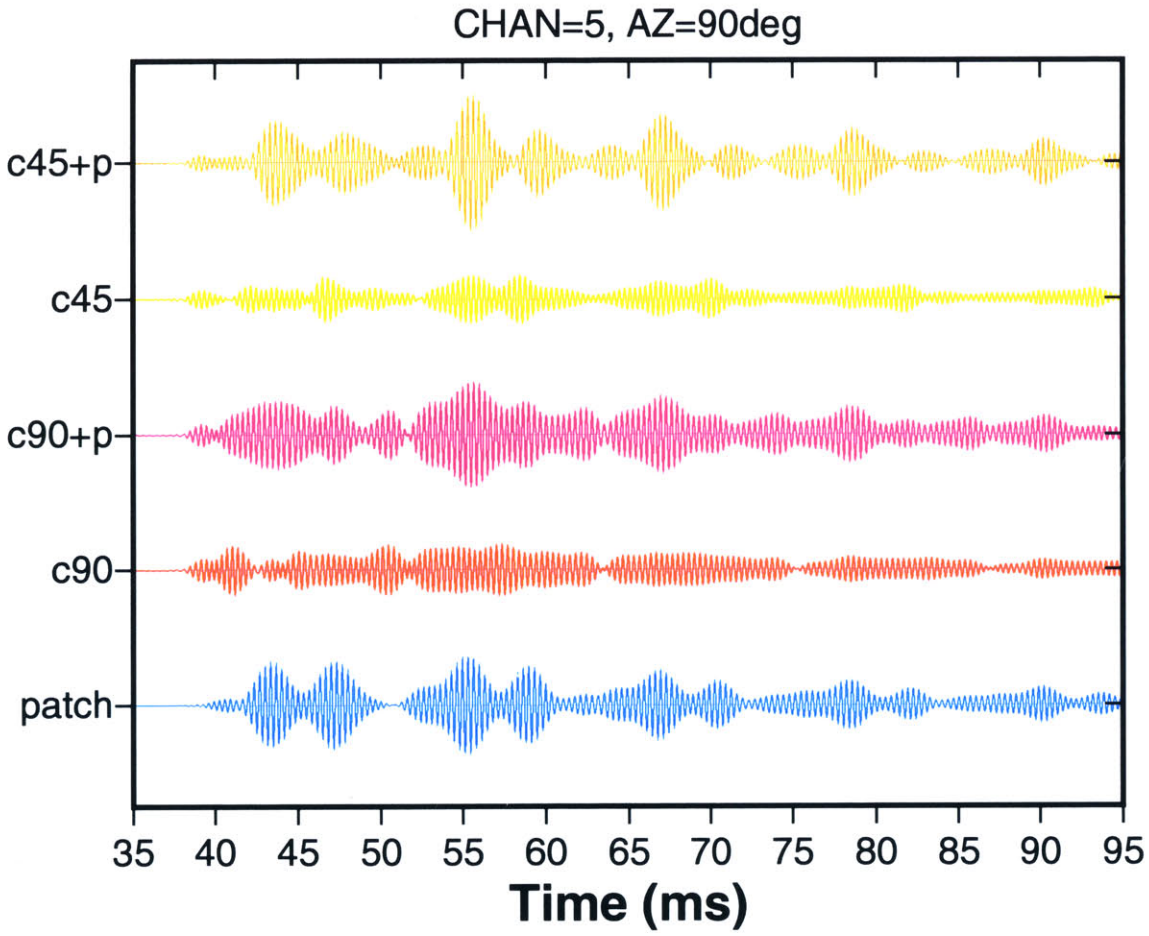

Figure 4-23: Time series received at the center channel from targets $C90$, $C45$, and rough interface. Array azimuth is $\theta_R = 90°$.

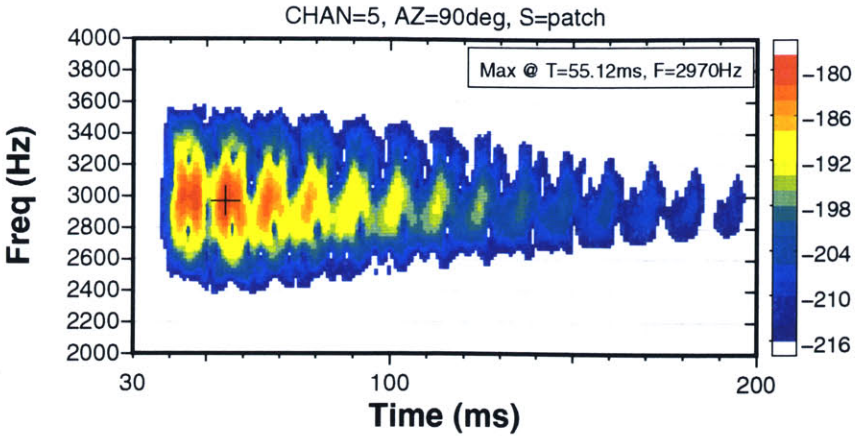

(a) Spectrogram of center channel.

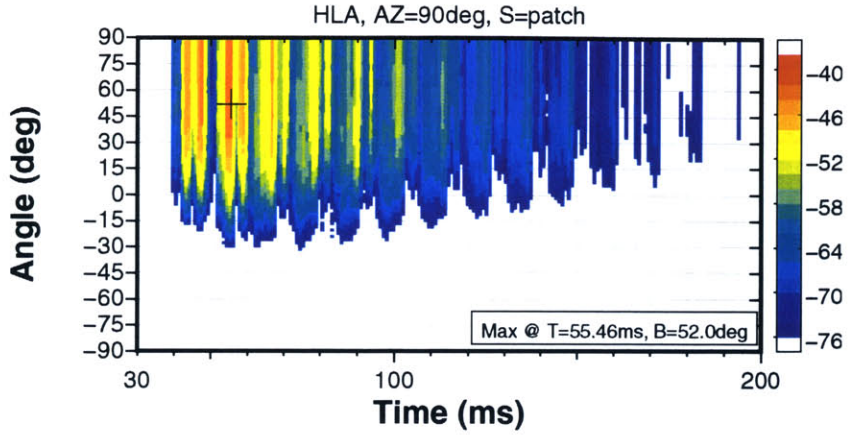

(b) Beamforming of HLA segment.

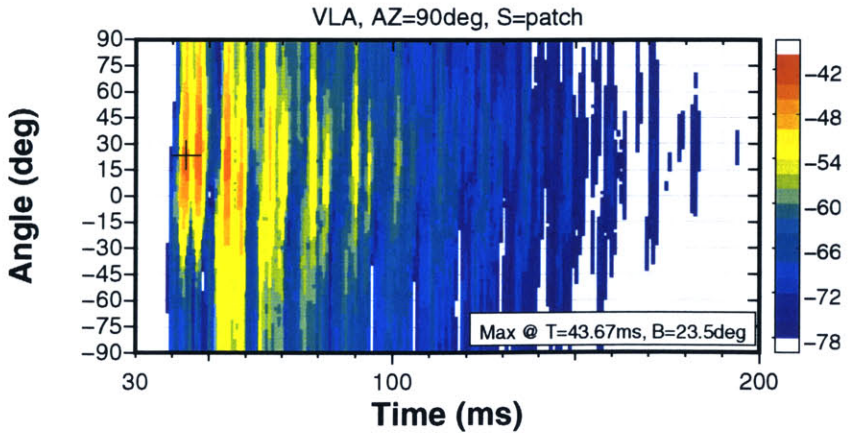

(c) Beamforming of VLA segment.

Figure 4-24: Patch : receiver array at $\theta_R = 90°$.

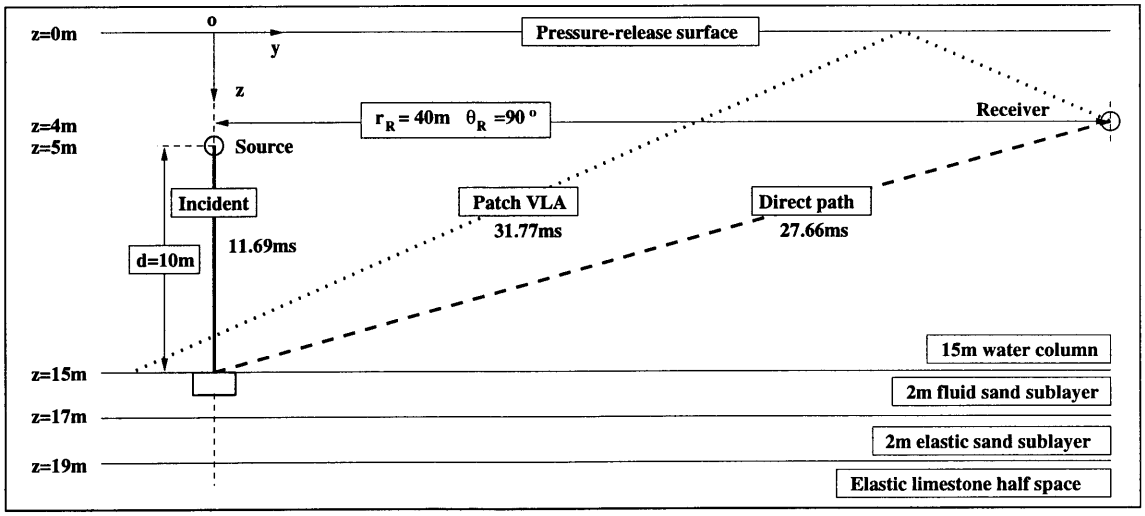

Figure 4-25: Arrival paths of scattered waves – rough interface scattering and target scattering in out-of-plane direction ($\theta_R = 90°$). The beam-angle from Figure 4-24(c) ($\phi_V = -39.5°$) is used to trace the path for the roughness patch. The path for the target signal is a direct path from the target to the receiver.

beam-angle at $t = 41ms$ in Figure 4-26(c). This time also corresponds to the time for the direct scattered wave from the target. The major difference between the case of the roughness patch and that of the target $C90$ is that the beamforming results of the VLA segment for $C90$ has multiple peaks with negative beam-angles.

Figure 4-27 shows the beamforming results of the receiver array for the case of the target $C90$ with the roughness patch. Overall, the reverberant field dominates the beamforming results and it is extremely difficult to locate the peaks from the target. But, the beamforming results of the VLA segment clearly show the direct arrival of the target signal at $t = 41ms$ with a negative beam-angle. As previously mentioned, some portion of target signals arrive at the receiver with negative beam-angles while the signals from the roughness patch have positive beam-angles. Therefore, the negative beam-angle provides an evidence that the signal originates from the target.

Figure 4-28 shows the post-processed results for the target $C45$. Compared to the spectrograms for the other cases, the spectrogram for $C45$ (Figure 4-28(a)) has a significant amount of energy (corresponding to the scattered signal) concentrated in the upper half of frequency band ($3.0kHz < f < 3.5kHz$). The beamforming results of the HLA and VLA segments show that the peaks are coming as pairs with a slight change in arrival angle and time. The most distinguishable peak is found at $t = 56.34ms$ and $\phi_V = -44.5°$ in Figure 4-28(c). Since the scattered field produced by the roughness patch does not have peaks near this peak, it likely provides the clue to find the target signal when the target signals are summed with the reverberant signals.

Figure 4-29 shows the beamforming results of the HLA and VLA segments for the target $C45$ with the roughness patch. Both beamforming results clearly show their peaks at the same position. According to the beamforming results of the VLA segment for the target only case, this peak corresponds to the target signal from the bottom direction. Even though the time series for this target have relatively low levels compared to those for the roughness patch, the beamforming results can clearly differentiate the target signal from the reverberant background. The path of the target signal with the peak value from the beamforming results is difficult to be traced back to the target position by a simple geometric calculation because of the multiple paths of the scattered

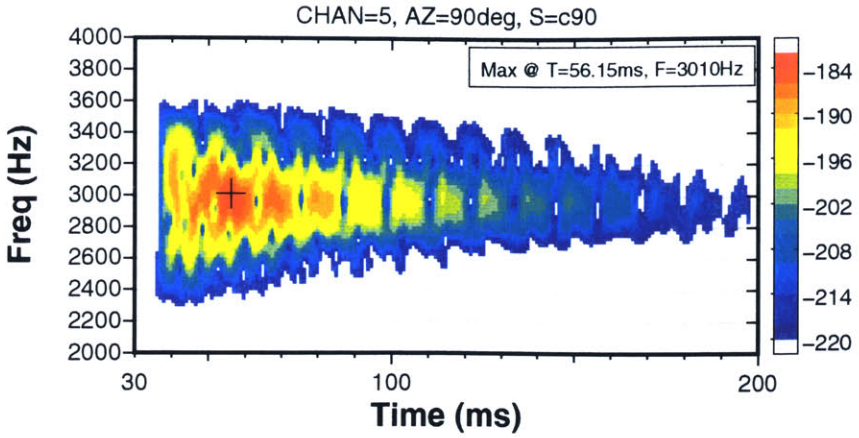

(a) Spectrogram of center channel.

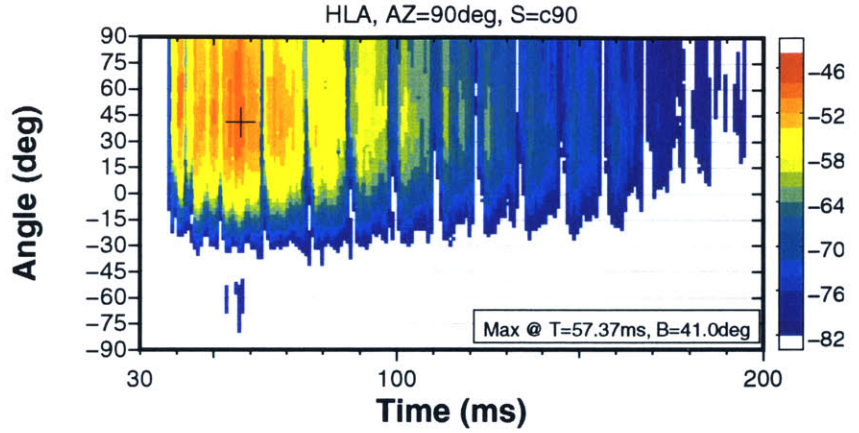

(b) Beamforming of HLA segment.

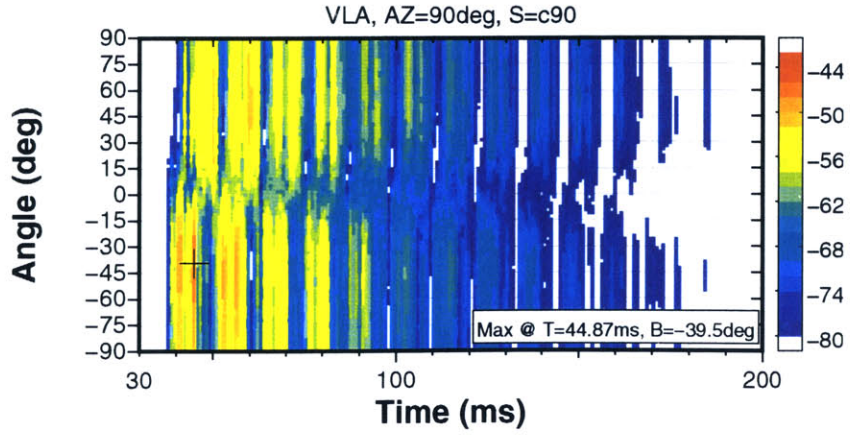

(c) Beamforming of VLA segment.

Figure 4-26: Target $C90$: receiver array at $\theta_R = 90°$.

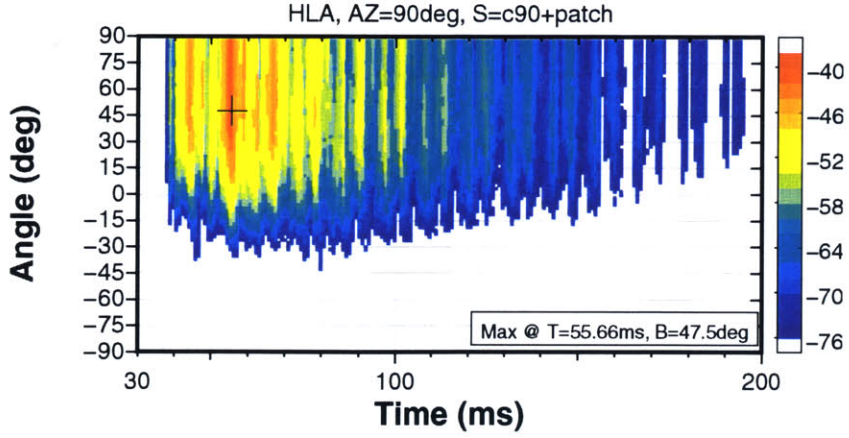

(a) Beamforming of HLA segment.

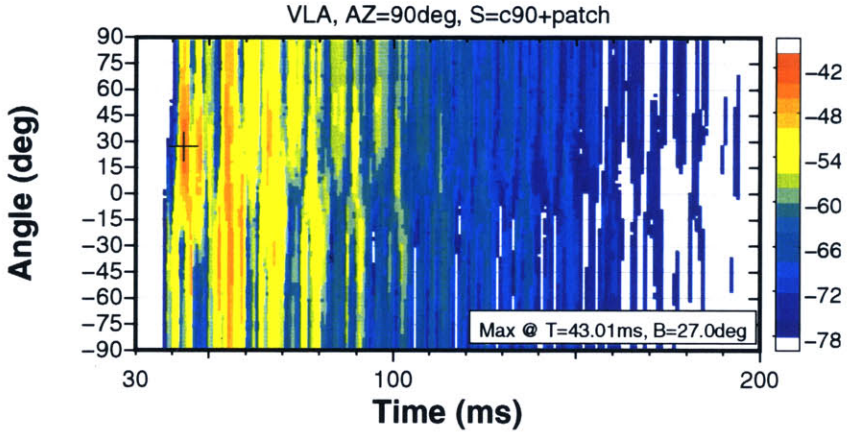

(b) Beamforming of VLA segment.

Figure 4-27: Target $C90$ + patch : receiver array at $\theta_R = 90°$.

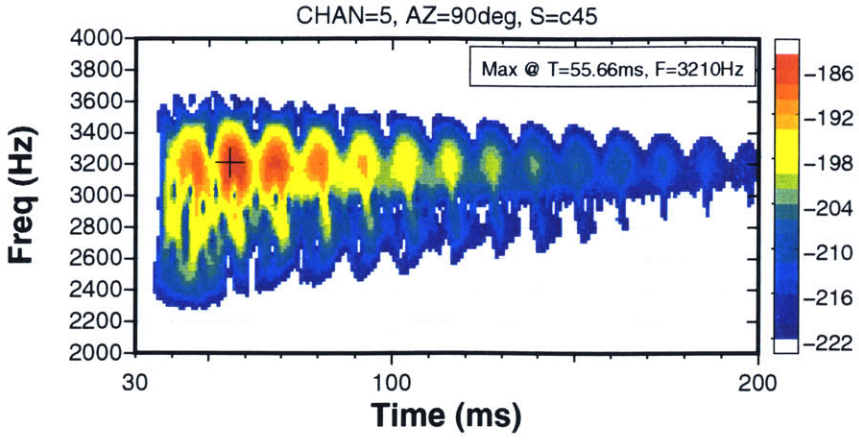

(a) Spectrogram of center channel.

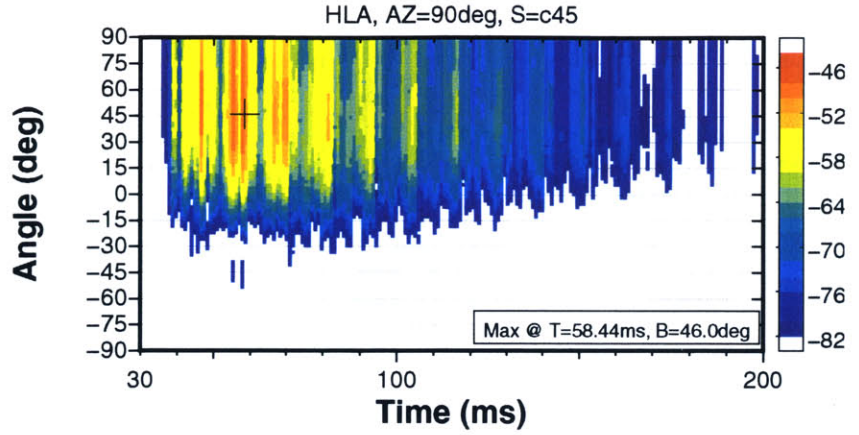

(b) Beamforming of HLA segment.

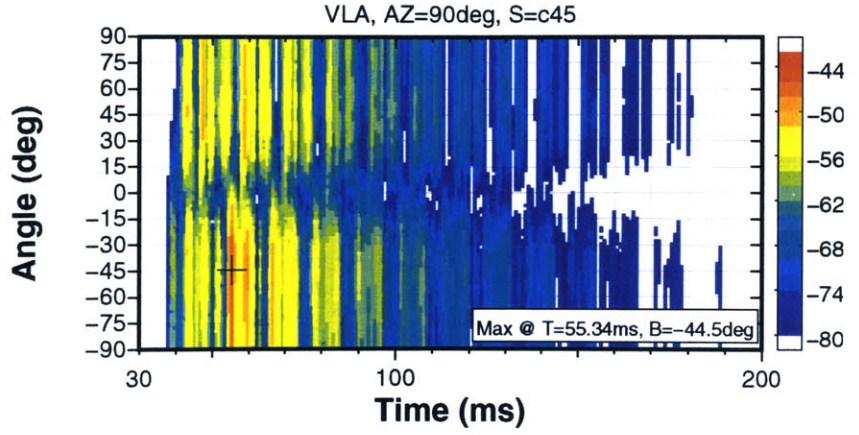

(c) Beamforming of VLA segment.

Figure 4-28: Target $C45$: receiver array at $\theta_R = 90°$.

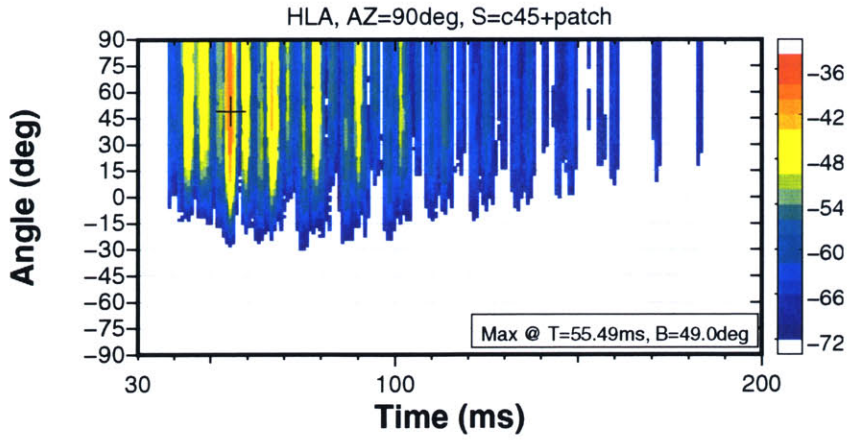

(a) Beamforming of HLA segment.

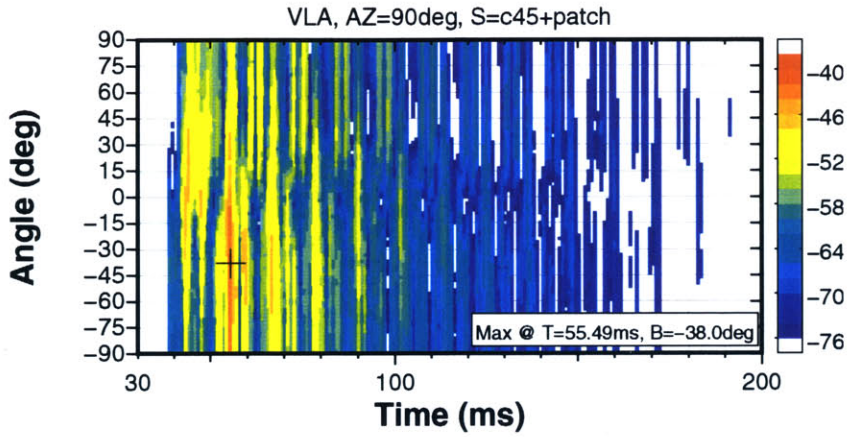

(b) Beamforming of VLA segment.

Figure 4-29: Target $C45$ + patch : receiver array at $\theta_R = 90°$.

waves.

Chapter 5

Conclusion

5.1 Model

In this thesis, two scattering theories were combined into a consistent numerical model framework and used to investigate the physics of seismo-acoustic scattering in a waveguide. Specifically, rough interface scattering and target scattering were considered. Various environmental complexities were investigated such as multiple layers, each scattering theory treats a scatterer as a distributed source function or a point source. Since scattering is an inherent 3-D phenomenon, the numerical models were developed to include 3-D aspects of scattering. In order to incorporate each scattering component in a common environment, they were integrated with the same propagation model – 3-D OASES. Benchmarks were performed to validate the numerical models. An integrated numerical simulator has been developed to simulate multi-static scattering scenarios.

5.1.1 Rough Interface Scattering

In this thesis, the method of small perturbation was combined with the wavenumber representation of scattering phenomena to model rough interface scattering in a multi-layered environment. The method of small perturbation was selected to take advantage of numerical Green's functions provided by the wavenumber integration technique. The numerical Green's function is essential to represent multi-layered environment in an efficient way. By using the perturbation of boundary conditions, the formulation of an equivalent forcing term was derived in the spectral domain. Instead of using a convolution-type spectral formulation of the scattered field, an equivalent spatial domain formulation was obtained for 2-D rough interfaces in a layered medium. In order to perform efficient evaluation of the equivalent scattering forcing term, the 2-D rough interface is modeled as a roughness patch with the size of sonar footprint. In addition, a 2-D fast Fourier integral (FFI. See Section C.2.) was introduced for the fast computation of scattered fields. The computational efficiency of this numerical model enables Monte-Carlo style simulations to compute the statistical properties of the scattered field.

A comparison with an analytic solution was used to validate the numerical model. A series of numerical simulations were conducted to investigate the scattered fields produced by various types of roughness such as anisotropy, correlation length, and fractal dimension. The effects of medium properties on the scattered fields were also studied. By using Fourier synthesis, time domain solutions of rough interface scattering were computed. The effects of roughness anisotropy were studied in the time domain as well.

5.1.2 Target Scattering

The single scattering approximation was utilized together with wavenumber integration to develop a model of target scattering in a waveguide. Since the primary purpose of the target model is to understand the physics of target scattering in a waveguide, only targets with simple geometric and material properties were used. Three target scattering models – rigid sphere, pressure-release sphere, and finite cylindrical elastic shell – were used to compute the effective target beampatterns extended to evanescent regime. Several benchmarks for the target scattering models were performed to validate the numerical model. In addition, a series of extensive numerical simulations were performed to study the effects of target and medium properties on the scattered field. Different layer thicknesses, waveguides, burial depths of target, target anisotropy, and bottom properties were used for the numerical simulations. Wideband simulations were also conducted using Fourier synthesis. The effects of target anisotropy were also studied in the time domain simulation.

5.1.3 Numerical Experiments

A numerical simulator for shallow water target scattering scenarios was developed integrating the numerical models for rough interface scattering and target scattering. In addition to the numerical scattering models, the simulator includes a pulse post-processing module, a spectral analysis module, and an array beamforming module. These extra modules were added to analyze the time domain solutions as if they were collected from real experiments. In order to demonstrate the capability of the numerical simulator and to investigate the practicability of multi-static target sonar systems, a series of numerical experiments were performed to simulate the scenarios of the GOATS '98 experiment. These numerical experiments include multi-static configuration of the receiver array, a shallow waveguide with a multi-layered bottom, an anisotropic rough interface at the bottom interface, and a cylindrical target flush buried in the bottom.

With a given source pulse, simulated time series were obtained by Fourier synthesis. Then, several sets of time series were chosen based on the possibility of detecting a target signal out of the reverberant background for further investigation. By applying an array beamforming technique on the synthesized time series of the receiver array, arrival structures of scattered signals were analyzed.

5.2 Scattering and Reverberation Physics

The physics of rough interface and target scattering has been studied through the extensive numerical simulation of scattered fields using the theories and numerical models developed in this thesis. Even though rough interface scattering and target scattering are due to different fundamental mechanisms, the numerical models in this thesis have been developed in a consistent framework through the wavenumber domain formulation. Two numerical models have been successfully tested with benchmark problems, comparing against analytic and semi-analytic solutions.

By using the numerical model of rough interface scattering developed in this thesis, the following physical conclusions were reached.

- Effects of bottom properties.
  - An elastic sub-bottom produces a stronger scattered field in the bottom because it allows conversion of scattered energy into SH and SV waves.
  - A faster and denser bottom produces a scattered field in steeper angular regime of the water because the critical angle becomes higher.

- An elastic bottom produces a scattered field with wider azimuthal range than a fluid bottom because the elastic bottom allows the shear conversion of scattered energy in the transverse direction.
- An scattered interface wave is noticeably observed for the case of an elastic sub-bottom with supersonic incidence.
- The effects of shear waves on the scattered field in the water becomes significant when the incident horizontal wavenumber approaches the shear wavenumber of the bottom. When the shear wave speed of the bottom is much lower than the incident phase speed, the scattered field becomes similar to that of the fluid bottom.

- Waveguide effects.
  - The scattered field has significant depth-structure because of the modal structure of the waveguide.
  - The waveguide effect is reduced for the case of supersonic incidence because a major portion of the energy is in the continuous spectrum.
  - A deeper waveguide produces more interference pattern at steeper grazing angles.

- Effects of sediment thickness.
  - The scattered field in the water exhibits interference patterns produced by the modal structure in the sediment.
  - Interference patterns in the water are observed at angles higher than the critical angle between the water and the sediment.
  - Below the critical angle, the scattering spectrum of an elastic sand layer over elastic limestone is similar to that of an elastic sand bottom. This is due to the fact that the transmission of scattered energy is evanescent in the sediment.
  - A thicker sediment layer produces more modal interference patterns in the water by the same reason as the case of a waveguide.

- Effects of roughness correlation length.
  - Backward scattering increases as the correlation length decreases because of the longer tail in the roughness spectrum.
  - The forward peak value of scattering increases and the width of the peak becomes narrower as the correlation length increases because the longer correlation length concentrates the roughness spectrum at low wavenumbers. Within the limits of the perturbation theory, the forward scattering peak is proportional to the value of the roughness spectrum at the origin.

- Effects of roughness fractal dimension.
  - When the fractal dimension increases, the roughness power spectrum becomes flatter. Therefore, the angular spreading of the scattered field increases as the fractal dimension becomes higher.
  - The forward scattered field is not affected significantly by the fractal dimension because the behavior of the low-wavenumber roughness spectrum near the origin is not changed by the fractal dimension.

- Except for the forward scattering lobe, roughness with a higher fractal dimension produces a stronger scattered field.

- Effects of roughness anisotropy.

  - An anisotropic roughness spectrum with a center peak produces a dominant scattered field between the forward direction and the specular direction of the incident field with respect to the anisotropic angle.
  - A ripple structure is generally characterized by a dominant wavenumber which results in a different distribution of scattered energy. Frequency dependency of the scattering produced by a ripple structure is relatively strong and it can be explained by a Bragg scattering argument.

From the time domain solutions of rough interface scattering presented in Chapter 2, the following conclusions were reached.

- Effects of medium properties.

  - As the compressional and shear wave speed of the bottom increase, backward scattering is enhanced because the transmitted energy in the bottom is reduced.
  - Interface waves (Scholte waves) become significant when the shear wave speed of the bottom becomes the same order as the compressional wave speed of the water. The phase speed of the scattered interface wave is slower than the compressional wave speed of the water.
  - An elastic sediment layer over a fast elastic half space enhances the scattered field in the water compared to the case of a plain elastic half space. This is caused by the strong upward reflection of compressional and shear waves at the interface between the sediment and the bottom.

- In the time domain, a spatial anisotropy of the scattered field is produced by roughness anisotropy. The trend of anisotropy is the same as the one observed in the frequency domain. Therefore, prior knowledge of the roughness anisotropy provides information about the preferred directions of the reverberant field.

The target scattering model using the single scattering approximation provides a simple way to compute the field scattered by a target in a layered medium. From the numerical simulations presented in Chapter 3, the following physical conclusions were reached.

- The elasticity of the medium below a target affects the resulting scattered field in the water by allowing the transmission of direct scattered energy as shear waves in the bottom. When the incident grazing angle is shallower than the compressional critical angle, the scattered field in the water becomes weak and the out-of-plane scattered field is decreased.

- The effects of layering depths are observed for buried targets.

  - The modal structure of a layer produces interference patterns in the scattered field in the water.
  - The scattered field in the water remains the same regardless of the layer thickness when the scattering angle is shallower than the critical angle. The evanescent scattered field in that angular regime is similar to that of the half space case.

- When a target is located in a waveguide, the resulting scattering pattern is governed by the physics of the waveguide. The scattered field has an interference in the depth direction because of the modal structure of the waveguide. The properties of the bottom are important because they determine the modal structure of the waveguide.

- Aspect-dependent targets such as cylindrical shells in general produce an asymmetric scattered field. A finite cylindrical elastic shell has two angular preferences of its scattered field – the forward direction and the specular direction of the incident wave with respect to the longitudinal axis of the target.

- The scattered field in the water is strongly dependent on burial depth.

  - For sub-critical incidence, the overall strength of the scattered field is reduced exponentially with respect to the burial depth because the excitation of the target by the incident wave is reduced by the same rate.
  - The scattered field in the water is predominantly within the critical cone (i.e. the angular regime of supersonic incidence) regardless of the burial depth.

From the wideband simulation of target scattering, the following conclusions were reached.

- Shear conversion of scattered energy is clearly observed in the elastic bottom which will result in less scattered field in the water than for a fluid bottom. The medium below a target affects the scattered field in the water to a significant degree.

- An aspect-dependent target produces an anisotropic scattered field. A 45° slanted cylindrical shell produces a scattered field predominantly in the forward and side ($\theta = 90°$) directions.

The scattering and propagation models have been combined into a consistent numerical simulator. Numerical experiments of multi-static scattered fields in a shallow water environment were conducted using the GOATS '98 experiment scenario [50]. The numerical experiment showed that the 3-D scattering features are different for targets and rough interfaces. An array beamforming technique was applied to the synthesized scattering data and the following conclusions were reached.

- Using horizontal and vertical line arrays together is useful for arrival identification.

- The aspect dependency of a target is significant for detection in an anisotropic reverberant background caused by a rough interface above the target.

- The multi-static configuration of a sonar system can take advantage of prior knowledge of the reverberant background field such as roughness anisotropy. The azimuthal position of the receiver array can be adjusted to avoid excessive reverberation and maximize the signal-to-noise ratio for better identification of the target.

5.3 Suggestion for Future Work

5.3.1 Feedback from the GOATS '98 Experiment

The GOATS '98 experiment provided high quality multi-static target scattering data. This data set can be compared with synthetic data produced by the numerical simulator designed in this thesis. The numerical models can be validated and improved by getting feedback from the real data.

5.3.2 Implementation of Medium Complexity

The bottom can be modeled as a poro-elastic material to allow the slow compressional scattered wave which may be important in certain frequency regimes. Since the formulation of rough interface scattering applies to any combination of wave types, it is possible to implement poro-elasticity into the rough interface scattering model. When the 3-D OASES includes the implementation of poro-elasticity, this extension of the scattering model will be readily possible. One of the major shortcomings of the target scattering model in this thesis is that the model cannot be applied to a target buried in an elastic medium. Allowing elasticity in the surrounding medium is expected to be especially important when the dominant portion of the incident energy is transfered to a target by shear waves.

5.3.3 Implementation of Other Targets

Even though rigid and pressure-release spheres are useful to understand the physics of target scattering, they are not commonly found in a real environment. A spherical elastic shell behaves differently from rigid and pressure-release spheres because it supports membrane waves which affect the spatial and temporal structures of scattering. Even though an analytic scattering solution for a spherical elastic shell is not available, a numerical solution of the full wave equation is available using the DGM (direct global matrix) formulation [43]. The derivation of scattering functions for spherical elastic shells with fluid and void inside is presented in Appendix E. Preliminary work for its numerical implementation was done but a validity check is necessary.

5.3.4 Implementation of Volume Reverberant Mechanism

Another type of reverberant mechanism is observed in the ocean environment. It is reverberation caused by volume inhomogeneities such as fluctuations of density and sound speed in a layer. Since the same perturbational formulation used in Chapter 2 was previously applied to model the scattered field of stochastically distributed inhomogeneities by Tracey [54], this type of volume reverberant mechanism can be integrated into the numerical simulator. Another implementation of volume reverberation was also done by Tang [52] and Li [31].

Appendix A

3-D DGM Formulation in Cylindrical Coordinate System

When the external forces are confined to a relatively small region compared to the total volume of interest, the natural choice of coordinate system is a cylindrical coordinate system with its origin close to the sources (i.e. external forces). The cylindrical coordinate system consists of three spatial variable (r, θ, z), which are the radial, azimuthal and vertical components shown in Figure A-1. For a horizontally stratified environment, the seismo-acoustic field can be solved by making several assumptions. In a given environment, all layers are assumed to be homogeneous and isotropic with either elastic or fluid medium properties. In the following derivation, the time dependency is set to be $\exp(\iota\omega t)$ and it is omitted for convenience. The field in each layer is a superposition of external source terms and the homogeneous solution to the Helmholtz equation for the layer. Unknown coefficients in the homogeneous solution can be determined by applying the boundary conditions at each interface. When the homogeneous equation of motion is derived with the polar displacement vector $\vec{u} = [u_n, v_n, w_n]^T$, it becomes :

$$(\lambda_n + 2\mu_n)\nabla\nabla\cdot\vec{u}_n - \mu_n\nabla\times\nabla\times\vec{u}_n - \rho_n\frac{\partial^2\vec{u}_n}{\partial t^2} = 0, \tag{A.1}$$

where λ_n and μ_n are the Lamé constants and ρ_n is the density of the n th layer. The compressional wave speed C_{pn} and shear wave speed C_{sn} are related to the Lamé constants and density.

$$C_{pn} = \sqrt{(\lambda_n + \mu_n)/\rho_n}, \qquad C_{sn} = \sqrt{\mu_n/\rho_n}. \tag{A.2}$$

The equation of motion is satisfied when the polar displacements $[u_n, v_n, w_n]^T$ are expressed by scalar potential $[\phi_n, \Lambda_n, \psi_n]^T$ shown as below.

$$\begin{aligned} u_n &= \frac{\partial\phi_n}{\partial r} + \frac{1}{r}\frac{\partial\psi_n}{\partial\theta} + \frac{\partial^2\Lambda_n}{\partial r\partial z}, \\ v_n &= \frac{1}{r}\frac{\partial\phi_n}{\partial\theta} - \frac{\partial\psi_n}{\partial r} + \frac{1}{r}\frac{\partial^2\Lambda_n}{\partial\theta\partial z}, \\ w_n &= \frac{\partial\phi_n}{\partial z} - \left(\frac{1}{r}\frac{\partial}{\partial r}r\frac{\partial}{\partial r} + \frac{1}{r^2}\frac{\partial^2}{\partial\theta^2}\right)\Lambda_n, \end{aligned} \tag{A.3}$$

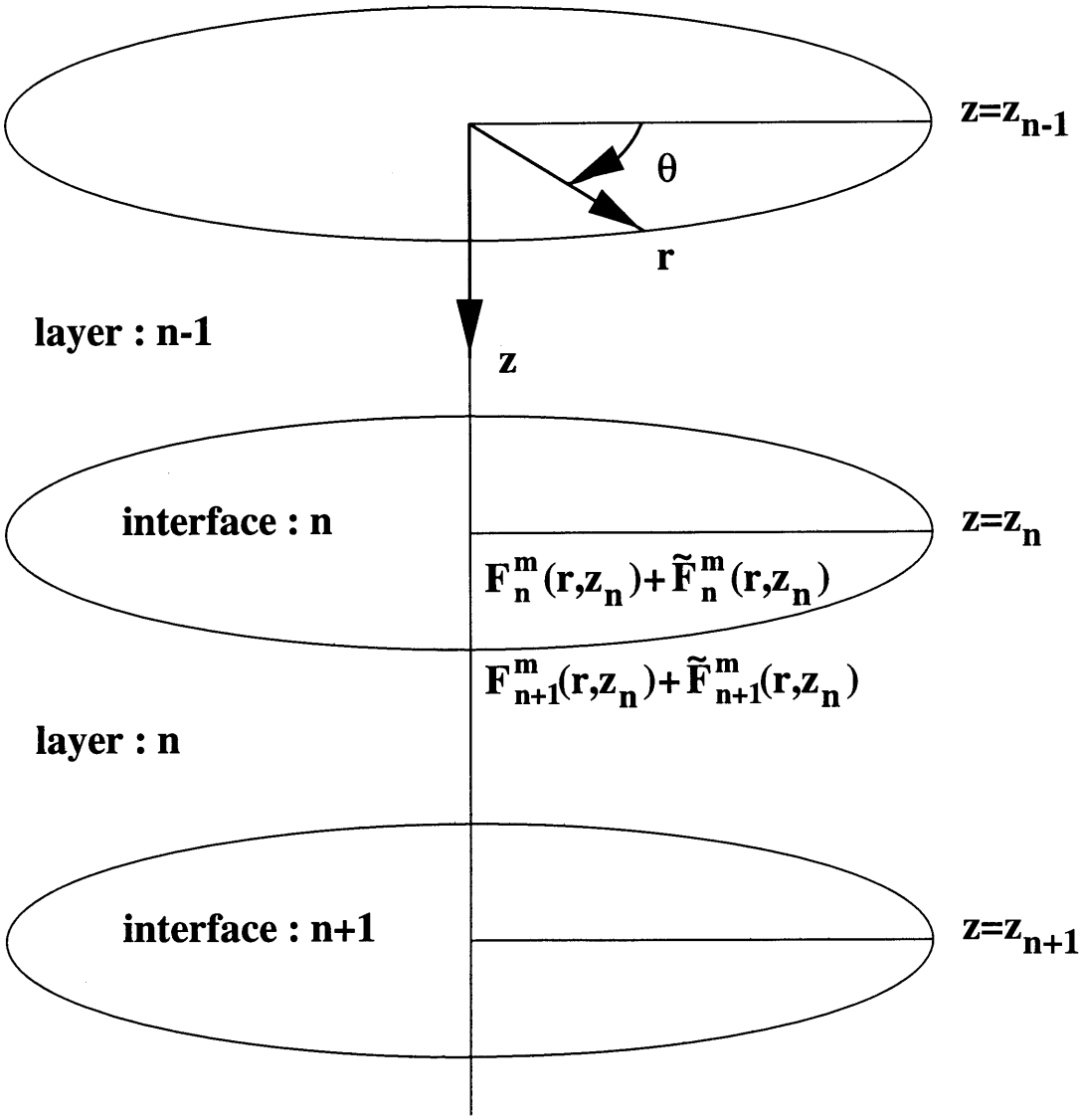

Figure A-1: Cylindrical coordinate system for 3-D DGM.

where each of potential satisfies a homogeneous Helmholtz equation with the stated time harmonic factor.

$$\left(\nabla^2 + h_n^2\right)\phi_n = 0, \qquad \left(\nabla^2 + k_n^2\right)(\Lambda_n, \psi_n) = 0, \tag{A.4}$$

where h_n and k_n are medium dependent compressional and shear wavenumbers, respectively.

Since the field can have angular variation, it is possible to expand the potentials in a set of discrete Fourier series with respect to θ.

$$\begin{aligned}
\phi(r,\theta,z) &= \sum_{m=0}^{\infty}\left[\phi_1^m(r,z)\cos(m\theta) + \phi_2^m(r,z)\sin(m\theta)\right], \\
\Lambda(r,\theta,z) &= \sum_{m=0}^{\infty}\left[\Lambda_1^m(r,z)\cos(m\theta) + \Lambda_2^m(r,z)\sin(m\theta)\right], \\
\psi(r,\theta,z) &= \sum_{m=0}^{\infty}\left[\psi_1^m(r,z)\sin(m\theta) - \psi_2^m(r,z)\cos(m\theta)\right].
\end{aligned} \tag{A.5}$$

By substituting the above solution forms into the Helmholtz equation and using the Hankel transform, each Fourier coefficient can be represented by the following integral form :

$$\begin{aligned}
\phi^m(r,z) &= \int_0^{\infty}\left[a_1^m(s)\,e^{-\alpha(z-z_{n-1})} + a_2^m(s)\,e^{\alpha(z-z_n)}\right] s J_m(rs)\,ds, \\
\Lambda^m(r,z) &= \int_0^{\infty}\left[b_1^m(s)\,e^{-\beta(z-z_{n-1})} + b_2^m(s)\,e^{\beta(z-z_n)}\right] J_m(rs)\,ds, \\
\psi^m(r,z) &= \int_0^{\infty}\left[c_1^m(s)\,e^{-\beta(z-z_{n-1})} + c_2^m(s)\,e^{\beta(z-z_n)}\right] s J_m(rs)\,ds,
\end{aligned} \tag{A.6}$$

where s is the horizontal wavenumber. The subscripts 1 and 2 of Fourier coefficients have been omitted and α and β are the vertical wavenumbers defined as :

$$\alpha(s) = \sqrt{s^2 - h^2}, \qquad \beta(s) = \sqrt{s^2 - k^2}. \tag{A.7}$$

The above integral forms imply the decomposition of field into downward and upward traveling wave components.

The Fourier coefficients of polar displacement are obtained by substituting the integral form of displacement potential into (A.3). The horizontal displacements $[u^m, v^n]^T$ are divided into the symmetric and anti-symmetric parts.

$$\begin{aligned}
w^m(r,z) = \int_0^{\infty}\Big[&-a_1^m\,\alpha\,e^{-\alpha(z-z_{n-1})} + a_2^m\,\alpha\,e^{\alpha(z-z_n)} \\
&+ b_1^m\,s\,e^{-\beta(z-z_{n-1})} + b_2^m\,s\,e^{\beta(z-z_n)}\Big] s J_m(rs)\,ds,
\end{aligned} \tag{A.8}$$

$$\begin{aligned}
u^m(r,z) \pm v^m(r,z) = \int_0^{\infty}\Big[&\mp a_1^m\,s\,e^{-\alpha(z-z_{n-1})} \mp a_2^m\,s\,e^{\alpha(z-z_n)} \\
&\pm b_1^m\,\beta\,e^{-\beta(z-z_{n-1})} \mp b_2^m\,\beta\,e^{\beta(z-z_n)} \\
&+ c_1^m\,s\,e^{-\beta(z-z_{n-1})} + c_2^m\,s\,e^{\beta(z-z_n)}\Big] s J_{m\pm1}(rs)\,ds.
\end{aligned} \tag{A.9}$$

By applying Hooke's law to the above expression, the Fourier coefficients of vertical and horizon-

tal stress components are obtained.

$$\sigma_{zz}^m(r,z) = \mu \int_0^\infty \left[a_1^m (2s^2-k^2) e^{-\alpha(z-z_{n-1})} + a_2^m (2s^2-k^2) e^{\alpha(z-z_n)} \right. \\ \left. - b_1^m 2s\beta e^{-\beta(z-z_{n-1})} + b_2^m 2s\beta e^{\beta(z-z_n)}\right] s J_m(rs)\, ds, \tag{A.10}$$

$$\sigma_{rz}^m(r,z) \pm \sigma_{\theta z}^m(r,z) = \mu \int_0^\infty \left[\pm a_1^m 2s\alpha e^{-\alpha(z-z_{n-1})} \mp a_2^m 2s\alpha e^{\alpha(z-z_n)} \right. \\ \mp b_1^m (2s^2-k^2) e^{-\beta(z-z_{n-1})} \mp b_2^m (2s^2-k^2) e^{\beta(z-z_n)} \\ \left. - c_1^m s\beta e^{-\beta(z-z_{n-1})} + c_2^m s\beta e^{\beta(z-z_n)}\right] s J_{m\pm1}(rs)\, ds. \tag{A.11}$$

For a fluid layer, the shear displacement potentials become zero and the vertical stress component is obtained as follows :

$$\sigma_{zz}^m = -\lambda h^2 \int_0^\infty \left[a_1^m e^{-\alpha(z-z_{n-1})} + a_2^m e^{\alpha(z-z_n)}\right] s J_m(rs)\, ds. \tag{A.12}$$

Because the horizontal components of displacements and stresses are decomposed into symmetric and anti-symmetric parts, the resulting coefficients of the unknown potential functions are independent of the Fourier orders and need to be computed only once.

Since the homogeneous part of the solution is expressed as the unknown Fourier coefficients in integral form, the source term (i.e. external forces) should be expanded in the azimuthal Fourier series and Hankel transform.

In order to solve for the unknown Fourier coefficients, the boundary conditions at each interface are applied. Depending on the layers adjacent to an interface, the number of boundary conditions are determined. At the interface between two elastic layers, the boundary condition implies the continuity of three displacements and three stresses. Since the Fourier series is based on the orthogonal function sets, matching the boundary conditions at every order is equivalent to satisfying the continuity of the whole series. The boundary condition can be expressed by a vector of displacements and tractions in each Fourier order.

$$F^m(r,z) = \begin{pmatrix} w^m(r,z) \\ u^m(r,z) + v^m(r,z) \\ u^m(r,z) - v^m(r,z) \\ \sigma_{zz}^m(r,z) \\ \sigma_{rz}^m(r,z) + \sigma_{\theta z}^m(r,z) \\ \sigma_{rz}^m(r,z) - \sigma_{\theta z}^m(r,z) \end{pmatrix}. \tag{A.13}$$

For the n th interface between the n th and the $n+1$ th layers, the boundary condition can be written as follows :

$$F_n^m(r,z_n) + \hat{F}_n^m(r,z_n) - F_{n+1}^m(r,z_n) - \hat{F}_{n+1}^m(r,z_n) = 0, \tag{A.14}$$

where $\hat{F}_n$ is the source term in the n th layer. Since the above condition should be satisfied for all values of r, the integrands of the above equation must be zero. Then, a set of linear equations are derived for the unknown potential functions of the horizontal wavenumber s :

$$A_n(s) E_n(s,z_n) B_n^m(s) - A_{n+1}(s) E_{n+1}(s,z_n) B_{n+1}^m(s) = R_{n+1}^m(s,z_n) - R_n^m(s,z_n), \tag{A.15}$$

where $B_n^m(s)$ is a column vector of the unknown potential functions for the n th layer :

$$B_n^m(s) = \begin{pmatrix} a_{1,n}^m(s) \\ b_{1,n}^m(s) \\ c_{1,n}^m(s) \\ a_{2,n}^m(s) \\ b_{2,n}^m(s) \\ c_{2,n}^m(s) \end{pmatrix}. \tag{A.16}$$

A diagonal matrix $E_n(s, z)$ represents the depth dependency terms :

$$E_n(s,z) = \begin{bmatrix} e^{-\alpha(z-z_{n-1})} & 0 & 0 & 0 & 0 & 0 \\ 0 & e^{-\beta(z-z_{n-1})} & 0 & 0 & 0 & 0 \\ 0 & 0 & e^{-\beta(z-z_{n-1})} & 0 & 0 & 0 \\ 0 & 0 & 0 & e^{\alpha(z-z_n)} & 0 & 0 \\ 0 & 0 & 0 & 0 & e^{\beta(z-z_n)} & 0 \\ 0 & 0 & 0 & 0 & 0 & e^{\beta(z-z_n)} \end{bmatrix}. \tag{A.17}$$

$A_n(s)$ is a six by six square matrix consisting of the coefficients independent of Fourier order for the n th layer. For an elastic layer,

$$A_n(s) = \begin{bmatrix} -\alpha & s & 0 & \alpha & s & 0 \\ -s & \beta & s & -s & -\beta & s \\ s & -\beta & s & s & \beta & s \\ (2s^2-k^2)\mu & -2s\beta\mu & 0 & (2s^2-k^2)\mu & 2s\beta\mu & 0 \\ 2s\alpha\mu & -(2s^2-k^2)\mu & -s\beta\mu & -2s\alpha\mu & -(2s^2-k^2)\mu & s\beta\mu \\ -2s\alpha\mu & (2s^2-k^2)\mu & -s\beta\mu & 2s\alpha\mu & -(2s^2-k^2)\mu & s\beta\mu \end{bmatrix}. \tag{A.18}$$

For a fluid layer, $A_n(s)$ is much simpler.

$$A_n(s) = \begin{bmatrix} -\alpha & 0 & 0 & \alpha & 0 & 0 \\ -s & 0 & 0 & -s & 0 & 0 \\ s & 0 & 0 & s & 0 & 0 \\ -\lambda h^2 & 0 & 0 & -\lambda h^2 & 0 & 0 \\ 0 & 0 & 0 & 0 & 0 & 0 \\ 0 & 0 & 0 & 0 & 0 & 0 \end{bmatrix}. \tag{A.19}$$

Column vectors $R_n^m(s, z_n)$ and $R_{n+1}^m(s, z_n)$ are the residual terms of linear matrix equation which represents the projection of the source on the interface $z = z_n$. They can be either rough interface or target scattering functions.

This page is blank.

Appendix B

Roughness Virtual Source

To evaluate the virtual forcing term $f_v(\vec{x})$ produced by interface roughness, each term of (2.20) is derived as follows. The physical variables to be matched on the interface are three displacement components (u, v, w) and three stress components $(\sigma_{xz}, \sigma_{yz}, \sigma_{zz})$. The corresponding boundary operator B_i is derived from the following equation.

$$B_i(\vec{x})\langle\chi_{i;i+1}(\vec{x})\rangle = \begin{pmatrix} u \\ v \\ w \\ \sigma_{xz} \\ \sigma_{yz} \\ \sigma_{zz} \end{pmatrix}_i - \begin{pmatrix} u \\ v \\ w \\ \sigma_{xz} \\ \sigma_{yz} \\ \sigma_{zz} \end{pmatrix}_{i+1} . \tag{B.1}$$

Only the compressional source (or array of compressional sources) was used as external forcing term in this thesis. With this condition and the assumption of horizontal stratification of the medium, the unperturbed field $\langle\chi(\vec{x})\rangle$ consists of P and SV waves only. As a results, the SH displacement potential $\psi(\vec{x})$ of the unperturbed field is zero. Therefore, the boundary operator $B(\vec{x})$ includes contributions from P and SV displacement potentials (ϕ, Λ) only. By definition, the displacement vector is related to displacement potentials as follows :

$$\begin{pmatrix} u \\ v \\ w \end{pmatrix} = \nabla\phi + \nabla\times\nabla\times(0,0,\Lambda) + \nabla\times(0,0,\psi) = \begin{pmatrix} \phi_{,x} + \Lambda_{,xz} \\ \phi_{,y} + \Lambda_{,yz} \\ \phi_{,z} - \Lambda_{,xx} - \Lambda_{,yy} \end{pmatrix}. \tag{B.2}$$

The traction vector is obtained from the displacements through Hooke's law :

$$\begin{pmatrix} \sigma_{xz} \\ \sigma_{yz} \\ \sigma_{zz} \end{pmatrix} = \begin{pmatrix} \mu(u_{,z} + w_{,x}) \\ \mu(v_{,z} + w_{,y}) \\ 2\mu w_{,z} + \lambda(u_{,x} + v_{,y} + w_{,z}) \end{pmatrix} = \begin{pmatrix} \mu(2\phi_{,xz} + \Lambda_{,xzz} - \Lambda_{,xxx} - \Lambda_{,xyy}) \\ \mu(2\phi_{,yz} + \Lambda_{,yzz} - \Lambda_{,xxy} - \Lambda_{,yyy}) \\ 2\mu(\phi_{,zz} - \Lambda_{,xxz} - \Lambda_{,yyz}) + \lambda(\phi_{,xx} + \phi_{,yy} + \phi_{,zz}) \end{pmatrix}. \tag{B.3}$$

Therefore, the contribution from the i th layer becomes :

$$\begin{pmatrix} u \\ v \\ w \\ \sigma_{xz} \\ \sigma_{yz} \\ \sigma_{zz} \end{pmatrix}_i = \begin{pmatrix} \phi_{,x} + \Lambda_{,xz} \\ \phi_{,y} + \Lambda_{,yz} \\ \phi_{,z} - \Lambda_{,xx} - \Lambda_{,yy} \\ \mu(2\phi_{,xz} + \Lambda_{,xzz} - \Lambda_{,xxx} - \Lambda_{,xyy}) \\ \mu(2\phi_{,yz} + \Lambda_{,yzz} - \Lambda_{,xxy} - \Lambda_{,yyy}) \\ 2\mu(\phi_{,zz} - \Lambda_{,xxz} - \Lambda_{,yyz}) + \lambda(\phi_{,xx} + \phi_{,yy} + \phi_{,zz}) \end{pmatrix}_i$$

$$= \begin{bmatrix} \dfrac{\partial}{\partial x} & \dfrac{\partial^2}{\partial x \partial z} \\ \dfrac{\partial}{\partial y} & \dfrac{\partial^2}{\partial y \partial z} \\ \dfrac{\partial}{\partial z} & -\left(\dfrac{\partial^2}{\partial x^2} + \dfrac{\partial^2}{\partial y^2}\right) \\ 2\mu_i \dfrac{\partial^2}{\partial x \partial z} & \mu_i\left(\dfrac{\partial^3}{\partial x \partial z^2} - \dfrac{\partial^3}{\partial x^3} - \dfrac{\partial^3}{\partial x \partial y^2}\right) \\ 2\mu_i \dfrac{\partial^2}{\partial y \partial z} & \mu_i\left(\dfrac{\partial^3}{\partial y \partial z^2} - \dfrac{\partial^3}{\partial x^2 \partial y} - \dfrac{\partial^3}{\partial y^3}\right) \\ 2\mu_i \dfrac{\partial^2}{\partial z^2} + \lambda_i\left(\dfrac{\partial^2}{\partial x^2} + \dfrac{\partial^2}{\partial y^2} + \dfrac{\partial^2}{\partial z^2}\right) & -2\mu_i\left(\dfrac{\partial^3}{\partial x^2 \partial z} + \dfrac{\partial^3}{\partial y^2 \partial z}\right) \end{bmatrix} \begin{pmatrix} \phi_i \\ \Lambda_i \end{pmatrix} \tag{B.4}$$

$$= \begin{bmatrix} \mathbf{D} \\ \mathbf{T}_i \end{bmatrix} \mathbf{P}_i,$$

where submatrices $\mathbf{D}$, $\mathbf{T}_i$ and vector $\mathbf{P}_i$ are defined as follows :

$$\mathbf{D} = \begin{bmatrix} \dfrac{\partial}{\partial x} & \dfrac{\partial^2}{\partial x \partial z} \\ \dfrac{\partial}{\partial y} & \dfrac{\partial^2}{\partial y \partial z} \\ \dfrac{\partial}{\partial z} & -\left(\dfrac{\partial^2}{\partial x^2} + \dfrac{\partial^2}{\partial y^2}\right) \end{bmatrix}, \tag{B.5}$$

$$\mathbf{T}_i = \begin{bmatrix} 2\mu_i \dfrac{\partial^2}{\partial x \partial z} & \mu_i\left(\dfrac{\partial^3}{\partial x \partial z^2} - \dfrac{\partial^3}{\partial x^3} - \dfrac{\partial^3}{\partial x \partial y^2}\right) \\ 2\mu_i \dfrac{\partial^2}{\partial y \partial z} & \mu_i\left(\dfrac{\partial^3}{\partial y \partial z^2} - \dfrac{\partial^3}{\partial x^2 \partial y} - \dfrac{\partial^3}{\partial y^3}\right) \\ 2\mu_i \dfrac{\partial^2}{\partial z^2} + \lambda_i\left(\dfrac{\partial^2}{\partial x^2} + \dfrac{\partial^2}{\partial y^2} + \dfrac{\partial^2}{\partial z^2}\right) & -2\mu_i\left(\dfrac{\partial^3}{\partial x^2 \partial z} + \dfrac{\partial^3}{\partial y^2 \partial z}\right) \end{bmatrix}, \tag{B.6}$$

and

$$\mathbf{P}_i = \begin{pmatrix} \phi_i \\ \Lambda_i \end{pmatrix}. \tag{B.7}$$

Using (B.5) through (B.7), the discontinuity vector across the interface can be expressed as shown below.

$$B_i(\vec{x})\langle\chi_{i;i+1}\rangle = \begin{bmatrix} \mathbf{D} & -\mathbf{D} \\ \mathbf{T}_i & -\mathbf{T}_{i+1} \end{bmatrix} \begin{bmatrix} \mathbf{P}_i \\ \mathbf{P}_{i+1} \end{bmatrix}. \tag{B.8}$$

Therefore, the first virtual source term becomes :

$$\left[\gamma \frac{\partial B_i(\vec{x})}{\partial z}\langle\chi_{i;i+1}(\vec{x})\rangle\right]\Big|_{z=z_i} = \gamma \begin{bmatrix} \mathbf{D}_{,z} & -\mathbf{D}_{,z} \\ \mathbf{T}_{i,z} & -\mathbf{T}_{i+1,z} \end{bmatrix} \begin{bmatrix} \mathbf{P}_i \\ \mathbf{P}_{i+1} \end{bmatrix}_{z=z_i}. \tag{B.9}$$

The second virtual forcing term is derived from the coordinate transform equations (2.11) and (2.12). Because the boundary condition states the continuity of the normal and tangential components across the interface at each point, the local displacements and stresses should be obtained by considering the surface normal vector. Originally, the coordinate transform is described by the roughness height function $\gamma(\vec{x})$. The subsequent transformation of displacements and stresses are computed by the tensor rotation [17]. When the coordinate axes are rotated by angles θ_x and θ_y with respect to the original coordinate system, the displacement vector $[U\ V\ W]^T$ in the rotated coordinate system is :

$$\begin{pmatrix} U \\ V \\ W \end{pmatrix} = \begin{bmatrix} \cos\theta_x & 0 & \sin\theta_x \\ 0 & \cos\theta_y & \sin\theta_y \\ -\sin\theta_x & -\sin\theta_y & \cos\theta_x \cos\theta_y \end{bmatrix} \begin{pmatrix} u \\ v \\ w \end{pmatrix}. \tag{B.10}$$

The stress vector $[\Sigma_{xz}\ \Sigma_{yz}\ \Sigma_{zz}]^T$ in the rotated coordinate system is :

$$\begin{aligned} \begin{pmatrix} \Sigma_{xz} \\ \Sigma_{yz} \\ \Sigma_{zz} \end{pmatrix} &= \begin{bmatrix} -\cos\theta_x \sin\theta_x & -\cos\theta_x \sin\theta_y & 0 \\ 0 & -\cos\theta_y \sin\theta_x & -\cos\theta_y \sin\theta_y \\ \sin^2\theta_x & 2\sin\theta_x \sin\theta_y & \sin^2\theta_y \end{bmatrix} \begin{pmatrix} \sigma_{xx} \\ \sigma_{xy} \\ \sigma_{yy} \end{pmatrix} \\ &+ \begin{bmatrix} \cos^2\theta_x \cos\theta_y - \sin^2\theta_x & -\sin\theta_x \sin\theta_y & \cos\theta_x \sin\theta_x \cos\theta_y \\ -\sin\theta_x \sin\theta_y & \cos\theta_x \cos^2\theta_y - \sin^2\theta_y & \cos\theta_x \cos\theta_y \sin\theta_y \\ -2\cos\theta_y \cos\theta_x \sin\theta_x & -2\cos\theta_x \cos\theta_y \sin\theta_y & \cos^2\theta_x \cos^2\theta_y \end{bmatrix} \begin{pmatrix} \sigma_{xz} \\ \sigma_{yz} \\ \sigma_{zz} \end{pmatrix}. \end{aligned} \tag{B.11}$$

With the above transformation, the components in the new coordinates can be expressed by the sum of the unrotated components and the remaining term.

$$\begin{pmatrix} U \\ V \\ W \\ \Sigma_{xz} \\ \Sigma_{yz} \\ \Sigma_{zz} \end{pmatrix}_i = \begin{pmatrix} u \\ v \\ w \\ \sigma_{xz} \\ \sigma_{yz} \\ \sigma_{zz} \end{pmatrix}_i + \vec{\Delta}_i(\theta_x, \theta_y), \tag{B.12}$$

where $\vec{\Delta}(\theta_x, \theta_y)$ represents the pure rotational contribution to the displacements and stresses in the new coordinate. The rotational contribution $\vec{\Delta}$ can be implemented without any assumptions because the local rotational angles of roughness can be evaluated explicitly from the roughness

height function.

$$\cos\theta_q = 1\Big/\sqrt{1+\left(\frac{\partial\gamma}{\partial q}\right)^2}, \qquad \sin\theta_q = \left(\frac{\partial\gamma}{\partial q}\right)\Big/\sqrt{1+\left(\frac{\partial\gamma}{\partial q}\right)^2}, \tag{B.13}$$

where q represents x or y coordinates. For a first order perturbation, the slope of roughness is assumed to be small. The leading order approximations of the cosine and sine become :

$$\cos\theta_q = 1 + O^2\left(\frac{\partial\gamma}{\partial q}\right), \qquad \sin\theta_q = \frac{\partial\gamma}{\partial q} + O^3\left(\frac{\partial\gamma}{\partial q}\right). \tag{B.14}$$

The rotational matrix Ψ of (2.12) then simplifies in the first order perturbation theory :

$$\Psi \sim \begin{bmatrix} 1 & 0 & \dfrac{\partial\gamma}{\partial x} \\ 0 & 1 & \dfrac{\partial\gamma}{\partial y} \\ -\dfrac{\partial\gamma}{\partial x} & -\dfrac{\partial\gamma}{\partial y} & 1 \end{bmatrix}. \tag{B.15}$$

Similarly, keeping first order terms only, the second virtual force term becomes a linear function of the local roughness slope $\nabla\gamma(\vec{x})$.

$$\vec{\Delta}_i - \vec{\Delta}_{i+1} \sim \nabla\gamma \circ b_i(\vec{x})\langle\chi_{i;i+1}(\vec{x})\rangle = \begin{bmatrix} w & 0 \\ 0 & w \\ -u & -v \\ \sigma_{zz}-\sigma_{xx} & -\sigma_{xy} \\ -\sigma_{xy} & \sigma_{zz}-\sigma_{yy} \\ -2\sigma_{xz} & -2\sigma_{yz} \end{bmatrix}_{i;i+1} \begin{pmatrix} \dfrac{\partial\gamma}{\partial x} \\ \dfrac{\partial\gamma}{\partial y} \end{pmatrix}. \tag{B.16}$$

The above term is rewritten by a combination of differential operators and displacement potentials. When the contributions from roughness slopes are separated into x and y components, x components become :

$$\gamma_{,x}\begin{pmatrix} w \\ 0 \\ -u \\ \sigma_{zz}-\sigma_{xx} \\ -\sigma_{xy} \\ -2\sigma_{xz} \end{pmatrix}_i = \frac{\partial\gamma}{\partial x}\begin{bmatrix} \dfrac{\partial}{\partial z} & -\left(\dfrac{\partial^2}{\partial x^2}+\dfrac{\partial^2}{\partial y^2}\right) \\ 0 & 0 \\ -\dfrac{\partial}{\partial x} & -\dfrac{\partial^2}{\partial x\partial z} \\ 2\mu_i\left(\dfrac{\partial^2}{\partial z^2}-\dfrac{\partial^2}{\partial x^2}\right) & -2\mu_i\left(2\dfrac{\partial^3}{\partial x^2\partial z}+\dfrac{\partial^3}{\partial y^2\partial z}\right) \\ -2\mu_i\dfrac{\partial^2}{\partial x\partial y} & -2\mu_i\dfrac{\partial^3}{\partial x\partial y\partial z} \\ -4\mu_i\dfrac{\partial^2}{\partial x\partial z} & -2\mu_i\left(\dfrac{\partial^3}{\partial x\partial z^2}-\dfrac{\partial^3}{\partial x^3}-\dfrac{\partial^3}{\partial x\partial y^2}\right) \end{bmatrix}\begin{pmatrix} \phi_i \\ \Lambda_i \end{pmatrix} \tag{B.17}$$

$$= \gamma_{,x}\mathbf{X}_i\mathbf{P}_i$$

and y components are :

$$\gamma_{,y}\begin{pmatrix} 0 \\ w \\ -v \\ -\sigma_{xy} \\ \sigma_{zz}-\sigma_{yy} \\ -2\sigma_{yz} \end{pmatrix}_i = \frac{\partial \gamma}{\partial y}\begin{bmatrix} 0 & 0 \\ \frac{\partial}{\partial z} & -\left(\frac{\partial^2}{\partial x^2}+\frac{\partial^2}{\partial y^2}\right) \\ -\frac{\partial}{\partial y} & -\frac{\partial^2}{\partial y \partial z} \\ -2\mu_i \frac{\partial^2}{\partial x \partial y} & -2\mu_i \frac{\partial^3}{\partial x \partial y \partial z} \\ 2\mu_i\left(\frac{\partial^2}{\partial z^2}-\frac{\partial^2}{\partial y^2}\right) & -2\mu_i\left(2\frac{\partial^3}{\partial y^2 \partial z}+\frac{\partial^3}{\partial x^2 \partial z}\right) \\ -4\mu_i \frac{\partial^2}{\partial y \partial z} & -2\mu_i\left(\frac{\partial^3}{\partial y \partial z^2}-\frac{\partial^3}{\partial y^3}-\frac{\partial^3}{\partial x^2 \partial y}\right) \end{bmatrix}\begin{pmatrix} \phi_i \\ \Lambda_i \end{pmatrix} \tag{B.18}$$

$$= \gamma_{,y}\mathbf{Y}_i\mathbf{P}_i,$$

where linear differential operators $\mathbf{X}_i$ and $\mathbf{Y}_i$ are defined as follows :

$$\mathbf{X}_i = \begin{bmatrix} \frac{\partial}{\partial z} & -\left(\frac{\partial^2}{\partial x^2}+\frac{\partial^2}{\partial y^2}\right) \\ 0 & 0 \\ -\frac{\partial}{\partial x} & -\frac{\partial^2}{\partial x \partial z} \\ 2\mu_i\left(\frac{\partial^2}{\partial z^2}-\frac{\partial^2}{\partial x^2}\right) & -2\mu_i\left(2\frac{\partial^3}{\partial x^2 \partial z}+\frac{\partial^3}{\partial y^2 \partial z}\right) \\ -2\mu_i \frac{\partial^2}{\partial x \partial y} & -2\mu_i \frac{\partial^3}{\partial x \partial y \partial z} \\ -4\mu_i \frac{\partial^2}{\partial x \partial z} & -2\mu_i\left(\frac{\partial^3}{\partial x \partial z^2}-\frac{\partial^3}{\partial x^3}-\frac{\partial^3}{\partial x \partial y^2}\right) \end{bmatrix}, \tag{B.19}$$

$$\mathbf{Y}_i = \begin{bmatrix} 0 & 0 \\ \frac{\partial}{\partial z} & -\left(\frac{\partial^2}{\partial x^2}+\frac{\partial^2}{\partial y^2}\right) \\ -\frac{\partial}{\partial y} & -\frac{\partial^2}{\partial y \partial z} \\ -2\mu_i \frac{\partial^2}{\partial x \partial y} & -2\mu_i \frac{\partial^3}{\partial x \partial y \partial z} \\ 2\mu_i\left(\frac{\partial^2}{\partial z^2}-\frac{\partial^2}{\partial y^2}\right) & -2\mu_i\left(2\frac{\partial^3}{\partial y^2 \partial z}+\frac{\partial^3}{\partial x^2 \partial z}\right) \\ -4\mu_i \frac{\partial^2}{\partial y \partial z} & -2\mu_i\left(\frac{\partial^3}{\partial y \partial z^2}-\frac{\partial^3}{\partial y^3}-\frac{\partial^3}{\partial x^2 \partial y}\right) \end{bmatrix}. \tag{B.20}$$

Therefore, the second virtual source term becomes :

$$\left[\nabla\gamma \circ b_i(\vec{x})\langle\chi_{i;i+1}(\vec{x})\rangle\right]\Big|_{z=z_i} = \left\{\gamma_{,x}\begin{bmatrix}\mathbf{X}_i & -\mathbf{X}_{i+1}\end{bmatrix} + \gamma_{,y}\begin{bmatrix}\mathbf{Y}_i & -\mathbf{Y}_{i+1}\end{bmatrix}\right\}\begin{bmatrix}\mathbf{P}_i \\ \mathbf{P}_{i+1}\end{bmatrix}_{z=z_i}. \tag{B.21}$$

Summing (B.9) and (B.21), the discontinuity vector of the virtual source term is expressed by linear differential operators and displacement potentials.

$$f_v(\vec{x}) = \left\{\gamma\begin{bmatrix}\mathbf{D}_{,z} & -\mathbf{D}_{,z} \\ \mathbf{T}_{i,z} & -\mathbf{T}_{i+1,z}\end{bmatrix} + \gamma_{,x}\begin{bmatrix}\mathbf{X}_i & -\mathbf{X}_{i+1}\end{bmatrix} + \gamma_{,y}\begin{bmatrix}\mathbf{Y}_i & -\mathbf{Y}_{i+1}\end{bmatrix}\right\}\begin{bmatrix}\mathbf{P}_i \\ \mathbf{P}_{i+1}\end{bmatrix}_{z=z_i}. \tag{B.22}$$

For time harmonic cases, the displacement potentials can be decomposed in the wavenumber domain. Partial derivatives in the spatial domain are then easily obtained by integration of corresponding spectral components. Time dependency was chosen as $\exp(\iota\omega t)$, which is omitted in the following equations.

When the unperturbed field is axisymmetric (i.e., case of point source or its combinations.), the displacement potentials (ϕ, Λ) are conveniently expressed in cylindrical coordinates (r, z). Using the Hankel transform, the potentials of the i th layer have the following forms.

$$\begin{aligned}\phi_i(r,z) &= \int_0^\infty \left[\tilde{\phi}_i^-(s)\, e^{-\alpha_i(z-z_{i-1})} + \tilde{\phi}_i^+(s)\, e^{\alpha_i(z-z_i)}\right] s J_0(rs)\, ds, \\ \Lambda_i(r,z) &= \int_0^\infty \left[\tilde{\Lambda}_i^-(s)\, e^{-\beta_i(z-z_{i-1})} + \tilde{\Lambda}_i^+(s)\, e^{\beta_i(z-z_i)}\right] J_0(rs)\, ds,\end{aligned} \tag{B.23}$$

with vertical wavenumbers α_i and β_i :

$$\alpha_i = \sqrt{s^2 - h_i^2}, \qquad \beta_i = \sqrt{s^2 - k_i^2}, \tag{B.24}$$

where h_i and k_i are the compressional and shear medium wavenumbers in the i th layer.

To compute the virtual source term from the above displacement potentials, the chain rule of differential operators is used for the coordinate transform. The highest order partial derivative is three, and the first three orders of partial derivative operators are derived in the following equations. The coordinate transform from cylindrical coordinates (r, θ) to rectangular coordinates (x, y) is defined by the following :

$$x = r\cos\theta, \qquad y = r\sin\theta. \tag{B.25}$$

The first order partial derivative operators are :

$$\frac{\partial}{\partial x} = \frac{x}{r}\frac{\partial}{\partial r} = \cos\theta\frac{\partial}{\partial r}, \qquad \frac{\partial}{\partial y} = \frac{y}{r}\frac{\partial}{\partial r} = \sin\theta\frac{\partial}{\partial r}. \tag{B.26}$$

The second order partial derivative operators are :

$$\begin{aligned}\frac{\partial^2}{\partial x^2} &= \frac{y^2}{r^3}\frac{\partial}{\partial r} + \frac{x^2}{r^2}\frac{\partial^2}{\partial r^2} = \frac{\sin^2\theta}{r}\frac{\partial}{\partial r} + \cos^2\theta\frac{\partial^2}{\partial r^2}, \\ \frac{\partial^2}{\partial x\partial y} &= -\frac{xy}{r^3}\frac{\partial}{\partial r} + \frac{xy}{r^2}\frac{\partial^2}{\partial r^2} = \cos\theta\sin\theta\left(\frac{\partial^2}{\partial r^2} - \frac{1}{r}\frac{\partial}{\partial r}\right), \\ \frac{\partial^2}{\partial y^2} &= \frac{x^2}{r^3}\frac{\partial}{\partial r} + \frac{y^2}{r^2}\frac{\partial^2}{\partial r^2} = \frac{\cos^2\theta}{r}\frac{\partial}{\partial r} + \sin^2\theta\frac{\partial^2}{\partial r^2}.\end{aligned} \tag{B.27}$$

The third order partial derivative operators are :

$$
\begin{aligned}
\frac{\partial^3}{\partial x^3} &= \frac{3xy^2}{r^4}\left(\frac{\partial^2}{\partial r^2}-\frac{1}{r}\frac{\partial}{\partial r}\right)+\frac{x^3}{r^3}\frac{\partial^3}{\partial r^3} \\
&= \frac{3}{r}\cos\theta\sin^2\theta\left(\frac{\partial^2}{\partial r^2}-\frac{1}{r}\frac{\partial}{\partial r}\right)+\cos^3\theta\frac{\partial^3}{\partial r^3}, \\
\frac{\partial^3}{\partial x^2\partial y} &= \left(\frac{3y^3}{r^4}-\frac{2y}{r^2}\right)\left(\frac{\partial^2}{\partial r^2}-\frac{1}{r}\frac{\partial}{\partial r}\right)+\frac{x^2y}{r^3}\frac{\partial^3}{\partial r^3} \\
&= \frac{\sin\theta}{r}(3\sin^2\theta-2)\left(\frac{\partial^2}{\partial r^2}-\frac{1}{r}\frac{\partial}{\partial r}\right)+\cos^2\theta\sin\theta\frac{\partial^3}{\partial r^3}, \\
\frac{\partial^3}{\partial x\partial y^2} &= \left(\frac{3x^3}{r^4}-\frac{2x}{r^2}\right)\left(\frac{\partial^2}{\partial r^2}-\frac{1}{r}\frac{\partial}{\partial r}\right)+\frac{xy^2}{r^3}\frac{\partial^3}{\partial r^3} \\
&= \frac{\cos\theta}{r}(3\cos^2\theta-2)\left(\frac{\partial^2}{\partial r^2}-\frac{1}{r}\frac{\partial}{\partial r}\right)+\cos\theta\sin^2\theta\frac{\partial^3}{\partial r^3}, \\
\frac{\partial^3}{\partial y^3} &= \frac{3x^2y}{r^4}\left(\frac{\partial^2}{\partial r^2}-\frac{1}{r}\frac{\partial}{\partial r}\right)+\frac{y^3}{r^3}\frac{\partial^3}{\partial r^3} \\
&= \frac{3}{r}\cos^2\theta\sin\theta\left(\frac{\partial^2}{\partial r^2}-\frac{1}{r}\frac{\partial}{\partial r}\right)+\sin^3\theta\frac{\partial^3}{\partial r^3}.
\end{aligned}
\tag{B.28}
$$

Since the kernel of the wavenumber integral has the zeroth order Bessel function with radial coordinate dependency, the first, second, and third order partial derivatives are required for the computation of displacement potential derivatives.

$$
\begin{aligned}
&\frac{\partial}{\partial r}J_0(rs) = -sJ_1(rs), \\
&\frac{\partial^2}{\partial r^2}J_0(rs) = -s^2\left[J_0(rs)-\frac{1}{rs}J_1(rs)\right], \\
&\frac{\partial^3}{\partial r^3}J_0(rs) = s^3\left[\frac{1}{rs}J_0(rs)+\left(1-\frac{2}{r^2s^2}\right)J_1(rs)\right].
\end{aligned}
\tag{B.29}
$$

Assuming that the source is far away from the roughness patch, the asymptotic forms of the Bessel functions and their derivatives approximate the integral kernels well. As the argument rs of the Bessel function becomes large, the first two terms of the expansions are derived in Reference [59] as follows :

$$
\begin{aligned}
J_0(rs) &\sim \sqrt{\frac{2}{\pi rs}}\left[\cos(rs-\pi/4)+\frac{1}{8rs}\sin(rs-\pi/4)\right], \\
\frac{\partial}{\partial r}J_0(rs) &\sim -s\sqrt{\frac{2}{\pi rs}}\left[\sin(rs-\pi/4)+\frac{3}{8rs}\cos(rs-\pi/4)\right], \\
\frac{\partial^2}{\partial r^2}J_0(rs) &\sim -s^2\sqrt{\frac{2}{\pi rs}}\left[\cos(rs-\pi/4)-\frac{7}{8rs}\sin(rs-\pi/4)\right], \\
\frac{\partial^3}{\partial r^3}J_0(rs) &\sim s^3\sqrt{\frac{2}{\pi rs}}\left[\sin(rs-\pi/4)+\frac{11}{8rs}\cos(rs-\pi/4)\right].
\end{aligned}
\tag{B.30}
$$

For the case of a plane unperturbed field in (x, z) (i.e., line sources parallel to y axis or incident

plane wave), the potentials expressed as Fourier transform become :

$$\begin{aligned}\phi_i(x,z) &= \int_{-\infty}^{\infty}\left[\tilde{\phi}_i^-(s)\,e^{-\alpha_i(z-z_{i-1})} + \tilde{\phi}_i^+(s)\,e^{\alpha_i(z-z_i)}\right]e^{-\imath sx}ds,\\ \Lambda_i(x,z) &= \int_{-\infty}^{\infty}\left[\tilde{\Lambda}_i^-(s)\,e^{-\beta_i(z-z_{i-1})} + \tilde{\Lambda}_i^+(s)\,e^{\beta_i(z-z_i)}\right]e^{-\imath sx}ds.\end{aligned} \tag{B.31}$$

The corresponding partial derivatives with respect to the Cartesian coordinates are simple compared to those for the cylindrical field. Since there is no y dependency in the wavenumber kernel, only three partial derivatives in the x direction are necessary.

$$\begin{bmatrix}\dfrac{\partial}{\partial x}\\ \dfrac{\partial^2}{\partial x^2}\\ \dfrac{\partial^3}{\partial x^3}\end{bmatrix}\left[e^{-\imath sx}\right] = e^{-\imath sx}\begin{bmatrix}-\imath s\\ -s^2\\ \imath s^3\end{bmatrix}. \tag{B.32}$$

For unperturbed fields in both cylindrical and plane geometries, the partial derivatives of the displacement potentials in depth (z) can be obtained in the same way. Since wavenumber kernels (both P and SV) consist of downward ($+z$) and upward ($-z$) traveling waves, depth derivatives are simply derivatives of exponential functions multiplied by potential amplitudes in the wavenumber domain. Depth derivatives are required up to the third order for boundary operators.

$$\begin{aligned}&\begin{bmatrix}\dfrac{\partial}{\partial z}\\ \dfrac{\partial}{\partial z^2}\\ \dfrac{\partial}{\partial z^3}\end{bmatrix}\left[e^{-\alpha_i(z-z_{i-1})} \quad e^{\alpha_i(z-z_i)} \quad e^{-\beta_i(z-z_{i-1})} \quad e^{\beta_i(z-z_i)}\right]\\ &= \begin{bmatrix}-\alpha_i & \alpha_i & -\beta_i & \beta_i\\ \alpha_i^2 & \alpha_i^2 & \beta_i^2 & \beta_i^2\\ -\alpha_i^3 & \alpha_i^3 & -\beta_i^3 & \beta_i^3\end{bmatrix}\begin{bmatrix}e^{-\alpha_i(z-z_{i-1})} & 0 & 0 & 0\\ 0 & e^{\alpha_i(z-z_i)} & 0 & 0\\ 0 & 0 & e^{-\beta_i(z-z_{i-1})} & 0\\ 0 & 0 & 0 & e^{\beta_i(z-z_i)}\end{bmatrix}.\end{aligned} \tag{B.33}$$

Appendix C

Representation of Cylindrical Virtual Source

This chapter describes the transform technique involving the roughness scattering virtual source in Chapter 2. In order for the scattering virtual source to be compatible with 3-D OASES, its spectral representation must be the coefficient function of a Fourier – Hankel transform in cylindrical coordinates. Since the virtual source function is evaluated at each grid point of a rectangular roughness patch, the transform also requires a transformation from Cartesian to cylindrical coordinates. There are several numerical algorithms to perform Hankel transformations. Johansen and Sørensen developed the fast Hankel transform by utilizing logarithmic sampling and a forward / inverse FFT [23]. The algorithm can compute the Hankel transform very accurately even to high orders, but the non-uniform sampling is incompatible with the rectangular sampling of the virtual source. Kausel and Bouchovalas also introduced a numerical Hankel transformation [26] of 2-D rectangular samples. The algorithm was only applied to zeroth and first orders of Hankel transforms because it becomes unstable at higher orders. The transform technique in this chapter shares the same mathematical formulation as the previous development in Reference [10]. However, the previous numerical implementation was not efficient for the moderate and high frequency cases. Each point in the wavenumber domain was evaluated numerically by double summation of spatial samples. Therefore, the computation time was proportional to the square of the sampling number in one direction :

$$(\text{CPU TIME}) \propto N_x^2 N_y^2, \tag{C.1}$$

where N_x and N_y are the spatial sampling numbers in each direction. In this thesis, a numerical technique based on a modified 2-D FFT (fast Fourier transform) is utilized to reduce the computational time to the following order without loss of accuracy.

$$(\text{CPU TIME}) \propto N_x N_y \log(N_x N_y). \tag{C.2}$$

C.1 Coordinate Transformation of Kernels from Cartesian to Cylindrical Coordinates

This coordinate transformation was first introduced in Reference [10]. Several errors have been found and they are corrected in this thesis. In order to evaluate the cylindrical virtual source

(CVS) efficiently, the coordinate transformation from Cartesian to cylindrical coordinates should be applied in the wavenumber domain.

In cylindrical coordinate system, an arbitrary vector $\vec{u}(r,\theta,z)$ is defined as :

$$\vec{u}(r,\theta,z) = u_r(r,\theta,z)\,\hat{\mathbf{e}}_r + u_\theta(r,\theta,z)\,\hat{\mathbf{e}}_\theta + u_z(r,\theta,z)\,\hat{\mathbf{e}}_z. \tag{C.3}$$

Since the forcing vector of the 3-D DGM formulation is expressed in Fourier orders, each component of $\vec{u}(r,\theta,z)$ is expanded by discrete Fourier series in the circumferential direction.

$$\begin{aligned}
u_r(r,\theta,z) &= \sum_{m=0}^{\infty}\left[U_{r1}^m(r,z)\cos(m\theta) + U_{r2}^m(r,z)\sin(m\theta)\right],\\
u_\theta(r,\theta,z) &= \sum_{m=0}^{\infty}\left[U_{\theta1}^m(r,z)\sin(m\theta) - U_{\theta2}^m(r,z)\cos(m\theta)\right],\\
u_z(r,\theta,z) &= \sum_{m=0}^{\infty}\left[U_{z1}^m(r,z)\cos(m\theta) + U_{z2}^m(r,z)\sin(m\theta)\right],
\end{aligned} \tag{C.4}$$

where the coefficients of the Fourier series can be transformed to the spectral domain by a Hankel transform. The resulting coefficients in (r,θ) coordinates are separated into symmetric and anti-symmetric parts for consistency with the 3-D DGM formulation.

$$\begin{aligned}
U_{ri}^m(r,z) + U_{\theta i}^m(r,z) &= \int_0^\infty \left[R_i^m(s,z) + \Theta_i^m(s,z)\right] s J_{m+1}(rs)\,ds,\\
U_{ri}^m(r,z) - U_{\theta i}^m(r,z) &= \int_0^\infty \left[R_i^m(s,z) - \Theta_i^m(s,z)\right] s J_{m-1}(rs)\,ds,\\
U_{zi}^m(r,z) &= \int_0^\infty Z_i^m(s,z)\, s J_m(rs)\,ds,
\end{aligned} \tag{C.5}$$

where $i = 1, 2$.

In Cartesian coordinates, the same vector $\vec{u}(r,\theta,z)$ is expressed in terms of Cartesian components u_x,u_y and u_z :

$$\vec{u}(r,\theta,z) = u_x(r,\theta,z)\,\hat{\mathbf{e}}_x + u_y(r,\theta,z)\,\hat{\mathbf{e}}_y + u_z(r,\theta,z)\,\hat{\mathbf{e}}_z. \tag{C.6}$$

Again, each component is expanded in a Fourier series and transformed to the wavenumber domain by Hankel transform.

$$\begin{aligned}
u_x(r,\theta,z) &= \sum_{m=0}^{\infty}\left[U_{x1}^m(r,z)\cos(m\theta) + U_{x2}^m(r,z)\sin(m\theta)\right],\\
u_y(r,\theta,z) &= \sum_{m=0}^{\infty}\left[U_{y1}^m(r,z)\sin(m\theta) - U_{y2}^m(r,z)\cos(m\theta)\right],\\
u_z(r,\theta,z) &= \sum_{m=0}^{\infty}\left[U_{z1}^m(r,z)\cos(m\theta) + U_{z2}^m(r,z)\sin(m\theta)\right],
\end{aligned} \tag{C.7}$$

and

$$
\begin{aligned}
U_{xi}^{m}(r,z) &= \int_0^{\infty} X_i^m(s,z)\, s J_m(rs)\, ds, \\
U_{yi}^{m}(r,z) &= \int_0^{\infty} Y_i^m(s,z)\, s J_m(rs)\, ds, \\
U_{zi}^{m}(r,z) &= \int_0^{\infty} Z_i^m(s,z)\, s J_m(rs)\, ds,
\end{aligned}
\tag{C.8}
$$

where $i = 1, 2$.

With a simple coordinate transformation from (x, y) to (r, θ),

$$
\begin{aligned}
u_r(r,\theta,z) &= u_x(r,\theta,z)\cos\theta + u_y(r,\theta,z)\sin\theta \\
&= \sum_{m=0}^{\infty}\Big[U_{x1}^{m}(r,z)\cos(m\theta)\cos\theta + U_{x2}^{m}(r,z)\sin(m\theta)\cos\theta \\
&\qquad + U_{y1}^{m}(r,z)\sin(m\theta)\sin\theta - U_{y2}^{m}(r,z)\cos(m\theta)\sin\theta\Big], \\
u_\theta(r,\theta,z) &= -u_x(r,\theta,z)\sin\theta + u_y(r,\theta,z)\cos\theta \\
&= \sum_{m=0}^{\infty}\Big[-U_{x1}^{m}(r,z)\cos(m\theta)\sin\theta - U_{x2}^{m}(r,z)\sin(m\theta)\sin\theta \\
&\qquad + U_{y1}^{m}(r,z)\sin(m\theta)\cos\theta - U_{y2}^{m}(r,z)\cos(m\theta)\cos\theta\Big].
\end{aligned}
\tag{C.9}
$$

By equating (C.4) and (C.9), the relationship between Fourier coefficients in cylindrical and Cartesian coordinates is obtained.

$$
U_{r1}^{m} = \frac{1}{2}\begin{cases} U_{x1}^{1} + U_{y1}^{1} & \text{for } m = 0 \\ 2U_{x1}^{0} + U_{x1}^{2} + U_{y1}^{2} & \text{for } m = 1, \\ U_{x1}^{m-1} + U_{x1}^{m+1} - U_{y1}^{m-1} + U_{y1}^{m+1} & \text{for } m \geq 2 \end{cases}
\tag{C.10}
$$

$$
U_{r2}^{m} = \frac{1}{2}\begin{cases} 0 & \text{for } m = 0 \\ U_{x2}^{2} - 2U_{y2}^{0} + U_{y2}^{2} & \text{for } m = 1, \\ U_{x2}^{m-1} + U_{x2}^{m+1} - U_{y2}^{m-1} + U_{y2}^{m+1} & \text{for } m \geq 2 \end{cases}
\tag{C.11}
$$

$$
U_{\theta 1}^{m} = \frac{1}{2}\begin{cases} 0 & \text{for } m = 0 \\ -2U_{x1}^{0} + U_{x1}^{2} + U_{y1}^{2} & \text{for } m = 1, \\ -U_{x1}^{m-1} + U_{x1}^{m+1} + U_{y1}^{m-1} + U_{y1}^{m+1} & \text{for } m \geq 2 \end{cases}
\tag{C.12}
$$

and

$$
U_{\theta 2}^{m} = \frac{1}{2}\begin{cases} U_{x2}^{1} + U_{y2}^{1} & \text{for } m = 0 \\ U_{x2}^{2} + 2U_{y2}^{0} + U_{y2}^{2} & \text{for } m = 1. \\ -U_{x2}^{m-1} + U_{x2}^{m+1} + U_{y2}^{m-1} + U_{y2}^{m+1} & \text{for } m \geq 2 \end{cases}
\tag{C.13}
$$

Thus,

$$U_{r1}^m + U_{\theta 1}^m = \begin{cases} \frac{1}{2}(U_{x1}^1 + U_{y1}^1) & \text{for } m = 0 \\ U_{x1}^2 + U_{y1}^2 & \text{for } m = 1 \\ U_{x1}^{m+1} + U_{y1}^{m+1} & \text{for } m \geq 2 \end{cases}, \tag{C.14}$$

$$U_{r1}^m - U_{\theta 1}^m = \begin{cases} \frac{1}{2}(U_{x1}^1 + U_{y1}^1) & \text{for } m = 0 \\ 2U_{x1}^0 & \text{for } m = 1 \\ U_{x1}^{m-1} - U_{y1}^{m-1} & \text{for } m \geq 2 \end{cases}, \tag{C.15}$$

$$U_{r2}^m + U_{\theta 2}^m = \begin{cases} \frac{1}{2}(U_{x2}^1 + U_{y2}^1) & \text{for } m = 0 \\ U_{x2}^2 + U_{y2}^2 & \text{for } m = 1 \\ U_{x2}^{m+1} + U_{y2}^{m+1} & \text{for } m \geq 2 \end{cases}, \tag{C.16}$$

and

$$U_{r2}^m - U_{\theta 2}^m = \begin{cases} -\frac{1}{2}(U_{x2}^1 + U_{y2}^1) & \text{for } m = 0 \\ -2U_{y2}^0 & \text{for } m = 1 \\ U_{x2}^{m-1} - U_{y2}^{m-1} & \text{for } m \geq 2 \end{cases}. \tag{C.17}$$

For the corresponding coefficients in the wavenumber-depth domain (s, z),

$$R_i^m + \Theta_i^m = \begin{cases} \frac{1}{2}(X_i^1 + Y_i^1) & \text{for } m = 0 \text{ and } i = 1, 2 \\ X_i^{m+1} + Y_i^{m+1} & \text{otherwise} \end{cases},$$

$$R_i^m - \Theta_i^m = \begin{cases} \frac{1}{2}(X_1^1 + Y_1^1) & \text{for } m = 0 \text{ and } i = 1 \\ -\frac{1}{2}(X_2^1 + Y_2^1) & \text{for } m = 0 \text{ and } i = 2 \\ 2X_1^0 & \text{for } m = 1 \text{ and } i = 1 \\ -2Y_1^0 & \text{for } m = 1 \text{ and } i = 2 \\ X_i^{m-1} - Y_i^{m-1} & \text{otherwise} \end{cases}. \tag{C.18}$$

The perturbation code in this thesis produces the displacement vector $\vec{u} = [u\, v\, w]^T$ and traction vector $\vec{t} = [\sigma_{zz}\, \sigma_{xz}\, \sigma_{yz}]^T$, which represent the scattering forcing terms on a rectangular patch at depth $z = z_0$. In order to feed these forcing vectors to 3-D OASES, the displacement and traction vectors are converted to cylindrical coordinates and expanded in Fourier series and transformed to spectral coefficients of m th Fourier order. This transformation can be done by series of coordinate transforms and by Hankel transform, but the procedure in this thesis utilizes the efficiency of the 2-D FFT to evaluate these forcing terms. Obviously, $[\tilde{X}_i^m(s, z_0)\, \tilde{Y}_i^m(s, z_0)\, \tilde{Z}_i^m(s, z_0)]^T$, a vector of coefficients from the Fourier transform, is different from the Hankel transforming vector of coefficients $[X_i^m(s, z_0)\, Y_i^m(s, z_0)\, Z_i^m(s, z_0)]^T$. This difference is found in the relationship between two transformations. They are related to each other as follows. Given the transformation from

Cartesian coordinates to cylindrical coordinates,

$$x = r\cos\theta, \qquad y = r\sin\theta, \tag{C.19}$$

$$k_x = s\cos\alpha, \qquad k_y = s\sin\alpha, \tag{C.20}$$

the x component becomes :

$$\begin{aligned}
&u_x(x, y, z_0) \\
&= \int_{-\infty}^{\infty}\int_{-\infty}^{\infty} \tilde{U}_x(k_x, k_y, z_0)\, e^{-\imath k_x x - \imath k_y y}\, dk_x\, dk_y \\
&= \int_0^{\infty} ds\, s \int_{-\pi}^{\pi} d\alpha\, \tilde{U}_x(s, \alpha, z_0)\, e^{-\imath rs\cos(\alpha-\theta)} \\
&= \int_0^{\infty} ds\, s \int_{-\pi}^{\pi} d\alpha\, e^{-\imath rs\cos(\alpha-\theta)} \sum_{m=0}^{\infty} \left[\tilde{X}_1^m(s, z_0)\cos m\alpha + \tilde{X}_2^m(s, z_0)\sin m\alpha\right] \\
&= \int_0^{\infty} ds\, s \int_{-\pi}^{\pi} d\beta\, e^{-\imath rs\cos\beta} \sum_{m=0}^{\infty} \left[\tilde{X}_1^m(s, z_0)\cos m(\beta+\theta) + \tilde{X}_2^m(s, z_0)\sin m(\beta+\theta)\right] \\
&= \int_0^{\infty} ds\, s \sum_{m=0}^{\infty} \left(\int_{-\pi}^{\pi} e^{-\imath rs\cos\beta}\cos m\beta\, d\beta\right)\left[\tilde{X}_1^m(s, z_0)\cos m\theta + \tilde{X}_2^m(s, z_0)\sin m\theta\right] \\
&= \sum_{m=0}^{\infty} 2\pi(-\imath)^m \int_0^{\infty} \left[\tilde{X}_1^m(s, z_0)\cos m\theta + \tilde{X}_2^m(s, z_0)\sin m\theta\right] J_m(rs)\, s\, ds,
\end{aligned} \tag{C.21}$$

where the integral over β is done by the following integral equalities.

$$\begin{aligned}
\int_{-\pi}^{\pi} \cos m(\beta+\theta)\, e^{-\imath rs\cos\beta} d\beta &= \cos m\theta \int_{-\pi}^{\pi} e^{-\imath rs\cos\beta}\cos m\beta\, d\beta, \\
\int_{-\pi}^{\pi} \sin m(\beta+\theta)\, e^{-\imath rs\cos\beta} d\beta &= \sin m\theta \int_{-\pi}^{\pi} e^{-\imath rs\cos\beta}\cos m\beta\, d\beta,
\end{aligned} \tag{C.22}$$

and according to (9.1.22) of Reference [1],

$$\int_{-\pi}^{\pi} e^{-\imath rs\cos\beta}\cos m\beta\, d\beta = 2\pi(-\imath)^m J_m(rs). \tag{C.23}$$

By comparing the above expression with the original definition of $u_x(r, \theta, z_0)$ in terms of $X_i^m(s, z_0)$ and applying the same technique to y and z components,

$$\begin{bmatrix} X_1^m & X_2^m \\ Y_1^m & Y_2^m \\ Z_1^m & Z_2^m \end{bmatrix} = 2\pi(-\imath)^m \begin{bmatrix} \tilde{X}_1^m & \tilde{X}_2^m \\ \tilde{Y}_1^m & \tilde{Y}_2^m \\ \tilde{Z}_1^m & \tilde{Z}_2^m \end{bmatrix}. \tag{C.24}$$

C.2 Two Dimensional Fast Fourier Integral (2-D FFI)

In order to transform the forcing distribution in the spatial domain to the spectral domain, a two dimensional Fourier transform is necessary. The approximation of the Fourier transform by 2-D FFT with finite sampling lengths does not provide enough resolution in the wavenumber domain. Since the convolution of the incident field and the roughness patch is always zero outside of the patch, the Fourier transform of the forcing on the finite patch has a form of 2-D definite

integral with integral ranges equal to the dimension of the patch. By these two justifications, the corresponding Fourier transform is evaluated by numerical 2-D Fourier integral.

$$\begin{aligned}\tilde{U}(s,\theta,z_0) &= \frac{1}{(2\pi)^2}\int_{-\infty}^{\infty}\int_{-\infty}^{\infty} u(x,y,z_0)\,e^{\imath k_x x+\imath k_y y}\,dx\,dy \\ &= \frac{1}{(2\pi)^2}\int_{-l_y/2}^{l_y/2}\int_{-l_x/2}^{l_x/2} u(x,y,z_0)\,e^{\imath k_x x+\imath k_y y}\,dx\,dy.\end{aligned} \tag{C.25}$$

Previously, the numerical Fourier transform in cylindrical coordinates was achieved by simple coordinate transform and trapezoidal numerical integration [10]. Even though this procedure is numerically simple and does not cause any significant computational efficiency problem for low frequency cases, it cannot meet the demand for moderate frequency cases, 'Monte-Carlo' style simulation for spatial statistics, and time-domain field computation. Therefore, there is a need to develop a new way for an efficient and accurate numerical transformation. Even though the 2-D FFT approximates the integral mathematically, its numerical results are likely to be wrong. The problem lies in the oscillatory nature of integrand and consequently the numerical approximation by 2-D FFT becomes worse when the wavenumber increases. A cure for this numerical instability is to use an interpolation function for the kernel values $u(x,y,z_0)$. The numerical 2-D fast Fourier integral (2-D FFI) has been implemented using its one dimensional version in Reference [39]. The beauty of the 2-D fast Fourier integral is that the resolution in the spectral domain can be arbitrarily controlled even with finite sampling length and a number of non trivial samples and it is still fast enough to match the speed of a conventional 2-D FFT. The interpolation method used by this 2-D FFI is a fourth order polynomial, which even improves the accuracy of 2-D FFI.

$$\begin{aligned}\int_{-l_x/2}^{l_x/2} u(x,y,z_0)e^{\imath k_{xn}x}dx &\approx \mathrm{F}FI_x\left[u(x,y,z_0),k_{xn}\right] \\ &= \Delta_x e^{-\imath k_{xn}l_x/2}\Big\{W(\theta_{xn})\mathrm{F}FT_x\left[u(x,y,z_0),k_{xn}\right] \\ &\quad+\left[\alpha_0(\theta_{xn})\,u(x_0,y,z_0)+\alpha_1(\theta_{xn})\,u(x_1,y,z_0)\right. \\ &\qquad\left.+\alpha_2(\theta_{xn})\,u(x_2,y,z_0)+\alpha_3(\theta_{xn})\,u(x_3,y,z_0)\right] \\ &\quad+e^{\imath k_{xn}l_x}\left[\alpha_3^*(\theta_{xn})\,u(x_{n-3},y,z_0)+\alpha_2^*(\theta_{xn})\,u(x_{n-2},y,z_0)\right. \\ &\qquad\left.+\alpha_1^*(\theta_{xn})\,u(x_{n-1},y,z_0)+\alpha_0^*(\theta_{xn})\,u(x_n,y,z_0)\right]\Big\},\end{aligned} \tag{C.26}$$

where $\theta_{xn}=k_{xn}\Delta_x$ and $\mathrm{F}FT_x[u(x,y,z_0),k_{xn}]$ is the FFT value of u in the x direction at $k_x=k_{xn}$. The weighting function $W(\theta)$ and coefficients $\alpha_{0,1,2,3}(\theta)$ are defined in Reference [39]. Transforms in the x direction are performed at each grid point of y and then the same transform in y is performed.

Based on the benchmark cases, there are noticeable differences between the FFT and FFI results. Since 3-D OASES uses a linear interpolation to compute the wavenumber kernels between two input wavenumbers, having fine wavenumber samples in the input cylindrical virtual source terms is necessary to avoid numerical artifacts caused by the linear interpolation. CVS by FFI generates a smooth angular spectrum which agrees with the analytic perturbation solution. However, CVS by FFT produces artificially repeating peaks in the angular spectrum if the spatial samples used are the same as in FFI. This proves that the approximated transformation by FFI is more accurate.

Appendix D

Formulation of Finite Cylindrical Elastic Shell

In this chapter, the formulation of cylindrical shell scattering derived by Rumerman [41] is reviewed. The geometry and the variables used here are shown in Figure D-1. The assumptions underling the mathematical derivation of the scattered field produced by a finite cylindrical elastic shell are as follows. The system impedance function of shell and supporting medium can be approximated by that of the the infinite-length shell with the same elastic properties, radius and thickness. The second assumption is that the supersonic membrane vibration of the shell dominates the other scattering mechanisms such as a flexural wave scattering caused by high wavenumber bending motion. Since the motion of the shell is in the supersonic regime, the acoustical energy can transfer from the shell surface to the surrounding fluid medium. The third assumption is that the membrane scattered energy is concentrated near the modal membrane resonance wavenumbers, which are zeros of the system impedance. With the third assumption, the scattered field generated by the elastic boundary is approximated as the sum of the modal resonance parameters. The following derivation expresses the physical quantities as a trigonometric series of circumferential angle.

If an incident field is time harmonic with time dependency $\exp(\imath\omega t)$, the incident plane wave with angle of incident ϕ_i with respect to the radial axis of shell and zero circumferential angle (i.e $\theta = 0$) is :

$$P_i(x,z,t) = P_0 \exp(\imath kx\cos\phi_i + \imath kz\sin\phi_i - \imath\omega t). \tag{D.1}$$

Given the following definitions,

$$\alpha_i = ka\sin\phi_i, \qquad K_i a = ka\cos\phi_i, \qquad \epsilon_n = \begin{cases} 1 & \text{for } n = 0 \\ 2 & \text{for } n > 0 \end{cases}, \tag{D.2}$$

the total pressure field on the surface of the shell ($r = a$) with infinite impedance (i.e. rigid shell) is :

$$\begin{aligned} P_b(z,\theta,t) &= P_i(a\cos\phi_i, z, t) + P_{s\infty}(a\cos\phi_i, z, t) \\ &= \frac{2\imath P_0}{\pi K_i a}\exp\left(\frac{\imath\alpha_i z}{a} - \imath\omega t\right)\sum_{n=0}^{\infty}\epsilon_n \imath^n \frac{\cos(n\theta)}{H'^{(1)}_n(K_i a)}, \end{aligned} \tag{D.3}$$

where $P_{s\infty}$ is the scattered pressure of a cylinder with infinite impedance and θ is the circumferen-

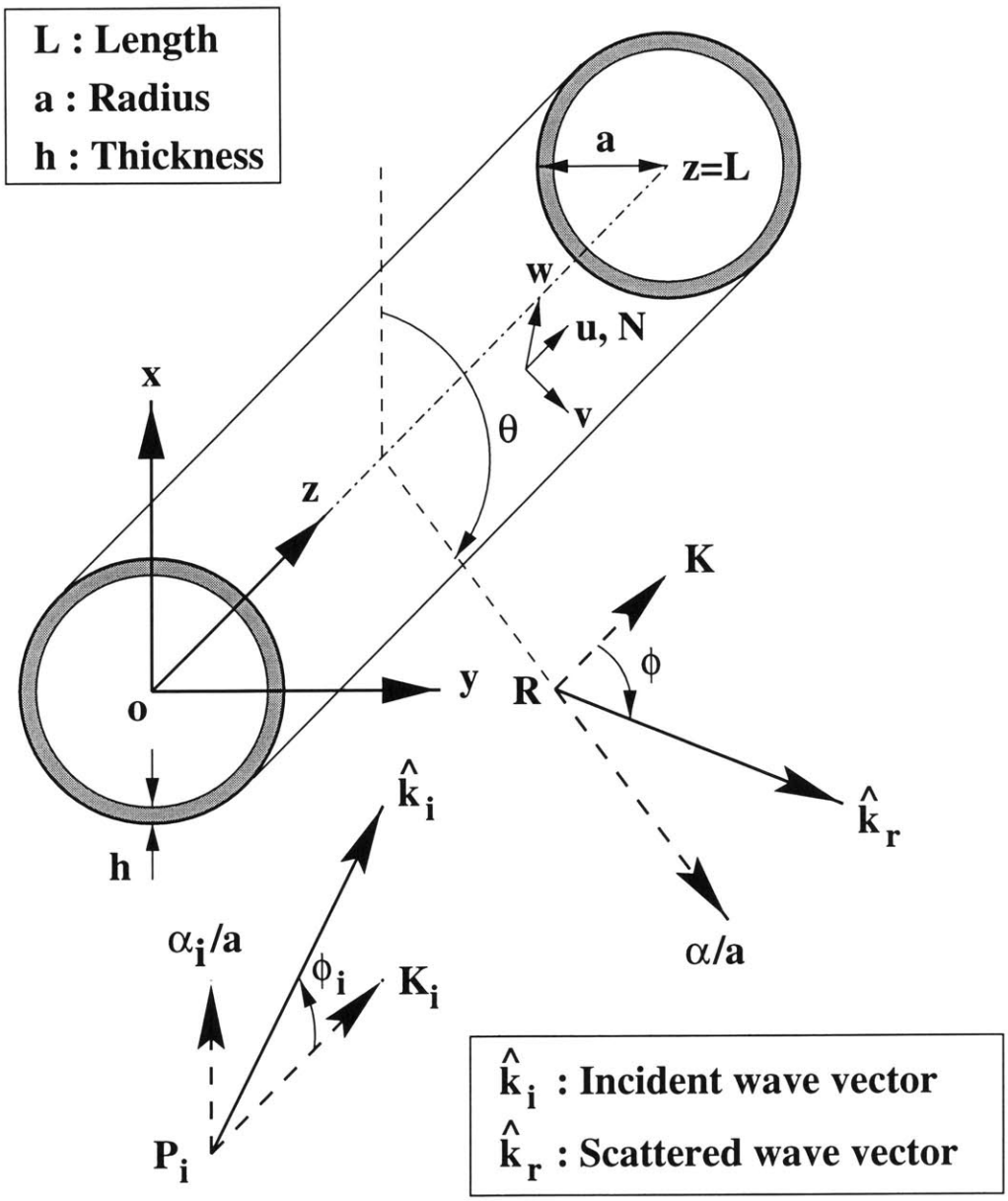

Figure D-1: Geometry of a finite cylindrical shell and the definitions of wave vectors.

tial angle between source and receiver directions. The corresponding forced radial velocity, $\dot{w}_0$ is obtained by the following relationship with the total pressure.

$$\dot{w}_0(z,\theta,t) = -\sum_{n=0}^{\infty} \frac{p_n \cos(n\theta)}{Z_n}, \tag{D.4}$$

where the p_n's are the Fourier coefficients of the total pressure and Z_n is the sum of Z_n^s, the structural impedance, and Z_n^f, the acoustic impedance of the surrounding fluid medium for the n th circumferential order. Then, the resulting forced radial velocity is :

$$\dot{w}_0(z,\theta,t) = (-\imath\omega)\exp\left(\frac{\imath\alpha_i z}{a} - \imath\omega t\right)\sum_{n=0}^{\infty} W_{0n}\cos(n\theta), \tag{D.5}$$

where the W_{0n}'s are the Fourier coefficients of the forced radial displacement and the same harmonic dependency is used to express the velocity in terms of the displacement coefficients.

$$\dot{W}_{0n} = (-\imath\omega)W_{0n} = \frac{-2\imath P_0 \imath^n \epsilon_n}{\pi K_i a H_n'^{(1)}(K_i a) Z_n(\Omega,\alpha_i)}, \tag{D.6}$$

where $\Omega = kac/c_p$ is known as the 'ring frequency'. It is the non-dimensional ratio of compressional phase speeds between the surrounding fluid and the shell. The modal impedance of the shell Z_n^s is derived in Reference [25]. Restricting the problem to membrane waves, the shell impedance is simplified by omitting higher wavenumber bending wave terms.

$$\begin{aligned}
&Z_n^s(\Omega,\alpha) = -\imath\left(\frac{\rho_s h\omega}{\Omega^2}\right)\frac{A\alpha^4 + B\alpha^2 + C}{D\alpha^4 + E\alpha^2 + F},\\
&A = (\Omega^2 + \nu^2 - 1)(1-\nu)/2,\\
&B = \Omega^2 n^2(1-\nu) - \Omega^2(\Omega^2-1)(1-\nu)/2 - \Omega^2(\Omega^2+\nu^2-1),\\
&C = \Omega^2[\Omega^2 - n^2(1-\nu)/2](\Omega^2 - 1 - n^2),\\
&D = (1-\nu)/2,\\
&E = n^2(1-\nu) - \Omega^2(3-\nu)/2,\\
&F = (\Omega^2 - n^2)[\Omega^2 - n^2(1-\nu)/2],
\end{aligned} \tag{D.7}$$

where ρ_s, h and ν are the density, thickness and Poisson's ratio of the shell, respectively. The shear wave speed (C_s) is related to the compressional wave speed (C_p) by Poisson's ratio in the following equation [53].

$$\frac{C_s}{C_p} = \sqrt{\frac{1-2\nu}{2(1-\nu)}}. \tag{D.8}$$

The modal acoustic impedance of the surrounding medium is :

$$Z_n^f(ka,\alpha) = \imath\rho c \frac{ka}{\sqrt{k^2a^2 - \alpha^2}} \frac{H_n^{(1)}\left(\sqrt{k^2a^2-\alpha^2}\right)}{H_n'^{(1)}\left(\sqrt{k^2a^2-\alpha^2}\right)}. \tag{D.9}$$

Therefore, the equation for the modal wavenumber is obtained as follows :

$$\left(\frac{h}{a}\right)\left(\frac{\rho_s}{\rho}\right)\left(\frac{c_p}{c}\right)^2 (ka)^{-2}\frac{A\alpha^4+B\alpha^2+C}{D\alpha^4+E\alpha^2+F} = \frac{H_n^{(1)}\left(\sqrt{k^2a^2-\alpha^2}\right)}{nH_n^{(1)}\left(\sqrt{k^2a^2-\alpha^2}\right)-\sqrt{k^2a^2-\alpha^2}H_{n+1}^{(1)}\left(\sqrt{k^2a^2-\alpha^2}\right)}. \tag{D.10}$$

Since the modal system impedance is an even function of the non-dimensional axial wavenumber α, it can possibly have 4 zeros. The maximum membrane mode number is short of $n = ka$. Two of the 4 zeros are the negative pairs of others, but not all of those zeros represent the contributions from supersonic modal membrane waves. Zeros outside of the supersonic membrane range should be eliminated.

In order to match the boundary conditions correctly, the shear and compressional components of each membrane mode must be distinguished properly. For each mode, the compressional wave travels faster than the shear wave in the helical direction of the shell and it consequently belongs to the lower axial wavenumber (or higher radial wavenumber). By comparing the real part of the radial wavenumber, the shear and compressional modes can be chosen [41]. Since the system impedance is a complex function, a complex root finding algorithm is required to find its zeros. Muller's method [34, 56] is used with the zeros of the same shell in vacuum as initial guesses.

Given the computed modal membrane wavenumbers, it is possible to derive the free membrane mode contribution to the scattered pressure field.

$$\begin{aligned} w_r(z,\theta,t) &= e^{-\iota\omega t}\sum_{n=0}^{\infty} W_{rn}\cos(n\theta), \\ W_{rn}(z) &= \begin{cases} A_n e^{\iota\alpha_n z/a} + B_n e^{\iota\beta_n z/a} + C_n e^{-\iota\alpha_n z/a} + D_n e^{-\iota\beta_n z/a} & \text{for } n>0 \\ B_n e^{\iota\beta_n z/a} + D_n e^{-\iota\beta_n z/a} & \text{for } n=0 \end{cases}, \end{aligned} \tag{D.11}$$

where α_n and β_n are the zeros of the modal system impedance for the n th circumferential order. α_n represents the shear wave contribution and β_n is the non-dimensional axial wavenumber of the n th modal compressional wave. Since the zeroth order shear mode represents a torsional motion with no radial component of displacement, it does not couple to the surrounding medium. Therefore, the zeroth order shear wave contribution is omitted throughout the formulation.

With the homogeneous equation of motion in Reference [25], the previously defined solution form and Hooke's law, the ratios of modal coefficients between displacements and axial stress are obtained as follows :

$$J_{\gamma n} \equiv \left.\frac{U}{W}\right|_{\gamma,n} = \begin{cases} \dfrac{-\iota\nu\gamma[\Omega^2-\gamma^2(1-\nu)/2-n^2]-\iota\gamma n^2(1+\nu)/2}{\{[\Omega^2-\gamma^2-n^2(1-\nu/2)][\Omega^2-n^2-\gamma^2(1-\nu/2)] \\ -\gamma^2n^2(1+\nu)^2/4\}} & \text{for } n>0 \\ \dfrac{\iota\nu\gamma}{\gamma^2-\Omega^2} & \text{for } n=0 \end{cases}, \tag{D.12}$$

$$S_{\gamma n} \equiv \left.\frac{V}{W}\right|_{\gamma,n} = \frac{n[\Omega^2-\gamma^2-n^2(1-\nu)/2]+\nu\gamma^2 n(1+\nu)/2}{\left\{[\Omega^2-\gamma^2-n^2(1-\nu/2)][\Omega^2-n^2-\gamma^2(1-\nu/2)]\right.} \\ \left. -\gamma^2 n^2(1+\nu)^2/4\right\}, \tag{D.13}$$

and

$$T_{\gamma n} \equiv \left.\frac{N}{W}\right|_{\gamma,n} = \left(\frac{E}{1-\nu^2}\right)\left(\frac{h}{a}\right)\left[\imath\gamma J_{\gamma n}+\nu(nS_{\gamma n}+1)\right] \tag{D.14}$$

where E is the Young's modulus of the shell. Since the free membrane contribution of the radial wave is expressed as the summation of circumferential orders with modal coefficients, it is natural to have the other physical quantities in the same form. The radial displacement of the forced and free membrane mode is :

$$\begin{aligned} w(z,\theta) &= \sum_{n=0}^{\infty} W_n(z)\cos(n\theta), \\ W_n(z) &= W_{rn}(z)+W_{0n}e^{\imath\alpha_i z/a}. \end{aligned} \tag{D.15}$$

The circumferential displacement field is :

$$\begin{aligned} v(z,\theta) &= \sum_{n=0}^{\infty} V_n(z)\sin(n\theta), \\ V_n(z) &= S_{\alpha_n n}A_n e^{\imath\alpha_n z/a}+S_{\beta_n n}B_n e^{\imath\beta_n z/a} \\ &\quad +S_{\alpha_n n}C_n e^{-\imath\alpha_n z/a}+S_{\beta_n n}D_n e^{-\imath\beta_n z/a}. \end{aligned} \tag{D.16}$$

The axial stress is :

$$\begin{aligned} N(z,\theta) &= \sum_{n=0}^{\infty} N_n(z)\cos(n\theta), \\ N_n(z) &= T_{\alpha_n n}A_n e^{\imath\alpha_n z/a}+T_{\beta_n n}B_n e^{\imath\beta_n z/a} \\ &\quad +T_{\alpha_n n}C_n e^{-\imath\alpha_n z/a}+T_{\beta_n n}D_n e^{-\imath\beta_n z/a}. \end{aligned} \tag{D.17}$$

By applying the boundary conditions that the axial stress N and the circumferential displacement v vanish at the ends of the shells ($z = 0, L$), the unknown coefficients of W_{rn} are derived as follows :

$$\begin{aligned} A_n &= \frac{W_{0n}}{2\imath\sin(\alpha_n\bar{L})}\frac{T_{\beta_n n}S_{\alpha_i n}-S_{\beta_n n}T_{\alpha_i n}}{\Delta_n}\left(e^{-\imath\alpha_n\bar{L}}-e^{\imath\alpha_i\bar{L}}\right) = \frac{W_{0n}}{2\imath\sin(\alpha_n\bar{L})}\bar{A}_n, \\ B_n &= \frac{W_{0n}}{2\imath\sin(\beta_n\bar{L})}\frac{T_{\alpha_n n}S_{\alpha_i n}-S_{\alpha_n n}T_{\alpha_i n}}{-\Delta_n}\left(e^{-\imath\beta_n\bar{L}}-e^{\imath\alpha_i\bar{L}}\right) = \frac{W_{0n}}{2\imath\sin(\beta_n\bar{L})}\bar{B}_n, \\ C_n &= \frac{W_{0n}}{2\imath\sin(\alpha_n\bar{L})}\frac{T_{\beta_n n}S_{\alpha_i n}-S_{\beta_n n}T_{\alpha_i n}}{\Delta_n}\left(e^{\imath\alpha_i\bar{L}}-e^{\imath\alpha_n\bar{L}}\right) = \frac{W_{0n}}{2\imath\sin(\alpha_n\bar{L})}\bar{C}_n, \\ D_n &= \frac{W_{0n}}{2\imath\sin(\beta_n\bar{L})}\frac{T_{\alpha_n n}S_{\alpha_i n}-S_{\alpha_n n}T_{\alpha_i n}}{-\Delta_n}\left(e^{\imath\alpha_i\bar{L}}-e^{\imath\beta_n\bar{L}}\right) = \frac{W_{0n}}{2\imath\sin(\beta_n\bar{L})}\bar{D}_n, \end{aligned} \tag{D.18}$$

where the common denominator Δ_n is defined as :

$$\Delta_n = T_{\beta_n n}S_{\alpha_n n}-S_{\beta_n n}T_{\alpha_n n}. \tag{D.19}$$

For $n = 0$, the coefficients for the shear scattered wave, A_n and C_n are zero while B_n and D_n are :

$$\begin{aligned} B_n &= \frac{W_{0n}}{2\imath \sin(\beta_n \bar{L})} \frac{T_{\alpha_i n}}{T_{\beta_n n}} \left(e^{-\imath \beta_n \bar{L}} - e^{\imath \alpha_i \bar{L}} \right) = \frac{W_{0n}}{2\imath \sin(\beta_n \bar{L})} \bar{B}, \\ D_n &= \frac{W_{0n}}{2\imath \sin(\beta_n \bar{L})} \frac{T_{\alpha_i n}}{T_{\beta_n n}} \left(e^{\imath \alpha_i \bar{L}} - e^{\imath \beta_n \bar{L}} \right) = \frac{W_{0n}}{2\imath \sin(\beta_n \bar{L})} \bar{D}. \end{aligned} \tag{D.20}$$

Therefore, the unknown radial displacement field generated by a free membrane wave are obtained. Its contribution to the time harmonic scattered pressure field is again derived from the boundary condition on the surface of shell ($r = a$).

$$\begin{aligned} p(r, \theta, z) &= \frac{1}{2\pi a} \int_{-\infty}^{\infty} \tilde{p}(r, \theta; \gamma) e^{\imath \gamma z / a} \, d\gamma, \\ \tilde{p}(r, \theta; \gamma) &= \sum_{n=0}^{\infty} \tilde{P}_n(\gamma) H_n^{(1)} \left(\bar{r} \sqrt{k^2 a^2 - \gamma^2} \right) \cos(n\theta), \end{aligned} \tag{D.21}$$

where $\bar{r} = r/a$. The surface radial displacements is :

$$\begin{aligned} w(z, \theta) &= \sum_{n=0}^{\infty} W_n(z) \cos(n\theta), \\ \tilde{w}(\gamma, \theta) &= \sum_{n=0}^{\infty} \tilde{W}_n(\gamma) \cos(n\theta), \\ \tilde{W}_n(\gamma) &= \int_{-\infty}^{\infty} W_n(z) e^{-\imath \gamma z / a} \, dz. \end{aligned} \tag{D.22}$$

Given the Fourier transform of the boundary condition at $r = a$,

$$\frac{\partial \tilde{p}(r, \theta; \gamma)}{\partial r} = -\rho(-\imath\omega)^2 \sum_{n=0}^{\infty} \tilde{W}_n(\gamma) \cos(n\theta), \qquad \text{at } r = a, \tag{D.23}$$

the Fourier transformed coefficient P_n is obtained :

$$\tilde{P}_n(\gamma) = \frac{a\rho\omega^2 \tilde{W}_n(\gamma)}{\sqrt{k^2 a^2 - \gamma^2} H_n'^{(1)} \left(\sqrt{k^2 a^2 - \gamma^2} \right)}. \tag{D.24}$$

By substituting the above coefficients into the original scattering pressure field, $p(r, \theta, z)$ becomes :

$$p(r, \theta, z) = \frac{\rho\omega^2}{2\pi} \sum_{n=0}^{\infty} \cos(n\theta) \left\{ \int_{-\infty}^{\infty} \frac{\tilde{W}_n(\gamma) H_n^{(1)} \left(\bar{r} \sqrt{k^2 a^2 - \gamma^2} \right)}{\sqrt{k^2 a^2 - \gamma^2} H_n'^{(1)} \left(\sqrt{k^2 a^2 - \gamma^2} \right)} e^{\imath \gamma z / a} \, d\gamma \right\}. \tag{D.25}$$

If the far-field is of interest, further simplifications can be done. With the change of variables

$$r = R\cos\phi, \qquad z = R\sin\phi \tag{D.26}$$

and the asymptotic approximation of the Hankel function with large arguments

$$H_n^{(1)}(x) \sim (-\imath)^n e^{\imath(x - \pi/4)} \sqrt{\frac{2}{\pi x}}, \qquad \text{as } x \to \infty, \tag{D.27}$$

the far-field pressure field becomes :

$$p(R,\phi,\theta) \sim \rho\omega^2 e^{-\imath\pi/4}\sqrt{\frac{a}{2\pi^3 R\cos\phi}}\sum_{n=0}^{\infty}(-\imath)^n\cos(n\theta) \times\left\{\int_{-\infty}^{\infty}\frac{\tilde{W}_n(\gamma)\exp\left[\imath R/a\left(\sqrt{k^2a^2-\gamma^2}\cos\phi+\gamma\sin\phi\right)\right]}{\left(k^2a^2-\gamma^2\right)^{3/4}H_n'^{(1)}\left(\sqrt{k^2a^2-\gamma^2}\right)}d\gamma\right\}. \tag{D.28}$$

The integral in the bracket is approximated by the stationary phase integral. The phase of the oscillating exponential term is :

$$\begin{aligned}\Psi &\equiv \frac{R}{a}\left(\sqrt{k^2a^2-\gamma^2}\cos\phi+\gamma\sin\phi\right),\\ \frac{\partial\Psi}{\partial\gamma} &= \frac{R}{a}\left(\frac{-\gamma}{\sqrt{k^2a^2-\gamma^2}}\cos\phi+\sin\phi\right),\\ \frac{\partial^2\Psi}{\partial\gamma^2} &= -\frac{R}{a}\frac{k^2a^2\cos\phi}{(k^2a^2-\gamma^2)^{3/2}}.\end{aligned} \tag{D.29}$$

When γ is equal to $\bar{\gamma} = ka\sin\phi$, the first derivative of the phase vanishes. The phase and its second derivative at $\gamma = \bar{\gamma}$ become :

$$\Psi(\bar{\gamma}) = kR, \qquad \frac{\partial^2\Psi(\bar{\gamma})}{\partial\gamma^2} = \frac{-R}{a}\frac{1}{ka\cos^2\phi}. \tag{D.30}$$

By substituting the above into the formulation of stationary phase, the bracket term is evaluated as follows :

$$I \sim \sqrt{\frac{2\pi}{k^2aR\cos\phi}}\frac{\tilde{W}_n(ka\sin\phi)}{H_n'^{(1)}(ka\cos\phi)}e^{\imath(kR-\pi/4)}. \tag{D.31}$$

The far-field radiated pressure is :

$$p(R,\phi,\theta) \sim \frac{\rho\omega^2 e^{\imath kR}}{\pi\imath kR\cos\phi}\sum_{n=0}^{\infty}(-\imath)^n\cos(n\theta)\frac{\tilde{W}_n(ka\sin\phi)}{H_n'^{(1)}(ka\cos\phi)}, \quad \text{as } R\to\infty. \tag{D.32}$$

Since the axial variations of the radial displacements are exponential functions in the region $0 < z < L$, the generic expression for the Fourier transformed displacement $\tilde{W}(\gamma)$ becomes :

$$\tilde{W}_{\gamma_0}(\gamma) = \int_0^L e^{\imath(\gamma_0-\gamma)z/a}dz = a\frac{\exp\left[\imath\bar{L}(\gamma_0-\gamma)\right]-1}{\imath(\gamma_0-\gamma)}, \tag{D.33}$$

where $\gamma_0 = \pm\alpha_n, \pm\beta_n$, and α_i . By substituting the coefficients of compressional and shear scattered radial displacements $\bar{A}_n, \bar{B}_n, \bar{C}_n, \bar{D}_n$ and the forced radial displacement field W_{0n} into the far-field radiated pressure, the pressure is obtained as :

$$P_r(R,\phi,\theta) = \frac{P_0}{\pi^2}\frac{\rho c(ka)^2}{(K_ia)(Ka)}\frac{e^{\imath kR}}{\imath kR}\sum_{n=0}^{\infty}\frac{\epsilon_n\cos(n\theta)Q_n}{H_n'^{(1)}(K_ia)H_n'^{(1)}(Ka)Z_n(\Omega,\alpha_i)}, \tag{D.34}$$

where K_i and K are the incident and receiver radial wavenumbers, respectively. The modal coeffi-

cient Q_n is the sum of the compressional, shear membrane, and forced scattering contributions :

$$\begin{aligned} Q_n =& Q_{n1} + Q_{n2} + Q_{n3} + Q_{n4} + Q_{n5} \\ =& \frac{\bar{A}_n}{\sin(\alpha_n \bar{L})} \frac{1-\exp\left[-\imath\bar{L}(\alpha_r-\alpha_n)\right]}{\alpha_n-\alpha_r} + \frac{\bar{B}_n}{\sin(\beta_n \bar{L})} \frac{1-\exp\left[-\imath\bar{L}(\alpha_r-\beta_n)\right]}{\beta_n-\alpha_r} \\ &+ \frac{(-\bar{C}_n)}{\sin(\alpha_n \bar{L})} \frac{1-\exp\left[-\imath\bar{L}(\alpha_r+\alpha_n)\right]}{\alpha_n+\alpha_r} + \frac{(-\bar{D}_n)}{\sin(\beta_n \bar{L})} \frac{1-\exp\left[-\imath\bar{L}(\alpha_r+\beta_n)\right]}{\beta_n+\alpha_r} \\ &+ 2\imath \frac{1-\exp\left[-\imath\bar{L}(\alpha_r-\alpha_i)\right]}{\alpha_i-\alpha_r}. \end{aligned} \tag{D.35}$$

The above pressure is a part of the total scattered pressure field. The total scattered pressure field is the sum of the scattering pressure by the infinite impedance boundary on the surface of the elastic scatterer ($P_{s\infty}$) and the remaining term (P_r) which is necessary to satisfy the elastic boundary conditions. Since the lengths of cylinders considered are finite, the corresponding scattered pressure by a finite rigid shell is to be obtained. The incident field omitting the time dependency is :

$$P_i = P_0 \exp\left(\frac{\imath\alpha_i z}{a}\right) \sum_{n=0}^{\infty} \epsilon_n \imath^n J_n(K_i x) \cos(n\theta), \tag{D.36}$$

where the following addition theorem of Bessel functions is used.

$$\exp(\imath z \cos\theta) = \sum_{n=0}^{\infty} \epsilon_n \imath^n J_n(z) \cos(n\theta), \tag{D.37}$$

which is derived from (9.1.41) and (9.1.42) of Reference [1]. Imposing the boundary condition at $x = a$, the radiated displacement field from the infinite-impedance cylinder of infinite length becomes :

$$W_{s\infty} = -W_i = -\frac{1}{\rho\omega^2}\frac{\partial P_i(a)}{\partial r} = -\frac{P_0 K_i}{\rho\omega^2} \sum_{n=0}^{\infty} \epsilon_n \imath^n J'_n(K_i a) \exp\left(\frac{\imath\alpha_i z}{a}\right) \cos(n\theta). \tag{D.38}$$

Using the previous technique used for evaluating the far-field pressure field (i.e. stationary phase approximation of the integral as $R \to \infty$), the scattered pressure produced by the rigid scatterer becomes :

$$P_{s\infty}(R, \phi, \theta) = -\frac{P_0}{2\pi} \frac{(ka)(K_i a)}{Ka} \frac{e^{\imath kR}}{\imath kR} \sum_{n=0}^{\infty} \frac{\epsilon_n \cos(n\theta) J'_n(K_i a) Q_{n5}}{H'^{(1)}_n(Ka)}. \tag{D.39}$$

Therefore, the total scattered field scattered by a finite cylindrical elastic shell P_{sc} becomes :

$$\begin{aligned} P_{sc} &= P_{s\infty} + P_r \\ &= \frac{\imath P_0 ka e^{\imath kR}}{2\pi KR} \sum_{n=0}^{N_{\max}} \left\{ \frac{\epsilon_n \cos(n\theta)}{H'^{(1)}_n(Ka)} \left[\frac{J'_n(K_i a) K_i Q_{n5}}{k} - \frac{2\rho c Q_n}{Z_n(\Omega, \alpha_i)\pi K_i a H'^{(1)}_n(K_i a)} \right] \right\}, \end{aligned} \tag{D.40}$$

where the summation is limited to the highest membrane mode number $N_{\max}$.

In order to implement evanescent incident and scattered waves by the analytic continuation, the angle θ in the solution D.40 is defined by the incident wave vector $\vec{k}_i$, the scattered (receiver)

wave vector $\vec{k}_r$, and the skew angle of the shell θ_{sk}.

$$\cos\theta = \frac{\vec{k}_i \Psi^T \Psi \vec{k}_r^T}{k_0^2}, \tag{D.41}$$

where Ψ is the coordinate rotational matrix from the global coordinates to the local coordinates of shell.

$$\Psi = \begin{pmatrix} 0 & 0 & -1 \\ -\sin\theta_{sk} & \cos\theta_{sk} & 0 \\ \cos\theta_{sk} & \sin\theta_{sk} & 0 \end{pmatrix}. \tag{D.42}$$

This page is blank.

Appendix E

Formulation of Spherical Elastic Shells

The homogeneous solution of the Helmholtz equation in a spherically symmetric geometry can be found by utilizing Legendre transformation.

$$\nabla^2 f(r,\theta) + k^2 f(r,\theta) = 0, \tag{E.1}$$

where k^2 is a wavenumber. In a spherically symmetric configuration, the Laplace operator becomes :

$$\nabla^2 = \frac{1}{r^2}\frac{\partial}{\partial r} r^2 \frac{\partial}{\partial r} + \frac{1}{r^2}\left(\frac{1}{\sin\theta}\frac{\partial}{\partial\theta}\sin\theta\frac{\partial}{\partial\theta}\right). \tag{E.2}$$

The Helmholtz equation can be separated in radius and angle coordinates by introducing the Legendre transform pair :

$$F(r,n) = \int_0^\pi f(r,\theta) P_n(\cos\theta)\sin\theta d\theta, \tag{E.3}$$

$$f(r,\theta) = \sum_{n=0}^{\infty}\left(n+\frac{1}{2}\right)F(r,n)P_n(\cos\theta), \tag{E.4}$$

where P_n is the Legendre polynomial of the n th order.

By replacing f with the above expression in the Helmholtz equation, an ordinary differential equation for F is obtained.

$$\left\{\frac{d^2}{dr^2} + \frac{2}{r}\frac{d}{dr} - \frac{1}{r^2}\left[n(n+1) - k^2 r^2\right]\right\} F(r,n) = 0. \tag{E.5}$$

The solutions to the above differential equation are n th order spherical Bessel functions. A general form of $F(r,n)$ is :

$$F(r,n) = a_n j_n(kr) + b_n y_n(kr), \tag{E.6}$$

where a_n and b_n are constant. j_n and y_n are spherical Bessel functions of the first and second kind. The above solution form can be used with careful choices of spherical Bessel function and time dependency for a physical problem. In order to have a finite solution at the origin $r = 0$, the coefficients b_n should be zero. In order to have an out-going field in the far field $r \to \infty$ (i.e. radiation condition), the asymptotic expression of the above solution can be used to find the

relation between a_n and b_n.

$$\lim_{kr\to\infty} F(r,n) = \frac{a_n}{z}\sin\left(z-\frac{n\pi}{2}\right) - \frac{b_n}{z}\cos\left(z-\frac{n\pi}{2}\right). \tag{E.7}$$

When $b_n = \pm\imath a_n$, the above solution becomes a propagating field. Given a time dependency of $\exp(-\imath\omega t)$, an out-going propagation field can be generated by $b_n = \imath a_n$ only. With $b_n = \imath a_n$, the far field solution becomes :

$$\lim_{kr\to\infty} F(r,n) = -\frac{\imath a_n}{z} e^{\imath(z-n\pi/2)} = a_n \lim_{kr\to\infty} h_n^{(1)}(kr). \tag{E.8}$$

The far field solution has the same asymptotic behavior as the spherical Hankel function of the first kind. Therefore, it is necessary to use a different solution form considering these two conditions.

$$F(r,n) = a_n j_n(kr) + b_n h_n^{(1)}(kr), \tag{E.9}$$

where $h_n^{(1)}$ is the n th order spherical Hankel function defined as :

$$h_n^{(1)}(z) = j_n(z) + \imath y_n(z). \tag{E.10}$$

This choice of solution form guarantees theoretical independence of the solutions as well as numerical independence [43].

When a physical problem involves compressional and shear components, the corresponding homogeneous displacement potentials ϕ and ψ of compressional and shear waves are as follows [43] :

$$\phi(r,\theta) = \sum_{n=0}^{\infty}\left(n+\frac{1}{2}\right)\left[A^j(n)\, j_n(hr) + A^h(n)\, h_n^{(1)}(hr)\right] P_n(\cos\theta), \tag{E.11}$$

$$\psi(r,\theta) = \sum_{n=0}^{\infty}\left(n+\frac{1}{2}\right)\left[B^j(n)\, j_n(kr) + B^h(n)\, h_n^{(1)}(kr)\right] P_n(\cos\theta), \tag{E.12}$$

where $h = \omega/c_p$ and $k = \omega/c_s$ are the wavenumbers of compressional and shear waves, respectively.

The above solutions represent wave components as a spherical harmonic sum of spherical Bessel functions j_n and $h_n^{(1)}$. In order to have a finite solution at the origin and satisfy the radiation condition, the coefficients $A^h(n)$ and $B^h(n)$ of the innermost spherical layer must vanish as well as $A^j(n)$ and $B^j(n)$ of the outermost spherical layer.

Besides the above two conditions, a set of boundary conditions along each interface between two adjacent layers is necessary to solve the system. The general boundary conditions are obtained by enforcing continuity of displacements and tractions on the spherical interfaces. Therefore, the expression for displacements and tractions are also necessary. The above displacement potentials are related to displacement by the definition and the stress components can be obtained by Hooke's law.

$$u_r = \frac{\partial\phi}{\partial r} + \frac{1}{r\sin\theta}\frac{\partial}{\partial\theta}\sin\theta\frac{\partial\psi}{\partial\theta}, \tag{E.13}$$

$$u_\theta = \frac{1}{r}\frac{\partial\phi}{\partial\theta} - \frac{1}{r}\frac{\partial}{\partial r}r\frac{\partial\psi}{\partial\theta}, \tag{E.14}$$

$$\sigma_{rr} = \lambda\nabla^2\phi + 2\mu\frac{\partial u_r}{\partial r}, \tag{E.15}$$

$$\sigma_{r\theta} = \mu\left[\frac{1}{r}\frac{\partial u_r}{\partial \theta} + \left(\frac{\partial}{\partial r} - \frac{1}{r}\right)u_\theta\right], \tag{E.16}$$

where the subscripts r and θ correspond to the radial and tangential coordinates, respectively. Since the displacement potentials are expressed in sums of spherical harmonics, the corresponding displacements and tractions can be expressed in similar form. When the differential operators in the above expression are applied to the homogeneous displacement potentials, the spherical harmonic coefficients for the displacements and tractions are obtained as follows. While the radial components u_r and σ_{rr} are spherically symmetric, the tangential components u_θ and $u_{r\theta}$ are anti-symmetric with respect to the tangential coordinate. The radial displacement is :

$$u_r(r,\theta) = \sum_{n=0}^{\infty}\left(n+\frac{1}{2}\right)u_r(r,n)P_n(\cos\theta), \tag{E.17}$$

where the n th order coefficient $u_r(r,n)$ is obtained as :

$$\begin{aligned} u_r(r,n) =& h\,j_n'(hr)A^j(n) + h\,h_n'^{(1)}(hr)A^h(n) \\ & - \frac{n(n+1)}{r}j_n(kr)B^j(n) - \frac{n(n+1)}{r}h_n^{(1)}(kr)\,B^h(n). \end{aligned} \tag{E.18}$$

The tangential displacement is :

$$u_\theta(r,\theta) = -\sin\theta\sum_{n=1}^{\infty}\left(n+\frac{1}{2}\right)u_\theta(r,n)P_n'(\cos\theta), \tag{E.19}$$

where the coefficient $u_\theta(r,n)$ is :

$$\begin{aligned} u_\theta(r,n) =& \frac{j_n(hr)}{r}A^j(n) + \frac{h_n^{(1)}(hr)}{r}A^h(n) \\ & - \left[\frac{j_n(kr)}{r} + k\,j_n'(kr)\right]B^j(n) - \left[\frac{h_n^{(1)}(kr)}{r} + h\,h_n'^{(1)}(kr)\right]B^h(n). \end{aligned} \tag{E.20}$$

The radial stress is :

$$\sigma_{rr}(r,\theta) = \sum_{n=0}^{\infty}\left(n+\frac{1}{2}\right)\sigma_{rr}(r,n)P_n(\cos\theta), \tag{E.21}$$

where the coefficient $\sigma_{rr}(r,n)$ becomes :

$$\begin{aligned} \sigma_{rr}(r,n) =& \left[-\lambda h^2 j_n(hr) + 2\mu h^2 j_n''(hr)\right]A^j(n) + \left[-\lambda h^2 h_n^{(1)}(hr) + 2\mu h^2 h_n''^{(1)}(hr)\right]A^h(n) \\ & + \frac{2n(n+1)\mu k}{r}\left[\frac{j_n(kr)}{kr} - j_n'(kr)\right]B^j(n) \\ & + \frac{2n(n+1)\mu k}{r}\left[\frac{h_n^{(1)}(kr)}{kr} - h_n'^{(1)}(kr)\right]B^h(n). \end{aligned} \tag{E.22}$$

The tangential stress is :

$$\sigma_{r\theta}(r,\theta) = -\sin\theta\sum_{n=1}^{\infty}\left(n+\frac{1}{2}\right)\sigma_{r\theta}(r,n)P_n'(\cos\theta), \tag{E.23}$$

where

$$\sigma_{r\theta}(r,n) = \frac{2\mu h}{r}\left[j_n'(hr) - \frac{j_n(hr)}{hr}\right]A^j(n) + \frac{2\mu h}{r}\left[h_n'^{(1)}(hr) - \frac{h_n^{(1)}(hr)}{hr}\right]A^h(n)$$
$$+ \frac{\mu k}{r}\left[[2-n(n+1)]\frac{j_n(kr)}{kr} - kr\,j_n''(kr)\right]B^j(n) \qquad \text{(E.24)}$$
$$+ \frac{\mu k}{r}\left[[2-n(n+1)]\frac{h_n^{(1)}(kr)}{kr} - kr\,h_n''^{(1)}(kr)\right]B^h(n).$$

When obtaining the above coefficients, the following equalities are utilized [1]. The second derivative of the Legendre polynomial with $\cos\theta$ argument becomes :

$$\frac{1}{\sin\theta}\frac{d}{d\theta}\left[\sin\theta\frac{d}{d\theta}P_n(\cos\theta)\right] = -n(n+1)P_n(\cos\theta). \qquad \text{(E.25)}$$

The first and second order derivatives of the spherical Bessel functions j_n and $h_n^{(1)}$ can be obtained by the following recurrence relations.

$$f_n'(z) = f_{n-1}(z) - \frac{n+1}{z}f_n(z), \qquad \text{(E.26)}$$

$$f_n''(z) = \left[\frac{(n+1)(n+2)}{z^2} - 1\right]f_n(z) - \frac{2}{z}f_{n-1}(z), \qquad \text{(E.27)}$$

where f_n is j_n or $h_n^{(1)}$.

For the target scattering problem in this thesis, only compressional plane waves and their combinations are considered as incident fields. A compressional plane wave can be expressed as a sum of spherical harmonics as follows :

$$\hat{\phi} = e^{ihr\cos\theta} = \sum_{n=0}^{\infty} 2\left(n+\frac{1}{2}\right)i^n\,j_n(hr)\,P_n(\cos\theta). \qquad \text{(E.28)}$$

The spherical shell considered in this thesis is surrounded by a fluid medium, loaded with fluid inside, and it has an homogeneous elastic layer. Therefore, the solution forms satisfying the radiation condition and including a particular solution are as follows.
In the surrounding medium :

$$\phi_w + \hat{\phi}_w = \sum_{n=0}^{\infty}\left(n+\frac{1}{2}\right)\left[2i^n\,j_n(h_w r) + A_w^h(n)\,h_n^{(1)}(h_w r)\right]P_n(\cos\theta). \qquad \text{(E.29)}$$

In the elastic wall :

$$\phi_s = \sum_{n=0}^{\infty}\left(n+\frac{1}{2}\right)\left[A_s^j(n)\,j_n(h_s r) + A_s^h(n)\,h_n^{(1)}(h_s r)\right]P_n(\cos\theta), \qquad \text{(E.30)}$$

$$\psi_s = \sum_{n=0}^{\infty}\left(n+\frac{1}{2}\right)\left[B_s^j(n)\,j_n(k_s r) + B_s^h(n)\,h_n^{(1)}(k_s r)\right]P_n(\cos\theta). \qquad \text{(E.31)}$$

Inside of the shell :

$$\phi_f = \sum_{n=0}^{\infty}\left(n+\frac{1}{2}\right)A_f^j(n)\,j_n(h_f r)\,P_n(\cos\theta). \qquad \text{(E.32)}$$

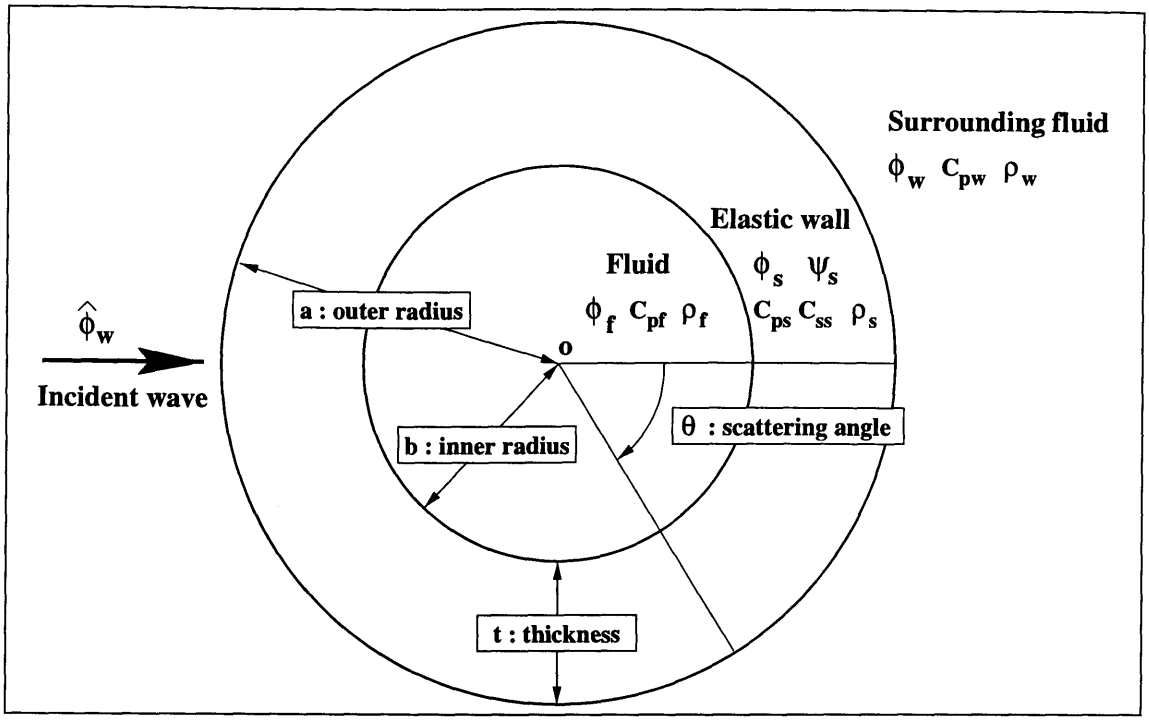

Figure E-1: The incident field and unknown displacement potentials of a spherical elastic shell.

With the above solution forms and the following six boundary conditions, the unknown potential coefficients $A_w^h(n)$, $A_s^j(n)$, $A_s^h(n)$, $B_s^j(n)$, $B_s^h(n)$, and $A_f^j(n)$ can be obtained.
Continuity of radial displacement at the outer radius $r = a$ requires that :

$$\begin{aligned} & h_w j_n'(h_w a) 2 i^n \phi_0 + h_w h_n'^{(1)}(h_w a) A_w^h(n) \\ & - h_s j_n'(h_s a) A_s^j(n) - h_s h_n'^{(1)}(h_s a) A_s^h(n) \\ & + \frac{n(n+1)}{a} j_n(k_s a) B_s^j(n) + \frac{n(n+1)}{a} h_n^{(1)}(k_s a) B_s^h(n) = 0. \end{aligned} \tag{E.33}$$

Continuity of radial stress at the outer radius $r = a$ leads to :

$$\begin{aligned} & -\lambda_w h_w^2 j_n(h_w a) 2 i^n \phi_0 - \lambda_w h_w^2 h_n^{(1)}(h_w a) A_w^h(n) \\ & -\left[-\lambda_s h_s^2 j_n(h_s a) + 2\mu_s h_s^2 j_n''(h_s a)\right] A_s^j(n) \\ & -\left[-\lambda_s h_s^2 h_n^{(1)}(h_s a) + 2\mu_s h_s^2 h_n''^{(1)}(h_s a)\right] A_s^h(n) \\ & -\frac{2n(n+1)\mu_s k_s}{a}\left[\frac{j_n(k_s a)}{k_s a} - j_n'(k_s a)\right] B_s^j(n) \\ & -\frac{2n(n+1)\mu_s k_s}{a}\left[\frac{h_n^{(1)}(k_s a)}{k_s a} - h_n'^{(1)}(k_s a)\right] B_s^h(n) = 0. \end{aligned} \tag{E.34}$$

Zero tangential stress at the outer radius $r = a$ means that :

$$\begin{aligned}
&\frac{2\mu_s h_s}{a}\left[j_n'(h_s a) - \frac{j_n(h_s a)}{h_s a}\right] A_s^j(n) + \frac{2\mu_s h_s}{a}\left[h_n'^{(1)}(h_s a) - \frac{h_n^{(1)}(h_s a)}{h_s a}\right] A_s^h(n) \\
&+ \frac{\mu_s k_s}{a}\left[[2 - n(n+1)]\,\frac{j_n(k_s a)}{k_s a} - k_s a\, j_n''(k_s a)\right] B_s^j(n) \\
&+ \frac{\mu_s k_s}{a}\left[[2 - n(n+1)]\,\frac{h_n^{(1)}(k_s a)}{k_s a} - k_s a\, h_n''^{(1)}(k_s a)\right] B_s^h(n) = 0.
\end{aligned} \tag{E.35}$$

Continuity of radial displacement at the inner radius $r = b = a - t$ implies that :

$$\begin{aligned}
&h_s\, j_n'(h_s b) A_s^j(n) + h_s\, h_n'^{(1)}(h_s b) A_s^h(n) - \frac{n(n+1)}{b} j_n(k_b b) B_s^j(n) - \frac{n(n+1)}{b} h_n^{(1)}(k_s b) B_s^h(n) \\
&- h_f\, j_n'(h_f b) A_f^j(n) = 0.
\end{aligned} \tag{E.36}$$

Continuity of radial stress at the inner radius $r = b$ leads to :

$$\begin{aligned}
&\left[-\lambda_s h_s^2\, j_n(h_s b) + 2\mu_s h_s^2\, j_n''(h_s b)\right] A_s^j(n) + \left[-\lambda_s h_s^2\, h_n^{(1)}(h_s b) + 2\mu_s h_s^2\, h_n''^{(1)}(h_s b)\right] A_s^h(n) \\
&+ \frac{2n(n+1)\mu_s k_s}{b}\left[\frac{j_n(k_s b)}{k_s b} - j_n'(k b)\right] B_s^j(n) + \frac{2n(n+1)\mu_s k_s}{b}\left[\frac{h_n^{(1)}(k_s b)}{k_s b} - h_n'^{(1)}(k b)\right] B_s^h(n) \\
&+ \lambda_f h_f^2\, j_n(h_f b) A_f^j(n) = 0.
\end{aligned} \tag{E.37}$$

Zero tangential stress at the inner radius $r = b$ means that :

$$\begin{aligned}
&\frac{2\mu_s h_s}{b}\left[j_n'(h_s b) - \frac{j_n(h_s b)}{h_s b}\right] A_s^j(n) + \frac{2\mu_s h_s}{b}\left[h_n'^{(1)}(h_s b) - \frac{h_n^{(1)}(h_s b)}{h_s b}\right] A_s^h(n) \\
&+ \frac{\mu_s k_s}{b}\left[[2 - n(n+1)]\,\frac{j_n(k_s b)}{k_s b} - k_s b\, j_n''(k_s b)\right] B_s^j(n) \\
&+ \frac{\mu_s k_s}{b}\left[[2 - n(n+1)]\,\frac{h_n^{(1)}(k_s b)}{k_s b} - k_s b\, h_n''^{(1)}(k_s b)\right] B_s^h(n) = 0.
\end{aligned} \tag{E.38}$$

Appendix F

Manual for SCATT Package

F.1 Introduction

The *SCATT* package has been developed to investigate rough interface scattering and target scattering in ocean waveguides. With a given scatterer and waveguide configuration, it computes the corresponding scattered field in space and time. Since the *SCATT* package utilizes several computational modules from 2-D and 3-D *OASES* [44], it is a must to know 2-D and 3-D *OASES* prior to using the *SCATT*. *OASES Ver.2.1 User Guide and Reference Manual* [44] should be referred to especially for using 2-D *oast* and the pulse post-processor *pp*.

The theoretical idea of *SCATT* is based on representing a scatterer as a 'virtual source'. The term 'virtual source' is used to differentiate itself from the 'physical' or 'real' source in the medium. A virtual source exists when a physical source insonifies a scatterer. It mathematically represents a scatterer as source term.

The package consists of six major modules. Table F.1 shows major modules and their programs. This manual describes the installation of these programs and how to use them along with several examples.

F.2 Installation

F.2.1 Computing Environment

Since the *SCATT* package has been developed on Digital UNIX and Linux platforms and it utilizes external X11 applications for post-processing, it has a better chance to run on UNIX platforms. The source codes are mostly written in standard FORTRAN 77 syntax with several widely used (or popular) UNIX extensions. Part of the source codes are written in ANSI C. Therefore, an ideal computing environment is UNIX with an X11 interface, native FORTRAN 77 and C compilers. A FORTRAN to C converter can be used if a native FORTRAN 77 compiler is not available. However, this method has not been tested and it is not recommended.

F.2.2 Building Package

From the file *scatt.tar.gz*, the source code tree can be built using *tar* and *gzip* commands.

```
gzip -d -c scatt.tar.gz | tar xvf -
```

This process will create the directory *scatt* and its subdirectories. Figure F-1 shows the file tree of

MODULE / Program	inputs	outputs
INCIDENT FIELD		
oast	<incidence>.dat	<incidence>.sck
ROUGH INTERFACE		
mp2	standard input (unit5) or <patch>.in	<patch>.dat, <patch>.mtv
sp2	<patch>.dat	<patch>.mtv
sfmask	<patch>.dat w/ command line parameters	<patch>.dat
fvdct	<incidence>.sck	<incidence>.dct
fvpcvs	<patch>.dat, <incidence>.sck	<patch>_<incidence>.cvs
SPHERE TARGET		
sphcvs_es	<incidence>.sck with command line parameters	<incidence>.cvs
CYLINDRICAL SHELL TARGET		
wkaxsam	<incidence>.sck w/ standard input (unit5) or <incidence>.sck, <cylinder>.geo	<incidence>.inc
cmfinder	standard input (unit5) or <shell>.par	<mode>.mod
cylcvs	<mode>.mod, <incidence>.inc with command line parameters	<mode>.mod_<incidence>.cvs
3D SCATTERED FIELD		
oast3	<field>.dat, <source>.cvs	<field>.trf, <field>.cdr, <filed>.bdr <field>.plp, <field>.plt
avpatch	<incidence>.dat, <patch>.in, <pro>.dat with command line parameters	<pro>_av.cdr, <pro>_av.bdr <pro>_av.plp, <pro>_av.plt
tspatch	<incidence>.dat, <patch>.dat, <pro>.dat with command line parameters	<pro>_pa.trf
tssphere	<incidence>.dat, <pro.dat> with command line parameters	<pro>_sp.trf
tsshell	<incidence>.dat, <cylinder>.geo, <shell>.par, <pro>.dat with command line parameters	<pro>_sh.trf
POST PROCESSOR		
tsbf	OASES' pp generated trace files (depth, range, azimuth stacks)	<trace>.ts.mtv, <trace>.sp.mtv, <trace>.bf.mtv

Table F.1: Major modules and programs of the SCATT package. The second column is for input files and arguments. The third column is for output files from each program.

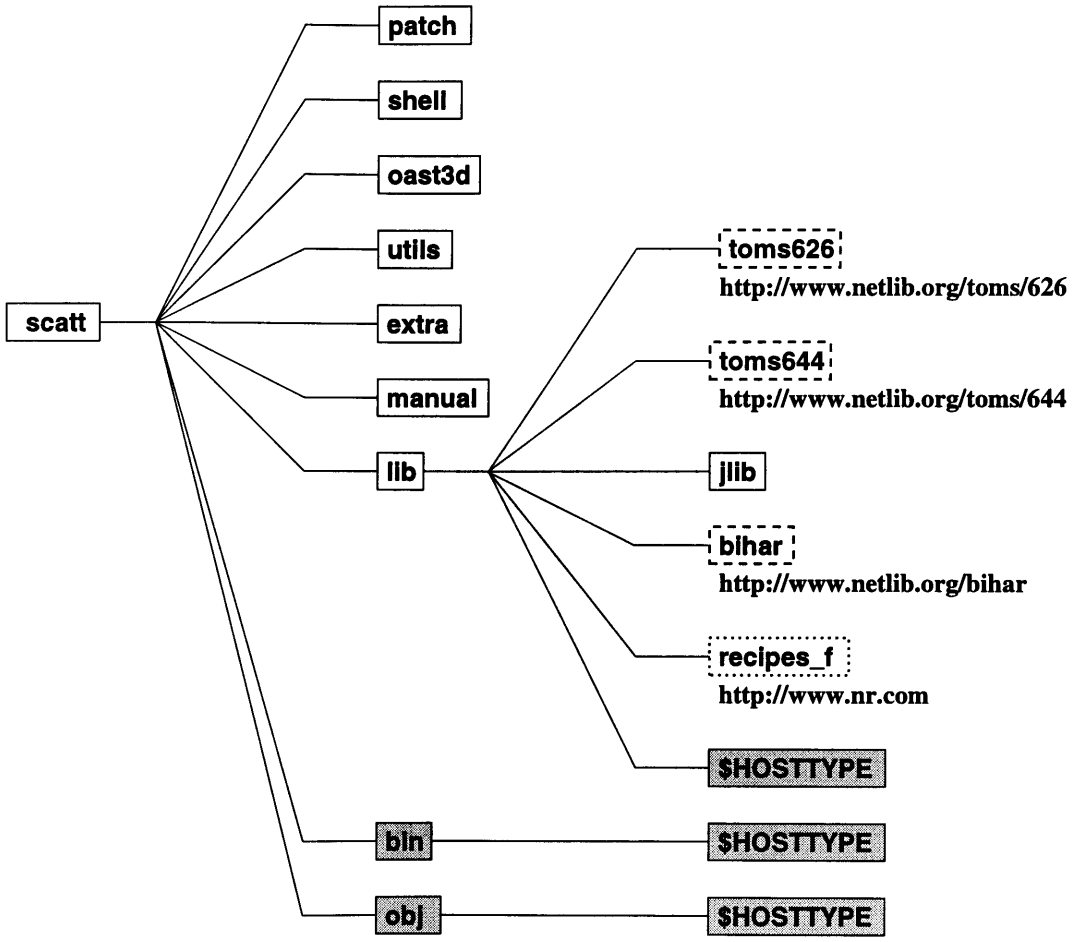

Figure F-1: File tree of the SCATT package. Except Numerical Recipes FORTRAN, original source codes of other libraries can be download from the corresponding URLs.

CPU Type	Operating System	FORTRAN 77 Compiler	C compiler	$HOSTTYPE
Alpha	Digital UNIX	Digital FORTRAN	Digital C	alpha
Intel x86	Linux	GNU FORTRAN 77	GNU C	i386-linux
Sparc	SunOS	SUN FORTRAN 77	SUN C	sun4
Mips	IRIX	MIPS FORTRAN 77	MIPS C	iris4d

Table F.2: Supported platforms and compilers. Values of `$HOSTTYPE$` variables are shown in the last column.

the *SCATT* package.

If the installation is performed on platforms other than Digital UNIX or Linux Intel PC, the *makefile* in every sub directory should be modified in order to take advantage of local compilers. Each *makefile* contains machine dependent compiler and linker options. These options are selected by reading an environmental variable `$HOSTTYPE`. The local configuration can be added as a target named `$HOSTTYPE` in the *makefile*. Examples of Alpha (Digital UNIX), Intel PC (Linux), SGI (IRIX), and SUN (SunOS) with their native compilers are included in each *makefile*. Table F.2 shows the list of supported platforms and their generic compilers.

F.2.3 Requirements of External Programs

Since the *SCATT* package utilizes Numerical Recipes FORTRAN version 2 [39], the license should be acquired and the library should be installed properly prior to the installation of *SCATT*. *jlib*, one of required libraries, has been developed together with *SCATT* and it is distributed with the source code. Other necessary libraries are included along with source codes and they are freely available through the Internet. In Figure F-1, the free libraries are boxed with a dashed line. In order to run the *SCATT* package, *OASES* should be installed and all of its executable files should be accessible. The export version of *OASES* is available in `ftp://keel.mit.edu/pub/oases` . As mentioned in Reference [44], *PLOTMTV* also has to be installed for graphic outputs. The source code and patch file are available in `ftp://keel.mit.edu/pub/Plotmtv` . In addition to the above programs, the *SCATT* package requires several UNIX utilities such as *gzip*, *sed*, *bc*, *perl*, and *grep*. If the animation output of the time series in FLI is desired, *netpbm utility*, *ghostscript*, and *ppm2fli* should be installed.

F.3 Incident Field

F.3.1 oast

oast is a part of 2-D *OASES*. It computes potential values for the incident field. Option 'E' should be activated to generate an .sck file. The output .sck file contains amplitudes of up and down plane waves in layers adjacent to a scatterer. Option 'E' in the input file will read one extra line of input. Otherwise, the input file structure is identical to an ordinary *oast* input file.

```
Usage: oast <input>
```

The source code of *oast* has the following line to read an additional line when option 'E' is enabled.

```
READ(1,*) PCENTER,INPATCH,NFFT_X,NFFT_Y,SPLEN_X,SPLEN_Y
```

- PCENTER : Horizontal range from the source to the center of scatterer in *km*.
- INPATCH : Interface number where a scatterer is located.
  1. The depth of the rough interface corresponds to the *INPATCH+1* th interface depth.
  2. For target scattering, the target is located at the middle depth between the *INPATCH* th and *INPATCH+1* th interfaces.
- NFFT_X : Number of patch grids in x direction. Meaningless for target.
- NFFT_Y : Number of patch grids in y direction. Meaningless for target.
- SPLEN_X :
  1. For rough interface, it is the length of the patch in the x direction in meters.
  2. For a spherical target, the target radius is half of SPLEN_X in meters.
  3. For a cylindrical shell, it is meaningless.
- SPLEN_Y : Length of patch in y direction in meter. Meaningless for target.

Remark 1: When the number of wavenumber samples is equal to 1 and $c_{min} = c_{max}$, wavenumber integration is not performed. *oast* will produce the case of single plane wave incidence. The grazing angle is equal to $\theta_i = \cos^{-1}(c_p/c_{min})$ where c_p is the medium compressional wave speed and c_{min} is minimum phase speed.
Remark 2: Other functionalities are exactly the same as *oast* run without option 'E'.

F.4 Rough Interface

F.4.1 mp2

mp2 synthesizes random roughness on the rectangular patches. Given the roughness parameters, roughness is randomly realized. The output is a .dat file.

```
Usage: mp2 [options]

Options:
 -detail     : generates plots for each process.
 -e <N>      : generates N ensembles.
 -f <prefix> : set the prefix of output files. Otherwise, the prefix
               is determined by power spectrum type and time stamp.
 -h          : show usage or howto.
 -ispect     : generate input power spectrum plots in plotmtv contour
               format.
 -p          : generates plot outputs in plotmtv contour format.
 -s          : computes roughness slopes (derivatives)
               in x and y directions.
```

Remark 1: *mp2* asks for the parameters of the roughness power spectrum and window type. Redirection of input can be used for batch jobs such as *avpatch*.
The input parameters for *mp2* are :

- nx : number of grid points in the x direction.
- ny : number of grid points in the y direction.
- sx : length of the patch in x direction in meters.
- sy : length of the patch in y direction in meters.
- $c1$: major correlation length in meters.
- $c2$: minor correlation length in meters.
- sk : angle of anisotropy in degrees.
- rm : *RMS* roughness height in meters.

Remark 2: The parameters nx and ny should be powers of two. If not, they will be changed to the next smallest powers of two. If nx is negative, both nx and ny will be the absolute value of input nx. When $c1$ is negative, $c1$ and $c2$ will be absolute value of input $c1$. Angle of anisotropy sk is measured in the counter-clockwise direction. sk is not required when $c1 = c2$ (i.e. isotropic case).

The type of power spectrum to use is specified after the general roughness parameters. Some of the power spectra require additional input parameters.

- Goff-Jordan : 2-D Goff-Jordan power spectrum. fd (fractal dimension of Goff-Jordan power spectrum) is required ($2 \leq fd < 3$).
- Gaussian : 2-D Gaussian power spectrum.
- Ripple (GJ) : Ripple structure modeled using a Goff-Jordan power spectrum with $fd = 2.5$.
- Ripple (GS) : Ripple structure modeled using a Gaussian power spectrum.
- Ripple (GS) + Isotropic Goff-Jordan : Ripple structure modeled using a Gaussian power spectrum with background roughness from an isotropic Goff-Jordan power spectrum. The *RMS* height (rb) and correlation length (cb) of the background roughness are additionally required. The fractal dimension of the background roughness is fixed at 2.5. The *RMS* height of the background roughness should be less than the total *RMS* roughness height (rm). Foreground *RMS* height will be $rm - rb$.
- Ripple (GS) + Isotropic Gaussian : Ripple structure modeled using a Gaussian power spectrum with background roughness from an isotropic Gaussian power spectrum. The *RMS* height (rb) and correlation length (cb) of the background roughness are also required.

Remark 3: For ripple structures, the roles of major and minor correlation lengths are different from the other power spectra. The inverse of the major correlation length $c1$ determines the spreading width of ripples in the wavenumber domain while the inverse of the minor correlation length $c2$ sets the separation between the two peaks (maxima) of the power spectrum in the wavenumber domain.
Remark 4: *RMS* height of background roughness should be less than total *RMS* roughness height (rm). The foreground *RMS* height will be $rm - rb$.

mp2 has two window models. If the roughness output is to be windowed externally such as by *sfmask*, one must chose the 'rectangular' window option.

- Hanning : 2-D Hanning window is applied.
- Rectangular : No window function is applied.

F.4.2 sp2

sp2 generates a plot of the roughness spectrum from the output of *mp2*. The plot format is *plotmtv*'s 2-D contour.

```
Usage: sp2 <input patch file>
```

F.4.3 sfmask

sfmask masks the roughness patch file from *mp2* with a 2-D Hanning window of the size of the sonar footprint. It truncates the patch data if necessary. The input patch roughness file should be generated with the rectangular window option in *mp2*.

```
Usage: sfmask -i <Iangle> -v <Vangle> -h <Hangle>
              -d <distance> <input patch> [output patch]

Arguments:
 -i <Iangle>   : incident grazing angle in degrees.
 -v <Vangle>   : vertical angular beam width in degrees.
 -h <Hangle>   : horizontal angular beam width in degrees.
 -d <distance> : vertical separation between source and patch in m.
```

Remark: If the input roughness patch is too small to cover the sonar footprint, *sfmask* will not produce the output.

Shape of sonar footprint is assumed to be rectangular and the area of the sonar footprint is determined by the above 4 parameters with a 25% margin. When the calculated sonar footprint is small enough, the output roughness patch can have fewer grid points.

F.4.4 fvdct

fvdct computes the potential discontinuity field on the grids of the roughness patch. The input is an .sck file generated by *oast* and the output suffix is .dct .

```
Usage: fvdct <sck file> [dct file] [-a <adjust parameter file>]
```

Remark: The format of the parameter file is same as the last line of the *oast* input file. The following is the file structure.

```
PCENTER,INPATCH,NFFT_X,NFFT_Y,SPLEN_X,SPLEN_Y
```

Each variable in the above line has the same definition as in the *oast* input file. This file is especially useful because the patch parameters can be changed without re-running *oast*.

The potential values in the wavenumber domain are integrated on the grid points to compute the potential discontinuity in the spatial domain. In the case of single plane wave incidence, no integration is performed.

F.4.5 fvcvs

fvpcvs convolves the patch roughness (.dat file) with the potential discontinuity field (.dct file) and generates a 'cylindrical virtual source' for 3-D *OASES*.

```
Usage: fvpcvs <patch dat> <dct>
```

The output file name is <prefix of 1st argument>_<prefix of 2nd argument>.cvs. The maximum wavenumber sampling and the azimuthal Fourier order are internally determined.

F.5 Spherical Target

F.5.1 sphcvs_es

sphcvs_es computes virtual source terms due to spherical targets. The output is a cvs file and it will serve as input to 3-D *oast*.

```
Usage: sphcvs_es [options] <sck> <SMAX> <NS>

Arguments:
 sck  : output of oast with Option 'E'
 SMAX : reference radius for sampling
 NS   : number of wavenumber samples

Options:
 -rigid : rigid sphere
 -soft  : pressure-release sphere
 -void  : elastic spherical shell with void inside
 -fluid : elastic spherical shell with fluid inside
 -plot  : plots scattering beampatterns in plotmtv format
```

Remark: With the option '-void' or '-fluid', additional parameters are necessary.

For a void spherical shell, the thickness, density, compressional wave speed, and shear wave speed of the shell are required. The dialogue for a void spherical shell is :

```
>> void elastic shell :
 thickness          (m) =
 Rho of shell (kg/m^3) =
 Cp of shell    (m/sec) =
 Cs of shell    (m/sec) =
```

For a fluid-loaded spherical shell, the density and compressional wave speed of the fluid are also required.

```
>> fluid loaded elastic shell case
 thickness          (m) =
 Rho of shell (kg/m^3) =
 Cp of shell    (m/sec) =
 Cs of shell    (m/sec) =
 Rho of fluid (kg/m^3) =
 Cp of fluid    (m/sec) =
```

F.6 Cylindrical Target

F.6.1 wkaxsam

wkaxsam converts values of the incident potential from *oast* (.sck file) to a local incident field. The local incident field is expressed as a function of the shell's axial wavenumber and the suffix of the output file is .inc .

```
Usage: wkaxsam
```

The input dialogue of *wkaxsam* is :

```
sck file name                    :
inc file name                    :
length of shell (m)              :
radius of shell (m)              :
range of shell center (m)        :
skew angle w.r.t shell center (deg) :
dynamic range of output (dB)     :
```

Remark: `inc file` is the output file name. If not specified, it uses the same prefix as .sck file name. Skew angle of shell is defined positive in counter clock wise sense and its valid range is between $-90°$ and $+90°$. Dynamic range of output is the *dB* level where output inc file is truncated. When it is zero, no truncation is done.

F.6.2 cmfinder

cmfinder finds finite cylindrical shell's modal values and produces .mod file.

```
Usage: cmfinder
```

Input dialogue of *cmfinder* is :

```
frequency (Hz)             :
density of shell (kg/m^3)  :
Cp of shell (m/sec)        :
Poison ration of shell (.) :
length of shell (m)        :
radius of shell (m)        :
thickness of shell (m)     :
density of fluid (kg/m^3)  :
Cp of fluid (m/sec)        :
Output file name (.mod)    :
```

Remark: Fluid in the above dialogue refers the external medium surrounding cylindrical shell.

F.6.3 cylcvs

cylcvs combines local incident field (.inc file) and shell's modal values (.mod file) to compute effective target beampatterns in a waveguide. cvs file is generated as an output.

```
Usage: cylcvs [-plot] <mod> <inc> <SMAX> <NS>

Arguments:
 mod  : mode file from cmfinder
 inc  : local incident field file from wkaxsam
 SMAX : reference radius for sampling
 NS   : number of wavenumber samples

Options:
 -plot : plots scattering beampatterns in plotmtv format
```

Remark: Consistency of shell's input parameters will be checked by examining .inc and .mod files.

F.7 3-D Scattered Field

F.7.1 oast3

oast3 is the transmission loss module of 3-D *OASES*. It has been modified to compute a scattered field from an external .cvs file. The field computation is performed in the spatial domain at a fixed frequency. A time domain solution can be achieved using Fourier synthesis. Fourier synthesis is implemented by several batch scripts and utilities. The output files are trf, bdr, cdr, plp, and plt files which can be further processed by *OASES*' plotting module and pulse post-processor.

```
Usage: oast3 <field> <cvs>

Arguments:
 <field> : prefix of input .dat file for 3-D oast .
 <cvs>   : prefix of cvs format file.
```

Structure of input file <field> for *oast3* is :

```
<TITLE>
<OPTIONS>
<FRC> [<COFF>] [<DFRC>]
<NL>
<D  1> <CC  1> <CS  1> <AC  1> <AS  1> <RO  1>  0
<D  2> <CC  2> <CS  2> <AC  2> <AS  2> <RO  2>  0
.
.
<D NL> <CC NL> <CS NL> <AC NL> <AS NL> <RO NL>  0
<ST> <FO>
<SD>
<RD1> <RD2> <NRD>
<CMIN> <CMAX>
<NW> <IC1> <IC2> <IF>
<R1> <DR> <NR>
```

Remark: The seventh column of the layer information is meaningless for *oast3*. In other *OASES*' modules, it represents the *RMS* interface roughness height.

Each variable shown in the above is described in Table F.3. The details regarding input parameters and options can be found in *OASP: 2-D WIDEBAND TRANSFER FUNCTIONS* section of *OASES* manual [44].

F.7.2 avpatch

avpatch is a UNIX shell script to computes the average scattered field due to roughness patches. The roughness patches are generated from the input parameter file. An average is performed in ensemble sense. The outputs are averaged transmission loss, angular spectrum, and wavenumber spectrum in *OASES'* bdr, cdr, plp, and plt format.

```
Usage: avpatch <INC> <PAT> <DAT> <NUM>

Arguments:
 <INC> : incident input file for oast
 <PAT> : patch input file for mp2
 <DAT> : input file for oast3
 <NUM> : number of ensemble

Required programs:
 oast, oast2, mp2, fvdct, fvpcvs, oast3, oast3d,
 trfbdr, cbt. splitbdr, avbdr, avplt
```

Remark 1: The input file for *oast3* should include option 'C' and 'd' for the *avpatch* run because those options produce angular/wavenumber spectra and scattering coefficients.
Remark 2: The second argument <PAT> has the same sequence of input parameters as *mp2* and its file suffix should be .in . In the batch script, this input file is fed to the standard input unit of *mp2* as follows :

```
mp2 -f ${PAT} < ${PAT}.in
```

Remark 3: *avpatch* will check required executable files and input files prior to actual computation. Without proper set up, the script will not run.

F.7.3 tspatch

tspatch is a UNIX shell script to perform wideband simulation of scattering from roughness patches. The output files are a series of single frequency trf files. When option '-c' is selected, the individual trf files are combined by *trfconc* at the end of the batch to produce a wideband trf file.

```
Usage: tspatch [-c] [-l <nl>] [-u <nu>]
         <FC> <T> <NF> <INC> <PAT> <PRO1> [PRO2] ...

Arguments:
 <FC>   : Center frequency (Hz)
 <T>    : Time window (sec)
 <NF>   : Number of frequencies
 <INC>  : Master incident input for oast
 <PAT>  : Roughness patch file
 <PRO1> : First propagation input for oast3
```

TITLE	title of run	
OPTIONS	N *	normal stress
	r *	roughness or target source (i.e. cvs input)
	d	scattering coefficients
	C	contours of integrand and angular spectra
	O	complex frequency integration
	f	full Bessel integration scheme
FRC	source frequency (Hz)	
COFF	integration contour offset (dB/λ)	
DFRC	frequency increment for wideband (Hz)	
NL	number of layers including half spaces	
D	depth of layer (m)	
CC	compressional wave speed (m/s)	
CS	shear wave speed (m/s)	
AC	compressional wave attenuation (dB/λ)	
AS	shear wave attenuation (dB/λ)	
RO	density (g/cm^3)	
ST	source type : ST=100 * for cvs file	
FO	maximum azimuthal Fourier order	
SD	source depth (m) : trivia for cvs input	
RD1	first receiver depth (m)	
RD2	last receiver depth (m)	
NRD	number of receiver depths	
CMIN	minimum phase velocity for wavenumber integration (m/s)	
CMAX	maximum phase velocity for wavenumber integration (m/s)	
NW	number of wavenumber samples	
IC1	first sampling point	
IC2	last sampling point	
IF	frequency sample increment for kernels : trivia for cvs input	
R1	first range sample (km)	
DR	increment of range sample (m)	
NR	number of range samples	

Table F.3: Input file structure for *oast3*. The superscript $*$ indicates necessary options and parameters for the scattered field computation.

```
 [PRO2] : Second propagation input for oast3 (optional)

Options:
 [-c]      : Concatenate trf files
 [-l <nl>] : Lower frequency sampling number
 [-u <nu>] : Upper frequency sampling number

Required programs:
  oast, oast2, fvdct, fvpcvs, oast3, oast3d, trfconc
```

Band width <BW>, pulse duration <DT>, and frequency increment <DF> are related to the above parameters as follows :

```
<BW>=1/<DT>=(<NF>-1)/<T>
<DF>=1/<T>
```

Remark 1: The input file for *oast3* (<PRO1>, [PRO2]...) should replace FRC with <tsfreq> and DFRC with <dfreq>, respectively.
Remark 2: The number of input files for *oast3* can be greater than one. If there are extra arguments after the first input file <PRO1>, those arguments will be used as *oast3*'s input files with the same cvs file.
Remark 3: Batch jobs can be run on multiple platforms by splitting the range of frequency sampling with options '-l' and '-u'.
Remark 4: Required external programs and input files will be checked prior to actual computation.

F.7.4 tssphere

tssphere is a UNIX shell script to compute the wideband transfer function (.trf file) for spherical target scattering. Concatenation of a single frequency trf file is performed in the same fashion as *tspatch*.

```
Usage: tssphere [-c] [-l <nl>] [-u <nu>]
         <[-r] [-s] [-v <vinput>] [-f <finput>]
         <FC> <T> <NF> <INC> <SMAX> <NS> <PRO1> [PRO2] ...

Arguments:
 <FC>   : Center frequency (Hz)
 <T>    : Time window (sec)
 <NF>   : Number of frequencies
 <INC>  : Master incident input for oast
 <SMAX> : Maximum sampling range
 <NS>   : Number of range samples
 <PRO1> : First propagation input for oast3
 [PRO2] : Second propagation input for oast3 (optional)

Options:
 [-c]        : Concatenate trf files
 [-l <nl>]   : Lower frequency sampling number
 [-u <nu>]   : Upper frequency sampling number
```

```
 -r          : Rigid sphere
 -s          : Pressure-release sphere
 -v <vinput> : Void spherical shell
               <vinput> = input parameter file
 -f <finput> : Fluid loaded spherical shell
               <finput> = input parameter file

Required programs:
  oast, oast2, sphcvs_es, oast3, oast3d, trfconc
```

For void or fluid loaded spherical shells, extra input parameter files are required. This input file will be fed into a standard input unit (unit 5) of *sphcvs_es*.
Remark 1: <vinput> has the following file structure.

```
<thickness of spherical shell in m>              ! line 1
<density of shell in kg per cubic meter>         ! line 2
<compressional wave speed of shell in m/s>       ! line 3
<shear wave speed of shell in m/s>               ! line 4
```

Remark 2: <finput> has the following file structure.

```
<thickness of spherical shell in m>              ! line 1
<density of shell in kg per cubic meter>         ! line 2
<compressional wave speed of shell in m/s>       ! line 3
<shear wave speed of shell in m/s>               ! line 4
<density of fluid inside in kg per cubic meter>  ! line 5
<compressional wave speed of fluid inside in m/s> ! line 6
```

Remark 3: The structure of the input file for *oast3* is identical to that of *tspatch*. Frequency sampling parameters are same as those of *tspatch*.
Remark 4: Options '-c','-l', and '-u' have the same definitions as in *tspatch*.

F.7.5 tsshell

tsshell is a UNIX shell script to compute the wideband transfer function (.trf file) for finite cylindrical elastic shell scattering. Structures of input arguments are similar to those of *tssphere*.

```
Usage: tsshell [-c] [-l <nl>] [-u <nu>]
         <FC> <T> <NF> <INC> <GEO> <PAR> <SMAX> <NS> <PRO1> [PRO2] ...

Arguments:
 <FC>   : Center frequency (Hz)
 <T>    : Time window (sec)
 <NF>   : Number of frequencies
 <INC>  : Master incident input for oast
 <GEO>  : Shell geometry input for wkaxsam
 <PAR>  : Shell parameter input for cmfinder
 <SMAX> : Maximum sampling range for cylcvs
 <NS>   : Number of range samples for cylcvs
 <PRO1> : First propagation input for oast3
```

```
 [PRO2] : Second propagation input for oast3 (optional)

Options:
 [-c]      : Concatenate trf files
 [-l <nl>] : Lower frequency sampling number
 [-u <nu>] : Upper frequency sampling number

Required programs:
  oast, oast2, wkaxsam, cmfinder, cylcvs, oast3, oast3d, trfconc
```

Remark 1: <GEO> has suffix .geo and it will be fed to *wkaxsam*. The structure of <GEO>.geo is :

```
<ifield>                                              ! shouldn't be changed.
<ifield>                                              ! shouldn't be changed.
<length of shell in meters>
<radius of shell in meters>
<horizontal distance of shell center from source>
<skew angle of shell in degrees>
<dynamic range of output in dB scale>
```

Remark 2: <PAR> has suffix .par and it will fed to *cmfinder*. The structure of <PAR>.par is :

```
<tsfreq>                                              ! shouldn't be changed.
<density of shell in kg per cubic meter>
<compressional wave speed of shell in m/s>
<Poison ratio of shell>
<length of shell in meter>
<radius of shell in meter>
<thickness of shell in meter>
<density of surrounding fluid in kg per cubic meter>
<compressional wave speed of fluid in m/s>
<mode>                                                ! shouldn't be changed.
```

Remark 3: The structure of the input file for *oast3* is identical to that of *tspatch*. Frequency sampling parameters are the same as those of *tspatch*.
Remark 4: Options '-c','-l', and '-u' have the same definitions as in *tspatch*.

F.8 Post-Processor

F.8.1 tsbf

tsbf is a time series array beam-former. It performs simple array processing based on trace files from range, depth, and azimuth stack trace files from *OASES' pp* (pulse post-processor). It generates stack plots, spectrograms, and beam-formed outputs of the time series. *tsbf* is a menu-driven program and its graphical output is handled by *plotmtv*.

```
Usage: tsbf [trace file]

Arguments:
 [trace file] : one of range, depth, and azimuth stack
                trace files from OASES' pp.
```

The main menu dialogue is :

```
>> TSBF Main Menu <<
 1. Trace file name :
 2. Tmin (sec)       : 0. / index= 0
 3. Tmax (sec)       : 0. / index= 0
 4. Time Series
 5. Spectrogram
 6. Beamforming
 7. Plot :
 8. END

SELECT
```

The time window can be set to reduce the amount of input data or select a specific time frame. Once a trace file is loaded, other options can be selected. Option 6 will shows the list of plot files generated from options 4, 5, and 6. When it is chosen, it will call *plotmtv* to plot all the results.

When option 4 is chosen in the main menu, a time series menu will appear as follows :

```
>> Time Series Menu <<
 1. Tmin            :   0. / index= 0
 2. Tmax            :   0. / index= 0
 3. Absolute Scale  :   -999.00
 4. Plot file (MTV) :
 5. Plot title      :
 6. Generate plot
 7. RETURN

SELECT
```

The scale of the stack plot can be specified using option 3. Otherwise, it uses the peak value of the time series as a scaling factor for plotting. The plot file name and title can be changed using option 4 and 5, respectively. When X11 GUI is available, option 6 calls *plotmtv* to plot stacked time series.

The following is the spectrogram menu.

```
>> Spectrogram Menu <<
 1. Tmin                :   0. / index= 0
 2. Tmax                :   0. / index= 0
 3. Channel number      :            1
 4. FFT size     (NFFT) :         1024
 5. Window size  (NW)   :          128
 6. Overlap size (NOL)  :          127
 7. Plot file (MTV)     :
 8. Plot title          :
 9. Generate plot
10. RETURN

SELECT
```

The spectrogram shows the temporal energy distribution in the time and frequency domains. The time resolution is controlled by changing the temporal window size (NW) while frequency resolution is changed using the FFT size ($NFFT$). NOL is the number of overlapped time bins between two adjacent temporal windows. The definition of the spectrogram is same as for *MATLAB Signal Processing Toolbox's specgram*. The receiver channel can be selected using option 3. The maximum amplitude will be indicated on the contour plot as a cross mark.

The following is the beamforming menu.

```
>> Beamforming Menu <<
 1. Tmin                      :   0. / index= 0
 2. Tmax                      :   0. / index= 0
 3. Minimum Beam Angle (deg)  :   -90.00000
 4. Maximum Beam Angle (deg)  :    90.00000
 5. Number of Beams           :          181
 6. Phase speed        (m/s)  :    1500.000
 7. Plot file (MTV)           :
 8. Plot title                :
 9. Generate plot
10. RETURN

SELECT
```

The angular resolution can be increased by increasing the number of beams. A positive angle points to the first element of the array while a negative angle points to the last. The maximum amplitude will be marked on the contour plot.

This page is blank.

Bibliography

[1] M. Abramowitz and I. A. Stegun. *Handbook of mathematical functions.* Dover Publications, 1970.

[2] G. Arfken. *Mathematical methods for physicists.* Academic Press, third edition, 1985.

[3] F. G. Bass and I. M. Fuks. *Wave scattering from statistically rough surfaces.* Pergamon press, 1979.

[4] M. A. Biot. Theory of propagation of elastic waves in a fluid saturated porous solid. *Journal of Acoustical Society of America*, 28:168–191, 1956.

[5] M. Bouchon. Simple, complete numerical solution to the problem of diffraction of SH waves by an irregular surface. *Journal of Acoustical Society of America*, 77:1–5, 1985.

[6] M. Bouchon and K. Aki. Discrete wavenumber representation of seismic source wavefields. *Bull. seism. Soc. Am.*, 67:259–277, 1977.

[7] L. M. Brekhovskikh and O. A. Godin. *Acoustics of layered media I.* Springer-Verlag, 1989.

[8] S. A. Chin-Bing and E. M. Murphy. A seismo-acoustic finite element model for underwater acoustic propagation. In J. M. Hovem, M. D. Richardson, and R. D. Stoll, editors, *Shear Waves in Sediments.* Kluwer, Doordrecht, NL, 1991.

[9] T. W. Dawson and J. A. Fawcett. A boundary integral equation method for acoustic scattering in a waveguide with nonplanar surfaces. *Journal of Acoustical Society of America*, 87:1110–1125, 1990.

[10] H. Fan. *Wave theory modeling of three-dimensional seismo-acoustic reverberation in ocean waveguides.* PhD thesis, Massachusetts Institute of Technology, September 1995.

[11] J. A. Fawcett. A plane-wave decomposition method for modeling scattering from objects and bathymetry in a waveguide. *Journal of Acoustical Society of America*, 100:183–192, 1996.

[12] J. A. Fawcett. Coupled-mode modeling of acoustic scattering from three-dimensional, axisymmetric objects. *Journal of Acoustical Society of America*, 102:3387–3393, 1997.

[13] J. A. Fawcett. Scattering from an elastic cylinder buried beneath a rough water/sediment interface. In N. G. Pace, E. Pouliquen, O. Bergem, and A. P. Lyons, editors, *High Frequency Acoustics in Shallow Water*, pages 147–154. NATO SACLANT Undersea Research Centre, LaSpezia, Italy, 1997.

[14] C. A. J. Fletcher. *Computational techniques for fluid dynamics.* Springer-Verlag, 1988.

[15] J. R. Fricke. *Acoustic scattering from elastic ice : a finite difference solution.* PhD thesis, Massachusetts Institute of Technology and Woods Hole Oceanographic Institution, June 1991.

[16] G. V. Frisk. *Ocean and seabed acoustics : a theory of wave propagation.* P T R Prentice Hall, 1994.

[17] Y. C. Fung. *Foundations of solid mechanics.* Prentice-Hall, 1965.

[18] P. Gerstoft and H. Schmidt. A boundary element approach to ocean seismoacoustic facet reverberation. *Journal of Acoustical Society of America*, 89:1629–1642, 1991.

[19] J. A. Goff and T. H. Jordan. Stochastic modeling of seafloor morphology : Inversion of sea beam data for second order statistics. *Journal of Geophysical Research*, B11:13589–13608, 1988.

[20] Benthos INC. *Underwater photography : scientific and engineering applications.* Van Nostrand Reinhold Company, 1984.

[21] F. Ingenito. Scattering from an object in a stratified medium. *Journal of Acoustical Society of America*, 82:2051–2059, 1987.

[22] F. B. Jensen, W. A. Kuperman, M. B. Porter, and H. Schmidt. *Computational ocean acoustics.* AIP press, 1994.

[23] H. K. Johansen and K. Sørensen. Fast Hankel transforms. *Geophysical Prospecting*, 27:876–901, 1979.

[24] D. H. Johnson and D. E. Dudgeon. *Array signal processing : concepts and techniques.* P T R Prentice Hall, 1993.

[25] M. C. Junger and D. Feit. *Sound, structures, and their interaction.* The MIT Press, second edition, 1986.

[26] E. Kausel and G. Bouchovalas. Computation of Hankel transforms using the fast-Fourier transform algorithm. Technical report, Massachusetts Institute of Technology, August 1979.

[27] W. A. Kuperman and H. Schmidt. Rough surface elastic wave scattering in a horizontally stratified ocean. *Journal of Acoustical Society of America*, 79:1767–1777, 1986.

[28] W. A. Kuperman and H. Schmidt. Self-consistent perturbation approach to rough surface scattering in stratified elastic media. *Journal of Acoustical Society of America*, 86:1511–1522, 1989.

[29] K. D. LePage. *Elastic scattering in ocean waveguides.* PhD thesis, Massachusetts Institute of Technology, September 1992.

[30] K. D. LePage and H. Schmidt. Modeling of low-frequency transmission loss in the central arctic. *Journal of Acoustical Society of America*, 96:1783–1795, 1994.

[31] D. Li. *Modeling of monostatic bottom backscattering from three-dimensional volume inhomogeneities and comparisons with experimental data.* PhD thesis, Massachusetts Institute of Technology and Woods Hole Oceanographic Institution, September 1997.

[32] J. Y. Liu, H. Schmidt, and W. A. Kuperman. Effect of a rough seabed on the spectral composition of deep ocean infrasonic ambient noise. *Journal of Acoustical Society of America*, 93:753–769, 1993.

[33] N. C. Makris, F. Ingenito, and W. A. Kuperman. Detection of a submerged object insonified by surface noise in an ocean waveguide. *Journal of Acoustical Society of America*, 96:1703–1724, 1994.

[34] M. J. Maron and R. J. Lopez. *Numerical analysis : a practical approach.* Wadsworth publishing company, third edition, 1990.

[35] P. M. Morse and H. Feshbach. *Methods of theoretical physics.* McGraw-Hill, 1953.

[36] J. A. Ogilvy. *Theory of wave scattering from random rough surfaces.* Institute of Physics Publishing, 1991.

[37] A. D. Pierce. *Acoustics : an introduction to its physical principles and applications.* The Acoustical Society of America, 1989.

[38] M. B. Porter. *The KRAKEN normal mode program.* SACLANT Undersea Research Centre, La Spezia, Italy, 1992.

[39] W. H. Press, S. A. Teukolsky, W. T. Vetteriling, and B. P. Flannery. *Numerical Recipes.* Cambridge University Press, second edition, 1992.

[40] D. C. Ricks. A bistatic scattering model for cylindrical shell. Internal memorandum, Alliant Techsystems, September 1996.

[41] M. L. Rumerman. Contribution of membrane wave reradiation to scattering from finite cylindrical shells in water. *Journal of Acoustical Society of America*, 93:55–65, 1993.

[42] H. Schmidt. *SAFARI : seismo-acoustic fast field algorithm for range independent environments. User's guide.* SACLANT ASW Research Centre, La Spezia, Italy, 1987.

[43] H. Schmidt. Numerically stable global matrix approach to radiation and scattering from spherically stratified shells. *Journal of Acoustical Society of America*, 94:2420–2430, 1993.

[44] H. Schmidt. *OASES, Version 2.1, User guide and reference manual.* Massachusetts Institute of Technology, 1997.

[45] H. Schmidt, E. Bovio, and A. Maguer. GOATS '98, Multistatic detection and imaging concepts for proud and buried seabed objects, Test plan. White paper, SACLANT Undersea Research Center and Massachusetts Institute of Technology, March 1997.

[46] H. Schmidt and J. Glattetre. A fast field model for three-dimensional wave propagation in stratified environments based on the global matrix method. *Journal of Acoustical Society of America*, 78:2105–2114, 1985.

[47] H. Schmidt and F. B. Jensen. A full wave solution for propagation in multilayered viscoelastic media with application to Gaussian beam reflection at fluid solid interface. *Journal of Acoustical Society of America*, 77:813–825, 1985.

[48] H. Schmidt and W. A. Kuperman. Spectral representations of rough interface reverberation in stratified ocean waveguides. *Journal of Acoustical Society of America*, 97:2199–2209, 1995.

[49] H. Schmidt and Jaiyong Lee. Physics of 3-d scattering from rippled seabed and buried targets in shallow water. *Journal of Acoustical Society of America*, 1998. Accepted for publication.

[50] H. Schmidt, A. Maguer, E. Bovio, W. L. J. Fox, K. LePage, N. G. Pace, R. Hollett, P. Guerrini, P. A. Sletner, E. Michelozzi, B. Moran, and R. Grieve. GOATS '98, AUV network sonar concepts for shallow water mine countermeasures. SR 302, SACLANT Undersea Research Centre, La Spezia, Italy, 1998.

[51] A. J. Tadeu. *Modeling and seismic imaging of buried structures.* PhD thesis, Massachusetts Institute of Technology, February 1992.

[52] D. Tang. *Acoustic wave scattering from a random ocean bottom.* PhD thesis, Massachusetts Institute of Technology and Woods Hole Oceanographic Institution, June 1991.

[53] S. P. Timoshenko and J. N. Goodier. *Theory of elasticity.* McGraw-Hill, third edition, 1982.

[54] B. H. Tracey. *An integrated modal approach to surface and volume scattering in ocean acoustic waveguides.* PhD thesis, Massachusetts Institute of Technology and Woods Hole Oceanographic Institution, January 1996.

[55] B. H. Tracey and H. Schmidt. Seismo-acoustic field statistics in shallow water. *IEEE Journal of Ocean Engineering*, 100(2):317–331, April 1997.

[56] J. F. Traub. *Iterative methods for the solution of equations.* Prentice-Hall, 1964.

[57] R. J. Urick. *Principles of underwater sound.* McGraw-Hill, third edition, 1983.

[58] A. G. Voronovich. *Wave scattering from rough surfaces.* Springer-Verlag, 1994.

[59] G. N. Watson. *A treatise on the theory of Bessel functions.* Cambridge University Press, second edition, 1966.